A Mechanism-based Approach to Constitutive Modelling of Quasi-Brittle Geomaterials with and without Fibre Reinforcement

A Thesis Submitted for the Degree of Doctor of Philosophy

School of Civil, Environmental and Mining Engineering, the University of Adelaide

by

Linh Anh Le

April 2019

Abstract

A Mechanism-based Approach to Constitutive Modelling of Quasi-Brittle Geomaterials with and without Fibre Reinforcement

A Thesis Submitted for the Degree of Doctor of Philosophy

Linh Anh Le

School of Civil, Environmental and Mining Engineering

The University of Adelaide, April 2019

The formation and development of localisation bands and/or cracks have been experimentally identified as the key failure mechanism governing responses of quasi-brittle geomaterials like concrete, sandstones and soft rocks. In fact, key features of the material behaviour, including Lode-angle dependence, size effect and brittle-ductile transition can be considered as consequences stemming from the localised failure mechanism in several loading conditions. For geomaterials with fibre reinforcement (i.e., fibre reinforced concrete), even though adding short fibres into the material significantly changes its mechanical characteristics and performances, the development of cracks and localisation bands remains the central mechanism driving the material responses. In this case, the bridging effect caused by fibres across cracks, together with the material cohesive-frictional resistance, refrains cracks from further developing and forces the material to form more cracks throughout the structure to dissipate the given energy. This prolongs the coalescence of diffuse micro/meso-cracks to form a macro-crack and considerably improve the material strength and ductility.

Classical continuum models, in principle, can capture the overall responses of the material with stress-strain relationships formulated from experimental observations at the macroscopic level. However, the material behaviour in these models is homogenous throughout the whole element domain, leading to an incorrect dependence of dissipated energy and specimen responses on the discretisation resolution. This is because they fail to capture the difference of deformation and behaviour between the localisation zone and its surrounding bulk material. As a result, with the presence of crack/localisation band, the definition of averaged quantities such as overall stress and strain is not adequate to describe the volume element and using them for analysing post-localisation behaviour of quasi-brittle

geomaterials is inappropriate, if not totally incorrect. Consequently, classical approaches that ignore the strong heterogeneity induced by the localisation of deformation suffer from mesh convergence issues in Boundary Value Problems (BVPs) analysis.

In this research, the localised failure mechanism is employed as the basis to develop a continuum-based constitutive model for quasi-brittle geomaterials with and without fibre reinforcement. The cracks/localisation bands are explicitly included as an intrinsic part of the model with its own behaviour in conjunction with the responses of the surrounding bulk material. This allows an additional constitutive relationship, together with its internal variables, to be defined inside the localisation band to describe its microstructural changes under the course of loading. The material inelastic behaviour and important features such as brittle-ductile transition, Lode-angle dependence, size effect and hydrostatic pressure dependence can thus be correctly captured in association with observable failure patterns at constitutive level. The model, constructed in this manner, is also capable of featuring multiple localisation bands/cracks inside the constitutive equations to account for any change of loading path and avoid unphysical stress-locking naturally. In addition, for modelling quasi-brittle geomaterials with fibre reinforcement, the incorporation of cracks within the constitutive model enables the inclusion of separate models describing the fibre bridging effect and material cohesive-frictional resistance. As a result, the interactions between these two components and their contributions to the stress transfer across a crack are naturally captured for different types of fibres and their volume contents. The transition from hardening to softening, corresponding to the change from diffuse cracking phase to localised failure can also be reflected as a consequence. Furthermore, owing to the explicit inclusion of cracks in the model, the resulting constitutive behaviour automatically scales with the discretisation resolution and the results are thus mesh-independent when solving BVPs, without requiring any additional regularisation.

Model validations against experimental data show that the proposed model is simple yet effective in capturing the localised failure of quasi-brittle geomaterials with and without fibre reinforcement at both constitutive and structural levels. The model is proven to be reliable and computationally inexpensive, with a few model parameters which can be identified and calibrated in a consistent and physically meaningful manner. The proposed model can thus be applied straightforwardly for the analysis and design of solids/structures made of rocks or concrete, with or without fibre reinforcements.

Declaration

I, Linh A. Le, certify that this work contains no material which has been accepted for the award of any other degree or diploma in my name, in any university or other tertiary institution and, to the best of my knowledge and belief, contains no material previously published or written by another person, except where due reference has been made in the text. In addition, I certify that no part of this work will, in the future, be used in a submission in my name, for any other degree or diploma in any university or other tertiary institution without the prior approval of the University of Adelaide and where applicable, any partner institution responsible for the joint-award of this degree.

I acknowledge that copyright of published works contained within this thesis resides with the copyright holder(s) of those works.

I also give permission for the digital version of my thesis to be made available on the web, via the University's digital research repository, the Library Search and also through web search engines, unless permission has been granted by the University to restrict access for a period of time.

April 9th 2019

Linh A. Le

Acknowledgements

First and foremost I want to thank my principal advisor Associate Professor Giang D. Nguyen, for his wholehearted support and encouragement from the very beginning of applying to the University of Adelaide to the last technical details and writing of my thesis. His guidance, in both academic and personal life, helped me overcome all the ups and downs in my long journey over the past four years. I also want to express my sincere gratitude to Dr. Ha H. Bui (Monash University) for his significant contributions in terms of ideas and technical review towards my research; to my co-advisors Associate Professor Abdul Hamid Sheikh and Professor Andrei Kotousov for their invaluable assistance and support.

The financial support from the Beacon of Enlightenment Premiers award is gratefully acknowledged. I would also like to thank the University of Adelaide for providing me with all the necessary facilities and final support during my PhD.

I am also grateful to Ms Leticia Mooney for her proofreading of the first draft of my second paper and Ms Alison-Jane Hunter for her proofreading of several chapters in my thesis.

My special thanks go to the Civil Engineering Postgraduate Liaison Committee members for making my life here colourful and interesting. I am really grateful for the numerous skills and lessons I have learned during my time serving in the committee. I also want to extend my appreciation to all my old friends in Vietnam who have always been there for me and new friends in Adelaide for their help and companionship which made my time here joyful and unforgettable.

I also greatly appreciate Professor Trung Nguyen-Thoi (Ton Duc Thang University), Associate Professor Hung Nguyen-Xuan (HUTECH University) and friends to whom I had the privilege to work with from my very first steps in research, for introducing me to solid mechanics.

Finally, my heartfelt thanks go to my wife, Khue M. Tran, for her love and understanding throughout the years of my PhD. It was her endless patience and attentive care that have given me the strength to endure years of working long hours. We both are very thankful to our parents for their love and encouragement during the course of my PhD.

List of publications

Le, L.A., Nguyen, G.D., Bui, H.H., Sheikh, A.H., Kotousov, A., Khanna, A., 2017. Modelling jointed rock mass as a continuum with an embedded cohesive-frictional model. *Engineering Geology* 228, 107–120. doi:10.1016/j.enggeo.2017.07.011

Le, L.A., Nguyen, G.D., Bui, H.H., Sheikh, A.H., Kotousove, A., 2018. Localised failure mechanism as the basis for constitutive modelling of geomaterials. *International Journal of Engineering Science* 133, 284–310.

Le, L.A., Nguyen, G.D., Bui, H.H., Sheikh, A.H., Kotousov, A., 2019. Incorporation of micro-cracking and fibre bridging phenomena in constitutive modelling of fibre reinforced concrete. *In preparation*

Le, L.A., Nguyen, G.D., Bui, H.H., Sheikh, A.H., Kotousov, A., 2018. Capturing localised failure of geomaterials at the constitutive level by embedding a cohesive crack in a continuum modelling approach. *The 3rd Australasian Conference on Computational Mechanics, ACCM 2018,* Geelong February 12-14

Le, L.A., Nguyen, G.D., Bui, H.H., Sheikh, A.H., Kotousov, A., 2018. Localisation and lode-angle dependence of geomaterial behaviour. *The 25th Australasian Conference on Mechanics of Structures and Materials, ACMSM25*, Brisbane, Australia, December 4 – 7

Table of Contents

List of figures

List of tables

CHAPTER 1

Introduction

1.1 Background

Quasi-brittle geomaterials such as concrete and rocks have been widely used in the construction of infrastructure from ancient pyramids in Egypt at the dawn of human civilization, to modern skyscrapers. Some other geomaterials, such as rocks and granites, are commonly used in the designing and planning of projects in mining and hydrocarbon extractions. Therefore, it is expected that the material would experience a wide range of stress conditions. For concrete and its structural applications, the dominant loading conditions are tension and shear under very low confinements. The associated response of the material in these cases is usually brittle and softening. Rocks or sandstones, on the other hand, are often under compression and shear under a wide range of confinements. The corresponding responses thus vary from brittle under lower confinements to ductile under high confinements.

In order to improve the toughness and durability of quasi-brittle geomaterials, short fibres can be added into the matrix to form a new generation of material (i.e., fibre reinforced geomaterials) with outstanding strength and energy absorption capability. Such materials have been increasingly utilised over the past several decades for infrastructure design and analysis. Reinforcing fibres can be steel, glass, synthetic or natural fibres, each of which contributes varying properties and characteristics to the resultant material. In addition to the material made of the fibres, their geometries, orientations and densities are also important factors governing the mechanical responses of the reinforced geomaterials. From a modelling point of view, despite changes in their mechanical performance, fibre reinforced geomaterials inherit many characteristics and properties from the original geomaterials.

Owing to its importance and popularity, constitutive modelling of quasi-brittle geomaterials with and without fibre reinforcement has been a focus of research among the civil engineering community over the past several decades. A reliable model with proper representations of material behaviour and intrinsic mechanisms would help facilitate a safe and economical solution for analysing and designing structures made from such materials. Nonetheless, the behaviour and underlying mechanism of quasi-brittle geomaterials are not

always faithfully reflected in constitutive models due to the complex deformation and inelasticity taking place within the material body. For quasi-brittle geomaterials with and without fibre reinforcement, the material failure always involves the formation and development of localisation bands and/or cracks whose deformation and behaviour are totally different from the surrounding bulk material. Besides the composite nature of geomaterials, the presence of these localisations introduces a new level of heterogeneity which has been proven to be the source of the inelasticity and complex behaviour of the material. In this sense, the challenging task for constitutive modelling and numerical simulation of such materials is not only to predict the overall macro responses but to capture the underlying mechanism of localised failure that leads to those responses in the first place appropriately. Only then does the model facilitate a proper analysis and reliable numerical simulation for large-scale structures, commonly encountered in mining and civil engineering fields.

1.2 Aims and Scope

The main objective of this study is to develop a continuum-based constitutive model for quasi-brittle geomaterials with and without fibre reinforcements. The study focuses on the identification of the failure mechanism and its correlation with mechanical behaviour, followed by incorporating the mechanism into a generic formulation for constitutive modelling of the material. This is the key feature that has been largely overlooked in previous studies in the current literature. To accomplish these aims, the formation and development of localisation zone are pinpointed as the underlying failure mechanism, governing several key features of the material behaviour in various loading conditions, including tension, shear, compression under low confinements and mixed-mode loadings. This localised failure mechanism is then employed as the fundamental basis for the constitutive model development within the rigorous and consistent framework of thermodynamics.

Important features of the material, including Lode-angle dependence, size effect and brittle-ductile transition can be captured as consequences of including the localised failure mechanism into the constitutive formulation. For modelling quasi-brittle geomaterials with fibre reinforcements, the interactions between the fibre bridging effect and cohesive resistance within a crack and their influence on the overall load-bearing capacity can also be captured properly. Since the localised failure is placed as the basis for the model development, the scope for application of the proposed model is set for loading conditions where localised failure is the main mechanism governing material responses (i.e., tension,

shear, compression under low confinement and their mixed-mode loading conditions). While this scope is broad enough for structural applications of concrete and soft rocks, the proposed constitutive model can straightforwardly be extended to cover a wider range of loading conditions. This will be covered at the end of this study as a potential future development.

Localised failure in quasi-brittle geomaterials leads to the dependence of constitutive behaviour on the size of volume on which it is defined. Specifically, besides material mechanical properties, the inelasticity and overall behaviour exhibited by the material also depends on the width and behaviour of the localisation band, both of which are predominantly governed by the microstructures and attributes of the material. This is the well-known deterministic size effect reported in several studies (Bažant, 1999, 1984; Karihaloo et al., 2003; Tang et al., 1992; van Mier, 1986). Furthermore, the mesh-dependence in solving BVPs where the dissipated energy and material response unphysically depend on the discretisation resolution, is a more severe issue related to the scale-effect in numerical simulation. Various regularisation techniques (i.e., fracture energy regularisation adopted from the smeared crack approach, viscous enhancements or nonlocal and gradient approaches) have been proposed to alleviate the mesh-dependence issue in continuum models. All these existing approaches of regularisation, despite having their own advantages, are external treatments, used on top of an existing model or separately from the constitutive formulations to remedy the mesh-dependence issue. This, in my opinion, is one of direct consequences of lacking the localised failure mechanism in the constitutive modelling in the first place. To this end, in the proposed model, localisation band is incorporated explicitly into the constitutive structure, with its own responses and relative size, separately from the surrounding bulk material. The inelasticity and dissipation of the band are thus reflected correctly, regardless of the mesh resolution. As a result, no external regularisation technique is needed in the proposed model for simulating softening-related problems, as shown throughout the study, while the deterministic size effect can be captured naturally.

Reflecting the nature and characteristics of the localisation band also falls into the scope of this study. Experimental results on the failure state of quasi-brittle geomaterials at both micro/meso-scale (Alam et al., 2014; Brooks, 2013; Ma and Haimson, 2016; Skarzyński and Tejchman, 2016) show that the localisation band is not a single entity as it appears to be but actually is a system of meso- and/or micro-cracks. This zone, termed fracture process zone (FPZ), usually comprises of both primary and secondary cracks, resulting from the development of pre-existing micro-cracks, together with the initiation and

progressive propagation of new cracks over the course of loading. In the modelling of quasi-brittle geomaterials, the existence of secondary cracks at lower scales is usually ignored and the FPZ is idealised as a single zero-thickness crack. Despite its practical usefulness, this simplification leads to unphysical stress-locking issues, where the FPZ does not propagate properly (see Haghighat and Pietruszczak, 2015; Zhang et al., 2015). Several treatments have been proposed and employed in numerical simulations to avoid this unphysical stress-locking issue. These include crack tracking/tracing (Haghighat and Pietruszczak, 2015; Lloberas-Valls et al., 2016; Parvaneh and Foster, 2016; Zhang et al., 2015) and rotating crack approach (He et al., 2006; Jirásek, 2000; Sancho et al., 2007). In spite of reproducing a reasonable crack path and structural responses, these treatments, being additive components to the constitutive formulation, unnecessarily complicate the model. Furthermore, as these treatments simply modify the crack orientation to obtain desired propagations, they may not resolve the problem of stress-locking in non-proportional loading conditions with changes of loading paths if a new (secondary) crack/band is not allowed in the models. In this study, the issue of stress-locking will be dealt with by allowing a secondary crack to initiate, alongside the primary one, at constitutive level, if appropriate conditions are met. This is possible in the proposed model due to its straightforwardness in featuring the localisation band inside the constitutive formulation. Allowing secondary cracking at the constitutive level, to the best of my knowledge, is a natural way to remove the stress-locking issue, leading to proper FPZ propagation and correctly reflecting the nature and characteristic of the FPZ observed in experiments.

From a numerical perspective, an appropriate iterative algorithm should be used to facilitate the implementation of the newly developed constitutive model for numerical simulation. As the localisation band is explicitly incorporated into the continuum-based constitutive model, extra internal variables and quantities are defined inside the band, beside the conventional volume-averaged stress and strain. More importantly, the presence of a secondary crack inside the constitutive model structure necessitates the development of a new iterative algorithm for numerical modelling. As there are more than one cracks featured in the model, different scenarios can happen for a given incremental step depending on the actual loading path and the current state of the material point (or integration point in Finite Element Analysis). Therefore, a new algorithm is needed to identify the appropriate state of each crack (i.e., inelastic opening, elastic closing) so that proper contributions from these cracks towards the material behaviour can be reflected and internal variables in the model

are correctly updated, accordingly. An implicit iterative algorithm is thus developed in the research to ensure the consistency and internal equilibrium conditions of all these quantities. As the aim of this research is to develop a constitutive approach within consistent and rigorous frameworks, the well-known Newton-Raphson method is employed as the nonlinear system solver for numerical simulations with finite element analysis.

The primary focus of the study is static and quasi-static material behaviour under monotonic loading conditions. Even though the model is proposed in a generic form and is capable of handling dynamic/damping-related problems or cyclic loading conditions where strength/stiffness reduction occurs, these aspects are beyond the scope of this study. In addition, as the nonlinearity taking place in the localisation band are normally under very small strain, continuum mechanics with the small strain assumption is used throughout the study.

1.3 Outline of the Thesis

This thesis is organised into seven chapters, including the current chapter, which serves as an introduction for the aims and scope of the study. The contents of the successive chapters are as follows.

Chapter 2 addresses the mechanical behaviour of the quasi-brittle geomaterials under different loading conditions and, more importantly, the underlying failure mechanism leading to those responses in the first place. Experimental results analyses show that important features of the material, such as sharp softening responses in tensile loading, brittle-to-ductile behaviour transition in compression, Lode-angle dependence and size effect, are all associated with the localised failure mechanism. In fact, these features can be considered as consequences stemming from this mechanism and thus they should not be a starting point for developing a constitutive model. In other words, localised failure leads to the observed features of the material behaviour and hence this failure mechanism should be the key for a model to possess the above-mentioned features. For geomaterials with fibre reinforcement (e.g., in fibre reinforced concrete), the transition from the diffuse cracking phase to the localisation phase is also considered to be a result of the initiation and development of cracks, where interactions between the fibre bridging effect and cohesive resistance takes place. Localisation band associated with the evolving crack density, can be considered as the underlying mechanism of the macro observed behaviour. The analyses and

conclusions in this chapter serve as a background for a comparison of existing models in the literature in the next chapter.

In chapter 3, we address recent developments in constitutive modelling of quasi-brittle geomaterials with and without fibre reinforcement. Major themes on modelling the material, along with the strengths, weaknesses and limitations of existing models and frameworks are compared, based on their capacity to reflect the underlying mechanisms associated with important characteristics of the mechanical behaviour. The review shows the inadequacy of using classical continuum models and common drawbacks of recently developed micromechanics approaches in modelling the material. This underlies the motivation to develop a mechanism-based approach for constitutive modelling of geomaterials in this study.

Chapter 4 of the thesis is concerned with describing the inelasticity and deformation inside the localisation band by a proposed cohesive-frictional model. Inspired from experimental observations, the model is constructed based on coupling damage-plasticity theories with a unified yield function to reflect the close relationship between fracture and irreversible deformation happening inside the band. The model is then incorporated into the double-scale approach (Nguyen et al., 2012b; Nguyen et al., 2014) for its validation against experiments of rock joint under mixed-mode conditions. Fair agreement between the results from the model and their experimental counterparts show that the model is capable of capturing key responses of the localisation band, such as residual deformations, stiffness reduction, evolution of dilation due to asperity damage, and unilateral behaviour upon unloading-reloading. This indicates the robustness of using the proposed cohesive-frictional model for capturing the behaviour of the localisation band in modelling quasi-brittle geomaterials.

Chapter 5 is dedicated to detailing the proposed constitutive model for quasi-brittle geomaterials based on the localised failure mechanism. The chapter starts with the necessity of removing unphysical stress locking, witnessed in several existing approaches, in order to capture the propagation of the macro-crack within the material body correctly. This is the motivation to improve the existing double-scale models by adding a secondary crack into the constitutive formulations. The chapter goes on to describe the resultant model with two embedded cracks, whose behaviour is represented by the cohesive-frictional model addressed in Chapter 4. The main features of the model and its parameter calibration are also detailed and illustrated numerically by various standard tests of both concrete, sandstone and

soft rock. The proposed model is then implemented into the commercial package ABAQUS as a user-defined material model (UMAT) for analysing BVPs with Finite Element Analysis. In addition to illustrating the effectiveness and robustness of the proposed model in capturing mechanical responses and failure patterns of the material, the results from analyses in this chapter also demonstrate the mesh-independence and locking-free features of the model.

In Chapter 6, the proposed model is extended to modelling of fibre reinforced concrete with the localised failure remaining the key mechanism of the material behaviour. To serve this purpose, the bridging effect from fibres is described as an integration of individual fibres across a crack with appropriate distribution density functions. The contribution from each fibre is represented by a single fibre pull-out force with respect to the pull-out displacement relationship. The formulations of this relationship for both polymer and hooked end steel fibres, the two most popularly used fibres in commercial products, are also detailed in this chapter. The implementation of the fibre bridging effect and cohesive-frictional resistance, described in Chapter 4, into the double-scale approach is then presented together with a proposed phenomenological relationship to reflect the connection between crack density, volume fracture and deformation. Towards the end of the chapter, numerical simulations of structures made of fibre reinforced concrete are carried out to illustrate the capacity of the model to capture material behaviour, from the diffuse crack phase to the localised deformation phase.

Chapter 7 concludes the study and provides discussions and proposes possible research directions for future studies.

CHAPTER 2

Quasi-brittle geomaterials: mechanical behaviour and failure mechanism

2.1 Introduction

In this chapter, the complex responses of quasi-brittle geomaterials, with and without fibre reinforcement, under different loading conditions are addressed, together with their important features and underlying causes. Because field study of the materials can only be carried out on existing fractured areas and thus the formation and development of these fractures cannot be monitored, the majority of material behaviour analyses in this study are based on experimental studies available in the literature. The focus in this chapter lies not only on the macroscopic behaviour typically represented by stress-strain curves, but also on the development of failure patterns and associated micro/meso-scopic changes within the materials to identify and understand the mechanisms behind those macro observable responses.

For quasi-brittle geomaterials without fibre reinforcement, experimental data from standard tests (i.e., tension, bending and compression tests under different confinements) and recent microscopic studies will be analysed to clarify the relationship between the localised failure and material responses. From that, the brittle-ductile transition of material behaviour, observed in triaxial tests under various confining pressure levels, is analysed in association with the change in failure patterns to demonstrate the key role of localised failure in governing these responses. The dependence of yield loci on the Lode-angle in true triaxial tests and the size effect in both tension and compression are also addressed and linked with the localisation of deformation and behaviour of the specimens.

In a similar manner, the overall behaviour of fibre reinforced concrete (FRC), the most commonly used geomaterials with fibre reinforcement, is addressed with its progressive failure from experimental data of tension, bending, shear and compression tests. The difference in behaviour between plain concrete and fibre reinforced concrete is identified to show the role that additive fibres play in enhancing material mechanical performances. In essence, the combination of the fibre bridging effect and cohesive-frictional resistance in

stress transferring within cracks and later within a localisation band is idenfied as the decisive factor that controls all of the improvements and failure characteristics of the material. This brings us back to localised failure being the key mechanism for the material responses and thus it should be the foremost factor to be considered before any other features when developing a model for such materials.

The analyses and conclusions in this chapter serve as a background for a comparison of existing models in the literature in the next chapter. The experimental support and findings from this chapter are also the inspiration for further formulations and development of the proposed constitutive model in this research. Therefore, some aspects and analyses from this chapter will be referred to in the successive chapters for justification of some of assumptions made during the model's development.

2.2 Mechanical responses and failure mechanism of quasi-brittle geomaterials

In this section, mechanical responses of quasi-brittle geomaterials, such as yield-failure surface, macro-behaviour in tension and compression under different confinements are examined together with specimen failure patterns, in order to understand the mechanism behind these responses. In addition, the Lode-angle dependence and phenomena related to the size-effect are addressed at length to identify the correlation between these features and the failure mechanism.

2.2.1 Macro behaviour and failure mechanism

2.2.1.1 Macro behaviour

Yield surface

The initial yield surface (i.e., elastic-limit surface), illustrated in Figure 2.1, is an important feature, defining the elastic regime of the material. It can be seen that in both triaxial and biaxial planes, the yield surface of quasi-brittle geomaterials is clearly dependent on hydrostatic pressure and gradually expands towards compression (see Figure 2.1a and b for both concrete and sandstone). In addition, the surface is also clearly curved in these planes. The yield loci in a deviatoric plane, presented in Figure 2.1c, show the effect of the intermediate principal stress (and thus the Lode angle) on the failure surface. As seen from experimental results presented in the Figure, the yield surface of the material generally has a triangular shape with smoothly rounded corners in one-sixth of the deviatoric plane.

Similar characteristics of the yield surface can also be observed in several other experimental studies conducted on different quasi-brittle geomaterials (Byerlee, 1967; Ely, 1968; Ingraham et al., 2013; Kupfer et al., 1969; Lade, 1977; Ma and Haimson, 2016; Macari and Hoyos, 2001; Vachaparampil and Ghassemi, 2017).

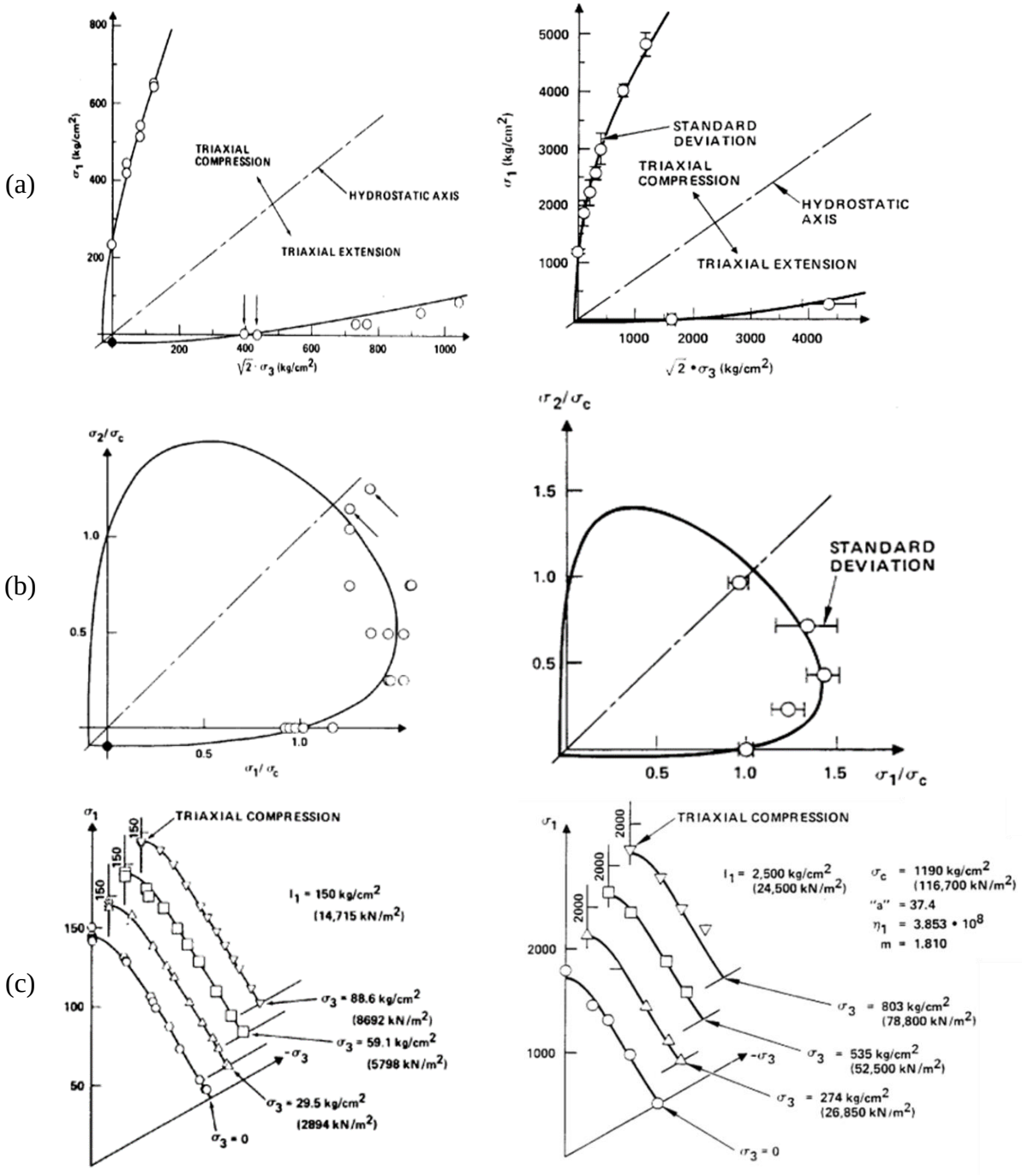

Figure 2.1. Typical experimental data on initial yield surface of concrete (Mills and Zimmerman, 1970) and sandstone (Akai and Mori, 1970) in different stress spaces: (a) Triaxial plane, (b) Biaxial plane and (c) Deviatoric plane. The results were interpreted and presented by Lade (1997).

From a modelling point of view, it is important to distinguish the concept of yield surface (i.e., the elastic-limit surface) from the ultimate failure surface, which characterises the residual strength envelope of the material. This final failure surface is generally identified when material strength is totally lost or residual strength exists, indicated by the shear strength remaining unchanged and/or no volume change in some cases. The ultimate failure surface is meaningful and critical for material modelling in the sense that it reveals the so-called final state of the material. By reflecting the evolution from the initial yield to the ultimate failure envelope, the overall behaviour of the material can be controlled consistently by the model. Figure 2.2a shows a typical evolution of the yield envelop of several types of sandstone, where black dots represent the initial yield points, white dots depict the ultimate failure states and solid lines are the paths of evolution. It can be seen that the loci of failure states are typically straight lines, which are illustrated by dotted lines in the Figure. A stress state in $p-q$ space (i.e., mean stress versus differential stress space) would move up or down towards the ultimate failure surface, depending on its position on the initial yield surface. The concepts of an initial yield surface and ultimate failure surface have been widely adopted in many numerical modelling studies, one of which is illustrated in Figure 2.2b.

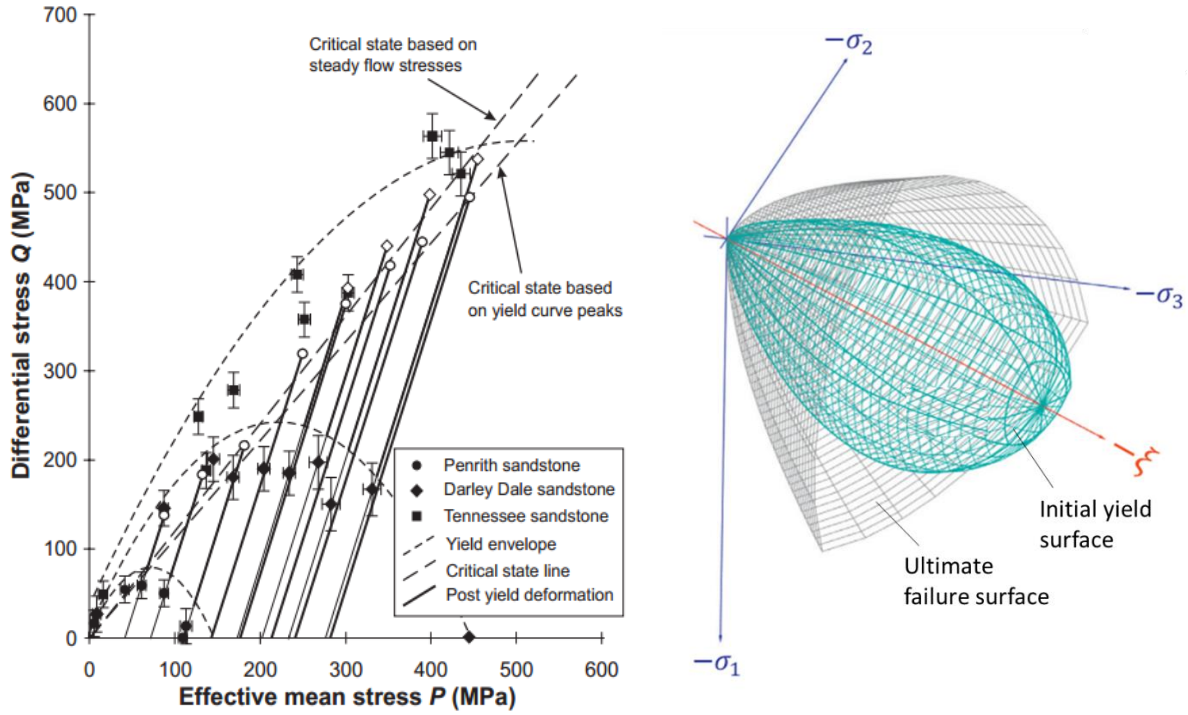

(a) (b)

Figure 2.2. Yield-failure surface evolution: (a) Experimental results from initial yield (black points) to final failure state (white points) of different sandstones (Cuss et al., 2003) and (b) An example of numerical representation for yield and failure surface evolution (Paliwal et al., 2017)

Macro behaviour in tension

The stress - deformation response of plain concrete in a direct tension test, plotted in Figure 2.3a, can be considered as typical behaviour of quasi-brittle geomaterials in tensile loading conditions. It can be seen that the material exhibits brittle behaviour, with a sharp softening where stress suddenly drops after reaching its peak. This sharp brittle behaviour can also be observed in the force – crack opening curve of 3-point bending tests conducted on plain concrete, as shown in Figure 2.3b. In normal conditions, the tensile strength of the material is very low compared to the compressive strength. Under uniaxial cyclic tensile loading, the material clearly shows that the stiffness reduction and hysteresis take place in each cycle of unloading and reloading, as shown in Figure 2.3a. This typical response of quasi-brittle geomaterials can also be observed in various experimental results of tension or bending tests throughout the literature (Di Prisco et al., 2000; Gálvez et al., 2003; Gopalaratnam and Shah, 1985; Reinhardt et al., 1986; van Mier and Schlangen, 1993).

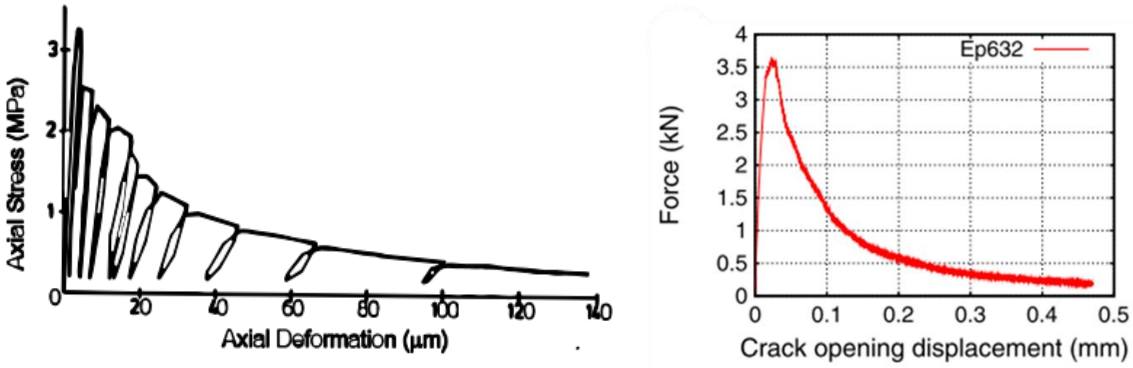

(a) (b)

Figure 2.3. Illustration of material behaviour in tension: (a) stress-deformation curve of concrete under uniaxial cyclic tensile loading (Reinhardt et al., 1986) and (b) Force - crack mouth opening in a three-point bending test (Grégoire et al., 2013)

Macro behaviour in compression

The material behaviour in compression, on the other hand, shows a wider range of responses from brittle softening to ductile hardening, depending on several factors such as confining pressure, temperature, loading rate and material microstructures. However, because the temperature and loading rate are beyond the scope of this study, the confining pressure associated with microstructural changes is the main focus to address the underlying failure mechanism of the material in this chapter. Typical experimental results of triaxial compression tests for concrete and sandstone under different confinements (with the notion that compressive stress is considered to be positive), plotted in Figure 2.4, show that with

the increase of confining pressure, the material responses become more ductile. Specifically, the Figure shows a softening in the axial stress at low confinement (i.e., $\sigma_{\text{confine}} < 6$ MPa), more ductile softening at higher confinement (i.e., $\sigma_{\text{confine}} = 12\sim40$ MPa) and hardening at very high confinement (i.e., $\sigma_{\text{confine}} > 40$ MPa) for both concrete and sandstone examined here. Figure 2.4 also shows that in compression, the volumetric/porosity changes are different, depending on the characteristics of the materials. In general, it can be seen that under low confinements, the material exhibits compaction at first and expansion later on (see Figure 2.4a for volumetric strain and Figure 2.4b for confinement 5 MPa) while under higher confinements, the dominant behaviour is compaction (see Figure 2.4b for confinement larger than 40 MPa). At different magnitude scales, similar responses can be observed in several other experiments of triaxial tests on cylindrical specimens (Candappa et al., 2001; Imran and Pantazopoulou, 1997; Xie et al., 1995) or recent true triaxial tests (Haimson and Rudnicki, 2010; Ingraham et al., 2013; Vachaparampil and Ghassemi, 2017).

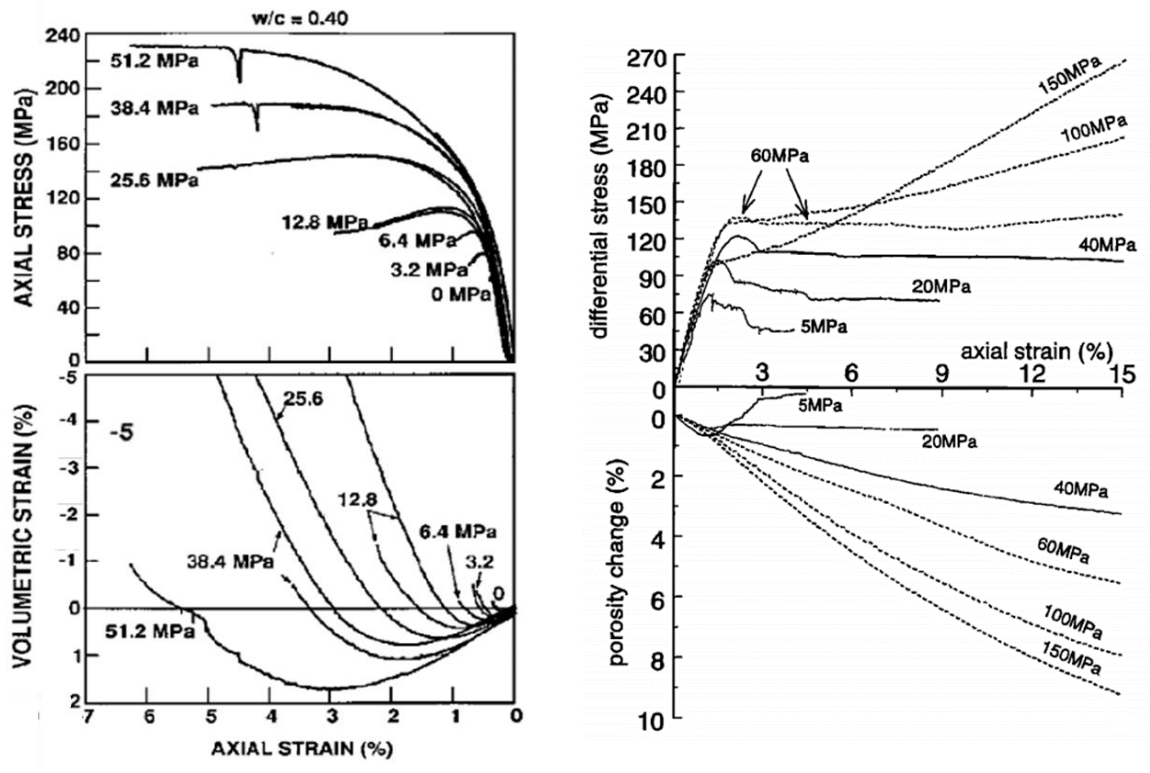

(a) (b)

Figure 2.4. Typical stress-strain responses of quasi-brittle geomaterials in a triaxial test of cylindrical specimens: (a) Test results on concrete (Imran and Pantazopoulou, 1997) and (b) on Adamswiller sandstone (Wong et al., 1997)

2.2.1.2 Failure patterns and underlying mechanisms

From a physical perspective, the low tensile strength of the material is a direct consequence of the low tensile strength in the bonding between the material constituents (e.g., aggregates-mortar bonding in concrete or bonding between mineral quartz/grains in rock or sandstone). These bonding interfaces are the weakest links of the composite materials, where cracks initiate and develop perpendicular to the tensile loading. The appearance of cracks reduces the load-carrying area, which in turn increases the stress concentration at critical crack tips, leading to crack coalescence to form a macro-crack, as shown in Figure 2.5. As investigated in several studies (Bažant and Chen, 1997; Bažant and Oh, 1983; Bažant, 2000), this major crack is, in fact, a Fracture Process Zone, which can also be called localisation band/zone. The rapid development of fracture results in a sudden drop in the loading capacity, hence the brittle nature of the material. During this process, energy is dissipated within the localisation band via the fracture of mortar and cohesion-friction between aggregates/fragments being pulled out of the mortar. The total amount of dissipated energy can be calculated by the area under the stress-deformation curve in tension test, as illustrated in Figure 2.5. Therefore, from the modelling point of view, the brittle nature of quasi-brittle geomaterials in tensile loading conditions is, in fact, a result of the formation of a localisation zone in which the dissipation, represented by tensile strength f_t and mode I fracture energy G_I, take place. The low tensile strength of quasi-brittle geomaterials is also clearly reflected on the yield locus, where the tensile part is very small compared to the compressive part, as shown in Figure 2.1a and b.

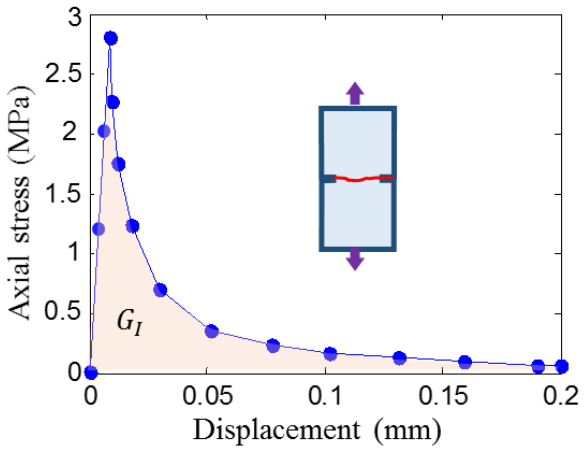

Figure 2.5. Typical quasi-brittle geomaterials behaviour and failure patterns under tensile loading conditions (Shi et al., 2000)

The underlying failure mechanism of quasi-brittle geomaterials under compressive loading conditions can be examined when the macro responses of specimens in triaxial compression tests are analysed together with their failure patterns. Typical behaviour and failure patterns of both conventional triaxial tests (conducted on cylindrical specimens) and true triaxial tests (conducted on cubic specimens), plotted in Figure 2.6, show that, together with the brittle-ductile transition as described in the previous section, the localisation band (i.e., the failure plane) becomes less inclined and disappears (in the figure, NA indicates no clear band observed) at very high confining pressure levels (i.e., σ_{confine}~90 MPa in Figure 2.6a and $\sigma_{\text{confine}} = 120\sim150$ MPa in Figure 2.6b). This phenomena can be understood with the help of experimental observations at microscopic level in recent studies (Alam et al., 2014; Lee and Haimson, 2011; Ma and Haimson, 2016; Seo et al., 2002). Micrographs of Bentheim sandstone specimens under various confinement levels in Figure 2.7 show that in compression, the micro-cracks, initiating from the weakest links, can be in any direction and can be either at grain boundaries or in the cementing matrix. As the micro-crack density increases with the increase of strain, these cracks concentrate in a localised zone where most of the inelasticity and dissipation happen. At this stage, the only two factors against the axial loading/movement are the lateral confining pressure and cohesive-frictional resistance inside the localisation band.

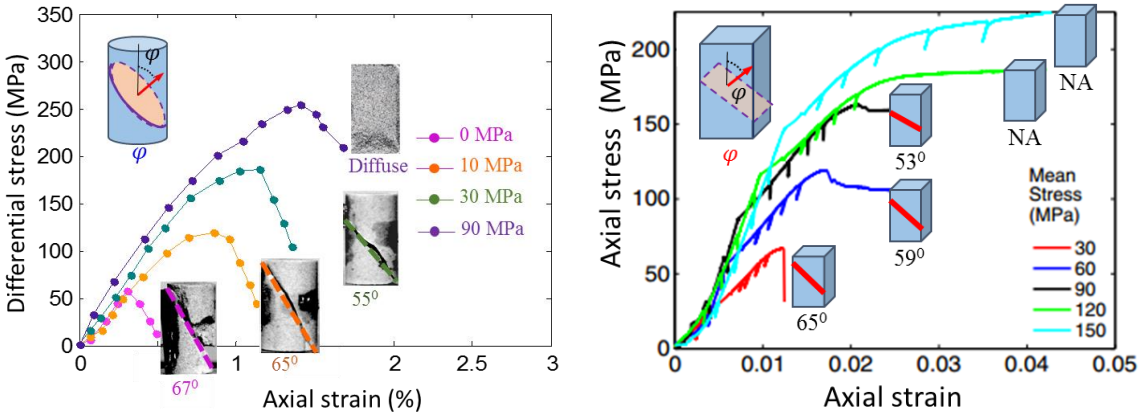

(a) (b)

Figure 2.6. Stress-strain and failure patterns of triaxial compression tests under different confinements: (a) On cylindrical specimens of Bentheim sandstone (Klein et al., 2001, 2003) and (b) On cubic specimens of Castlegate sandstone (Ingraham et al., 2013)

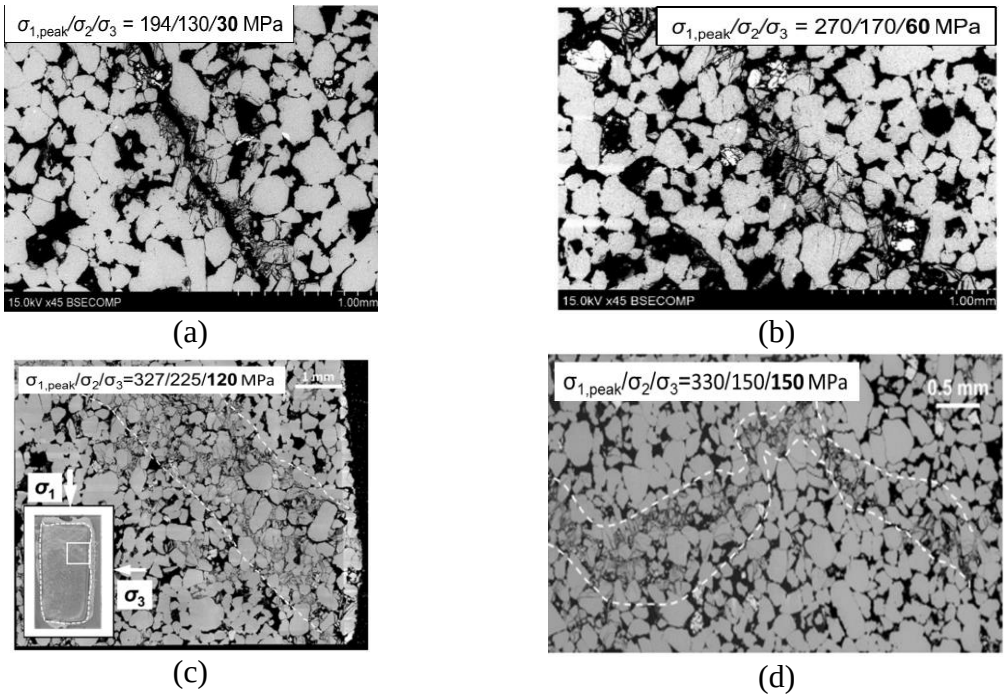

Figure 2.7. Scanning electron microscopic (SEM) micrograph mosaic of failed Bentheim sandstone specimens under different confinements (Ma and Haimson, 2016)

Under low confinements, as the lateral resistance is small, the failure happens quickly via a steep shear band, as illustrated in Figure 2.7a and b, where grains/fragments tend to slide on top of each other, leading to dilation inside the band. Simultaneously, due to the reduction of axial stress in the softening regime, the bulk material surrounding the localisation zone expands elastically. Therefore, the overall expansion exhibited by the material shown in Figure 2.4 is, in fact, a combination of dilation inside the localisation zone and expansion due to elastic unloading of the surrounding bulk material. This explains the transition from compaction (due to elastic deformation when the localisation zone has not appeared) to expansion, as observed in the specimens under low confinements. With the increase of lateral confining pressure, it is harder for the sliding in a band to happen. This gives time for the initiation and development of more microcracks, leading to proliferation and accumulation of damage within the cementitious matrix. The damage concentration in the matrix gives rise to grain-to-grain contacts and increases the chances of grains being broken. This grain crushing takes place simultaneously with the shearing inside a localised band, hence the term shear-enhanced compaction band (Ma and Haimson, 2016). The band becomes less inclined with the increase of confining pressure, as a consequence of the transition from shear band to shear-enhanced compaction band, as illustrated in Figure 2.7c. Since the compaction increases with the decrease of localisation plane orientation, the

specimen can bear more load, leading to more ductile and hardening stress-strain responses, as illustrated in Figure 2.6. The interaction between dilation at low confining pressures and grain crushing at high confining pressures explains the curvature of the yield locus in compressive parts, as seen in Figure 2.1. Specifically, under high confining pressures, the crushing failure suppresses the effects of shearing and results in a curved envelope.

Under very high confinements, the compaction and grain crushing become the dominant mechanism governing all material responses, leading to pure compaction, as illustrated in Figure 2.4b (i.e., for confinements larger than 40 MPa). In this case, the deformation does not concentrate in a straight band anymore but rather clusters in a zig-zag strip, termed a compaction band, as illustrated in Figure 2.7d. This results in the closed shape of initial yield loci in the meridian plane, as illustrated in Figure 2.8, with a shear band at low confinement, transitioning to shear-enhanced compaction and compaction band under high confining pressures (see Figure 2.8b).

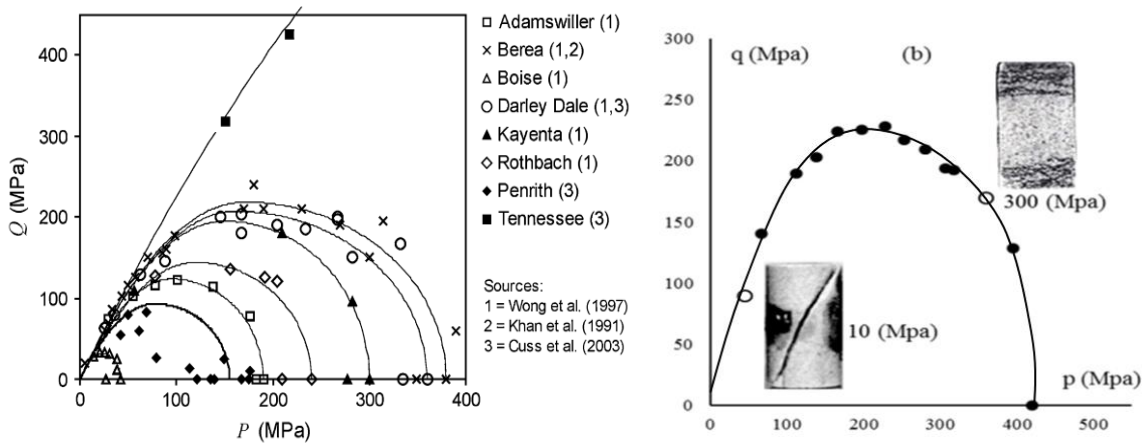

(a) (b)

Figure 2.8. Initial yield loci of (a) Different rocks and stones (Sheldon et al., 2006) and (b) Bentheim sandstone with failure patterns under low and very high confining pressure levels (Wong et al., 2001; Wong and Baud, 2012).

2.2.2 Lode-angle dependency

Recent true triaxial tests on cubic specimens (Ingraham et al., 2013; Ma and Haimson, 2016; Macari and Hoyos, 2001; Vachaparampil and Ghassemi, 2017) conducted on sandstone, concrete and soft rock show that the yield locus of quasi-brittle geomaterials is highly dependent on the Lode-angle θ, defined by $\cos 3\theta = \frac{3\sqrt{3}}{2} J_3 / J_2^{3/2}$ where J_2 and J_3 are the second and third invariants of the deviatoric stress tensor. The yield loci and stress-strain responses, together with the corresponding localisation failure patterns from tests conducted

on Castlegate sandstone in Figure 2.9, can be considered as a good illustration of the Lode-angle dependence of the material. It can be seen that for different Lode angle values, the material yields at different deviatoric stress levels. Specifically, the yielding state in axisymmetric extension $\theta = 0^0$ (i.e. $\sigma_1 = \sigma_2 > \sigma_3$) falls below that in pure shear $\theta = 30^0$ and axisymmetric compression $\theta = 60^0$ (i.e. $\sigma_1 > \sigma_2 = \sigma_3$). This Lode-angle dependence is further illustrated in Figure 2.10 by plotting yield loci in the hydrostatic-deviatoric stress space (i.e., $p - q$ coordinate system), whose results were extracted from true triaxial tests conducted on Laxiwa granite by Li et al. (1994) and later interpreted by Yu et al. (2002). As shown in Figure 2.9, this phenomenon is more evident at low confining stress, where the yield loci have triangle-like shapes in deviatoric planes. As addressed in the previous section, at such stress levels, the material responses are usually brittle and the failure planes appear to have high inclination angles (see Figure 2.9b). With the increase of confining stress, the dependence of the yield surface on the Lode angle becomes less dominant. This can be seen in the yield locus becoming more rotationally symmetrical and almost circular at high confining stress (see Figure 2.9a). This change of yield locus occurs simultaneously with the brittle-ductile transition and reduction of failure plane orientation, described in the preceding section.

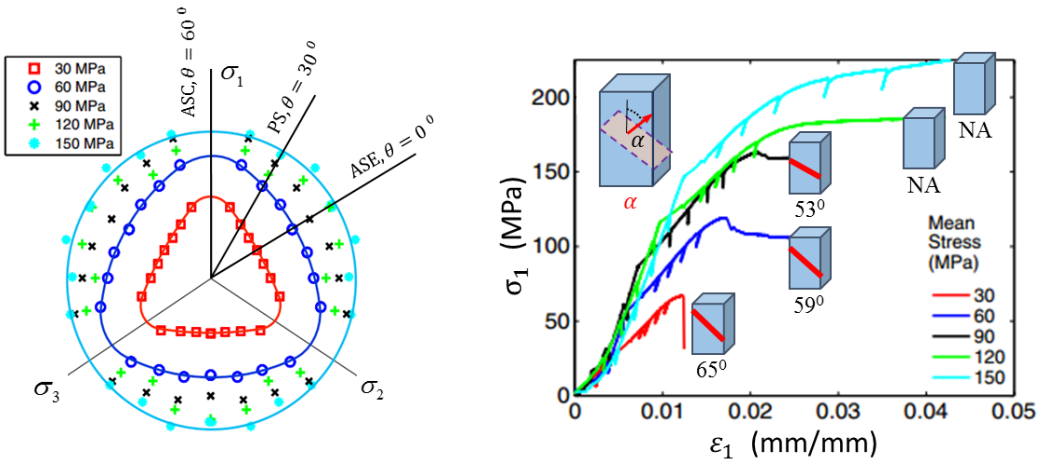

(a) (b)

Figure 2.9. Experimental observations of Castlegate sandstone (Ingraham et al., 2013): (a) Yield loci at different confining stress levels and (b) Corresponding stress-strain responses and failure patterns for $\theta = 0^0$

From the above experimental results, it is seen that the dependence of the yield surface on the Lode-angle is closely related to the failure mechanism of the material. To the best of my knowledge, this dependence should be interpreted as one of the consequences of the failure mechanism. In particular, at low confining stress, along with highly inclined failure

planes, shear band is the mechanism responsible for material failure (Ma and Haimson, 2016; Wong and Baud, 2012). The stress acting on this shear band is closely linked with the true triaxial stress conditions, represented by the stress invariants I_1, J_2 and J_3. Because the shear stress component is dominant in controlling the behaviour of the shear band, for different values of the invariants J_2, J_3 and consequently the Lode angle θ, the material responses would change accordingly. The change of the yield surface with respect to different Lode angle values thus comes naturally as a result of shear band failure mechanism. As the confining stress increases, the failure plane becomes less inclined and the failure mechanism changes from a localised shear band to a shear-enhanced compaction band, in conjunction with the brittle-ductile transition (Ma and Haimson, 2016; Wong and Baud, 2012). As a result, the influence of shear stress on the material yielding/failure decreases. This explains why the yield locus gradually becomes less dependent on the Lode angle during this transition, as shown in Figure 2.9a. Based on this analysis, the dependence of the yield surface on the Lode angle can be considered as an indirect consequence of the failure mechanism and closely links with the localised failure band orientation.

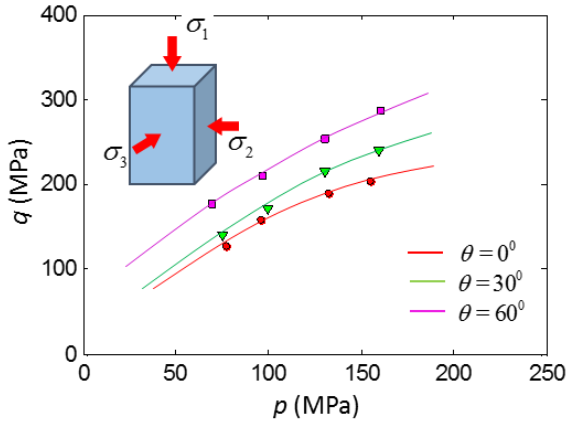

Figure 2.10. Yield loci from experimental results for Laxiwa granite in $p - q$ space (Li et al. 1994)

2.2.3 Size effect

The deterministic part of size effect, observed in experiments on concrete and rock (Bažant, 1999, 1984; Grégoire et al., 2013; Karihaloo et al., 2003; Tang et al., 1992; van Mier, 1986) and investigated numerically (Karihaloo et al., 2006; Le Bellégo et al., 2003; Rezakhani and Cusatis, 2014; Scholtès et al., 2011; Syroka-Korol et al., 2013; Tejchman and Gorski, 2008), is also among the most important features, strongly affecting the modelling of the material. The size effect of the material in tension can be seen in three-point bending tests conducted on various specimen sizes of different beam types, as illustrated in Figure

2.11. Although a comparison in terms of strength could not be made due to the difference in size of these specimens, it can be observed that the bigger the specimen is, the more brittle its behaviour becomes. This applies for all beam types (with different notch depths and un-notched beams) in this experimental study (see Grégoire et al., 2013). This change in response with respect to specimen size can be clearly observed in experimental results of direct tension tests of dog-bone specimens made from concrete and sandstone, as shown in Figure 2.12. With the increase in specimen size, the tensile strength slightly reduces and more importantly, the overall behaviour becomes more brittle. Furthermore, the deterministic size effect is also clearly observed through the stress-strain results of uniaxial compression tests, shown in Figure 2.13a, conducted on concrete specimens with three different heights by van Mier (1986). Similar to the bending and direct tension tests, it can be seen that the longer the specimen is, the more brittle the behaviour becomes.

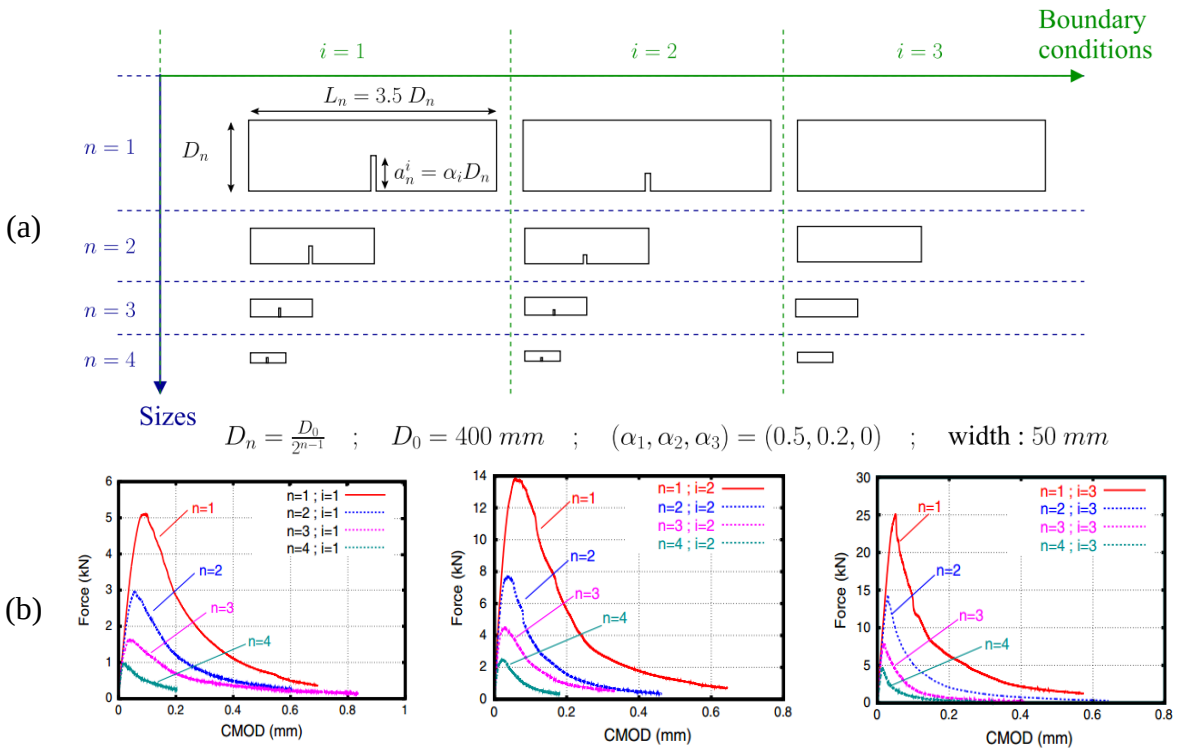

Figure 2.11. An illustration of the size-effect in 3-point bending tests: (a) Problem boundary conditions and (b) Corresponding averaged load versus crack mouth opening displacement (CMOD) responses (Grégoire et al., 2013)

As suggested by Gopalaratnam and Shah (1985), the change of responses, described above, implies that there is no unique stress-strain relationship to represent the materials' behaviour, as it tends to vary depending on the specimen size used. The reason behind this is that the softening branch of a stress-strain curve is, in fact, a mixture of the material and

structural property (Chen and Han, 1988). As a result, the quantifying of inelastic or fracture-related quantities, such as fracture energy, using stress-strain curves alone is unreasonable. This leads to a problematic issue when it comes to solving Boundary Value Problems (BVPs) by continuum models, where the stress-strain relationship needs to be provided as a constitutive behaviour for the modelling. Even though several methods and approaches have been proposed to tackle this issue and obtained fairly satisfactory results, they are of mathematical or phenomenological treatments, and thus fail to address the underlying mechanism leading to such behaviour at the first place. This issue in current models will be discussed at length in the next chapter.

(a)

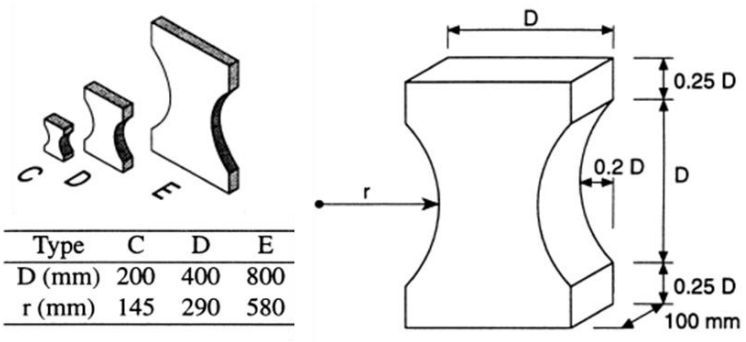

Type	C	D	E
D (mm)	200	400	800
r (mm)	145	290	580

(b)

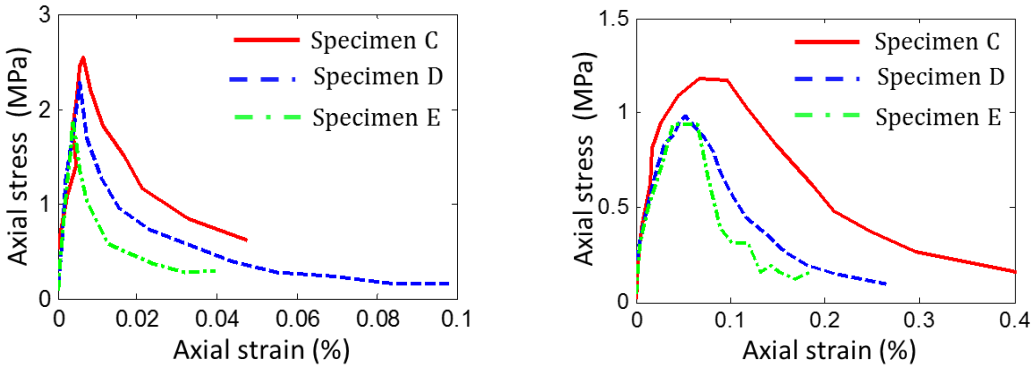

Concrete Red Felser Sandstone

Figure 2.12. An illustration of the size-effect in direct tension tests on concrete and red Felser Sandstone: (a) Problem boundary conditions and (b) Corresponding stress-strain responses (van Vliet and van Mier, 2000)

Different from the statistical size effect caused by the randomness of material strengths, the deterministic size effect, described above, is a result of stress redistributions caused by the stable propagation of fractures or damage and the inherent energy release (Bažant, 1999). Therefore, the deterministic size effect is highly connected with the contribution from the localised failure into the overall structural system. The intimate link of the deterministic size effect and the localisation zone can be explained by further analyses of the uniaxial compression tests conducted by van Mier (1986). In particular, when the post-

peak relative displacement (i.e., subtract displacement at peak, $u_{1,\sigma_{1,\mathrm{p}}}$, from total displacement, $u_{1,\mathrm{tot}}$) rather than the strain is plotted against the stress, as shown in Figure 2.13b, the responses are almost identical, regardless of specimen heights. This discrepancy can be explained as follows. As the surrounding bulk material behaves elastically once localisation appears, the majority of displacements measured on the specimen are due to the deformations inside the localisation band. The Figure shows that the displacements inside the localisation band are the same for all specimen sizes. However, this same value of displacement is then divided by different heights to calculate the strain of each specimen. This will result in different strain values, which are not real ones measured from the experiments but just the averaged strain over the whole specimens. As a result, we would have different stress-strain curves from the same stress-displacement behaviour inside the localisation band, as shown in typical experimental results by van Mier (1986) in Figure 2.13a. In other words, the change in specimen heights results in a variation of contributions ratio between the localised band and its surrounding bulk material to the macro behaviour. As a result, the overall mechanical responses change with respect to different specimen sizes.

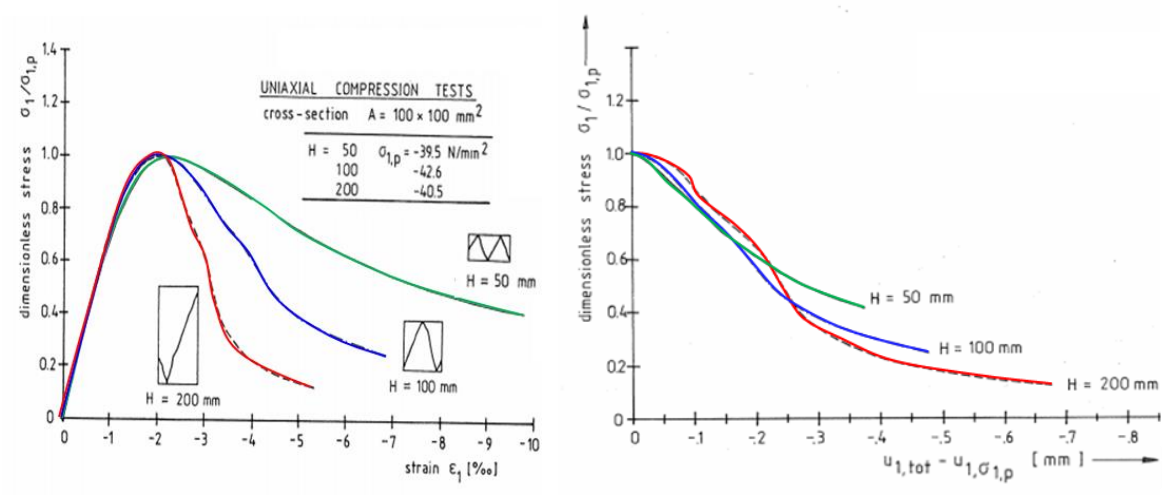

(a) (b)

Figure 2.13. Uniaxial compression test results on concrete with different specimen heights: (a) Dimensionless stress-strain curves and (b) Corresponding dimensionless stress-displacement curves (after van Mier, 1986)

The above analysis shows that the size effect observed in experiments is actually a consequence of the difference in deformation and behaviour between the localisation band and the material surrounding it. This difference, and consequently the size effect, cannot be captured by continuum models where averaged stress and strain are the only quantities used to describe the material responses. Instead, the deformation and inelasticity within the

localisation band should be captured separately from the behaviour of the surrounding bulk material, so that the structural properties are distinguished from the material properties. The size effect can then be captured properly, with its underlying mechanism.

2.3 Mechanical responses and failure mechanisms of fibre reinforced concrete (FRC)

Alongside fibre reinforced concrete, reinforcing other geomaterials, such as soils and sand with randomly short fibres, has been proved to be effective in improving their mechanical properties. Over the past few decades, this method of reinforcement has been employed in geotechnical engineering for thin layers of soil, repairing failed slopes, soil strengthening around footings or earth retaining structures. Therefore, numerous studies have been devoted to investigating the influence and effectiveness of different fibre types (i.e., natural and artificial fibres) on behavioural characteristics of the materials, with emphasis put mostly on its strength and ductility. Noteworthy experimental studies on uniaxial and triaxial compression tests on cylindrical specimens (Ahmad et al., 2010; Diambra et al., 2010; Hamidi and Hooresfand, 2013; Ibraim et al., 2012, 2010; Kumar and Gupta, 2016; Russell et al., 2017) and direct shear tests (Consoli et al., 2007; Hazirbaba, 2018; Yetimoglu and Salbas, 2003) quantified the impact of adding fibres on the compressive and shear strength of soils and sands. Despite the traditional conception that the tensile strength of soils/sands is almost zero, experimental results on tension tests conducted recently (Cristelo et al., 2017; Li et al., 2014, 2018; Liu et al., 2018; Plé and Lê, 2012; Tang et al., 2016) have revealed that the tensile strength can be improved considerably with fibre reinforcement. Even though more research is needed to extend their application, these findings show the promising potential of using fibre reinforced soils/sands for large-scale and complex geotechnical structures in the near future.

Nonetheless, despite providing comprehensive data on strength improvement, experimental data on failure mechanisms of fibre reinforced soils/sands are very limited in the current database. This is probably due to difficulties in traditional measurement methods and the fact that specimens will disintegrate when being removed from the experimental cell. This necessitates further research using more advanced experimental techniques, such as X-ray MicroCT (Khaddour et al., 2018; Soriano et al., 2017; Wiebicke et al., 2017) or Digital Image Correlation (DIC) (Aparna et al., 2018; Dias-da-Costa et al., 2017; Kan et al., 2018; Paegle and Fischer, 2016; Rasheed and Prakash, 2018; Robert et al., 2007; Srikar et al.,

2016) to observe and measure deformation inside the specimens at different stages of loading. All of these aspects, alongside fibre reinforced soils/sands, are generally beyond the scope of this study. The research in this study focuses mainly on Fibre Reinforced Concrete (FRC) in tension and compression, under no or low confining pressure levels which are common loading conditions of concrete and its applications.

2.3.1 Behaviour and failure of FRC in tension

It is well-known that adding randomly distributed short fibres into cementitious concrete can substantially improve the overall ductility, energy absorption and meso/macro-cracking control of the FRC. Short fibres help improve the tensile strength and toughness significantly (Bashar et al., 2016; Gopalaratnam and Shah, 1987; Kamal et al., 2008; Li et al., 2001, 1996, 1998; Park et al., 2012; Wille et al., 2014, 2011). This is illustrated in Figure 2.14a for tension tests where responses of FRC with various fibre types (i.e., hooked end steel fibres, polymer PVA fibres) and volume fraction ($V_f = 3.5$ and 6%) show a significant improvement on strength and ductility compared with that of plain concrete. Similar responses can be observed in flexural behaviour in bending tests, illustrated in Figure 2.14b.

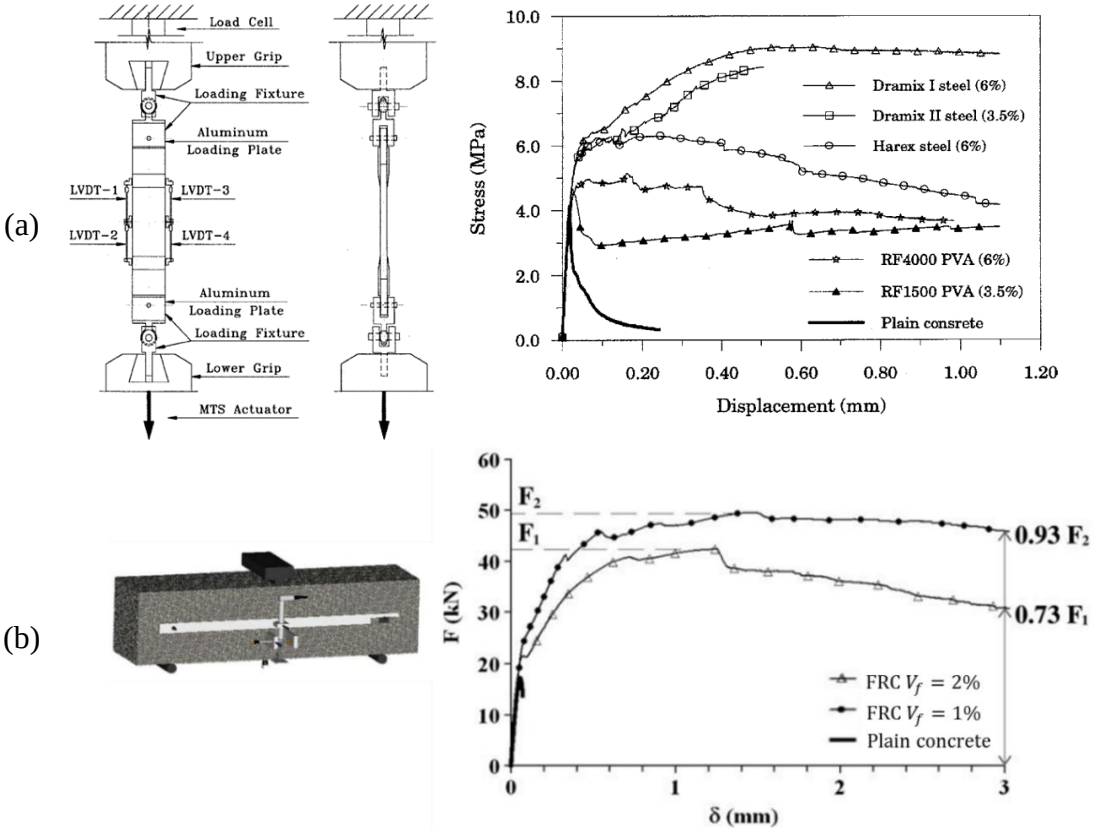

Figure 2.14. Illustration of improvements made by fibres in FRC: (a) Tension test results of plain and FRC of various fibre types and volume contents (Li et al., 1998) and (b) Flexural behaviour in 3-point bending tests of FRC with Dramix fibre (Bencardino et al., 2010)

The mechanism governing the behaviour of FRC can be addressed and identified using typical experimental results of tension tests on dog-bone specimens, shown in Figure 2.15, for both plain and reinforced concrete. The first set of experimental results, shown in Figure 2.15a, is from high-performance fibre reinforced cement composites (HPFRCC) reinforced by Spectra fibre, which is an ultra-high molecular weight polyethylene fibre with diameter $d_f = 0.038$ mm, length $L_f = 38$ mm and volume content $V_f = 1\%$. Figure 2.15b plots both the stress - strain responses and the progressive failure pattern of tension tests on concrete reinforced by Polyvinyl alcohol (PVA) fibres 12 mm in length, 40 μm in diameter and a ratio of 2% by volume. As seen in the Figure, the response of the plain concrete specimen is sharp softening after the stress reaches tensile strength with the appearance of a major crack (illustrated by a red curve in Figure 2.15a). As explained in Section 2.2.1, this is because a single, localised crack quickly develops and dissipates all of the given energy, resulting in brittle behaviour, as also observed in many experiments (Gopalaratnam and Shah, 1987; Li et al., 1996, 1998; Wille et al., 2014).

On the other hand, substantial improvements in toughness and fracture resistance can be observed in the FRC responses (Kamal et al., 2008; Li et al., 2001; Park et al., 2012; Wille et al., 2014, 2011), which can be divided into three phases. In phase I, illustrated by the curve AB in Figure 2.15a, the response of the FRC is relatively linear elastic, similar to the plain concrete case. This means that the responses of fibres have not yet been mobilised and the FRC behaves just like plain concrete in this phase. However, a significant increase in strength and ductility is observed in phase II from point B to point C, with numerous cracks distributed throughout the specimen. This is because when the first crack initiates and opens, the fibres across the crack are activated and begin to debond from the matrix. These bridging fibres help transfer stresses between two sides of the crack and hamper it from opening freely. This forces the material to form new small cracks to dissipate the given energy. The density of cracks throughout the specimen and the elongation of phase II depend on the fibre bridging forces, governed by the number of fibres across the crack plane, the mechanical properties of fibres, matrices and their interactions. As small cracks are uniformly distributed, the strain is relatively homogenous throughout the specimen length during this phase. In phase III, the material behaviour becomes softening with the formation of a localisation band at the weakest crack plane, illustrated by a red curve in the experimental failure pattern in Figure 2.15a. In this phase, the fibres across this localisation band are subsequently pulled out of the matrix, making the bridging effect weaker and consequently fostering the

localisation to develop further. The deformation in the localisation band increases quickly, while cracks at other locations close owing to the decrease in stress, as illustrated in Figure 2.15. This process takes place until the specimen fails.

(a)

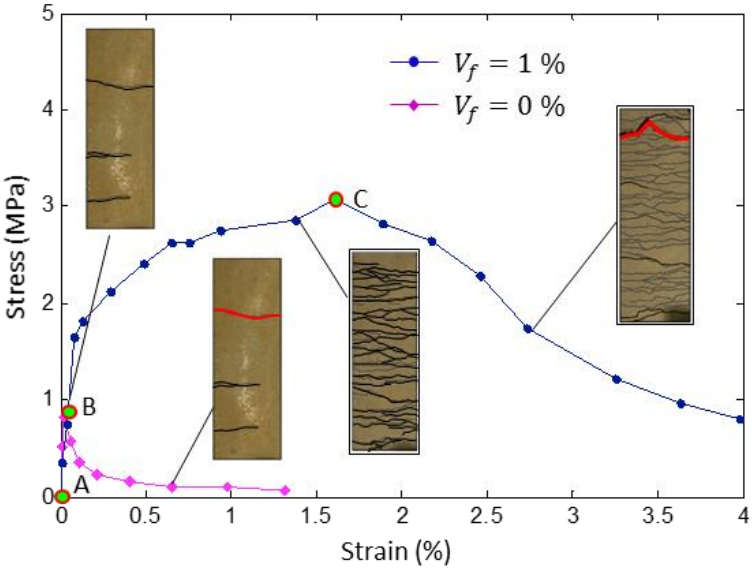

(b)

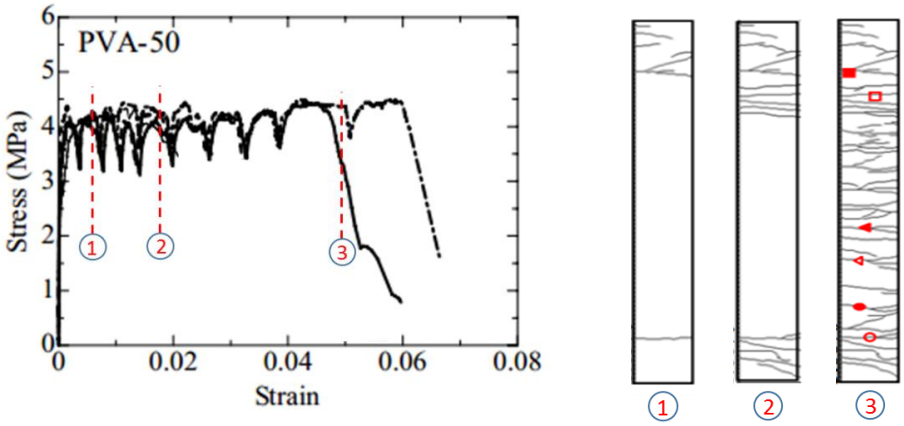

Figure 2.15. Typical uniaxial tensile responses and failure patterns of FRC: (a) FRC reinforced by Spectra fibres (Sirijaroonchai et al., 2010) and (b) FRC reinforced by PVE fibres (Rokugo et al., 2007)

The analyses and arguments made above from the direct tension tests can also be applied to the flexural behaviour of FRC beams due to the fact that the dominant loading condition borne by material, in this case, is also tension. This is illustrated by experimental results of a 4-point bending test, shown in Figure 2.16, with different volume fraction values (in percentages) denoted after the fibre type (L: long, M: medium, S: short fibre). The beams were made from ultra-high performance concrete (UHPC) reinforced by three types of straight steel fibres (i.e., L, M and S), whose aspect ratios are 65, 97 and 100. The final failure patterns, plotted in Figure 2.16b, show that the specimen containing a total of 2% of

steel fibres by volume exhibits multiple cracks and one localised zone at the failure stage. The best cracking properties in terms of the number of cracks and average crack spacing were obtained in the L0.5-M1.5 specimen (contains 0.5% long fibre and 1.5% medium fibre by volume), which is also the specimen with the best post-cracking flexural properties, including the highest values of strength and toughness. This again confirms the analyses made above that the formation of cracks and diffuse cracking have a strong relationship with the load-bearing capacity of the structures.

(a)

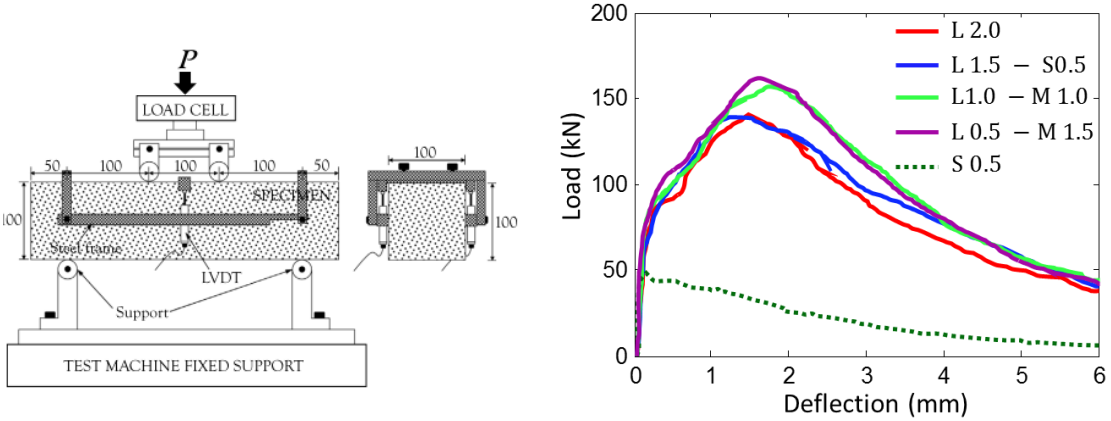

(b)

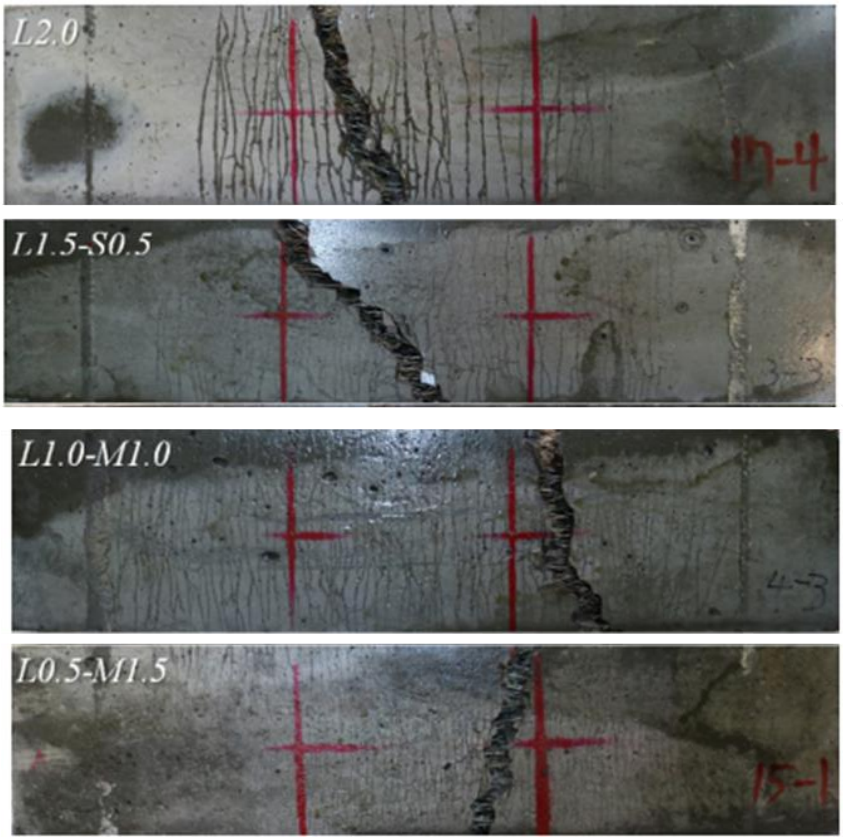

Figure 2.16. Flexural behaviour of FRC beams: (a) Experimental set-up and load-deflection behaviour and (b) Corresponding final failure pattern (Yoo et al., 2017)

Similar observations can be found in shear behaviour of FRC, as illustrated in Figure 2.17. With the experimental set-up shown in Figure 2.17a, the shear stress on the localisation zone is calculated and plotted against the shear strain. Analogous to tension and bending cases described above, the progressive failure patterns at different loading stages, captured by the DIC technique in Figure 2.17b, show a system of smaller cracks (diffuse cracking) developing in an R/ECC specimen (i.e., normal concrete reinforced by both conventional rebar and short fibres). On the other hand, there is only one major crack propagating in the R/C specimen (i.e., normal concrete with only conventional rebar reinforcement). This observation, once again, shows the importance of the fibre bridging effect, alongside cohesive resistance inside cracks, in controlling failure patterns at the material level and the overall responses of the structures.

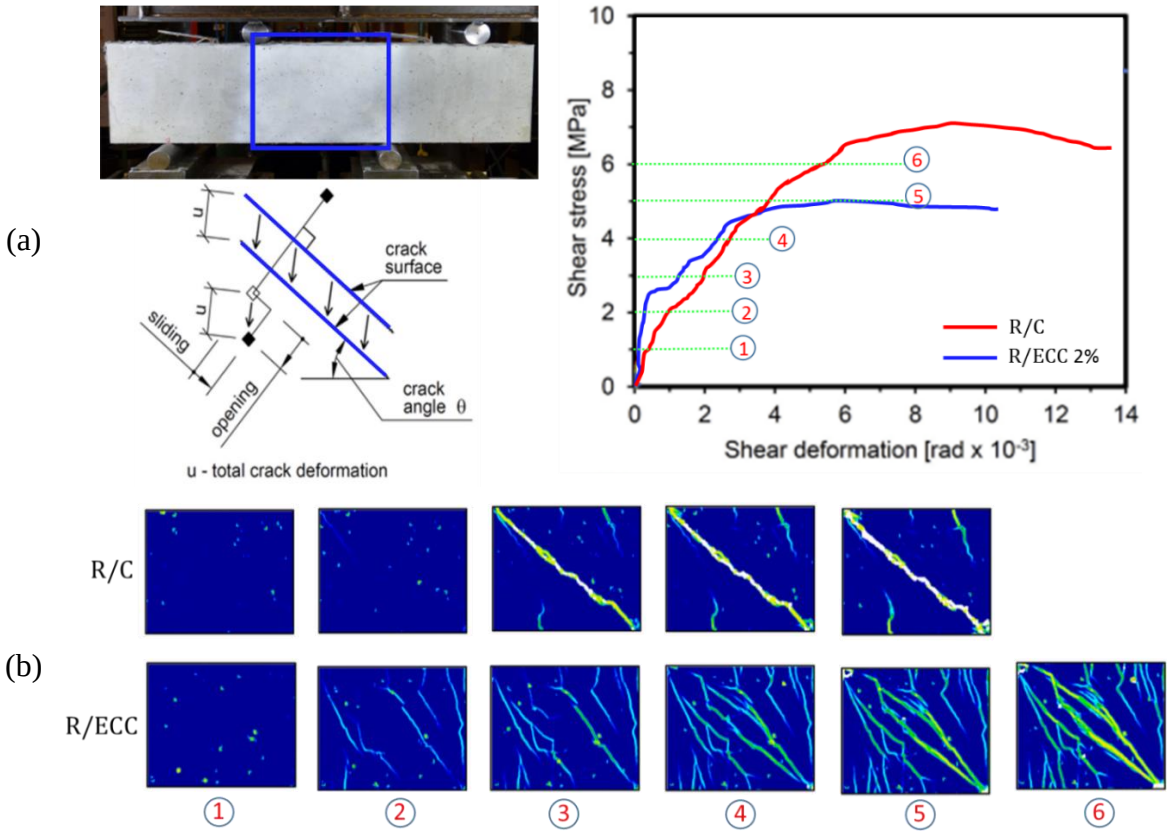

Figure 2.17. Shear behaviour of conventional and fibre reinforced concrete beams: (a) Experimental set-up and stress-deformation responses and (b) Progressive failure patterns obtained with DIC (Paegle and Fischer, 2016)

2.3.2 Behaviour and failure of FRC in compression

Experimental studies (Bencardino et al., 2008; Ding and Kusterle, 2000; Hassan et al., 2012; Lu and Hsu, 2006; Mo et al., 2017; Nataraja et al., 1999; Ou et al., 2012; Ezeldin and Balaguru 1992) show the marginal enhancement that adding fibres makes to compressive strength, as illustrated by the experimental results of uniaxial compression tests on normal and high strength concrete specimens reinforced by steel hooked end fibres, shown in Figure 2.18. These are predictable observations, as the original purpose of adding short fibres into quasi-brittle geomaterials like concrete is to overcome its brittleness in tensile loading conditions.

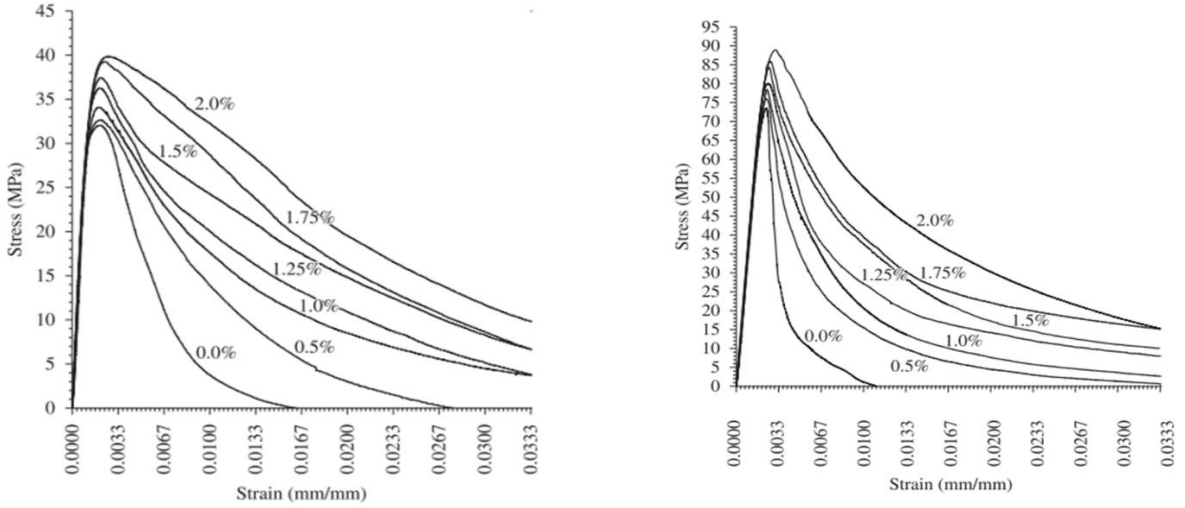

Figure 2.18. Uniaxial compression test results of FRC with various values of volume fraction: (a) Normal strength steel fibre reinforced concrete mixes and (b) High strength fibre reinforced concrete mixes (Marara et al., 2011)

The material behaviour in compressive loadings, illustrated by uniaxial compression test results of FRC plotted in Figure 2.19a, shows modest improvements on strength. The experiments were conducted by Ou et al. (2012) with concrete whose compressive strength is $f_c = 40$ Mpa, and hooked-end steel fibres with a diameter $d_f = 1$ mm; fibre length $L_f = 60$ mm. With different volume fracture values, ranging from $V_f = 0.7$ to $2.8\,\%$, the compressive strength is almost the same, while notable enhancements of material ductility are observed. The failure patterns of the FRC also exhibit a localisation band whose plane becomes less inclined with the increase of volume content, as presented in Figure 2.19b. This can be explained by the interaction of the fibre bridging effect and the cohesive-frictional resistance in the localisation band. Specifically, similar to the tension case, when

a crack appears within the material, fibres across that crack will be activated and start bearing the load. It should be noted that in terms of load carrying, a fibre would act as a cable, which only resists the tensile loading applied to it. For low fibre content, as the effect of fibre bridging is still weak, the specimen forms a steep shear band upon which the two remaining parts of the specimen can slide until failure, similar to the plain concrete (PC) case. When the fibre bridging force becomes stronger with the increase in volume fracture, it refrains the formation and sliding of steep localisation bands. In this sense, the influence of fibre bridging forces on the failure of the FRC is similar to that of confining pressure on the failure pattern of PC as described previously. As a result, the increase in volume fracture shifts the failure mechanism in the localisation band from shear to shear-enhanced compaction and consequently changes the failure plane angle, as observed in the experiments. Similar to the case of quasi-brittle geomaterials under high confining pressure levels, the failure patterns of FRC, plotted in Figure 2.19b, show zig-zag localisation bands for high fibre volume fractures. This again confirms the coupling effect of shear and compaction, which originates from the interaction of fibre bridging forces and material cohesive-frictional resistance within the crack/band.

(a)

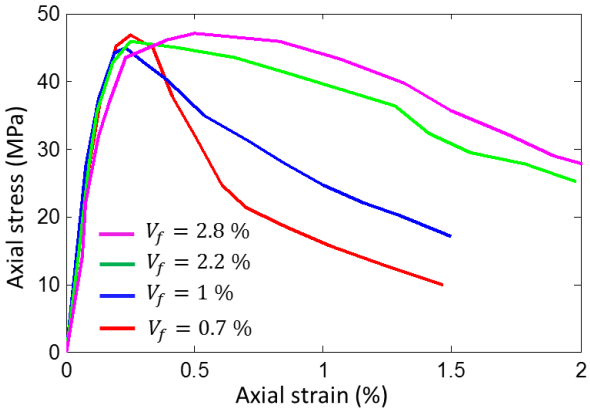

(b)

V_f = 0.7 % V_f = 1 % V_f = 2.2 % V_f = 2.8 %

Figure 2.19. Uniaxial compression test results on FRC with different volume fractures: (a) Stress-strain responses and (b) Corresponding failure patterns (Ou et al., 2012)

(a)

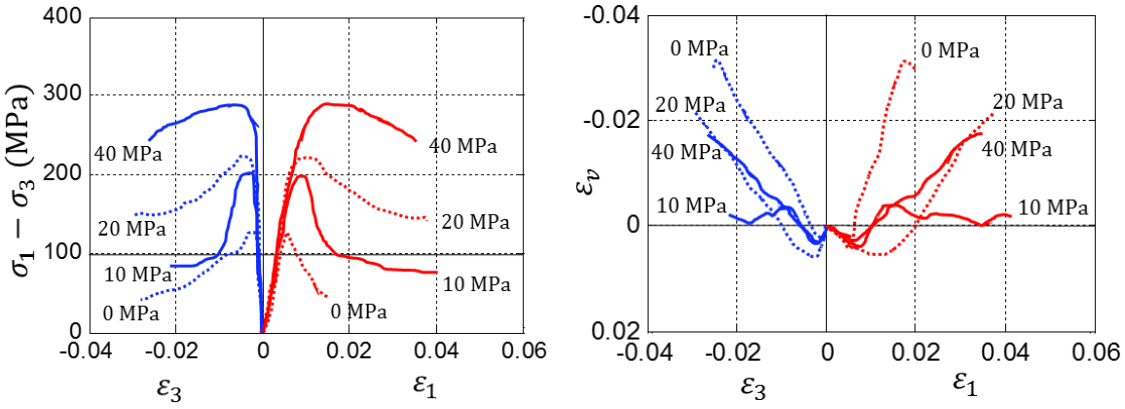

(b)

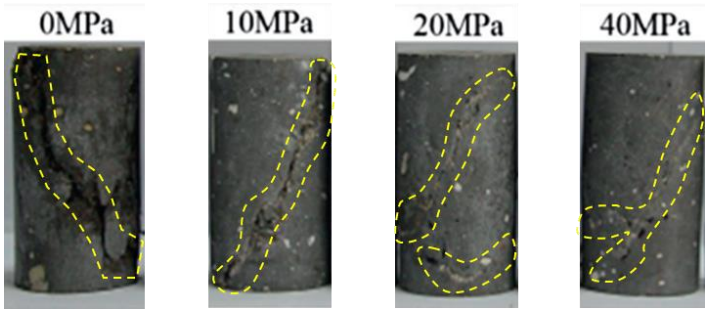

Figure 2.20. Triaxial compression test results on FRC with volume fracture $V_f = 2\%$ under different confinements: (a) Overall responses and (b) Corresponding failure patterns (Ren et al., 2016)

Behaviour of FRC in compression is further investigated through triaxial compression tests under different levels of confinements. The experimental results used for illustration here were obtained by Ren et al., (2016) from compression tests on 50 x 100 mm cylindrical specimens of ultra-high performance cement-based composite (UHPCC) whose compressive strength is $f_c = 95$ Mpa. The concrete was reinforced with straight steel fibre with the volume content $V_f = 2\%$. The results, plotted in Figure 2.20a, show that the overall stress-strain responses of the FRC at different confinements are relatively similar to those of plain concrete. Specifically, with an increase of confining pressure, its behaviour becomes more ductile towards hardening. The volumetric strain evolution is similar to that of plain concrete where compaction due to elastic compression takes place first and then expansion due to dilation inside and relaxation of the outside the localisation band occurs. The analogy of responses between FRC and PC is understandable as the compressive characteristics of concrete are little changed with the addition of fibres, as has been observed in many studies (Bencardino et al., 2008; Ding and Kusterle, 2000; Hassan et al., 2012; Lu and Hsu, 2006; Mo et al., 2017; Nataraja et al., 1999; Ou et al., 2012; Ezeldin and Balaguru 1992). The failure patterns, presented in Figure 2.20b, exhibit a clear localisation band under low

confinement and more zig-zag bands under higher confinement. This brings us back to the analyses made in Section 2.2.1 on the combining effect of shear band and shear-enhanced compaction band.

From analyses addressed above, it can be seen that, even though the responses and performances of FRC in both tension and compression are different from those in quasi-brittle geomaterials, localisation remains the intrinsic failure mechanism governing the behaviour of the material. Once localisation bands appear within the body of the material, the inelasticity and energy dissipation take place mainly inside the band, where stresses are transferred via: (i) cohesive-frictional resistance from the material and (ii) bridging fibres across the band. This stress transfer in the localisation band is the source of strength and ductility improvements in the FRC compared with plain concrete at mesoscale, as well as structural level.

2.4 Summary and discussion

Experimental data from different tests have shown that quasi-brittle geomaterials feature a wide range of behaviour under different loading conditions. In tension, the material shows sharp softening and brittle behaviour, with a thin localisation band that forms and develops quickly within the material body. On the other hand, the response of quasi-brittle geomaterials in triaxial compression tests gradually alters from being brittle with steep failure planes, to ductile with less steep planes and/or zig-zag failure patterns when the confining pressure increases. Together with this transition of macro responses, experimental results show the dependence of yield loci on the Lode-angle, which is clearly observed at low confining pressure levels and becomes less evident at high confinements. Furthermore, the experimental data also reveals the significant influence of specimen sizes on material responses, which become more brittle with the increase in specimen height.

Experimental results on fibre reinforced concrete clearly show the significant influence of adding short fibres into the cementitious concrete in both tension and compression. Both the strength and the ductility of the material increase substantially in tensile loading conditions. Together with this enhancement, the failure patterns first show a system of small cracks scattering among the whole specimen and then all the inelastic activities are localised into a narrow band until complete failure. This failure is totally different from that of plain concrete (i.e., quasi-brittle geomaterial), described above, where a major crack forms and develops quickly until the specimen completely fails. Under compression, the FRC shows

notable improvement in material ductility, while only modest change of compression strength can be found with an increase of fibre volume fracture. The experimental observations also show that the corresponding failure patterns transition gradually from narrow steep planes to less steep and/or zig-zag localisation bands with the increase in fibre volume fracture and confining pressures.

Via analyses of experimental data, all of the above-mentioned features and characteristics of material failure patterns are closely tied to the localised failure mechanism. In fact, the failure in form of localisation band is identified as the governing mechanism causing these features in several loading conditions (e.g., mixed-mode loading conditions of tension, shear and compression under low confining pressure levels). Whether it is a thin band in which cohesive-frictional resistance and fibre bridging forces interact with each other under tensile loading, or a shear band transitioning to a shear-enhanced compaction band in compression, localised failure is always the mechanism governing both the macro responses and the failure patterns of the material. The localisation of deformation and behaviour within the material body is also the primary cause of the Lode-angle dependence of yield loci and the size effect observed in experiments.

This conclusion of the localised failure being the underlying mechanism of the material responses, indicates a significant change in the way we should approach material modelling. If we solely use conventional theories such as plasticity or damage-plasticity to formulate the constitutive continuum model, this localised failure mechanism and consequently the material features and responses will never be captured faithfully. It is possible that the yield surface can be modified phenomenologically to bring in the Lode-angle dependence or to produce a good fit with macro responses observed in the experiments, but its constitutive behaviour could not truthfully reflect the failure in a localisation band and its transition from shear to shear-enhanced compaction. It is clear that the responses inside and outside the localisation band are totally different, the sole stress and strain or other averaged quantities such as damage or plastic strain cannot describe the localised deformation and inelasticity properly. Even if such models capture the macro localised failure with Finite Element Analysis, this localisation and its responses, in this case, are incorrectly dependent on the discretisation resolution of the mesh. Furthermore, it is even more problematic to model the interaction of the fibre bridging effect and cohesive-frictional resistance without variables describing the actual deformation in cracks/localisation bands where such interactions take place. In this sense, these models can only capture the overall responses exhibited by

specimens under different loading conditions but not the intrinsic mechanisms behind these responses. As a result, there is no inter-connection between features of the material, and consequently, external treatments are needed on top of the constitutive model to alleviate the lack of mechanism and obtain the desired characteristics. These limitations and problems, existing in current constitutive models, will be addressed at length in Chapter 3, which identifies the research gaps and serves as a motivation for this research.

For modelling quasi-brittle geomaterials with and without fibre reinforcement, the aim now is to apply these understandings of failure and responses from basic (material) tests to the development of a model that can predict the behaviour at both "material" and "structural" levels. If the mechanisms are not properly incorporated into the model development, it will be challenging to create a reliable model, as the outcome will be more curve fitting than predicting from physical relationships. In this sense, an appropriate approach, to the best of my knowledge, should take the localised failure mechanism as the foremost basis for the model development, before any other response or feature exhibited by the material. This means that instead of trying different formulations to capture the responses observed in experiments, the model development should start from the underlying mechanism of localisation as the key from which all of these responses can be captured as consequences. The constitutive model should feature the localised failure mechanism in a way that enables the addition of internal variables and quantities to describe the behaviour of the localisation band, alongside the conventional stress and strain in a continuum-based approach. Modelling of quasi-brittle geomaterials with fibre reinforcement is then straightforward, as the interactions of the fibre bridging effect and cohesive-frictional resistance within the crack/localisation band and their influences on material responses are portrayed naturally. The model, in this sense, would be more faithful in capturing material behaviour and more reliable in simulating engineering structures made from such materials.

CHAPTER 3

Constitutive modelling of quasi-brittle geomaterials: a review

3.1 Introduction

The complex behaviour of quasi-brittle geomaterials under various loading conditions, addressed in the preceding chapter, necessitates an adequate constitutive model for analysing applications of quasi-brittle geomaterials in infrastructure and geotechnical engineering. A constitutive model that can realistically reflect the key aspects of the material, with its underlying mechanisms, is of the utmost importance for a successful and reliable numerical simulation in an engineering design project. Therefore, over the past few decades, a large number of noteworthy contributions have been devoted to constitutive modelling of the materials with a wide range of complexity and applicability. Behavioural modelling has been approached from different perspectives, focusing on various aspects and obtaining different levels of success.

This chapter is thus dedicated to reviewing constitutive models for quasi-brittle geomaterials with and without fibre reinforcement, from which critical discussions of their features and capabilities will be drawn. Instead of reviewing a large number of models on a case by case basis, they will be classified into certain groups, depending on their original approach/theory. Given the importance of localised failure mechanism in governing material behaviour, the capability of each group will be examined, based on how faithfully they can reflect the underlying localisation mechanism, associated with important features of the material. In this regard, continuum-based models constructed from plasticity theory, damage mechanics, their coupling and micromechanical considerations are the main focus when addressing the modelling of quasi-brittle geomaterials. On the other hand, because geomaterials with fibre reinforcement, represented by fibre reinforced concrete (FRC), are highly heterogeneous at macroscopic level, discrete and semi-discrete modelling, in addition to continuum-based approaches, are also reviewed in this chapter. The main aspects, advantages, along with shortcomings and limitations of these approaches, drawn from the review and analyses in this chapter, serve as general background and motivation for the development of the constitutive models in this study.

3.2 Constitutive modelling of quasi-brittle geomaterials

The desire here is to create a constitutive model that can capture all important macroscopic aspects, so that the material can be simulated with a high level of accuracy and reliability. However, incorporating all of these features into a single model is quite difficult, especially for continuum constitutive modelling, which includes a few macroscopic quantities and thus cannot always reflect what truly happens at the microscopic level. Even though this is a disadvantage compared with explicit modelling at microscopic level, macroscopic constitutive modelling is superior in terms of simplicity and low computational cost when it comes to implementation for analysing large-scale structures in infrastructural and geotechnical engineering.

Therefore, over the past few decades, an extensive amount of effort has been paid to developing continuum-based constitutive models for quasi-brittle geomaterials. The majority of the existing models were constructed based on classical continuum theories, including plasticity theory, damage mechanics and their coupling damage-plasticity approach. These well-known theories have been widely utilised to describe the inelasticity, strength/stiffness reduction and/or irreversible deformation observed in many experiments conducted on concrete, rocks and sandstone. However, they fail to capture the essential localised failure and its micro-/meso-structural changes, revealed in recent studies (Alam et al., 2014; Lee and Haimson, 2011; Ma and Haimson, 2016; Seo et al., 2002). Other models, inspired by experimental observations and considerations at micro/mesoscopic level, have proved their superiority over classical continuum models in describing localised failures of the material. This approach, termed micromechanics-based approach, is thus also the focus of this section, alongside other advanced models in continuum approach proposed recently. In what follows, the pros and cons of these models and approaches in capturing the essential features of quasi-brittle geomaterials will be addressed at length.

3.2.1 Basics of constitutive modelling for quasi-brittle geomaterials

This section covers the basic developments in constitutive modelling of quasi-brittle geomaterials over the past decades. Classical continuum models such as elastoplastic models, elastic-damage and their coupling elastoplastic-damage models will be reviewed, together with more recently developed, advanced versions.

3.2.1.1 Elastoplastic models

Plasticity theory, originally developed to capture the irreversible deformation of metallic materials, has been extensively employed to describe the inelastic responses of geomaterials. In summary, apart from the fundamental elastic constitutive relationship, any model developed based on plasticity theory requires three other prerequisites, including: (i) decomposition of the total strain to describe the relationship between reversible and irreversible deformation; (ii) the definition of a yield function with hardening/softening rules to control when and how the inelasticity takes place, and (iii) flow rules to govern how irreversible deformation (i.e., plastic strain) evolves with further loading.

From a modelling point of view, in order to avoid excessive inelastic dilatancy, which is usually the case when using pressure-dependent yield criteria, a non-associated flow rule is generally recommended for geomaterials (Chen and Han, 1988; Grassl et al., 2002; Lee and Fenves, 1998). For this purpose, the plastic potential for the flow rule is usually formulated by slightly modifying the yield function with one or more additive parameters. Therefore, the majority of models proposed within plasticity framework are different from each other in their formulations of the yield function. A large number of yield criteria have been proposed under different considerations and can be classified based on their shapes and essential features in the principal stress space. For convenience, apart from the principal stress space $\sigma_1, \sigma_2, \sigma_3$ and their stress invariants I_1, J_2, J_3, the yield surfaces are often expressed in Haigh-Westergaard space, in which the position of a stress state is represented by three coordinates ξ, ρ, θ, defined as:

$$\xi = \frac{\mathrm{I}_1}{\sqrt{3}};\ \text{where } I_1 = \delta_{ij}\sigma_{ij} = \sigma_{11} + \sigma_{22} + \sigma_{33} \tag{3.1}$$

$$\rho = \sqrt{2J_2};\ \text{where } J_2 = \frac{1}{2}\sigma'_{ij}\sigma'_{ij} \text{ and } \sigma'_{ij} = \sigma_{ij} - \frac{1}{3}\delta_{ij}\sigma_{kk} \tag{3.2}$$

$$\cos 3\theta = \frac{3\sqrt{3}}{2}\frac{J_3}{J_2^{3/2}};\ \text{where } J_3 = \frac{1}{3}\sigma'_{ij}\sigma'_{jk}\sigma'_{ki} \tag{3.3}$$

Further explanations and illustrations of this space, together with definitions of other important notions, such as hydrostatic axis and deviatoric plane, can be found in Chen and Han (1988).

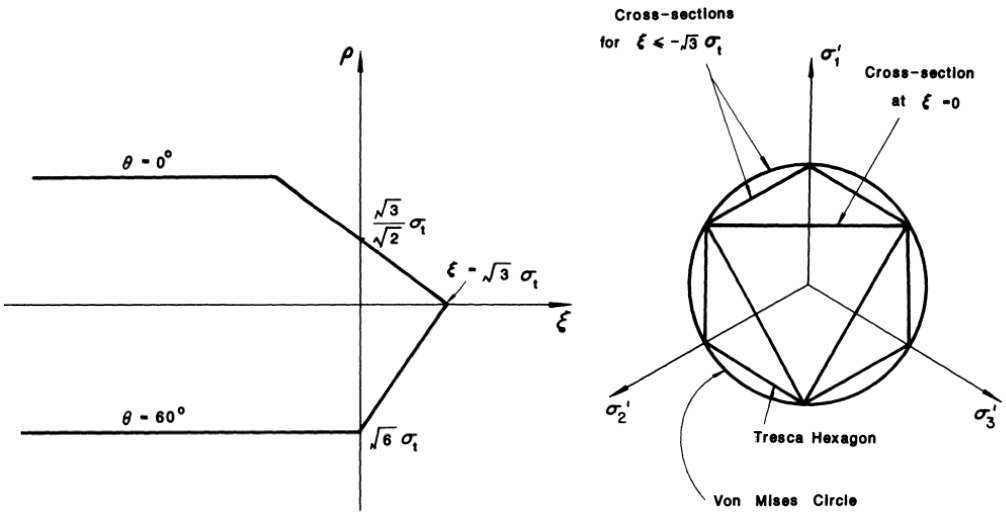

(a) b)

Figure 3.1. Graphical representations of Tresca and von Mises criteria with Rankie's tension cut-off: (a) Meridian sections and (b) Cross sections in the deviatoric plane (Chen and Han, 1988)

When it comes to modelling the inelastic behaviour, Tresca and Von Mises criteria are among the most classic pressure-independent models. Their yield functions are, respectively, written as:

$$f_{\text{Tresca}}(\rho,\theta) = \sqrt{2}\,\rho\sin(\theta + \frac{1}{3}\pi) - k = 0 \qquad 0^o \le \theta \le 60^o \tag{3.4}$$

$$f_{\text{V-M}}(J_2) = {J_2}^2 - k^2 = 0 \tag{3.5}$$

As these models are incapable of modelling the behavioural difference in tension and compression, they are usually augmented by adding tensile cut-off surfaces to facilitate the modelling of geomaterials in tension. An example of such models with Rankie's criterion cut-off is illustrated in Figure 3.1, where meridian and cross sections of both Tresca and Von Mises criteria are plotted in different stress spaces. Even though such augmentations can help these models capture the material behaviour in tension and roughly in biaxial loading, they cannot faithfully reflect the material responses in compression due to their pressure-independent nature, as illustrated in Figure 3.1a.

To overcome this pressure-independence issue of criteria like Tresca and Von Mises, many studies have been dedicated to pressure-dependent yield surfaces, among which classic Mohr-Coulomb and Drucker-Prager criteria are probably the simplest and most widely-used models. The yield surfaces of these two models, illustrated in Figure 3.2, indicate different yielding states when compressive hydrostatic pressure (represented by $-\xi$) increases, as has

also been shown experimentally (Baud et al., 2004; Klein et al., 2001; Wong et al., 2001; Wong and Baud, 2012). In this regard, these models had obtained one step further towards modelling the compressive behaviour of quasi-brittle geomaterials. They, however, adopt linear and open yield surfaces (see Figure 3.2), while experiments clearly show nonlinear and closed yield loci, as illustrated in Figure 2.8. Furthermore, the yield loci of both criteria in deviatoric planes do not properly reflect the dependence on the Lode angle θ, which contradicts with the experimental observations (see Section 2.2.2 and Figure 2.9). These are two major drawbacks of the classic Mohr-Coulomb and Drucker-Prager criteria that motivate further studies (Grassl et al., 2002; Kang and William, 1999) to adopt a nonlinear $\xi - \rho$ relationship in the meridian plane and Lode-angle dependence within their yield formulations.

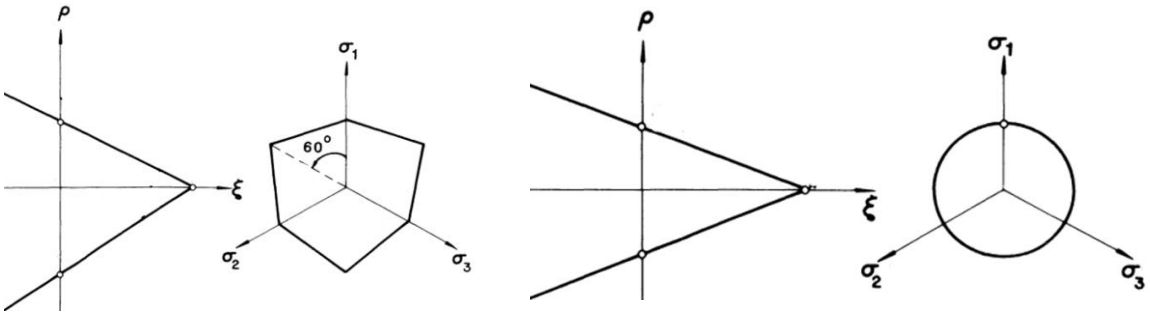

(a) (b)

Figure 3.2. Graphical representations of (a) Mohr-Coulomb criterion and (b) Drucker-Prager in the meridian plane and deviatoric plane (Chen and Han, 1988)

To avoid the open shape of the yield surface, which cannot properly reflect the behaviour of the geomaterials in compression, a "cap surface" can be added into the existing yield surface to handle the material under compression (Borja and Aydin, 2004; Grueschow and Rudnicki, 2005; Schultz and Siddharthan, 2005; Sfer et al., 2002). A more popular solution for this problem is to modify the yield function formulation, so that the initial yield surface has a closed shape. Under further loading, it gradually opens towards the compression direction: an example is illustrated in Figure 3.3. This approach was adopted in several studies for modelling the compressive behaviour of concrete and rocks (Borja, 2004; Imran and Pantazopoulou, 1997; Kang and William, 1999; Unteregger et al., 2015).

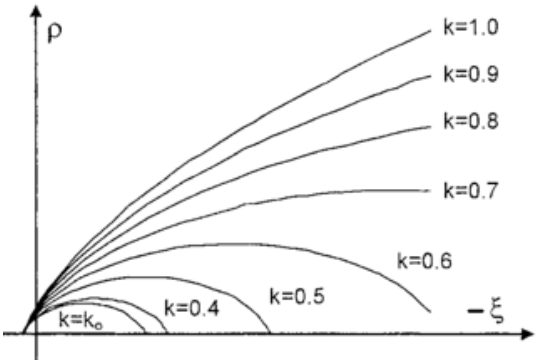

Figure 3.3. An example of the evolution of the closed yield surface in the meridian plane (Imran and Pantazopoulou, 2001)

Recently, with sufficiently extensive data sets from experiments in various loading conditions, more meticulous models with complex yield surfaces and evolution have been proposed (Chemenda and Mas, 2016; Das and Buscarnera, 2014; Jouanne et al., 2014; Liolios and Exadaktylos, 2017; Lu et al., 2016; Marinelli and Buscarnera, 2015; Navarro et al., 2010; Shen and Shao, 2016a; Spiezia et al., 2016), one of which is shown in Figure 3.4, as an illustration. Both nonlinear pressure-dependence and Lode-angle dependence, together with the material responses in compression are captured relatively well by such models. The sections of yield surface in different deviatoric planes, plotted in Figure 3.4, highlight that the model is also able to reflect the evolution of Lode-angle dependence with the increase of confining pressure, as previously addressed in Section 2.2.2.

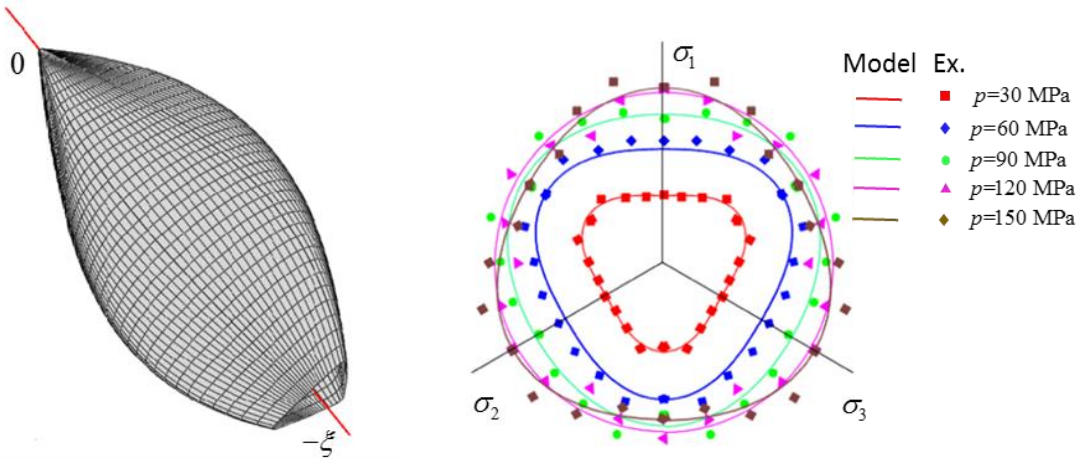

(a) (b)

Figure 3.4. Example of a recently developed initial yield surface: (a) Yield surface in principal stress space and (b) Comparison with experimental results in the deviatoric plane (Chemenda and Mas, 2016)

Even though models based on plasticity theory can successfully capture some of the material responses, such as irreversible deformation and strain hardening/softening in monotonic loading conditions, they are not favourable options when it comes to modelling quasi-brittle geomaterials. Since the plasticity theory emerges from solving metallic problems, where fracture is not a serious issue, the theory generally does not account for the effect of micro/meso-crack, as well as localisation bands. As described in Section 2.2.1, the initiation, formation and propagation of these factors are extremely important, causing the nonlinear behaviour of quasi-brittle geomaterials where pre-existing cracks are always present, even in rocks under natural conditions or freshly cast concrete. Therefore, the fracture-related aspects (e.g., stiffness reduction under unloading) and their underlying mechanism (i.e., crack formation and propagation) cannot be described solely by plasticity theory at this stage. This brings us to continuum damage mechanics, which characterises the fracture within the material as a progressive process of material breaking by which stiffness reduction can be described.

3.2.1.2 Elastic-Damage Models

Continuum damage mechanics (CDM), first proposed by Kachanov (see Lemaitre and Chaboche, 1990) and further developed by Rabotnov (see Lemaitre, 2012), has been proved to feature several superior characteristics over plasticity theory in modelling the fracture of materials. Due to the fact that the approach has a long history and has been well-documented in many studies (see Lemaitre, 1992; Voyiadjis et al., 1998), only its basic concepts and recent developments related to modelling quasi-brittle geomaterials will be addressed in this section.

The basic concept of CDM is to use a set of variables, termed damage variables, to reflect the degradation of the material elastic stiffness in a representative volume element (RVE) due to the progressive growth and coalescence of micro-cracks. As it is clearly impossible to describe the actual evolution of micro/meso-cracks explicitly via continuum-based modelling, the damage variable, in this case, is an averaged quantity to account for the behavioural heterogeneity due to the presence of cracks inside the material. As a result, the damage variable can be in the form of a tensor describing the stiffness reduction in multiple directions, or it can just be a scalar representing the overall deterioration in the whole RVE. While the tensorial representation of damage is more accurate in modelling the anisotropic nature of the material with the presence of cracks (see Maleki and Pouya, 2010; Shao and Rudnicki, 2000; Shao et al., 2006; Swoboda and Yang, 1999a, 1999b), it significantly

complicates the formulation and modelling process. On the other hand, even though the assumption of damage (or micro/meso- cracks) scattering uniformly in all directions used in scalar damage representation (see Addessi et al., 2002; Cauvin and Testa, 1999; Jirásek et al., 2004; Li and Ansari, 1999; Liu et al., 2016; Lyakhovsky et al., 2015) is not realistic, it has still been adopted widely among the engineering community due to its simplicity in formulation, numerical implementation and parameter identification (Burlion et al., 2000; Einav et al., 2007).

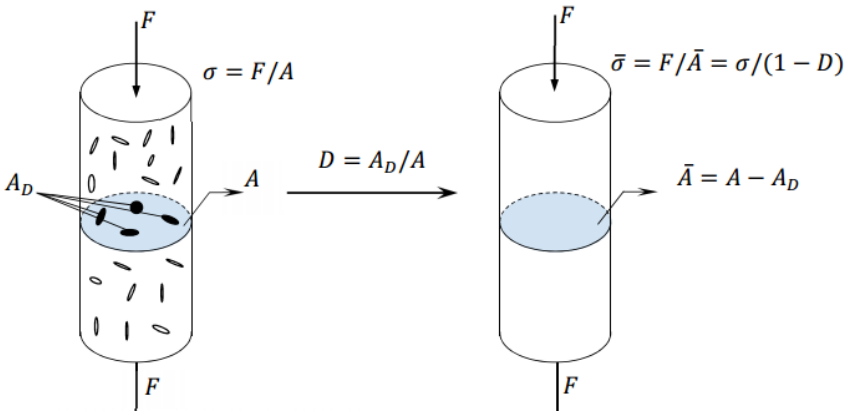

Figure 3.5. Concept of damage mechanics with scalar damage variable (Mir, 2017)

The conceptual idea of the CDM with scalar damage variable is illustrated in Figure 3.5 where the total area of damage due to micro-cracks presence is denoted by A_D out of original cross-sectional area A. The effective cross-sectional area can thus be defined as $\bar{A} = A - A_D$ and the damage variable is described as $D = A_D/A$. The effective stress, in this case, is calculated as:

$$\bar{\sigma} = \frac{F}{\bar{A}} = \frac{F}{A - A_D} = \frac{\sigma}{1 - D} \tag{3.6}$$

As the damage variable is defined independent of direction, the extension of the above equation to multi-axial stress state is straightforward and the following relationship holds:

$$\bar{\boldsymbol{\sigma}} = \frac{\boldsymbol{\sigma}}{1 - D} \tag{3.7}$$

where $\bar{\boldsymbol{\sigma}}$ and $\boldsymbol{\sigma}$ are the effective stress and stress in Voigt notation form, respectively.

Application of the strain equivalence hypothesis (Lemaitre, 1972) results in the state coupling between damage and elasticity straightforwardly as:

$$\boldsymbol{\sigma} = (1 - D)\mathbf{C}\boldsymbol{\varepsilon} \tag{3.8}$$

where $\mathbf{C}$ is the stiffness matrix of the material in the elastic range and $\boldsymbol{\varepsilon}$ is denoted for the strain vector of the RVE. With this equation as the basic, an evolution for the damage variable is needed to complete the constitutive equation. The most popular approach is to describe the damage evolution as a function of the effective stress or strain (Cauvin and Testa, 1999; Jirásek et al., 2004; Krajcinovic, 1985; Liu et al., 2016; Mazars and Pijaudier-Cabot, 1989; Peerlings, 1999; Simo and Ju, 1987). Few others formulate this evolution in association with the progressive change of a function, termed damage loading function, with its consistency conditions (Addessi et al., 2002; Comi and Perego, 2001; Comi, 2001), or just a decreasing function (Li and Ansari, 1999). Nonetheless, the above-mentioned descriptions of the damage variable are not always directly related to its geometrical definition in Eq. (3.6). In fact, in continuum constitutive modelling, physical representation of damage variables is not straightforward, as it totally depends on the identification of the microscopic mechanism underlying the observed macroscopic response (DeSimone et al., 2001). This is an intrinsic shortcoming of damage mechanics-based models.

From a modelling point of view, because continuum damage mechanics can successfully reproduce the softening responses of the material without the presence of irreversible deformation, it can be used to analyse structures under monotonic loading with certain levels of accuracy. However, because continuum-based damage models are usually based on a quantity termed fracture energy G_F to establish the stress-strain relationship, they usually encounter the issue of non-uniqueness of the model parameters. As illustrated in Figure 3.6a, the parameters that can produce the same amount of specific fracture energy g_F (calculated from fracture energy G_F and specimen length) are not unique. This means that for any given set of material properties (i.e., strength, strain with respect to stress peak) and input specific fracture energy g_F, there are many possible parameter sets that can produce different stress-strain relationships with the same area under the curves, two of which (the orange and green areas) are illustrated in Figure 3.6a. This issue is evident in several damage-based models (Borino et al., 2003; Comi and Perego, 2001; Comi, 2001; Jirásek et al., 2004) and hampers the physical meaning of such models.

In addition, even though the above-mentioned pure damage models can reflect the macro stress-strain responses in tensile and compressive loading cases, they did not pay proper attention to other observed macroscopic features of the material behaviour (i.e. Lode-angle dependence, size effect, or mixed-mode loading). Furthermore, since damage theory considers fracture as the only mechanism for energy dissipation without the participation of

plastic deformations, they fail to capture the irreversible deformation of the material. As a result, they tend to overestimate the stiffness degradation, as illustrated in Figure 3.6b, in comparison with the experimental results presented in Section 2.2.1 (see illustration in Figure 2.3 a)

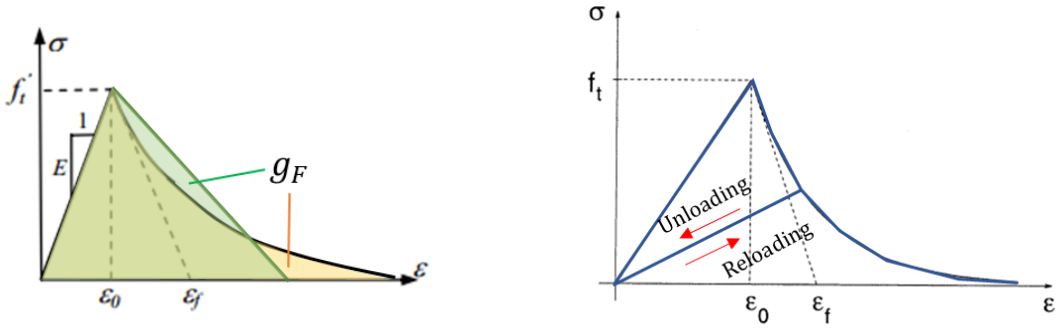

(a) (b)

Figure 3.6. Exponential stress-strain softening law: (a) With associated specific fracture energy and (b) Under unloading-reloading (Jirásek and Patzák, 2002; Jirásek et al., 2004)

This brief conclusion, together with the remarks drawn about plasticity models in the preceding section, points out that neither the elastoplastic approach nor the elastic-damage model are capable of capturing the behaviour of quasi-brittle geomaterials on their own, let alone the underlying mechanism. Therefore, the coupling between damage and plasticity comes into the picture of quasi-brittle geomaterials modelling as a potential approach to reflect essential macroscopic features of the material. The literature review in this chapter will thus continue with this damage-plasticity approach in the succeeding section.

3.2.1.3 Coupled Elastoplastic-Damage Models

As addressed in previous sections, during the course of loading, irreversible deformations always take place in quasi-brittle geomaterials simultaneously with material deterioration. This is because of the aggregates-mortar de-cohesion, mortar/grain crushing and fragments sliding happening inside cracks or localisation bands. The important results of these changes at microscopic level are residual strains and stiffness reductions observed in the macroscopic behaviour of the material. Therefore, coupling between damage and plasticity is necessary to capture these important features of the material. This is illustrated in Figure 3.7, where a coupled damage-plasticity approach balances the extreme effects of damage and plasticity theories and is able to capture the stiffness reduction together with residual strains. Owing to this advantage, a large number of coupled damage-plasticity

models have been proposed over the past few decades for modelling the behaviour of quasi-brittle geomaterials.

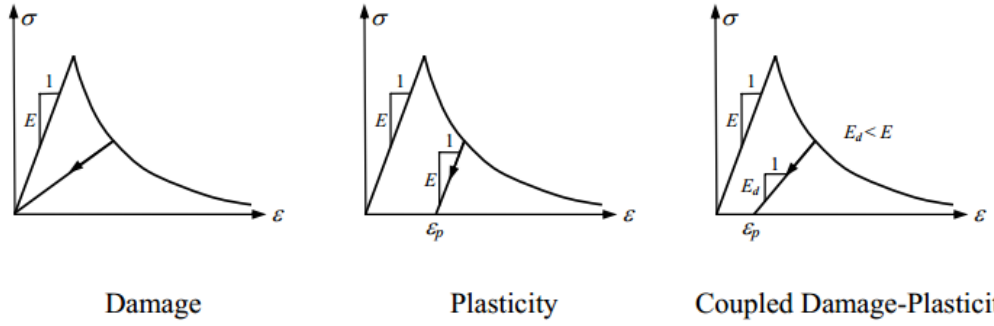

Figure 3.7. An example of uniaxial stress-strain constitutive behaviour to illustrate the advantage of coupled damage-plasticity over damage and plasticity models (Nguyen, 2005)

To construct a coupled damage-plasticity model, a common approach is to control the evolution of damage and plastic strain variables by two separate loading functions (Cicekli et al., 2007; Contrafatto and Cuomo, 2006; Grassl et al., 2013; Nguyen and Korsunsky, 2008; Nguyen et al., 2015; Parisio et al., 2015; Salari et al., 2004; Shao et al., 2006b; Voyiadjis et al., 2008; Zhu et al., 2016). The simultaneous evolution of damage variable and plastic strain is coupled through the governing stress-strain relationship, whose typical formulation is given as:

$$\boldsymbol{\sigma} = (1 - D)\mathbf{C}(\boldsymbol{\varepsilon} - \boldsymbol{\varepsilon}^{\mathrm{p}}) \tag{3.9}$$

where $\boldsymbol{\varepsilon}$ and $\boldsymbol{\varepsilon}^{\mathrm{p}}$ are, respectively, the total and plastic strain of the RVE. The damage evolution can be an implicit function of the plastic strain (e.g. Grassl et al., 2013; Parisio et al., 2015), or the material strength is a decreasing function of the damage variable (e.g. Salari et al., 2004). In these cases, the corresponding internal variables (i.e. damage and plastic strain) do not depend on each other explicitly but they are connected and interact with each other implicitly. This is the key for the coupling of damage and plasticity with separate loading functions in such models. Even though separating the evolution of damage and plasticity gives these models certain flexibility over controlling their contributions towards the dissipated energy, the numerical implementation, in this case, is unnecessarily complicated, as extra iterations are needed to update variables and other quantities following two separate loading functions consistently.

Another approach for the coupling damage-plasticity, adopted in several studies (Burlion et al., 2000; Contrafatto and Cuomo, 2006; Einav et al., 2007; Krätzig and Pölling, 2004; Lee and Fenves, 1998; Ma et al., 2016; Mir et al., 2018; Nguyen and Einav, 2010;

Paliwal et al., 2017; Pouya et al., 2015; Vu et al., 2017; Zhu, 2017), is to define only one loading function to control the dissipation process. In most of the cases, the loading function is the plastic yield function, which evolves from the initial yield to final failure with a hardening parameter related only to plastic deformation. As a result, *ad hoc* assumptions are usually needed to describe the interaction between damage evolution and plastic strain (see Paliwal et al., 2017; Zhu, 2017). Alternatively, it can be a unified damage-plasticity loading function with the explicit presence of damage variable in the formulation (see Arash Mir et al., 2018; Paliwal et al., 2017). In these cases, the evolution of the loading function, whether it is in closed or open shape, is directly governed by both plastic deformation (e.g. via effective plastic strain) and damage variable as illustrated in Figure 3.8. The evolution of all internal variables, in this case, can be controlled by the consistency condition of the unified loading function and thus would minimise the use of *ad hoc* assumptions.

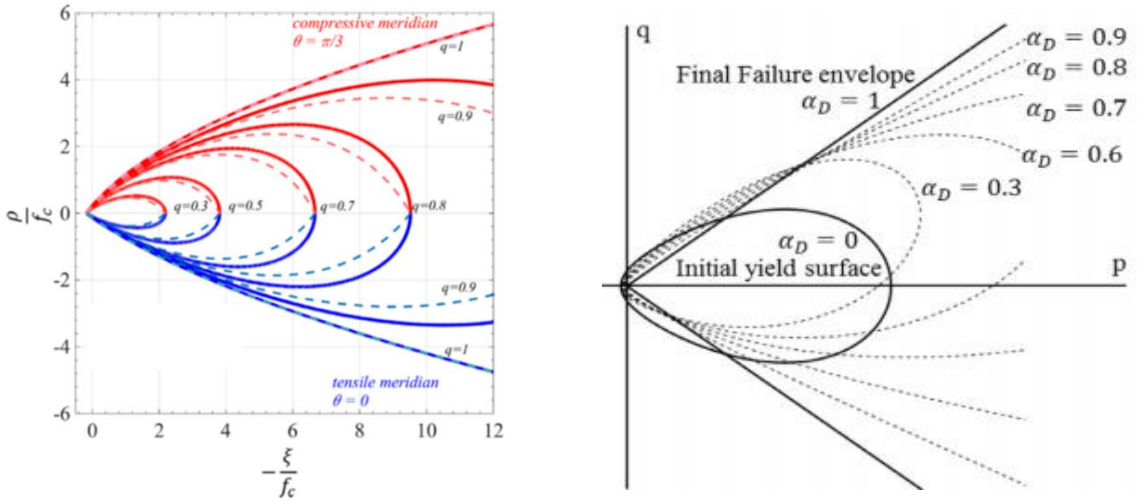

(a) (b)

Figure 3.8. Examples of evolution of unified damage-plasticity loading function in the meridian plane: (a) Model by Paliwal et al., (2017) and (b) Model by Mir et al. (2018)

Even though the coupled damage-plasticity approach is superior in terms of capturing the stiffness reduction and irreversible deformation compared with damage or plasticity on their own, it still suffers from serious limitations as a pure continuum approach. As addressed in the previous chapter, it is clear that the failure of quasi-brittle geomaterials is always accompanied with the formation and development of cracks or localisation bands. Once they appear within the material body, the deformation, anisotropy and behaviour of the localisation zone are totally different from those of the surrounding material. As a result, averaged quantities such as macro stress and strain are not adequate representations to

describe the volume element when localisation occurs and using them for analysing post-localisation behaviour of quasi-brittle geomaterials is inappropriate.

A direct consequence of using macro stress and strain alone to model such materials is the phenomenological nature of the loading function in fitting the yield loci of the materials. As the initial yielding in these continuum models is governed by the macro loading criteria (i.e., either separate damage/plastic or unified damage-plasticity loading functions), the yield states of the material only depend on their actual formulations, which are functions of stress (and sometimes damage variable). However, the macro stress alone cannot describe the behaviour and anisotropy of the localisation band, which is the main mechanism for the Lode-angle dependence of the yield loci, as addressed in Section 2.2.2. As a result, the formulation of the loading functions in these models is usually modified phenomenologically so that the predicted yield surfaces fit with the yield loci obtained from experiments. Specifically, expressions of the yield functions contain the third stress invariant J_3 (or alternatively the Lode angle parameter θ) in order to capture the Lode-angle dependence (see Chemenda and Mas, 2016; Grassl et al., 2013; Paliwal et al., 2017; Veiskarami and Tamizdoust, 2017). In a similar manner, the first stress invariant I_1 (or alternatively the hydrostatic pressure p or ξ) is added into the formulation of the loading function to make the resultant yield surface become pressure-dependent (see Červenka and Papanikolaou, 2008; Grassl and Jirásek, 2006; Grassl et al., 2013; Paliwal et al., 2017). Although providing good improvements to the constitutive behaviour, these treatments are usually of phenomenological nature due to missing the underlying intrinsic mechanism of the material failure. The characteristics of the yield loci, in this case, can be mimicked but the underlying mechanism leading to such features is still neglected. This, from a modelling point of view, is a shortcoming, as there are numerous characteristics of the material that need to be reflected and it is not rational to capture them individually by phenomenological modifications. Instead, the model should capture the underlying mechanism and then those characteristics would naturally be featured as consequences.

Furthermore, with the presence of cracks, continuum models using solely macro stress and strain could not capture the localised failure of the material properly. At constitutive level, these models assume that the material behaviour, described by stress, strain and internal variables such as plastic strain and/or damage is homogenous throughout the whole material domain, as illustrated in Figure 3.9a. This means that the fracture, represented by a scalar damage variable in most of the existing damage-plasticity models, is the same in all

directions and locations of the material. This completely ignores the presence of the localisation band (i.e. the shear band in this example) and its anisotropic behaviour. Therefore, the localised failure and its consequences (see Section 2.2) cannot be reflected at constitutive level by such continuum models.

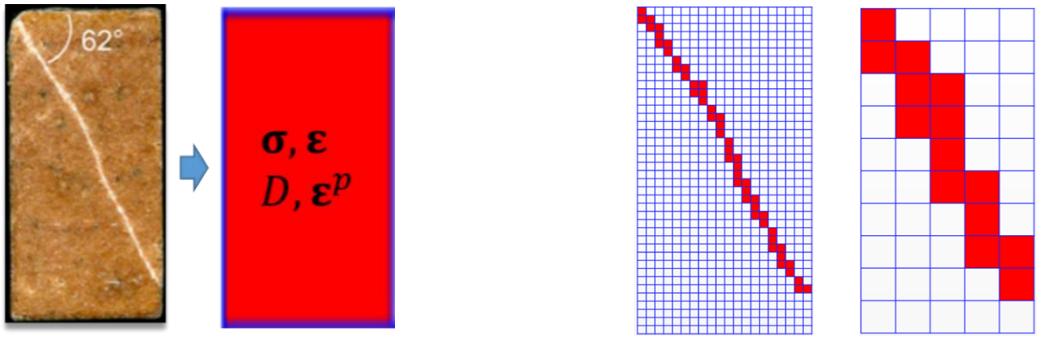

(a) (b) (c)

Figure 3.9. (a) An illustration of modelling using a continuum constitutive model and (b-c) Illustration of the dependence of the localisation band on mesh size

With the help of Finite Element Analysis (FEA), even though these continuum models can reflect such localisations (see Červenka and Papanikolaou, 2008; Grassl et al., 2013; Jirásek and Patzák, 2002; Pouya et al., 2015; Unteregger et al., 2015), they still could not capture the underlying mechanism and consequently evoke more issues. For illustration purposes, let me assume that the specimen in Figure 3.9a is now simulated by a continuum model that correctly predicts the crack path with a series of elements, denoted in red as illustrated in Figure 3.9b. As shown in the Figure, a series of homogenous "yielded" elements forms a band of elements across the problem domain, which plays the role of the localisation band observed in the specimen. Elements in this band, together with the surrounding "un-yielded" elements, create a system resembling what truly happens to the specimen in reality. In this sense, the model is capable of capturing the overall stress-strain responses and the failure mode exhibited by the specimens. However, in this case, the thickness of the localisation band in the model totally depends on the size of the element used in the simulation. This is illustrated in Figure 3.9b and c, showing that the width of the localisation band in the model significantly increases with the increase of mesh size. It is clear that the contribution from the localisation band towards the specimen responses would change accordingly. As a consequence, the results from such simulations would vary in accordance with the mesh size, hence its mesh-dependence.

At the other end of the spectrum, in the case of mesh refinement, the inelasticity and dissipated energy of the localisation band would unphysically approach zero. This phenomenon is more evident in tension tests where softening is more dominant. The observed failure mode of the material, in this case, is a thin crack, illustrated by a red line perpendicular to the load in Figure 3.10a. For the sake of illustration, let me assume that this problem is simulated by a simple bi-linear softening model whose stress-strain relationship in 1D is described in Figure 3.10b, where E_0 is the elastic modulus and E_t is the post-peak softening modulus. During the modelling, one of the elements, illustrated by a red element in Figure 3.10a, would be the "yielded" location where inelastic softening takes place, while the rest of the elements undergo elastic unloading. As the stress-strain relationship is unique and the material behaviour is now governed by this yielded element, the force-displacement curve obtained from the model (i.e., $P - \delta_n$) is not unique but dependent on element width L. For example, under the same strain increment, $\Delta\varepsilon_e$, in the yielded element, the resultant displacement increment for this element from the model, $\Delta\delta_e = \Delta\varepsilon_e L$, varies with respect to the element size L. Since inelastic loading is assumed to take place only in this yielded element, while the rest are under elastic unloading, the displacement of the whole specimen, δ_n, is governed by the displacement of this yielded element and varies with respect to element size L, as illustrated in Figure 3.10c. Under mesh refinement (i.e., $L \to 0$), the stress-strain response becomes more brittle as the displacement increment approaches zero (i.e., $\Delta\delta_e \to 0$). This change leads to an incorrect decrease of the dissipated energy, as illustrated in Figure 3.10c. From a physical point of view, this mesh-dependence and vanishing of resultant energy are serious limitations when using classical continuum models for modelling quasi-brittle geomaterials. For this reason, together with the above-mentioned limitations, the use of pure continuum models for capturing the failure of quasi-brittle geomaterials is considered to be inadequate (Comi, 2001; Jirásek and Bažant, 2002).

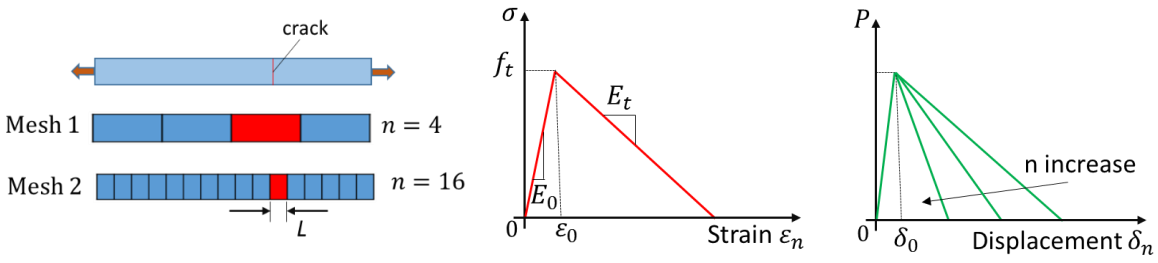

(a) (b) (c)

Figure 3.10. Illustration of using continuum models for a tension test: (a) Failure mode and different meshes used for the modelling example; (b) Bi-linear stress-strain relationship used in modelling example and (c) Example of model predictions with mesh refinement

To alleviate the mesh-dependence issue described above, additional phenomenological treatments are usually needed in the analysis of BVPs, as remedies for the lack of intrinsic localised failure mechanism. These include regularisations based on the smeared crack approach (Cervera and Chiumenti, 2006; Grassl et al., 2013; Schreyer et al., 2006; Tran et al., 2015), viscous enhancements (Das et al., 2014; Loret and Prevost, 1991; Oka et al., 1995; Tengattini et al., 2014; Zhao et al., 2018) or nonlocal enrichment (Adachi et al., 1991; Bažant and Gambarova, 1984; Eringen, 1972; Nguyen and Korsunsky, 2008a; Xenos et al., 2015). Without going into details of such regularisations, which are not the focus of the research, it can be seen that these regularisations are of external treatments, used on top of the proposed models to compensate for the lack of localised failure mechanism. In other words, these regularisations are not intrinsic characteristics, but external factors added into the models to help them obtain desired features (i.e., the size effect or mesh-independence). From a modelling point of view, even though the merits, along with success of the above models in capturing stress-strain responses are unquestionable, using such external treatments is not a natural/good approach for material modelling and sometimes evokes more issues that complicate the modelling. For example, in nonlocal approaches, as the constitutive behaviour of a material point is linked with those in neighbouring points to smooth out the deformation across a localisation zone, discretisation resolution (e.g., the finite element size) must be below the thickness of the localisation zone to have sufficient regularisation effects. The use of the smeared crack approach in continuum modelling causes unphysical snapback when certain conditions are met (see Nguyen et al., 2014).

Another approach to remedy the lack of localised failure mechanism in continuum models is to employ element-based enhancements for the analysis of boundary value problems (BVPs). The main theme of these approaches is modifying the formulation (i.e., interpolation functions, nodal kinematic relationship, or discretisation scheme) of the conventional finite element method (FEM) to describe the discontinuity/localisation band explicitly in the computing mesh when solving BVPs. These include the eXtended Finite Element (Borja, 2008; Samaniego and Belytschko, 2005; Sanborn and Prevost, 2011; Wells and Sluys, 2000), Enhanced Assume Strain (Borja, 2000; Foster et al., 2007; Larsson et al., 1996) or the Strong Discontinuity Approach (Dias et al., 2018a, 2018b, 2016; Dias-da-Costa et al., 2009; Gálvez et al., 2013; Guzmán et al., 2012; Lloberas-Valls et al., 2016; Oliver, 1996; Oliver et al., 2015, 2002; Planas et al., 2016; Reyes et al., 2009; Suárez et al., 2018). Although the importance and success of these models in capturing stress-strain responses

are unquestionable, explicit representations of cracks/localisation bands and/or enrichments to interpolation functions usually complicate the modelling due to extra degrees of freedom or effort to handle the enrichment in the interpolation. In addition, as these approaches include enhancements involving numerical discretisation in the formulations, they cannot capture the localised failure at the constitutive level. They are also bounded to conditions of the spatial discretisation size with respect to the width of the localisation band, which is usually one order of magnitude lower than the specimen size. This makes the extension of such models to cases involving complex crack patterns such as multiple branching/intersecting fractures become cumbersome and difficult compared with continuum-based modelling, which is the focus of this study.

3.2.2 Micromechanics-based approach for quasi-brittle geomaterials

Since the formulation with solely averaged stress and strain as descriptive quantities is not adequate to describe the behaviour of quasi-brittle geomaterials, advanced continuum models, termed micromechanics-based approaches, have been developed to overcome this drawback of classical continuum models. The main theme of this approach is to incorporate or mimic micro-scale behaviours of the material, with the aim of capturing its real responses at macro-scale. For that purpose, traction-displacement relationships are usually added into the constitutive equations alongside the conventional stress and strain to represent the inelasticity inside the micro-cracks incorporated in these models. This helps them overcome the drawback of the classical continuum model, as addressed in the previous section. The idea of incorporating the behaviour of cracks into the constitutive model formulation to capture the failure of geomaterials is not actually new (see Budiansky and O'connell, 1976; Kachanov, 1992) but at that time they were mostly at conceptual stage with limited validations against experimental data. The idea has been recently picked up again in several studies with different levels of complexity and success in modelling quasi-brittle geomaterials.

The most popular approach for the formulation of micromechanics-based models is to describe the failure of the representative volume element (RVE) through assembling of numerous weak planes in all directions with their own constitutive behaviour. Following this approach, a series of models with different names has recently been proposed for various geotechnical problems. These include micro-damage models (Shen and Shao, 2016b; Xie et al., 2012, 2011; Zeng et al., 2015; Zhu and Shao, 2015), multilaminate models (Galavi and Schweiger, 2010; Sadrnejad and Shakeri, 2017; Schädlich and Schweiger, 2013; Schweiger

et al., 2009), microplane models (Bažant and Caner, 2014; Caner and Bažant, 2013; Chen and Bažant, 2014; Ghadrdan et al., 2015; Li et al., 2017; Zreid and Kaliske, 2016) and some other models (Chang and Yin, 2009, 2010, 2011; Fang et al., 2017; Misra and Poorsolhjouy, 2016; Misra and Yang, 2010; Yin and Chang, 2013; Yin et al., 2014). In these models, the micro-cracks are considered either to have particular shapes and thicknesses (Shen and Shao, 2016b; Xie et al., 2012, 2011; Zeng et al., 2015; Zhu and Shao, 2015) or to be shapeless and simply formulated as contacts (Caner and Bažant, 2013; Li et al., 2017; Misra and Poorsolhjouy, 2016; Yin and Chang, 2013; Yin et al., 2014), as illustrated in Figure 3.11, but the key factor that is described consistently in such models is the relationship between the force/traction and the displacement/strain across the cracks or contacts.

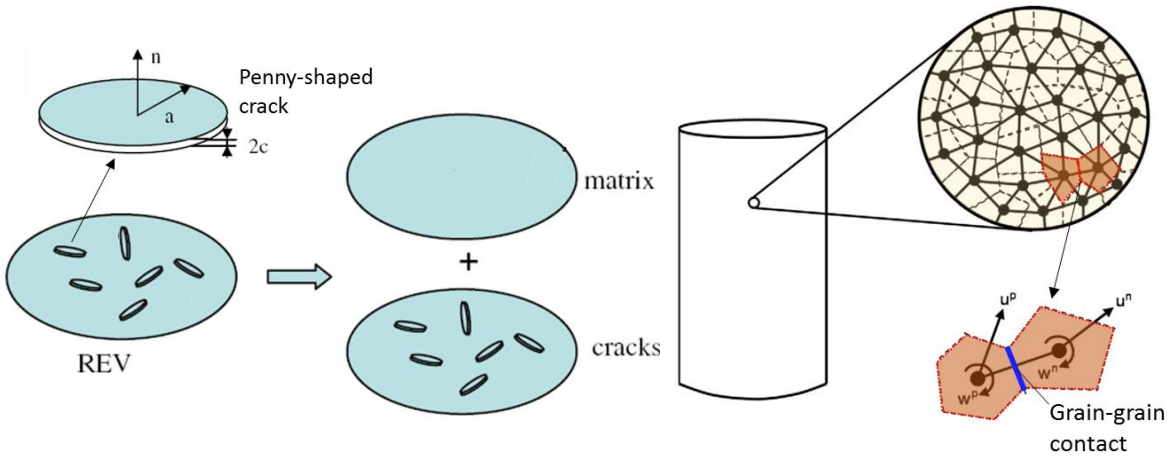

(a) (b)

Figure 3.11. Conceptual ideas of typical micromechanics-based models: (a) Micro-damage models with penny-shaped cracks (Xie et al., 2012) and (b) Model based on contact connections (Misra and Yang, 2010)

The basis for the model development here is that the macroscopic behaviour of materials is acquired as a sum/combination of local behaviour at all pre-existing or loading-induced contacts via a homogenisation procedure. The main difference between these groups of models lies in the method of connecting the local and macro responses. In multilaminate models, microscopic strains are calculated from local constitutive relationships with microscopic stresses, obtained by projecting the macroscopic stress onto the contact surfaces. This type of formulation follows a static hypothesis where static equilibriums of the system, including the balance of forces between the micro- and macro-levels, are enforced. The recovery of macroscopic strain is then obtained by summing the microscopic strains in all of the local weak planes. On the other hand, micro-plane and micro-damage models employ a kinematic hypothesis, where microscopic stresses are determined from

microscopic strains projected from macroscopic strain onto local contact surfaces. The macroscopic stress is then formulated as a sum of such microscopic stresses. Over the years, the static hypothesis has been refined and modified by introducing an intermediate layer of particle clusters at mesoscale, from which the inter-granular force vector is calculated by minimizing an error function using the least squares approximation scheme. This scheme, termed best-fit hypothesis, has been adopted in several studies (Cambou et al., 2000; Misra and Poorsolhjouy, 2016, 2013; Nguyen et al., 2009, 2012c; Tordesillas et al., 2011) and has been proven to be more effective than the original static hypothesis.

These micromechanics-based models, even though can handle some complex loading conditions due to the inclusion of different weak plane orientations, still do not account for the mechanism of localised failure. Specifically, although they include the behaviour of cracks in the constitutive equations, these crack/weak planes are "uniformly distributed" in the volume element and the behaviour of all the cracks in a group (i.e., all those having the same orientation) are the same. This contradicts with the experimental observations addressed in Section 2.2.1, where the behaviour and deformation concentrate within a localisation zone. Therefore, these cracks cannot reflect the behaviour of a localisation band in a strong sense and thus the localised failure mechanism cannot be captured properly. As a result, they still rely on external regularisations (see Bažant and Caner, 2014; Caner and Bažant, 2013; Chen and Bažant, 2014; Galavi and Schweiger, 2010; Li et al., 2017; Sadrnejad and Shakeri, 2017; Schädlich and Schweiger, 2013; Schweiger et al., 2009) to capture the energy dissipated by the localisation zone and avoid mesh-dependence when solving BVPs. Similarly, several other micromechanics-based models developed recently (Cheng et al., 2016; Das et al., 2014; Qi et al., 2016; Tengattini et al., 2014; Zhao et al., 2018) also aim to enhance the model's performance based on diverse micromechanical processes, but they all ignore the localised failure mechanisms. Therefore, despite obtaining good results, they all fail to deliver a meaningful constitutive relationship once localisation occurs.

In addition, since the weak planes in these models are fictitious representations, there are no clear physical links or indicators as to how many of them should be included in the model to yield realistic material behaviour. Furthermore, they need contributions from as many orientations (directly proportional with the integration points) as possible to form the macro quantities (i.e., the stress and strain). The number of integration points in three most common integration schemes used in these models, including regular meshing based on

McLaren (McLaren, 1963), Gaussian integration (Bažant and Oh, 1986) and spherical harmonics (Sloan and Womersley, 2004), are illustrated in Figure 3.12. As analysed by Daneshyar and Ghaemian (2017), to obtain more accuracy, the number of integration points needed increases rapidly, from 32 points in the method based on McLaren to 122 points in Gaussian integration and 380 points in spherical harmonics integration. Such integration has to be performed in each quadrature point of every element, and for all the iterations of every load increment. On top of that, the internal variables of the local constitutive relationships of all planes need to be stored and updated in each step of the finite element implementation. Therefore, the computational cost for simulation of just a lab-scale specimen would be prohibitively high, let alone large-scale structure.

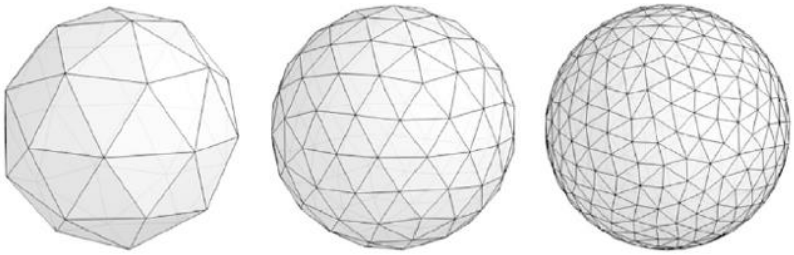

(a) (b) (c)

Figure 3.12. Distribution of integration points (located at the vertices) in different models: (a) McLaren, (b) Bažant and Oh, (c) Sloan and Womersley (Sloan and Womersley, 2004)

3.2.3 Critical review of current approaches and potential developments

It is clear that all approaches of modelling quasi-brittle geomaterials in the literature have their own advantages and limitations depending on the expectations and complexity of the problem under consideration. In addition, the choice of model is also subject to the expertise of users in material modelling. Nonetheless, given the importance of the localised failure mechanism in governing material responses, existing models have been assessed based on how faithful they can be in reflecting the mechanism from a constitutive modelling point of view. From these assessments, research gaps can be identified and further developments in modelling quasi-brittle geomaterials can be withdrawn.

As addressed in previous sections, the use of averaged stress and strain as descriptive quantities is not adequate to describe the behaviour of the volume element when localisation occurs. Therefore, due to their homogenous nature, pure continuum models, such as damage, plasticity or their coupling, suffer from several serious limitations in modelling quasi-brittle geomaterials. This has been discussed at length and illustrated in Section 3.2.1.

Micromechanics-based models, enhancing the constitutive structure with weak planes in different orientations, are more advantageous in describing the anisotropy of the materials, compared with pure continuum models. They all, however, fail to capture the localised failure mechanism properly at constitutive level, despite being computationally expensive. As a consequence, various forms of external regularisation techniques have to be employed on top of the model formulations and used separately from the constitutive equations to control the resultant behaviour and avoid mesh-dependence issues.

To overcome the disadvantages of micromechanics-based models, a few approaches have been proposed, by incorporating a localisation band into continuum constitutive equations, to obtain a balance between the computational cost and adequacy of reflecting the localised failure mechanism of the material at mesoscopic level. These include models proposed by Pietruszczak and co-authors (Haghighat and Pietruszczak, 2016; Moallemi and Pietruszczak, 2017; Moallemi et al., 2017; Mohammadi and Pietruszczak, 2019; Pietruszczak and Haghighat, 2015; Pietruszczak and Mroz, 2001; Pietruszczak et al., 2002), which focus on crack propagation, as well as the failure of quasi-brittle geomaterials and the model proposed by Gajo and co-authors (Gajo et al., 2004) emphasising on the localisation of granular materials. In such models, localisation band is explicitly described by additive local variables such as traction, displacement jumps besides macro stress and strain. The behaviour of the localisation band, in these cases, is linked with the overall responses of the material by a kinematic enhancement, which represents the high strain gradient of deformation inside the band and the traction continuity which reflects the static equilibrium of the macro stress versus the traction on the localisation band. By incorporating a localisation band into the constitutive formulations, these models are able to provide an adequate description of the material with underlying localised failure mechanism, while maintaining a computationally simple structure with a few variables and parameters. However, a strong basis for the development of constitutive models that can capture a wide range of behaviour under different loading conditions was not addressed in these models. Both kinematic enhancement and traction continuity conditions, being the backbones of such models, should be derived from a more rigorous theoretical background, instead of using assumptions which, in principle, weaken the consistency and robustness of the model. In addition, although the regularisation effects and crack propagations were satisfactory for benchmark problems, the use of a single localisation band required extra treatments, such as level-set method (see Haghighat and Pietruszczak, 2016; Moallemi and Pietruszczak, 2017;

Moallemi et al., 2017; Mohammadi and Pietruszczak, 2019; Pietruszczak and Haghighat, 2015), to control the crack propagation better and avoid stress-locking issues.

In another line of approach to capture the localised failure mechanism at constitutive level by enhancing the continuum modelling framework, the double-scale approach proposed by Nguyen and co-authors (Nguyen et al., 2012a, 2012b, 2014, 2016a, 2016b, 2017a, 2017b) was built on thermodynamics framework with employment of the work balance using the Hill-Mandel condition (Hill, 1963) that make the approach more consistent and reduce arbitrary assumptions. The approach was also formulated in a more generic form that can feature any law for the behaviour of a localisation band and thus can be used for any constitutive models for materials exhibiting localised failure. The key idea of the approach is to build a constitutive model from a representative volume element (RVE), featuring a localisation zone, as shown in Figure 3.13a, so that the constitutive descriptions can be enhanced directly with an additional kinematics mode and a corresponding length scale to describe the localised failure of materials correctly. As a consequence, the difference in behaviour of the inside and outside of the localisation zone under loading can be reflected, as illustrated in Figure 3.13b, even at a constitutive level. This means that the size effect, addressed in Section 2.2.3, can be captured naturally without requiring any regularisation techniques. As consequences of featuring the localisation band and its behaviour, the Lode-angle dependency, together with the change of responses and orientation of failure planes, can, in principle, be accounted for at the constitutive level by this approach. The robustness and capability of the approach in capturing some features of quasi-brittle geomaterials have been demonstrated for different loading cases (see Nguyen et al., 2016a, 2016b, 2017a, 2017b).

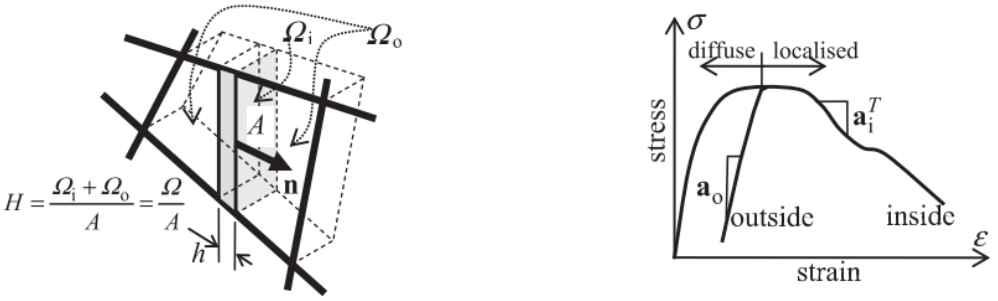

(a) (b)

Figure 3.13. Illustration of the double-scale approach: (a) Conceptual idea of a RVE featuring a localisation zone (shaded) and (b) Material responses inside and outside the localisation zone (Nguyen et al., 2012a).

Nonetheless, the current form of the double-scale approach still suffers from serious drawbacks and needs further improvements to move forward a robust and reliable model for quasi-brittle geomaterials. Despite being built on the rigorous theoretical framework of thermodynamics, the current models still have to employ additional relationships outside the thermodynamic formulation to connect all components together (see Nguyen et al., 2012a, 2014). In addition, in these studies, a sound and rigorous model to describe the behaviour of the localisation zone has been either missing or not properly explored at length (see Nguyen et al., 2016b, 2017a, 2017b). A good model, with physically meaningful parameters to represent the localisation band behaviour, is extremely important in the context of capturing the localised failure mechanism, given that the majority of inelastic responses take place within the localisation zone. More importantly, similar to those proposed by Pietruszczak and co-authors (Haghighat and Pietruszczak, 2016; Moallemi and Pietruszczak, 2017; Moallemi et al., 2017; Mohammadi and Pietruszczak, 2019; Pietruszczak and Haghighat, 2015), due to the fact that double-scale models only feature a single localisation zone, they inevitably suffer from stress-locking when solving boundary value problems. This drawback of the current double-scale modelling approach will be further addressed at length in Chapter 5, with appropriate numerical examples and demonstrations.

From the above analyses, it can be seen that the double-scale approach possesses advantageous features for capturing the localised failure mechanism exhibited by quasi-brittle geomaterials. Significant improvements including: (i) a more rigorous theoretical background for model development; (ii) an adequate sub-model to describe the behaviour of the localisation zone and (iii) an intrinsic enhancement within the constitutive structure to release the model from stress-locking problem, can be made to upgrade the current approach towards a robust and reliable model for quasi-brittle geomaterials. Once the structures and its components at constitutive level are validated and proven to be effective, the model can then be cast into a micromechanics framework to utilise its advantages and, at the same time, overcome its drawbacks in modelling the material. One of the possible improvements in this line is to describe the surrounding bulk material in the double-scale approach using micromechanics-based formulations of multiple weak planes to reflect the grain crushing associated with diffuse cracking under very high confining pressure levels. Another possible improvement is to implement the idea of multiple weak planes from micromechanics-based models to the current form of the double-scale model. Instead of incorporating one or two cracks/localisation bands into the constitutive equations, multiple cracks/localisation bands

of different orientations can be used in the model to capture more complex crack patterns such as multiple branching/intersecting fractures in large-scale structures. These points will be further addressed at the end of this study as future development of the proposed model.

3.3 Modelling of quasi-brittle geomaterials with fibre reinforcement

Despite the fact that fibre reinforced concrete (FRC) has been widely used in many contemporary engineering projects, constitutive modelling of such materials still lags behind despite the intensive growth in computational mechanics. This is mainly because of the high heterogeneity caused by randomly distributed short fibres, alongside the composite nature of concrete. Instead, several empirical models have been proposed for modelling the FRC due to the high demand for a tool to analyse and design its structural applications. On the other hand, several studies have focused on explicit modelling, where fibres and concrete together with its constituents are included in the numerical modelling explicitly. Even though the focus of the research is constitutive modelling, empirical and explicit modelling are also reviewed in this section to provide a more comprehensive view of the options available in the literature for modelling geomaterials with fibre reinforcement. As the majority of fibre reinforcements applied for quasi-brittle geomaterials are in concrete (i.e., fibre reinforced concrete), this is the main object of the review in this section.

Over the past decades, efforts have been made to capture the behaviour of FRC either by using statistical regression of experimental results for specific groups of tests (Abdul-Razzak and Mohammed Ali, 2011a, 2011b; Blanco et al., 2014; Slowik et al., 2006; Sousa and Gettu, 2006) or by exploiting fracture mechanics formulations of damage variables to account for the presence of fibres (Fanella and Krajcinovic, 1985; Li and Li, 2001) or merely by proposing empirical stress-strain responses (Barros and Figueiras, 1999; Ezeldin and Balaguru, 1992; Nataraja et al., 1999). Even though these models are simple and useful for structural modelling, they rely heavily on curve-fitting for the calibration of the model parameters, since the real failure mechanism governing the macro behaviour is missing. For example, in the work by Abdul-Razzak and Mohammed (2011a, 2011b), the material behaviour in different loading conditions (i.e., tension, compression and biaxial loading) is modelled separately by means of analytical formulations. For each loading case, empirical expressions of key quantities (e.g., strengths, critical strains, parameters controlling the stress-strain softening response), illustrated in red circles in Figure 3.14a, are obtained by regression analysis of existing experimental data. The formulation of compressive strength f_{cf} with respect to the fibre volume content V_f and aspect ratio L_f/d_f presented in Eq. (3.10),

for instance, is a result of regression analysis from various sources of experimental data (Bencardino et al., 2008; Mansur et al., 1999; Ezeldin and Balaguru 1992; Thomas and Ramaswamy, 2007).

$$f_{cf} = f_c + 0.33F{f_c}^{0.65} \tag{3.10}$$

where f_c is the compressive strength of plain concrete and $F = V_f L_f / d_f$ is termed the fibre reinforcing index. This equation, in this case, is then considered as robust and put to use if it fits well with the experimental results from another source, as illustrated in Figure 3.14b.

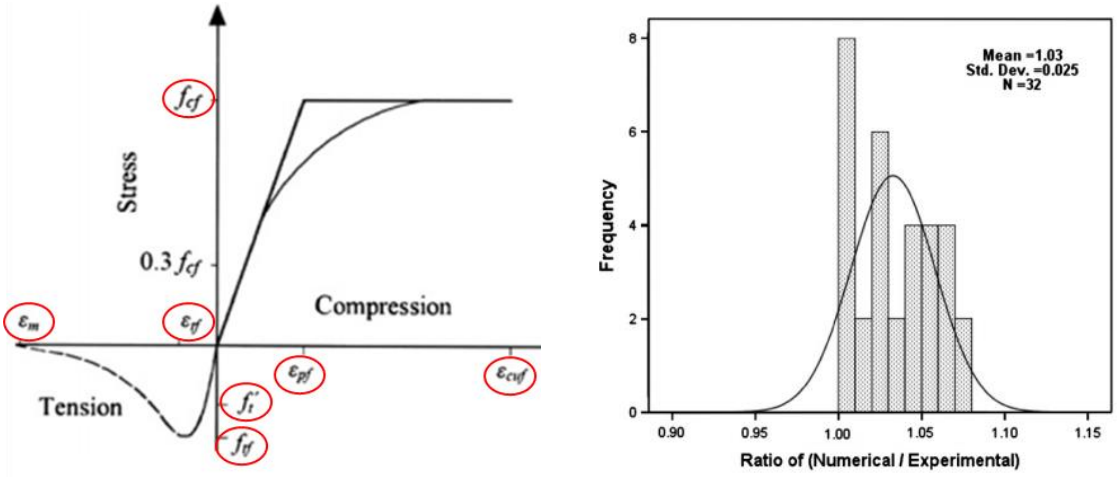

(a) (b)

Figure 3.14. An example of an empirical model: (a) Illustrations of some key quantities for regression analysis in tension and compression and (b) histogram of compressive strength (Abdul-Razzak and Mohammed, 2011b)

From a physical point of view, these models are of phenomenological nature, as they totally ignore the underlying mechanisms of failure addressed in Section 2.3. They thus rely heavily on the experimental data, which needs to be obtained for different loading conditions and for a particular composition and material properties of the FRC. As the number of tests is usually limited due to high costs or time restraints, there is always a risk of underestimating the failure load conditions or misinterpreting other important features of mechanical behaviour. Furthermore, the predictive capabilities of these models are bounded by the types of FRC and testing conditions from which they were built and calibrated.

Alternatively, discrete models (Alnaggar et al., 2019; Jin et al., 2016; Kang et al., 2014; Schauffert and Cusatis, 2011; Schauffert et al., 2012) can successfully capture both complex meso-structural changes and fibre bridging mechanism by explicit modelling of coarse aggregates and individual fibre responses with their embedded lengths and orientations. An

example of such models is illustrated in Figure 3.15a, where aggregates in concrete are represented by particles in different sizes, and randomly distributed fibres are described explicitly as separate subjects in the model (see Jin et al., 2016). The bonding between the aggregates and fibre-aggregate interactions can be reflected by cohesive-frictional models describing the traction-displacement relationship in these contacts, as well as the fibre slip and fibre pull-out. In a similar way, semi-discrete models account for the contribution of fibres by mapping the individual fibre's influence back to the finite mesh, using the partition of unity property of enriched shape functions (Radtke et al., 2010, 2011), immerse boundary formulations (Pros et al., 2012), strong discontinuity formulations (Octávio et al., 2016), morphological kinematical descriptors (Huespe et al., 2013; Oliver et al., 2012), fibre-aligned meshes with interface elements (Zhang et al., 2018) or meshless formulations (Yaghoobi and Chorzepa, 2015). In these cases, the effect of each fibre on the overall mechanical behaviour is reflected via a kinematic relationship with the numerical discretisation mesh behind. As a result, even though every fibre is explicitly described, the models do not need extra degrees of freedom for those fibres. However, in these models, extra care needs to be paid to meshing or interpolation schemes (see Octávio et al., 2016; Radtke et al., 2010, 2011) to facilitate the smooth kinematic connection between the fibres and the matrix. An example of these special requirements can be found in the model by Zhang et al., (2018) where the element edges in the mesh have to be aligned with scattering fibres so that the displacement of fibres can be linked with the nodal displacement on the mesh, as illustrated in Figure 3.15b. On the other hand, the approximation of displacement field from extended finite element method (Pike and Oskay, 2015a, 2015b) or adding additional degrees of freedom for the fibres (Cunha et al., 2012, 2011) is used to reflect the discontinuity of the material or fibre contributions. Even though these models have obtained relatively good results and are very useful for understanding the failure mechanism of FRC, it is clear that the high computational cost is a major drawback that impedes them from being applied extensively to analysing large-scale structures where hundreds of thousands of fibres are used.

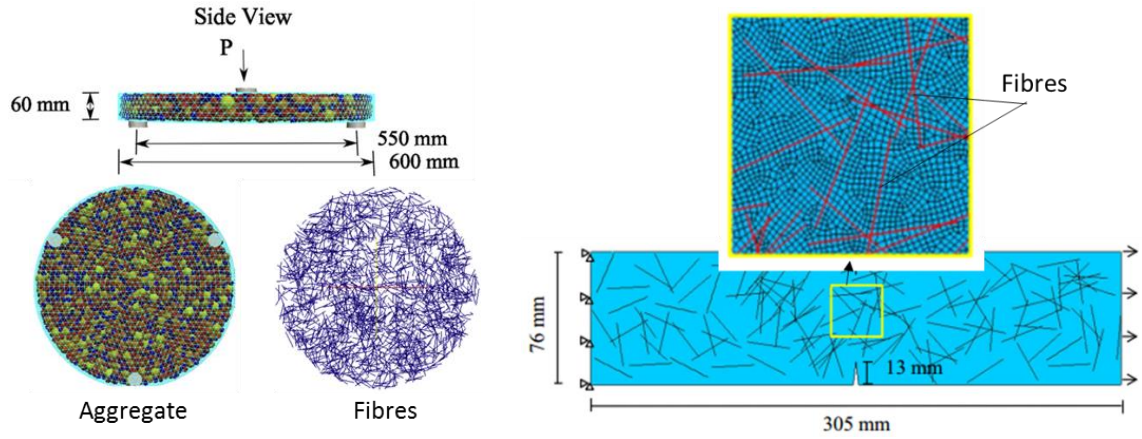

(a) (b)

Figure 3.15. An example of explicit modelling: (a) lattice model (Jin et al., 2016) and (b) fibre-aligned mesh model (Zhang et al., 2018)

Micro-mechanics based continuum modelling, on the other hand, opts for a balance between accuracy and computational expense by incorporating the failure mechanism into constitutive models to reflect the complex meso-structural changes while, at the same time, maintaining computational efficiency for structural simulations. In such models, the mechanical mechanisms of the fibre-matrix interactions are integrated at meso/macro-scopic level in a compact form where only the key variables (i.e. the fibre orientation distribution, volume fraction and fibre shape in general) are employed. The models hence are able to capture the macroscopic behaviour of the material with physical representations at the meso-scale, while still remaining simple and computationally efficient thanks to the continuum formulations. The incorporation of fibre bridging into constitutive models can be carried out via damage variables, which represent the stiffness degeneration of cracks bridged by fibres (Hameed et al., 2013; Lee and Simunovic, 2001; Lee et al., 2004; Nguyen and Khaleel, 2004; Peng and Meyer, 2000; Yan et al., 2019), or by superposition of stresses borne by fibres and that by matrix materials within a homogenisation framework with respect to their volume fractions (Diambra et al., 2010, 2011, 2013). Other models (Huang et al., 2016; Pasa Dutra et al., 2013) included the fibres' contribution to the material strength by using a static approach of limit analysis, implemented in the context of homogenisation scheme at meso-scale. Despite bringing insightful understandings, these studies focus only on the macro strength without full material responses with a constitutive relationship describing the mechanical responses from intact to ultimate failure is required.

Alternatively, the microplane models (Beghini et al., 2007; Caner et al., 2013), extended from a series of models for plain concrete, included the effect of fibre bridging by using multiple failure plane orientations with the implicit homogeneous deformation assumption. Because the differences in deformation between the inside and outside of cracks were ignored in these models, the strain in each crack had to be calculated by projecting the overall macro strain on that crack plane. Similar to the microplane models for plain concrete addressed in the previous section, the models required as many plane orientations as possible, with complex surfaces and evolution functions, to reflect the interaction between the crack and its surrounding intact bulk material correctly. On the other hand, the micromechanical constitutive models proposed by Mihai and Jefferson (Mihai and Jefferson, 2017; Mihai et al., 2016) took fibre bridging and aggregates interlocking in multiple directional microcracks into account by using Budiansky and O' Connell's solution (Budiansky and O'connell, 1976) for an elastic solid containing penny-shaped microcracks, in combination with the Mori-Tanaka homogenisation scheme for the interactions of the two phases. Similar to microplane models, the macro strain in these models was obtained by integrating the contributions from several directional microcracks. In addition, on each crack plane, two contact surface functions were employed for various crack states (i.e., open, interlocked and close crack states) to capture the tension/compression differences.

Even though the above-mentioned approaches obtained relatively good results for benchmark problems and have their own advantages, they still do not fully account for the failure mechanism of localisation/cracking, where fibre bridging takes place. As a consequence, in addition to being computationally expensive, these models still rely on regularisations on top of the models for the analysis of Boundary Value Problems (see Beghini et al., 2007; Mihai and Jefferson, 2017; Mihai et al., 2016). Essentially, the constitutive behaviour scales with the resolution of the discretisation used in the Finite Element Analysis (FEA), so that the requirement of the energy dissipation is met (i.e. cracked elements should reproduce an invariant dissipation with respect to the size of the element). This important length scale is either missing (Cunha et al., 2012, 2011; Pike and Oskay, 2015a, 2015b), or had to be obtained by phenomenological treatments of characteristic length from crack band theory (see Beghini et al., 2007; Mihai and Jefferson, 2017; Mihai et al., 2016) or by changing the model parameters for every analysis (Caner et al., 2013) to fit the fracture properties produced by the experiments.

3.4 Summary and discussion

Being the centre of any analysing and planning of civil engineering projects, numerical simulation, especially finite element analysis, has proven itself as a powerful tool to secure an economical and safe design for structural applications of geomaterials. The core of such simulations is a robust and stable constitutive model, establishing the relationship between the applied stresses and the resultant deformations (or vice versa) at a material point. The reliability and robustness of the constitutive model largely depend on how faithful it can be in reflecting the characteristics and intrinsic mechanism behind material behaviour. In the case of quasi-brittle geomaterials with and without fibre reinforcement, the localisation of deformation and behaviour within a band is identified as the key failure mechanism governing the material behaviour under several loading conditions (i.e., tension, shear, compression with low confinement and their mixed-mode loading conditions), as pointed out from the analyses presented in the previous chapter. The whole review of existing models in the literature for modelling quasi-brittle geomaterials with and without fibre reinforcement, in this chapter, was thus based mainly on this criterion to measure their advantages and limitations.

From a modelling point of view, the choice of model for a particular engineering application basically depends on the actual requirements and loading conditions. Simple models can still yield satisfactory results in relevant cases and more sophisticated models can have a larger scope of capability but at the same time require more computational expense. However, in any case, a model with rigorous theoretical formulations, accurately describing the macroscopic behaviour of the material, is always needed. Therefore, numerous studies, approaching the modelling issue in various aspects and angles, have been proposed over the past few decades. They all have their own advantages in certain aspects and loading cases but, at the same time, suffer from some limitations related to either their intrinsic nature, capability or numerical implementation.

Classical continuum approaches such as elastoplastic, elastic-damage models or their coupling can, at a certain level, capture the overall responses of the material in basic loading conditions. With the coupling of damage and plasticity theories, the simultaneous evolution of irreversible deformation and fracture within the material body can be captured fairly at a macroscopic level via finite element analysis. The models are thus capable of describing the stiffness reduction and residual strain, which are important features shown by the material in experiments. Nonetheless, as the underlying mechanism of localisation is totally ignored

in such models, many other significant aspects of material responses are not reflected properly. In particular, capturing Lode-angle dependences of the yield loci (i.e. the yield envelope) in these models relies on the formulation of the macro yield function, while it should be linked with the transition of the failure mode of the material, as presented in the previous chapter. In addition, as the inelasticity of the material is described by solely macro stress and strain, the difference in behaviour of the inside and outside localisation zones cannot be reflected at constitutive level. As a result, the results from such models are dependent on the mesh resolution and thus using external regularisation techniques (i.e., smear crack approach, non-local enrichment, viscous enhancements) on top of the constitutive equations is necessary to avoid this issue.

The micromechanics-based approach, on the other hand, could give a better representation of the material failure at micro-scale by using weak planes in different orientations to mimic the distributions and development of micro-cracks within the material body. Depending on the way these weak planes are incorporated into the model, several attributes of the material can be captured at different levels of success, while still maintaining the continuum structure that is straightforward for implementation in FEA. Such models thus boast many advantages over classical continuum models and their recent variants in capturing the behaviour of quasi-brittle geomaterials. Thanks to the inclusion of cracks/weak planes in the constitutive relationship, the interaction of cohesive-frictional resistance and fibre bridging effects in fibre reinforced geomaterials can also be fairly captured. These models, however, cannot reflect the localised failure mechanism to deliver a proper constitutive relationship once localisation occurs and they thus still rely on regularisation treatments to avoid mesh-dependence issues. A few advanced continuum models developed recently, by enhancing their constitutive equations with explicit contributions from the localisation zone, have obtained remarkable results in terms of capturing the localised failure mechanism. Since the localisation zone is featured as an intrinsic component of the model, several important features of the material (i.e., the size effect, Lode-angle, and pressure dependence) can be captured naturally. Nonetheless, these approaches still suffer from some limitations and need further improvements to become a better modelling approach. They either lack a rigorous theoretical basis for the inclusion of localised failure or are still far too expensive in terms of computational costs. On top of that, they either suffer from stress-locking issues or need crack-controlling techniques as external supplements to avoid stress-locking and obtain desired features/propagations.

In a nutshell, the review and analysis of models in the current literature show that even though numerous noteworthy models have been proposed, with different levels of complexity and applicability, there is still massive space for further development on the modelling of quasi-brittle geomaterials. Developed from previous studies, this research is dedicated to the advancement of a constitutive model with an emphasis on reflecting the localised failure mechanism of quasi-brittle geomaterials with or without fibre reinforcement. In the proposed model, the localisation band is incorporated directly into the constitutive equations with its own behaviour alongside the responses of the surrounding bulk materials. The proposed modelling structure is generic in the sense that it allows any type of constitutive sub-models for the bulk and localisation band, including classical continuum models or micromechanics-based models, to be used with minimal changes in the constitutive structure. In this research, a cohesive-frictional model is proposed to describe the behaviour of the localisation band, while linear elastic behaviour is employed for the bulk material. In addition, to obtain a more rigorous basis for the model's development, the constitutive equations will be cast within the generalised thermodynamics framework (Houlsby and Puzrin, 2000) with appropriate physical representations and connections among all components of the model. As a result, the localised failure mechanism can be captured even at constitutive level and no regularisation is needed on top of the model for solving BVPs. To overcome the stress-locking issues, the model is further improved by opening up the possibility of featuring a secondary crack/localisation zone in the structure of the constitutive model. This will later be proved to be a natural way to facilitate proper propagation of the fracture process zone and to deal with non-proportional loading conditions effectively. Due to the fact that localised failure is the key to the model development throughout this study, the scope of application for the proposed model is loading conditions where the localised failure is the dominant mechanism of the material failure (e.g., the tension, shear, compression under low confinements and their mixed modes). The descriptions and technical details of the proposed model will thus be presented in the following chapters, together with its numerical applications in numerous engineering problems, to demonstrate its capacity to capture localised failure, as well as the material's behaviour under various loading conditions.

CHAPTER 4

A cohesive-frictional model and application to modelling rock joints

4.1 Introduction

The literature review, presented in the preceding chapter, shows that a prerequisite for constructing any model that can capture localised failure at constitutive level, is a behavioural description of the crack/localisation band. This is also the case for the model proposed in this research, which incorporates localisation bands and its behaviour into the constitutive formulation at the very beginning of the model development. This chapter is thus dedicated to presenting the proposed cohesive-frictional model for describing the inelastic behaviour within the localisation zone. Inspired by the interactions of fracture and irreversible deformations taking place within the localisation zone, the proposed model is based on the damage-plasticity coupling, with a unified yield-failure function to govern the behaviour of the zone from initial yielding to final failure.

In a broader sense, apart from jointed rock mass, the developed cohesive-frictional model can be extended for modelling many other structures/problems in the engineering field where the cohesive and/or frictional zone plays an important role in the load-bearing capacity and progressive failure. These include the delamination of layers in laminate composites (Benzeggagh and Kenane, 1996; Colombo and Vergani, 2014; Grilo et al., 2013; Hao et al., 2012; Langdon et al., 2013; Panda et al., 2013; Sayer et al., 2010), fibre reinforced polymer (FRP) – concrete delamination (Biscaia and Chastre, 2018; Fang et al., 2016; Mazzotti et al., 2008; Nerilli and Vairo, 2018; Teng et al., 2007; Wu and Yin, 2003; Yazdani et al., 2019; Zhou et al., 2017), mortar-brick interaction in masonry wall (Dizhur and Ingham, 2013; Kaushik et al., 2007; Lotfi and Shing, 1994; Lumantarna et al., 2014; Mosallam, 2007) and adhesive bonds in cracks under hydro-mechanical coupling in hydraulic fracturing problems (Alm, 1999; Cammarata et al., 2007; Fidelibus, 2007; Petrovitch et al., 2014, 2013; Souley et al., 2015; Yeo et al., 1998). As a result, following pioneering work in the early 60s by Dugdale (1960) and Barenblatt (1962), numerous models have been devoted to encapsulating the complex behaviour inside these cohesive and frictional localisation zones. These models range from simple mathematical curves such as

bi-linear (Bazănt and Planas, 1998), exponential (Barenblatt, 1962; Cornelissen et al., 1986) or power law (Reinhardt, 1984), to much more complicated models focusing on several other crucial aspects, such as coupling damage and plasticity (Kolluri et al., 2014; Kumar et al., 2014; Pouya et al., 2015; Spada et al., 2009) and thermodynamic consistency (Dimitri et al., 2015; Guiamatsia and Nguyen, 2012, 2014; Parrinello et al., 2016; Simon et al., 2017).

Even though reviewing cohesive models for all the above-mentioned applications is outside the scope of this study and can be found in recent critical studies (Park and Paulino, 2011; Simon et al., 2017), it can be seen that thermodynamics-based formulation is a common approach to constructing a cohesive zone model (see Confalonieri and Perego, 2019; Guiamatsia and Nguyen, 2012, 2014; Mir, 2017; Modelling et al., 1993; Nguyen et al., 2017c; Parrinello et al., 2016). In these models, the traction (cohesive interactions) over fracture surfaces and the constitutive relationship (material tangent modulus) can be derived from potential functions within the framework of thermodynamics. Whilst these models would automatically comply with the First and Second Laws of thermodynamics and can also capture mixed mode responses under different loading conditions (e.g. both tension and compression in Guiamatsia and Nguyen, 2014), they are usually complicated. In other models (e.g., Camanho et al., 2003; Cornec et al., 2003; Högberg, 2006; Scheider and Brocks, 2003; van den Bosch et al., 2008; Yuan and Fish, 2016), the traction-separation laws and their coupling are often directly postulated. Despite the risk of being thermodynamically inconsistent, these models typically allow a straightforward modelling of mixed modes loading conditions and thus have been adopted for many practical applications.

The proposed cohesive-frictional model in this study features some advantageous characteristics in the modelling of localisation band in quasi-brittle geomaterials, which is the focus of this research. These include the simplicity in formulation of the traction-separation relationship, following the well-established damage-plasticity framework with a unified yield-failure function evolving gradually from the initial yield to final failure during the course of loading. In addition, the model covers mixed-mode behaviour in both tension and compression, which will be very beneficial for modelling a wide range of quasi-brittle geomaterials under both tensile and compressive loading conditions. The model also possesses an in-built fracture locus, which can naturally reflect the difference in fracture energies in mixed-mode loading conditions (i.e., mode I – tension/compression and mode II – shear). This helps the proposed constitutive model capture the failure of geomaterials in mixed mode conditions, such as triaxial compressive loadings where shear bands with

different inclination angles are observed, or four-point bending tests where a shear band under tension is the dominant failure mechanism. In conjunction with the model development, a procedure for calibration and identification of model parameters from standard experiments is proposed based on their physical representations. These parameters include those defining the elastic limit (i.e., the yield surface) and those controlling the evolution from yield to failure. For those controlling the evolution, not only fracture energies but also dilation behaviour are taken into account. Such calibrations are usually not addressed at length in several models in the literature, including the above-mentioned models.

In this section, the capability of the proposed cohesive-frictional model is validated against experimental results of jointed rock mass. The experiments of jointed rock mass have been chosen for validation purposes at this stage of the research due to the fact that such experiments mostly focus on the behaviour of the joint, which is similar to the localisation zone in quasi-brittle geomaterials; the main subject of this research. To serve this purpose, the proposed cohesive-frictional model is implemented into the double-scale modelling approach (Nguyen et al., 2012a; 2014), which incorporates a localisation band into the constitutive model. Even though this approach still suffers from some drawbacks and needs further improvement for modelling the failure of quasi-brittle geomaterials, it is quite suitable for modelling the jointed rock mass, where the behaviour of the localisation zone (i.e., the rock joint) is emphasised.

Via validation against experimental data, it is shown that the proposed cohesive-frictional model is able to capture the post-peak behaviour of rock joints, together with its dilation responses and other intrinsic features. This demonstrates the potential for using the model to describe the localisation zone, being the failure mechanism of quasi-brittle geomaterials. This work on jointed rock mass was published in the form of a journal paper (Le et al., 2017), which is presented in Appendix A. The cohesive-frictional model was later generalised to be suitable for formulation in 3D and was incorporated into the proposed constitutive model for quasi-brittle geomaterials (Le et al., 2018). Therefore, the majority of the content in this chapter is extracted from these two particular publications, with additional details and illustrations. It should also be noticed that, throughout the formulation process in this chapter, tensile stresses and dilative strains are considered to be positive.

4.2 A proposed cohesive-frictional crack model

As previously addressed in many studies (Antoni, 2017; Bažant, 1996; Landis et al., 2003; Reinhardt and Cornelissen, 1984), the development of cracks/localisation bands is always accompanied by irreversible deformations where friction plays the dominant role in contributing to the total dissipation energy. The importance of friction in the progressive failure of the material and the coupling between micro-cracking and friction in constitutive modelling has also been addressed at length in several studies by Nguyen and co-authors (Mir et al., 2015; Mukherjee et al., 2017; Nguyen and Houlsby, 2008b, 2008c; Nguyen and Bui, 2017; Nguyen et al., 2012b, 2012d). A model proposed to describe the behaviour of cracks/localisation bands should be able to capture both the stiffness reduction and irreversible/residual deformations, as well as their connections and interactions. Therefore, a cohesive-frictional model based on damage-plasticity coupling is proposed in this research. In general, the proposed model focuses on reproducing important features of the post-peak deformation and damage development of the fracture zone under mixed mode loading conditions in both tensile and compressive regimes. These include stiffness reductions, irreversible displacements, residual frictional strength at the failure state and the evolution of dilation under the effects of asperity degradation.

In the context of modelling quasi-brittle geomaterials by incorporating localisation bands into the constitutive equations, the traction - displacement jumps relationship is the primary target of formulation in the model. To serve this purpose, the cohesive-frictional model was built surrounding this relationship with a unified yield function describing the evolution of traction with respect to damage induced by displacement jumps across crack surfaces. In addition, the constitutive traction – displacement jumps relationship features the damage variables and plastic displacement jumps to strengthen the coupling of damage and plasticity observed in experiments.

In this section, the formulation of the cohesive-frictional model is presented with its details and explanations. Other important aspects of the model, including tangent stiffness and stress return algorithm of the proposed model, are also addressed, alongside the parameters identification and calibration. It is worth noting that the cohesive-frictional model and its variables, described in this section, are defined in the local coordinate system of the localisation band. They are thus transformed into the global coordinate system, where needed, using the transformation matrix **R** during the simulation with the constitutive model later.

4.2.1 Cohesive-frictional model description

Experimental observations, illustrated in Figure 4.1 show that the interlocking and cohesion of aggregates in a localisation band of finite thickness govern the behaviour of the material at macro-scale. From a modelling point of view, it is reasonable and practical to idealise the localisation band as a zero thickness zone (called crack hereafter for convenience) and describe its responses using a cohesive-frictional model. The description of the localisation band in this form naturally facilitates its integration into the constitutive model without any adjustment as shown later.

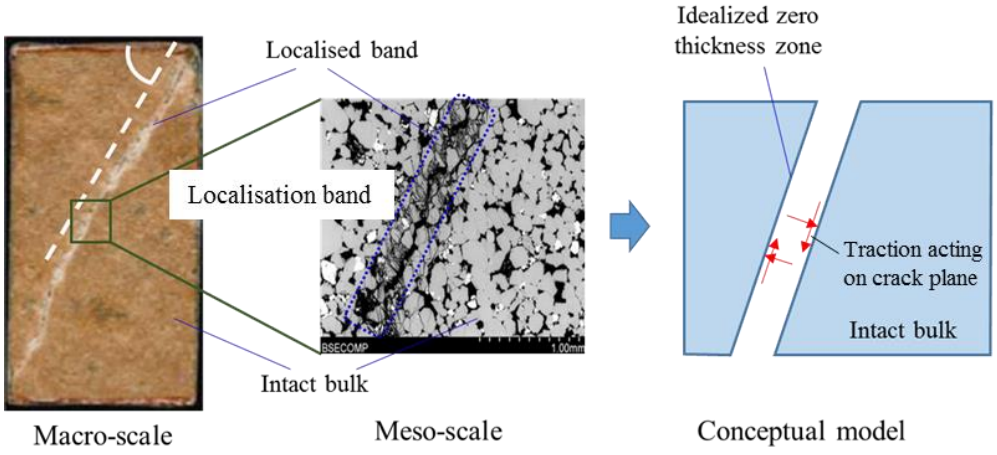

Figure 4.1. Experimental observation of localisation zone at Coconino sandstone (after Ma and Haimson, 2016) and the proposed conceptual model

To facilitate the coupling between damage and plasticity, the cohesive-frictional zone is assumed to comprise of two parts: the damaged part represented by damage variable D (i.e. $0 \leq D \leq 1$), and the undamaged part represented by $(1 - D)$. Following conventional notation, $D = 0$ represents the intact state of the material while $D = 1$ represents fully damaged material state where asperities are worn off and no cohesion left. The traction acting on two faces of the crack in the local coordinate system is denoted as $\mathbf{t}_{\mathrm{c}} = [t_n \quad t_{s1} \quad t_{s2}]^{\mathrm{T}}$, representing the normal and two shear tractions, respectively. These representations of damage variable and tractions are illustrated in Figure 4.2. Similarly, the displacement jump between the two crack faces, $\mathbf{u}_{\mathrm{c}}$, is decomposed into an elastic part $\mathbf{u}_{\mathrm{c}}^{\mathrm{e}}$ and an irreversible (plastic) part $\mathbf{u}_{\mathrm{c}}^{\mathrm{p}}$ as $\mathbf{u}_{\mathrm{c}} = \mathbf{u}_{\mathrm{c}}^{\mathrm{e}} + \mathbf{u}_{\mathrm{c}}^{\mathrm{p}}$.

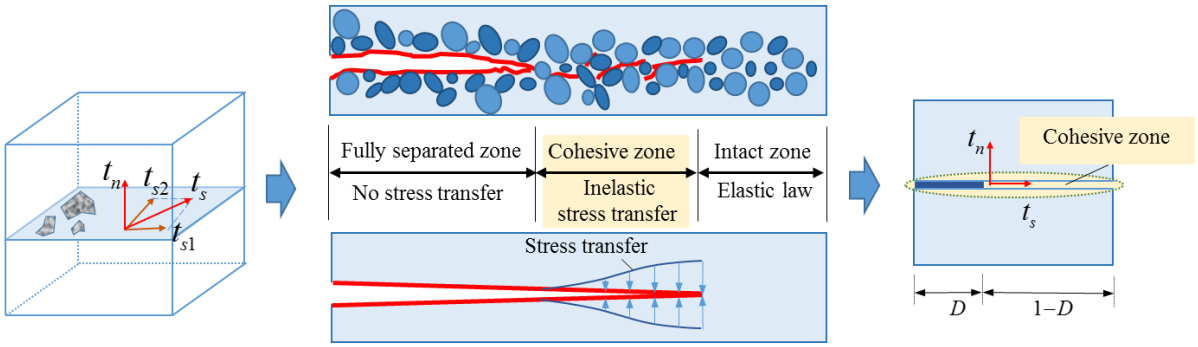

Figure 4.2. Tractions and damage representations in a cohesive zone

Based on these considerations, the traction-displacement relationship is described as:

$$\mathbf{t}_c = \begin{bmatrix} t_n \\ t_{s1} \\ t_{s2} \end{bmatrix} = \begin{bmatrix} 1-DH(t_n) & 0 & 0 \\ 0 & 1-D & 0 \\ 0 & 0 & 1-D \end{bmatrix} \begin{bmatrix} K_n & 0 & 0 \\ 0 & K_s & 0 \\ 0 & 0 & K_s \end{bmatrix} \begin{bmatrix} u_n - u_n^p \\ u_{s1} - u_{s1}^p \\ u_{s2} - u_{s2}^p \end{bmatrix} \quad (4.1)$$
$$= \mathbf{HK}\left(\mathbf{u}_c - \mathbf{u}_c^p\right)$$

where $\mathbf{K}_c^{sec} = \mathbf{HK}$ is the secant stiffness of the cohesive zone in the local coordinate system; K_n, K_s represent the normal and shear elastic stiffness of the cohesive crack; $u_n, u_{s1,2}$ are the normal and shear displacement jumps, and $u_n^p, u_{s1,2}^p$ represent the plastic displacement jumps. The normal traction is defined as positive in tension, and the sign of the displacement jump follows its corresponding traction. The inclusion of the Heaviside function $H(t_n)$ here means that the damaged part only affects the normal traction in the case where tension exists. This means that the nonlinear behaviour of the crack in pure normal direction due to the breaking of asperities leading to compaction (Schreyer and Sulsky, 2016) is not accounted for. Although for all validation examples in this study this is not an issue, we acknowledge this shortcoming and will address it in future work. The presence of damage and irreversible displacements in the traction-displacement jump relationship also allows the model to naturally capture the stiffness reduction due to micro-cracking.

Along with the tractions-displacement jumps relation, a loading function is needed to determine whether the behaviour of the joint is in elastic or inelastic regime. A loading function is also necessary for computing the elastic/plastic displacement parts, as well as the evolution of tractions during loading/unloading. A unified yield-failure function including damage as a function of accumulated plastic displacement is used in this research to capture this interaction. In general, this function needs to be smooth to ensure a continuous transition from pure normal/compression or shear to mixed mode conditions. In addition, experimental observations of shearing tests (Barton, 1976; Liao et al., 2011) show a residual shear strength

at the end of cracking due to friction caused by the waviness and roughness of asperities. Based on the foregoing considerations, the proposed damage-plastic yield model takes the form:

$$y = (t_{s1}^2 + t_{s2}^2) - [(1-D)\mu_0^2 + D\mu^2][t_n - (1-D)f_t]^2 + mf_c(1-D)[t_n - (1-D)f_t] \quad (4.2)$$

in which f_t is the tensile strength; f_c is the compressive strength of the material; and m, μ_0 are the parameters controlling the shape of the initial yield surface. It can be seen from the formulation that in case of final failure (i.e., $D = 1$), the yield surface becomes $t_s = \sqrt{t_{s1}^2 + t_{s2}^2} = \pm\mu t_n$, which is the classical frictional Mohr-Coulomb criterion, where μ plays the role of internal frictional coefficient of the material (i.e. $\mu = \tan\phi$ where ϕ is the friction angle). As a result, the residual shear strength can be described by the current yield surface.

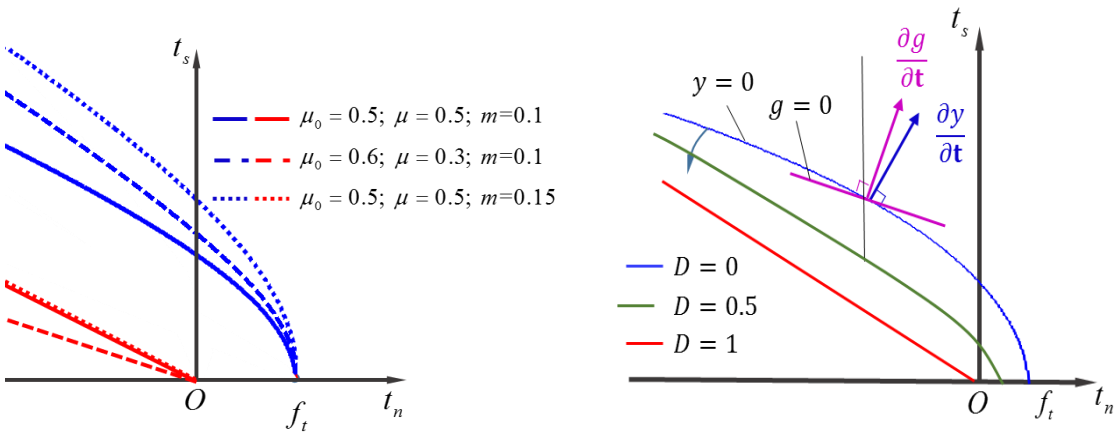

Figure 4.3. Illustration of yield surface: (a) Various yield surfaces with respect to different sets of parameters and (b) Yield surface evolution from initial yield to final failure state and non-associated flow rule.

It should be noted that by changing the values of these parameters, the shape of the yield surface could be adapted to different responses corresponding to different geological settings. This is illustrated in Figure 4.3a where blue and red curves, respectively, represent initial yield and final failure surface. This gives the model a certain level of flexibility while dealing with different types of material and loading paths. It can also be seen from the formulation of the model that both damage and plasticity together with their coupling are taken into account in a unified form of loading function. This helps the model evolve from initial yield to failure smoothly without any additional separate criteria for damage and plasticity. This evolution is illustrated in Figure 4.3b where an initial yield surface (blue

curve corresponding to the case of $D = 0$) gradually evolves as the damage variable D increases and reaches the final failure surface (red line corresponding to $D = 1$).

As non-associated flow rule is needed in modelling crack to better describe the dilation and plastic deformation of the crack interface (Wang et al., 2003), the corresponding plastic potential is defined by:

$$g = \gamma(t_{s1}^2 + t_{s2}^2) - [(1-D)\mu_0^2 + D\mu^2][t_n - (1-D)f_t]^2 + mf_c(1-D)[t_n - (1-D)f_t] \tag{4.3}$$

where γ is the parameter controlling the non-associativity. With $\Delta\lambda$ being the plastic multiplier, the flow rules are:

$$\Delta u_n^p = \Delta\lambda \frac{\partial g}{\partial t_n};\ \ \Delta u_{s1}^p = \Delta\lambda \frac{\partial g}{\partial t_{s1}};\ \ \ \Delta u_{s2}^p = \Delta\lambda \frac{\partial g}{\partial t_{s2}} \tag{4.4}$$

To complete the cohesive model, an evolution law of damage variable *D* is provided to capture the damage propagation caused by the plastic displacement jumps. The experimental data for different loading cases on concrete and sandstone (Ingraham et al., 2013; Liao et al., 2011; Shi et al., 2000) shows that the material responses change rapidly just after reaching its yielding point, and then the rate of variation slows down with further loading. This indicates that a reasonable damage evolution should increase quickly at first, and then more slowly. Hence, in the paper, an exponential function is used for damage evolution:

$$D = 1 - e^{-u_p}, \text{ with } \Delta u_p = \sqrt{\left(\frac{\alpha\Delta u_n^p}{\delta_0}\right)^2 + \left(\frac{\beta\Delta u_{s1}^p}{\delta_0}\right)^2 + \left(\frac{\beta\Delta u_{s2}^p}{\delta_0}\right)^2} \tag{4.5}$$

where u_p is the accumulated plastic displacement parameter in non-dimensional form; α and β are non-dimensional parameters controlling the contributions of normal and shear plastic displacements to the damage evolution; δ_0 is defined as the displacement corresponding to peak stress in pure tension, and is used just to make u_p non-dimensional. In the case of shearing under compression, the normal plastic displacement is a result of the dilation behaviour due to sliding of asperities against each other. Therefore, its contribution to the damage development should be smaller than that in pure tension where normal displacement is the direct cause of the damage development. This effect is taken into account in the model using the following function:

$$\alpha = \alpha_0 e^{\frac{-\langle -t_n \rangle}{f_t}} \tag{4.6}$$

where $\langle . \rangle$ are the Macaulay brackets; α_0 is calculated from mode I fracture energy G_I as shown in the next section. The appearance of tensile strength f_t in the formulation is just to make α non-dimensional as it should be. The use of Eq. (4.6) in this case, is satisfactory as demonstrated later in all numerical examples, and we acknowledge that this should be backed up with further investigations based on micromechanics in future work.

As presented above, a traction – displacement jumps relationship, a non-associated flow rule together with the evolutions of internal variables (i.e. damage D, plastic displacement jump $\mathbf{u}_c^p$) complete the cohesive-frictional model for describing the behaviour of crack. In the proposed cohesive-frictional model, only one unified loading surface is employed from the initial yield to the final failure surface. This allows a natural description of softening/harderning with the transition to frictional behaviour under mixed-mode loading. Because the damage evolution is associated with the plastic strain, the effects of coalescence and frictional sliding are taken into account together during the material failure. These features give the model a good prediction capability under different loading cases.

4.2.2 Parameter identification

The identification and calibration of model parameters play a crucial role in the development and utilisation of a constitutive model. It not only provides us with values of the model parameters with respect to certain material type for numerical analyses but also helps relate model parameters with the material properties measured in experiments from a physical point of view. This section focuses on the identification and calibration of parameters in the proposed model to create a link between model parameters and physical representations as well as material properties.

From a physical point of view, K_s, K_n are the elastic stiffness which are the slope of the stress-displacement curve of the crack in normal and shear loading. They can thus be theoretically calculated from elastic Young's Modulus E and shear modulus G divided by the thickness of the crack. Since in this research, crack is considered to have zero thickness, i.e. $h \to 0$, these elastic stiffness theoretically equals to infinity i.e. $K_s, K_n \to \infty$. However, such values would cause trouble for the numerical implementation of the model. Thus, for numerical simulation, K_s, K_n are chosen to be large enough compared to other stiffness (i.e.,

Young's Modulus E) without affecting results of the simulation. This will be supported by numerical results from the modelling of quasi-brittle geomaterials in the following chapter.

As seen from the model formulation presented above, apart from material properties (i.e. tensile strength f_t, compressive strength f_c, friction angle ϕ), parameters that need to be calibrated include $\mu_0, m, \alpha_0, \beta$ and γ. Their physical meanings and calibrations will be presented as follows.

Calibration of μ_0 and m

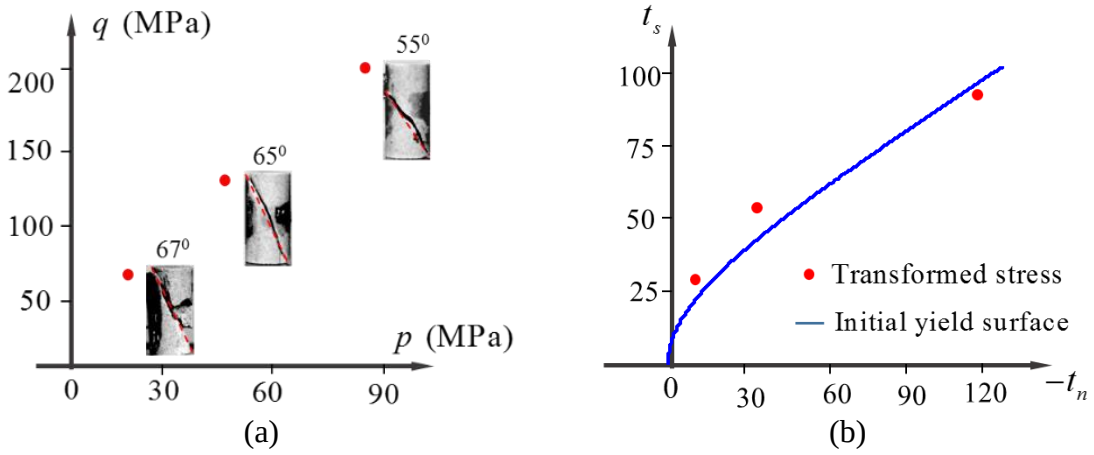

Figure 4.4. Illustration of yield surface calibration: (a) Experimental data (Klein et al., 2001, 2003) and (b) Converted traction and calibrated yield surface by the model

As discussed earlier, the parameters μ_0 and m control the shape of the initial yield surface, which defines the crack initiation. Therefore, in order to calibrate these parameters, an experimental dataset of localisation onset (i.e. yielding points) should be used. As the majority of the yield surface is in compression, the ideal dataset should be obtained from triaxial compression tests in which the stress states at yielding are recorded along with the crack patterns. To illustrate the calibration of these parameters, the triaxial test results of Bentheim sandstone conducted by Klein et al. (2001, 2003) are used. The experimental results of the differential stress $q = |\sigma_1 - \sigma_3| = \sqrt{3J_2}$ and the hydrostatic stress $p = \frac{\sigma_1 + 2\sigma_3}{3} = -I_1/3$, where localisation initiates, are plotted in Figure 4.4a along with their failure plane orientation extracted from the experiments. In association with these orientation of failure, stress states are converted to stresses (tractions) in the local coordinate system of the localisation band as illustrated in Figure 4.1. The two parameters μ_0 and m are then calibrated to fit the experimental data in the local coordinate system. The calibrated initial yield surface is illustrated in Figure 4.4 using two parameters: $\mu_0 = 0.55$ and $m = 1.1$.

Calibration of α_0 and β

As seen from the above formulations of the proposed model, the parameters α_0 and β control the contributions of normal and shear plastic deformations to the evolution of damage variable (see Eq. (4.5)). They are thus directly related to the fracture energy dissipated under loading, especially energies in pure separation in the normal direction (fracture energy in mode I failure, G_I) and pure shear (fracture energy in mode II failure, G_{II}) which are illustrated in Figure 4.5a and b. The calibration/identification of these two parameters, in the proposed model, is thus naturally based on these two fracture energy values.

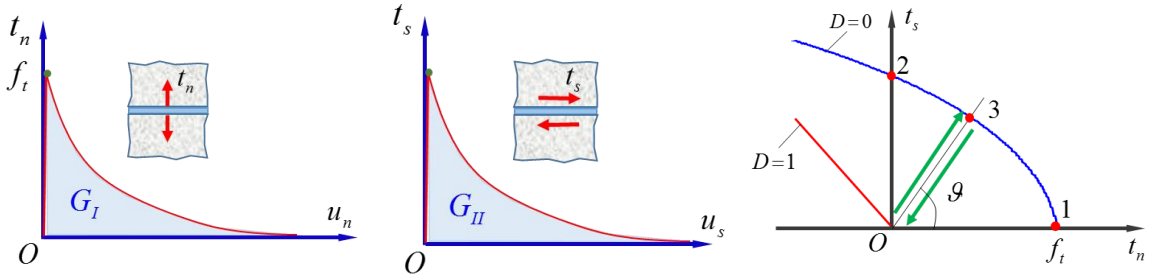

(a) (b) (c)

Figure 4.5. Illustration of fracture energy calculation: (a) in tension, (b) in pure shear and (c) traction path with respect to the yield function

The relationship between the parameter α_0 and mode I fracture energy G_I is found from the analytical derivation of pure tension case ($\vartheta = 0^o$ as illustrated in Figure 4.5c) where shear traction is considered to be zero, $t_s = 0$. The plastic shear displacement increment is thus written as:

$$\Delta u_s^p = \Delta\lambda \frac{\partial g}{\partial t_s} = 2\Delta\lambda t_s \gamma = 0 \tag{4.7}$$

As a result, the normal plastic displacement jump solely drives the damage evolution. The increment of accumulated displacement parameter then becomes:

$$\Delta u_p = \alpha_0 \frac{\Delta u_n^p}{\delta_0} = \frac{1}{1-D}\Delta D \text{ and thus } \Delta u_n^p = \frac{\delta_0}{\alpha_0}\frac{1}{1-D}\Delta D \tag{4.8}$$

From the yielding condition $y = 0$, in association with the condition $t_s = 0$, the normal traction is calculated by:

$$t_n = (1-D)f_t = (1-D)K_n(u_n - u_n^p) \tag{4.9}$$

By using Eqs. (4.8)-(4.10), the mode I fracture energy can be analytically calculated by:

$$\mathrm{G}_I = \int_0^{+\infty} t_n \mathrm{d}u_n = \int_0^1 (1-D) f_t \frac{\delta_0}{\alpha_0} \frac{1}{1-D} \mathrm{d}D = f_t \frac{\delta_0}{\alpha_0} \rightarrow \alpha_0 = \frac{f_t \delta_0}{G_I} \tag{4.10}$$

Similarly, the relationship between parameter β and mode II fracture energy G_{II} can be established via pure shear test. In this case, the normal traction t_n is considered to be zero and the stress path follows the vertical axis as shown in Figure 4.5c (i.e., $\vartheta = 90^0$ passing point 2). The normal and shear plastic displacements could then be calculated as:

$$\begin{gathered} \Delta u_s^p = \Delta\lambda \frac{\partial g}{\partial t_s} = 2\gamma\Delta\lambda t_s \text{ and} \\ \Delta u_n^p = \Delta\lambda \frac{\partial g}{\partial t_n} = -2[(1-D)\mu_0^2 + D\mu^2][t_n - (1-D)f_t] - m f_c (1-D) \end{gathered} \tag{4.11}$$

The effective plastic displacement, in this case, becomes:

$$\Delta u_p = \sqrt{\left(\frac{\alpha \Delta u_n^p}{\delta_0}\right)^2 + \left(\frac{\beta \Delta u_{s1}^p}{\delta_0}\right)^2 + \left(\frac{\beta \Delta u_{s2}^p}{\delta_0}\right)^2} \tag{4.12}$$

It can be seen from this equation that both normal and shear displacements contribute to damage development and thus will have effects on the produced fracture energy. As a result, different from the tension case, there is no explicit relationship between mode II fracture energy G_{II} and β. The parameter β is thus calibrated by a numerical procedure, given that α_0 is already known. In this process, the pure shear behaviour is modelled, and then β is fine-tuned until the fracture energy G_{II}, produced by the model, matches the given energy of the material.

Thanks to the coupling of normal and shear component within both the yield criterion and damage evolution, the model features an in-built fracture locus which is very useful for modelling geomaterials in mixed-mode loading conditions. A preliminary result is presented here to demonstrate this feature in the model. A series of numerical modelling is carried out under mixed-mode loading cases, as shown in Figure 4.5c (i.e. $0^0 \leq \vartheta \leq 90^0$). The material used for this illustration is concrete whose properties are adopted from tension test: tensile strength $f_t = 2.86$ MPa; compressive strength $f_c = 38.4$ MPa; mode I fracture energy $G_I = 0.063$ KN/m. Because there were no shear properties recorded in this experiment, shear properties are taken from a shear test conducted by Reinhardt and Xu (2000) with shear stress peak at $\sigma_{12}^0 = 20$ MPa, and mode II fracture energy $G_{II} = 20G_I = 1.26$ KN/m. The parameters are $\mu_0 = 0.1$; $m = 4.5$; $\alpha_0 = 0.63$; $\beta = 0.0017$; and $\gamma = 1.47$. For each mixed mode simulation (i.e. $\vartheta = \vartheta_0$), the fracture energy produced in mode I and mode II were

computed from corresponding traction-displacement responses and plotted in a fracture locus as shown in Figure 4.6. It can be seen that the total fracture energy (i.e., $G_I + G_{II}$) produced by the material in this case linearly transforms from pure tension G_I to pure shear G_{II}. This linear coupling of fracture in mode I and mode II produced by the model somewhat agrees with a few experimental results conducted on laminate composite (Reeder and Crews, 1990; Reeder, 2006). Nonetheless, this contradicts with nonlinear and curvy fracture locus reported in many other experimental studies (Agastra, 2004; Benzeggagh and Kenane, 1996; Crews and Reeder, 1998; Reeder and Crews, 1990; Reeder, 2006). This preliminary results, even though still need a lot of improvements, show the potential of the proposed cohesive-frictional model in capturing the mixed-mode loading conditions. It should be noted that the fracture locus, presented here, is an in-built feature of the model without requiring analytical criterions for mix-mode fracture as seen in several studies (Bui, 2011; Hashemi et al., 1990; Kenane and Benzeggagh, 1997; Reeder, 1993; Yan et al., 1991). Based on this preliminary results, further investigations and developments on fracture energy dissipated by the material in mixed-mode loadings can be carried out in a more rigorous and systematic way as seen in recent work (Alfaiate and Sluys, 2017a, 2017b; Guiamatsia and Nguyen, 2012). This is outside the scope of this study for now and will be addressed in future work.

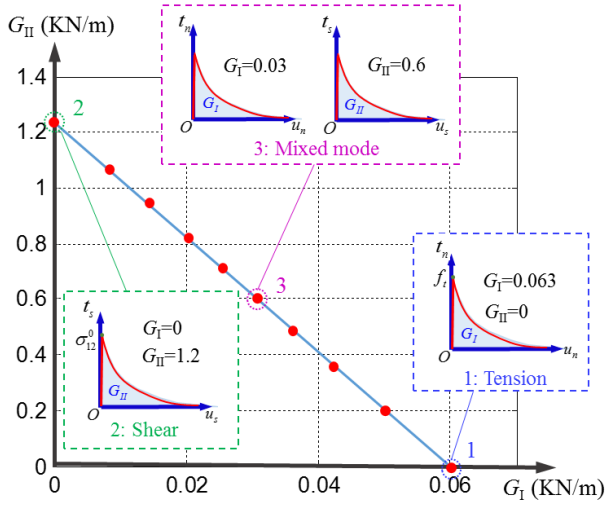

Figure 4.6. Fracture locus predicted by the model from tension to pure shear

Calibration of γ

This brings us to the calibration of parameter γ. Via the flow rule, γ controls the ratio between plastic normal and shear displacement jumps (i.e. Δu_n^p and Δu_s^p) by adjusting the potential function g. This means that γ implicitly governs the dilation angle ψ, as illustrated in Figure 4.3a. The blue vector in the figure is the normal vector of the yield surface y at a

specific point, and the purple one is the displacement jump vector, which is the normal vector of the potential function g. By changing γ, the potential function, its normal vector and the value of dilation angle $\tan\psi = \frac{\Delta u_n^p}{\Delta u_s^p}$ change correspondingly. Based on this consideration, γ can be calibrated through experiments where the dilation effect exists. In doing so, γ is tuned so that the dilation predicted by the model fits with that observed in the the experiment. The calibration of γ can also be achieved via shear under constant, normal stiffness; triaxial test; or a mixed mode test where dilation is recorded in the form of normal displacement or volumetric strain.

The above analysis shows that parameters in the model are physically meaningful and can be calibrated using experimental data from standard tests. When it comes to modelling a specific type of material in a specific condition, there might not be enough information to conduct an ideal calibration. In such situations, similar types of experiments (i.e. bending test, shear under constant normal stiffness, punch-through test) can be used for the calibration. The physical representation of parameters in the model presented above would then be very useful for such calibrations.

4.2.3 Tangent stiffness

To facilitate the implementation of the proposed cohesive-frictional model into numerical approaches for modelling purposes, it is necessary to have the formulation of the tangent stiffness matrix in the local coordinate system $\mathbf{K}_{\mathrm{c}}^{\tan}$ that is $\Delta\mathbf{t}_{\mathrm{c}} = \mathbf{K}_{\mathrm{c}}^{\tan}\Delta\mathbf{u}_{\mathrm{c}}$. This tangent stiffness is withdrawn from the consistency condition of the yield function. To serve this purpose, the governing equation (4.1) is rewritten in the compact form as:

$$\mathbf{t}_{\mathrm{c}} = f(D, \mathbf{u}_{\mathrm{c}}, \mathbf{u}_{\mathrm{c}}^{\mathrm{p}}) \tag{4.13}$$

By taking derivative of this equation, the incremental form of this relation is then obtained as:

$$\Delta\mathbf{t}_{\mathrm{c}} = \frac{\partial\mathbf{t}_{\mathrm{c}}}{\partial\mathbf{u}_{\mathrm{c}}}\Delta\mathbf{u}_{\mathrm{c}} + \frac{\partial\mathbf{t}_{\mathrm{c}}}{\partial\mathbf{u}_{\mathrm{c}}^{\mathrm{p}}}\Delta\mathbf{u}_{\mathrm{c}}^{\mathrm{p}} + \frac{\partial\mathbf{t}_{\mathrm{c}}}{\partial D}\Delta D \tag{4.14}$$

From Eq. (4.5), the damage increment is presented by:

$$\Delta D = e^{-u_p}\Delta u_p = \frac{e^{-u_p}}{\delta_0}\sqrt{\left(\alpha\frac{\partial g}{\partial t_n}\right)^2 + \left(\beta\frac{\partial g}{\partial t_{s1}}\right)^2 + \left(\beta\frac{\partial g}{\partial t_{s2}}\right)^2}\,\Delta\lambda = R\Delta\lambda \tag{4.15}$$

The consistency condition requires that at any step of calculation when traction and damage variable evolves from step n (i.e., $\mathbf{t}_{\mathrm{c}}^n, D^n$) to step $n+1$ (i.e., $\mathbf{t}_{\mathrm{c}}^{n+1}, D^{n+1}$), the

traction always has to be on the yield surface (i.e., $y(\mathbf{t}_c^n, D^n) = y(\mathbf{t}_c^{n+1}, D^{n+1}) = 0$). This results in:

$$\Delta y = \frac{\partial y}{\partial \mathbf{t}_c}\Delta \mathbf{t}_c + \frac{\partial y}{\partial D}\Delta D = 0 \tag{4.16}$$

By substituting Eqs. (4.4), (4.13) and (4.14) into consistency condition in Eq. (4.16) and solving for $\Delta\lambda$, one obtains:

$$\Delta\lambda = \frac{-\frac{\partial y}{\partial \mathbf{t}_c}\frac{\partial \mathbf{t}_c}{\partial \mathbf{u}_c}}{\frac{\partial y}{\partial \mathbf{t}_c}\frac{\partial \mathbf{t}_c}{\partial \mathbf{u}_c^p}\frac{\partial g}{\partial \mathbf{t}_c} + \frac{\partial y}{\partial \mathbf{t}_c}\frac{\partial \mathbf{t}_c}{\partial D}R + \frac{\partial y}{\partial D}R}\Delta \mathbf{u}_c = \mathbf{N}\Delta \mathbf{u}_c \tag{4.17}$$

This equation is then substituted back into Eqs. (4.4) to compute increments of plastic displacement jumps as:

$$\Delta u_n^p = \frac{\partial g}{\partial t_n}\mathbf{N}\Delta \mathbf{u}_c;\ \ \Delta u_{s1}^p = \frac{\partial g}{\partial t_{s1}}\mathbf{N}\Delta \mathbf{u}_c;\ \ \ \Delta u_{s2}^p = \frac{\partial g}{\partial t_{s2}}\mathbf{N}\Delta \mathbf{u}_c \tag{4.18}$$

Increments of internal variables in Eq. (4.14) can now be replaced by the above increments, together with the increment of damage variable in Eq. (4.15). The tangent stiffness in the loading case for the traction – displacement jump relationship is then withdrawn as:

$$\Delta \mathbf{t}_c = \left[\frac{\partial \mathbf{t}_c}{\partial \mathbf{u}_c} + \frac{\partial \mathbf{t}_c}{\partial \mathbf{u}_c^p}\frac{\partial g}{\partial \mathbf{t}_c}\mathbf{N} + R\frac{\partial \mathbf{t}_c}{\partial D}\right]\Delta \mathbf{u}_c = \mathbf{K}_c^{\tan}\Delta \mathbf{u}_c \tag{4.19}$$

4.2.4 Stress return algorithm for the cohesive-frictional model

As seen from Section 4.2.3, the increment of the traction could be directly calculated from incremental displacement jump using the tangent stiffness. However, because this tangent stiffness is explicitly calculated from the current state (state A as illustrated in Figure 4.7) which does not lie on the yield surface, it only provides good results when the incremental step is sufficiently small. Thus, an implicit calculation is usually preferred in the numerical simulation as it could produce relatively good results with larger steps. In addition, similar to the plasticity formulation where a stress return is needed for the implicit calculation, a stress return procedure is also required for the proposed cohesive model to work well with the overall stress – strain implicit calculation. The proposed stress return is based on a special form of the backward-Euler scheme presented by Crisfield (2000). The idea of this method is illustrated in Figure 4.7 where the yield surface is approximated by First Taylor expansion at trial point B and the yield criteria (i.e. $y(\mathbf{t}_c, D) = \mathbf{0}$) is applied to

obtain the increment of the scalar factor $\Delta\lambda$ for the yield evolution. By doing so, the procedure does not have to calculate the exact yielding point X and the yielding criteria is still satisfied.

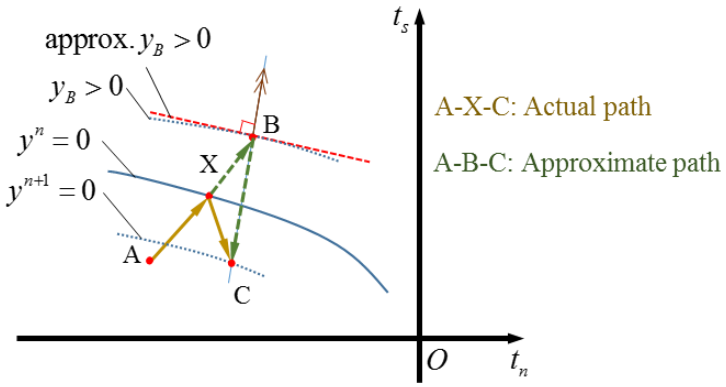

Figure 4.7. Illustration of stress return for the proposed cohesive model: A is current state, X is yielding state, B is a trial state, C is a new state.

The increment of the traction from the current point A to trial point B is elastic $\Delta\mathbf{t}_c^{tr} = \mathbf{HK}\Delta\mathbf{u}_c$ where matrices **H** and **K** is defined as in Eq. (4.1). The yield surface at point B is approximated at trial point B by first-order Taylor expansion and then in association with Eq. (4.14), the stress state is moved from trial point B to new yielding point C on the new yielding surface. The new yielding surface is then enforced to be zero as:

$$\begin{aligned} y^{n+1} &= y_B + \left.\frac{\partial y}{\partial \mathbf{t}_c}\right|_B (\mathbf{t}_c^C - \mathbf{t}_c^B) + \left.\frac{\partial y}{\partial D}\right|_B \Delta D \\ &= y_B + \left.\frac{\partial y}{\partial \mathbf{t}_c}\right|_B \left[\frac{\partial \mathbf{t}_c}{\partial \mathbf{u}_c^p}\Delta\mathbf{u}_c^p + \frac{\partial \mathbf{t}_c}{\partial D}\Delta D\right] + \left.\frac{\partial y}{\partial D}\right|_B R\Delta\lambda \end{aligned} \tag{4.20}$$

Noted that in the above equation, the elastic part when moving from B to C is equal to zero due to the fact that it was already used to move from A to trial point B as presented. By substituting Eqs. (4.4) and (4.15) into Eq. (4.16) and solving for scalar $\Delta\lambda$, one obtains:

$$\Delta\lambda = \frac{-y_B}{\left.\frac{\partial y}{\partial \mathbf{t}_c}\right|_B \frac{\partial \mathbf{t}_c}{\partial \mathbf{u}_c^p}\frac{\partial g}{\partial \mathbf{t}_c} + \left.\frac{\partial y}{\partial \mathbf{t}_c}\right|_B \frac{\partial \mathbf{t}_c}{\partial D}R + \left.\frac{\partial y}{\partial D}\right|_B R} \tag{4.21}$$

From this scalar factor, increments for other internal variables can be calculated following Eqs. (4.4), (4.5) and (4.15) easily. The traction increment is then computed by:

$$\Delta\mathbf{t}_c = \Delta\mathbf{t}_c^{tr} + \frac{\partial \mathbf{t}_c}{\partial \mathbf{u}_c^p}\Delta\mathbf{u}_c^p + \frac{\partial \mathbf{t}_c}{\partial D}R\Delta\lambda \tag{4.22}$$

4.3 A double-scale modelling

As seen from the formulation presented in the preceding section, the cohesive-frictional model was proposed to describe the behaviour of the localisation zone, characterised by traction –displacement jumps relationship. Therefore, this model on its own cannot be used for numerical simulation of any material yet. In general, it can be implemented into a constitutive model such as embedded crack model (Gálvez et al., 2013; Guzmán et al., 2012; Haghighat and Pietruszczak, 2016), microplane model (Caner and Bažant, 2013; Chen and Bažant, 2014; Cusatis et al., 2014; Kedar and Bažant, 2015; Li et al., 2017) or micromechanics-based models (Chang and Yin, 2010, 2011; Fang et al., 2017; Misra and Poorsolhjouy, 2016; Misra and Yang, 2010; Yin and Chang, 2013; Yin et al., 2014), where stress-strain relationship is concerned, for simulation purposes. Alternatively, it can also be used as interface element or discontinuity entities in Strong Discontinuity Approach (Dias et al., 2018a, 2018b, 2016; Dias-da-Costa et al., 2009; Lloberas-Valls et al., 2016; Oliver, 1996; Oliver et al., 2015, 2002).

In this study, the proposed cohesive-frictional model will be implemented into the double-scale modelling approach (Nguyen et al., 2012a, 2012b, 2014) to validate the capability at this stage. The key idea of this framework is to enhance the constitutive behaviour with an additional kinematics mode and a corresponding length scale related to the relative width of the localisation zone to correctly describe the localised failure of materials. This fits well with the validation against experimental results of jointed rock mass, which will be presented later. In this double-scale model, the interaction between the localisation zone and the surrounding bulk material is described by the internal equilibrium conditions between the overall stress and traction acting on the zone plane. This creates space to incorporate the proposed cohesive-frictional model into the continuum framework. By doing so, the two scales including the behaviour of the localisation zone and the overall stress-strain relationship of the material are incorporated into a single constitutive model. In other words, the framework connects these two scales to obtain a constitutive relationship at the macro-level in which inelastic behaviour is governed by the mechanisms of localisation band at a lower scale. This explains why the terminology “double-scale” is used for this model.

This section goes on to present key formulations of the double-scale constitutive framework specifically tailored for accommodating the proposed cohesive model. More details are available in Nguyen et al. (2012a, 2012b, 2014) for interested readers. It is then

followed by an implicit stress return algorithm, proposed to ensure the consistency and equilibrium among all quantities and internal variables defined in the model.

4.3.1 Double-scale model description

The double-scale model is developed for a Representative Volume Element (RVE) Ω comprising an outer bulk material Ω_o and a localisation band $\Omega_i = \Gamma_i h$, represented by its area Γ_i and thickness h as shown in Figure 4.8a. The localisation band is also characterised by its orientation, which can be represented by normal vector $\mathbf{n}$. Assuming homogeneous behaviour, the stress and strain vectors of the band are denoted as $\boldsymbol{\varrho}$ and $\boldsymbol{\xi}$ respectively. The stress and strain vectors of the outer bulk material are $\boldsymbol{\sigma}_o$ and $\boldsymbol{\varepsilon}_o$, while the volume-averaged stress and strain vectors of the RVE are denoted as $\boldsymbol{\sigma}$ and $\boldsymbol{\varepsilon}$. It should be noted that the notation "i" and "o" in above notations, respectively, represent "inside" and "outside" the localisation zone, where those quantities are defined and has nothing to do with index notation. Following the Voight notations, these above quantities are expressed in the global coordinate system as:

$$\begin{gathered}\boldsymbol{\varepsilon} = [\varepsilon_1 \quad \varepsilon_2 \quad \varepsilon_3 \quad \gamma_{12} \quad \gamma_{23} \quad \gamma_{31}]^T;\ \boldsymbol{\sigma} = [\sigma_1 \quad \sigma_2 \quad \sigma_3 \quad \sigma_{12} \quad \sigma_{23} \quad \sigma_{31}]^T \\ \boldsymbol{\varepsilon}_o = [\varepsilon_{o,11}\ \varepsilon_{o,22}\ \varepsilon_{o,33}\ \gamma_{o,12}\ \gamma_{o,23}\ \gamma_{o,31}]^T;\ \boldsymbol{\sigma}_o = [\sigma_{o,11}\ \sigma_{o,22}\ \sigma_{o,33}\ \sigma_{o,12}\ \sigma_{o,23}\ \sigma_{o,31}]^T \\ \boldsymbol{\xi} = [\xi_1 \quad \xi_2 \quad \xi_3 \quad 2\xi_{12} \quad 2\xi_{23} \quad 2\xi_{31}]^T;\ \boldsymbol{\varrho} = [\varrho_{11}\ \varrho_{22}\ \varrho_{33}\ \varrho_{12}\ \varrho_{23}\ \varrho_{31}]^T\end{gathered} \tag{4.23}$$

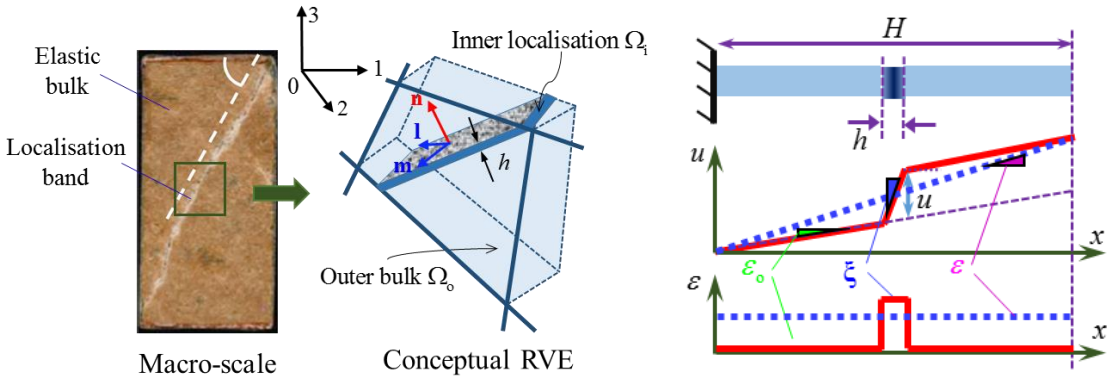

(a) (b)

Figure 4.8. Illustration of double-scale modelling: (a) The conceptual model based on failure mechanism at mesoscale and (b) 1D illustration of kinematic enhancement across the localisation zone in a general case

In order to link the behaviour of the localisation zone to the overall stress-strain relationship of the RVE as a whole, the strain increment inside the zone can be expressed in

terms of the strain increment of the bulk material and a kinematically enhanced strain increment component as (Kolymbas, 2009; Neilsen and Schreyer, 1993):

$$\Delta\boldsymbol{\xi} = \Delta\boldsymbol{\varepsilon}_{\mathrm{o}} + \frac{1}{h}\mathbf{n}\Delta\mathbf{u} \approx \frac{1}{h}\mathbf{n}\Delta\mathbf{u} \tag{4.24}$$

where $\Delta\mathbf{u} = [\Delta u_1 \quad \Delta u_2 \quad \Delta u_3]^T$ is the increment of relative displacements (i.e., displacement jumps) between two sides of the localisation zone in the global coordinate system. In this equation, the first term of Eq. (4.24) are much smaller than the other component and can be neglected as the localisation band can be reasonably idealised as a zero thickness crack plane, $h \to 0$. Assuming homogeneous behaviour inside and outside the band, the overall strain increment of the RVE is approximated using the rule of mixtures as:

$$\Delta\boldsymbol{\varepsilon} = \eta\Delta\boldsymbol{\xi} + (1-\eta)\Delta\boldsymbol{\varepsilon}_{\mathrm{o}} = \Delta\boldsymbol{\varepsilon}_{\mathrm{o}} + \frac{1}{H}\mathbf{n}\Delta\mathbf{u} \tag{4.25}$$

where $\eta = \frac{\Omega_{\mathrm{i}}}{\Omega} = \frac{\Gamma_{\mathrm{i}} h}{\Omega}$ is the volume fraction of localisation band in relation to the RVE and $H = \frac{\Omega}{\Gamma_{\mathrm{i}}} = \frac{h}{\eta}$ is defined as the characteristic length of the RVE. This kinematic enhancement is illustrated in Figure 4.8b for a general case (i.e. h is finite) in 1D where the inhomogeneous deformation over the element is illustrated by the red solid line and the averaged macro strain is presented by the dotted blue line. It can be seen that even though the overall strain appears to be constant over the region, it actually comprises of deformations from both the localisation band and the outer bulk material. This helps take the contribution of the localisation band into account naturally. The incorporation of the localisation band behaviour into the overall responses of the RVE is also carried out via the virtual work conservation (Hill, 1963) which requires that the summation of virtual work done by the localisation band and its surrounding bulk material is equal to the work done by the RVE:

$$\boldsymbol{\sigma}^T\delta\boldsymbol{\varepsilon} = \eta\boldsymbol{\varrho}^T\delta\boldsymbol{\xi} + (1-\eta)\boldsymbol{\sigma}_{\mathrm{o}}^T\delta\boldsymbol{\varepsilon}_{\mathbf{o}} \tag{4.26}$$

where $\delta\boldsymbol{\xi}$, $\delta\boldsymbol{\varepsilon}_{\mathrm{o}}$ and $\delta\boldsymbol{\varepsilon}$ are, respectively, the virtual strain increments of the inner localisation band, the outer bulk material and the volume element. By substituting the kinematic enhancement in Eqs. (4.24) and (4.25) into the work conservation in Eq. (4.26), one obtains:

$$(1-\eta)(\boldsymbol{\sigma}^T - \boldsymbol{\sigma}_{\mathrm{o}}^T)\delta\boldsymbol{\varepsilon}_{\mathbf{o}} + \frac{1}{H}(\boldsymbol{\sigma}^T\mathbf{n} - \boldsymbol{\varrho}^T\mathbf{n})\delta\mathbf{u} = 0 \tag{4.27}$$

in which $\delta\mathbf{u}$ is the virtual displacement increment across the localisation band. Since the work conservation has to be satisfied for arbitrary values of virtual deformations $\delta\boldsymbol{\varepsilon}_{\mathbf{o}}$ and $\delta\mathbf{u}$, two following equilibriums are obtained: i) the averaged stress of the volume element

coincides with the stress of the outer bulk material $\boldsymbol{\sigma} = \boldsymbol{\sigma}_{\mathrm{o}}$ and ii) traction continuity across the crack plane $\boldsymbol{\sigma}^T\mathbf{n} = \boldsymbol{\varrho}^T\mathbf{n} = \mathbf{t}^T$, where $\mathbf{t} = [t_1 \quad t_2 \quad t_3]^T$ is the traction acting on the boundaries between the localisation band and the bulk material in the global coordinate system.

The relationship between traction and displacement jumps inside the localisation zone, described by the cohesive-frictional model in Section 4.2, is now put to use here with the help of the transformation matrix from the global to the local coordinate system as:

$$\mathbf{t} = \mathbf{R}\mathbf{t}_{\mathrm{c}} = \mathbf{R}\mathbf{K}_{\mathrm{c}}^{\tan}\mathbf{u}_{\mathrm{c}} = \mathbf{R}\mathbf{K}_{\mathrm{c}}^{\tan}\mathbf{R}^T\mathbf{u} = \mathbf{K}^{\tan}\mathbf{u} \tag{4.28}$$

where $\mathbf{t}_{\mathrm{c}}$ and $\mathbf{u}_{\mathrm{c}}$ are, respectively, traction and displacement jump in the local coordinate system and were defined in Section 4.2. $\mathbf{K}_{\mathrm{c}}^{\tan}$ is the tangent stiffness of the traction-displacement jump, whose calculation was presented in Eq. (4.19) of Section 4.2.3. $\mathbf{R}$ is the transformation matrix from the global to local coordinate system, written as:

$$\mathbf{R} = \begin{bmatrix} n_1 & m_1 & l_1 \\ n_2 & m_2 & l_2 \\ n_3 & m_3 & l_3 \end{bmatrix} \text{ and } \mathbf{R}^{-1} = \mathbf{R}^{\mathrm{T}} \tag{4.29}$$

in which $n_i, l_i, m_i, i = 1, 2, 3$ are the three components of the unit vectors in the local coordinate system of the localisation band (respectively denoted as $\mathbf{n}, \mathbf{l}, \mathbf{m}$) with respect to the global coordinate system $0_{1,2,3}$ (drawn in black) as illustrated in Figure 4.8.

Now the condition of traction continuity, in its incremental form, $\mathbf{n}^T\Delta\boldsymbol{\sigma} = \mathbf{n}^T\Delta\boldsymbol{\sigma}_{\mathrm{o}} = \Delta\mathbf{t}$ can be rewritten using the constitutive relationship of the outer bulk material ($\Delta\boldsymbol{\sigma}_{\mathrm{o}} = \mathbf{a}_{\mathrm{o}}\Delta\boldsymbol{\varepsilon}_{\mathrm{o}}$) along with Eq. (4.25) as:

$$\mathbf{n}^T\mathbf{a}_{\mathrm{o}}\left(\Delta\boldsymbol{\varepsilon} - \frac{1}{H}\mathbf{n}\Delta\mathbf{u}\right) = \mathbf{K}^{\tan}\Delta\mathbf{u} \tag{4.30}$$

After some arrangements of the above equation, the increment of displacement jump can be derived as:

$$\Delta\mathbf{u} = \left(\frac{1}{H}\mathbf{n}^T\mathbf{a}_{\mathrm{o}}\mathbf{n} + \mathbf{K}^{\tan}\right)^{-1}\mathbf{n}^T\mathbf{a}_{\mathrm{o}}\Delta\boldsymbol{\varepsilon} = \mathbf{C}^{-1}\mathbf{n}^T\mathbf{a}_{\mathrm{o}}\Delta\boldsymbol{\varepsilon} \tag{4.31}$$

In the above formulation, the intact bulk material is assumed to be elastic with stiffness $\mathbf{a}_{\mathrm{o}}$ and the inelasticity of the material happens only in the embedded crack. The constitutive relation of the FRC can be then written as:

$$\Delta\boldsymbol{\sigma} = \Delta\boldsymbol{\sigma}_{\mathrm{o}} = \mathbf{a}_{\mathrm{o}}\left[\Delta\boldsymbol{\varepsilon} - \frac{1}{H}\mathbf{n}\Delta\mathbf{u}\right] = \left[\mathbf{a}_{\mathrm{o}} - \frac{1}{H}\mathbf{a}_{\mathrm{o}}\mathbf{n}\left(\frac{1}{H}\mathbf{n}^T\mathbf{a}_{\mathrm{o}}\mathbf{n} + \mathbf{K}^{\tan}\right)^{-1}\mathbf{n}^T\mathbf{a}_{\mathrm{o}}\right]\Delta\boldsymbol{\varepsilon} \tag{4.32}$$

As seen in the above formulation, both of the localisation band and the surrounding bulk material responses contribute to the constitutive model through a set of kinematic parameter and internal equilibrium conditions across the boundary of the band. This helps to incorporate the elastic response of the bulk material and the inelastic behaviour of the band into the overall response of the volume element. It can be seen from the above formulations that the length scale H is physically meaningful, reflects the size of the cracked RVE while the dissipation of this RVE is totally independent of this size H (Nguyen et al, 2014; Nguyen & Bui, 2019). The formulation in Eq. (4.25) is thus expected to be applicable within the behaviour range of quasi-brittle geomaterials. In extreme cases, if a very large RVE ($H \to \infty$) is examined, the contribution of displacement jump inside the localisation band toward the overall strain would reduce ($1/H \to 0$) which is reasonable given the size of the RVE. However, the contribution of this localisation band to the dissipation of the RVE still remains the same while the macro response in such cases would exhibit snap-back behaviour. This is due to excess strain energy (as RVE size increases) exceeding the dissipation capacity of the RVE (dissipation governed by localisation band remains the same).

4.3.2 Stress return algorithm for double-scale approach

Once the tractions – displacements jumps inside the localisation is implemented into the double-scale model, the constitutive model is completed in terms of formulation. As seen from the above equations, the responses of the localisation zone and the surrounding bulk material are included in a single constitutive stress-strain equation and interact with each other via traction continuity condition. Thus, it is necessary to have an appropriate numerical algorithm to cope with this coupling so that both the overall stress - strain of the material and the traction – displacement jumps of the localisation band are updated and compatible with each other iteratively. This section hence presents the numerical algorithm for stress update based on a given total strain increment and previous state of the material point. The implicit algorithm is employed here as it could give a relatively good result with a larger increment as compared to the explicit algorithm.

For a given strain increment, $\Delta\boldsymbol{\varepsilon}$, the trial stress and traction inside the localisation band are firstly computed with the assumption of elastic localisation band behaviour as:

$$\boldsymbol{\sigma}^{\mathrm{tr}} = \boldsymbol{\sigma} + \Delta\boldsymbol{\sigma}^{\mathrm{tr}} = \boldsymbol{\sigma} + \mathbf{a}_{\mathrm{o}}\left[\Delta\boldsymbol{\varepsilon} - \frac{1}{H}\mathbf{n}\Delta\mathbf{u}^{\mathrm{tr}}\right] \tag{4.33}$$

$$\mathbf{t}_{\mathrm{c}}^{\mathrm{tr}} = \mathbf{t}_{\mathrm{c}} + \Delta\mathbf{t}_{\mathrm{c}}^{\mathrm{tr}} = \mathbf{t}_{\mathrm{c}} + \mathbf{R}\mathbf{n}^{T}\Delta\boldsymbol{\sigma}^{\mathrm{tr}}$$

where $\Delta\mathbf{u}^{\mathrm{tr}}$ is calculated by:

$$\begin{aligned} \Delta\mathbf{u}^{\mathrm{tr}} &= \mathbf{C}^{-1}\mathbf{n}^{T}\mathbf{a}_{\mathrm{o}}\Delta\boldsymbol{\varepsilon} \\ \mathbf{C} &= \frac{1}{H}\mathbf{n}^{T}\mathbf{a}_{\mathrm{o}}\mathbf{n} + \mathbf{R}\mathbf{K}_{\mathrm{c}}^{\mathrm{sec}}\mathbf{R}^{T} \end{aligned} \tag{4.34}$$

It should be noted that with the assumption of elasticity, the stiffness used for calculating trial state is the secant stiffness defined in Eq. (4.1). The trial state is then substituted back to the yield function of the cohesive-frictional model to see if the assumption of elasticity is correct.

If the assumption is correct, $y(\mathbf{t}_{\mathrm{c}}^{\mathrm{tr}}) < 0$, the new state takes the form of trial state:

$$\boldsymbol{\sigma} = \boldsymbol{\sigma}^{\mathrm{tr}};\ \mathbf{t}_{\mathrm{c}} = \mathbf{t}_{\mathrm{c}}^{\mathrm{tr}} \text{ and } \mathbf{u} = \mathbf{u}^{\mathrm{tr}} \tag{4.35}$$

If the assumption is incorrect, $y(\mathbf{t}_{\mathrm{c}}^{\mathrm{tr}}) \geq 0$, the trial displacement jump is transfomed to the local cooridnate system, $\Delta\mathbf{u}_{\mathrm{c}}^{\mathrm{tr}} = \mathbf{R}\Delta\mathbf{u}^{\mathrm{tr}}$ and used to calculate corrective traction $\Delta\mathbf{t}_{\mathrm{c}}$ following the return algorithm described in Section 4.2.4. The traction in both local and global coordinate system is then updated $\mathbf{t}_{\mathrm{c}} = \mathbf{t}_{\mathrm{c}} + \Delta\mathbf{t}_{\mathrm{c}}$ and $\mathbf{t} = \mathbf{t} + \mathbf{R}^{T}\Delta\mathbf{t}_{\mathrm{c}}$. In this process, internal variables in the cohesive model are also updated correspondingly. Up to this point, the traction in crack is returned to its proper value with respect to the crack state, but the overall stress is still at the trial state $\boldsymbol{\sigma}^{\mathrm{tr}} = \boldsymbol{\sigma} + \Delta\boldsymbol{\sigma}^{\mathrm{tr}}$. Therefore, the internal equilibrium condition, $\mathbf{n}^{T}\boldsymbol{\sigma} - \mathbf{t} = \mathbf{0}$, is not met. To ensure that the traction continuity is obtained within a certain pre-defined tolerance, an iterative procedure is applied to correct the current stress and tractions. To serve this purpose, a vector of residual traction is defined in the global coordinate system as:

$$\mathbf{r} = \mathbf{n}^{T}\boldsymbol{\sigma} - \mathbf{t} \tag{4.36}$$

By using the first order Taylor expansion of the residual vector at a state of the last iteration n, the residual of the current iteration $n+1$ is given by:

$$\mathbf{r}^{n+1} = \mathbf{r}^{n} + \mathbf{n}^{\mathrm{T}}\delta\boldsymbol{\sigma} - \delta\mathbf{t} = \mathbf{r}^{n} - \frac{1}{H}\mathbf{n}^{T}\mathbf{a}_{\mathrm{o}}\mathbf{n}\delta\mathbf{u} - \mathbf{K}^{\tan}\delta\mathbf{u} \tag{4.37}$$

where $\delta\boldsymbol{\sigma}$, $\delta\mathbf{t}$ and $\delta\mathbf{u}$ are, respectively, the corrective stress, traction and displacement jump vectors at step n. It should be noted that in comparison with Eq. (4.32), the strain increment $\Delta\boldsymbol{\varepsilon}$ in this equation is omitted because it had already been used in the explicit step. By zeroing the residual for the current iteration $\mathbf{r}^{n+1} = 0$, the corrective displacement for the current step is calculated by:

$$\delta\mathbf{u} = \left(\frac{1}{H}\mathbf{n}^T\mathbf{a}_o\mathbf{n} + \mathbf{K}^{\tan}\right)^{-1}\mathbf{r}^n \tag{4.38}$$

This corrective displacement is then transformed to the local coordinate system, $\delta\mathbf{u}_c = \mathbf{R}\delta\mathbf{u}$ and used to calculate corrective traction $\delta\mathbf{t}_c$ following the return algorithm described in Section 4.2.4. The tractions in the local and global coordinate system are updated $\mathbf{t}_c^{n+1} = \mathbf{t}_c^n + \delta\mathbf{t}_c$ and $\mathbf{t}^{n+1} = \mathbf{t}^n + \mathbf{R}^T\delta\mathbf{t}_c$. During this process, internal variables inside the localisation zone are also updated. The corrective stress is now computed as:

$$\delta\boldsymbol{\sigma} = -\frac{1}{H}\mathbf{a}_o\mathbf{n}\delta\mathbf{u} \tag{4.39}$$

The stress and residual traction are then updated as:

$$\boldsymbol{\sigma}^{n+1} = \boldsymbol{\sigma} + \delta\boldsymbol{\sigma} \text{ and } \mathbf{r}^{n+1} = \mathbf{n}^T\boldsymbol{\sigma}^{n+1} - \mathbf{t}^{n+1} \tag{4.40}$$

The process of correcting the stress and tractions is performed until convergence is obtained (i.e., $\|\mathbf{r}\| < \epsilon$) and the traction continuity is then satisfied within a pre-defined tolerance, which is taken as $\epsilon = 10^{-4}$ in this study.

The constitutive model in the previous section, together with its stress return algorithm, described above, completes a model and is ready for numerical simulation.

4.4 Application to jointed rock mass

In this section, the capability of the proposed cohesive-frictional model is validated against the experimental results of jointed rock mass. In general, the mechanical and hydraulic properties of a rock mass are strongly affected by the presence of discontinuities such as joints, fractures or faults. The effects of these features, generally referred to as joint, can be very significant in many problems in geology or geophysics, mining or petroleum engineering, hydrogeology and waste management. Therefore, it is important to be able to locate and characterise them remotely within a rock mass using geophysical methods (Cook, 1992). In general, the behaviour of a rock mass is discontinuous, anisotropic, inhomogeneous and inelastic (Harrison and Hudson, 2000). This makes jointed rock mass an ideal subject for the validation of the proposed cohesive-frictional model, which is dedicated to describing the inelastic behaviour of discontinuities or localisation zones. In addition, as jointed rock mass has numerous similarities with quasi-brittle geomaterials, good results in modelling such problems would show a good potential for capturing the failure of the geomaterials.

One of the difficulties in analysing jointed rock masses is its diversity in natural characteristics. Because rock mass is a natural material, rock joints are formed under different stress states and continuous loadings from dynamic movements of the upper crust of the Earth such as tectonic movements, earthquakes, glaciation cycles. This complex and long history of formation makes the *in situ* characteristics of rock joints hard to be determined. However, in any situation, mechanical behaviour of both the joint and the surrounding intact rocks and their interactions are always important factors governing the responses of a jointed rock mass. In this sense, the double-scale approach with embedded cohesive-frictional model is very suitable for modelling such problems since it is developed from an RVE featuring a localisation zone inside, which is analogous to a rock mass with a joint inside. The interactions between responses of joint and its surrounding rocks can be captured naturally thanks to the links between the localisation zone and its surrounding bulks within the same constitutive model. In addition, the flexibility of the proposed cohesive-frictional model controlled by a few parameters, as presented in the previously, allows the model to cope with different *in situ* characteristics of the jointed rock mass. Furthermore, the unified yield-failure surface, gradually transforming from initial yield to ultimate failure, enables the modelling of a joint at different stages of deformation under mixed-mode loading conditions.

The parameter identification for jointed rock mass will be presented in this section, followed by numerical simulation for shear tests under constant normal load of rock joints with different levels of roughness. Numerical results, validated against experimental data, show that the proposed model is able to capture key responses of the rock joint including residual deformations, strength and stiffness reduction and evolution of dilation due to asperity damage. Moreover, as the constitutive model incorporates the mechanical behaviour of the joint along with its relative size and behaviour of the surrounding rock, the deterministic size effect of the rock mass is reflected naturally even at the constitutive level. The size effect, captured by the simple double-scale model at both constitutive level and Finite Element Analysis, will be presented in a separated segment at the end of this section.

4.4.1 Material properties and model parameters calibration for jointed rock mass

Different from the localisation zone in quasi-brittle geomaterials which initiates and develops over the course of loading, the joint in rock mass is a pre-existing entity formed

during the long history of rock mass formation. As a result, most of experiments for rock joint were conducted on replicas or samples having two parts separated from each other with a joint in the middle as illustrated in Figure 4.9a. Therefore, the cohesive-frictional model, proposed for modelling quasi-brittle geomaterials from intact states until failure, needs to be tailored to fit with the conditions in such experiments. Since the focus of the model validation in this section is the shear test of rock joint under constant normal loading, parameters and representations, especially ones related to shear, will be altered/calibrated based on the characteristics of rock joints.

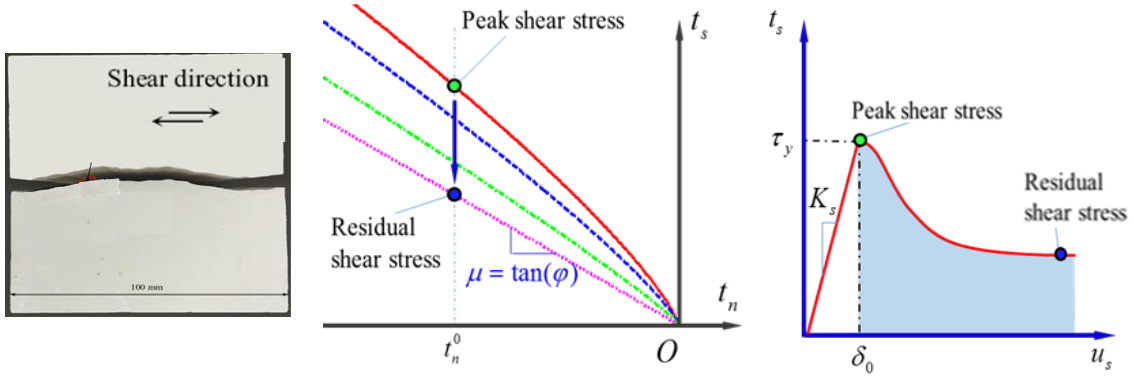

(a) (b) (c)

Figure 4.9. Illustration for rock joint simulation: (a) Example of rock joint test (Li et al., 2016a), (b) Tailored yield function for rock joint modelling and (c) Typical responses for parameters calibration

Due to the completely separated state of the two parts in the experiments, there would be no cohesion and tension resistance left in the joint. To cope with this condition, tensile strength in the proposed cohesive-frictional model is set to be zero $f_t = 0$. As a result, the yield-failure surface of the joint, in this case, starts from the origin of the $t_n - t_s$ coordinate system as illustrated in Figure 4.9b. In addition, the complete separation of the two rock joint sides also change the physical meaning of elastic stiffness in the original cohesive-frictional model. The shear elastic stiffness K_s now represents for the slope of the stress-displacement curve in the shear test experiments. Thus, given a data set of shear experiment, K_s can be calculated by $K_s = \tau_y/\delta_0$ where τ_y is the shear stress peak and δ_0 is the corresponding displacement as illustrated in Figure 4.9c.

The model parameters calibration also needs to be adjusted to fit with the types of material as well as experimental characteristics of rock joint before being used for simulation. Shear stress-displacement results, whose typical form is illustrated in Figure

4.9c, can be used for the calibration of parameters μ_0, μ and m. As in these experiments, shear is superposed with compression ($t_n < 0$), the peak of the shear stress, denoted by a green point on Figure 4.9b and c, would correspond to initial yielding states shows locus is represented by the red curve in Figure 4.9b. In addition, the locus of residual shear stress, represented by a blue point in Figure 4.9b and c, corresponds to the final failure surface which is illustrated by the red curve in Figure 4.9b. The stress peak and residual stress, in this case, are thus used for the calibration of μ_0, μ and m by fitting the shape of the yield-failure surface of the model to these values correspondingly. Since two sides of the joint are already separated and the normal loading is in compression, parameters α_0 is not related to the fracture energy in mode I, as presented in Section 4.2.2, anymore. In addition, in such shear tests, most of the displacement happens in shear direction, meaning that shear displacement is the dominant factor to induce damage in the model. The normal displacement, consequently, has a modest impact on the results of the modelling. Therefore, for the validation in this chapter, α_0 is taken as β (i.e., $\alpha_0 = \beta$), which is not accurate but convenient given that no fracture energy values are recorded in experiments of rock joints. The rest of parameters can still be calibrated by procedures described in Section 4.2.2.

Table 4.1. Rock material/joint properties and model parameters for numerical simulation

	Material/Joint properties from experimental data							Model's parameters				
Parameter	E GPa	ν	f_c MPa	K_n GPa/m	K_s GPa/m	δ_0 mm	H mm	μ	m	μ_0	β	γ
Ex. 1	30.8	0.2	75	10^3	34.73	0.55	90	0.8	0.2	0.7	1.2	1.9
Ex. 2	14.9	0.2	46	10^3	3.07	2.1	100	1.1	0.15	0.7	1.8	1.6
Ex. 3	48.4	0.2	173	10^3	7.07	0.65	140	0.8	0.015	0.5	0.7	1.8

The material properties from published data and the parameters of the model obtained from the calibration are summarised in Table 4.1 for all three examples considered in this chapter. As seen from the formulations presented in the previous section, the double-scale approach is based on the stress-strain relationship of a volume element Ω containing a localisation zone and its responses. Therefore, the model is capable of simulating the shear test at constitutive level (material point level) as long as the characterised length H is provided. As described earlier, the characterised length H is defined as the ratio between the area of the joint and the volume of the considered material body $H = \frac{\Omega}{\Gamma_i}$. Therefore, the values of H for all examples are calculated from the given geometry of the specimens and

are presented in Table 4.1. It should also be noted that in all examples, besides the peak and residual strengths used to calibrate the yield and failure surfaces, a single data set including shear stress – shear strain response and dilation behaviour at a given normal pressure was used for the calibration of other model parameters. The calibrated parameters are then utilised to predict the mechanical response of the joint under other normal pressures. The behaviour predicted by the model is compared with those obtained from experimental studies as well as previous models by other authors.

4.4.2 Example 1: Data from Gentier and co-authors.

The first example is a simulation of the direct shear test of granite mortar replicas, carried under various constant compressive normal stress $\sigma_n = 7, 14$ and 21 MPa. The samples of these replicas were cored across a natural joint of Guéret granite from France. The experiments, whose geometry and arrangement are shown in Figure 4.10, was conducted by Gentier et al. (2000) and was later investigated numerically by Mihai and Jefferson (2013). The shear plane of the specimen is circular with a diameter of 90 mm as shown in the figure. In this example, the first data test ($\sigma_n = 7$ MPa) was used to calibrate the model. The calibrated parameters and other model parameters are presented in the first row of Table 4.1. The results for other normal stress level tests were generated using these calibrated parameters.

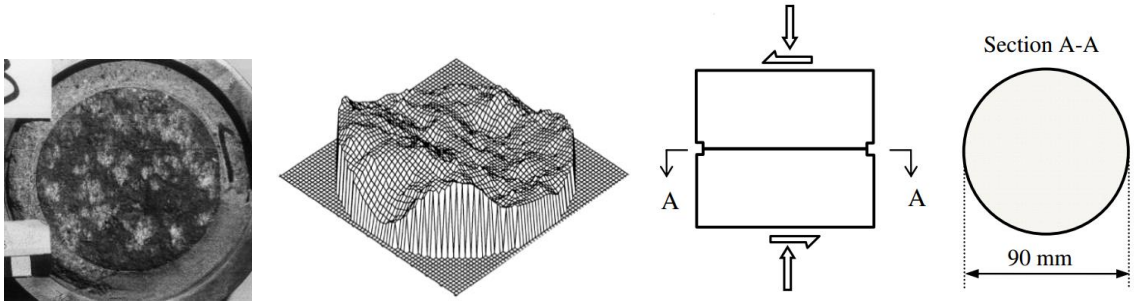

(a) (b) (c)

Figure 4.10. The Gentier's experiment set up (a) Real upper surface of the specimen, (b) 3D representation of the specimen upper surface and (c) Test arrangement (Gentier et al., 2000)

The shear stress – shear displacement responses predicted by the proposed model are plotted in Figure 4.11, Figure 4.12 and Figure 4.13 along with the experimental data by Gentier et al. (2000) as well as results of the model simulation by Mihai and Jefferson (2013). Because four separate tests were conducted for each normal stress level in the experiment

scheme adopted by Gentier et al., there are four experimental results for each case. It is seen from the figures that the results from the proposed model agree well with the experimental data and also those by Mihai and Jefferson (2013) in terms of both shear responses and dilation behaviour. It also can be seen that in all three cases, the peak stresses predicted by the proposed model are in good agreement with its experimental counterparts. This indicates that the initial yield surface governing the peak shear strengths follows well the observed behaviour at different normal stress levels. It should also be noted that the proposed model does not require geometrical characteristics of the joints roughness. Instead, this information is lumped in the evolution of the yield-failure surface from initial yield to final failure. This feature would be useful for modelling the jointed rock in reality where the information about the joint geometries is usually limited. In addition, even though the initiation of dilation is slightly different, the magnitude predicted by the model is in good agreement compared with experimental results. This implies that the dilative responses of the jointed rock behaviour can be well captured by the proposed evolution from initial yield to final failure and non-associated flow rule.

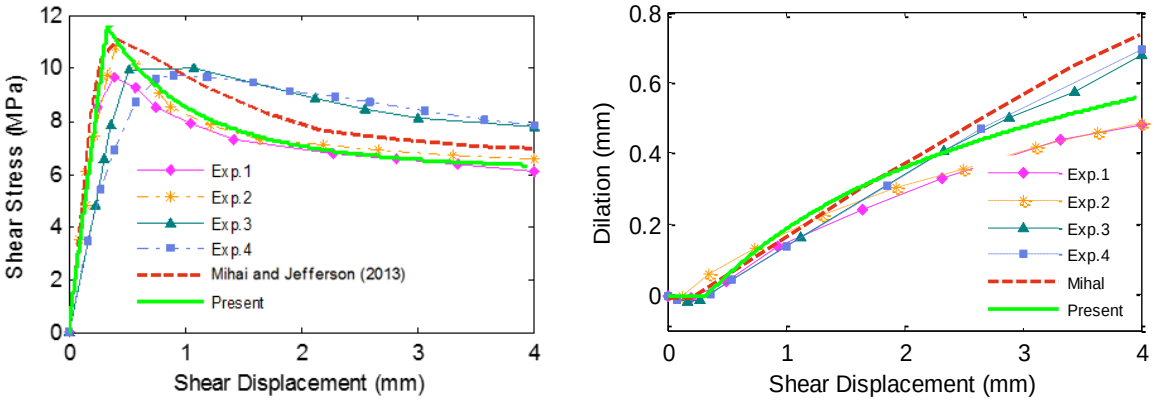

Figure 4.11. Shear and dilation responses under normal compression $\sigma_n = 7$ MPa

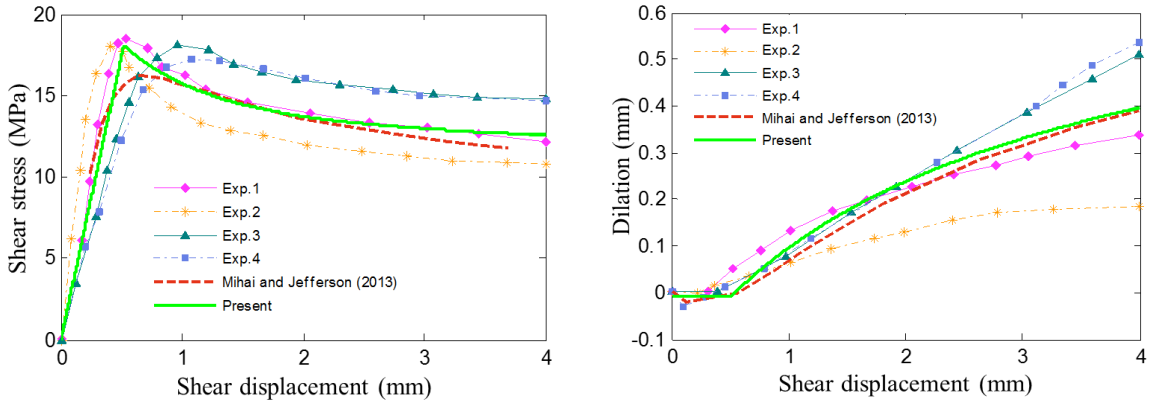

Figure 4.12. Shear and dilation responses under normal compression $\sigma_n = 14$ MPa

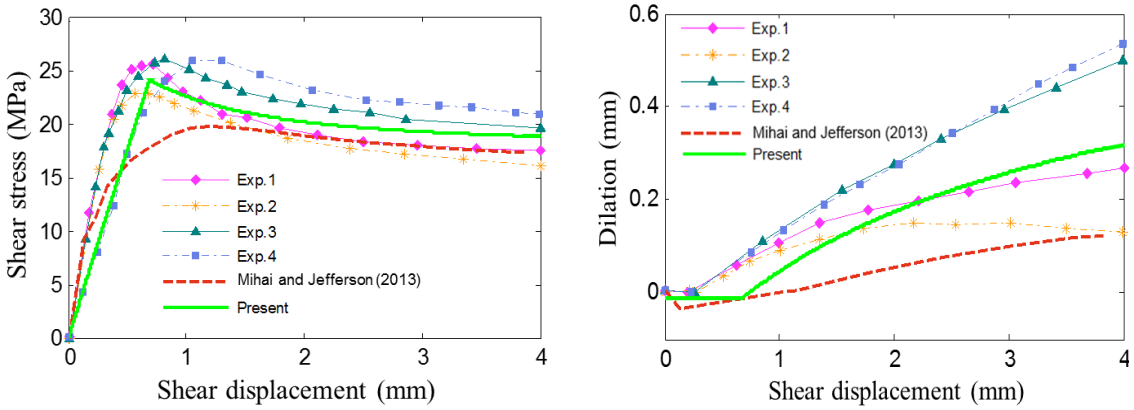

Figure 4.13. Shear and dilation responses under normal compression $\sigma_n = 21$ MPa

It is noted that the patterns of the stress and the dilation evolution from the model are relatively similar to those from experiments. Specifically, the shear stress-displacement curve brought by the model includes 4 phases. Firstly, it begins with a linear elastic part where the contact area between two sides of the joint increases. In this stage, the specimen also experiences contraction owing to the misfit of the two crack sides. This contraction mostly depends on the nature of the joint surfaces and their contacts with each other. The value of the contraction is usually small compared to the dilation (Barton, 1976) and thus is not a focus of the research. This phase keeps going until the shear stress reaches its peak. At this point, the traction state (i.e. t_n, t_s) lies on the initial yield surface. The second phase is the peak shear stress phase where asperities of the joint begin to be worn off and slide on each other. In this phase, the dilation initiates with the maximum rate since most of the asperities have not been worn off yet and these asperities slide on each other, resulting in more dilation. The damage, as well as plastic displacements, also start increasing from zero with the highest rate in this phase. This pattern of damage evolution agrees well with the experimental observation made by Gentier (2000). The shear stiffness hence begins to degrade with the highest rate in this phase. The third phase is the post-peak phase, where softening takes place. In this phase, the failure of asperities progressively increases along with the increase of the contact area between two sides of the joint. As a result, the damage increases together with the contraction of yield surface during this phase. The dilation still increases in this phase but with a lower rate compared to the previous one. Finally, the residual strength is reached. Since there is only friction caused by the remaining roughness of the joint, the shear stress is relatively constant with further shearing in this phase. The dilation might be unchanged or continue increasing at a lower rate compared to previous phases. From the above analysis, it can be seen that the progress of shearing obtained by the

model is totally similar to that observed from experiment except for the first phase where a short pre-peak inelastic part presents. This leads to five phases of shearing instead of four as obtained from the proposed model. However, the general pattern and the magnitude of the results brought by the model agree well with the experimental results.

4.4.3 Example 2: Data from Li and co-authors

The validation of cohesive-frictional model continues with shear tests of precast rock joints from replicas, recently conducted by Li et al. (2016). The geometry and roughness of the jointed rock sample are shown in Figure 4.14. The sample was fabricated with an estimated joint roughness coefficient (JRC) profile 14-16 representing undulating rock joint (Barton and Choubey, 1977). The length of the specimen is 100 mm. The tests were conducted under various constant normal loads (CNL) $\sigma_n = 2, 3.5$ and 5 MPa. The material properties and model parameters for this example were presented in Table 4.1. For this example, the experimental data set in the case $\sigma_n = 2$ MPa was used for the calibration of model parameters.

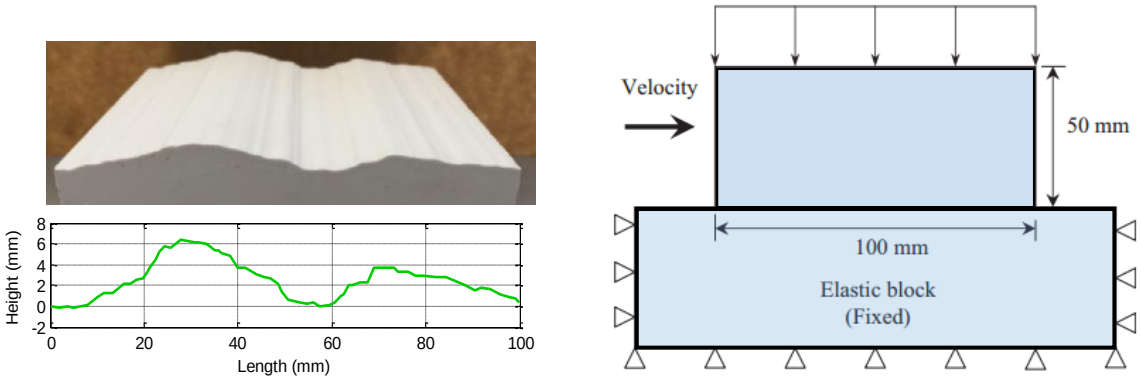

(a) (b)

Figure 4.14. The experiment set up for the second example (a) The geometry of the sample and (b) Test arrangement (Li et al., 2016)

The shear stress against shear displacement and dilation behaviour predicted by the model are plotted in Figure 4.15 in comparison with their experimental counterparts for different levels of normal stress. The results from the model proposed by Li et al. (2016) are also presented in the figure for comparison purpose. It can be seen from the figure that the results from the current model are generally in good agreement with those from the experiments. Although there are still discrepancies between these two sets of results, it can be said that the performance of the model is satisfactory. In spite of the difference of the

dilation initiation, the magnitude of the dilation predicted by the model agrees well with those from the experiments, especially for the case $\sigma_n = 5$ MPa. It is also seen that the dilation decreases with the increase of the normal stress. This is understandable because for shearing under higher normal stresses, the normal tractions between two sides of the joint increases. As a result, the asperities tend to be damaged more at higher normal stresses and the dilation under shearing hence becomes smaller correspondingly. Another noteworthy point is that the proposed model uses limited information from the experiments for the calibration. This would be useful in the simulation of rock joint in the practical context where details on the joint geometries are difficult to obtain. Along with its simplicity and easiness for implementation in conventional Finite Element Analysis, the proposed model could also be a good choice for modelling brittle/quasi-brittle material or further developing for rock mass in practice.

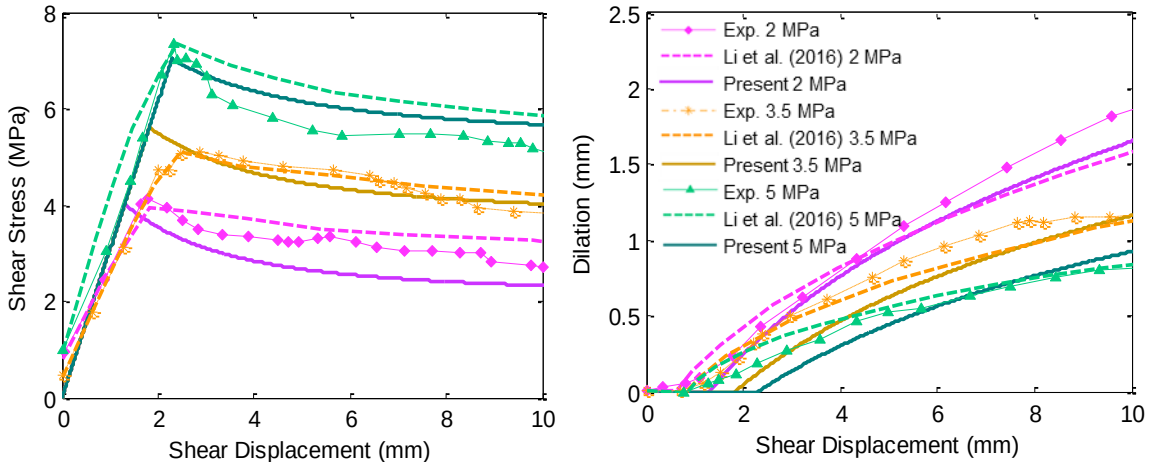

Figure 4.15. Shear stress-displacement and dilation results under different normal stress.

From the results plotted in Figure 4.15, it can also be seen that the behaviour of the jointed rock before the peak is linear and it exhibits a nonlinear softening response immediately after the peak. This is due to the assumption that the degradation of asperities takes place only after the peak and thus damage is activated only after that point. This may not be always the case for all rock joints as damage of the asperities may start even before the peak due to the mismatch of the two surfaces of the joint (Gentier et al., 2000). However, this pre-peak degradation does not significantly affect the post-peak behaviour, which is the focus of the paper, as can be seen in the model predictions. Nonetheless, we acknowledge this shortcoming and would address it in our future study.

4.4.4 Example 3: Data from Grasselli and Egger

In this section, the model is validated with data set from experiments whose geometries and set-up are shown in Figure 4.16. The experiment was conducted by Grasselli and Egger (2003) on samples having joint roughness coefficient, JRC = 18 (Grasselli and Egger, 2003). The replicas were sheared under different values of constant normal stress levels $\sigma_n =$ 1.275, 2.55, 5.1 and 6.1 MPa. The material properties and model parameters for this test was presented in Table 4.1. For this example, the experimental data for the case $\sigma_n =$ 6.1 MPa was used for calibration.

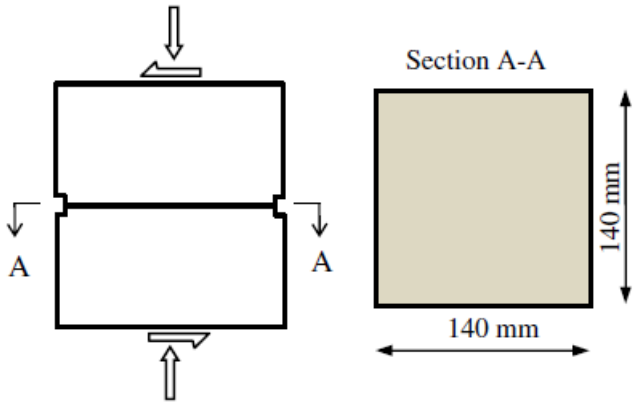

Figure 4.16. Geometry and test arrangement of rock joint (Grasselli and Egger, 2003)

The numerical shear stress-shear displacement results of the test are plotted in Figure 4.17 in comparison with those from experiments and numerical simulation (Mihai and Jefferson, 2013). Because there are no experimental data regarding dilation provided, the dilation of this test is not included here. It is seen from the figure that the results from the proposed model are comparable with those by experiment and numerical simulation by Mihai and Jefferson (2013), confirming the robustness of the proposed approach in modelling rock joint. It should also be noted that after the first yielding, the shear stress in experiments goes slightly higher than the initial yielding stress, especially for the cases of $\sigma_n =$ 5.1 and 6.1 MPa However, as presented by Barton (1976) and confirmed by many experimental results (Asadollahi et al., 2010; Bahaaddini et al., 2014, 2013; Barton, 2013; Fardin et al., 2001; Li et al., 2016b; Saeb and Amadei, 1992), the slight hardening after peak is not the typical behaviour of jointed rock mass in shear under constant normal stress. And because the main focus of the proposed model is to reflect the responses of the rock joint, the model fails to accurately capture this untypical response of this experiment. Nonetheless, the overall responses are adequately described by the proposed model.

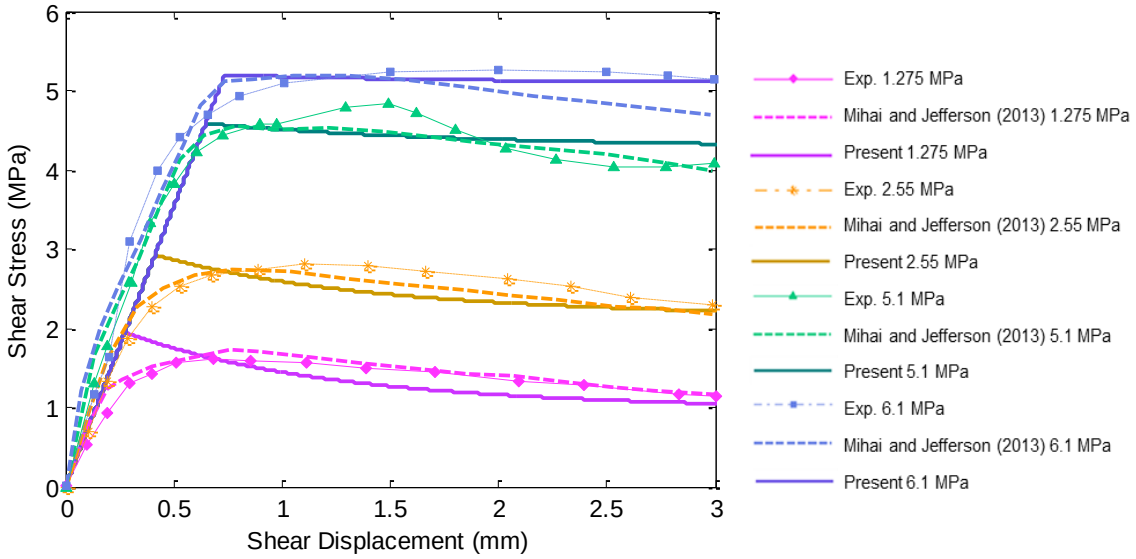

Figure 4.17. Shear stress-displacement and dilation results under different normal stress.

4.4.5 Size effects of jointed rock mass

The possession of a length scale in the constitutive structure, as seen in the model description in Section 4.3, allows capturing the spatial scaling of the constitutive behaviour due to the localisation of deformation. In the context of jointed rock mass behaviour, localised inelastic deformation concentrates mostly at the joint, while the surrounding rock mass can be reasonably assumed to be under elastic deformation. A parametric study is presented in this section to demonstrate the capability of the double-scale approach in capturing the deterministic size effects in modelling rock mass. It should be noted that this deterministic size effect due to localised failure is different from the statistical ones due to randomness of strength along the joint surface (Bažant and Yu, 2009; Bažant, 2000), which has been both experimentally (Yoshinaka et al., 1993) and numerically (Bahaaddini et al., 2014) investigated.

Similar to the analysis made in Section 2.2.3, the deterministic size effect of a jointed rock mass is due to the change in relative size of the joint with respect to its surrounding intact rock. The thickness and behaviour of the joint contained within a rock mass are invariant, irrespective of the rock mass size. This causes the change in contributions of the joint and the surrounding rock when specimen size increase, leading to the scaling in the behaviour of the jointed rock mass. In the proposed model, apart from the inclusion of the characterised length H to represent the relative size of the joint and the surrounding rock, the difference in deformation and behaviour inside the joint and its surrounding rock is also described in the model. This helps the model obtain the deterministic scale effect naturally

with respect to the change in specimen size. The model is thus capable of simulating a jointed rock mass at constitutive level (or one element based simulation) and hence can help save computational costs in modelling jointed rock masses.

To illustrate the scale effect in the model, the jointed rock mass in the first experiment (carried out by Gentier 2000) with normal stress $\sigma_n = 7$ MPa is chosen for this parametric study. By changing the rock mass size, the relative size of the rock joint and the surrounding bulk body would be changed and the resultant responses of the material will be obtained. The experiment will be simulated with four different scales as shown in Figure 4.18a in which the specimen 1 is the original sample with the length of $L = 0.09$ m and the lengths of other specimens (2 3 4) are respectively $0.18, 0.36$ and 0.72 m.

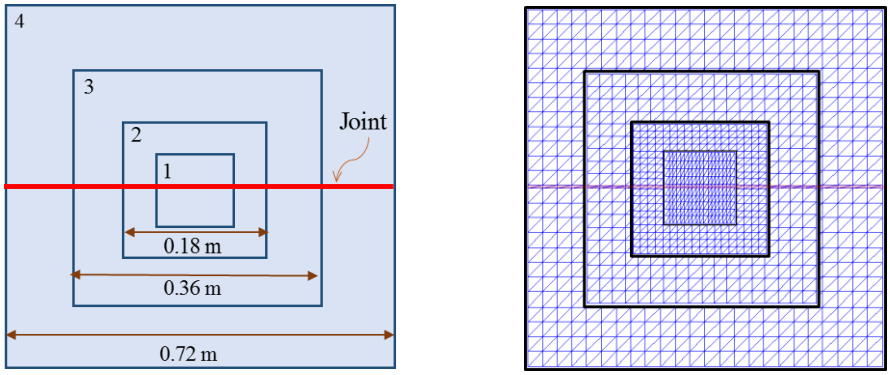

Figure 4.18. Geometries of specimens used for scale effect investigation: (a) Four specimen sizes and (b) Four corresponding discretisation meshes in FEM simulation

In addition to the simulation at constitutive level as described in the previous sections, numerical simulations using Finite Element Analysis (FEA) are also carried out to verify the performance of the proposed size-dependent constitutive model. For the FEA, the proposed constitutive model is implemented into the commercial software ABAQUS in the form of a user-defined material model (UMAT). In such simulations by FEA, a layer of elements (the red layer shown in Figure 4.18b) is used to represent the rock joint with the proposed double-scale constitutive model while the remaining elements represent the surrounding intact rock with elastic behaviour. The thickness of this layer is taken as constant $h = 0.5$ cm for simulations of all rock mass specimens having different sizes to reflect the fact that the joint thickness is the same for different rock mass specimens. Each specimen simulation is discretised with approximately 1200 elements, which means element sizes are different for simulations of different specimens. In these simulations, the elastic parameters of the FE model are obtained by matching its elastic responses with that of the proposed double-scale

constitutive model, while all other parameters governing inelastic behaviour are the same in both models (as taken from example 1).

The corresponding stress-displacement responses under shear predicted by the proposed constitutive model and the FE analysis are plotted in Figure 4.19 for different specimen sizes. It can be seen that the increase of sample size results in a reduction of elastic shear stiffness of the rock mass and an increase of peak displacement δ_0. This shows that by taking both the joint and the surrounding rock behaviour into the developing the constitutive model, the deterministic size effect can be captured even at the constitutive level. However, the values of the shear strengths by the model are unchanged with different scales. This is because the statistical size effects is missing in the current model. The present constitutive approach does not possess such a capability as it represents the constitutive relation with a few variables to save computational costs. It is, of course, natural for a much richer micromechanical approach (e.g. Bahaaddini et al., 2014, 2013) to have such statistical details for better predictions, at a price of much higher computational costs. It can also be seen in Figure 4.19 that the results obtained from the FE analysis and constitutive model are almost the same. This highlights the capability of the proposed model in capturing the behaviour of a jointed rock mass at different spatial scales. This advantage of the model helps save computational cost while being able to capture essential features of a jointed rock mass.

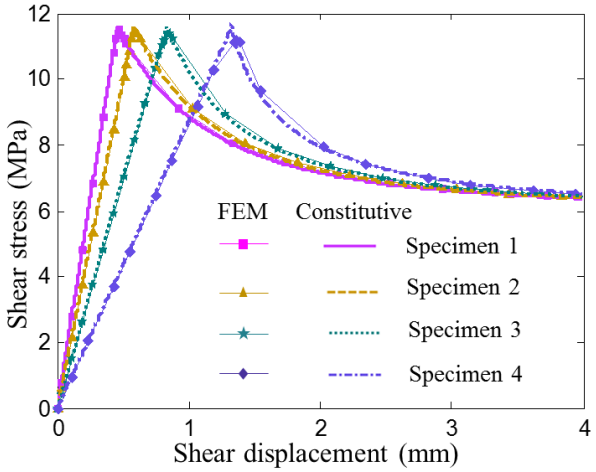

Figure 4.19. Shear stress displacement from the FEM and constitutive simulation

4.5 Summary and discussion

The first step in modelling quasi-brittle geomaterials, which is to describe the responses of the localisation zone, is presented in this chapter with the proposed cohesive-frictional model. The model was built based on damage-plasticity coupling, demonstrated at both the traction – displacement jump relationship and yield-failure surface, to capture the intimate connection between progressive fracture and irreversible deformation taking place simultaneously within the localisation band. The proposed unified yield-failure surface with the presence of damage variable helps to facilitate the evolution and interactions of the damage and plasticity smoothly. The use of a cohesive model defined in traction-separation space, in association with elastic bulk material outside the localisation band, within a continuum framework also helps bridge pure constitutive approaches and popular discretisation techniques widely used in the literature. The obtained results in this research is thus a continuum constitutive model featuring the effect of the discontinuity caused by localisation band inside the material, all described at the constitutive level independent from any numerical schemes for the solutions of BVPs. The parameters in the model were shown to be meaningful and strongly related to physical representations of the materials. As a result, they can be calibrated via standard tests. The details of the model were described, together with its formulation of tangent stiffness and the stress return algorithm for implementation into a constitutive model serving numerical simulation purposes.

The validation against experimental data shows that the proposed cohesive-frictional model is capable of capturing post-peak behaviour of rock joints of different profiles and roughness levels. The numerical results by the proposed model show good agreement with the experimental data, as well as the numerical results from previous studies. Thanks to the coupling of damage and plasticity, the dilation due to the abrasion and slide of asperities in mixed-mode loading conditions can be captured, together with the evolution of traction acting on the joint surface. The behaviour of the rock joint, in this case, is strongly analogous to the localisation zone in quasi-brittle geomaterials, especially the shear or shear-enhanced compaction bands in triaxial compressive conditions. Therefore, this successful validation against rock joint experiments is a direct demonstration of the reliability and applicability of the proposed cohesive-frictional model in describing the localisation zone in quasi-brittle geomaterials. Further investigations into the model's capabilities in other loading cases (i.e., tension and tension-shear mixed mode) will be carried out in the next chapter for quasi-brittle geomaterials; the main aim of this research.

Furthermore, the validation against rock joint experiments also shows some key features of the double-scale approach, used in the research for modelling quasi-brittle geomaterials. Since the double-scale approach, even in its simplest form, incorporates the mechanical behaviour of the joints and the surrounding rock into a constitutive model, the contributions of these two components are naturally taken into account, along with their interactions. This gives the model a better description of the jointed rock mass in different loading cases. In addition, the coupling between the joint and surrounding rock, together with the relative size and orientation of the joint, enable the double-scale approach to capture the scale effects of jointed rock mass behaviour naturally. This size effect, due to the interaction of the localisation zone (i.e., the rock joint in this case) and the outer bulk materials, is one of the key features of quasi-brittle geomaterials. The double-scale model thus proves itself as a potential approach for capturing the localised failure mechanism of quasi-brittle geomaterials. Nonetheless, at this stage, the double-scale model still suffers from some serious limitations and needs further improvements to become a robust and reliable tool for modelling the material. This issue will be addressed at length at the beginning of the next chapter and serves as a motivation for the development of the constitutive model proposed in this research.

CHAPTER 5

An approach to mechanism-based constitutive modelling of quasi-brittle geomaterials

5.1 Introduction

The double-scale approach (Nguyen et al., 2012a, 2012b, 2014), as shown in the previous chapter, features many advantages in modelling quasi-brittle geomaterials, since the localised failure mechanism of the material is directly incorporated into the constitutive model formulation. By explicitly incorporating the localisation band with its relative size and behaviour into constitutive relationships via kinematic enhancements and traction continuity conditions across the band surface, the effect of localised failure is taken into account naturally. In spite of being formulated within a continuum mechanics framework, the model possesses quantities defined inside the localisation zone (i.e., traction and displacement jump) besides the conventional volume-averaged stress and strain. The anisotropy and responses inside the localisation zone are thus described directly with their own internal variables (i.e., plastic deformation and damage). As a result, the deformation and behaviour of the localisation zone are genuinely separated from those of the surrounding bulk material. Other important features of the material (i.e., Lode-angle dependence, size effect, pressure dependence and brittle-ductile transition) are thus expected to be captured as consequences (see Chapter 2) without requiring additional phenomenological constitutive relationships. This highlights the advantages of this approach in comparison with existing models in the current literature. Nonetheless, the double-scale model, at this stage, suffers from severe limitations due to the fact that only one localisation band is featured in the representative volume element (RVE). This issue will be addressed at length in the following section, with appropriate illustrations and analyses, which serve as motivation for further improvements to meet expectations in modelling quasi-brittle geomaterials.

This chapter, thus, presents the proposed mechanism-based constitutive modelling approach for quasi-brittle geomaterials. The proposed model is based on the double-scale approach, with further improvements to overcome its drawbacks in capturing the localised failure of the material. In addition, this chapter investigates several aspects that were not addressed in the original double-scale approach. The validation at both constitutive and

structural levels will be carried out against experimental data from different quasi-brittle geomaterials (e.g., sandstone, granite, limestone and concrete) under various loading conditions. This work has been published in the form of a journal paper (Le et al., 2018) whose content (see Appendix B) is extracted and presented in this chapter.

5.2 Motivation for the proposed model

From a microscopic point of view, the localisation band is, in fact, a system of meso- and/or micro-cracks which are formed during loading, as addressed by Hillerborg et al. (1976) and later confirmed by experimental observations at micro/meso-scale (Alam et al., 2014; Brooks, 2013; Lee and Haimson, 2011; Ma and Haimson, 2016; Seo et al., 2002; Skarzyński and Tejchman, 2016) as well as field scales (Savage and Brodsky, 2011). As analysed in these studies and illustrated in Figure 5.1, a fracture process zone (FPZ) usually consists of both primary and secondary cracks with different orientations. They are results of the coalescence of pre-existing micro-cracks, as well as the initiation and progressive propagation of new cracks over the course of loading (see Seo et al., 2002). The formation and evolution of this zone affect the toughness and ductility of the material significantly (Hu and Duan, 2008).

In modelling of quasi-brittle geomaterials, this finite-width FPZ is usually and practically idealised as a single zero-thickness crack, lumping the contributions of several cracks at lower (micro-/meso-) scales into a cohesive-frictional model. Despite the practical usefulness, this simplification contains potential issues in the calculation of fracture energy from standard experiments, and also in the numerical simulation of structural failure/fracture. The former is the boundary effect on the produced fracture energy and is not the focus of this work, given that averaged fracture energy from standard tests can be used for simulation. The latter is related to the evolution of the FPZ during failure. It is well-known that unphysical stress-locking issue in numerical simulations of concrete fracture, even under proportional loading conditions, is due to taking and fixing the orientation of a single crack at the onset of cracking (see Haghighat and Pietruszczak, 2015; Zhang et al., 2015).

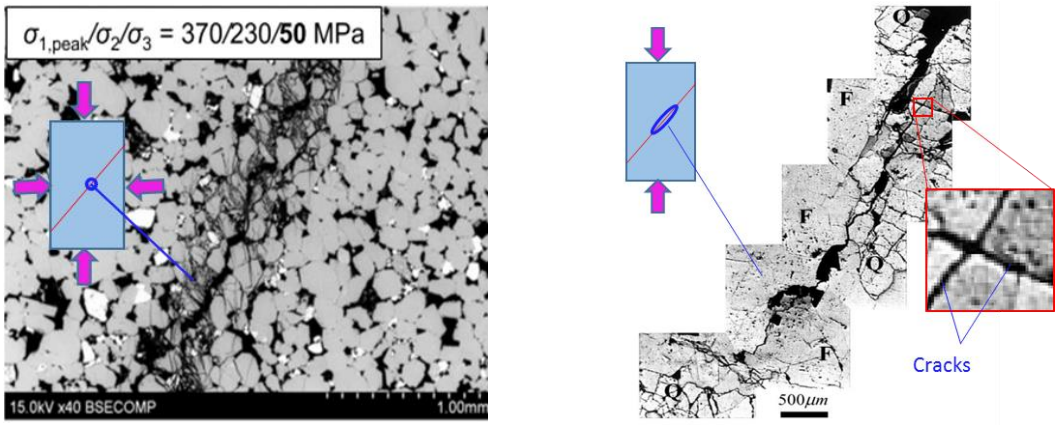

(a) (b)

Figure 5.1. Examples of photomicrograph regarding quasi-brittle geomaterials failure: (a) Coconino sandstone under true triaxial compressive stress (Ma and Haimson, 2016) and (b) Coarse-grained granite under uniaxial compressive stress (Seo et al., 2002)

Due to the fact that it only features one fixed crack inside the RVE, the double-scale approach, proposed by Nguyen et al. (2012a, 2012b, 2014), also suffers from the above-mentioned "artificial" stress-locking, which significantly affects the capacity of the approach in modelling quasi-brittle geomaterials. To illustrate this point, the original double-scale approach with cohesive-frictional model, presented in the previous chapter, is used to simulate a square RVE under a series of loading conditions, as shown in Figure 5.2. The RVE experiences four different displacement-controlled loading phases as follows. Phase 1 is tensile loading in the vertical direction up to $\Delta\delta_1 = 0.3$ mm. Phase 2 is tensile loading in the horizontal direction up to $\Delta\delta_2 = 0.5$ mm. Phase 3 is unloading in the horizontal direction up to $\Delta\delta_3 = 0.2$ mm. Phase 4 is reloading in both directions up to $\Delta\delta_4 = 0.9$ mm. It should be noted that during the loading/unloading in one direction, displacement in the other direction is kept constant. For this simulation, the material properties of concrete are taken as follows: tensile strength $f_t = 2.86$ MPa; compressive strength $f_c = 38.4$ MPa; mode I fracture energy $G_I = 0.063$ KN/m. The model parameters are $\mu_0 = 0.1$; $m = 4.5$; $\alpha_0 = 0.63$, $\beta = 0.0017$; $\gamma = 1.9$; $K_n = K_s = 10^{10}$ and the RVE size $H = 0.1$ m.

The stress-strain responses produced by this one-crack model, plotted in Figure 5.3, show that in phase 1, the vertical stress σ_{11} increases linearly up to the tensile strength, where a crack appears, and then comes to softening, as expected. The stress σ_{22}, however, keeps increasing during phase 2, passing the tensile strength, and reaches 12 MPa at the end of phase 2, as seen in Figure 5.3b. It then reduces to 8 MPa in phase 3, owing to the unloading, before increasing up to 30 MPa at the end of phase 4. Because only one crack is allowed in

this one-crack model, it cannot cope with the change in loading path and the stress unphysically goes far beyond the tensile strength (i.e., $f_t = 2.86$). As discussed previously, this is a serious issue with several existing models in the literature that allow only a single localisation band or crack in the model (see Haghighat and Pietruszczak, 2015; He et al., 2006; Jirásek, 2000; Sancho et al., 2007; Zhang et al., 2015).

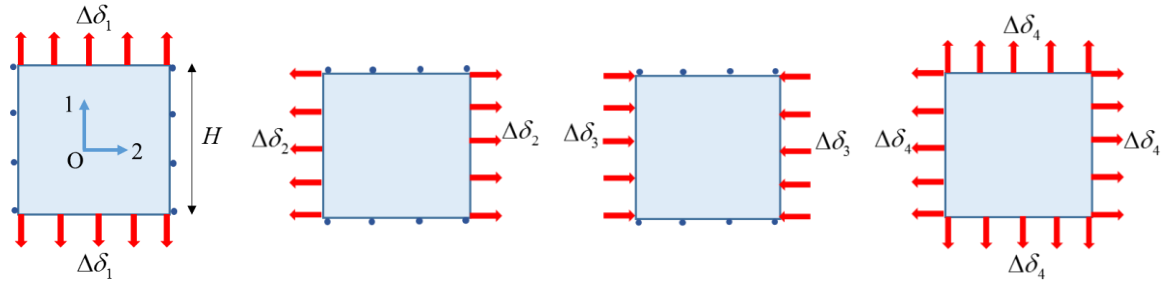

(a) (b) (c) (d)

Figure 5.2. Different loading phases (i.e. phase 1 to phase 4) to examine the original double-scale approach

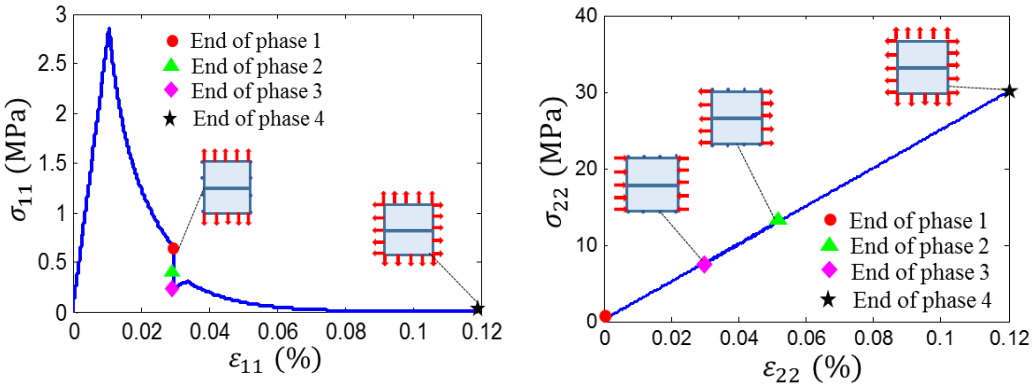

(a) (b)

Figure 5.3. Behaviour of the original model during loading phases: (a) Responses in vertical direction $\sigma_{11} - \varepsilon_{11}$ and (b) Responses in horizontal direction $\sigma_{22} - \varepsilon_{22}$

To avoid this unphysical stress-locking issue during the FEA, special attentions and numerical treatments are needed at the level of the discretisation scheme to obtain a proper crack propagation. These include crack tracking/tracing (Haghighat and Pietruszczak, 2015; Lloberas-Valls et al., 2016; Parvaneh and Foster, 2016; Zhang et al., 2015) and rotating crack approach (He et al., 2006; Jirásek, 2000; Sancho et al., 2007). The main idea of such tracking techniques is to use the information about the crack path in previous elements (e.g., Parvaneh and Foster, 2016) or the average direction of propagation in neighbouring elements (e.g., Haghighat and Pietruszczak, 2015) to calculate the crack orientation in an element. A review of different external techniques for crack propagation used commonly in both continuum-

based and strong discontinuity approaches can be found in the study by Jäger et al. (2008). Despite reproducing reasonable crack path and structural responses, these techniques are artificial, ignoring the fact that the FPZ in fact contains several micro/meso-cracks and hence its orientation can be adjusted naturally with the change in stress path. Besides, these tracking/rotating techniques require additive schemes applied throughout the numerical modelling, which complicate the models and increase the computational cost of the simulation.

Based on the considerations and illustrations described above, the problem of stress-locking will be dealt with in this research by allowing a secondary crack to initiate and develop within the constitutive model if appropriate conditions are met, despite the presence of the primary crack. Due to the straightforwardness of the model's formulation, presented in Section 4.3, the initiation and development of a secondary crack can be featured with minimal changes to the model structure. It will be shown later in this chapter that allowing secondary cracking at the constitutive level is a natural way to remove the stress-locking issue and capture the propagation of the macro-crack during the modelling of quasi-brittle geomaterials correctly. It is true that having more cracks would improve the flexibility of the model but, at the same time, but it would complicate the implementation and computation (for the stress update at both macro and localisation band level). Therefore, in this research, we only use a maximum of two cracks/localisation bands at a material point, which is sufficient to capture the behaviour of quasi-brittle geomaterials in several cases, as will be shown later in the numerical examples. Since this enhancement is at the constitutive level, the implementation of the proposed approach in any mesh-based or mesh-free methods is essentially the same, as it requires only a length scale related to the size of the volume element to bridge the constitutive and structural responses.

Furthermore, to provide a more rigorous and consistent theoretical background for the proposed model, a new thermodynamic formulation is used to connect all the components of the proposed kinematically enriched constitutive model. This has not been achieved in earlier work (Nguyen et al., 2012a, 2012b, 2014, 2016a, 2016b, 2017a, 2017b) where ad hoc relationships outside the thermodynamic formulation were needed. The proposed approach is developed in a generic form and hence can be used with any constitutive models to describe the nonlinear responses inside the localisation zone. This paves the way for a better description of the failure mechanism of quasi-brittle geomaterials.

5.3 A mechanism-based constitutive model

A mechanism-based model featuring two localisation zones will be presented in this section. The model is cast within a new thermodynamic formulation, based the framework of generalised thermodynamics proposed by Houlsby and Puzrin (2000), where the Helmholtz free energy potential and dissipation potential serve as the basis for the model derivation. In the model formulation, the newly-developed cohesive-frictional relationship, presented in the previous chapter, is implemented to describe the behaviour of the localisation bands of quasi-brittle geomaterials. In addition, other aspects of the proposed model related to its implementation including crack initiation, together with its orientation and stress return algorithm, are also described.

5.3.1 Model formulation and derivation

Thermodynamic formulation of the kinematically enriched approach

The constitutive model is developed for a Representative Volume Element (RVE) Ω comprising an outer bulk material Ω_o and two localisation bands $\Omega_k = \Gamma_k h_k$ $(k = 1, 2)$, represented by its area Γ_k and thickness h_k as shown in Figure 5.4. The localisation bands are also characterised by their orientations, which are represented by normal vectors $\mathbf{n}_k$. It should be noted that the two localisation zones can be of any directions depending on stress state of the considered point. Assuming homogeneous behaviour, the tractions at the boundaries between the localisation bands and the bulk material in the global coordinate system and strain vectors of the bands are denoted as $\mathbf{t}_k$ and $\boldsymbol{\xi}_k$ respectively. The stress and strain vectors of the outer bulk material are $\boldsymbol{\sigma}_o$ and $\boldsymbol{\varepsilon}_o$, while the volume-averaged stress and strain vectors of the RVE are denoted as $\boldsymbol{\sigma}$ and $\boldsymbol{\varepsilon}$. It should be noted that the notation k represents localisation band number and has nothing to do with index notation (i.e. $\boldsymbol{\xi}_1$ denotes the strain vector of the localisation band #1).

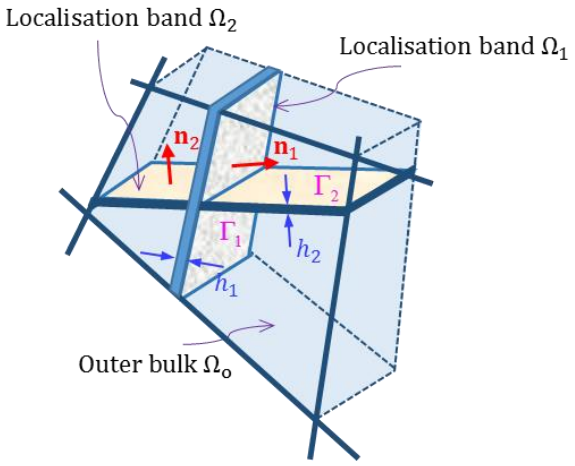

Figure 5.4. Illustration of a representative volume element (RVE) with two cracks.

Similar to the original double-scale modelling, to link the behaviour of the localisation bands to the overall stress-strain relationship of the RVE, the strain increment $\Delta\boldsymbol{\xi}_k$ inside the localisation bands can be expressed in terms of the homogeneous strain increment of the bulk material $\Delta\boldsymbol{\varepsilon}_o$ and an enhancing strain increment from the displacement jump (Neilsen and Schreyer, 1993):

$$\Delta\boldsymbol{\xi}_1 = \Delta\boldsymbol{\varepsilon}_o + \frac{1}{h_1}\mathbf{n}_1\Delta\mathbf{u}_1 \text{ and } \Delta\boldsymbol{\xi}_2 = \Delta\boldsymbol{\varepsilon}_o + \frac{1}{h_2}\mathbf{n}_2\Delta\mathbf{u}_2 \tag{5.1}$$

where $\Delta\mathbf{u}_1$ and $\Delta\mathbf{u}_2$ are the velocity jumps between two sides of the bands in the global coordinate system. The inclusion of the bulk behaviour in this approach allows the use of only a few localisation bands to capture material behaviour with and without localised failure. This is different from some existing micromechanics-based approaches (Caner and Bažant, 2013; Kedar and Bažant, 2015; Misra and Poorsolhjouy, 2016) that require contributions from as many orientations as possible to form the macro strain. The macro strain increment is obtained using Eq. (5.1) and a simple volume averaging homogenisation, assuming the strain in each region is uniform:

$$\Delta\boldsymbol{\varepsilon} = (1-\eta_1-\eta_2)\Delta\boldsymbol{\varepsilon}_o + \eta_1\Delta\boldsymbol{\xi}_1 + \eta_2\Delta\boldsymbol{\xi}_2 = \Delta\boldsymbol{\varepsilon}_o + \frac{1}{H_1}\mathbf{n}_1\Delta\mathbf{u}_1 + \frac{1}{H_2}\mathbf{n}_2\Delta\mathbf{u}_2 \tag{5.2}$$

where $\eta_k = \frac{\Omega_k}{\Omega} = \frac{\Gamma_k h_k}{\Omega}\,(k=1,2)$ is the volume fraction of localisation band k in the RVE. For $H_k = \frac{\Omega}{\Gamma_k}$, defined as the characteristic length of the RVE in relation to the localisation band k, we have $\eta_k = \frac{h_k}{H_k}$. Eq. (5.2) shows that the characteristic length is directly withdrawn from the model formulations and represents the relative size between the localisation band and the RVE. The resulting constitutive behaviour thus automatically scales with the

discretisation used in the Finite Element Analysis (FEA) and the energy dissipated by the localisation in the element is invariant as illustrated later by numerical examples. This feature is one of the main advantages, distinguishing the proposed model from previous studies (Beghini et al., 2007; Caner et al., 2013; Mihai and Jefferson, 2017; Mihai et al., 2016), where characteristic length has to be used after the model formulations as a parameter to scale the energy with respect to the element resolution during the FEA.

The above kinematic enrichment is then employed in the framework of generalised thermodynamics proposed by Houlsby and Puzrin (2000) for the model formulation. Following this framework, the constitutive relation of the material, its internal variables and their evolutions will be derived from two explicitly defined energy potentials: free energy potential, and dissipation potential. The enhanced kinematic condition in Eq. (5.2) will be treated as a kinematic constraint. The procedures established beforehand by Houlsby and Puzrin (2000) will directly result in a kinematically enriched model involving the combined responses of two localisation bands idealised as two cohesive-frictional cracks and the bulk material. No further assumptions, as used previously by Nguyen et al (2012a, 2012b, 2014), will be required. For isothermal processes, the Helmholtz free energy potential Ψ takes the following form, with contributions from both the bulk (Ψ_{o}) and crack faces (Ψ_{Γ_1} and Ψ_{Γ_2}):

$$\Psi = \Psi_{\mathrm{o}} + \frac{1}{\Omega}\left(\Psi_{\Gamma_1}\Gamma_1 + \Psi_{\Gamma_2}\Gamma_2\right) + \mathbf{C}^{\mathrm{T}}\boldsymbol{\Lambda} = \frac{1}{2}\boldsymbol{\varepsilon}_{\mathrm{o}}{}^{\mathrm{T}}\mathbf{a}_{\mathrm{o}}\boldsymbol{\varepsilon}_{\mathrm{o}} + \frac{1}{H_1}\Psi_{\Gamma_1} + \frac{1}{H_2}\Psi_{\Gamma_2} + \mathbf{C}^{\mathrm{T}}\boldsymbol{\Lambda} \tag{5.3}$$

where $\boldsymbol{\Lambda}$ is the vector of Lagrangian multipliers; $\mathbf{a}_{\mathrm{o}}$ is the stiffness matrix of the material in elastic range; $\mathbf{C}$ is the kinematic constraint based on Eq. (5.2):

$$\mathbf{C} = \boldsymbol{\varepsilon} - \left(\boldsymbol{\varepsilon}_{\mathrm{o}} + \frac{1}{H_1}\mathbf{n}_1^{\mathrm{T}}\mathbf{u}_1 + \frac{1}{H_2}\mathbf{n}_2^{\mathrm{T}}\mathbf{u}_2\right) = \mathbf{0} \tag{5.4}$$

The dissipation potential, in this case, consists of two components corresponding to two cracks, assuming the bulk is always elastic:

$$\Phi = \frac{1}{\Omega}\left(\Phi_{\Gamma_1}\Gamma_1 + \Phi_{\Gamma_2}\Gamma_2\right) = \frac{1}{H_1}\Phi_{\Gamma_1}\left(\mathbf{u}_1^{\mathrm{p}}, D_1\right) + \frac{1}{H_2}\Phi_{\Gamma_2}\left(\mathbf{u}_2^{\mathrm{p}}, D_2\right) \tag{5.5}$$

We note that Ψ_{Γ_1}, Ψ_{Γ_2}, Φ_{Γ_1} and Φ_{Γ_2} are surface-based quantities, corresponding to the dissipation per unit surface of area. This naturally leads to the involvement of the length scale $H_k = {\Omega}/{\Gamma_k}$ when writing the energy potential and dissipation potential for a unit volume. The assumption of elastic bulk is generally not correct for the case of shearing under very high confining pressure, but provides reasonable responses for a wide enough range of responses under both tension and compression. We acknowledge this shortcoming and will address it in future studies. The behaviour across crack surfaces Γ_1 and Γ_2 can be reasonably

assumed to be cohesive-frictional, represented by the cohesive-frictional cohesive model, presented in Section 4.2, where $\mathbf{u}_k^{\mathrm{p}}$ and D_k are respectively the plastic displacement jump and damage variable.

Following the procedures established in Houlsby and Puzrin (2000) for the derivation of constitutive models, the true and generalised stresses are:

$$\boldsymbol{\sigma} = \frac{\partial \Psi}{\partial \boldsymbol{\varepsilon}} = \boldsymbol{\Lambda} \tag{5.6}$$

$$\bar{\boldsymbol{\chi}}_{\mathrm{o}} = -\frac{\partial \Psi}{\partial \boldsymbol{\varepsilon}_{\mathrm{o}}} = -(\mathbf{a}_{\mathrm{o}}\boldsymbol{\varepsilon}_{\mathrm{o}} - \boldsymbol{\Lambda}) \tag{5.7}$$

$$\bar{\boldsymbol{\chi}}_{\Gamma_1} = -\frac{\partial \Psi}{\partial \mathbf{u}_1} = -\frac{1}{H_1}\left(\frac{\partial \Psi_{\Gamma_1}}{\partial \mathbf{u}_1} - \mathbf{n}_1^{\mathrm{T}}\boldsymbol{\Lambda}\right) \tag{5.8}$$

$$\bar{\boldsymbol{\chi}}_{\Gamma_2} = -\frac{\partial \Psi}{\partial \mathbf{u}_2} = -\frac{1}{H_2}\left(\frac{\partial \Psi_{\Gamma_2}}{\partial \mathbf{u}_2} - \mathbf{n}_2^{\mathrm{T}}\boldsymbol{\Lambda}\right) \tag{5.9}$$

The corresponding dissipative generalised stresses are obtained from the dissipation potential as follows:

$$\boldsymbol{\chi}_{\mathrm{o}} = \frac{\partial \Phi}{\partial \dot{\boldsymbol{\varepsilon}}_{\mathrm{o}}} = \mathbf{0} \tag{5.10}$$

$$\boldsymbol{\chi}_{\Gamma_1} = \frac{\partial \Phi}{\partial \dot{\mathbf{u}}_1} = \mathbf{0} \tag{5.11}$$

$$\boldsymbol{\chi}_{\Gamma_2} = \frac{\partial \Phi}{\partial \dot{\mathbf{u}}_2} = \mathbf{0} \tag{5.12}$$

The orthogonality conditions (Houlsby and Puzrin, 2000; Ziegler, 1983), $\bar{\boldsymbol{\chi}}_{\mathrm{o}} = \boldsymbol{\chi}_{\mathrm{o}}$, $\bar{\boldsymbol{\chi}}_{\Gamma_1} = \boldsymbol{\chi}_{\Gamma_1}$, and $\bar{\boldsymbol{\chi}}_{\Gamma_2} = \boldsymbol{\chi}_{\Gamma_2}$ lead to the following relationships:

$$\boldsymbol{\sigma} = \boldsymbol{\Lambda} = \mathbf{a}_{\mathrm{o}}\boldsymbol{\varepsilon}_{\mathrm{o}} \tag{5.13}$$

$$\mathbf{t}_1 = \frac{\partial \Psi_{\Gamma_1}}{\partial \mathbf{u}_1} = \mathbf{n}_1^{\mathrm{T}}\boldsymbol{\Lambda} = \mathbf{n}_1^{\mathrm{T}}\boldsymbol{\sigma} \tag{5.14}$$

$$\mathbf{t}_2 = \frac{\partial \Psi_{\Gamma_2}}{\partial \mathbf{u}_2} = \mathbf{n}_2^{\mathrm{T}}\boldsymbol{\Lambda} = \mathbf{n}_2^{\mathrm{T}}\boldsymbol{\sigma} \tag{5.15}$$

in which $\mathbf{t}_1$ and $\mathbf{t}_2$ are the tractions acting on crack surfaces Γ_1 and Γ_2, respectively. It can be seen that, in addition to the kinematic condition in Eq. (5.2), the bulk material and the cracks are linked through the internal equilibrium conditions Eqs. (5.14) – (5.15). As the terms in the energy and dissipation potentials are separated into three parts, corresponding to the bulk material and two cracks as seen in Eq. (5.3) and Eq. (5.5), the constitutive descriptions of these two cracks can be decoupled and dealt with separately. The elastic bulk

in this case does not produce dissipation and its behaviour can be directly obtained from the Helmholtz free energy Ψ_{o}, while the free energy potential Ψ_{Γ_k} and dissipation potential Φ_{Γ_k} written for a unit surface area can be used to obtain the constitutive behaviour of cohesive-frictional crack *k*, following procedures in Houlsby and Puzrin (2000). This separation of models facilitates the formulation of the proposed cohesive-frictional model naturally without any modification or change in the model structure.

Structure of the proposed constitutive model

The proposed model now consists of two traction – displacement jumps relationships of each crack in the global coordinate system, $\Delta\mathbf{t}_{\mathrm{k}} = \mathbf{K}_{\mathrm{k}}^{\tan}\Delta\mathbf{u}_{\mathrm{k}}, (k = 1, 2)$ and the constitutive equation of the outer bulk material, $\Delta\boldsymbol{\sigma} = \mathbf{a}_{\mathrm{o}}\Delta\boldsymbol{\varepsilon}_{\mathrm{o}}$, connected through the internal equilibrium conditions in Eqs. (5.14) – (5.15). The derivation of the macro response connecting macro stress increment $\Delta\boldsymbol{\sigma}$ with macro strain increment$\Delta\boldsymbol{\varepsilon}$ will give us a better idea about the links between several components in the structure of the proposed constitutive model.

By substituting $\Delta\mathbf{t}_{\mathrm{k}} = \mathbf{K}_{\mathrm{k}}^{\tan}\Delta\mathbf{u}_{\mathrm{k}}$ into the incremental forms of traction continuity conditions in Eqs. (5.14) – (5.15), we have

$$\begin{cases}\mathbf{n}_1^{\mathrm{T}}\Delta\boldsymbol{\sigma} = \mathbf{n}_1^{\mathrm{T}}\mathbf{a}_{\mathrm{o}}\Delta\boldsymbol{\varepsilon} = \mathbf{K}_1^{\tan}\Delta\mathbf{u} \\ \mathbf{n}_2^{\mathrm{T}}\Delta\boldsymbol{\sigma} = \mathbf{n}_2^{\mathrm{T}}\mathbf{a}_{\mathrm{o}}\Delta\boldsymbol{\varepsilon} = \mathbf{K}_2^{\tan}\Delta\mathbf{u}\end{cases} \tag{5.16}$$

From Eq. (5.2), the bulk strain increment $\Delta\boldsymbol{\varepsilon}_{\mathrm{o}}$ can be expressed in terms of macro strain increment $\Delta\boldsymbol{\varepsilon}$ and velocity jump $\Delta\mathbf{u}_k$. Substitution of $\Delta\boldsymbol{\varepsilon}_{\mathrm{o}}$ into Eq. (5.16), followed by some transformations and arrangements results in:

$$\begin{cases}\left(\frac{1}{H_1}\mathbf{n}_1^{\mathrm{T}}\mathbf{a}_{\mathrm{o}}\mathbf{n}_1 + \mathbf{K}_1^{\tan}\right)\Delta\mathbf{u}_1 + \frac{1}{H_2}\mathbf{n}_1^{\mathrm{T}}\mathbf{a}_{\mathrm{o}}\mathbf{n}_2\Delta\mathbf{u}_2 = \mathbf{n}_1^{\mathrm{T}}\mathbf{a}_{\mathrm{o}}\Delta\boldsymbol{\varepsilon} \\ \frac{1}{H_1}\mathbf{n}_2^{\mathrm{T}}\mathbf{a}_{\mathrm{o}}\mathbf{n}_1\Delta\mathbf{u}_1 + \left(\frac{1}{H_2}\mathbf{n}_2^{\mathrm{T}}\mathbf{a}_{\mathrm{o}}\mathbf{n}_2 + \mathbf{K}_2^{\tan}\right)\Delta\mathbf{u}_2 = \mathbf{n}_2^{\mathrm{T}}\mathbf{a}_{\mathrm{o}}\Delta\boldsymbol{\varepsilon}\end{cases} \tag{5.17}$$

This equation can be re-arranged in matrix form as:

$$\begin{bmatrix}\frac{1}{H_1}\mathbf{n}_1^{\mathrm{T}}\mathbf{a}_{\mathrm{o}}\mathbf{n}_1 + \mathbf{K}_1^{\tan} & \frac{1}{H_2}\mathbf{n}_1^{\mathrm{T}}\mathbf{a}_{\mathrm{o}}\mathbf{n}_2 \\ \frac{1}{H_1}\mathbf{n}_2^{\mathrm{T}}\mathbf{a}_{\mathrm{o}}\mathbf{n}_1 & \frac{1}{H_2}\mathbf{n}_2^{\mathrm{T}}\mathbf{a}_{\mathrm{o}}\mathbf{n}_2 + \mathbf{K}_2^{\tan}\end{bmatrix}\begin{bmatrix}\Delta\mathbf{u}_1 \\ \Delta\mathbf{u}_2\end{bmatrix} = \begin{bmatrix}\mathbf{n}_1^{\mathrm{T}}\mathbf{a}_{\mathrm{o}} \\ \mathbf{n}_2^{\mathrm{T}}\mathbf{a}_{\mathrm{o}}\end{bmatrix}\Delta\boldsymbol{\varepsilon} \tag{5.18}$$

The velocity jumps of the two cracks can be then calculated from a given macro strain increment as:

$$\begin{bmatrix}\Delta\mathbf{u}_1\\ \Delta\mathbf{u}_2\end{bmatrix}=\begin{bmatrix}\frac{1}{H_1}\mathbf{n}_1^{\mathrm{T}}\mathbf{a}_{\mathrm{o}}\mathbf{n}_1+\mathbf{K}_1^{\tan} & \frac{1}{H_2}\mathbf{n}_1^{\mathrm{T}}\mathbf{a}_{\mathrm{o}}\mathbf{n}_2\\ \frac{1}{H_1}\mathbf{n}_2^{\mathrm{T}}\mathbf{a}_{\mathrm{o}}\mathbf{n}_1 & \frac{1}{H_2}\mathbf{n}_2^{\mathrm{T}}\mathbf{a}_{\mathrm{o}}\mathbf{n}_2+\mathbf{K}_2^{\tan}\end{bmatrix}^{-1}\begin{bmatrix}\mathbf{n}_1^{\mathrm{T}}\mathbf{a}_{\mathrm{o}}\\ \mathbf{n}_2^{\mathrm{T}}\mathbf{a}_{\mathrm{o}}\end{bmatrix}\Delta\boldsymbol{\varepsilon}=\begin{bmatrix}\mathbf{M}_1\\ \mathbf{M}_2\end{bmatrix}\Delta\boldsymbol{\varepsilon} \tag{5.19}$$

where $\mathbf{M}_1$ and $\mathbf{M}_2$ are 3-by-6 matrices for 3D cases. The constitutive relation of the RVE crossed by two cracks can then be written as

$$\Delta\boldsymbol{\sigma}=\mathbf{a}_{\mathrm{o}}\left[\Delta\boldsymbol{\varepsilon}-\frac{1}{H_1}\mathbf{n}_1\Delta\mathbf{u}_1-\frac{1}{H_2}\mathbf{n}_2\Delta\mathbf{u}_2\right]=\mathbf{a}_{\mathrm{o}}\left[\mathbf{1}-\frac{1}{H_1}\mathbf{n}_1\mathbf{M}_1-\frac{1}{H_2}\mathbf{n}_2\mathbf{M}_2\right]\Delta\boldsymbol{\varepsilon} \tag{5.20}$$

As shown in the above formulation, both responses of the cracks and their surrounding bulk are included in the constitutive model through the application of a set of kinematic enrichments and internal equilibrium conditions across the boundaries of the cracks. Because the constitutive model is constructed within the thermodynamic framework, the model automatically complies with the First and Second Laws of thermodynamics. It can also be seen that the orientations, relative sizes and mechanical responses of the cracks, along with the behaviour of the surrounding bulk material, are incorporated in the macro behaviour. Size effect can thus be captured naturally at the constitutive level, and the generic model also possesses in-built regularisation effects thanks to the natural appearance of the sizes H_k in the constitutive structure. We will show later that this will naturally lead to convergence of numerical results with respect to the discretisation in the analysis of BVPs and no other regularisations are needed. In addition, it can also be seen in the constitutive structure Eq. (5.20) that the macro behaviour is governed by the responses of two embedded localisation bands that can be activated or deactivated depending on the stress conditions. This generic structure requires appropriate models at the scale of the localisation band, where inelastic behaviour actually takes place. Therefore, incorrect smearing of inelastic behaviour over the whole volume element is totally removed. In other words, phenomenology in this case has been transferred to the lower scale of the localisation band which is described by the proposed cohesive-frictional model, presented and validated in the previous chapter.

5.3.2 Model implementation

It is seen from Figure 5.4 and the model formulation in the previous section that crack/localisation bands are directly incorporated into the model and its orientation is taken into account in the constitutive formulations. This means that for each element (or alternatively integration point), the onset of crack and its orientation have to be determined and put to use for the rest of the computation. In this research, the cohesive-frictional model, describing the behaviour of the localisation band, provides the model with a natural way to

do so at constitutive level without requiring any additional criterion. Therefore, a scheme for crack initiation and its orientation as well as an implicit stress return algorithm of the proposed constitutive model will be presented in this section to facilitate its implementation into numerical methods (i.e., Finite Element Analysis) for solving Boundary Value Problems.

5.3.2.1 Crack initiation and its orientation

When solving Boundary Value Problems (BVPs) by Finite Element Analysis (FEA), it is necessary to have a criterion based on which crack initiation and its orientation are determined for each integration point. There are numerous approaches and criteria proposed in the literature to tackle this issue. Studies such as (Červenka and Papanikolaou, 2008; Dong et al., 2010; Unger et al., 2011) used the Rankine criterion, where crack initiates when the maximum principal stress exceeds the material tensile strength. In this case, the crack orientation is always perpendicular to the maximum principal direction. Although this criterion is useful in tension, it is not applicable to cases where tension is not the failure mechanism (i.e. compression, shear loadings). Originated from the pioneering work by Rudnicki and Rice (1975), acoustic tensor has been used for the onset of localisation and given reasonable results in several studies (Chemenda, 2009; Das et al., 2011, 2013, 2014; Nguyen et al., 2016a, 2016b; Tengattini et al., 2014). Following this approach, the orientation associated with the minimum determinant of the acoustic tensor is selected as localisation band orientation. Given the lack of localisation mechanisms and associated models, the use of the acoustic tensor for the determination of localisation band orientation is reasonable in classical continuum models.

However, in this study, the cohesive-frictional model used to describe the behaviour of the localisation band gives us a more natural way to not only detect the onset and orientation of the band but also to track its evolution. In particular, for a given stress state, all possible crack orientations are scanned and checked for crack initiation. For each potential orientation, the normal traction t_n and shear traction t_s acting on that plane are calculated using continuum mechanics equations:

$$t_n = n_i \sigma_{ij} n_j \text{ and } t_s = \sqrt{\left\|\sigma_{ij} n_j\right\|^2 - {t_n}^2} \tag{5.21}$$

where n_i is the normal vector of the plane, and σ_{ij} is stress state of the material in index notation form. A crack will appear if there exists a traction vector $({t_n}^*, {t_s}^*)$ that maximises

the initial yield function: $y(t_n{}^*, t_s{}^*) = \max_{\forall \mathbf{n}}\{y(t_n, t_s, D = 0)\} \geq 0$. The orientation corresponding to this traction vector is the crack orientation at that material point, and it is used for the rest of the calculation. The determination of the characteristic length as the ratio between the RVE volume and the surface area of the localisation band (Eq. (5.2) and Figure 5.4) can then be performed automatically. In the research, this procedure will be used as the crack initiation criterion for both first and second cracks: if the material is intact, the criterion is used to check if the first crack is formed; and if a crack already exists, it will check for the activation of the second crack.

5.3.2.2 Stress return algorithm

Similar to the original double-scale model, an implicit algorithm is employed to update the stress state given a strain increment because it can give relatively good results for larger increments compared to the explicit algorithm. Given that the algorithm for the model featuring one crack was clearly described previously in Section 4.3.2, only the case where two cracks with two orientations $\mathbf{n}_1$ and $\mathbf{n}_2$ have been triggered, is presented here.

For a given strain increment, if a crack is under loading (i.e. opening, shearing), its behaviour is inelastic and if it is under unloading (i.e. closing), the behaviour is elastic and hence secant stiffness is used. Therefore, both cracks are first assumed to be elastic to calculate the trial displacement increment in the global coordinate system $\Delta\mathbf{u}_k^{\mathrm{tr}}$ $(k = 1, 2)$ following Eq. (5.19), with $\mathbf{K}_k^{\tan}$ replaced by $\mathbf{K}_k^{\sec}$. The secant stiffness of crack k in the global coordinate system is $\mathbf{K}_k^{\sec} = \mathbf{R}_k^T \mathbf{K}_{ck}^{\sec} \mathbf{R}_k$, where $\mathbf{K}_{ck}^{\sec}$ is secant stiffness, presented in Eq. (4.1) of the previous chapter, in the local coordinate system and $\mathbf{R}_k$ is the transformation matrix of crack k. The trial stress increment $\Delta\boldsymbol{\sigma}^{\mathrm{tr}}$ is calculated by using Eq. (5.20) and the trial traction in the global coordinate system is then computed by:

$$\Delta\mathbf{t}_k^{\mathrm{tr}} = \mathbf{n}_k^{\mathrm{T}} \Delta\boldsymbol{\sigma}^{\mathrm{tr}} \text{ and } \mathbf{t}_k^{\mathrm{tr}} = \mathbf{t}_k + \Delta\mathbf{t}_k^{\mathrm{tr}}, k = 1, 2 \tag{5.22}$$

The trial traction of each crack is transformed to the local coordinate system and then substituted back into the yield function in Eq. (4.2) to test the assumptions of elasticity made previously. If the yield function value of a crack is negative, the assumption of elasticity is correct. Otherwise, the assumption is not correct and the crack is in inelastic state. As there are two cracks in the model, one of the following four possible scenarios will happen: (i) both cracks are closing; (ii) crack 1 is closing, crack 2 is opening; (iii) crack 1 is opening, crack 2 is closing; and (iv) both cracks are activated. For each scenario, the tractions are updated by corrective traction $\Delta\mathbf{t}_k^{\mathrm{cor}}$ in the global coordinate system corresponding to each

crack state ($\Delta\mathbf{t}_k^{\mathrm{cor}} = \mathbf{0}$ if the crack is closing). The algorithm for calculating the corrective traction in inelastic case follows procedures described in Section 4.2.4 of the preceding chapter with appropriate transformation. The traction in the global coordinate system is then updated by:

$$\mathbf{t}_k = \mathbf{t}_k^{\mathrm{tr}} + \Delta\mathbf{t}_k^{\mathrm{cor}};\ k = 1, 2 \tag{5.23}$$

Up to this point, the traction in each crack is returned to its proper value with respect to the crack state, but the overall stress is still at the trial state $\boldsymbol{\sigma}^{\mathrm{tr}} = \boldsymbol{\sigma} + \Delta\boldsymbol{\sigma}^{\mathrm{tr}}$. Therefore, the internal equilibrium conditions in Eqs. (5.14) – (5.15), $\mathbf{n}_k^{\mathrm{T}}\boldsymbol{\sigma}^{\mathrm{tr}} - \mathbf{t}_k = \mathbf{0}$, are not met. An iterative procedure is thus used to correct the stress with the aim of meeting internal equilibrium conditions. To do this, two residual traction vectors corresponding to two cracks are defined as

$$\mathbf{r}_1 = \mathbf{n}_1^{\mathrm{T}}\boldsymbol{\sigma} - \mathbf{t}_1 \text{ and } \mathbf{r}_2 = \mathbf{n}_2^{\mathrm{T}}\boldsymbol{\sigma} - \mathbf{t}_2 \tag{5.24}$$

By using the first order Taylor expansion for the residual at the current iteration n, the traction residual of the next iteration $n+1$ is given by:

$$\boldsymbol{r}_1^{n+1} = \boldsymbol{r}_1^n + \boldsymbol{n}_1^T\delta\boldsymbol{\sigma} - \delta\boldsymbol{t}_1 \ \textit{and}\ \boldsymbol{r}_2^{n+1} = \boldsymbol{r}_2^n + \boldsymbol{n}_2^T\delta\boldsymbol{\sigma} - \delta\boldsymbol{t}_2 \tag{5.25}$$

where $\delta\boldsymbol{\sigma}, \delta\mathbf{t}_1$ and $\delta\mathbf{t}_2$ are the iterative stress and tractions from iteration n to $n+1$. Then, the stress increment in Eq. (5.20) is substituted into Eq. (5.25) with suitable tangent stiffness $\mathbf{K}_k^{\tan}$ to solve for the iterative displacement increment $\delta\mathbf{u}_1$ and $\delta\mathbf{u}_2$. With some arrangements, one obtains:

$$\begin{cases}\boldsymbol{r}_1^{n+1} = \mathbf{0}\\ \boldsymbol{r}_2^{n+1} = \mathbf{0}\end{cases} \rightarrow \begin{bmatrix}\delta\boldsymbol{u}_1\\ \delta\boldsymbol{u}_2\end{bmatrix} = \begin{bmatrix}\frac{1}{H_1}\boldsymbol{n}_1^T\boldsymbol{a}_o\boldsymbol{n}_1 + \boldsymbol{K}_1^{tan} & \frac{1}{H_2}\boldsymbol{n}_1^T\boldsymbol{a}_o\boldsymbol{n}_2\\ \frac{1}{H_1}\boldsymbol{n}_2^T\boldsymbol{a}_o\boldsymbol{n}_1 & \frac{1}{H_2}\boldsymbol{n}_2^T\boldsymbol{a}_o\boldsymbol{n}_2 + \boldsymbol{K}_2^{tan}\end{bmatrix}^{-1}\begin{bmatrix}\boldsymbol{r}_1^n\\ \boldsymbol{r}_2^n\end{bmatrix} \tag{5.26}$$

It is worth noting that in the calculation of $\delta\mathbf{u}_1$ and $\delta\mathbf{u}_2$, the strain increment is neglected because it is already used in the trial step. The obtained displacement increments are then transformed back to the local coordinate system and used to update tractions following standard procedures described in Section 4.2.4 of Chapter 4. The iterative stress is then calculated as

$$\delta\boldsymbol{\sigma} = -\frac{1}{H_1}\boldsymbol{a}_o\boldsymbol{n}_1\delta\boldsymbol{u}_1 - \frac{1}{H_2}\boldsymbol{a}_o\boldsymbol{n}_2\delta\boldsymbol{u}_2 \tag{5.27}$$

This process is repeated until a convergence criterion is satisfied: $\|\mathbf{r}_k\| < \text{tolerance}$. At that stage, the traction continuity would be satisfied within a pre-defined tolerance and all quantities and internal variables are updated in consistence with their proposed descriptions and constitutive equations.

5.4 Application to modelling geomaterials

In this section, the capability and robustness of the proposed model will be investigated at both constitutive and structural levels. Some general features of the model including stress-locking removal and predicted yield locus with Lode-angle dependence are presented, followed by model validation against tri-axial tests results from sandstone and concrete together with illustrations of size effect featured in the model. The validation goes on to demonstrate the model capability in capturing the localised failure and responses of quasi-brittle geomaterials by simulating structural applications of the materials.

5.4.1 Model behaviour and validation at constitutive level

5.4.1.1 Stress-locking removal illustration

To show that incorporating two cracks in the constitutive model naturally helps overcome the stress-locking encountered in the above analysis, the problem described in Section 5.2 is now solved by the proposed two-crack model with the same material properties and parameters as presented earlier in that section. The stress-strain responses, plotted in Figure 5.5, show that during phase 1, σ_{11} quickly reaches tensile strength and then experiences softening after the appearance of a horizontal crack (the primary crack) as seen in Figure 5.5a. In this phase, owing to displacement restraint in the horizontal direction and the Poisson effect, σ_{22} increases up to 0.7 MPa while σ_{11} increases, and then decreases to 0.3 MPa when σ_{11} decreases. In phase 2, with the applied displacement along the horizontal direction, σ_{22} linearly increases up to the tensile strength, and decreases after the formation of a vertical crack (a secondary crack). These two cracks divide the RVE into 4 blocks as illustrated in Figure 5.5b. At the beginning of phase 2, owing to the increase of σ_{22} and the displacement restraint along the vertical direction, the intact blocks shrink vertically and force the primary crack to continue opening. However, after σ_{22} reaches tensile strength, and experiences softening, all four blocks expand vertically leading to closure of the primary crack. In phase 3, because the unloading is applied in the horizontal direction, the secondary crack closes and thus σ_{22} decreases. This phase shows that the secant stiffness of the cracks is degraded because of the damage development during previous phases (shown in Figure

5.5b). Similar to phase 2, the primary crack keeps closing in phase 3, resulting in a vertical drop of σ_{11} (Figure 5.5a). During phase 4, because displacements are applied to both directions, it is clear that both cracks should further open. Therefore, stresses σ_{11} and σ_{22} both increase elastically at first (as they are both in the elastic state) and then experience inelastic softening once they reach their yield points again. This analysis shows that a secondary crack is a must to better describe the behaviour of geomaterials in general loading cases where loading/unloading or change of loading paths occur. It should be noted that by using the same argument, a third crack might be necessary for 3D formulations to stop stress σ_{33} from increasing. However, this is beyond the scope of this paper and will be addressed in future studies.

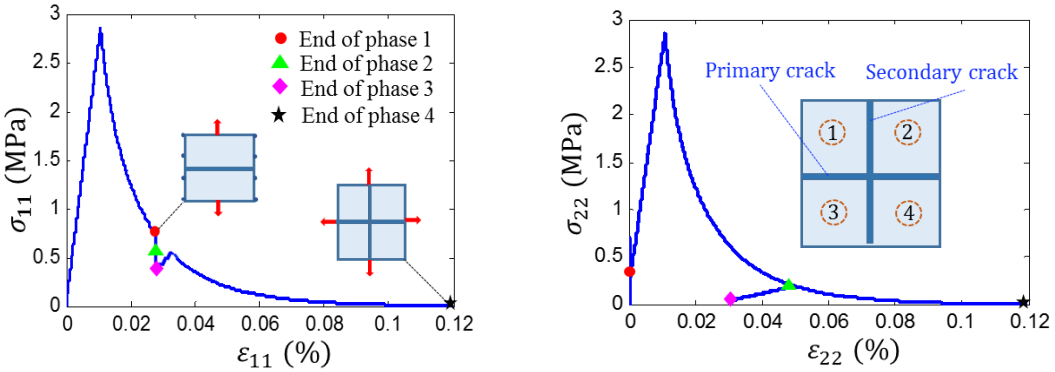

(a) (b)

Figure 5.5. Behaviour of the proposed model during loading phases: (a) Responses in vertical direction $\sigma_{11} - \varepsilon_{11}$ and (b) Responses in horizontal direction $\sigma_{22} - \varepsilon_{22}$

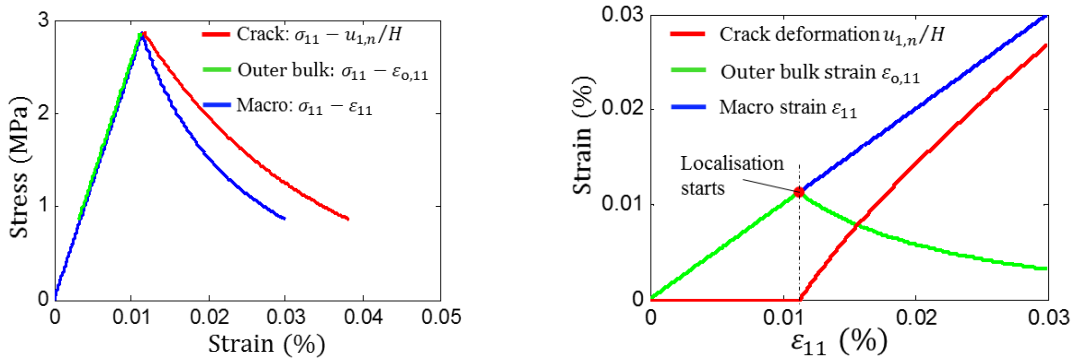

(a) (b)

Figure 5.6. Detailed stress-strain responses and deformation during phase 1: (a) Stress-strain responses and (b) Deformation responses

In addition, Figure 5.6 shows details of the localisation band, the outer bulk material and the overall (macro) responses during phase 1 to further illustrate the capability of the

proposed model in capturing the localised deformation observed in geomaterials. It can be seen that the outer bulk strain in 1-axis direction, $\varepsilon_{o,11}$, is equal to the macro (overall) strain ε_{11} before localisation takes place. Once localisation of deformation initiates, the outer bulk material is under unloading, with both strain and stress decreasing (see Figure 5.6). The localisation band, on the other hand, is under inelastic loading (i.e. opening) with a decrease in stress and an increase in $u_{1,n}$ which is the normal displacement jump of the first crack in its local coordinate system. The macro behaviour of the material, presented by the blue curve in Figure 5.6a and b, is a combination of these two responses with respect to their contributions as described in the constitutive equation Eq. (5.20). This change of loading paths in both intact bulk material and the localisation band within a continuum model is a key feature that distinguishes the proposed model from other continuum-based model (Brünig and Michalski, 2017; Grassl et al., 2013; Karrech et al., 2011; Mir et al., 2018; Paliwal et al., 2017; Zhu et al., 2016) and micromechanics based models (i.e. Das et al., 2011, 2013, 2014, Tengattini et al., 2014) where such responses cannot be captured.

A different loading path, shown in Figure 5.7, is used to further illustrate a more general case with two cracks not perpendicular to each other. The same material properties and model parameters, employed in the above problem, are used for this example. In this loading path, the RVE experiences two displacement-controlled loading phases. Phase 1 is a mixed-mode loading with normal displacement in the vertical direction up to $\Delta\delta_1 = 0.1$ mm, shear displacement $\Delta\delta_{12} = 2\Delta\delta_1$ and $\Delta\delta_2 = 0$. Phase 2 is tensile loading in the horizontal direction up to $\Delta\delta_2 = 0.5$ mm while $\Delta\delta_1 = \Delta\delta_{12} = 0$.

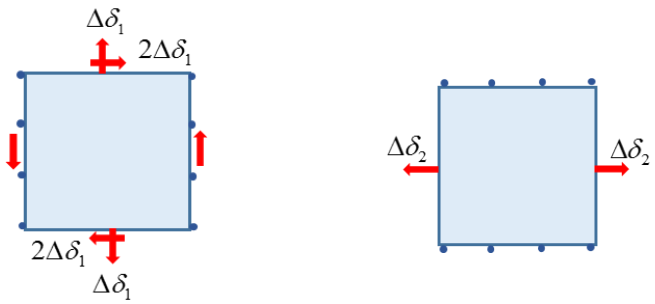

Figure 5.7. Different loading phases: (a) Phase 1 and (b) Phase 2

The stresses in two directions with respect to the calculation step (6000 steps in total) are plotted in Figure 5.8 for both one-crack and two-crack models. It is seen that for the one-crack model, a crack with an inclination angle of 30^0 is formed at the end of phase 1. In phase 2, even though this crack opens under the given horizontal displacement, stress can

still be transferred through it, leading to an unphysical increase of σ_{22} up to 10 MPa as shown in Figure 5.8a. This is the well-known stress locking issues, described in previous studies (Jirásek, 2000; Rots, 1991; Sancho et al., 2007). When secondary cracking is introduced, it helps avoid this unphysical locking as shown in Figure 5.7b. As shown in this figure, the first and second cracks are not necessarily perpendicular with each other which gives the proposed constitutive model flexibilities in capturing the formation and evolution of FPZ that consists of several smaller cracks in different orientations as illustrated in Figure 5.1.

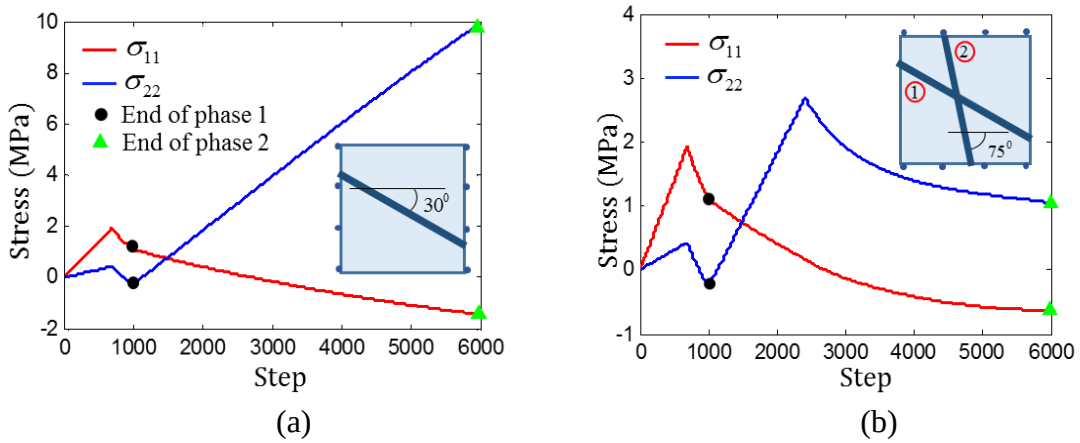

(a) (b)

Figure 5.8. Model behaviour: (a) One-crack model and (b) Two-crack model

5.4.1.2 General features and validation of the yield locus

A typical yield locus produced by the proposed model, plotted in Figure 5.9, clearly shows its dependence on the hydrostatic pressure and the Lode angle. As can be seen, this is a characteristic of macro behaviour generated by the embedded mechanism of localisation in the proposed constitutive structure while the third stress invariant is not present in the proposed model. In tension range, the resulting yield locus has a triangular shape in the deviatoric plane (Figure 5.9b). With an increase of compressive pressure, the triangular yield locus gradually becomes more radically symmetrical. This feature by the model distinguishes itself from the Mohr-Coulomb yield model which has the same shape in different deviatoric planes given the same set of parameters. Although the yield locus has non-smooth corners, the proposed model will not encounter singularity problems when taking derivatives of the yield function, as in the Rankine, Tresca and Mohr-Coulomb models. This is because the material yielding in the model is produced from the embedded localised failure mechanism, controlled by the cohesive-frictional model whose yield surface is continuous and defined on the failure plane. Therefore, there is no explicit macro yield

function as in classical continuum models and thus the singularity issues experienced in such models do not present here.

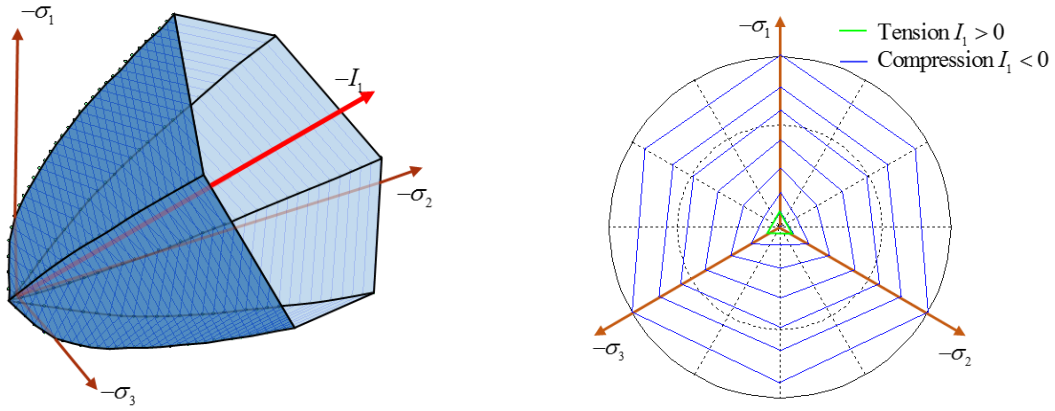

(a) (b)

Figure 5.9. A typical yield locus produced by the proposed model: (a) Yield locus in principal stress space and (b) Yield locus in the deviatoric plane at different hydrostatic pressure levels.

However, it can be seen that the yield locus is not a closed surface in the compressive direction, which indicates that if a material point is loaded along the compressive hydrostatic path ($\sigma_1 = \sigma_2 = \sigma_3 < 0$), it never yields. This is a direct consequence of the open-shaped cohesive model defined on the failure plane, meaning that failure will not appear in pure compression and the bulk behaviour is elastic (see Section 4.2). This problem can be overcome by introducing a close-shaped cohesive model and/or inelastic bulk behaviour to mimic failure due to material crushing under high confining pressures. This issue will be resolved in future work.

Another important feature of the proposed model is that every yielding point on the yield locus is associated with a corresponding failure plane as illustrated in Figure 5.10 and Figure 5.11 for typical loading paths, including tension, triaxial compression (TXC), shear and triaxial extension (TXE). In the tension case, the crack orientation only changes when the direction of the maximum principal stress changes. This is reasonable because, in this case, the crack orientation only depends on the maximum principal stress direction, which coincides with the Rankine criterion. For compression, the failure plane orientation by the model evolves with changes in the loading path as also observed in experiments (Ingraham et al., 2013; Klein and Reuschlé, 2003; Ma and Haimson, 2016; Vachaparampil and

Ghassemi, 2017). All of these results are naturally produced by the model without requiring adding the third stress invariant (or Lode angle parameter) in the yield function.

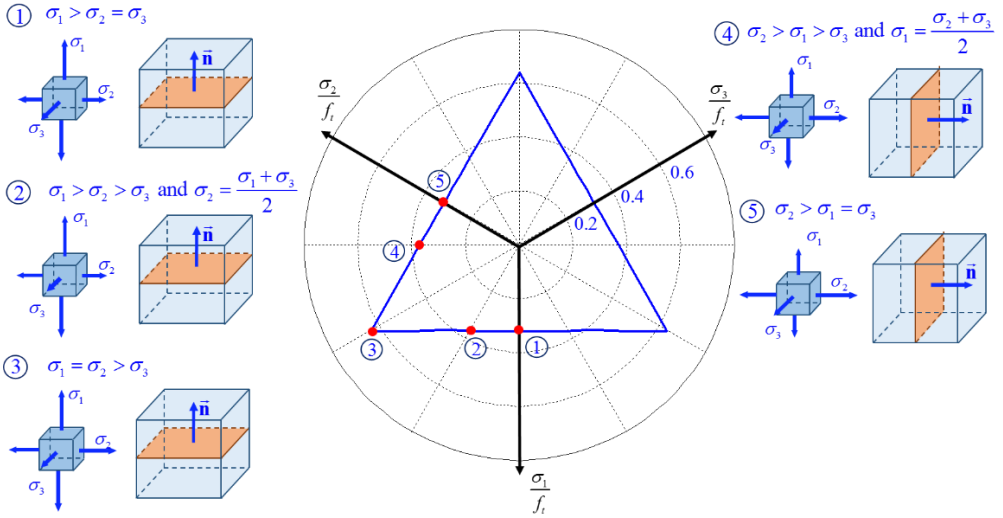

Figure 5.10. Example of dimensionless failure locus in the deviatoric plane for tension

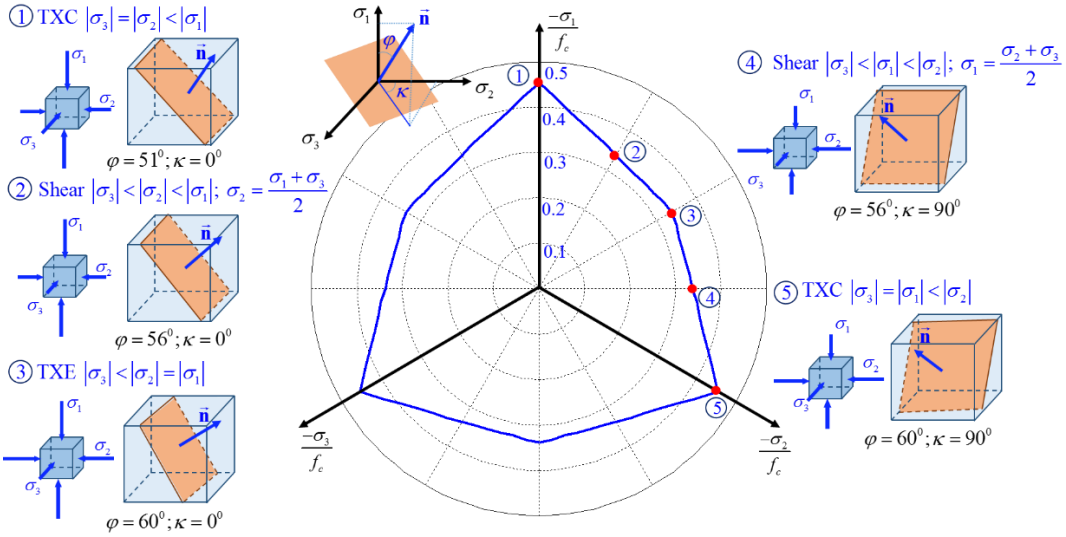

Figure 5.11. Example of dimensionless failure locus in the deviatoric plane for compression

Validation against yield loci of Laxiwa granite

The experimental data from true triaxial tests conducted on Laxiwa granite by Li et al. (1994) and later interpreted by Yu et al. (2002) is used to validate the yield loci produced by the model. The tests were performed at different hydrostatic pressure levels $p = 75, 100, 130, 160$ MPa and for each test, the stresses at yielding states are recorded to calculate the deviatoric stress component $q = \sqrt{3J_2}$. The rock properties are taken as: $f_c = 157$ MPa and $f_t = 9.3$ MPa. To produce the yield loci for validation purpose, the model only needs parameters that are related to the initial yield described in Section 5.3.2.1 which

are m and μ_0. In this example, these model parameters are $m = 0.6$ and $\mu_0 = 0.54$, which were calibrated from the case of $p = 75$ MPa and then used for other cases.

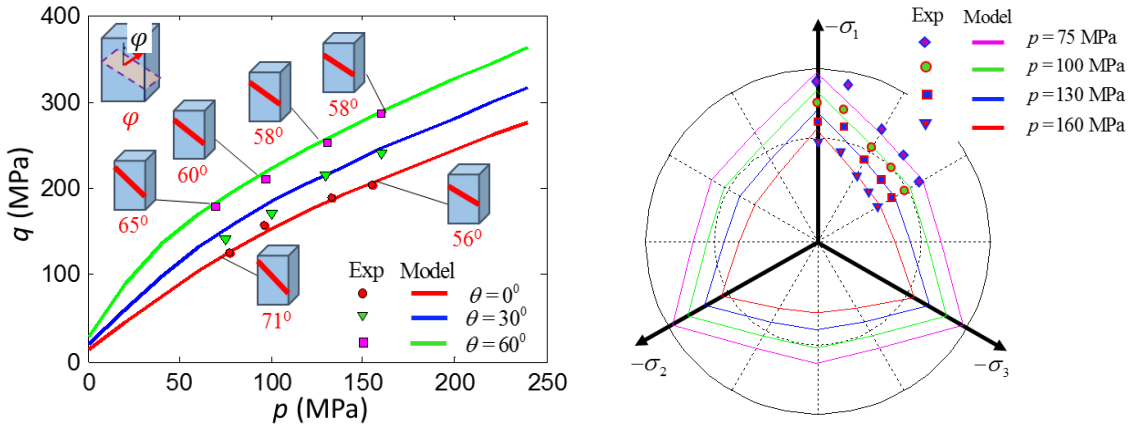

Figure 5.12. Failure locus produced by the model against experimental results for Laxiwa granite: (a) Yield loci in $p - q$ space and (b) Yield loci in deviatoric plane

The results of yield loci, predicted by the model in Figure 5.12, show good agreements with experimental observations. Thanks to the inclusion of the localised failure in the constitutive relationship, the model can naturally capture the Lode-angle dependence of the yield loci without requiring the third stress invariant (or Lode angle parameter) in the expression of the macro yield function. In addition, each yielding state predicted by the proposed model is also accompanied by an orientation of the localisation failure plane. It can be seen that with an increase of hydrostatic stress, the failure plane orientation decrease as also observed in experiments (Ingraham et al., 2013; Ma and Haimson, 2016; Vachaparampil and Ghassemi, 2017). Moreover, at the same level of mean stress, the failure plane orientation of the axisymmetric compression (i.e. $|\sigma_1| > |\sigma_2| = |\sigma_3|$) is smaller than that in axisymmetric extension (i.e. $|\sigma_1| = |\sigma_2| > |\sigma_3|$) as experimentally observed (Ingraham et al., 2013; Ma and Haimson, 2016). This feature highlights the importance and benefits of embedding the mechanisms of localised failure in the proposed model, and also its advantage in removing the phenomenological use of third stress invariant over other continuum models in the literature.

Validation against yield loci of Castlegate sandstone

The capability of the model in predicting yield loci is also validated against experimental data for Castlegate sandstone whose properties are taken as $f_t = 1$ MPa and

$f_c = 16$ MPa. Model parameters including $m = 1.7$ and $\mu_0 = 0.5$ are calibrated from the case of $p = 30$ MPa.

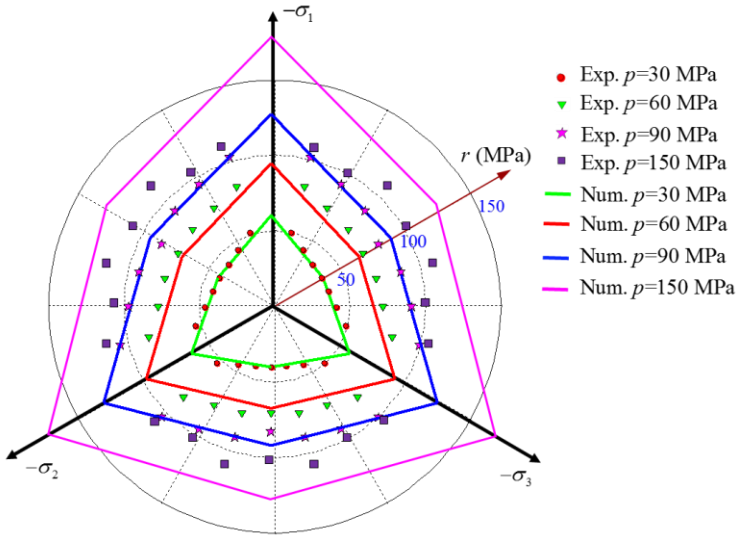

Figure 5.13. Yield loci in the deviatoric plane under different confining pressure levels against experimental results of Castlegate sandstone

Results of yield loci predicted by the model in Figure 5.13 agree well with their experimental counterparts (Ingraham et al., 2013) at low confining stress levels. However, for the case of higher confining stress (i.e. $p = 150$ MPa), the model is not successful in capturing the shape of the yield locus. This is because at high confining stresses the failure mechanism gradually changes from localisation to diffusion associated with grain crushing, a mechanism that the proposed model does not possess yet. This is why the experimental data shows a circular-shaped yield locus at high confining stress levels, while the model prediction is still a hexagon. As explained earlier, work is underway to take into account this transition of failure mechanism governing the observed behaviour.

Validation against yield loci of Indiana limestone

The yield loci produced by the proposed model is further validated against experimental data conducted by Robinson (1985) for Indiana limestone and later interpreted by Aubertin et al. (1999). The material properties are taken as: compression strength $f_c = 28$ MPa; tensile strength $f_t = 4$ MPa and model parameters are $\mu_0 = 0.7$ and $m = 0.28$. The yield surface in the hydrostatic – deviatoric stress space and the deviatoric plane, predicted by the model, are presented in Figure 5.14 along with the experimental data. It can be seen that the yielding predicted by the model agrees well with its experimental

counterpart. The Lode-angle dependence of the yield surface is seen clearly in the hydrostatic – deviatoric stress space where yield locus of axisymmetric extension $\theta = 0^0$ falls below that of axisymmetric compression $\theta = 60^0$.

Figure 5.14 also shows the orientation of the localised failure predicted by the model for the case $I_1 = 30, 60$ and 90 MPa. The figure shows that when the confining stress increases, the failure plane orientation decreases, which coincides with experimental observations and also the analyses made in Section 2.2.2 of Chapter 2 . In addition, at the same mean stress level, the orientation of failure plane in axisymmetric compression is smaller than that in axisymmetric extension, which agrees with experimental observations (Ingraham et al., 2013; Ma and Haimson, 2016). All of these results are naturally produced by the proposed model without adding the third stress invariant (or Lode angle) to the expression of the yield surface. This again highlights the benefits of considering the intrinsic failure mechanism at the very beginning step of the model construction.

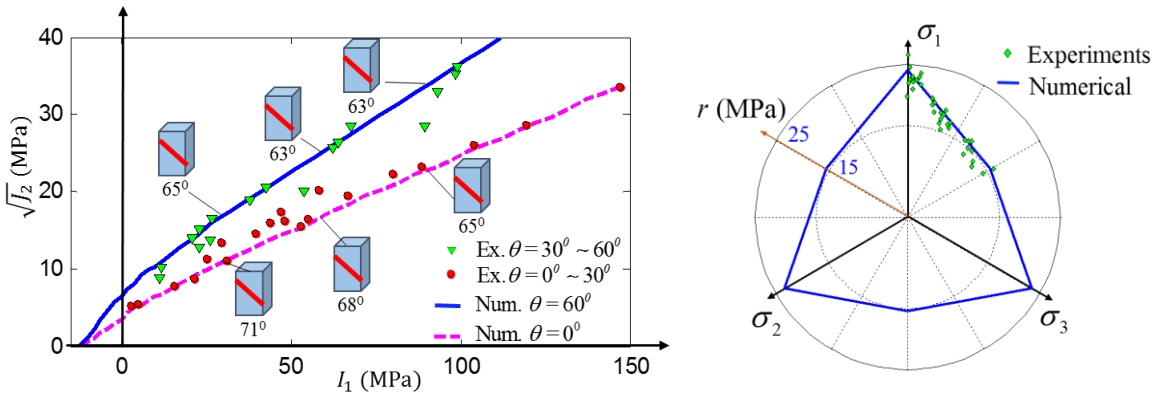

(a) (b)

Figure 5.14. Failure locus: (a) In hydrostatic – deviatoric stress space and (b) In deviatoric plane ($I_1 = 50\ MPa$) against experimental results of Limestone

5.4.1.3 Model validation against cyclic tensile loading

In this section, the capability of the proposed model in capturing material behaviour under cyclic tensile loading conditions is validated against experimental results by Gopalaratnam and Shah (1985). The tests were conducted by Gopalaratnam and Shah (1985) on rectangular specimens made of concrete whose properties are taken as Young's modulus $E = 30$ GPa; Poisson's ratio $\nu = 0.18$; compressive strength $f_c = 40$ MPa; tensile strength $f_t = 3.6$ MPa; mode I fracture energy $G_I = 0.05$ kNm/m^2. Other parameters of the model are: $\alpha_0 = 1.1$; $\beta = 1.2$; $m = 0.2$; $\mu_0 = 0.77$; $\mu = 0.84$; $\gamma = 1.8$. The elastic stiffness of the cohesive-frictional model in this case is $K_n = 10^9$ KPa/m.

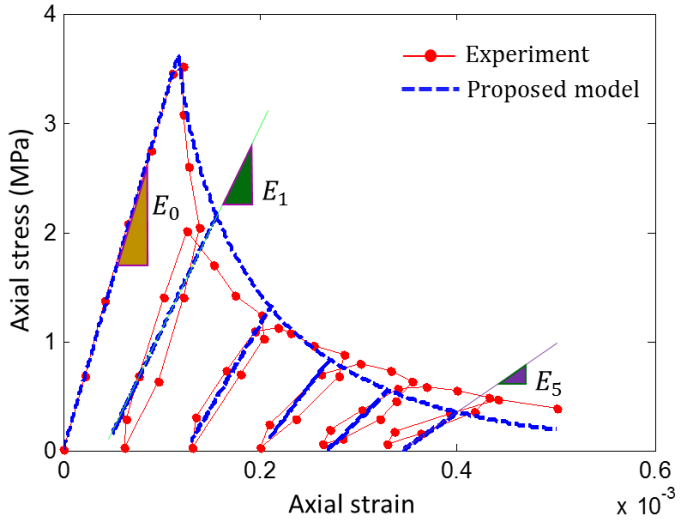

Figure 5.15. Cyclic uniaxial tension test results predicted by the model compared to experimental results reported by Gopalaratnam and Shah (1985)

The stress-strain response of the specimen under 5 unloading-reloading cycles predicted by the proposed model is plotted in Figure 5.15 together with its experimental counterpart. Fair agreements in the comparison show that the model is able to capture the sharp softening of the material in tension. In addition, thanks to the coupling of damage and plasticity in formulations of the cohesive-frictional model, both stiffness reduction and residual deformation are captured effectively. This is clearly illustrated in the figure where the original stiffness, E_0, gradually reduces after each cycle of unloading-reloading; from E_0 to E_1 (after 1 cycle) and E_5 (after 5 cycles).

5.4.1.4 Model validation against triaxial tests on Bentheim sandstone

In this section, the performance of the proposed model is assessed against triaxial tests conducted by Klein et al. (2001, 2003) on cylindrical Bentheim sandstone samples having a diameter of 20 mm and height of 40 mm. For convenience, the pressure in this example follows geomechanics conventions, where compressive stress is considered to be positive. The tests were carried out at different confining pressure levels $(0, 10, 30 \text{ and } 90 \text{ MPa})$ where the axial and lateral strains were recorded to calculate the volumetric strain throughout the experiment. The differential stress q and mean stress p were then calculated, along with the axial/volumetric strain for each stage of the test.

In this example, the material properties are taken as follows: Young's modulus $E = 21$ GPa; Poisson's ratio $\nu = 0.24$; compressive strength $f_c = 60$ MPa; tensile strength $f_t = 1$ MPa; mode I fracture energy $G_I = 0.146\ \text{kNm/m}^2$. For modelling the triaxial test, the

parameters of the model were calibrated using the experimental data at confining stress $\sigma_3 =$ 10 MPa, resulting in the following model parameters: $\alpha_0 = 0.34$; $\beta = 0.046$; $m = 1.1$; $\mu_0 = 0.55$; $\mu = 0.32$; $\gamma = 0.8$. The elastic stiffness of the cohesive-frictional model in this case can take a large value, $K_n = K_s = 10^{10}$ KPa/m. Once the localisation band appears, the characteristic length H is calculated as $H = {\Omega}/{\Gamma} = L\cos\varphi$, where L is the specimen height and φ is the localisation band orientation as illustrated in Figure 5.16a.

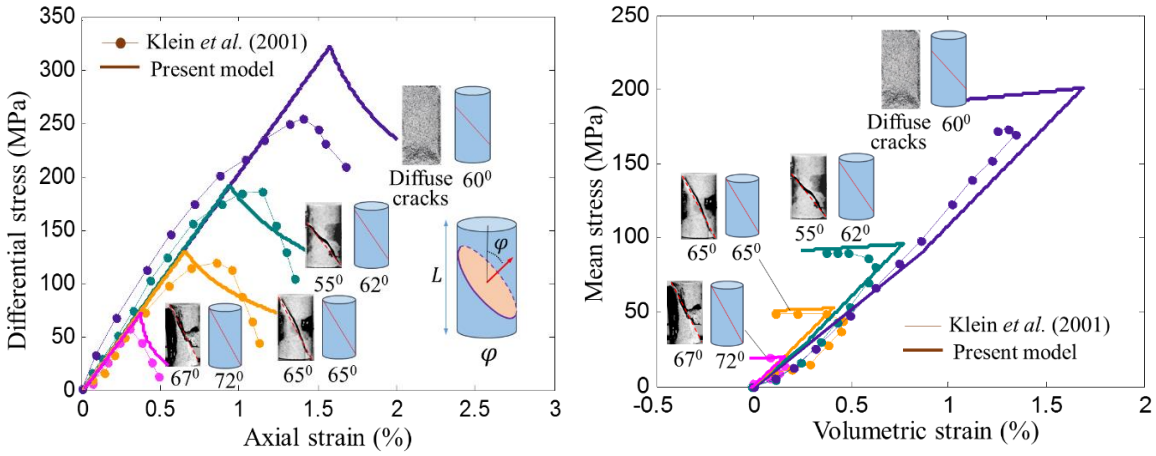

(a) (b)

Figure 5.16. Triaxial test results for Bentheim sandstone: (a) Differential stress – axial strain and (b) Mean stress – volumetric strain

Figure 5.17 shows that both experimental stress-strain results and failure patterns (Klein et al., 2001, 2003) are fairly captured by the model. In particular, the orientations of the localisation bands under different confining pressures are predicted following the procedures described in Section 5.3.2.1 and compared well with their experimental counterparts. For each confining pressure, the material behaviour is accompanied by a failure plane as experimentally observed in the tests. This is one of the key features produced by the model that cannot be found in classical continuum models. It is seen that an increase in the confining pressure results in a decrease in the angle between the failure plane and the horizontal axis, reflecting the experimental observations. The dilation behaviour associated with this change of failure plane orientation can also be captured well, as shown in Figure 5.16b. However at high confining pressure (90 MPa), because the model fails to capture the compaction failure mechanism associated with grain crushing, the predicted results are much higher than their experimental counterparts.

As presented in Section 5.3, because the proposed model includes the behaviour of the localisation band, it is capable of capturing size effect responses at the constitutive level. A

parametric study is performed on the same sandstone using confining pressure $\sigma_3 = 30$ MPa to illustrate the size-despendent behaviour of the material at constitutive level. Figure 5.17a shows the stress-strain results of the triaxial test for different specimen lengths $L = 40, 60$ and 80 mm, respectively, while keeping the radius unchanged. It is seen that the longer the specimen is, the more brittle the behaviour becomes. This prediction by the model agrees well with experimental observations on size effects (van Mier, 1986). Figure 5.17b shows the invariance of traction-displacement responses in the local coordinate system of the failure plane, which indicates the invariance of energy dissipation regardless of specimen sizes. These features are direct outcomes of incorporating the localised failure mechanism in the proposed constitutive model and also show the in-built regularisation effects of the proposed model.

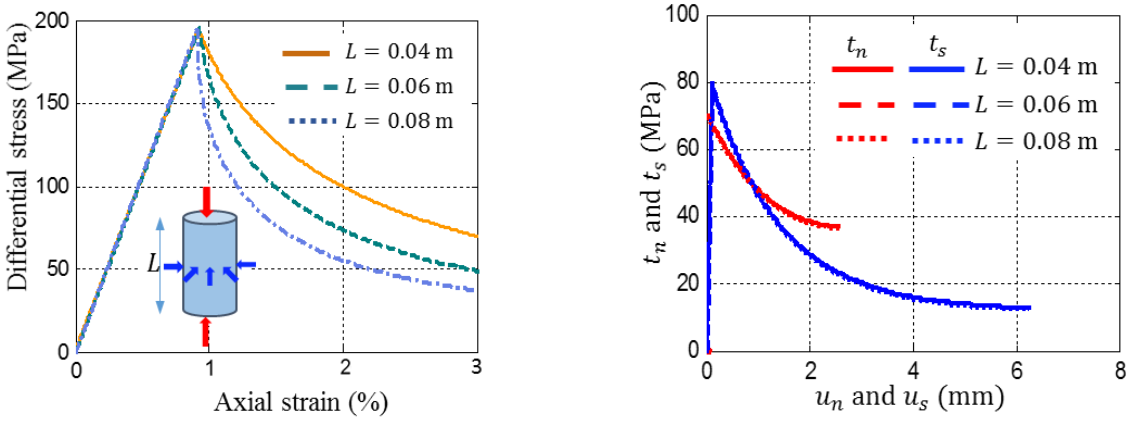

(a) (b)

Figure 5.17. Parametric study on size effect: (a) Stress-strain responses for different specimen lengths and (b) traction-displacement responses in local failure plane up to the same damage level ($D = 0.9$)

5.4.1.5 Model validation against triaxial tests on concrete

The proposed model is also validated against triaxial tests conducted by Imran and Pantazopoulou (1997) on cylindrical concrete specimens with a length of 115 mm and diameter of 54 mm. The material properties are: Young's modulus $E = 21.25$ GPa; Poisson's ratio $\nu = 0.21$; compressive strength $f_c = 21.2$ MPa; tensile strength $f_t = 2.86$ MPa and mode I fracture energy $G_I = 0.063$ kN. m/m^2. Other model parameters are: $\alpha_0 = 0.63$; $m = 0.48$; $\mu_0 = 0.1$; $\mu = 1.05$; $\gamma = 1.5$; $\beta = 0.006$; $K_n = K_s = 10^{10}$ KPa/m. The characteristic length H is calculated once the localisation band appears using the same formulation described in the preceding example on sandstone.

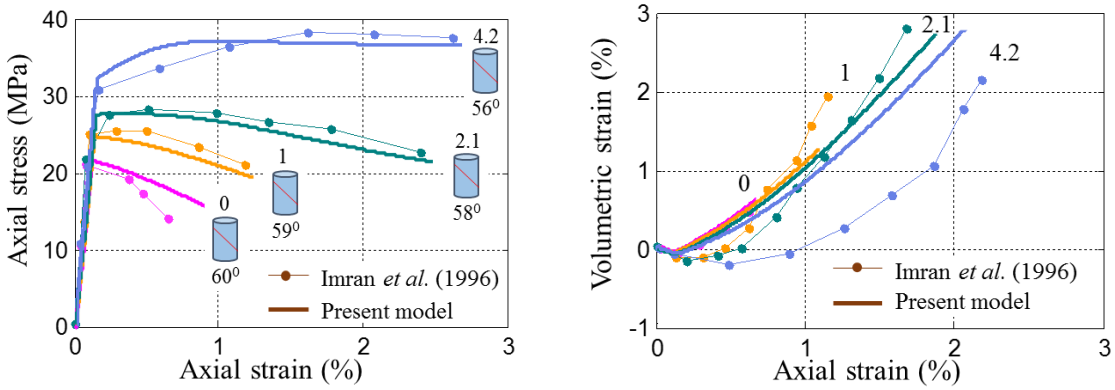

(a) (b)

Figure 5.18. Triaxial test results for concrete at different confinement levels (0, 1, 2.1 and 4.2 MPa): (a) Axial stress–axial strain and (b) Volumetric strain–axial strain

The predictions, plotted in Figure 5.18, show that the transition from softening (at zero or low confining pressure) to hardening behaviour (at higher confining pressure) exhibited by the specimen is well-captured by the model. The model prediction of failure patterns, characterised by the failure plane angle φ in Figure 5.18, also reflects the general trend of localised failure in triaxial compression tests, where an increase of confining pressure leads to a decrease in the failure plane angle. While the stress-strain results show a good agreement, there are discrepancies between volumetric strain measured in the experiments and that predicted by the model for high confining pressure cases, despite the agreement in the trend. This could be due to the measuring method used in the experiment where only one strain gauge with a limited length was attached to the specimen at mid-height to measure the lateral strain (Imran and Pantazopoulou, 1997). The volumetric strain calculated from this lateral strain, therefore, might not be a good representative for the volumetric response of the specimen.

The size-dependent behaviour is also illustrated in Figure 5.19 for the case of confining pressure $\sigma_3 = 2.1$ MPa using three different lengths $L_1 = 115$ mm, $2L_1$ and $4L_1$. The traction-displacement responses in the local coordinate system are the same, regardless of the length scale as illustrated in Figure 5.19b. This again highlights the importance and benefits of including localised failure mechanism in the development of constitutive models.

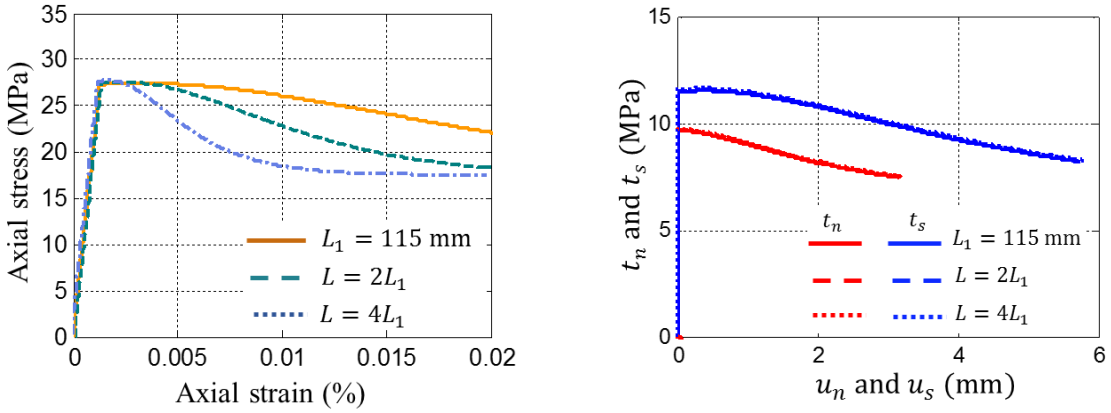

(a) (b)

Figure 5.19. Parametric study on size effect: (a) stress-strain curves for different specimen lengths and (b) traction-displacement responses in local failure plane up to the same damage level ($D = 0.9$)

5.4.2 Model validation at the structural level

In this section, the proposed model is implemented into the commercial package ABAQUS as a user-defined material model (UMAT) for the analysis of BVPs including tension tests of double-edge notch specimens, mixed-mode tests of a double-edge notch specimen and L-shaped structure. Because the responses of the materials in those experiments are mostly softening, displacement-controlled loading is used for the simulations. The mechanical properties of the materials are summarised in Table 5.1. The friction angle of concrete is taken as 37^0, based on a generally-accepted value in Fujita et al. (1998) for all examples. The elastic normal and shear stiffness of the cohesive-frictional model are taken as $K_n = K_s = 10^{10}$ and dilation parameter $\gamma = 1.1$ is used. Other model parameters needed for the cohesive-frictional model are presented in Table 5.2.

Table 5.1. Mechanical properties of the material used in experiments

Properties	Example 1 and 2	Example 3	Example 4
Young's Modulus E(GPa)	24	32	25.8
Poisson's ratio ν	0.2	0.2	0.18
Compressive strength f_c(MPa)	38.4	38.4	31
Tensile strength f_t(MPa)	2.86	3	2.7
Fracture energy G_I (N/mm)	0.063	0.11	0.065
Specimen thickness (mm)	10	50	100

Table 5.2. Model parameters for structural simulation

Parameters	Example 1 and 2	Example 3	Example 4
α_0	0.63	0.38	0.58
β	0.002	0.002	0.001
m	0.4	0.43	0.4
μ_0	0.4	0.35	0.5

In this section, all simulations are performed in 2D using 3-node triangular elements. Strictly, the characteristic length of each element should be calculated by definition as $H = \frac{\Omega}{\Gamma} = \frac{A}{l}$ where A is the area of the element and l is the length of the localisation band crossing the element as illustrated in Figure 5.20. Theoretically, H can be calculated during the simulation using the predicted localisation orientation φ, nodal coordinates of the element and geometric manipulations. However, to avoid this dependence on element geometry and also reduce the computational time, a simple and more practical way, with $H = \sqrt{A}$, is employed in this study. This simple approximation also helps facilitate the discretisation independence of the implementation for both mesh-free and mesh-based methods. The convergence of numerical solutions upon mesh refinement in this section demonstrates that this simplification works well and hence can be adopted.

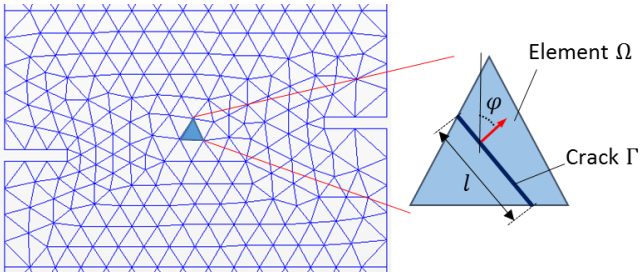

Figure 5.20. Illustration for the characteristic length calculation in FEAs

5.4.2.1 Illustration of mesh-independence in tension tests of concrete specimens

To illustrate the mesh-independence featured in the proposed model, a simple tension test is simulated in this section with three different mesh resolutions shown in Figure 5.21a. For illustration purpose, the material is taken from concrete used in experiments conducted by Shi et al. (2000) whose mechanical properties are summarised in Table 5.1. Model parameters used in this simulation are presented in Table 5.2. As the crack orientation is predictable (i.e., perpendicular to the load) in this case, the characteristic length H in the

constitutive equation is directly determined from its definition (i.e., Eq. 5.2) as shown in Figure 5.21a, instead of using the approximation described above.

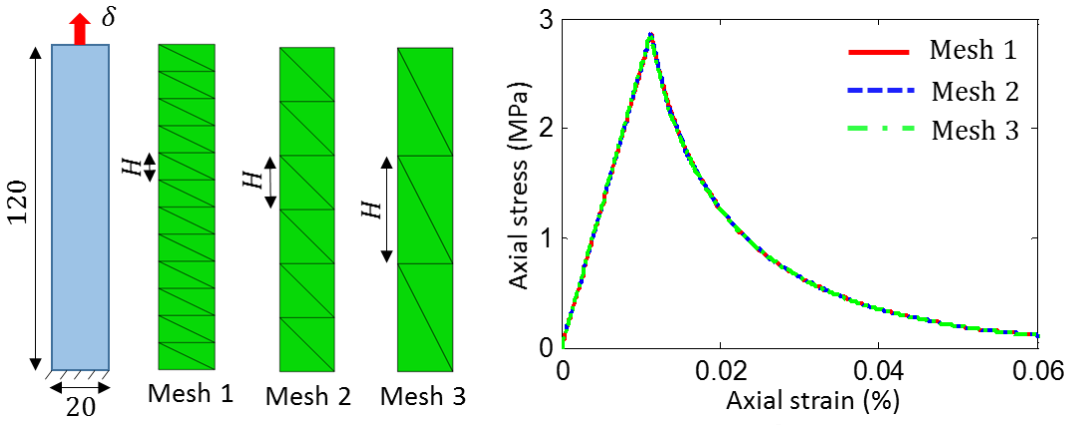

(a) (b)

Figure 5.21. Illustration of mesh-independence in tension: (a) Tension test set-up (dimension in mm) & three meshes used in simulation and (b) Stress-strain responses

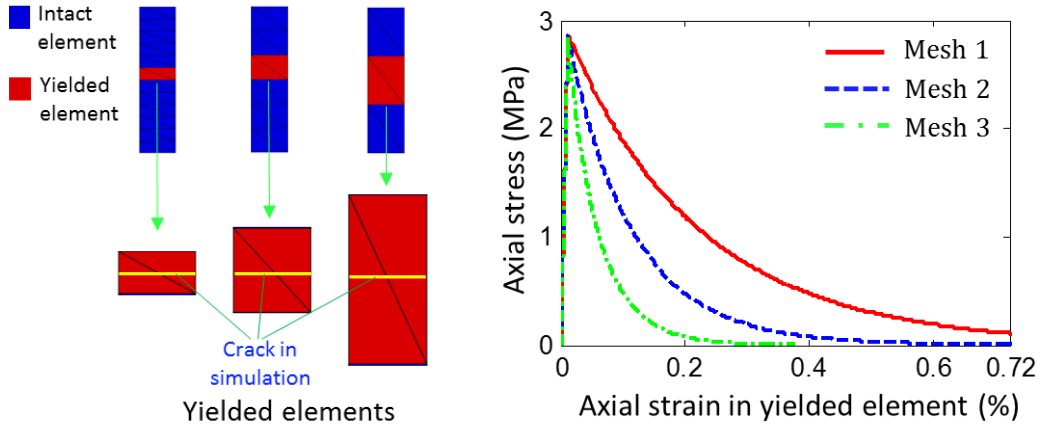

(a) (b)

Figure 5.22. Detailed analysis in different meshes: (a) Embedded crack featured in yielded elements and (b) Stress-strain responses in yielded elements

It can be seen from overall stress-strain responses of the specimens, plotted in Figure 5.21b, that that the results are almost identical despite different mesh resolutions. This means that unlike numerous continuum models analysed in Chapter 3, the results predicted by the model would not be dependent on the mesh used in the simulations. This can be explained by detailed analyses of the "yielded" elements where crack initiates and inelastic process mainly takes place. Figure 5.22 shows that together with the increase of element size, the corresponding averaged stress-strain response in the element automatically changes (see Figure 5.22b). This is completely different from what happens in classical continuum models, discussed at length Section 3.2 of Chapter 3 that the constitutive relationship used

in simulations is unchanged, leading to the non-uniqueness of numerical results with different discretisation resolutions (illustrated in Figure 3.10).

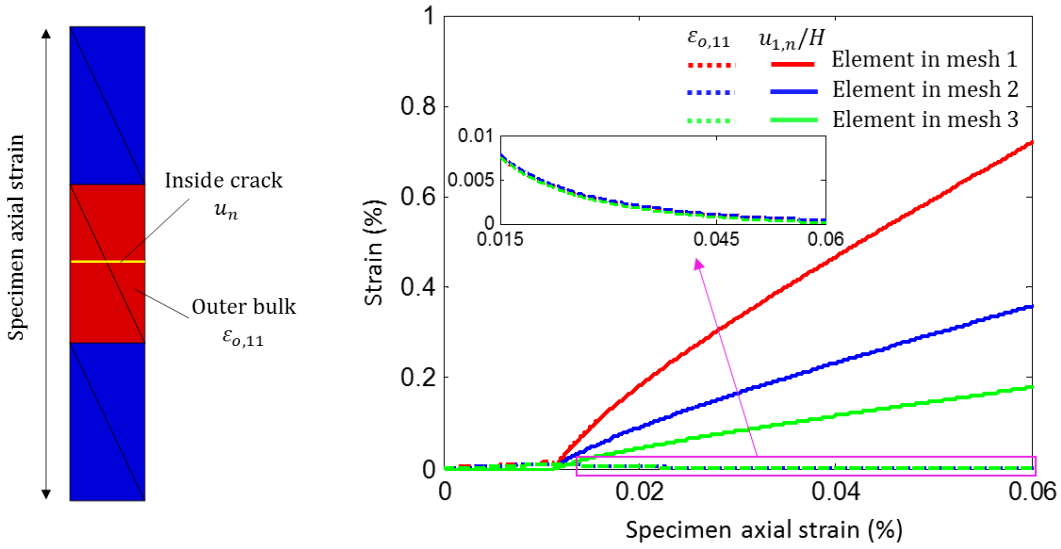

Figure 5.23. Detailed strain and displacement analysis in the yielded elements for different meshes used in the simulation

The change of constitutive relationship featured in the proposed model is a direct consequence of featuring crack/localisation band in the model as described in Section 4.2 of Chapter 4 and Section 5.2 of Chapter 5. Even though the sizes of the yielded elements, illustrated by red elements in Figure 5.22a, are different for three meshes, they all possess the same crack (illustrated by yellow lines in yielded elements). However, because of the difference in element size, the ratio of contributions between the embedded crack and surrounding bulk materiel towards averaged element strain are different, for different mesh resolutions. This difference can be seen clearly in Figure 5.23 where contributions from crack towards averaged strain, following the kinematic enhancement in the model (see Eq. 5.2), are plotted for the three different mesh resolutions above. It can also be seen from this figure that once a crack appears within the material body, the surrounding bulk material undergoes elastic unloading, exhibited by a reduction in strain as shown in the zoom-in figure. The averaged strain of the element, being the summation of contributions from the crack and the surrounding bulk material, would consequently change with respect to mesh sizes. All of these interactions of the inside and outside of crack are incorporated within the proposed constitutive equations, leading to a natural change in constitutive stress-strain relationship with respect to different mesh resolutions. Such responses captured in the proposed model are very similar to the material behaviour analysed in Section 2.2.3

regarding the underlying mechanism of size-effect. As a result, even though the contours from the simulations by the proposed model look similar to those by other continuum models, they actually feature the behaviour of crack at a lower scale and thus naturally lead to mesh-independent results. This is one of the key features distinguishing the proposed model from many other continuum models where additional treatments and regularisations are needed to achieve the mesh-independence when solving BVPs (see Section 3.2 of Chapter 3).

5.4.2.2 Tension test of the double-edge-notched specimen

Tension tests of two double-edge-notched concrete specimens, shown in Figure 5.24 (in cm), are simulated to illustrate the model capability. Based on the experimental setup (Shi et al., 2000), the top edge is pulled upwards and the bottom edge is fixed in the simulation. The tests were conducted with two different values of the vertical distance a between two notches (i.e. symmetrical, $a = 0$, and asymmetric, $a = 5$ cm).

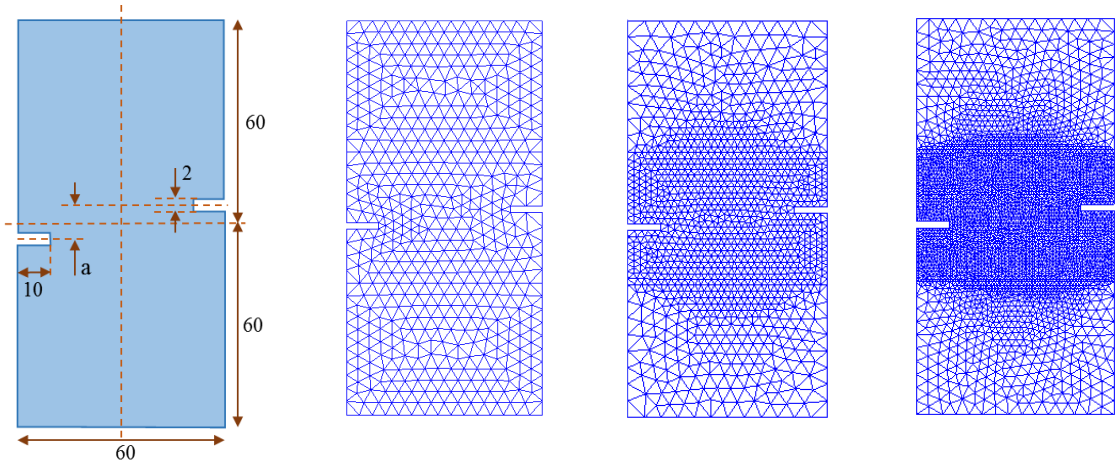

(a) Geometry (b) coarse mesh 1 (c) medium mesh 2 (d) fine mesh 3

Figure 5.24. Specimen geometry and mesh sizes for tension test

The predicted force-displacement responses are presented in Figure 5.25, for three different meshes, mesh 1 (635 elements), mesh 2 (1242 elements) and mesh 3 (2598 elements). It can be seen that the model prediction fairly agrees with the experimentally measured response which shows sharp softening after the peak due to the brittle attribute of concrete behaviour. During this process, a large amount of energy is quickly dissipated via the crack development, and the load-displacement curve hence drops down rapidly. It can also be observed from this figure that the numerical results converge upon mesh refinement, thanks to the characteristic length H included in the model. The results corresponding to two values of cohesive stiffness K (K=10^{10} and K=10^{11}), presented in Figure 5.25 for the case of

$a = 0$, are almost unchanged. This shows that as long as these stiffness values are high enough, the choice of the actual values does not significantly affect the simulation results.

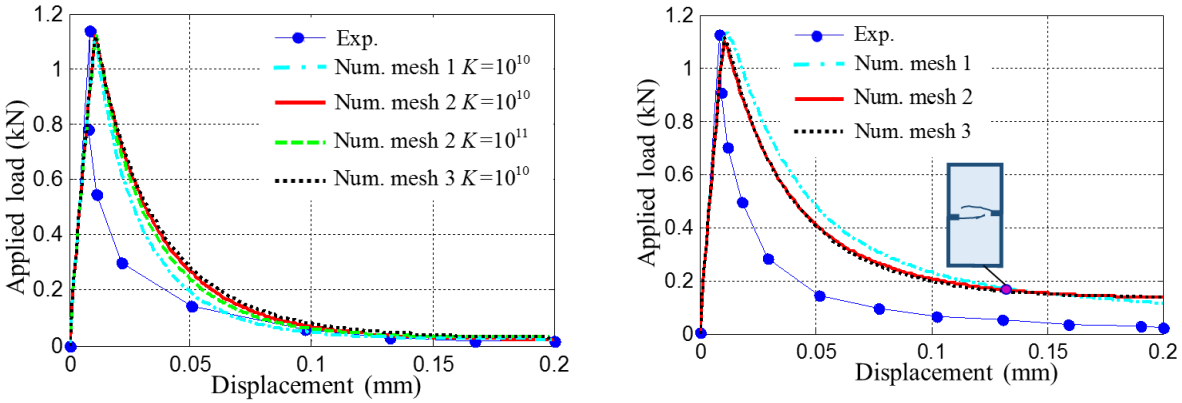

(a) (b)

Figure 5.25. Load-displacement responses for tension test: (a) $a = 0$ and (b) $a = 5$

The formation of the fracture process zone (FPZ) around the crack tips is shown in Figure 5.26a and Figure 5.27a. During the simulation, a system of smaller primary and secondary cracks forms and develops during the evolution of the two major cracks. These cracks will close (i.e. under elastic unloading) when the major cracks develop. This somewhat coincides with the experimental observations (Brooks, 2013; Janssen et al., 2001; Otsuka and Date, 2000; Skarzyński and Tejchman, 2016; Vermilye and Scholz, 1998) on the evolution of the fracture process zone, and demonstrates another advantage of the proposed model. The contours of damage in Figure 5.26b and Figure 5.27b show localised major cracking despite the numerically observed finite width FPZs. There is also no stress-locking issue experienced as can be confirmed from the macro responses in Figure 5.25. Figure 5.26 and Figure 5.27 also shows a good agreement between simulated crack patterns (using medium mesh) and the crack patterns from experiments. For the case of $a = 0$, cracks initiate from two notches of the specimen. These cracks then coalesce to form a major horizontal crack connecting the two notches together. For the case where $a = 5$, two major cracks initiate from two notches and then grow parallel to each other, forming an intact area in between. Because this area has loading capacity, there exists residual stress in the simulation results at the final stage. It should be noted that the incremental step in numerical simulation should be small enough to enable the implicit stress return algorithm to capture the rapid reduction in load-carrying capacity observed in experiments. In addition, due to the fact that greater surface area (i.e. more irregular/rough cracks) might be induced in the real specimen

compared to what the model assumes, calibration of parameters related to fracture energy needs extra attention to ensure the consistency between model assumptions and parameters used for the simulation. In this research, the fracture energy calculated from the macro responses and is used to calibrate the model parameters. This means that the effect of the fracture process zone (FPZ) containing numerous cracks is lumped into the value of fracture energy. Therefore it is just an averaged quantity and hence is not a perfect match for the cohesive crack in the model. For calibration purpose, this FPZ is simplified as a single crack having the same fracture energy value as the FPZ. This approach yields reasonable results as illustrated in this research but its accuracy and robustness should still be further examined in future studies.

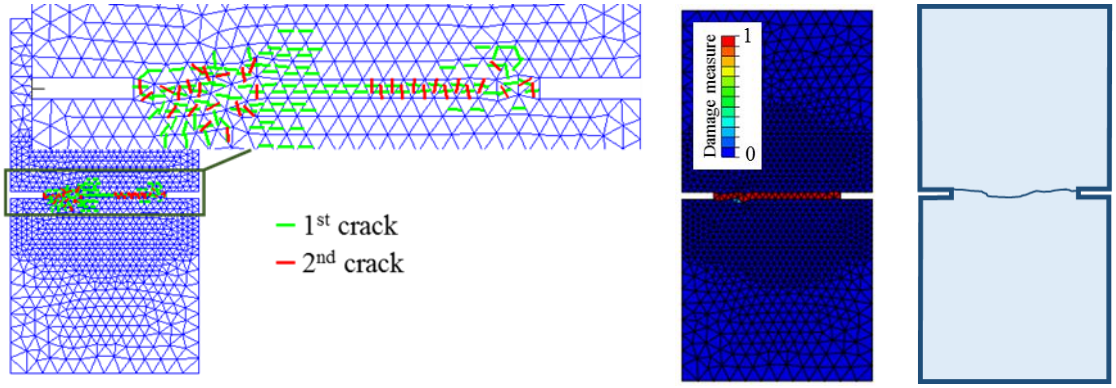

Figure 5.26. Crack patterns symmetrical notch a = 0: (a) FPZ prediction from the simulation; (b) Macro crack by the model and (c) Failure pattern in the experiment (redrawn from Shi et al. 2000).

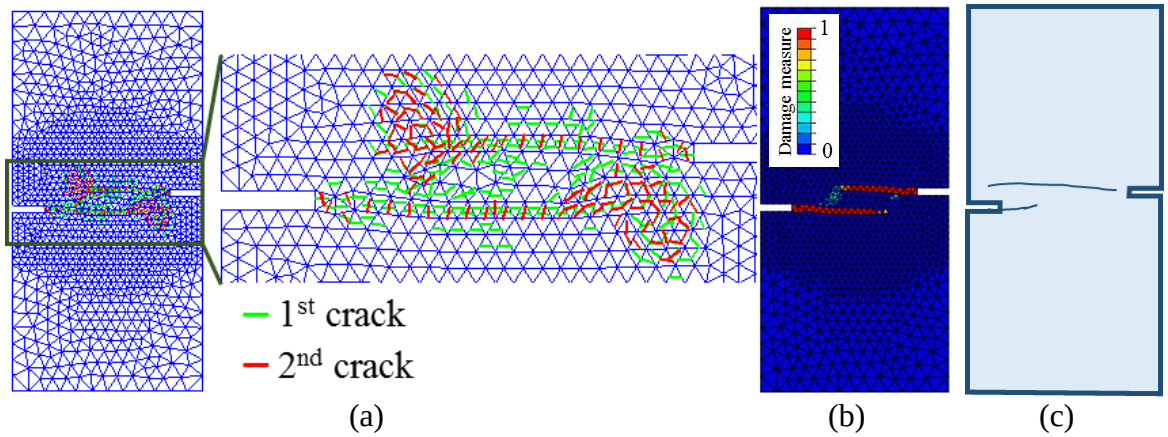

Figure 5.27. Crack patterns unsymmetrical notch a = 5: (a) FPZ prediction from the simulation; (b) Macro crack by the model and (c) Failure pattern in the experiment (redrawn from Shi et al. 2000).

5.4.2.3 Mixed-mode loading test of the double-edge-notched specimen

The capability of the model in capturing mixed-mode responses is demonstrated via the simulation of a double-edge-notched concrete specimen under combined shear and tension, shown in Figure 5.28. The loading path 2a (Nooru-Mohamed et al., 1993), where a normal (horizontal) and shear (vertical) displacements are applied equally ($\delta_n = \delta_s$) on the specimen, is considered here. In the experiment, displacements were measured at points M, M', N, N', P and P' and then used to calculate the average displacement as $\delta_n = (\delta_n^M - \delta_n^{M\prime} + \delta_n^N - \delta_n^{N\prime})/2$ and $\delta_s = (\delta_s^P - \delta_s^{P\prime})/2$. However, because incorporating such conditions in numerical simulation is difficult, an alternative boundary condition, proposed by Jefferson (2003), is used in this study. Following this alternative, the movements of two rigid plates were applied to the upper-left and top edges of the specimens while the lower-right and bottom edges were fixed in both directions.

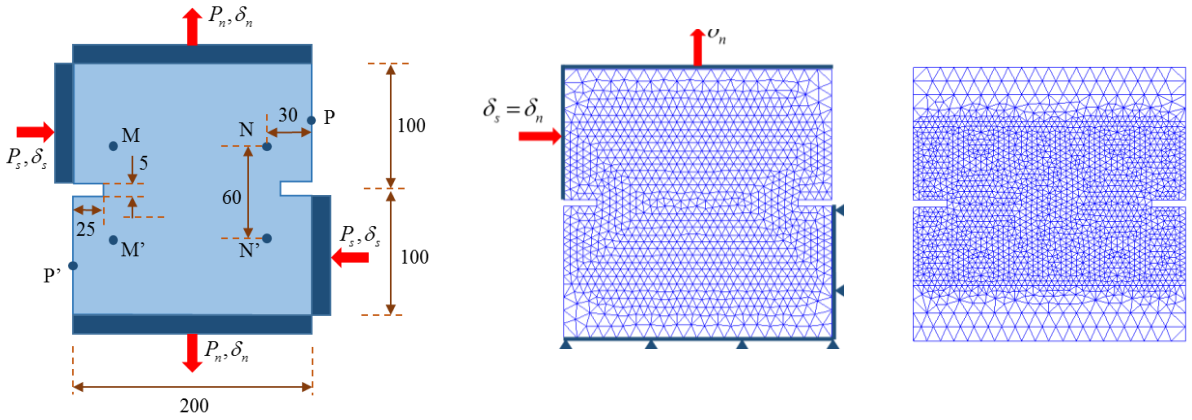

(a) (b) (c)

Figure 5.28. Mixed mode test: (a) experiment set-ups; (b) mesh 1 and (c) mesh 2

The results in Figure 5.29 show reasonable agreements in trends between the numerical results and their corresponding experimental counterparts. The vertical force, after reaching the peak, decreases and gradually becomes negative, while the horizontal force increases quickly at first then increases at a lower rate. This is because the two major cracks propagate in parallel to each other, as seen in Figure 5.30c, leaving a relatively undamaged area in between. Because this area has loading capacity in the horizontal direction, the resulting horizontal force keeps increasing. As the results produced by two meshes (mesh 1, 1821 elements and mesh 2, 3984 elements shown in Figure 5.28) are almost the same, they again demonstrate the convergence of the numerical results upon mesh refinement. Figure 5.30 also highlights the agreement between the predicted and experimentally observed crack patterns. The failure pattern including FPZs in Figure 5.30a and damage contour in Figure

5.30b are assessed against the experimental observation in Figure 5.30c. The damage variable values at the final state of the simulation in Figure 5.30b demonstrates that only two major macro cracks formed and propagated during the simulation, as also experimentally observed (Nooru-Mohamed et al., 1993), while the FPZ in this case spreads out over a larger area.

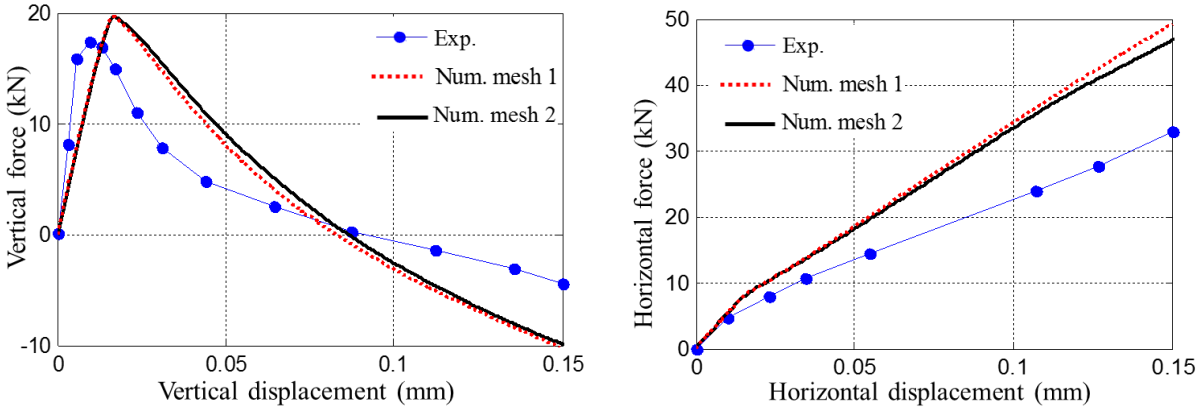

Figure 5.29. Load-displacement responses for the mixed-mode test: (a) in vertical and (b) in the horizontal direction

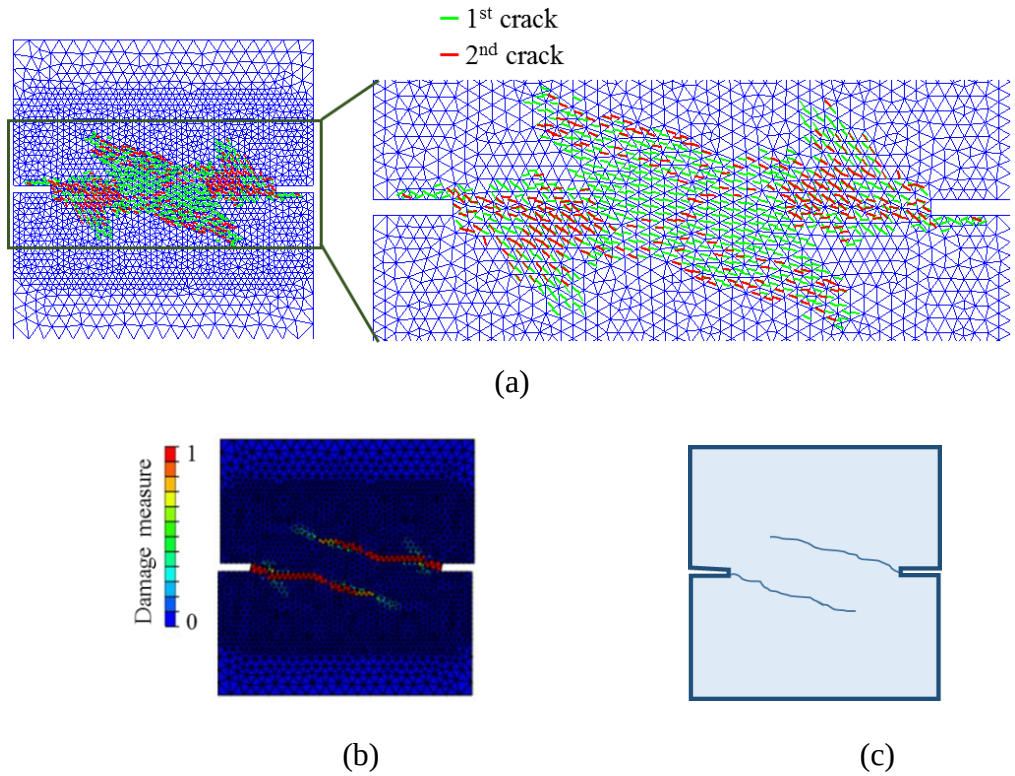

Figure 5.30. Crack pattern of the mixed-mode test: (a) FPZ prediction from the simulation; (b) macro crack from simulation with scale =10 and (c) from experiments (redrawn from Nooru-Mohamed et al., 1993)

5.4.2.4 Mixed-mode test of the L-shaped structure.

The final example, presented in this chapter, to illustrate the model capability is a mixed-mode test of an L-shaped structure carried out by Winkler et al. (2001) with structural geometry and boundary condition shown in Figure 5.31. Vertical displacement was applied through a loading plate near the right edge while the bottom of the specimen was fixed in both directions. This figure also shows the two meshes used in the numerical simulation: mesh 1 (1432 elements) and mesh 2 (2563 elements).

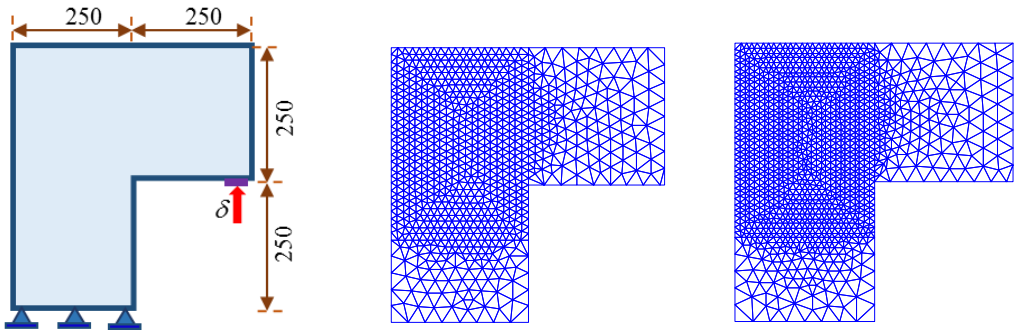

(a) (b) (c)

Figure 5.31. The L-shaped test: (a) Experiment set-ups (b) Mesh 1 and (c) Mesh 2

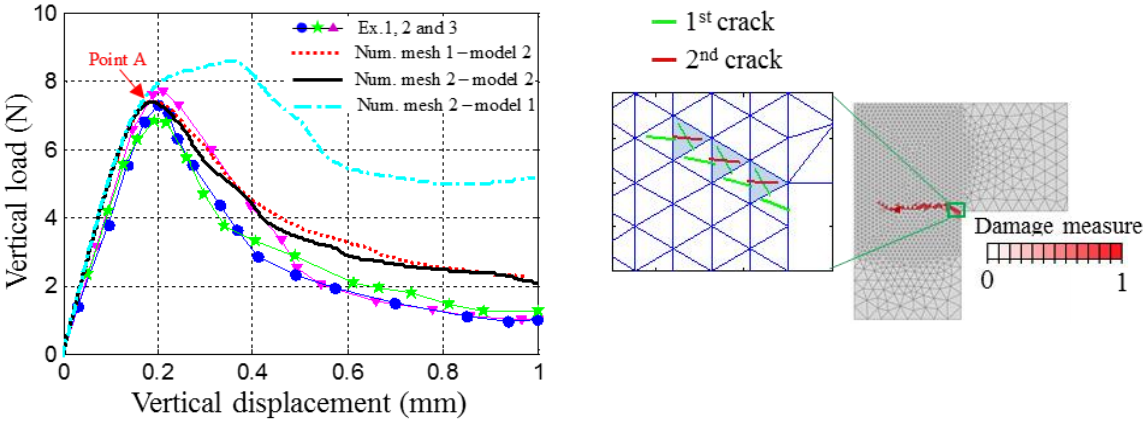

(a) (b)

Figure 5.32. Results of L-shaped structure test: (a) Load-displacement responses, (b) Embedded crack development at point A

The load versus vertical displacement presented in Figure 5.32a shows a relatively good agreement between responses predicted by the model and the experimentally observed ones. Although there is a slight difference in residual force values in the final stage of failure, the softening branch of the results is captured by the proposed two-crack model (model 2). The Figure also shows the result obtained using a model that allows the activation of a single

crack only (model 1) with the same set of parameters. It can be seen that the result obtained by this single crack model is much stiffer showing a remarkable hardening response before the softening. This discrepancy can be explained in Figure 5.32b, where the crack development at the early stage of cracking (point A in Figure 5.32a) is plotted. As can be seen, the primary cracks, denoted by green lines, in shaded elements are not well aligned with the overall macroscopic crack direction, which is almost horizontal as shown in Figure 5.33b. For the one-crack model (Nguyen et al., 2012a, 2012b, 2014, Le et al., 2017), a significant amount of stress is still transferred through these shaded elements as illustrated previously in Section 5.2, leading to over-stiff responses. In the two-crack model is used, secondary cracks, denoted by red lines in Figure 5.32b, are activated and help release this spurious stress transfer. This allows the macroscopic crack to develop in an appropriate direction and yield more reasonable results. This again illustrates the necessity of having secondary cracks at the constitutive level to capture the structural responses of during the FEA simulation.

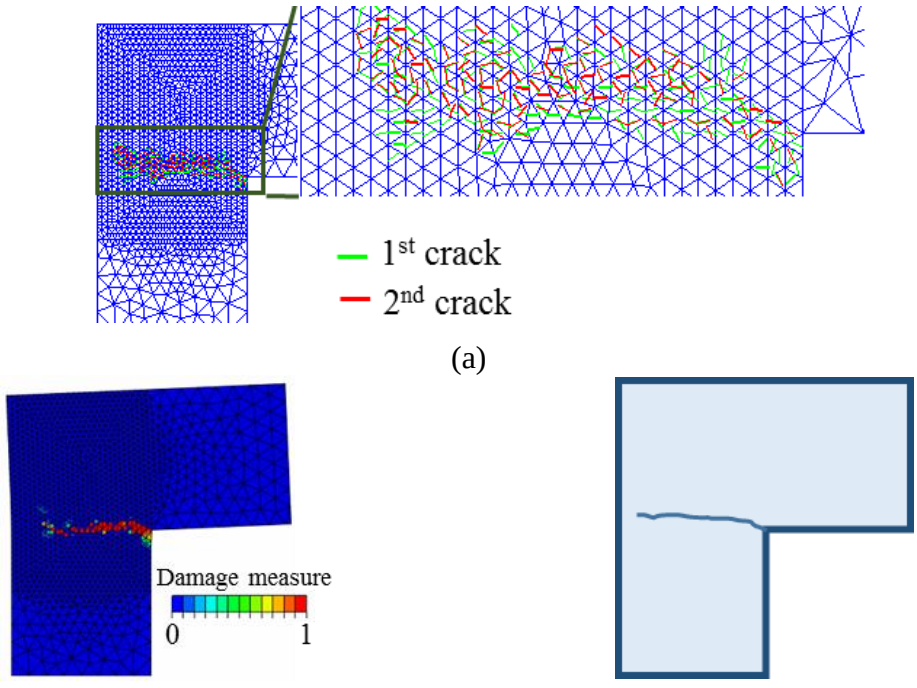

Figure 5.33. Crack pattern of the mixed-mode test: (a) FPZ prediction from the simulation; (b) Macro crack from simulation with scale =50 and (c) Failure pattern from experiments (redrawn from Winkler et al. 2001).

As shown in Figure 5.33b and c, the crack pattern obtained by the model agrees well with the crack pattern from the experiment, while a finite thickness FPZ is also obtained naturally and stress locking issue is simply resolved with the introduction of secondary

cracking. As shown in Figure 5.33b and c, the crack pattern obtained from the model agrees well with its experimental counterpart with a major crack initiating from the corner and then propagating to the left side of the specimen within a FPZ shown in Figure 5.33a.

5.5 Summary and discussion

In this chapter, a mechanism-based model is developed for quasi-brittle geomaterials by incorporating the localised failure mechanism into the constitutive equations as the basis of the model development. The proposed approach is developed within the framework of thermodynamics, with new forms of energy potentials proposed to encapsulate localised failure mechanisms. The thermodynamics-based formulation naturally leads to a new constitutive structure containing the responses of both the bulk and localisation bands, whose orientations depend on both the stress state and material properties. The interactions of these phases (the bulk and localisation bands) are obtained as part of the standard procedures in the thermodynamic formulation and help connect them to drive the macro response of the volume element.

The proposed constitutive model possesses key features of the materials, all of which are consequences of the underlying localised failure mechanism embedded in the proposed constitutive structure. Despite being formulated within a continuum mechanics framework, the proposed model can describe the anisotropy and responses inside the localisation zone explicitly. The deformation and behaviour inside the localisation zone and its surrounding bulk material are separated, even at constitutive level. Consequently, the dissipation of the material is reflected correctly with respect to the discretisation resolution in Finite Element Analysis. As a result, no phenomenological treatments is needed to reflect the Lode angle dependence and no regularisation is required in the analysis of Boundary Value Problems, as is usually the case in classical continuum models.

Furthermore, the introduction of secondary cracking helps to remove stress-locking issues naturally when modelling the localised failure of the material at a structural scale. Opening the possibility of having more than one crack inside the constitutive equations helps the model reflect the nature of the Fracture Process Zone (FPZ), which is a system of numerous meso/micro-cracks crossing each other. The propagation of the FPZ can thus be captured naturally, without requiring any additional crack tracking technique as seen in other embedded crack models. Possible improvements to this issue in the model will be addressed

in Chapter 7, together with potential developments to move towards a better model for simulating quasi-brittle geomaterials.

Good agreement with the experimental results at both constitutive and structural levels illustrate the capacity of the proposed model in analysing the materials responses and their failure patterns in a wide range of loading cases, from tension to triaxial compression, under different confining pressure levels. The proposed approach thus shows promising features for constitutive modelling of geomaterials, based on their underlying mechanisms of localised failure. The capabilities of the approach can be further extended in the near future to capture the compaction failure mechanism by introducing compaction modes with grain crushing to the elastic bulk and/or to the cohesive-frictional model at the scale of the compaction band.

CHAPTER 6

A mechanism-based constitutive modelling of fibre reinforced concrete

6.1 Introduction

In this chapter, the model proposed for quasi-brittle geomaterials in previous chapters will be extended for fibre reinforced concrete (FRC). The application of the proposed model for FRC is straightforward, since the failure mechanism of FRC shares several similarities with that of quasi-brittle geomaterials. As analysed in Chapter 2, the formation and development of the localisation zone among the FRC body still remain the underlying mechanism governing the material responses. For the case of FRC, in addition to the cohesive resistance from cementitious bulk material, the fibre bridging effect, caused by short fibres across cracks, is also a decisive factor affecting the initiation and evolution of the localisation band. Given that the crack/localisation zone and its responses were explicitly incorporated into the constitutive model alongside the surrounding bulk material, the fibre bridging effect can now simply be added into the constitutive equations for the modelling of FRC. As the behaviour of the localisation zone is linked with the overall responses of the material through a traction continuity condition, the fibre bridging forces can be added into this equilibrium to take the contribution of bridging fibres into account. This enables the employment of a separate model for the fibre bridging effect, in association with the cohesive-frictional model for material cohesive resistance, as described in the previous chapter. The model is flexible and can be applied for various types of fibres with different mechanical characteristics and geometries. The model in this form can capture the overall responses of the FRC naturally, as consequences of the interactions between the fibre bridging effect and the cohesive resistance at the material (constitutive) level, as shown by the numerical examples.

The study in this chapter focuses on concrete reinforced by straight polymer fibre and hooked-end steel fibre, which are the most two commonly used fibres among the engineering community for infrastructure applications. Simple bridging models for these fibre types will be presented with details and derivations, together with their integration into the proposed mechanism-based constitutive model. To investigate the capability of the double-scale

approach in modelling the FRC, the fibre bridging laws will be integrated into the model featuring one crack/localisation band, presented in Chapter 4, for simplicity. The extension to double-scale model with more cracks/localisation bands (see Chapter 5) can be carried out straightforwardly in future work for more complex loading conditions/scenarios. The validation in this chapter will be conducted against single fibre pull-out tests, as well as standard experiments of the FRC with different volume fractions and fibre types at both constitutive and structural simulation. The work done for modelling FRC has been written up in the form of a journal paper (Le et al., 2019 - Appendix C) from which the theoretical methodology and numerical validations presented in this chapter are extracted.

6.2 A mechanism-based constitutive model for fibre reinforced concrete

In this section, the incorporation of fibre bridging forces into the double-scale approach, described in Chapter 4, is presented. It can be seen that the addition of the fibre bridging effect into the constitutive relationship of the proposed model is very straightforward with minimal modification, thanks to the inclusion of the localised failure mechanism. The section then goes on to describe fibre bridging models for straight and hooked-end fibres, together with their integration into the double-scale model to form a complete model for FRC.

6.2.1 A double-scale model featuring fibre bridging effect

With the presence of bridging fibres across opening crack/localisation zone, the representative volume element (RVE) used for the model development in Chapter 4 is tailored to feature both cohesive resistance and fibre bridging effect as illustrated in Figure 6.1. It is seen from the Figure that inside the localisation zone, besides cohesive forces (illustrated by the blue vectors) from the cementitious material, there are now bridging forces (illustrated by red vectors in the Figure) caused by fibres across the zone, called bridging fibres. This is the main modification made to the overall structure of the constitutive equation for modelling of FRC. Other representations (i.e., the zone thickness, normal vector, surface area) remains the same as described in Chapter 4.

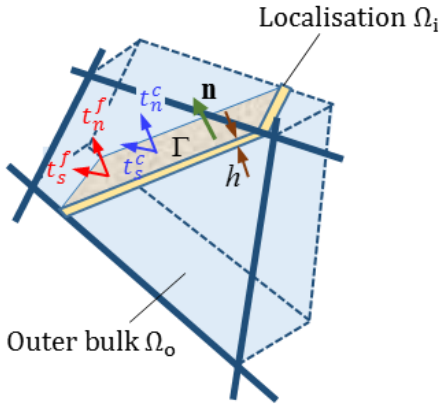

Figure 6.1. Illustration of a representative volume element made from FRC

By using the same formulation described in Eq. (4.24)-(4.27) of Section 4.3.1, the two following equilibriums still hold: i) the averaged stress of the volume element coincides with the stress of the outer bulk material $\boldsymbol{\sigma} = \boldsymbol{\sigma}_o$ and ii) satisfaction of traction continuity across the crack plane $\boldsymbol{\sigma}^T\mathbf{n} = \boldsymbol{\varrho}^T\mathbf{n} = \mathbf{t}^T$, where $\mathbf{t} = [t_1 \quad t_2 \quad t_3]^T$ is the traction acting on the crack plane in the global coordinate system. It should also be noted that the procedure used in Eq. (5.1)-(5.15) of Chapter 5 can be applied here to cast the proposed model into thermodynamics framework and obtain the same equilibriums presented above.

As stated earlier, when a crack opens, both bridging forces from fibres $\mathbf{t}^f = [t_1^f \quad t_2^f \quad t_3^f]^T$ and cohesive resistance from plain concrete $\mathbf{t}^c = [t_1^c \quad t_2^c \quad t_3^c]^T$ are activated simultaneously. The traction acting on this crack plane thus comprises these two components as:

$$\Delta\mathbf{t} = \Delta\mathbf{t}^f + \Delta\mathbf{t}^c = \mathbf{K}^f\Delta\mathbf{u} + \mathbf{K}^c\Delta\mathbf{u} = (\mathbf{K}^f + \mathbf{K}^c)\Delta\mathbf{u} \tag{6.1}$$

where $\mathbf{K}^c$ is the tangent stiffness of the cohesion law expressed in the global coordinate system, which was addressed in Section 4.2.3 of Chapter 4; $\mathbf{K}^f$ is the tangent stiffness of the fibre bridging force which will be address in the following section. By substituting Eq. (6.1) back into the incremental form of traction continuity ($\mathbf{n}^T\Delta\boldsymbol{\sigma} = \mathbf{n}^T\Delta\boldsymbol{\sigma}_o = \Delta\mathbf{t}$), together with the kinematic enhancement presented in Eq. (4.25) and some arrangements, the velocity jump from a given strain increment can be written as:

$$\Delta\mathbf{u} = \left(\frac{1}{H}\mathbf{n}^T\mathbf{a}_o\mathbf{n} + \mathbf{K}^f + \mathbf{K}^c\right)^{-1}\mathbf{n}^T\mathbf{a}_o\Delta\boldsymbol{\varepsilon} \tag{6.2}$$

In the above formulation, the intact bulk material is assumed to be elastic with stiffness $\mathbf{a}_o$ and the inelastic response of the material is assumed to happen only in the embedded crack. The constitutive relation of the FRC can be then written as:

$$\begin{aligned}\Delta\boldsymbol{\sigma} = \Delta\boldsymbol{\sigma}_o &= \mathbf{a}_o\left[\Delta\boldsymbol{\varepsilon} - \frac{1}{H}\mathbf{n}\Delta\mathbf{u}\right] \\ &= \left[\mathbf{a}_o - \frac{1}{H}\mathbf{a}_o\mathbf{n}\left(\frac{1}{H}\mathbf{n}^T\mathbf{a}_o\mathbf{n} + \mathbf{K}^f + \mathbf{K}^c\right)^{-1}\mathbf{n}^T\mathbf{a}_o\right]\Delta\boldsymbol{\varepsilon}\end{aligned} \tag{6.3}$$

The obtained constitutive relationship shows that the response of localisation band, driven by both the fibre bridging effect and concrete cohesion, is systematically and directly incorporated into a continuum-based constitutive model. As seen in Eqs. (6.2) and (6.3), the constitutive model, in this form, is generic and able to feature any type of fibre bridging and cohesive laws via the tangent stiffness $\mathbf{K}^f$ and $\mathbf{K}^c$. As a result, it can be used for different types of fibres with different geometries and mechanical specifications while maintaining the localised failure mechanism as the central component of modelling. In addition to cohesive resistance, described in Section 4.2, a fibre bridging law is now needed to complete the constitutive model. After that, other aspects of numerical calculation including tangent stiffness for cohesive-frictional resistance, stress return algorithm and crack initiation will be executed similar to those presented in Section 4.2.3, 4.2.4 and 5.3.2.1 in previous chapters.

6.2.2 Fibre pull-out and fibre bridging models

The constitutive equation in Eq. (6.3) indicates that apart from a cohesive law for the cementitious matrix, the model also requires a fibre bridging law, describing the stress transfer by randomly distributed fibres across the crack. Since the model is formulated in a generic form as mentioned earlier, either phenomenological fibre bridging laws (Abdallah et al., 2016; Cunha et al., 2010; Laranjeira et al., 2010) or more complicated micromechanics-based models (Lu and Leung, 2017; Naaman et al., 1992; Stang and Shah, 1986) can be used within the constitutive model described above. In this study, the pull-out force-displacement relationship (i.e., $P - \delta$) of smooth polymer fibres follows formulations proposed by Lin and Li (1997) which is based on micromechanical analysis of single fibre pull-out test. The model is simple with a few parameters and was proven to be effective for modelling the fibre bridging effect of FRC (Mihai and Jefferson, 2017; Mihai et al., 2016). For hooked-end fibre, the pull-out force – displacement relationship is obtained by solving

the differential equation in Lin and Li (1997) with slip-softening law in association with the pull-out resistance of the fibre hooks proposed by Alwan et al. (1999).

The fibre bridging stress t^f in the local coordinate system of the crack plane is then derived by integrating the individual pull-out contribution of all fibres across the crack plane using probability density functions for the fibre orientation $p(\varpi)$ and for fibre centroidal distance from the crack plane $p(z)$ as (Lin and Li, 1997):

$$t^f(\delta) = \frac{4V_f}{\pi {d_f}^2} \int_{\varpi} \int_{z} P(\delta)\, p(\varpi) p(z) dz d\varpi \tag{6.4}$$

where d_f is the diameter of the fibre; V_f is the fibre volume fraction within the material; ϖ is the orientation angle of the fibre and z is the distance between the centroid of a fibre and the crack plane as illustrated in Figure 6.2; $P(\delta)$ is the pull-out force carried by a single fibre with respect to crack opening, $\delta = \|\mathbf{u}\|$.

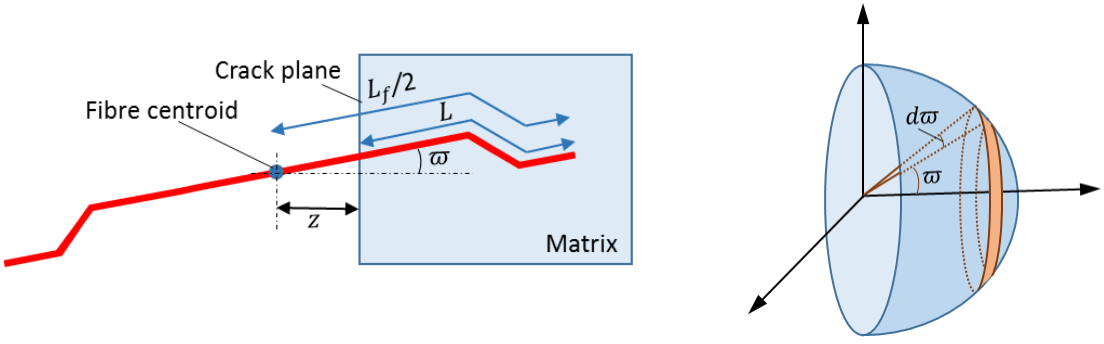

(a) (b)

Figure 6.2. Illustration of fibre bridging effect integration: (a) z and ϖ definitions for a hooked fibre and (b) Integration scheme

Thanks to the integration with corresponding probability density functions, the fibre bridging force can be constructed from the contributions of individual fibres without having to explicitly take into account the influence of every fibre. This allows the calculation of fibre bridging stress from single fibre pull-out where micro-structural changes and failure mechanisms are taken into consideration. The macro responses of the FRC can thus be captured with a proper bridging force from fibres. In addition, the model can be flexibly used for different types of fibre distributions (i.e., unidirectional fibres, random fibres) by changing these density functions appropriately. The formulations of bridging stress t^f for two most common fibres, including smooth polymer fibres and hook-end steel fibre, are presented in the following.

6.2.2.1 Fibre bridging effect for smooth polymer fibres

As proposed by Lin and Li (1997), the pull-out process of a single polymer fibre comprises two stages: (i) debonding stage where interfacial fibre-matrix cohesion is debonded and (ii) subsequent pull-out stage governed by the frictional slipping of fibres over the matrix. The relationship between the fibre-matrix interfacial shear stress τ and the slip S is assumed to be linear hardening as follows:

$$\tau = \tau_0(1 + \beta_f \frac{S}{d_f}) \tag{6.5}$$

where d_f is the diameter of the fibre; τ_0 is the initial cohesion between fibre and matrix and $\beta_f > 0$ is the hardening parameter for the frictional sliding. For the case of uniformly random distribution of fibres (i.e., $p(\varpi) = \sin\varpi$; $p(z) = \frac{2}{L_f}$), together with fibre snubbing effect, the fibre bridging law can be written as (Lin and Li, 1997):

$$\frac{t^f}{t^*} = \begin{cases} \frac{2}{k}\left\{\left[1 - \frac{1}{k}cosh^{-1}\left(1 + \zeta\frac{\delta}{\delta^*}\right)\right]\sqrt{\left(1 + \zeta\frac{\delta}{\delta^*}\right)^2 - 1} + \frac{\zeta\delta}{k\delta^*}\right\} & 0 \le \delta \le \delta^* \\ \left(1 + \frac{\beta_f}{d_f}\delta\right)\left(1 - \frac{2\delta}{L_f}\right) & \delta^* \le \delta \le \frac{L_f}{2} \end{cases} \tag{6.6}$$

with $t^* = 0.5w\tau_0 V_f(1+\varsigma)\frac{L_f}{d_f}$; $w = \frac{2}{4+f^2}\left(1 + e^{\pi f/2}\right)$; $k = \frac{\omega L_f}{2d_f}$; $\zeta = \cosh(k) - 1$; $\omega = \sqrt{4\tau_0\beta_f(1+\varsigma)/E_f}$; $\varsigma = \frac{V_f E_f}{(1-V_f)E_m}$; $\delta^* = \frac{2d_f}{\beta_f}[\cosh(k) - 1]$. In the above formulations, L_f is the fibre length; f is snubbing coefficient of the fibre; E_f and E_m are, respectively, Young's modulus of the fibre and the cement matrix.

6.2.2.2 Fibre bridging effect for hooked-end steel fibres

Different from the straight fibre, the behaviour and mechanism of hooked-end fibre is more complicated and has not been fully investigated in previous studies. With the emphasis on theoretical methodology for constitutive modelling of geomaterials, the current research will integrate concepts proposed by previous studies (Alwan et al., 1999; Lin and Li, 1997) to obtain a bridging model for hooked-end fibre. As presented in Eq. (6.4), the fibre bridging stress is obtained by integrating the individual pull-out contribution of all fibres across the crack plane with appropriate probability density functions for the fibre orientation and for fibre centroidal distance from the crack plane. The pull-out force – displacement for a single hooked-end fibre is thus presented in this section. It is then put into the integration to

calculate the bridging stress which can be used within the double-scale framework for modelling FRC.

Single fibre pull-out

Experimental results of single fibre pull-out tests (Abdallah et al., 2016; Laranjeira et al., 2010) show that hooked-end fibres have greater load-bearing capacity compared to straight fibre owing to the extra effort needed to straighten the hooks before pulling it out of the matrix. The present study followed the concepts used in the analytical formulation of Alwan et al. (1999) to determine the mechanical contribution from the hooks to the fibre load-resistance by formulating the hook straightening as a pulling process through frictional pulleys where plastic hinges are integrated. This contribution from hook-straightening is incorporated into the model of straight fibre by Lin and Li (1997) to obtain a pull-out model for hooked-end fibre. As a result, in addition to debonding and pull-out phase as for straight fibre, the pull-out process of a hooked-end fibre is considered to experience two extra phases for hook straightening process, as illustrated in Figure 6.3. During phase 1, the fibre is debonded from the cementitious matrix by a pull-out force as illustrated by the blue curve in Figure 6.3b. In phase 2, both parts of the hook (i.e., h_{f1} and h_{f2}) are straightened at two plastic hinges illustrated by image (2) in Figure 6.3a. The additional pull-out force to perform the cold work needed to for this process is $\Delta P_1 = P_2 - P_1$, corresponding to the extra pull-out distance h_{f1}. The force-displacement relationship in this phase is illustrated in Figure 6.3b by the red curve. In phase 3, the remaining part of the hook, h_{f2}, is straightened and pulled out by an additional force $\Delta P_2 = P_3 - P_1$, as illustrated by a purple curve in the Figure. After being straightened, the fibre is then pulled out of the matrix by the same frictional pulling mechanism as experienced by a normal straight fibre in phase 4. The force-displacement relationship for this phase is illustrated by a green curve in the Figure. By using an equivalent frictional pulley model to calculate the cold work needed for straightening the steel hooks at plastic hinges, ΔP_1 and ΔP_2 can be calculated as (Alwan et al., 1999):

$$\Delta P_1 = \frac{f_y \pi {d_f}^2}{12\cos\theta \left(1 - \mu_f \sin\frac{\theta}{2}\right)^2} \tag{6.7}$$

$$\Delta P_2 = \frac{f_y \pi {d_f}^2}{24\cos\theta \left(1 - \mu_f \sin\frac{\theta}{2}\right)} \tag{6.8}$$

where f_y is the fiber yield strength; θ is the hook angle and μ_f is the frictional coefficient between the fibre surface and the surrounding cementitious matrix.

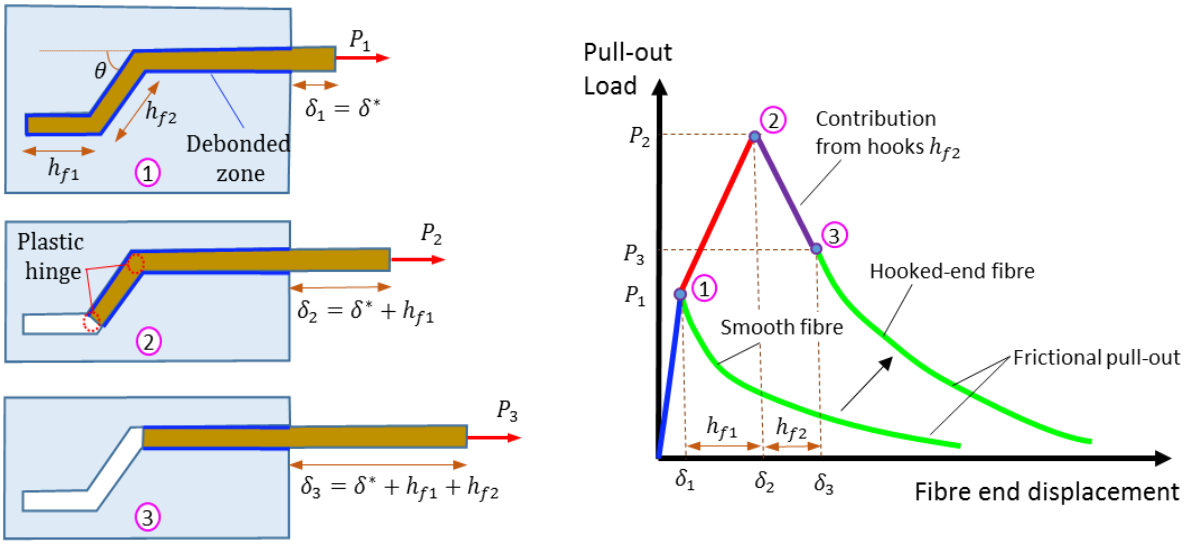

(a) (b)

Figure 6.3. Illustration of a hooked-end fibre pull-out: (a) Pull-out process and (b) Corresponding load-displacement curve

From these considerations, the formulations of the four-phase fibre pull-out model is as follows.

Debonding phase

Different from polymer fibres where fibre debris from surface abrasion creates "jamming" effect and results in slip-hardening behaviour, experimental results for steel fibres (Abdallah et al., 2016; Alwan et al., 1999; Laranjeira et al., 2010) show a softening shear-slip relationship, which can be represented as:

$$\tau = \tau_0(1 - \beta_f \frac{S}{d_f}) \tag{6.9}$$

Following the concept proposed by Lin and Li (1997) for pull-out process of a straight fibre depicted in Figure 6.4, interfacial fibre-matrix slip, S in the debonding phase can be calculated from the differential equation:

$$\frac{d^2S}{dx^2} + \frac{\omega^2}{{d_f}^2} S = \frac{\omega^2}{\beta_f d_f} \tag{6.10}$$

where ω and other parameters are defined earlier as in Eq. (6.6). The boundary conditions of this equation are $S = 0$ and $\frac{dS}{dx} = 0$ at $x = 0$.

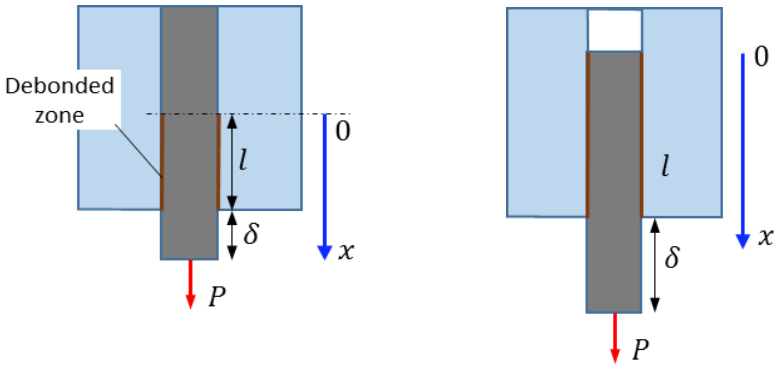

(a) (b)

Figure 6.4. Schematic of straight fibre pull-out: (a) Debonding phase and (b) Pull-out phase

The solution for this second order differential equation (6.10) can be found as:

$$S(x) = \frac{d_f}{\beta_f}\left[1 - \cos\left(\frac{\omega x}{d_f}\right)\right] \tag{6.11}$$

It can be seen that due to the difference in the shear-slip relationship, the solution of the differential equation for the pull-out force, in this case, is totally different from that for straight fibre presented in Lin and Li (1997). This thus yields a different pull-out load – displacement relationship. By substituting Eq. (6.11) into Eq. (6.9), the shear stress acting along the fibre can be expressed as:

$$\tau(x) = \tau_0 \cos\left(\frac{\omega x}{d_f}\right) \tag{6.12}$$

The averaged interfacial shear stress in the debonded region can thus be obtained as:

$$\bar{\tau} = \frac{1}{l}\int_0^l \tau(x)dx = \frac{d_f}{\omega l}\tau_0 \sin\left(\frac{\omega l}{d_f}\right) \tag{6.13}$$

where l is the debonded length of the fibre as shown in Figure 6.4. Using the same formulation described by Lin and Li (1997), the pull-out force in the debonding phase can be written as:

$$P = \pi d_f l \bar{\tau}(1+\varsigma) = \frac{\pi {d_f}^2 \tau_0}{\omega}(1+\varsigma)\sin(\frac{\omega l}{d_f}) \tag{6.14}$$

By eliminating l from Eq. (6.14) and using two-side pull-out distance $\delta = 2S(x = l)$, the pull-out force with respect to pull-out displacement is obtained as:

$$P = \frac{\pi {d_f}^2 \tau_0}{\omega}(1+\varsigma)\sqrt{1-(1-\frac{\beta_f \delta}{2d_f})^2} \tag{6.15}$$

Finally, the force and displacement corresponding to the stage of fully debonded (i.e., end of phase 1) can be expressed as:

$$P_0 = \frac{\pi {d_f}^2 \tau_0}{\omega}(1+\varsigma)\sqrt{1-(1-\frac{\beta_f \delta^*}{2d_f})^2} \tag{6.16}$$

$$\delta^* = 2S(x=l) = \frac{2d_f}{\beta}\left[1-\cos(\frac{\omega l}{d_f})\right] \tag{6.17}$$

Straightening hook h_{f1}

Starting from the end of phase 1, the relationship of pull-out force and pull-out displacement of a fibre in this phase is simply assumed to be linear. This means that it would start from point (P_0; δ^*) whose formulation is presented in Eq. (6.16)-(6.17) and end at the point ($P_0 + \Delta P_1$; $\delta^* + h_{f1}$) where ΔP_1 is calculated from Eq. (6.7) and h_{f1} is the length of the first part of fibre hook. This process is illustrated in Figure 6.3b by a red line from point 1 to 2. The pull-out force – displacement relationship can thus be written as:

$$P = P_0 + \frac{\Delta P_1}{h_{f1}}(\delta - \delta^*) \tag{6.18}$$

This phase will end when the pull-out distance reaches $\delta^* + h_{f1}$ and the first part of the hook is completely straightened as illustrated by the second image of Figure 6.3a.

Straightening hook h_{f2}

Similar to the second phase, the force-displacement relationship during the third phase (i.e., straightening the second part of the hook, h_{f2}) is also considered to be linear with the end-point $P_0 + \Delta P_2$ and the corresponding displacement $\delta^* + h_{f1} + h_{f2}$. The pull-out force in this phase is thus formulated as:

$$P = P_0 + \Delta P_1 + \frac{\Delta P_2 - \Delta P_1}{h_{f2}}\left(\delta - h_{f1} - \delta^*\right) \tag{6.19}$$

Pull-out phase

In this phase, the fibre is assumed to be frozen and pulled out of the matrix with frictional sliding as illustrated in Figure 6.4b. Therefore, the distribution of slip distance along embedded fibre length remains the same as in Eq. (6.11). Its formulation is now expressed as:

$$S = \frac{d_f}{\beta_f}\left[1-cos(\frac{\omega x}{d_f})\right] + (\delta - \delta^*) \tag{6.20}$$

Consequently, the expression for the pull-out force can be written as:

$$P = \pi d_f \int_0^{L-\delta+\delta^*} \tau(x)dx = \frac{\pi {d_f}^2 \tau_0}{\omega} \sin\left[\frac{\omega}{d_f}(L-\delta+\delta^*)\right] - \pi\beta_f\tau_0(\delta-\delta^*)(l-\delta+\delta^*) \tag{6.21}$$

This phase will end when the fibre is completely pulled out of the matrix; $\delta = l + \delta^*$.

The final formulation of four-phase pull-out force – displacement of a single hooked-end fibre is summarised as:

$$P = \begin{cases} P_I = \dfrac{\pi {d_f}^2 \tau_0}{\omega}(1+\varsigma)\sqrt{1-\left(1-\dfrac{\beta_f\delta}{2d_f}\right)^2} & 0 \le \delta \le \delta^* \\ P_{II} = P_0 + \dfrac{\Delta P_1}{h_{f1}}(\delta-\delta^*) & \delta^* \le \delta \le \delta^* + h_{f1} \\ P_{III} = P_0 + \Delta P_1 + \dfrac{\Delta P_2 - \Delta P_1}{h_{f2}}\left(\delta - h_{f1} - \delta^*\right) & \delta^* + h_{f1} \le \delta \le \delta^* + h_{f1} + h_{f2} \\ P_{IV} = \dfrac{\pi {d_f}^2 {\tau_0}'}{\omega}\sin\left[\dfrac{\omega}{d_f}(l-\delta+\delta^*)\right] & \\ \quad -\pi\beta_f\tau_0'(\delta-\delta^*)(l-\delta+\delta^*) & \delta^* + h_{f1} + h_{f2} \le \delta \le l + \delta^* \end{cases} \tag{6.22}$$

where $\delta^* = \frac{2d_f}{\beta}\left[1-\cos(\frac{\omega l}{d_f})\right]$; ${\tau_0}' = \frac{P_0+\Delta P_2}{\frac{\pi {d_f}^2}{\omega}\sin\left[\frac{\omega}{d_f}(l-h_{f1}-h_{f2})\right]-\pi\beta_f(h_{f1}+h_{f2})(l-h_{f1}-h_{f2})}$; $P_0 = \frac{\pi {d_f}^2\tau_0}{\omega}(1+\varsigma)\sqrt{1-(1-\frac{\beta_f\delta^*}{2d_f})^2}$; ω and ς are defined in Eq. (6.6) and l is the fibre embedded length within the cementitious matrix.

Fibre bridging stress

As described in Eq. (6.4), the fibre bridging law for hooked-end fibre can be obtained by integrating the pull-out contributions of fibres across the crack plane. Figure 6.2 shows the relative position of a fibre to the matrix, represented by its orientation ϖ and centrodial distance to the crack plane, from which the embedded length can be determined as:

$$l = \frac{L_f}{2} - \frac{z}{\cos\varpi} \rightarrow z = \left(\frac{L_f}{2} - l\right)\cos\varpi \tag{6.23}$$

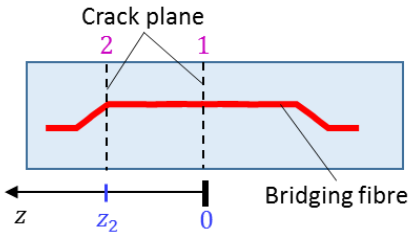

Figure 6.5. Illustration of fibre boundaries for the integration

Because the proposed pull-out force expression for hooked-end fibre in Eq. (6.22) is valid only for the embedded length $h_{f1} + h_{f2} \leq l \leq L_f/2$, the integration of bridging law, for simplicity purpose, only counts the contributions from fibres in this range as illustrated in Figure 6.5. As a result, the boundaries for the integration are $0 \leq \varpi \leq \pi/2$ and $0 \leq z \leq \left(\frac{L_f}{2} - h_{f1} - h_{f2}\right)\cos\varpi = z_2\cos\phi$ and the density functions for uniformly random distribution are taken as $p(\varpi) = \sin\varpi$ and $p(z) = \frac{1}{z_2}$. In addition, the pull-out force for inclined fibres (i.e., $\varpi \neq 0$) can be calculated from fibres perpendicular to crack surface (i.e., $\varpi = 0$) as:

$$P|_{\varpi} = e^{f\varpi}P|_{\varpi=0} \tag{6.24}$$

where f is the snubbing coefficient, proposed by Li et al. (1990, 1991). The integration for the fibre bridging effect is now expressed as:

$$t^f(\delta) = \frac{4V_f}{\pi z_2 {d_f}^2}\int_{\varpi=0}^{\frac{\pi}{2}}\int_{z=0}^{z_2 cos\varpi} P(\delta)e^{f\varpi}sin\,\varpi dz\,d\varpi \tag{6.25}$$

As the pull-out force P is obtained separately for four different phases (i.e., debonding, straightening hook h_{f1}, straightening hook h_{f2} and frictional pull-out), the integration in (6.25) can simply be calculated for four phases. To simplify the integration process, the force P of fibres whose embedded lengths range from 0 to $L_f/2$, is approximated by taking an averaged embedded length of $L_f/4$. This approximation helps obtain a simple yet effective model for fibre bridging effect in this study but we acknowledge that a more accurate calculation can be used to acquire better consistencies throughout the model.

In phase I ($0 \le \delta \le \delta^*$), the fibre bridging stress can be obtained from the pull-out force as:

$$\begin{aligned} t^f(\delta) &= \frac{4V_f}{\pi z_2 {d_f}^2}\int_{\varpi=0}^{\frac{\pi}{2}}\int_{z=0}^{z_2 cos\varpi} P_I e^{f\varpi} sin\varpi dz\, d\varpi \\ &= P_I \frac{4V_f}{\pi z_2 {d_f}^2}\int_{\varpi=0}^{\frac{\pi}{2}}\int_{z=0}^{z_2 cos\varpi} e^{f\phi} sin\,\varpi dz d\varpi = \frac{4V_f}{\pi {d_f}^2}\frac{1+e^{\frac{\pi f}{2}}}{4+f^2}P_I = t^* P_I \end{aligned} \tag{6.26}$$

Similarly, the bridging law for phase II and III can be simply written as $t^* P_{\mathrm{II}}$ and $t^* P_{\mathrm{III}}$. However, since during phase IV, some fibres are completely pulled out of the matrix and no longer contribute to the bridging effect, the upper limit of the integration changes. As formulated in Eq. (6.22), a fibre contributes to the bridging as long as its embedded length satisfies $\delta \le l + \delta^*$. By substituting Eq. (6.23) into this condition, one obtains:

$$\delta \le \frac{L_f}{2} - \frac{z}{\cos\varpi} + \delta^* \rightarrow z \le \left(\frac{L_f}{2} - \delta + \delta^*\right)\cos\varpi = z_4 \cos\varpi \tag{6.27}$$

This upper integration limit ensures that for a given crack opening, only fibres that are actually bridging the crack, are counted. The bridging stress is then calculated as:

$$\begin{aligned} t^f(\delta) &= \frac{4V_f}{\pi z_2 {d_f}^2}\int_{\phi=0}^{\frac{\pi}{2}}\int_{z=0}^{z_4 cos\phi} P_{IV}(\delta) e^{f\phi} sin\,\phi dz\, d\phi = \frac{4V_f}{\pi z_2 {d_f}^2} P_{IV} z_4 \frac{1+e^{\frac{\pi f}{2}}}{4+f^2} \\ &= \frac{4V_f z_4}{\pi {d_f}^2 z_2}\frac{1+e^{\frac{\pi f}{2}}}{4+f^2}P_{IV} = \sigma^* \frac{z_4}{z_2} P_{IV} \end{aligned} \tag{6.28}$$

The four-phase bridging force of hooked-end fibre is finally summarised as:

$$\frac{t^f}{t^*} = \begin{cases} \dfrac{\pi {d_f}^2 \tau_0}{\omega}(1+\varsigma)\sqrt{1-\left(1-\dfrac{\beta_f \delta}{2d_f}\right)^2} & 0 \le \delta \le \delta^* \\ P_0 + \dfrac{\Delta P_1}{h_{f1}}(\delta - \delta^*) & \delta^* \le \delta \le \delta^* + h_{f1} \\ P_0 + \Delta P_1 + \dfrac{\Delta P_2 - \Delta P_1}{h_{f2}}\left(\delta - h_{f1} - \delta^*\right) & \delta^* + h_{f1} \le \delta \le \delta^* + h_{f1} + h_{f2} \\ \dfrac{z_4}{z_2}\dfrac{\pi {d_f}^2 \tau_0'}{\omega} sin\left[\dfrac{\omega}{d_f}\left(\dfrac{L_f}{4} - \delta + \delta^*\right)\right] & \\ -\dfrac{z_4}{z_2}\pi\beta_f \tau_0'(\delta - \delta^*)\left(\dfrac{L_f}{4} - \delta + \delta^*\right) & \delta^* + h_{f1} + h_{f2} \le \delta \le \dfrac{L_f}{2} + \delta^* \end{cases} \tag{6.29}$$

where δ^*, $\tau_0{}'$ are calculated as in Eq. (6.22) with $L = L_f/4$; $z_2 = \frac{L_f}{2} - h_{f1} - h_{f2}$; $z_4 = \frac{L_f}{2} - \delta + \delta^*$ and $t^* = \frac{4V_f}{\pi {d_f}^2}\frac{1+e^{\frac{\pi f}{2}}}{4+f^2}$.

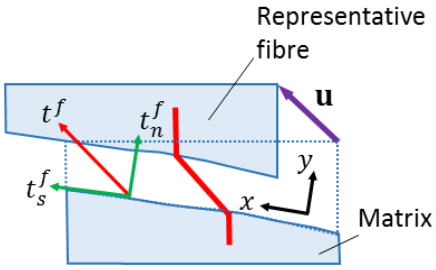

Figure 6.6. Deformation and projections of force transferred by a bridging fibre due to crack opening

With the assumption that the bridging fibres deform in accordance with the relative displacement of the crack faces as illustrated in Figure 6.6 for 2D case, the increment of fibre bridging stress, $\Delta t^f = K_l^f \Delta\delta$, along the fibre axis can be projected onto the local coordinate system of the crack plane to get the local bridging law as:

$$\Delta \mathbf{t}_l^f = \begin{bmatrix} \Delta t_n^f \\ \Delta t_{s1}^f \\ \Delta t_{s2}^f \end{bmatrix} = \begin{bmatrix} K_l^f & 0 & 0 \\ 0 & K_l^f & 0 \\ 0 & 0 & K_l^f \end{bmatrix} \begin{bmatrix} \Delta u_n \\ \Delta u_{s1} \\ \Delta u_{s2} \end{bmatrix} = \mathbf{K}_l^f \Delta \mathbf{u}_l \tag{6.30}$$

The incremental form of fibre bridging law in the global coordinate system, $\Delta \mathbf{t}^f = \mathbf{K}^f \Delta \mathbf{u}$, can now be obtained from its local relationship by using coordinate transformations technique. Then, it can be incorporated into the double-scale model presented in Section 4.3 of Chapter 4 for modelling FRC.

6.2.3 Enhancement to account for effects of fibre content on cracking and mechanical response

It is known that the inhomogeneity of material in specimens could not be captured by using solely homogenous models with Finite Element Analysis, especially for FRC where crack development is strongly affected by the randomness of fibre distribution. In addition, as shown in experimental results (Li et al., 2001; Park et al., 2012; Wille et al., 2011), for a specific set of material mixture (i.e. concrete and fibre), fibre content (i.e. volume fraction) is the decisive factor, controlling the crack density and elongation of phase II where cracks are diffusely distributed among specimens as addressed in Section 2.3 of Chapter 2. Crack

density, in this case, can be considered as a "property" of a material mixture which is closely related to the density of fibre (i.e., fibre volume fraction) and its random distribution among the material body. However, to the best of my knowledge, there is no explicit relationship between fibre content and crack density in the failure of FRC that was reported in the literature so far. Given limited experimental proofs and theoretical supports on the issue, a phenomenological law is used in the model to reflect this intimate relationship and to alleviate the mismatch of inhomogeneity between the real material and that in the modelling. The relationship of the so-called crack density and fibre volume content V_f is reflected through the number of crack, n_c, initiating throughout the considered RVE, formulated as:

$$n_c = \frac{1}{\varepsilon_0} V_f e^{100V_f - \vartheta - \frac{0.01\varepsilon_m}{\varepsilon_0}} + 1 \tag{6.31}$$

where $\varepsilon_m = \max(\varepsilon_1,\ \varepsilon_2,\ \varepsilon_3)$ is the largest value of principal strain of the RVE; $\varepsilon_0 = \delta_0/H$ with δ_0 defined as the displacement corresponding to peak stress in pure tension as previously presented in Eq. (4.5) and H is the characteristic length of considered RVE (or element during the simulation by FEA) defined in Eq. (4.25); ϑ is a parameter controlling the crack density throughout the considered volume. This law is inspired from experimental observations (Kamal et al., 2008; Li et al., 2001; Paegle and Fischer, 2016; Park et al., 2012; Soulioti et al., 2011; Zhang and Ju, 2011) that the number of crack increases with the increase of volume content. The number of crack, formulated in this form, also approaches 1 with the increase of strain to reflect the transition from diffuse cracking to localisation mode as earlier analysed in Section 2.3 of Chapter 2.

A parametric study, shown in Figure 6.7a, further illustrates this relationship by plotting the number of crack, calculated over a length $L = 20\text{cm}$ at a stage $\varepsilon_m = 2\varepsilon_0$ with various values of volume fraction (i.e., $V_f = 0 - 4\%$) and parameter ϑ (i.e., $\vartheta = 5 - 8$). It can be seen that for the case of plain concrete (i.e., $V_f = 0\%$), the number of crack across the RVE is 1 (shown in the zoom-in image) which agrees with experimental observations (Gopalaratnam and Shah, 1987; Li et al., 1996, 1998; Wille et al., 2014) and the analyses made in Section 2.3. With the increase of the fibre volume fraction, the number of crack increases at different rates depending on the parameter ϑ. In addition, the crack number is plotted against various deformation values (i.e., ε_m ranges from ε_0 to 3%) in Figure 6.7b for volume fraction $V_f = 3\%$. It is seen that with the increase of deformation, the number of crack gradually decreases and approaches 1. The phenomenological law, in this form, would

help the model reflect the transition from diffuse cracking phase to localised failure mode smoothly. It also gives the model flexibility to adapt itself to different types of FRC.

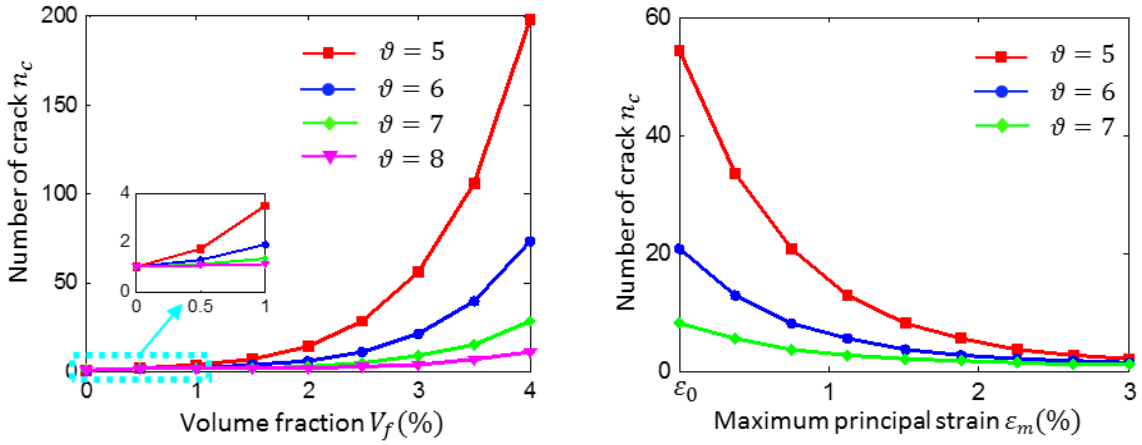

(a) (b)

Figure 6.7. Parametric study on parameter ϑ: (a) Number of crack with different volume fraction values and (b) With deformation evolution

With the increase in the number of cracks/localisation bands, as illustrated in Figure 6.8a, the volume fraction of localisation band with respect to the RVE now becomes $\eta = \frac{n_c \Omega_{\mathrm{i}}}{\Omega} = \frac{n_c h}{H}$. Following the same procedure in Section 6.2.1, the constitutive equation, (6.3) can now be rewritten as:

$$\Delta\boldsymbol{\sigma} = \mathbf{a}_o \left[\Delta\boldsymbol{\varepsilon} - \frac{n_c}{H}\mathbf{n}\Delta\mathbf{u}\right] = \left[\mathbf{a}_o - \frac{n_c}{H}\mathbf{a}_o\mathbf{n}\left(\frac{n_c}{H}\mathbf{n}^T\mathbf{a}_o\mathbf{n} + \mathbf{K}^f + \mathbf{K}^c\right)^{-1}\mathbf{n}^T\mathbf{a}_o\right]\Delta\boldsymbol{\varepsilon} \qquad (6.32)$$

The reasoning behind this enhancement is illustrated through an example of a RVE of FRC having the length $L = 20$ cm and $V_f = 1$ % as shown in Figure 6.8 (the experimental failure pattern is taken from Sirijaroonchai et al. (2010)). Under tensile loading, let me assume that there are 20 cracks appearing in the considered RVE, making the averaged crack density $\zeta_{\mathrm{cr}} = 20/0.2 = 100$ cracks/m. In the modelling, if the RVE is meshed with two elements using the proposed model, each element, having characteristic length $H = 10$cm, has to theoretically reflect the interactions of 10 cracks and their surrounding bulk material. By using Eq. (6.31) with $\vartheta = 2.94$ and $\varepsilon_m = 2\varepsilon_0$, the number of crack in each element is calculated as $n_c = 10.4$ (cracks). On the other hand, when the RVE is simulated using only one element having characteristic length $H = 20$cm, the number of cracks can be recalculated using the same parameter $\vartheta = 2.96$ and the result is $n_c = 19.8$ (cracks). This means that in both cases, the crack density remains constant of approximately $\zeta_{\mathrm{cr}} = 100$ cracks/m as it should be. This simple modification allows the proposed model to

properly capture the diffuse cracking phase at different discretisation resolutions during the modelling with FEA. It should also be noticed that the number of crack used in the model described above is just a value to represent for the level of diffuse cracking in the specimen and thus it can be a real number. The use of Eq. (6.31) is satisfactory as demonstrated by numerical examples and we acknowledge that it should be backed up with further investigations based on micromechanics and experiments in future work.

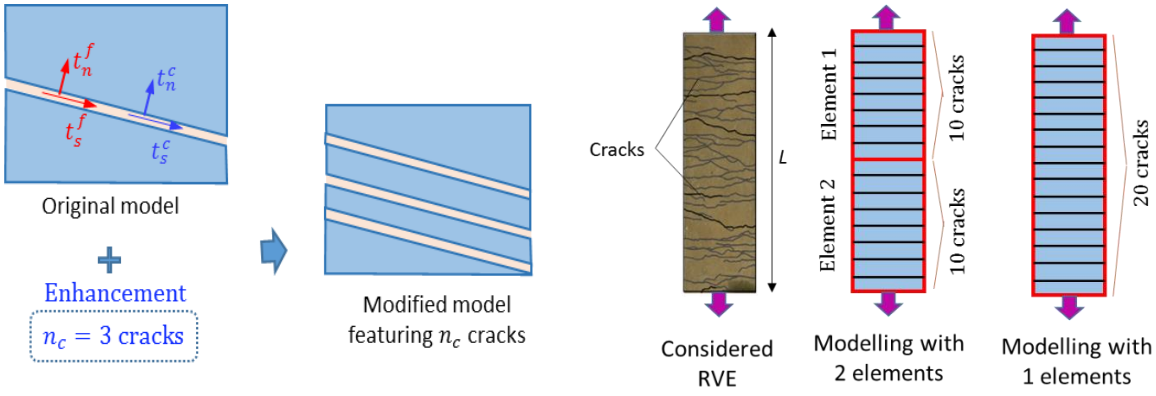

Figure 6.8. Illustration of phenomenological enhancement (a) Implementation into the proposed model and (b) Capturing constant crack density during simulation

6.3 Application to fibre reinforced concrete modelling

This section presents the application of the proposed model to fibre reinforced concrete (FRC) modelling. The fibre pull-out model for hooked-end fibre, described above, is validated via experimental results of single fibre pull-out tests to prove its applicability in capturing the behaviour of bridging fibres in cracks. The model validation is then carried out at both constitutive and structural levels against experiments of various types of fibres and volume contents.

6.3.1 Single fibre pull-out test

The proposed pull-out model for hooked-end fibres is validated via a series of pull-out tests, shown in Figure 6.9, where a hooked steel fibre is pulled out of a cementitious matrix. The experiments were performed by Alwan et al. (1999) with commercial Dramix fibres having a diameter $d_f = 0.5$ mm and two embedded lengths $L = 12.5$ and 25 mm while the cement Young's modulus is $E_m = 20$ GPa. The fibre properties are: yield strength $f_y = 896$ MPa; Young's modulus $E_f = 210$ GPa; hook geometries $h_{f1} = h_{f2} = 1.5$ mm and

hook angle $\theta = 45^0$. The model parameters in this example are $\tau_0 = 1.1$ KPa; $\beta_f = 0.04$; $\mu_f = 0.5$.

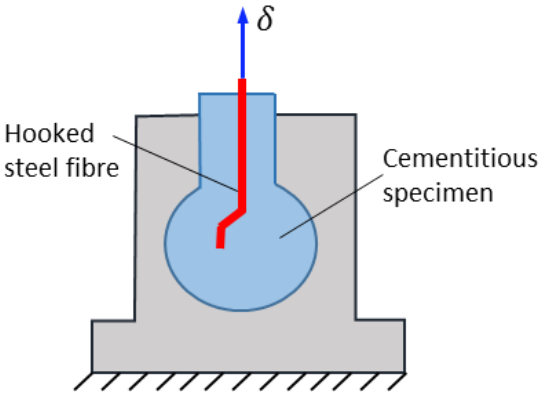

Figure 6.9. Pull-out test set-up of a single hooked-end steel fibre

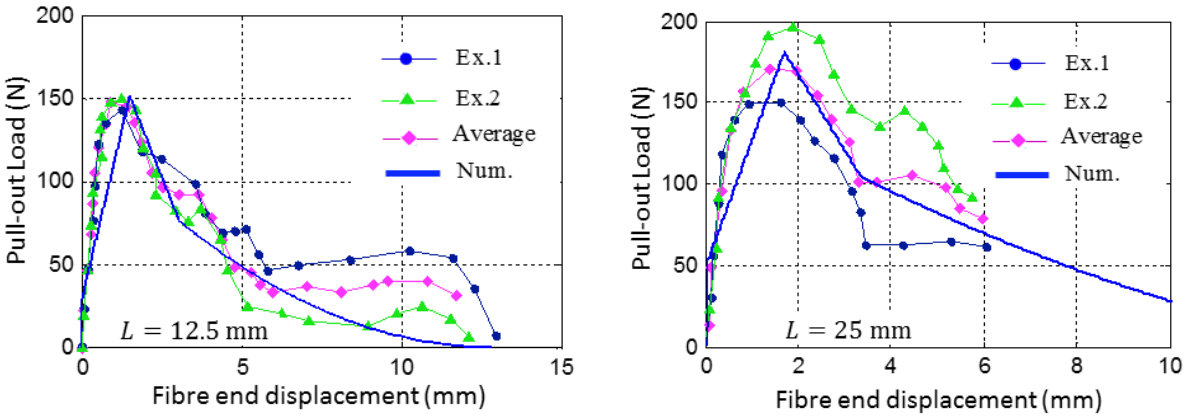

Figure 6.10. Pull-out test results for different embedded lengths L

The load-displacement responses, plotted in Figure 6.10 for two embedded lengths, show good agreements between the model results and experimental counterparts. Following the model, under a very small displacement, the fibres are debonded from the matrix and the straightening process starts quickly. The softening behaviour, where all hooks are straightened and the fibre is subsequently pulled out of the matrix, is well-captured by the model. Thanks to the considerations of fibre-matrix slip and hook straightening at micro-/mesoscopic level, the model can predict the overall pull-out force with a few physically meaningful parameters, which can be experimentally determined. The responses, including the contributions from the hooks, are produced from fibre mechanical properties and geometries without requiring information about the force-displacement curve in advance as in previous models (Laranjeira et al., 2010) or phenomenological models heavily based on curve-fitting (Abdallah et al., 2016; Cunha et al., 2010). Even though the fibre pull-out

responses from the model are not smooth, this simple model is capable of capturing the general trend and behaviour of single fibre pull-out thanks to the mechanism of debonding and hook straightening.

6.3.2 Constitutive simulations of uniaxial tension tests

The uniaxial tension tests, with set-up shown in Figure 6.11, are used to investigate the capability of the proposed constitutive model for FRC. A series of tests were conducted by Li et al. (1998) with commercial Dramix fibres and polymer polyvinyl alcohol (PVA) fibres with different volume fraction $V_f = 0\%, 2\%, 3\%$ and 6%. The properties of the concrete are taken as: Young's modulus $E_m = 50$ GPa; Poisson's ratio $\nu = 0.18$; uniaxial compressive strength $f_c = 46.3$ MPa; tensile strength $f_t = 3.7$ MPa; fracture energy $G_I = 0.27$ N/mm from which the model parameter α can be calculated as $\alpha = 0.2$. As the plain concrete used for all specimens comes from the same batch, model parameters for the matrix are: $m = 0.3$; $\beta = 0.05$; $\mu_0 = 0.6$; $\gamma = 1.2$. The mechanical properties of fibres used in the experiments and related model parameters are listed in Table 6.1.

Table 6.1. Mechanical properties and parameters of the fibres used in experiments

	Fibre properties						Model parameters			
	E_f (GPa)	d_f (mm)	L_f (mm)	τ_0 (MPa)	h_{f1} (mm)	h_{f1} (mm)	μ_f	f	β_f	ϑ
Dramix	200	0.5	30	1.2	2	2	0.5	0.8	0.03	7.9
PVA	30	0.66	30	1.1	-	-	-	0.85	1.9	10.6

Numerical results of the model for Dramix fibre reinforced concrete, plotted in Figure 6.12, show fair agreements with its corresponding experimental counterparts for different values of fibre volume fraction. It is seen that the general trend of the material response from softening to hardening is well-captured by the model. Figure 6.12b shows detailed contributions of both concrete cohesion and fibre bridging effect at a crack plane for the case $V_f = 3\%$. It can be seen that after the first crack appears in the specimen (point A in the Figure), fibres bridging stress t_1^f, illustrated by a green curve, is activated and starts transferring stress across the crack plane while the matrix cohesion t_1^c begins to gradually lose its strength (illustrated by the blue curve). The overall stress of the specimen, σ_{11}, illustrated by the red curve, is a combination of these two responses as shown in the Figure. This verifies that the failure mechanism of FRC where fibres help bear the loading and stop

crack from opening, addressed in Section 2.3.1 of Chapter 2, is well captured by the proposed model.

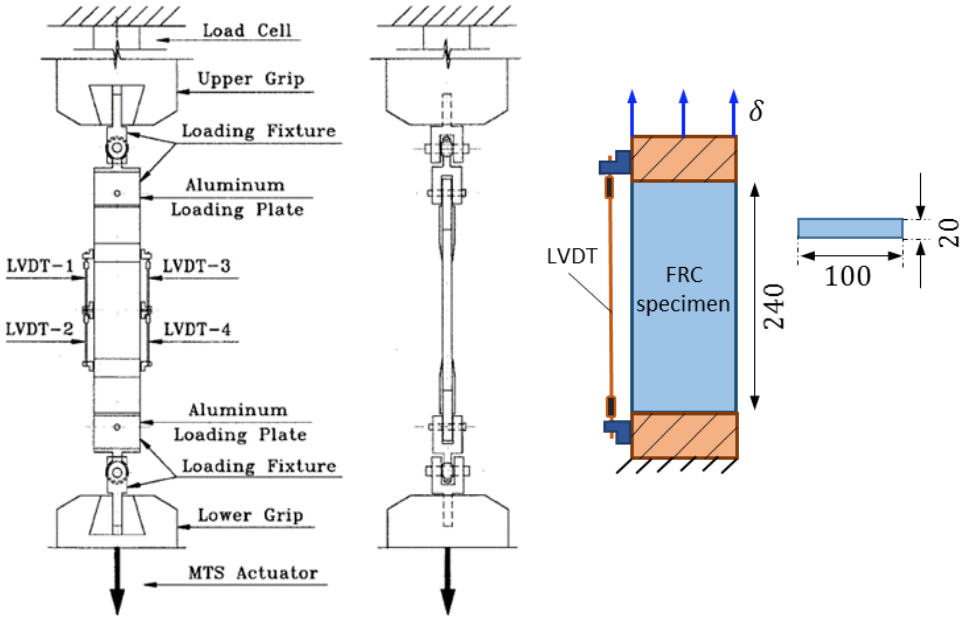

Figure 6.11. Schematic set-up of tension tests, measured in mm.

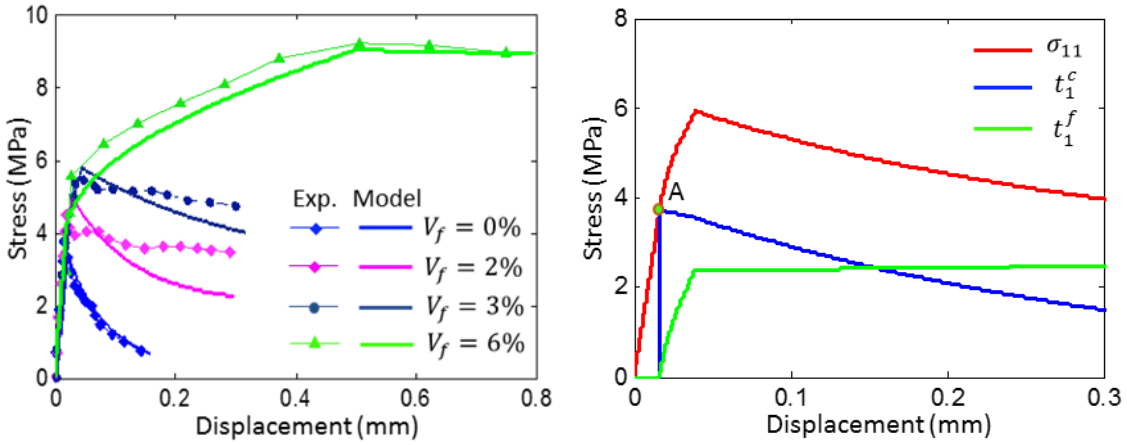

(a) (b)

Figure 6.12. Tension test results of concrete reinforced by Dramix fibres: (a) Stress-displacement responses for different volume fractions and (b) Detailed contributions within a crack for the case $V_f = 3\%$.

A parametric study is conducted for the two values of volume fraction $V_f = 3$ and 6% to investigate the influence of parameter ϑ on the overall responses of the specimen. Figure 6.13, plotting the stress – displacement responses with respect to different values of ϑ, shows that with larger values of the parameter, the material behaviour becomes more ductile. This is understandable as when ϑ increases ($\vartheta = 7.3;\ 7.9$ and 8.5), the number of cracks (and

hence crack density) also increases (at displacement $\delta = 0.1mm$, $n_c = 2.9;\ 4.8;\ 7.5$ for the case $V_f = 3\%$; and $n_c = 79;\ 144;\ 262$ for the case $V_f = 6\%$). This allows the energy to be dissipated gradually via the formation and development of more cracks, leading to more ductile behaviour. The impact of parameter ϑ (and also the phenomenological law) on the behaviour is also seen to be stronger in the case of higher volume fraction.

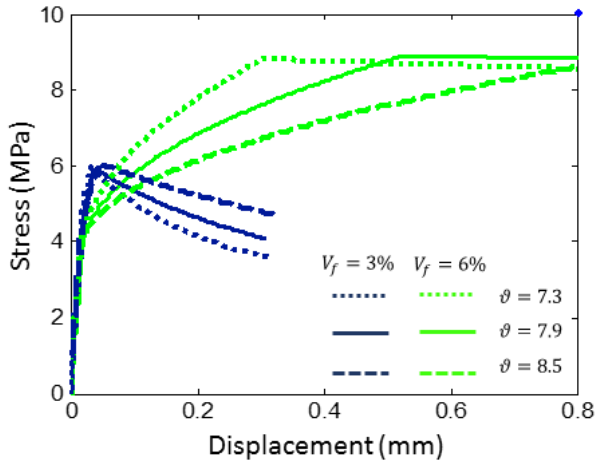

Figure 6.13. Stress-displacement responses with different values of parameter ϑ

Figure 6.14 shows reasonable agreements between numerical results and its experimental counterparts for concrete reinforced with PVA fibres. As observed in experimental studies, the results for PVA fibres show modest improvements of strength and ductility with low volume fractions (i.e., 2-3%) and they only become significant with very high contents of fibres (i.e., 6%). Similar to the case of Dramix reinforced concrete, the detailed responses, plotted in Figure 6.14b, show that the overall specimen response is a combination of the fibre bridging effect and the matrix cohesion. In addition, the Figure shows that after a crack initiates (i.e., point A), the stress $\sigma_{o,11}$ and strain $\varepsilon_{o,11}$ of the intact bulk material, illustrated by the cyan curve, continue to increase up to the peak owing to the increase of the overall stress σ_{11}. However, when the overall stress decreases, they both decrease (i.e., the outer bulk shrinks) making stress-train response a straight line on the elastic trajectory, which contrasts with the increase of deformations in the opening crack. This shows that both linear-elastic behaviour of the outer bulk material and inelastic responses of the crack where cohesion and fibre bridging take place, are interconnected within a continuum model and they all contribute to the overall responses of the material following their own constitutive relationships. This is one of the key features that distinguishes the proposed model from other continuum-based model (Beghini et al., 2007;

Caner et al., 2013; Mihai and Jefferson, 2017; Mihai et al., 2016) where such behaviour cannot be captured.

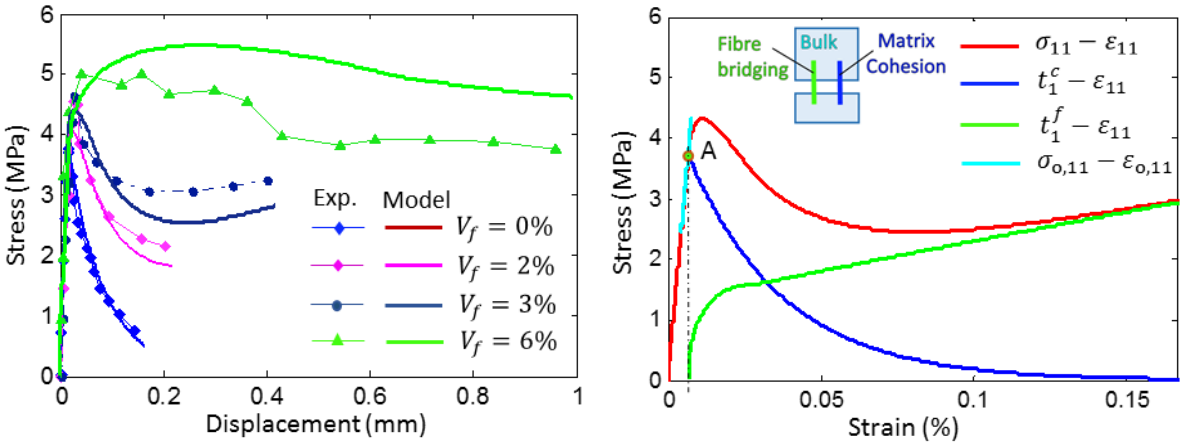

(a) (b)

Figure 6.14. Tension test results of concrete reinforced with PVA fibre: (a) Stress-displacement for different volume fractions and (b) Detailed contributions within a crack for the case $V_f = 3\%$.

6.3.3 Finite element analysis (FEA) of dog-bone tension tests

In this section, the proposed model is implemented into the commercial package ABAQUS as a user-defined material model (UMAT) for the FEA of dog-bone tension tests, whose set-up is shown in Figure 6.15a. The simulations are performed in 2D plane stress using a mesh comprising of 1347 three-node triangular elements as shown in Figure 6.15b, with displacement-controlled loading condition. The experiments were conducted by Kamal et al. (2008) with ultra-high performance concrete (UHPC) reinforced by high strength polyethylene (PE) fibres whose geometries and properties are listed in Table 6.2 and Table 6.3.

As addressed previously in Section 5.4.2, the characteristic length of each element can be calculated by definition once a crack appears by using the predicted crack orientation and nodal coordinates of the element. However, for simplicity purpose, the characteristic length is approximated as the square root of element area $H_i = \sqrt{A_i}, i = 1, 2, \ldots N_e$ where N_e is the number of element in the simulation. The previous examples in Section 5.4.2 shows that this simple approximation is effective in facilitating the implementation during the simulation without losing the effectiveness of the regularisation and hence can be adopted.

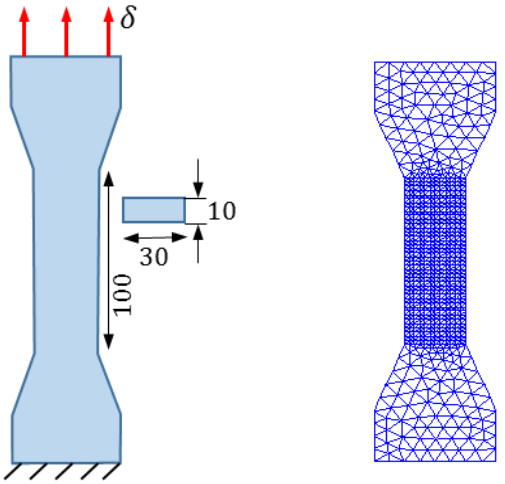

(a) (b)

Figure 6.15. Dog-bone tests: (a) Schematic experimental set-up and (b) Finite element mesh used in the simulations

Table 6.2. Fibres properties and related model parameters

	Fibre properties						Related parameters			
	E_f GPa	d_f mm	L_f mm	τ_0 MPa	h_{f1} mm	h_{f1} mm	μ_f	f	β_f	ϑ
PE	32	0.012	6	1.1	-	-	-	0.92	0.001	4.5
Dramix	210	0.63	50	1.8	2	2	0.6	0.85	0.015	5.2

Table 6.3. Concrete properties and related model parameters

	Concrete properties					Related parameters			
	E_m GPa	ν	f_c MPa	f_t MPa	G_I N/mm	β	m	μ_0	γ
Dog-bone	33	0.2	94	3.7	0.15	0.1	0.9	0.8	1.1
Bending	40	0.2	81	2.5	0.07	0.08	0.8	0.78	2.2

Figure 6.16 shows fair agreements between numerical results and those from the experiment for three volume fractions $V_f = 0.5, 1$ and 1.5%. With the increase of fibre content, the fibre bridging force becomes stronger, resulting in more cracks within the specimen and significant improvement in material ductility as also observed in experiments (Kamal et al., 2008; Li et al., 2001; Park et al., 2012). The damage profiles, in Figure 6.17a, show that for the case of $V_f = 0.5$ %, after the appearance of the first crack, a localisation

band forms and develops quickly among the specimen. This is clearly seen in the strain profiles across the specimen length at three instants of the analysis (see Figure 6.17b). With high volume content (i.e., for the case $V_f = 1.5$ %), the deformation is more homogenous, thanks to the stronger fibre bridging force shown in Figure 6.17c. The homogeneity of strain is maintained in the hardening phase, during which cracks form and develop uniformly throughout the specimen as seen in the damage contours in Figure 6.17a. This reflects the analysis made in Section 2.3.1 of Chapter 2 that the fibre bridging stress forces the specimen to form a system of uniformly distributed small cracks to dissipate the given energy.

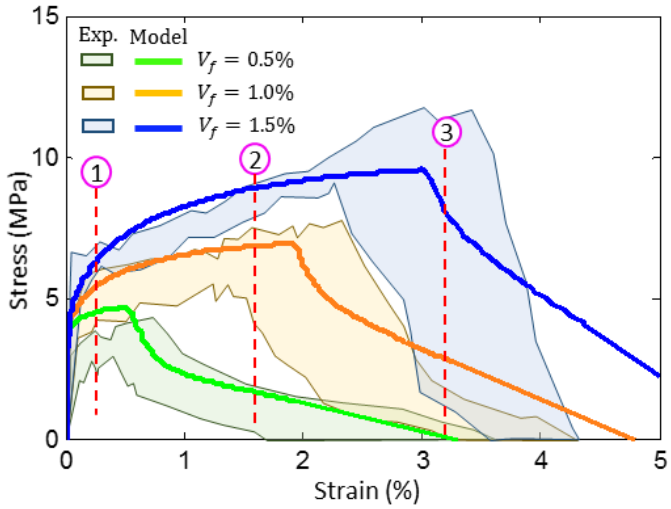

Figure 6.16. Stress-strain responses of dog-bone tests

In all cases of fibre content, once a localisation is formed, most of the deformations take place in this region causing bridging fibres to be quickly pulled out of the concrete matrix and the material response becomes softening as observed in experiments. In this sense, the addition of fibres, represented by the fibre bridging effect illustrated in Figure 6.17c, prolongs the formation and development of localisation within the specimen and thus enhances its capability of energy absorption. The plot of tractions in the localisation band (i.e., Figure 6.17c) with respect to local strain shows that the overall load resistance of the specimen comes from both the matrix cohesion, vanishing quickly and the fibre bridging force, being the main load-bearing component until failure. The influence of fibre bridging effect is stronger with the increase of fibre content, leading to the change of specimen behaviour, described above. These underlying mechanisms driving the macro responses and failure patterns that match experimental counterparts are naturally captured by the model thanks to the embedded localisation zone in the constitutive equations. This highlights the benefits of the in-built intrinsic failure mechanism of the model.

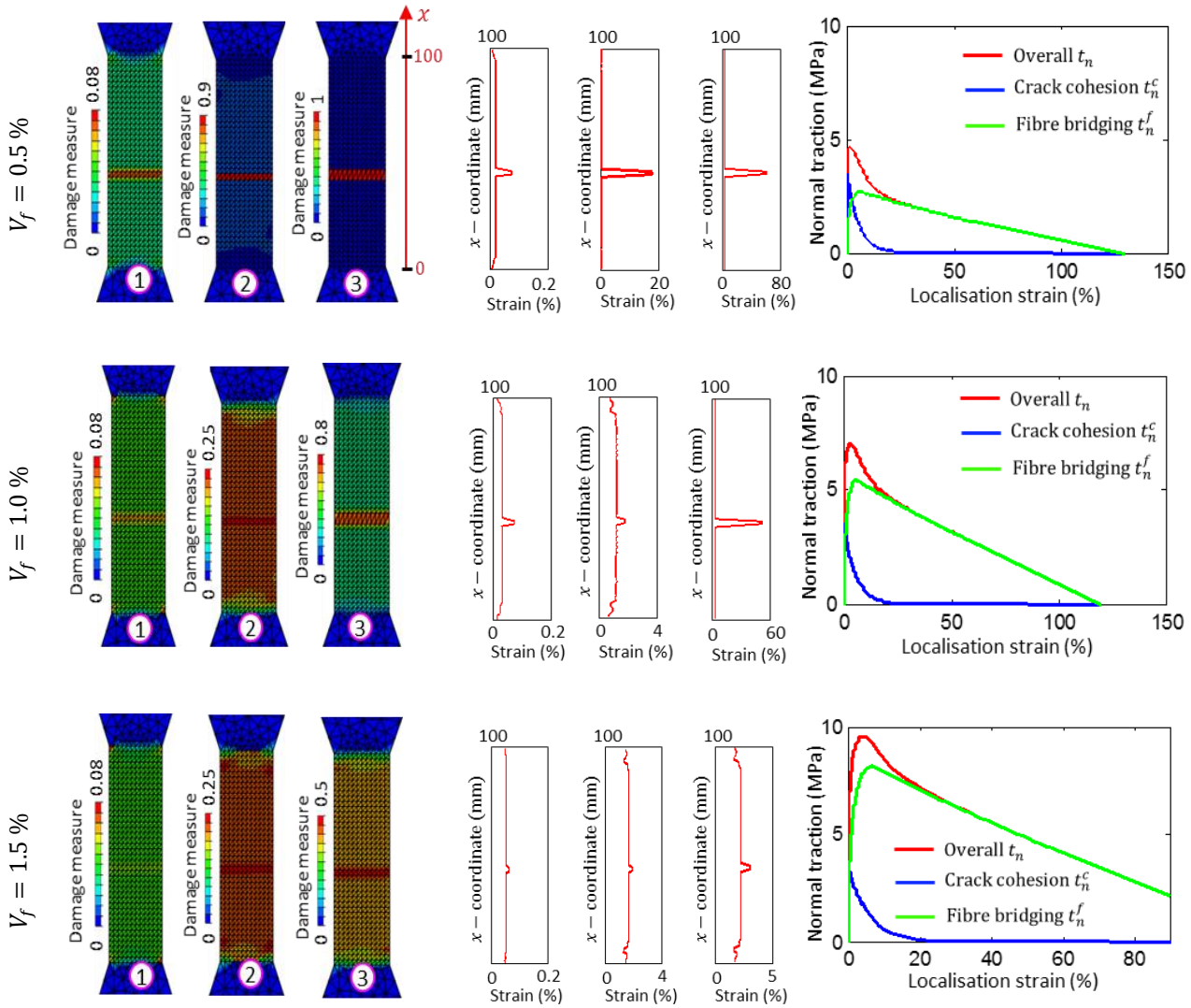

(a) (b) (c)

Figure 6.17. Dog-bone tests results: (a) Damage contour; (b) Strain profiles and (c) Detailed contribution at the localisation

Further detailed analyses of strains at two sections (i.e., A-A and B-B) for the case $V_f = 1$ % in Figure 6.18 clearly shows the difference in the deformations inside and outside the localisation band during the loading. At first, strains of the two sections are relatively the same, which verifies the homogeneous deformation profiles shown in Figure 6.17a. A sudden increase in strain at section A-A, compared to section B-B, indicates the formation of a localisation band. After that, the localisation band keeps opening while the strain in other regions, represented by section B-B, decreases as shown by the zoom-in image in Figure 6.18. This, together with the examples presented in Section 6.3.2, shows the robustness of the proposed model capturing the interaction of the localisation and its outer bulk material at both constitutive and structural modelling levels.

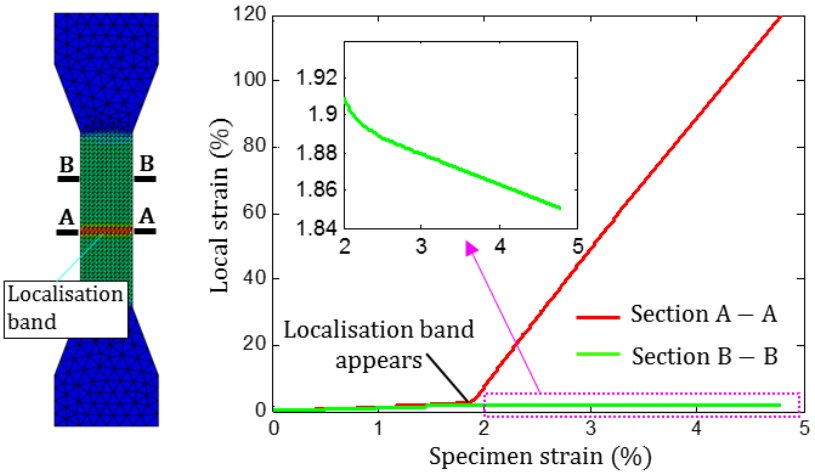

Figure 6.18. Detailed analysis of local strains at 2 sections in the case $V_f = 1$ %

6.3.4 Finite element analysis of 3-point bending tests

In this section, the capability of the proposed model is validated against experimental results of 3-point bending tests, conducted by Bencardino et al. (2010) with set-up and boundary condition shown in Figure 6.19a. The specimens in these tests were cast with high-performance concrete, whose mechanical properties are listed Table 6.3 and steel hooked-end Dramix fibres whose geometries and properties are presented in Table 6.2. The simulations in this example use 3-node triangular elements and displacement-controlled loading in 2D plane stress condition with two meshes, mesh 1 (1107 elements) and mesh 2 (2636 elements), as shown in Figure 6.19b.

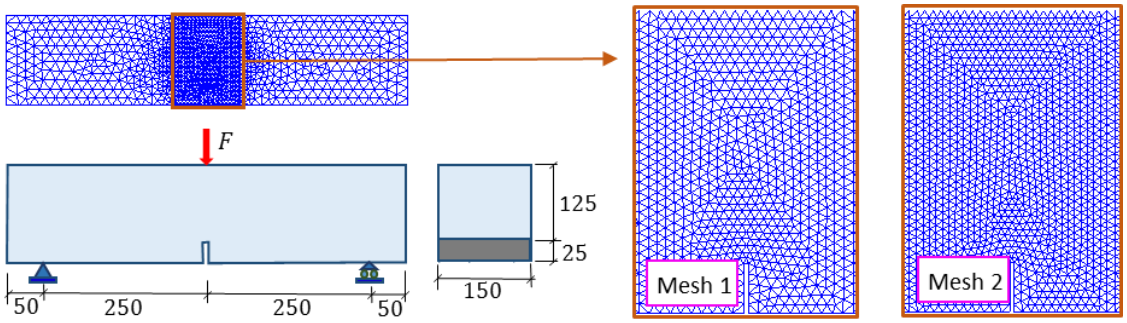

Figure 6.19. Three-point bending tests: (a) Schematic experiment set-up and (b) Meshes used for the FEA simulations

The load-displacement responses by the model, presented in Figure 6.20, show good agreements with their experimental counterparts. While the plain concrete shows a sharp softening response after reaching its peak, FRC vividly shows significant improvements in ductility and strength with hardening behaviour. These improvements again have an intimate

relationship with the failure mechanism of the material. Fracture patterns at different stages, depicted in Figure 6.21a, show that for the case of plain concrete, a narrow crack band initiates from the notch and quickly develops towards the top of the specimen. Section cuts across the damaged area in Figure 6.21b further show that the horizontal strain of plain concrete beam concentrates on a narrow region (i.e. a localisation) throughout the analysis. In this case, a small amount of energy, represented by the small area under the load-displacement curve in Figure 6.20, is dissipated via the formation and rapid development of this major crack. The failure pattern of the FRC beam, on the other hand, shows that a bigger region of damage forms and develops up to the end of the experiments with respect to the increase of fibre content, as also observed in experimental data (Paegle and Fischer, 2016; Soulioti et al., 2011; Zhang and Ju, 2011). This is further illustrated by section cuts of deformation in Figure 6.21b, where strain spreads in a wider area and cracks are more diffused with higher fibre volume fraction.

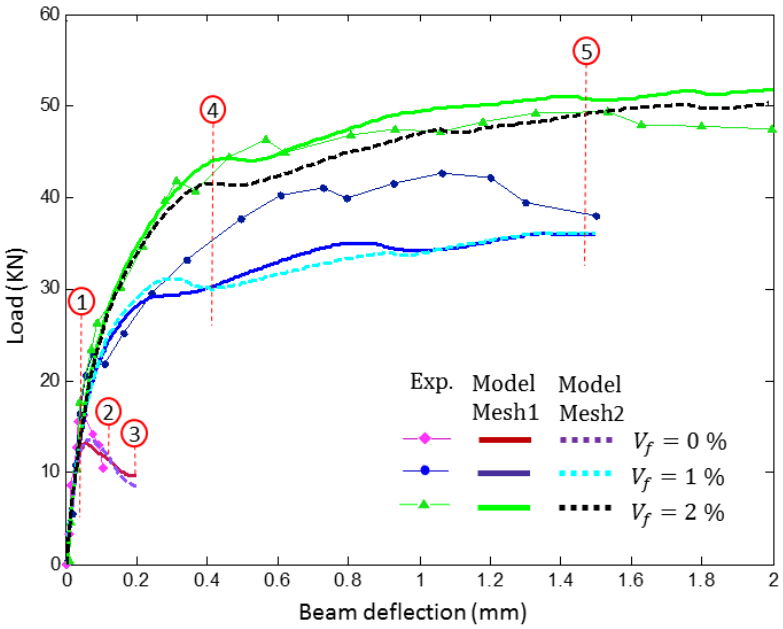

Figure 6.20. Load-deflection responses of 3-point bending tests

In addition, Figure 6.20 also shows that the numerical results for the two meshes are comparable, demonstrating the convergence of the proposed model with mesh refinement. Even though the structural responses, in this case, are hardening, the material behaviour at the major crack shown in Figure 6.21c is, in fact, softening, followed by a hardening period. Regularisation is thus always needed when solving BVPs to reflect the proper amount of energy dissipated within a crack for different mesh resolutions. As crack is included in the model with its relative size, represented by the characteristic length H, the constitutive

behaviour naturally scales with the resolution of discretisation while the dissipation in crack remains the same. Results from the proposed model are thus independent of the mesh size without employing any external regularisation. This advantage is one of the features distinguishing the proposed model from existing ones (Beghini et al., 2007; Caner et al., 2013; Mihai and Jefferson, 2017; Mihai et al., 2016).

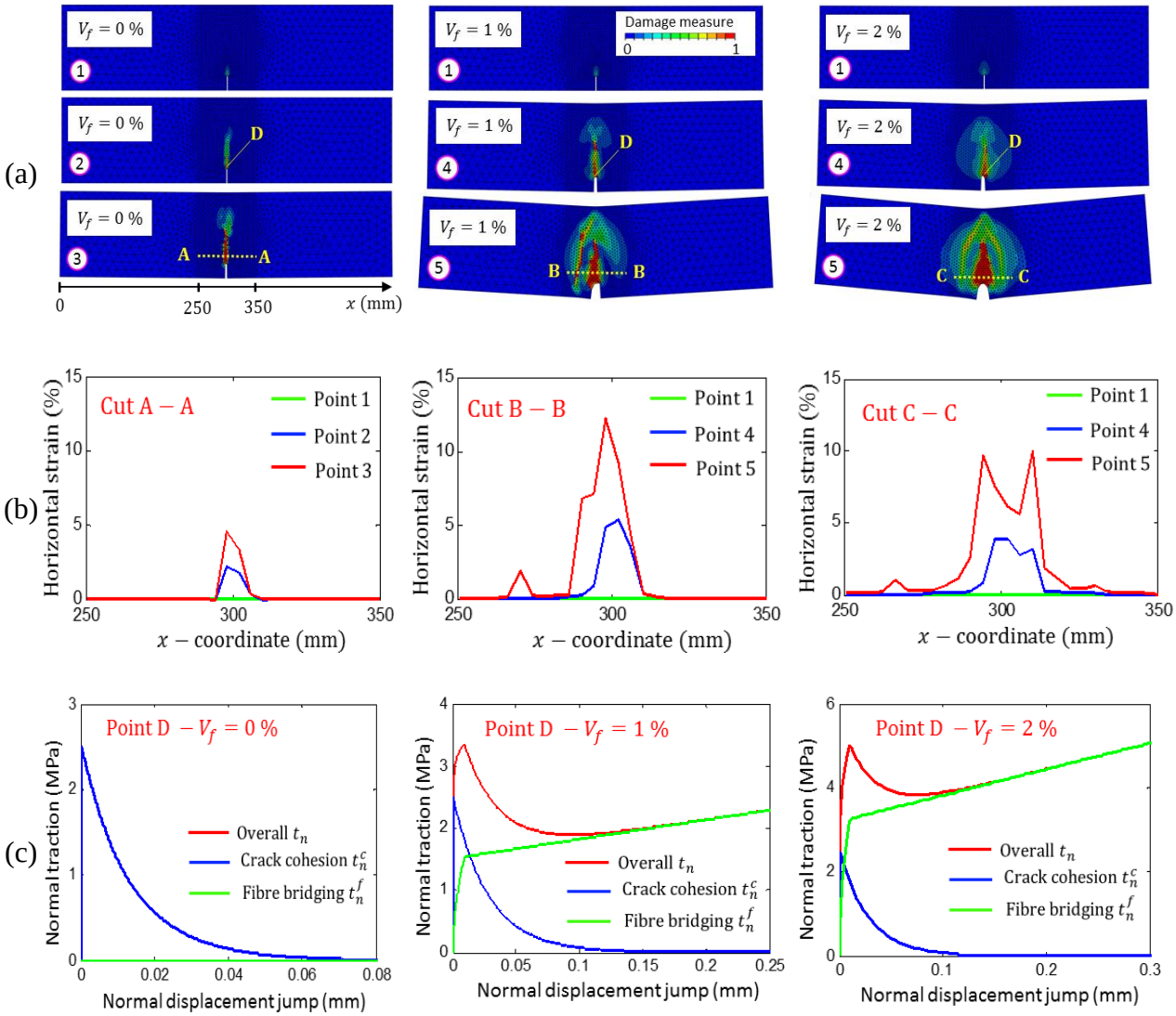

Figure 6.21. Detailed analysis of 3-point bending tests: (a) Damage contour with magnification factor of 10 (mesh1); (b) Corresponding section cut of horizontal strain and (c) Local traction-displacement at point D of the beam

All of these structural responses and failure pattern, described above, are actually driven by the constitutive behaviour shown in Figure 6.21c at a point just above the beam notch (i.e. point D in Figure 6.21a) for all three cases. Under loading, the material quickly loses its cohesive resistance, represented by blue curves and activates the fibre bridging forces, described as green curves in the Figure. The loading resistance of the element is a

combination of both cementitious cohesion and the fibre bridging effect as previously addressed in Section 2.3. The cohesive resistance from plain material and bridging effect from fibres hinders a crack from opening and force the specimen to initiate more cracks in surrounding areas to dissipate the provided energy. The interaction between these two contributions is further illustrated in Figure 6.22, where normal tractions contour at point 4 of the analysis are plotted for the case $V_f = 2\%$. It shows that up to this point, concrete loses the majority of its cohesive resistance in the major crack. This is presented in the Figure by a blue thin area where local cohesive traction is approximately zero. However, stresses are still transferred across this crack, thanks to the fibre bridging effect illustrated in the Figure. The overall traction, being a sum of both fibre bridging effect and cohesion, still can carry a significant amount and thus the structure can absorb much more energies before failure, shown by a substantially bigger area under the load-displacement curve compared to that of plain concrete (see Figure 6.20). This detailed analysis again shows that the structural responses are naturally captured with corresponding failure patterns driven by the underlying mechanism of fibre bridging effect at constitutive level. This proves the robustness and effectiveness of featuring the crack as the failure mechanism in the constitutive modelling.

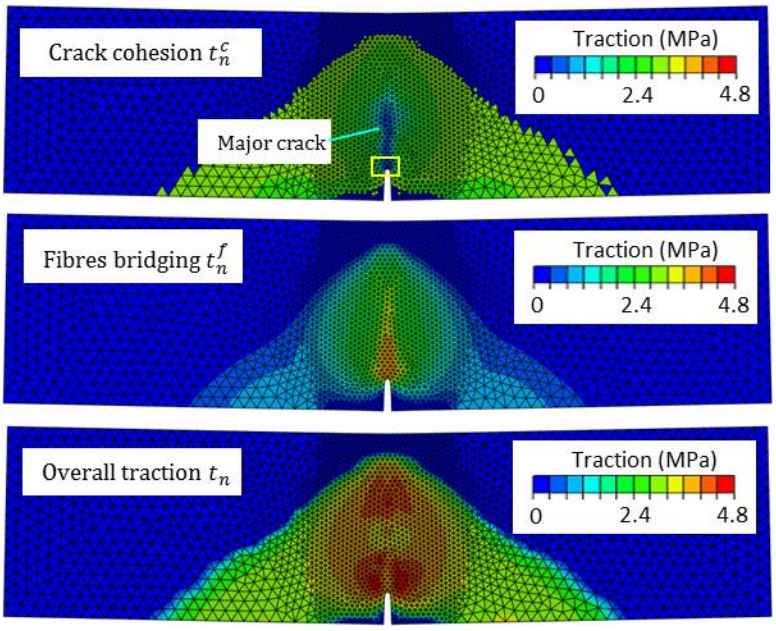

Figure 6.22. Normal traction contour in the whole beam at point 4 of the loading for the case $V_f = 2\%$

6.4 Summary and discussion

This chapter was dedicated to applying the proposed model for modelling fibre reinforced concrete, an iconic fibre reinforced geomaterials. The fibre bridging effect and cohesive resistance acting on an opening crack are taken as the fundamental mechanism governing the material behaviour and are incorporated as an intrinsic part of the proposed model. Both the effect of fibres-matrix bonding and aggregates interlocking/cohesion within a crack are incorporated into a continuum-based constitutive model via kinematic enhancements and traction continuity conditions. The enrichment in the present form allows the inclusion of separate laws/models for the fibre bridging effect caused by fibres across crack and cohesive resistance from cementitious material. The model, in this generic form, is capable of simulating the FRC of various fibres types with different geometries and mechanical properties.

Validation against experimental results of single fibre pull-out tests shows that this simple model, proposed by integrating available concepts in the literature, can capture key responses of hooked-end fibres in bridging cracks (i.e., fibre debonding, hook straightening and fibre pull-out). Good agreements of numerical results in both constitutive modelling and Boundary Value Problem simulations against experimental data prove the robustness and reliability of the proposed approach in modelling the FRC. Macro responses and failure patterns of the material, from hardening with multiple-cracking to softening with a localisation band, are captured naturally. All of these responses are consequences of the interactions between fibre bridging effect and cohesive resistance inside opening cracks. The direct inclusion of the crack with its relative size into the constitutive model also produces an in-built regularisation effect to overcome the mesh-dependency problem during the simulation of Boundary Value Problems. The proposed approach shows good potential to be extended to other materials, such as fibre reinforced soil or sand, with more complex underlying mechanisms and micro/meso constitutive laws.

CHAPTER 7

Conclusions and further research

7.1 Summary and conclusions

A continuum-based constitutive model has been proposed in this study for quasi-brittle geomaterials with and without fibre reinforcement. Emphasis is placed on the identification of the underlying failure mechanism governing mechanical behaviour and key features of the material failure. This is followed by the development of a constitutive model in which the failure mechanism is the basis for all the characteristics of the model. In particular, through analysing numerous experimental results, the formation and propagation of localisation bands are pinpointed as the failure mechanism behind several important features of the material behaviour in various loading conditions including tension, shear, compression under low confinement and their responses under mixed-mode loading conditions. The localised failure mechanism is then employed as the fundamental basis for the model development by explicitly incorporating localisation bands into the constitutive equations within the framework of thermodynamics. The main contributions of this research are:

- Development of a cohesive-frictional model based on damage-plasticity theory to describe the behaviour of localisation band wherein the progressive failure of quasi-brittle geomaterials mainly takes place (see Section 4.2 in Chapter 4). The different responses of the localisation band in tension, compression, shear and their mixed-mode loadings, together with key features such as dilation, residual deformations, stiffness reduction, size-effect are captured appropriately (see Section 4.4 in Chapter 4 and Section 5.4 in Chapter 5).
- Development of a mechanism-based constitutive model for quasi-brittle geomaterials by integrating the localised failure mechanism into constitutive equations within the framework of generalised thermodynamics. This mechanism-based approach, in association with featuring a secondary localisation band inside the constitutive equations, results in a more advantageous model for capturing the material behaviour when compared with existing approaches in the literature (see Sections 5.3 and 5.4 in Chapter 5). These novel features include the Lode angle dependent behaviour without relying on phenomenological expressions for the yield/failure surface, brittle-ductile

transition associated with the evolution of the shear band angle, size-dependent behaviour and in-built regularisation. The incorporation of a secondary crack or shear band automatically removes the need of additional treatments for stress-locking in the numerical analysis of Boundary Value Problems.

- Incorporation of fibre bridging effects alongside the cohesive resistance, taking place in crack/localisation band, into the generic form of the proposed constitutive model for analysing fibre reinforced concrete (FRC), an iconic fibre reinforced geomaterials (see Sections 6.2 and 6.3 in Chapter 6). This naturally leads to diffuse-localised failure mechanism underpinning the macro behaviour of FRC and minimise the employment of phenomenological relationships.

In the subsequent sections, the above-mentioned contributions and findings, together with weaknesses of the present research, will be discussed further.

7.1.1 A cohesive-frictional model to describe the behaviour of localisation band

Given the central role of the localised failure mechanism in developing a constitutive model for quasi-brittle geomaterials, the first step taken in this research is to capture the inelastic behaviour occurring inside the localisation band. In order to describe the irreversible deformation and stiffness reduction happening simultaneously inside the band, a cohesive-frictional model has been proposed, based on damage-plasticity theory. The proposed unified yield-failure surface, together with the damage-plasticity coupling in a traction-displacement jump relationship, help to facilitate the evolution and interaction of damage and plasticity smoothly. This approach to modelling a cohesive zone features some advantageous characteristics in the context of modelling of the localisation band in quasi-brittle geomaterials. These include simplicity, mixed mode behaviour in both tension and compression and an in-built fracture locus, each of which has been addressed and illustrated in Chapter 4. Since the model was proposed based on experimental observations and considerations, the parameters in the model are shown to be physically meaningful and can be calibrated via standard tests commonly practised among the research community.

The validation against experimental results shows that the proposed cohesive-frictional model is capable of capturing post-peak behaviour in the localisation band, such as residual deformations, stiffness reduction and the evolution of dilation. Thanks to the strong coupling of damage and plasticity, the interaction between irreversible deformation

and progressive fracture taking place inside the localisation band during the course of loading, can be captured properly. As the behaviour of the localisation band under mixed-mode loading can be reflected, the dissipated energy and consequently the fracture locus can be reflected naturally in the model. The proposed model, thus, shows itself as a simple yet effective tool to simulate the inelastic behaviour inside the localisation band of quasi-brittle geomaterials. Furthermore, it also provides an in-built criterion to predict not only the onset but also the orientation of the localised deformation. This helps the model, proposed later for quasi-brittle geomaterials, capture the correlation between the confining pressures and failure plane orientation in triaxial compressive loading, as seen in the experimental observations addressed in Chapter 2. The macro responses of the material can thus be predicted as a result of the underlying localised mechanism, as it should be.

7.1.2 A mechanism-based constitutive model for quasi-brittle geomaterials

A mechanism-based model is developed in this study for quasi-brittle geomaterials by incorporating the localised failure mechanism as the basis of the model development. The model is constructed from new forms of energy potential, proposed to encapsulate the localised failure mechanisms within the framework of thermodynamics. The thermodynamics-based formulation leads to direct contributions from both the localisation bands and the surrounding bulk material to the overall responses of the materials. As a result, the proposed model, despite being a continuum approach, can properly describe the localised failure of quasi-brittle geomaterials by quantities and variables defined inside these localisation bands, alongside conventional averaged quantities such as stress and strain. This helps overcome the drawback encountered in several continuum models that (incorrectly) employ solely macro stress and strain to describe the failure of quasi-brittle geomaterials.

The proposed constitutive model encompasses key features of the materials, including brittle softening in tension, brittle-to-ductile behaviour in compression, Lode-angle dependence of the yield locus and size-effect, all of which are consequences of the underlying localised failure mechanism embedded in the proposed constitutive structure. Since the behaviour and relative size of localisation bands are integrated into the constitutive equations, alongside the responses of the surrounding bulk material, the energy dissipated is properly reflected when solving boundary value problems. As a consequence, the numerical results produced by the proposed model are independent of the discretisation resolution, without requiring any additional regularisation treatment. Furthermore, the introduction of a secondary crack in the constitutive structure helps the proposed model to reflect the nature

of the Fracture Process Zone (FPZ). This allows a proper propagation of the FPZ and thus stress-locking is naturally removed in modelling the material at structural scale. These are key features distinguishing the proposed model from other micromechanics-based and/or advanced continuum models in the literature.

7.1.3 Incorporation of fibre bridging effects and cohesive resistance for modelling FRC

By incorporating fibre bridging effects, alongside the existing cohesive resistance in the localisation band into the constitutive equations, the proposed model is extended for the modelling of fibre reinforced concrete, an iconic fibre reinforced geomaterials. The presence of the crack/localisation band in the constitutive model allows the inclusion of contributions from the fibre bridging effect caused by fibres across crack and cohesive resistance from cementitious material. The fibre bridging effect is obtained from the integration of the pull-out force-displacement relationship of all fibres across the crack, while the cohesive resistance is captured by the cohesive-frictional model proposed in the first part of the study. Thanks to the incorporation of the localisation band inside the constitutive structure, the interaction between these two components, being the fundamental mechanism governing material behaviour, is captured properly by the proposed model. Good agreements in the model validation against experimental results at both constitutive and structural levels demonstrate the capacity of the proposed model in capturing the responses and failures of FRC. Macro responses and failure patterns of the material, from hardening with multiple-cracking to softening with a localisation band, are captured as consequences of the interactions of fibre bridging and cohesive resistance inside cracks at the material level. This again highlights the robustness of the method used in this study; by approaching the material from its underlying mechanism, its mechanical behaviour and key features could be captured as consequences.

7.1.4 Limitations and weaknesses of the proposed models

Even though the proposed model does possess some advantageous features and characteristics in capturing the responses of quasi-brittle geomaterials with and without fibre reinforcement, the model still suffers from some weaknesses and limitations. They can be summarised as follows:

- The cohesive-frictional model proposed in this study, even though can capture several important post-peak responses, cannot account for the pure compressive responses of

the localisation band. This is a direct consequence of the open shape of the proposed yield surface, as seen in Figure 4.3 of Chapter 4, which implies that failure will not occur in pure compression (i.e., $t_s = 0;\ t_n < 0$). This means that the compaction or grain crushing in the localisation zone cannot be reflected. As a result, the proposed model for quasi-brittle geomaterials, with the cohesive-frictional being a core, fails to capture the material behaviour in compression under very high confining pressure levels, where grain crushing in a compaction band is the dominant mechanism for the material failure. An example of this limitation is the inability to capture the yield locus of sandstone under high confining pressure, as pointed out in Section 5.4.1.2. The inadequacy of the proposed model in predicting the stress-strain responses in triaxial compression tests under high confinements in Section 5.4.1.3 is another example of the model's weakness, stemming from the open-shaped yield surface in the proposed cohesive-frictional model. This limitation can be overcome by employing a better yield function with a closed shape to capture the behaviour of the localisation band in compression. This is, however, beyond the scope of this study and will be discussed further as a possible future development for the proposed model in the following section.

- As addressed and illustrated in Chapter 5, featuring a secondary crack in the constitutive model is a natural way to remove stress-locking issues in several loading cases. However, this approach, in principle, still cannot completely remove stress-locking and capture the crack propagation of the material in more complex loading scenarios (i.e., un-proportional loadings with multiple branching/intersecting fractures). This is because having two localisation zones in the constitutive model might not be enough to capture the real, complex nature of cracking within the material body, especially for simulation in 3D, where crack propagation is even more complicated with numerous branches. The enhancement of featuring a secondary crack is effective for benchmark structures and standard experiments with simple loading paths as presented in this study, but it might not be enough for the aim of a robust and reliable model to capture the failure of large-scale, real-life engineering structures. Potential improvements on this issue using ideas taken from the micromechanics-based approach, will be discussed further in the following section as possible future work.

- As analysed in Section 2.3 of Chapter 2, specimens of FRC generally show a diffuse cracking stage, where numerous small cracks are uniformly distributed throughout the material body, especially for the case of high fibre volume fraction values. Since the

proposed model is constructed from a representative volume element containing a few localisation bands inside, it could not capture the diffuse cracking stage completely. Instead, a phenomenological law for crack density, presented in Section 6.2.3, has to be employed as an external remedy to capture the failure mechanism of the material in this stage. Even though the use of this phenomenological law is satisfactory, as demonstrated by numerical examples in this study, it can still be improved and, in principle, avoided if sufficient details on the evolution of the diffuse-localised failure are available. In particular, with more experimental data at a lower scale and investigations, together with formulations inspired from the micromechanics-based approach, a better description based on more rigorous evidence can be used to capture this stage and thus remove the use of such phenomenological laws.

7.2 Further research directions

Based on the limitations and weaknesses, as well as considerations on the potential of the proposed model, addressed in previous sections, possible research directions for the model are presented, as follows.

7.2.1 Improvements for compaction behaviour

Apart from adopting the proposed cohesive-frictional model for other engineering problems, such as modelling the delamination of layers in laminate composites, mortar-brick interactions in masonry walls, fibre reinforced polymer (FRP) – concrete delamination or adhesive bonds in cracks under hydro-mechanical coupling in hydraulic fracturing problems, it can be further improved to capture compaction behaviour under compressive loading. As addressed in the previous section, one of the possible improvements to achieve this aim is to re-formulate the loading function in Eq. (4.2) in Chapter 4 to feature a closed yield surface. Along with this re-formulation of the yield surface, several other definitions and quantities, including non-associated flow rules with corresponding plastic potential, damage development and parameter identification, have to be modified and/or re-formulated to capture dilation, compaction and dilation-to-compaction transition smoothly. In addition, the progressive evolution of normal and shear tractions under different loading conditions also needs to be re-examined to ensure consistent behaviour with other components of the proposed model. Alongside such improvements for the cohesive-frictional model describing the localisation band, the structure of the double-scale model might also need to be modified to better reflect failure due to compaction in association with grain crushing, where no

localisation band is observed. An example of such modifications to the current double-scale approach can be found in the study by Nguyen and co-authors (2017a), where the activation and deactivation of multiple localisation bands are incorporated at constitutive level to imitate arrays of discrete compaction bands. Another possible modification that can be made is to employ formulations from micromechanics models, which will be discussed in the following section.

Even though there is still a long way to go to achieve the aim describe above, such developments and improvements can significantly widen the application scope of the proposed model. The mechanical behaviour of quasi-brittle geomaterials in various loading conditions, from tension to compression under low to very high confining pressure levels, can then be modelled effectively with their underlying failure mechanisms.

7.2.2 Integration of micromechanics-based considerations

As discussed in Section 7.1.4, ideas and considerations from current micromechanics-based models can be integrated into the double-scale approach to yield a better description for modelling quasi-brittle geomaterials. One of the potential research directions to be considered in this theme is to employ the formulations of multiple weak planes to describe the bulk material, alongside the current localisation band in the constitutive model. This is possible and straightforward in the double-scale approach because the constitutive behaviour of the localisation band and surrounding bulk material are separated from each other in the model formulation, as seen in Section 4.3 of Chapter 4 and Section 5.3.1 of Chapter 5. Specifically, even though their contributions are both taken into account towards a single stress-strain constitutive relationship, the behaviour of the localisation band is described by the proposed cohesive-frictional model, while the surrounding bulk material is assumed to be elastic following Hooke's law with elastic stiffness matrix $\mathbf{a}_o$. Therefore, the constitutive law from micromechanics-based models with multiple weak planes can be used directly to replace the elastic stiffness matrix in the model formulation. The effect of uniformly distributed micro-cracks from micromechanics-based formulations would potentially help the model to account for the diffuse cracking phase observed in quasi-brittle geomaterials under compression with high confining pressure and fibre reinforced concrete under tension with high fibre volume fraction, naturally. The presence of the localisation band in the model is still necessary to ensure a good description of the localised failure where necessary (i.e., changing of the loading paths from compression to tension or shear and the transition from diffuse to localised failure in FRC).

Another way of improving the current double-scale model using micromechanics considerations is to feature multiple localisation bands in different orientations at the first place of the model development. This system of localisation bands is inspired by the multiple weak plane formulations in several micromechanics-based models, to imitate the complex nature of crack systems in a fracture process zone. Since several localisation bands representing meso-crack can initiate at the same time in any direction, the model may possibly remove the stress-locking completely and be able to capture complex crack patterns such as multiple branching/intersecting fractures in large-scale structures. The implementation of such improvements can also be carried out straightforwardly by using the same procedure of formulation, described in Section 5.3.1 of Chapter 5, with not two but multiple localisation bands.

Even though the ideas and formulations of the two above-mentioned proposals are straightforward, there is a considerable amount of work that needs to be done and reviewed in terms of their numerical implementation (i.e., a stress return algorithm and updating internal variables in each iteration). In addition, investigations into the computational cost once the idea of micromechanics is incorporated into the model should also be conducted to ensure a cost-effective model. Nonetheless, these are valuable and promising research directions that can be carried out from the current research to achieve a further step towards a robust and reliable tool for designing various infrastructural applications in the geotechnical and civil engineering fields.

References

Abdallah, S., Fan, M., Rees, D.W.A., 2016. Analysis and modelling of mechanical anchorage of 4D/5D hooked end steel fibres. Mater. Des. 112, 539–552. doi:10.1016/j.matdes.2016.09.107

Abdul-Razzak, A.A., Mohammed Ali, A.A., 2011a. Modelling and numerical simulation of high strength fibre reinforced concrete corbels. Appl. Math. Model. 35, 2901–2915. doi:10.1016/j.apm.2010.11.073

Abdul-Razzak, A.A., Mohammed Ali, A.A., 2011b. Influence of cracked concrete models on the nonlinear analysis of High Strength Steel Fibre Reinforced Concrete corbels. Compos. Struct. 93, 2277–2287. doi:10.1016/j.compstruct.2011.03.016

Adachi, T., Oka, F., Yashima, A., 1991. A finite element analysis of strain localization for soft rock using a constitutive equation with strain softening. Arch. Appl. Mech. 61, 183–191.

Addessi, D., Marfia, S., Sacco, E., 2002. A plastic nonlocal damage model. Comput. Methods Appl. Mech. Eng. 191, 1291–1310. doi:10.1016/S0045-7825(01)00325-5

Agastra, P., 2004. Mixed-mode Delamination of Glass Fiber Polymer Matrix Composite Material. Master Thesis, Montana State University.

Ahmad, F., Bateni, F., Azmi, M., 2010. Performance evaluation of silty sand reinforced with fibres. Geotext. Geomembranes 28, 93–99. doi:10.1016/j.geotexmem.2009.09.017

Akai, K., Mori, H., 1970. Ein versuch ber bruchmecanismus von sandstein under mehrachsigen spannungszustand, in: Proceedings of the Second Congress of the International Society for Rock Mechanics. Belgrade, pp. 3–30.

Alam, A.K.M.B., Niioka, M., Fujii, Y., Fukuda, D., Kodama, J., 2014. Effects of confining pressure on the permeability of three rock types under compression. Int. J. Rock Mech. Min. Sci. 65, 49–61. doi:10.1016/j.ijrmms.2013.11.006

Alfaiate, J., Sluys, L.J., 2017a. On the modelling of mixed-mode discrete fracture: Part I – Damage models. Eng. Fract. Mech. 182, 157–186. doi:10.1016/j.engfracmech.2017.07.019

Alfaiate, J., Sluys, L.J., 2017b. On the modeling of mixed-mode discrete fracture: Part II – Inclusion of dilatancy. Eng. Fract. Mech. 182, 245–264. doi:10.1016/j.engfracmech.2017.07.020

Alm, P., 1999. Hydro-mechanical behavior of a pressurized single fracture: an in situ experiment. Chalmers University, Sweden.

Alnaggar, M., Asce, A.M., Pelessone, D., Cusatis, G., Asce, M., 2019. Lattice Discrete Particle Modeling of Reinforced Concrete Flexural Behavior. J. Struct. Eng. 145, 1–14. doi:10.1061/(ASCE)ST.1943-541X.0002230.

Alwan, J.M., Naaman, A.E., Guerrero, P., 1999. Effect of mechanical clamping on the pull-out response of hooked steel fibers embedded in cementitious matrices. Concr. Sci. Eng. 1, 15–25.

Antoni, N., 2017. A further analysis on the analogy between friction and plasticity in Solid Mechanics. Int. J. Eng. Sci. 121, 34–51. doi:10.1016/j.ijengsci.2017.08.012

Aparna, L.L., Chaitanya, G., Srisnivas, K., 2018. Characterization of continuous GFRP composites using Digital Image Correlation (DIC) technique. Int. J. Innov. Res. Sci. Technol. 5, 118–125.

Asadollahi, P., Invernizzi, M.C.A., Addotto, S., Tonon, F., 2010. Experimental validation of modified Barton's model for rock fractures. Rock Mech. Rock Eng. 43, 597–613. doi:10.1007/s00603-010-0085-6

Aubertin, M., Li, L., Simon, R., Khalfi, S., 1999. Formulation and application of a short-term strength criterion for isotropic rocks. Can. Geotech. J. 36, 947–960.

Bahaaddini, M., Hagan, P.C., Mitra, R., Hebblewhite, B.K., 2014. Scale effect on the shear behaviour of rock joints based on a numerical study. Eng. Geol. 181, 212–223. doi:10.1016/j.enggeo.2014.07.018

Bahaaddini, M., Sharrock, G., Hebblewhite, B.K., 2013. Numerical direct shear tests to model the shear behaviour of rock joints. Comput. Geotech. 51, 101–115. doi:10.1016/j.compgeo.2013.02.003

Barenblatt, G., 1962. The mathematical theory of equilibrium cracks in brittle fracture. Adv. Appl. Mech. 7, 55–129.

Barros, J.A.O., Figueiras, J.A., 1999. Flexural behaviour of SFRC: Testing and modelling. J. Mater. Civ. Eng. 11, 331–339.

Barton, N., 2013. Shear strength criteria for rock, rock joints, rockfill and rock masses: Problems and some solutions. J. Rock Mech. Geotech. Eng. 5, 249–261. doi:10.1016/j.jrmge.2013.05.008

Barton, N., 1976. Rock mechanics review: the shear strength of rock and rock joints. Int. J. Rock Mech. Min. Sci. 13, 255–279. doi:10.1016/0148-9062(76)90003-6

Barton, N., Choubey, V., 1977. The shear strength of rock joints in theory and practice. Rock Mech. 10, 1–54. doi:10.1007/BF01261801

Bashar, I.I., Alengaram, U.J., Jumaat, M.Z., Islam, A., Santhi, H., Sharmin, A., 2016. Engineering properties and fracture behaviour of high volume palm oil fuel ash based fibre reinforced geopolymer concrete. Constr. Build. Mater. 111, 286–297. doi:10.1016/j.conbuildmat.2016.02.022

Baud, P., Klein, E., Wong, T. fong, 2004. Compaction localization in porous sandstones: Spatial evolution of damage and acoustic emission activity. J. Struct. Geol. 26, 603–624. doi:10.1016/j.jsg.2003.09.002

Bažant, P., Oh, B.H., 1986. Efficient Numerical Integration on the Surface of a Sphere. J. Appl. Math. Mech. 66, 37–49. doi:10.1002/zamm.19860660108

Bažant, Z.P., 2000. Size effect. Int. J. Solids Struct. doi:doi: DOI: 10.1016/S0020-7683(99)00077-3

Bažant, Z.P., 1999. Size effect on structural strength: a review. Arch. Appl. Mech. 69, 703–725. doi:10.1007/s004190050252

Bažant, Z.P., 1996. Analysis of work-of-fracture method for measuring fractuer energy of concrete. J. Eng. Mech. 122, 138–144.

Bažant, Z.P., 1984. Size Effect in Blunt Fracture: Concrete, Rock, Metal. J. Eng. Mech. 110, 518–535. doi:10.1061/(ASCE)0733-9399(1984)110:4(518)

Bažant, Z.P., Caner, F.C., 2014. Impact comminution of solids due to local kinetic energy of high shear strain rate: I. Continuum theory and turbulence analogy. J. Mech. Phys. Solids 64, 223–235. doi:10.1016/j.jmps.2013.11.008

Bažant, Z.P., Chen, E.P., 1997. Scaling of Structural Failure. Appl. Mech. Rev. 50, 593–627. doi:10.1115/1.3101672

Bažant, Z.P., Gambarova, B., 1984. Shear crack in concrete: Crack band microplane model. J. Struct. Eng. 110, 2015–2035.

Bažant, Z.P., Oh, B.H., 1983. Crack band theory of concrete. Mater. Struct. 16, 155–177. doi:10.1007/BF02486267

Bazănt, Z.P., Planas, J., 1998. Fracture and size effect in concrete and other quasibrittle materials.

Bažant, Z.P., Yu, Q., 2009. Universal Size Effect Law and Effect of Crack Depth on Quasi-Brittle Structure Strength. J. Eng. Mech. 135, 78–84. doi:10.1061/(ASCE)0733-9399(2009)135:2(78)

Beghini, A., Bažant, Z.P., Zhou, Y., Gouirand, O., Caner, F.C., 2007. Microplane model M5f for multiaxial behavior and fracture of fiber-reinforced concrete. J. Eng. Mech. 133, 66–75. doi:10.1061/(asce)0733-9399(2007)133:1(66)

Bencardino, F., Rizzuti, L., Spadea, G., Swamy, R.N., 2010. Experimental evaluation of fiber reinforced concrete fracture properties. Compos. Part B Eng. 41, 17–24. doi:10.1016/j.compositesb.2009.09.002

Bencardino, F., Rizzuti, L., Spadea, G., Swamy, R.N., 2008. Stress-Strain Behavior of Steel Fiber-Reinforced Concrete in Compression. J. Mater. Civ. Eng. 20, 255–263. doi:10.1061/(ASCE)0899-1561(2008)20:3(255)

Benzeggagh, M.L., Kenane, M., 1996. Measurement of mixed-mode delamination fracture toughness of unidirectional glass/epoxy composites with mixed-mode bending aparatus. Compos. Sci. Technol. 56, 439–449. doi:10.1016/0266-3538(96)00005-X

Biscaia, H.C., Chastre, C., 2018. Design method and verification of steel plate anchorages for FRP-to-concrete bonded interfaces. Compos. Struct. 192, 52–66. doi:10.1016/j.compstruct.2018.02.062

Blanco, A., Pujadas, P., Cavalaro, S., De La Fuente, A., Aguado, A., 2014. Constitutive model for fibre reinforced concrete based on the Barcelona test. Cem. Concr. Compos. 53, 327–340. doi:10.1016/j.cemconcomp.2014.07.017

Borino, G., Failla, B., Parrinello, F., 2003. A symmetric nonlocal damage theory. Int. J. Solids Struct. 40, 3621–3645. doi:10.1016/S0020-7683(03)00144-6

Borja, R.I., 2008. Assumed enhanced strain and the extended finite element methods : A unification of concepts. Comput. Methods Appl. Mech. Eng. 197, 2789–2803. doi:10.1016/j.cma.2008.01.019

Borja, R.I., 2004. Computational modeling of deformation bands in granular media. II. Numerical simulations. Comput. Methods Appl. Mech. Eng. 193, 2699–2718. doi:10.1016/j.cma.2003.09.018

Borja, R.I., 2000. A finite element model for strain localization analysis of strongly discontinuous fields based on standard Galerkin approximation. Comput. Methods Appl. Mech. Eng. 190, 1529–1549.

Borja, R.I., Aydin, A., 2004. Computational modeling of deformation bands in granular media. I. Geological and mathematical framework. Comput. Methods Appl. Mech. Eng. 193, 2667–2698. doi:10.1016/j.cma.2003.09.019

Brooks, Z., 2013. Fracture Process Zone : Microstructure and Nanomechanics in quasi-brittle materials. PhD Thesis, Massachusetts Institute of Technology.

Brünig, M., Michalski, A., 2017. A stress-state-dependent continuum damage model for concrete based on irreversible thermodynamics. Int. J. Plast. 90, 31–43. doi:10.1016/j.ijplas.2016.12.002

Budiansky, B., O'connell, R.J., 1976. Elastic moduli of a cracked solid. Int. J. Solids Struct. 12, 81–97. doi:10.1016/0020-7683(76)90044-5

Bui, Q. V., 2011. A modified Benzeggagh-Kenane fracture criterion for mixed-mode delamination. J. Compos. Mater. 45, 389–413. doi:10.1177/0021998310376105

Burlion, N., Gatuingt, F., Pijaudier-Cabot, G., Daudeville, L., 2000. Compaction and tensile damage in concrete: Constitutive modelling and application to dynamics. Comput. Methods Appl. Mech. Eng. 183, 291–308. doi:10.1016/S0045-7825(99)00223-6

Byerlee, J.D., 1967. Frictional characteristics of granite under high confining pressure. J. Geophys. Res. 72, 3639–3648.

Camanho, P.P., Dávila, C.G., Moura, M.F. de, 2003. Mixed-Mode decohesion finite elements in for the simulation composite of delamination materials. J. Compos. Mater. 37, 1415–1438. doi:10.1177/002199803034505

Cambou, B., Chaze, M., Dedecker, F., 2000. Change of scale in granular materials. Eur. J. Mech. A/Solids 19, 999–1014. doi:10.1016/S0997-7538(00)01114-1

Cammarata, G., Fidelibus, C., Cravero, M., Barla, G., 2007. The hydro-mechanically coupled response of rock fractures. Rock Mech. Rock Eng. 40, 41–61. doi:10.1007/s00603-006-0081-z

Candappa, D.C., Sanjayan, J.G., Setunge, S., 2001. Complete triaxial stress-strain curves of high-strength concrete. J. Mater. Civ. Eng. 13, 209–215.

Caner, F.C., Bažant, Z.P., 2013. Microplane Model M7 for Plain Concrete. I: formulation. J. Eng. Mech. 139, 1724–1735. doi:10.1061/(ASCE)EM.1943-7889.0000571

Caner, F.C., Bažant, Z.P., Wendner, R., 2013. Microplane model M7f for fiber reinforced concrete. Eng. Fract. Mech. 105, 41–57. doi:10.1016/j.engfracmech.2013.03.029

Cauvin, A., Testa, R.B., 1999. Damage mechanics : Basic variables in continuum theories. Int. J. Solids Struct. 36, 747–761. doi:10.1016/S0020-7683(98)00044-4

Červenka, J., Papanikolaou, V.K., 2008. Three dimensional combined fracture-plastic material model for concrete. Int. J. Plast. 24, 2192–2220. doi:10.1016/j.ijplas.2008.01.004

Cervera, M., Chiumenti, M., 2006. Smeared crack approach: Back to the original track. Int. J. Numer. Anal. Methods Geomech. 30, 1173–1199. doi:10.1002/nag.518

Chang, C., Yin, Z., 2009. Modeling stress-dilatancy for sand under compression and extension loading conditions. J. Eng. Mech. 136, 777–786. doi:10.1061/(ASCE)EM.1943-7889.0000116

Chang, C.S., Yin, Z., 2010. Micromechanical Modeling for Inherent Anisotropy in Granular Materials. J. Eng. Mech. 136, 830–839. doi:10.1061/(ASCE)EM.1943-7889.0000125

Chang, C.S., Yin, Z.Y., 2011. Micromechanical modeling for behavior of silty sand with influence of fine content. Int. J. Solids Struct. 48, 2655–2667. doi:10.1016/j.ijsolstr.2011.05.014

Chemenda, A.I., 2009. The formation of tabular compaction-band arrays: Theoretical and numerical analysis. J. Mech. Phys. Solids 57, 851–868. doi:10.1016/j.jmps.2009.01.007

Chemenda, A.I., Mas, D., 2016. Dependence of rock properties on the Lode angle: Experimental data, constitutive model, and bifurcation analysis. J. Mech. Phys. Solids 96, 477–496. doi:10.1016/j.jmps.2016.08.004

Chen, W.F., Han, D.J., 1988. Plasticity for Structural Engineers. Springer-Verlag, Newyork Inc.

Chen, X., Bažant, Z.P., 2014. Microplane damage model for jointed rock masses Xin. Int. J. Numer. Anal. Methods Geomech. 38, 1431–1452. doi:10.1002/nag

Cheng, J., Qian, X., Zhao, T., 2016. Rheological viscoplastic models of asphalt concrete and rate-dependent numerical implement. Int. J. Plast. 81, 209–230. doi:10.1016/j.ijplas.2016.01.004

Cicekli, U., Voyiadjis, G.Z., Abu Al-Rub, R.K., 2007. A plasticity and anisotropic damage model for plain concrete. Int. J. Plast. 23, 1874–1900. doi:10.1016/j.ijplas.2007.03.006

Colombo, C., Vergani, L., 2014. Influence of delamination on fatigue properties of a fibreglass composite. Compos. Struct. 107, 325–333. doi:10.1016/j.compstruct.2013.07.028

Comi, C., 2001. A non-local model with tension and compression damage mechanisms. Eur. J. Mech. - A/Solids 20, 1–22.

Comi, C., Perego, U., 2001. Fracture energy based bi-dissipative damage model for concrete. Int. J. Solids Struct. 38, 6427–6454. doi:10.1016/S0020-7683(01)00066-X

Confalonieri, F., Perego, U., 2019. A new framework for the formulation and validation of cohesive mixed-mode delamination models. Int. J. Solids Struct. 164, 168–190. doi:10.1016/j.ijsolstr.2018.12.032

Consoli, N.C., Casagrande, M.D.T., Coop, M.R., 2007. Performance of a fibre-reinforced sand at large shear strains. Géotechnique 57, 751–756. doi:10.1680/geot.2007.57.9.751

Contrafatto, L., Cuomo, M., 2006. A framework of elastic-plastic damaging model for concrete under multiaxial stress states. Int. J. Plast. 22, 2272–2300. doi:10.1016/j.ijplas.2006.03.011

Cook, N.G.W., 1992. Natural joints in rock: Mechanical, hydraulic and seismic behaviour and properties under normal stress. Int. J. Rock Mech. Min. Sci. 29, 198–223. doi:10.1016/0148-9062(92)93656-5

Cornec, A., Scheider, I., Schwalbe, K.H., 2003. On the practical application of the cohesive model. Eng. Fract. Mech. 70, 1963–1987. doi:10.1016/S0013-7944(03)00134-6

Cornelissen, H., Hordijk, D., Reinhardt, H., 1986. Experimental determination of crack softening characteristics of normal weight and lightweight concrete. Heron 31, 45–56.

Crews, J.H., Reeder, J.R., 1998. A Mixed-mode Bending Apparatus for Delamination Testing. Nasa Tech. Memo. 100662.

Crisfield, M.A., 2000. Non-linear Finite Element analysis of solids and structures, John Wiley and Sons Ltd. John Wiley and Sons Ltd, New York. doi:10.1017/CBO9781107415324.004

Cristelo, N., Cunha, V.M.C.F., Topa Gomes, A., Araújo, N., Miranda, T., Lurdes Lopes, M. de, 2017. Influence of fibre reinforcement on the post-cracking behaviour of a cement-stabilised sandy-clay subjected to indirect tensile stress. Constr. Build. Mater. 138, 163–173. doi:10.1016/j.conbuildmat.2017.02.010

Cunha, V.M.C.F., Barros, J.A.O., Sena-Cruz, J.M., 2012. A finite element model with discrete embedded elements for fibre reinforced composites. Comput. Struct. 94-95, 22–33. doi:10.1016/j.compstruc.2011.12.005

Cunha, V.M.C.F., Barros, J.A.O., Sena-cruz, J.M., 2011. An integrated approach for modelling the tensile behaviour of steel fibre reinforced self-compacting concrete. Cem. Concr. Res. 41, 64–76. doi:10.1016/j.cemconres.2010.09.007

Cunha, V.M.C.F., Barros, J.A.O., Sena-Cruz, J.M., 2010. Pullout Behavior of Steel Fibers in Self-Compacting Concrete. J. Mater. Civ. Eng. 22, 1–9. doi:10.1061/(ASCE)MT.1943-5533.0000001

Cusatis, G., Asce, M., Zhou, X., 2014. High-order microplane theory for quasi-Brittle materials with multiple characteristic lengths. J. Eng. Mech. 140, 1–10. doi:10.1061/(ASCE)EM.1943-7889.0000747.

Cuss, R.J., Rutter, E.H., Holloway, R.F., 2003. The application of critical state soil mechanics to the mechanical behaviour of porous sandstones. Int. J. Rock Mech. Min. Sci. 40, 847–862. doi:10.1016/S1365-1609(03)00053-4

Daneshyar, A., Ghaemian, M., 2017. Coupling microplane-based damage and continuum plasticity models for analysis of damage-induced anisotropy in plain concrete. Int. J. Plast. 95, 216–250. doi:10.1016/j.ijplas.2017.04.011

Das, A., Buscarnera, G., 2014. Simulation of localized compaction in high-porosity calcarenite subjected to boundary constraints. Int. J. Rock Mech. Min. Sci. 71, 91–104. doi:10.1016/j.ijrmms.2014.07.004

Das, A., Nguyen, G.D., Einav, I., 2013. The propagation of compaction bands in porous rocks based on breakage mechanics. J. Geophys. Res. Solid Earth 118, 2049–2066. doi:10.1002/jgrb.50193

Das, A., Nguyen, G.D., Einav, I., 2011. Compaction bands due to grain crushing in porous rocks: A theoretical approach based on breakage mechanics. J. Geophys. Res. 116, 1–14. doi:10.1029/2011JB008265

Das, A., Tengattini, A., Nguyen, G.D., Viggiani, G., Hall, S.A., Einav, I., 2014. A thermomechanical constitutive model for cemented granular materials with quantifiable internal variables. Part II - Validation and localization analysis. J. Mech. Phys. Solids 70, 382–405. doi:10.1016/j.jmps.2014.05.022

DeSimone, A., Marigo, J.J., Teresi, L., 2001. A damage mechanics approach to stress softening and its application to rubber. Eur. J. Mech. A/Solids 20, 873–892. doi:10.1016/S0997-7538(01)01171-8

Di Prisco, M., Ferrara, L., Meftah, F., Pamin, J., De Borst, R., Mazars, J., Reynouard, J.M., 2000. Mixed mode fracture in plain and reinforced concrete: Some results on benchmark tests. Int. J. Fract. 103, 127–148. doi:10.1023/A:1007613001402

Diambra, A., Ibraim, E., Muir Wood, D., Russell, A.R., 2010. Fibre reinforced sands: Experiments and modelling. Geotext. Geomembranes 28, 238–250. doi:10.1016/j.geotexmem.2009.09.010

Diambra, A., Ibraim, E., Russell, A., Muir Wood, D., 2011. Modelling the undrained response of fibre reinforced sands. Soils Found. 51, 625–636.

Diambra, A., Ibraim, E., Russell, A.R., Muir Wood, D., 2013. Fibre reinforced sands: from experiments to modelling and beyond. Int. J. Numer. Anal. Methods Geomech. 37, 2427–2455. doi:10.1002/nag

Dias, I.F., Oliver, J., Lemos, J. V., Lloberas-Valls, O., 2016. Modeling tensile crack propagation in concrete gravity dams via crack-path-field and strain injection techniques. Eng. Fract. Mech. 154, 288–310. doi:10.1016/j.engfracmech.2015.12.028

Dias, I.F., Oliver, J., Lloberas-Valls, O., 2018a. Strain Injection Techniques for Modeling 3D Crack Propagation. Key Eng. Mater. 774, 774.

Dias, I.F., Oliver, J., Lloberas-Valls, O., 2018b. Strain-injection and crack-path field techniques for 3D crack-propagation modelling in quasi-brittle materials. Int. J. Fract. 212, 67–87. doi:10.1007/s10704-018-0293-8

Dias-da-Costa, D., Alfaiate, J., Sluys, L.J., Júlio, E., 2009. A discrete strong discontinuity approach. Eng. Fract. Mech. 76, 1176–1201. doi:10.1016/j.engfracmech.2009.01.011

Dias-da-Costa, D., Valença, J., Júlio, E., Araújo, H., 2017. Crack propagation monitoring using an image deformation approach. Struct. Control Heal. Monit. 24, 1–14. doi:10.1002/stc.1973

Dimitri, R., Trullo, M., De Lorenzis, L., Zavarise, G., 2015. Coupled cohesive zone models for mixed-mode fracture: A comparative study. Eng. Fract. Mech. 148, 145–179. doi:10.1016/j.engfracmech.2015.09.029

Ding, Y., Kusterle, W., 2000. Compressive stress - strain relationship of steel fibre-reinforced concrete at early age. Cem. Concr. Res. 30, 1573–1579.

Dizhur, D., Ingham, J.M., 2013. Diagonal tension strength of vintage unreinforced clay brick masonry wall panels. Constr. Build. Mater. 43, 418–427. doi:10.1016/j.conbuildmat.2013.02.015

Dong, Y., Wu, S., Xu, S.S., Zhang, Y., Fang, S., 2010. Analysis of concrete fracture using a novel cohesive crack method. Appl. Math. Model. 34, 4219–4231. doi:10.1016/j.apm.2010.04.019

Dudgale, D.S., 1960. Yielding of steel sheets containing slits. J. Mech. Phys. Solids 8, 100–104. doi:10.1016/0022-5096(60)90013-2

Sousa, J.L.A. de O., Gettu, R., 2006. Determining the tensile stress-crack opening curve of concrete by inverse analysis. J. Eng. Mech. 132, 141–148. doi:10.1061/_ASCE_0733-9399_2006_132:2_141

Einav, I., Houlsby, G.T., Nguyen, G.D., 2007. Coupled damage and plasticity models derived from energy and dissipation potentials. Int. J. Solids Struct. 44, 2487–2508. doi:10.1016/j.ijsolstr.2006.07.019

Ely, R.E., 1968. Strength of magnesium silicate and graphite under biaxial stresses. Ceram. Bull. 47, 489–492.

Eringen, A.C., 1972. Nonlocal polar elastic continua. Internaltional J. Eng. Sci. 10, 1–16.

Ezeldin, S.A., Balaguru, P.N., 1992. High strength fiber reinforced concrete under compression. J. Mater. Civ. Eng. 4, 415–429.

Fanella, D., Krajcinovic, D., 1985. Continuum damage mechanics of fibre reinforced concrete. J. Eng. Mech. 111, 995–1009.

Fang, H., Xu, X., Liu, W., Qi, Y., Bai, Y., Zhang, B., Hui, D., 2016. Flexural behavior of composite concrete slabs reinforced by FRP grid facesheets. Compos. Part B Eng. 92, 46–62. doi:10.1016/j.compositesb.2016.02.029

Fang, H.L., Zheng, H., Zheng, J., 2017. Micromechanics-based multimechanism bounding surface model for sands. Int. J. Plast. 90, 242–266. doi:10.1016/j.ijplas.2017.01.011

Fardin, N., Stephansson, O., Jing, L., 2001. The scale dependence of rock joint surface roughness. Int. J. Rock Mech. Min. Sci. 38, 659–669. doi:10.1016/S1365-1609(01)00028-4

Fidelibus, C., 2007. The 2D hydro-mechanically coupled response of a rock mass with fractures via a mixed BEM–FEM technique. Int. J. Numer. Anal. Methods Geomech. 31, 1329–1348. doi:10.1002/nag

Foster, C.D., Borja, R.I., Regueiro, R.A., 2007. Embedded strong discontinuity finite elements for fractured geomaterialswith variable friction. Int. J. Numer. Methods Eng. 72, 549–581. doi:10.1002/nme

Fujita, Y., Ishimaru, R., Hanai, S., Suenga, Y., 1998. Study on Internal Friction Angle and Tensile Strength. Proc. Fram. 325–334.

Gajo, A., Bigoni, D., Wood, D.M., 2004. Multiple shear band development and related instabilities in granular materials. J. Mech. Phys. Solids 52, 2683–2724. doi:10.1016/j.jmps.2004.05.010

Galavi, V., Schweiger, H.F., 2010. Nonlocal multilaminate model for strain softening analysis. Int. J. Geomech. 10, 30–44. doi:10.1061/(ASCE)1532-3641(2010)10:1(30)

Gálvez, J.C., Cendón, D.A., Planas, J., 2003. Influence of shear parameters on mixed – mode fracture of concrete. Int. J. Fract. 118, 163–189.

Gálvez, J.C., Planas, J., Sancho, J.M., Reyes, E., Cendón, D.A., Casati, M.J., 2013. An embedded cohesive crack model for finite element analysis of quasi-brittle materials. Eng. Fract. Mech. 109, 369–386. doi:10.1016/j.engfracmech.2012.08.021

Gentier, S., Riss, J., Archambault, G., Flamand, R., Hopkins, D., 2000. Influence of fracture geometry on shear behavior. Int. J. Rock Mech. Min. Sci. 37, 161–174. doi:10.1016/S1365-1609(99)00096-9

Ghadrdan, M., Sadrnejad, S.A., Shaghaghi, T., 2015. Numerical evaluation of geomaterials behavior upon multiplane damage model. Comput. Geotech. 68, 1–7. doi:10.1016/j.compgeo.2015.03.008

Gopalaratnam, V.S., Shah, S.P., 1987. Tensile failure of steel fiber-reinforced mortar. J. Eng. Mech. 113, 635–652. doi:10.1061/(ASCE)0733-9399(1987)113:5(635)

Gopalaratnam, V.S., Shah, S.P., 1985. Softening response of plain concrete in direct tension. ACI J. 82, 310–323.

Grasselli, G., Egger, P., 2003. Constitutive law for the shear strength of rock joints based on three-dimensional surface parameters. Int J Rock Mech Min Sci. 40, 25–40.

Grassl, P., Jirásek, M., 2006. Damage-plastic model for concrete failure. Int. J. Solids Struct. 43, 7166–7196. doi:10.1016/j.ijsolstr.2006.06.032

Grassl, P., Lundgren, K., Gylltoft, K., 2002. Concrete in compression: a plasticity theory with a novel hardening law. Int. J. Solids Struct. 39, 5205–5223. doi:10.1016/S0020-7683(02)00408-0

Grassl, P., Xenos, D., Nyström, U., Rempling, R., Gylltoft, K., 2013. CDPM2: A damage-plasticity approach to modelling the failure of concrete. Int. J. Solids Struct. 50, 3805–3816. doi:10.1016/j.ijsolstr.2013.07.008

Grégoire, D., Rojas-Solano, L.B., Pijaudier-Cabot, G., 2013. Failure and size effect for notched and unnotched concrete beams. Int. J. Numer. Anal. Methods Geomech. 37, 1434–1452. doi:10.1002/nag

Grilo, T.J., Paulo, R.M.F., Silva, C.R.M., Davim, J.P., 2013. Experimental delamination analyses of CFRPs using different drill geometries. Compos. Part B Eng. 45, 1344–1350. doi:10.1016/j.compositesb.2012.07.057

Grueschow, E., Rudnicki, J.W., 2005. Elliptic yield cap constitutive modeling for high porosity sandstone. Int. J. Solids Struct. 42, 4574–4587. doi:10.1016/j.ijsolstr.2005.02.001

Guiamatsia, I., Nguyen, G.D., 2014. A thermodynamics-based cohesive model for interface debonding and friction. Int. J. Solids Struct. 51, 647–659. doi:10.1016/j.ijsolstr.2013.10.032

Guiamatsia, I., Nguyen, G.D., 2012. A generic approach to constitutive modelling of composite delamination under mixed-mode loading conditions. Compos. Sci. Technol. 72, 269–277. doi:10.1016/j.compscitech.2011.11.012

Guzmán, S., Gálvez, J.C., Sancho, J.M., 2012. Modelling of corrosion-induced cover cracking in reinforced concrete by an embedded cohesive crack finite element. Eng. Fract. Mech. 93, 92–107. doi:10.1016/j.engfracmech.2012.06.010

Haghighat, E., Pietruszczak, S., 2016. On modeling of fractured media using an enhanced embedded discontinuity approach. Extrem. Mech. Lett. 6, 10–22. doi:10.1016/j.eml.2015.11.001

Haghighat, E., Pietruszczak, S., 2015. On modeling of discrete propagation of localised damage in cohesive-frictional material. Int. J. Numer. Anal. Methods Geomech. 39, 1774–1790.

Haimson, B., Rudnicki, J.W., 2010. The effect of the intermediate principal stress on fault formation and fault angle in siltstone. J. Struct. Geol. 32, 1701–1711. doi:10.1016/j.jsg.2009.08.017

Hameed, R., Sellier, A., Turatsinze, A., Duprat, F., 2013. Metallic fiber-reinforced concrete behaviour: Experiments and constitutive law for finite element modeling. Eng. Fract. Mech. 103, 124–131. doi:10.1016/j.engfracmech.2012.11.022

Hamidi, A., Hooresfand, M., 2013. Effect of fiber reinforcement on triaxial shear behavior of cement treated sand. Geotext. Geomembranes 36, 1–9. doi:10.1016/j.geotexmem.2012.10.005

Hao, W., Ge, D., Ma, Y., Yao, X., Shi, Y., 2012. Experimental investigation on deformation and strength of carbon/epoxy laminated curved beams. Polym. Test. 31, 520–526. doi:10.1016/j.polymertesting.2012.02.003

Harrison, J.P., Hudson, J.A., 2000. Engineering rock mechanics. Part 2: illustrative workable examples. Elsevier, Oxford: Pergamon.

Hashemi, S., Kinloch, A.J., Williams, J.G., 1990. The effects of geometry, rate and temperature on the mode I, mode II and mixed-mode I/II interlamina fracture of Carbon-firbre/poly (ether-ether ketone) Composite. J. Compos. Mater. 24, 918–956. doi:10.4028/www.scientific.net/kem.37.199

Hassan, A.M.T., Jones, S.W., Mahmud, G.H., 2012. Experimental test methods to determine the uniaxial tensile and compressive behaviour of ultra high performance fibre reinforced concrete (UHPFRC). Constr. Build. Mater. 37, 874–882. doi:10.1016/j.conbuildmat.2012.04.030

Hazirbaba, K., 2018. Large-scale direct shear and CBR performance of geofibre-reinforced sand. Road Mater. Pavement Des. 19, 1350–1371. doi:10.1080/14680629.2017.1310667

He, W., Wu, Y.F., Liew, K.M., Wu, Z., 2006. A 2D total strain based constitutive model for predicting the behaviors of concrete structures. Int. J. Eng. Sci. 44, 1280–1303. doi:10.1016/j.ijengsci.2006.07.007

Hill, R., 1963. Elastic properties of reinforced solids: Some theoretical principles. J. Mech. Phys. Solids 11, 357–372. doi:10.1016/0022-5096(63)90036-X

Hillerborg, A., Modéer, M., Petersson, P.E., 1976. Analysis of crack formation and crack growth in concrete by means of fracture mechanics and finite elements. Cem. Concr. Res. 6, 773–781. doi:10.1016/0008-8846(76)90007-7

Högberg, J.L., 2006. Mixed mode cohesive law. Int. J. Fract. 141, 549–559. doi:10.1007/s10704-006-9014-9

Houlsby, G.T., Puzrin, A.M., 2000. Thermomechanical framework for constitutive models for rate-independent dissipative materials. Int. J. Plast. 16, 1017–1047. doi:10.1016/S0749-6419(99)00073-X

Hu, X., Duan, K., 2008. Size effect and quasi-brittle fracture: The role of FPZ. Int. J. Fract. 154, 3–14. doi:10.1007/s10704-008-9290-7

Huang, T., Zhang, Y.X., Yang, C., 2016. Multiscale modelling of multiple-cracking tensile fracture behaviour of engineered cementitious composites. Eng. Fract. Mech. 160, 52–66. doi:10.1016/j.engfracmech.2016.04.006

Huespe, A.E., Oliver, J., Mora, D.F., 2013. Computational modeling of high performance steel fiber reinforced concrete using a micromorphic approach. Comput. Mech. 52, 1243–1264. doi:10.1007/s00466-013-0873-4

Ibraim, E., Diambra, A., Muir Wood, D., Russell, A.R., 2010. Static liquefaction of fibre reinforced sand under monotonic loading. Geotext. Geomembranes 28, 374–385. doi:10.1016/j.geotexmem.2009.12.001

Ibraim, E., Diambra, A., Russell, A.R., Muir Wood, D., 2012. Assessment of laboratory sample preparation for fibre reinforced sands. Geotext. Geomembranes 34, 69–79. doi:10.1016/j.geotexmem.2012.03.002

Imran, I., Pantazopoulou, S.J., 2001. Plasticity model for concrete under triaxial compression. J. Eng. Mech. 127, 281–290.

Imran, I., Pantazopoulou, S.J., 1997. Experimental Study of plain concrete under triaxial stress. ACI Mater. J. 93, 589–601.

Ingraham, M.D., Issen, K.A., Holcomb, D.J., 2013. Response of Castlegate sandstone to true triaxial states of stress. J. Geophys. Res. Solid Earth 118, 536–552. doi:10.1002/jgrb.50084

Jäger, P., Steinmann, P., Kuhl, E., 2008. Ultrasonic thickness of middle trapezius muscle in young healthy men. Internaltional J. Numer. Methods Eng. 76, 1328–1352. doi:10.1002/nme

Jefferson, A.D., 2003. Craft – a plastic-damage-contact model for concrete. II. Model implementation with implicit return-mapping algorithm and consistent tangent matrix. Int. J. Solids Struct. 40, 6001–6022.

Jin, C., Buratti, N., Stacchini, M., Savoia, M., Cusatis, G., 2016. Lattice discrete particle modeling of fiber reinforced concrete: Experiments and simulations. Eur. J. Mech. A/Solids 57, 85–107. doi:10.1016/j.euromechsol.2015.12.002

Jirásek, M., 2000. Comparative study on finite elements with embedded discontinuities. Comput. Methods Appl. Mech. Eng. 188, 307–330. doi:10.1016/s0045-7825(99)00154-1

Jirásek, M., Bažant, Z.P., 2002. Inelastic analysis of structures. John Wiley & Sons Ltd.

Jirásek, M., Patzák, B., 2002. Consistent tangent stiffness for nonlocal material models. Solids, Struct. Coupled Probl. Eng. 80, 1279–1293.

Jirásek, M., Rolshoven, S., Grassl, P., 2004. Size effect on fracture energy induced by non-locality. Int. J. Numer. Anal. Methods Geomech. 28, 653–670. doi:10.1002/nag.364

Jouanne, F., Awan, A., Pêcher, A., Kausar, A., Mugnier, J.L., Khan, I., Khan, N.A., Van Melle, J., 2014. Journal of Geophysical Research : Solid Earth. J. Geophys. Res. Solid Earth 119, 1882–1903. doi:10.1002/2013JB010776.Received

Kachanov, M., 1992. Effective Elastic Properties of Cracked Solids: Critical Review of Some Basic Concepts. Appl. Mech. Rev. 45, 304. doi:10.1115/1.3119761

Kan, W.H., Albino, C., Dias-da-Costa, D., Dolman, K., Lucey, T., Tang, X., Cairney, J., Proust, G., 2018. Fracture toughness testing using photogrammetry and digital image correlation. MethodsX 5, 1166–1177. doi:10.1016/j.mex.2018.09.012

Kamal, A., Kunieda, M., Ueda, N., Nakamura, H., 2008. Evaluation of crack opening performance of a repair material with strain hardening behavior. Cem. Concr. Compos. 30, 863–871. doi:10.1016/j.cemconcomp.2008.08.003

Kang, H.D., William, K., 1999. Localisation characteristics of triaxial concrete model. J. Eng. Mech. 125, 941–950.

Kang, J., Kim, K., Lim, Y.M., Bolander, J.E., 2014. Modeling of fiber-reinforced cement composites: Discrete representation of fiber pullout. Int. J. Solids Struct. 51, 1970–1979. doi:10.1016/j.ijsolstr.2014.02.006

Karihaloo, B.L., Abdalla, H.M., Xiao, Q.Z., 2006. Deterministic size effect in the strength of cracked concrete structures. Cem. Concr. Res. 36, 171–188. doi:10.1016/j.cemconres.2005.04.007

Karihaloo, B.L., Abdalla, H.M., Xiao, Q.Z., 2003. Size effect in concrete beams. Eng. Fract. Mech. 70, 979–993. doi:10.1016/S0013-7944(02)00161-3

Karrech, A., Regenauer-Lieb, K., Poulet, T., 2011. A damaged visco-plasticity model for pressure and temperature sensitive geomaterials. Int. J. Eng. Sci. 49, 1141–1150. doi:10.1016/j.ijengsci.2011.05.005

Kaushik, H.B., Rai, D.C., Jain, S.K., 2007. Stress-strain characteristics of clay brick masonry under uniaxial compression. J. Mater. Civ. Eng. 19, 728–739. doi:10.1061/(asce)0899-1561(2007)19:9(728)

Kedar, K., Bažant, Z.P., 2015. Microplane damage model for fatigue of quasibrittle materials : Sub-critical crack growth, lifetime and residual strength. Int. J. Fatigue 70, 93–105. doi:10.1016/j.ijfatigue.2014.08.012

Kenane, M., Benzeggagh, M.L., 1997. Mixed-mode delamination fracture toughness of unidirectional glass epoxy composites under-fatigue loading. Compos. Sci. Technol. 57, 597–605.

Khaddour, G., Riedel, I., Andò, E., Charrier, P., Bésuelle, P., Salager, S., Desrues, J., Viggiani, G., Salager, S., 2018. Grain-scale characterization of water retention behaviour of sand using X-ray CT. Acta Geotech. 13, 497–512. doi:10.1007/s11440-018-0628-7

Klein, E., Baud, P., Reuschlé, T., Wong, T.F., 2001. Mechanical behaviour and failure mode of bentheim sandstone under triaxial compression. Phys. Chem. Earth, Part A Solid Earth Geod. 26, 21–25. doi:10.1016/S1464-1895(01)00017-5

Klein, E., Reuschlé, T., 2003. A model for the mechanical behaviour of bentheim sandstone in the brittle regime. Pure Appl. Geophys. 160, 833–849. doi:10.1007/PL00012568

Kolluri, M., Hoefnagels, J.P.M., Van Dommelen, J.A.W., Geers, M.G.D., 2014. Irreversible mixed mode interface delamination using a combined damage-plasticity cohesive zone enabling unloading. Int. J. Fract. 185, 77–95. doi:10.1007/s10704-013-9899-z

Kolymbas, D., 2009. Kinematics of shear bands. Acta Geotech. 4, 315–318. doi:10.1007/s11440-009-0092-5

Krajcinovic, D., 1985. Continuous damage mechanics revisited: basic concepts and definitions. J. Appl. Mech. 52, 829. doi:10.1115/1.3169154

Krätzig, W.B., Pölling, R., 2004. An elasto-plastic damage model for reinforced concrete with minimum number of material parameters. Comput. Struct. 82, 1201–1215. doi:10.1016/j.compstruc.2004.03.002

Kumar, A., Gupta, D., 2016. Behavior of cement-stabilized fiber-reinforced pond ash, rice husk ash-soil mixtures. Geotext. Geomembranes 44, 466–474. doi:10.1016/j.geotexmem.2015.07.010

Kumar, N., Amirtham, R., Pandey, M., 2014. Plasticity based approach for failure modelling of unreinforced masonry. Eng. Struct. 80, 40–52. doi:10.1016/j.engstruct.2014.08.021

Kupfer, H., Hilsdorf, H.K., Rusch, H., 1969. Behaviour of concrete under biaxial stresses. Am. Concr. Inst. J. 66, 656–666.

Lade, P. V, 1997. Modelling the strength of engineering materials in three dimensions. Mech. Cohesive-Frictional Mater. 2, 339–356.

Lade, P. V, 1977. Elasto-plastic stress–strain theory for cohesionless soil with curved yield surfaces. Int. J. Solids Struct. 13, 1019–1035.

Landis, E.N., Nagy, E.N., Keane, D.T., 2003. Microstructure and fracture in three dimensions. Eng. Fract. Mech. 70, 911–925. doi:10.1016/S0013-7944(02)00157-1

Langdon, G.S., Karagiozova, D., Von Klemperer, C.J., Nurick, G.N., Ozinsky, A., Pickering, E.G., 2013. The air-blast response of sandwich panels with composite face sheets and polymer foam cores: Experiments and predictions. Int. J. Impact Eng. 54, 64–82. doi:10.1016/j.ijimpeng.2012.10.015

Laranjeira, F., Molins, C., Aguado, A., 2010. Predicting the pullout response of inclined hooked steel fibers. Cem. Concr. Res. 40, 1471–1487. doi:10.1016/j.cemconres.2010.05.005

Larsson, R., Runesson, K., Sture, S., 1996. Embedded localization band in undrained soil based on regularized strong discontinuity theory and FE-Analysis. Int. J. Solids Struct. 33, 3081–3101. doi:10.1016/0020-7683(95)00272-3

Le Bellégo, C., Dubé, J.F., Pijaudier-Cabot, G., Gérard, B., 2003. Calibration of nonlocal damage model from size effect tests. Eur. J. Mech. A/Solids 22, 33–46. doi:10.1016/S0997-7538(02)01255-X

Le, L.A., Nguyen, G.D., Bui, H.H., Sheikh, A.H., Kotousov, A., Khanna, A., 2017. Modelling jointed rock mass as a continuum with an embedded cohesive-frictional model. Eng. Geol. 228, 107–120. doi:10.1016/j.enggeo.2017.07.011

Le, L.A., Nguyen, G.D., Bui, H.H., Sheikh, A.H., Kotousove, A., 2018. Localised failure mechanism as the basis for constitutive modelling of geomaterials. Internaltional J. Eng. Sci. 133, 284–310.

Le, L.A., Nguyen, G.D., Bui, H.H., Sheikh, A.H., Kotousov, A., 2019. Incorporation of micro-cracking and fibre bridging phenomena in constitutive modelling of fibre reinforced concrete. In preparation

Lee, H., Haimson, B.C., 2011. True triaxial strength, deformability, and brittle failure of granodiorite from the San Andreas Fault Observatory at Depth. Int. J. Rock Mech. Min. Sci. 48, 1199–1207. doi:10.1016/j.ijrmms.2011.08.003

Lee, H.K., Simunovic, S., 2001. A damage constitutive model of progressive debonding in aligned discontinuous fiber composites. Int. J. Solids Struct. 38, 875–895. doi:10.1016/S0020-7683(00)00060-3

Lee, H.K., Simunović, S., Shin, D.K., 2004. A computational approach for prediction of the damage evolution and crushing behavior of chopped random fiber composites. Comput. Mater. Sci. 29, 459–474. doi:10.1016/j.commatsci.2003.12.008

Lee, J., Fenves, G.L., 1998. Plastic-damage model for cyclic loading of concrete structures. J. Eng. Mech. 124, 892–900. doi:https://doi.org/10.1061/(ASCE)0733-9399(1998)124:8(892)

Lemaitre, J., 2012. A course on damage mechanics. Springer Science & Business Media.

Lemaitre, J., 1972. Evaluation of dissipation and damage in metals submitted to dynamic loading. Mech. Behav. Mater. 540–9.

Lemaitre, J., Chaboche, J.L., 1990. Mechanics of solid materials. Cambridge University Press, Cambridge.

Li, C., Caner, F.C., Chau, V.T., Bažant, Z.P., 2017. Spherocylindrical microplane constitutive model for shale and other anisotropic rocks. J. Mech. Phys. Solids 103, 155–178. doi:10.1016/j.jmps.2017.03.006

Li, F., Li, Z., 2001. Continuum damage mechanics based modeling of fiber reinforced concrete in tension. Int. J. Solids Struct. 38, 777–793. doi:10.1016/S0020-7683(00)00034-2

Li, J., Tang, C., Wang, D., Pei, X., Shi, B., 2014. Effect of discrete fibre reinforcement on soil tensile strength. J. Rock Mech. Geotech. Eng. 6, 133–137. doi:10.1016/j.jrmge.2014.01.003

Li, Q., Ansari, F., 1999. Mechanics of damage and constitutive relationship for high-strength concrete in triaxial compression. J. Eng. Mech. 89, 490–507. doi:10.1109/IPECON.2010.5697021

Li, V.C., Hwai-Chung, W., Mohamed, M., Dhanada, M., 1996. Tensile behaviour of cement-based composite with random discontinuous steel fibers. J. Am. Ceram. Soc. 79, 74–78.

Li, V.C., Wang, S., Wu, C., 2001. Tensile strain-hardening behaviour of Polyvinyl Alcohol Engineered Cementitious Composites (PVA-ECC). ACI Mater. J. 483–492. doi:10.14359/10851

Li, V.C., Wang, Y., Backer, S., 1991. A micromechanical model of tension- softening and bridging toughening of short random fiber reinforced brittle. J. Mech. Phys. Solids 39, 607–625.

Li, V.C., Wang, Y., Backer, S., 1990. Effect of inclining angle, bundling and surface treatment on synthetic fibre pull-out from a cement matrix. Composites 21, 132–140. doi:10.1016/0010-4361(90)90005-H

Li, X.C., Xu, D.J., Liu, S.H., 1994. The experimental research of the strength, deformation and failure properties of Laxiwa granite under the status of true triaxial stresses, in: Proceedings of the Third Conference of Chinese Society of Rock Mechanics and Engineering. China Science and Technology Press, Beijing, China, pp. 153–159.

Li, Y., Ling, X., Su, L., An, L., Li, P., Zhao, Y., 2018. Tensile strength of fiber reinforced soil under freeze-thaw condition. Cold Reg. Sci. Technol. 146, 53–59. doi:10.1016/j.coldregions.2017.11.010

Li, Y., Oh, J., Mitra, R., Hebblewhite, B., 2016a. A constitutive model for a laboratory rock joint with multi-scale asperity degradation. Comput. Geotech. 72, 143–151. doi:10.1016/j.compgeo.2015.10.008

Li, Y., Oh, J., Mitra, R., Hebblewhite, B., 2016b. A constitutive model for a laboratory rock joint with multi-scale asperity degradation. Comput. Geotech. 72, 143–151. doi:10.1016/j.compgeo.2015.10.008

Li, Z., Li, F., Chang, T.Y., Mai, Y.-W., 1998. Uniaxial tensile behaviour of concrete reinforced with randomly distributed short fibres. ACI Mater. J. 95, 564–574.

Liao, C.J., Lee, D.H., Wu, J.H., Lai, C.Z., 2011. A new ring-shear device for testing rocks under high normal stress and dynamic conditions. Eng. Geol. 122, 93–105. doi:10.1016/j.enggeo.2011.03.018

Lin, Z., Li, V.C., 1997. Crack bridging in fiber reinforced cementitious composites with slip-hardening interfaces. J. Mech. Phys. Solids 45, 763–787.

Liolios, P., Exadaktylos, G., 2017. Hyperbolic hardening model for quasibrittle materials. Int. J. Solids Struct. 120, 1339–1351. doi:10.1016/j.ijsolstr.2017.05.011

Liu, J., Chen, Z., Song, Z., Bai, Y., Qian, W., Wei, J., Kanungo, D.P., 2018. Tensile behavior of polyurethane organic polymer and polypropylene fiber-reinforced sand. Polymers (Basel). 10, 499. doi:10.3390/polym10050499

Liu, X.S., Ning, J.G., Tan, Y.L., Gu, Q.H., 2016. Damage constitutive model based on energy dissipation for intact rock subjected to cyclic loading. Int. J. Rock Mech. Min. Sci. 85, 27–32. doi:10.1016/j.ijrmms.2016.03.003

Lloberas-Valls, O., Huespe, A.E., Oliver, J., Dias, I.F., 2016. Strain injection techniques in dynamic fracture modeling. Comput. Methods Appl. Mech. Eng. 308, 499–534. doi:10.1016/j.cma.2016.05.023

Loret, B., Prevost, J.H., 1991. Dynamic strain localization in fluidsaturated porous media. J. Eng. Mech. 117, 907–922.

Lotfi, H.R., Shing, P.B., 1994. Interface model applied to fracture of masonry structures. J. Struct. Eng. 120, 63–80.

Lu, C., Leung, C.K.Y., 2017. Theoretical evaluation of fiber orientation and its effects on mechanical properties in Engineered Cementitious Composites (ECC) with various thicknesses. Cem. Concr. Res. 95, 240–246. doi:10.1016/j.cemconres.2017.02.024

Lu, D., Du, X., Wang, G., Zhou, A., Li, A., 2016. A three-dimensional elastoplastic constitutive model for concrete. Comput. Struct. 163, 41–55. doi:10.1016/j.compstruc.2015.10.003

Lu, X., Hsu, C.T.T., 2006. Behavior of high strength concrete with and without steel fiber reinforcement in triaxial compression. Cem. Concr. Res. 36, 1679–1685. doi:10.1016/j.cemconres.2006.05.021

Lumantarna, R., Biggs, D.T., Ingham, J.M., 2014. Compressive, flexural bond, and shear bond strengths of in situ New Zealand unreinforced clay brick masonry constructed using lime mortar between the 1880s and 1940s. J. Mater. Civ. Eng. 26, 559–566. doi:10.1061/(asce)mt.1943-5533.0000685

Lyakhovsky, V., Zhu, W., Shalev, E., 2015. Visco-poroelastic damage model for brittle-ductile failure of porous rocks. J. Geophys. Res. Solid Earth 120, 2179–2199. doi:10.1002/2014JB011805

Ma, J., Zhao, G., Khalili, N., 2016. A fully coupled flow deformation model for elasto-plastic damage analysis in saturated fractured porous media. Int. J. Plast. 76, 29–50. doi:10.1016/j.ijplas.2015.07.011

Ma, X., Haimson, B.C., 2016. Failure characteristics of two porous sandstones subjected to true triaxial testing. J. Geophys. Res. Solid Earth 121, 6477–6498. doi:10.1002/2016JB012979

Macari, M., Hoyos, L., 2001. Mechanical Behavior of an Unsaturated Soil Under Multi-Axial Stress States. Am. Soc. Test. Mater. 24, 14–22. doi:10.1520/GTJ11278J

Maleki, K., Pouya, A., 2010. Numerical simulation of damage-Permeability relationship in brittle geomaterials. Comput. Geotech. 37, 619–628. doi:10.1016/j.compgeo.2010.03.009

Mansur, M.A., Chin, M.S., Wee, T.H., 1999. Stress-strain relationship of high-strength fibre concrete in compression. J. Mater. Civ. Eng. 11, 21–29.

Marara, K., Erenb, Ö., Yitmena, İ., 2011. Compression specific toughness of normal strength steel fiber reinforced concrete (NSSFRC) and high strength steel fiber reinforced concrete (HSSFRC). Mater. Res. 14, 239–247. doi:10.1590/s1516-14392011005000042

Marinelli, F., Buscarnera, G., 2015. Parameter calibration for high-porosity sandstones deformed in the compaction banding regime. Int. J. Rock Mech. Min. Sci. 78, 240–252. doi:10.1016/j.ijrmms.2015.05.004

Mazars, J., Pijaudier-Cabot, G., 1989. Continuum damage theory - application to concrete. J. Eng. Mech. 115, 345–365.

Mazzotti, C., Savoia, M., Ferracuti, B., 2008. An experimental study on delamination of FRP plates bonded to concrete. Constr. Build. Mater. 22, 1409–1421. doi:10.1016/j.conbuildmat.2007.04.009

McLaren, 1963. Optimal numerical integration on a sphere. Math. Comput. 17, 361–383.

Mihai, I., Jefferson, A., 2013. A multi-asperity plastic-contact crack plane model for geomaterials. Int. J. Numer. Anal. Methods Geomech. 37, 1492–1509. doi:10.1002/nag

Mihai, I.C., Jefferson, A.D., 2017. A micromechanics based constitutive model for fibre reinforced cementitious composites. Int. J. Solids Struct. 110-111, 152–169. doi:10.1016/j.ijsolstr.2017.01.032

Mihai, I.C., Jefferson, A.D., Lyons, P., 2016. A plastic-damage constitutive model for the finite element analysis of fibre reinforced concrete. Eng. Fract. Mech. 159, 35–62. doi:10.1016/j.engfracmech.2015.12.035

Mills, L.L., Zimmerman, R.M., 1970. Compressive strength of plain concrete under multiaxial loading conditions. ACI J. Proc. 67, 802–807. doi:10.14359/7310

Mir, A., 2017. A thermodynamic approach to modelling brittle-ductile and localised failure of rocks using damage mechanics and plasticity theory. PhD thesis, The University of Adelaide.

Mir, A., Nguyen, G.D., Sheikh, A.H., 2018. A Thermodynamics-based Model for brittle to ductile behaviour and localised failure of porous rocks. Int. J. Solids Struct. In press, 161–184. doi:10.1016/j.ijsolstr.2018.06.025

Mir, A., Nguyen, G.D., Sheikh, A.H., 2015. A continuum model with an embedded fracture process zone modelled as a cohesive frictional interface. Appl. Mech. Mater. 846, 360–365.

Misra, A., Poorsolhjouy, P., 2016. Granular micromechanics model of anisotropic elasticity derived from Gibbs potential. Acta Mech. 227, 1393–1413. doi:10.1007/s00707-016-1560-2

Misra, A., Poorsolhjouy, P., 2013. Micro-macro scale instability in 2D regular granular assemblies. Contin. Mech. Thermodyn. 27, 63–82. doi:10.1007/s00161-013-0330-9

Misra, A., Yang, Y., 2010. Micromechanical model for cohesive materials based upon pseudo-granular structure. Int. J. Solids Struct. 47, 2970–2981. doi:10.1016/j.ijsolstr.2010.07.002

Mo, K.H., Yeoh, K.H., Bashar, I.I., Alengaram, U.J., Jumaat, M.Z., 2017. Shear behaviour and mechanical properties of steel fibre-reinforced cement-based and geopolymer oil palm shell lightweight aggregate concrete. Constr. Build. Mater. 148, 369–375. doi:10.1016/j.conbuildmat.2017.05.017

Moallemi, S., Pietruszczak, S., 2017. Analysis of localized fracture in 3D reinforced concrete structures using volume averaging technique. Finite Elem. Anal. Des. 125, 41–52. doi:10.1016/j.finel.2016.10.004

Moallemi, S., Pietruszczak, S., Mróz, Z., 2017. Deterministic size effect in concrete structures with account for chemo-mechanical loading. Comput. Struct. 182, 74–86. doi:10.1016/j.compstruc.2016.10.003

Modelling, A.N., Mater, S., Eng, S., 1993. Modelling and Simulation in Materials Science and Engineering Related content Void nucleation by inclusion debonding in a crystal matrix.

Mohammadi, H., Pietruszczak, S., 2019. Description of damage process in fractured rocks. Int. J. Rock Mech. Min. Sci. 113, 295–302. doi:10.1016/j.ijrmms.2018.12.003

Mosallam, A.S., 2007. Out-of-plane flexural behavior of unreinforced red brick walls strengthened with FRP composites. Compos. Part B Eng. 38, 559–574. doi:10.1016/j.compositesb.2006.07.019

Mukherjee, M., Nguyen, G.D., Mir, A., Bui, H.H., Shen, L., El-Zein, A., Maggi, F., 2017. Capturing pressure- and rate-dependent behaviour of rocks using a new damage-plasticity model. Int. J. Impact Eng. 110, 208–218. doi:10.1016/j.ijimpeng.2017.01.006

Naaman, A.E., Namur, G.G., Alwan, J.M., Najm, H.S., 1992. Fiber Pullout and Bond Slip. I: Analytical Study. J. Struct. Eng. 117, 2769–2790. doi:doi:10.1061/(ASCE)0733-9445(1991)117:9(2791)

Nataraja, M.C., Dhang, N., Gupta, A.P., 1999. Stress - strain curves for steel- fiber reinforced concrete under compression. Cem. Concr. Compos. 21, 383–390.

Nataraja, M.C., Dhang, N., Gupta, A.P., 1999. Stress–strain curves for steel-fiber reinforced concrete under compression. Cem. Concr. Compos. 21, 383–390. doi:10.1016/S0958-9465(99)00021-9

Navarro, V., Alonso, J., Calvo, B., Sánchez, J., 2010. A constitutive model for porous rock including effects of bond strength degradation and partial saturation. Int. J. Rock Mech. Min. Sci. 47, 1330–1338. doi:10.1016/j.ijrmms.2010.08.003

Neilsen, M.K., Schreyer, H.L., 1993. Bifurcations in elastic-plastic materials. Int. J. Solids Struct. 30, 521–544. doi:https://doi.org/10.1016/0020-7683(93)90185-A

Nerilli, F., Vairo, G., 2018. Experimental investigation on the debonding failure mode of basalt-based FRP sheets from concrete. Compos. Part B Eng. 153, 205–216. doi:10.1016/j.compositesb.2018.07.002

Nguyen, B.N., Khaleel, M.A., 2004. A mechanistic approach to damage in short-fiber composites based on micromechanical and continuum damage mechanics descriptions. Compos. Sci. Technol. 64, 607–617. doi:10.1016/S0266-3538(03)00293-8

Nguyen, G.D., 2005. A thermodynamic approach to constitutive modelling of concrete using damage mechanics and plasticity theory. PhD dissertation, University of Oxford.

Nguyen, G.D., Korsunsky, A.M., 2008a. Development of an approach to constitutive modelling of concrete: Isotropic damage coupled with plasticity. Int. J. Solids Struct. 45, 5483–5501. doi:10.1016/j.ijsolstr.2008.05.029

Nguyen, G.D., Houlsby, G.T., 2008b. Acoupled damage–plasticity model for concrete based on thermodynamic principles: Part I: model formulation and parameter identification Giang. Int. J. Numer. Anal. Methods Geomech. 32, 189–213. doi:10.1002/nag

Nguyen, G.D., Houlsby, G. T., 2008c. Implementation, Acoupled damage–plasticity model for concrete based on thermodynamic principles: Part II: non-local regularization and numerical. Int. J. Numer. Anal. Methods Geomech. 32, 189–213. doi:10.1002/nag

Nguyen, N.S., Magoariec, H., Cambou, B., 2009. Analysis of structure and strain at the meso-scale in 2D granular materials. Int. J. Solids Struct. 46, 3257–3271. doi:10.1016/j.ijsolstr.2009.04.019

Nguyen, G.D., Einav, I., 2010. Nonlocal regularisation of a model based on breakage mechanics for granular materials. Int. J. Solids Struct. 47, 1350–1360. doi:10.1016/j.ijsolstr.2010.01.020

Nguyen, G.D., Einav, I., Korsunsky, A.M., 2012a. How to connect two scales of behaviour in constitutive modelling of geomaterials. Géotechnique Lett. 2, 129–134. doi:10.1680/geolett.12.00030

Nguyen, G.D., Einav, I., Guiamatsia, I., 2012b. On the partition of fracture energy in constitutive modelling of quasi-brittle materials. Eng. Fract. Mech. 79, 225–244. doi:10.1016/j.engfracmech.2011.11.002

Nguyen, N.S., Magoariec, H., Cambou, B., 2012c. Local stress analysis in granular materials at a mesoscale. Int. J. Numer. Anal. Methods Geomech. 36, 1609–1635. doi:10.1002/nag

Nguyen, G.D., Einav, I., Guiamatsia, I., Korsunsky, A.M., 2012d. From diffuse to localized damage: the role of friction, in: The International Conference on Advances in Computational Mechanics (ACOME). August 14-16, Ho Chi Minh City, Vietnam.

Nguyen, G.D., Korsunsky, A.M., Einav, I., 2014. A constitutive modelling framework featuring two scales of behaviour : Fundamentals and applications to quasi-brittle failure. Eng. Fract. Mech. 115, 221–240. doi:10.1016/j.engfracmech.2013.11.006

Nguyen, G.D., Korsunsky, A.M., Belnoue, J.P.H., 2015. A nonlocal coupled damage-plasticity model for the analysis of ductile failure. Int. J. Plast. 64, 56–75. doi:10.1016/j.ijplas.2014.08.001

Nguyen, G.D., Nguyen, C.T., Bui, H.H., Nguyen, V.P., 2016a. Constitutive modelling of compaction localisation in porous sandstones. Int. J. Rock Mech. Min. Sci. 83, 57–72. doi:10.1016/j.ijrmms.2015.12.018

Nguyen, G.D., Nguyen, C.T., Nguyen, V.P., Bui, H.H., Shen, L., 2016b. A size-dependent constitutive modelling framework for localised failure analysis. Comput. Mech. 58, 257–280. doi:10.1007/s00466-016-1293-z

Nguyen, C.T., Nguyen, G.D., Das, A., Bui, H.H., 2017a. Constitutive modelling of progressive localised failure in porous sandstones under shearing at high confining pressures. Int. J. Rock Mech. Min. Sci. 93, 179–195. doi:10.1016/j.ijrmms.2017.01.014

Nguyen, V.P., Nguyen, G.D., Nguyen, C.T., Shen, L., Dias-da-Costa, D., El-Zein, A., Maggi, F., 2017b. Modelling complex cracks with finite elements: a kinematically enriched constitutive model. Int. J. Fract. 203, 21–39. doi:10.1007/s10704-016-0114-x

Nguyen, N.H.T., Kodikara, J., Bui, H.H., Nguyen, G.D., Jitsangiam, P., Arooran, S., 2017c. A thermodynamics-based cohesive model for discrete element modelling of fracture in cemented materials. Int. J. Solids Struct., In press

Nguyen, G.D., Bui, H.H., 2017. The Roles and effects of friction in cohesive zone modelling: A thermodynamics-based formulation, in: Lecture Notes in Civil Engineering, V. 8. (Ed.), Proceedings of the 4th Congrès International de Géotechnique - Ouvrages - Structures. CIGOS. Springer, Singapore.

Nguyen, G.D., Bui, H.H., 2019. A constitutive modelling framework featuring two scales of behaviour: fundamentals and applications to quasi-brittle failure. Int. J. Solids Struct. 117, 159–176. doi:10.1016/j.ijsolstr.2017.03.027

Nooru-Mohamed, Schlangen, E., Van Mier, J.G., 1993. Experimental and numerical study on the behavior of concrete subjected to biaxial tension. Adv. Cem. Based Mater. 1, 22–37.

Octávio, C., Dias-da-Costa, D., Alfaiate, J., Júlio, E., 2016. Modelling the behaviour of steel fibre reinforced concrete using a discrete strong discontinuity approach. Eng. Fract. Mech. 154, 12–23. doi:10.1016/j.engfracmech.2016.01.006

Oka, F., Adachi, T., Yashima, A., 1995. A strain localization analysis of clay using a strain softening viscoplastic model. Int. J. Plast. 37, 271–283.

Oliver, J., 1996. Modelling strong discontinuities in solid mechanics via strain softening constitutive equations. Part 1: Fundamentals. Int. J. Numer. Methods Eng. 39, 3575–3600. doi:10.1002/(SICI)1097-0207(19961115)39:21<3575::AID-NME65>3.0.CO;2-E

Oliver, J., Caicedo, M., Roubin, E., Huespe, A.E., Hernández, J.A., 2015. Continuum approach to computational multiscale modeling of propagating fracture. Comput. Methods Appl. Mech. Eng. 294, 384–427. doi:10.1016/j.cma.2015.05.012

Oliver, J., Huespe, A.E., Pulido, M.D.G., Chaves, E., 2002. From continuum mechanics to fracture mechanics: the strong discontinuity approach. Eng. Fract. 69, 113–136. doi:10.1016/S0013-7944(01)00060-1

Oliver, J., Mora, D.F., Huespe, A.E., Weyler, R., 2012. A micromorphic model for steel fiber reinforced concrete. Int. J. Solids Struct. 49, 2990–3007. doi:10.1016/j.ijsolstr.2012.05.032

Ou, Y., Tsai, M., Liu, K., Chang, K., 2012. Compressive behavior of steel-fiber-reinforced concrete with a high reinforcing index. J. Mater. Civ. Eng. 24, 207–215. doi:10.1061/(ASCE)MT.1943-5533.0000372.

Paegle, I., Fischer, G., 2016. Phenomenological interpretation of the shear behavior of reinforced Engineered Cementitious Composite beams. Cem. Concr. Compos. 73, 213–225. doi:10.1016/j.cemconcomp.2016.07.018

Paliwal, B., Hammi, Y., Moser, R.D., Horstemeyer, M.F., 2017. A three-invariant cap-plasticity damage model for cementitious materials. Int. J. Solids Struct. 108, 186–202. doi:10.1016/j.ijsolstr.2016.12.015

Panda, H.S., Sahu, S.K., Parhi, P.K., 2013. Hygrothermal effects on free vibration of delaminated woven fiber composite plates - Numerical and experimental results. Compos. Struct. 96, 502–513. doi:10.1016/j.compstruct.2012.08.057

Parisio, F., Samat, S., Laloui, L., 2015. Constitutive analysis of shale: A coupled damage plasticity approach. Int. J. Solids Struct. 75-76, 88–98. doi:10.1016/j.ijsolstr.2015.08.003

Park, K., Paulino, G.H., 2011. Cohesive Zone Models: A critical review of traction-separation relationships across fracture surfaces. Appl. Mech. Rev. 64, 060802. doi:10.1115/1.4023110

Park, S.H., Kim, D.J., Ryu, G.S., Koh, K.T., 2012. Tensile behavior of ultra high performance hybrid fiber reinforced concrete. Cem. Concr. Compos. 34, 172–184. doi:10.1016/j.cemconcomp.2011.09.009

Parrinello, F., Marannano, G., Borino, G., 2016. A thermodynamically consistent cohesive-frictional interface model for mixed mode delamination. Eng. Fract. Mech. 153, 61–79. doi:10.1016/j.engfracmech.2015.12.001

Parvaneh, S.M., Foster, C.D., 2016. On numerical aspects of different updating schedules for tracking fracture path in strain localization modeling. Eng. Fract. Mech. 152, 26–57. doi:10.1016/j.engfracmech.2015.11.011

Pasa Dutra, V.F., Maghous, S., Campos Filho, A., 2013. A homogenization approach to macroscopic strength criterion of steel fiber reinforced concrete. Cem. Concr. Res. 44, 34–45. doi:10.1016/j.cemconres.2012.10.009

Peerlings, R.H.J., 1999. Enhanced damage modelling for fracture and fatigue. PhD dissertation, Eindhoven University of Technology, Eindhoven, The Netherlands.

Peng, X., Meyer, C., 2000. A continuum damage mechanics model for concrete reinforced with randomly distributed short fibers. Comput. Struct. 78, 505–515.

Petrovitch, C.L., Nolte, D.D., Pyrak-Nolte, L.J., 2013. Scaling of fluid flow versus fracture stiffness. Geophys. Res. Lett. doi:10.1002/grl.50479

Petrovitch, C.L., Pyrak-Nolte, L.J., Nolte, D.D., 2014. Combined scaling of fluid flow and seismic stiffness in single fractures. Rock Mech. Rock Eng. 47, 1613–1623. doi:10.1007/s00603-014-0591-z

Pietruszczak, S., Haghighat, E., 2015. Modeling of deformation and localized failure in anisotropic rocks. Int. J. Solids Struct. 67-68, 93–101. doi:10.1016/j.ijsolstr.2015.04.004

Pietruszczak, S., Lydzba, D., Shao, J.F., 2002. Modelling of inherent anisotropy in sedimentary rocks. Int. J. Solids Struct. 39, 637–648. doi:10.1016/S0020-7683(01)00110-X

Pietruszczak, S., Mroz, Z., 2001. On failure criteria for anisotropic cohesive-frictional materials. Int. J. Numer. Anal. Methods Geomech. 25, 509–524. doi:10.1002/nag.141

Pike, Oskay, C., 2015a. Three-dimensional modeling of short fiber-reinforced composites with Extended Finite-Element Method. J. Eng. Mech. 1–12. doi:10.1061/(ASCE)EM.1943-7889.0001149.

Pike, Oskay, C., 2015b. XFEM modeling of short microfiber reinforced composites with cohesive interfaces. Finite Elem. Anal. Des. 106, 16–31. doi:10.1016/j.finel.2015.07.007

Planas, J., Sanz, B., Sancho, J.M., 2016. Transition from smeared to localized cracking in macro-defect-free quasibrittle structures. Procedia Struct. Integr. 2, 3676–3683. doi:10.1016/j.prostr.2016.06.457

Plé, O., Lê, T.N.H., 2012. Effect of polypropylene fiber-reinforcement on the mechanical behavior of silty clay. Geotext. Geomembranes 32, 111–116. doi:10.1016/j.geotexmem.2011.11.004

Pouya, A., Bemani Yazdi, P., Yazdi, P.B., 2015. A damage-plasticity model for cohesive fractures. Int. J. Rock Mech. Min. Sci. 73, 194–202. doi:10.1016/j.ijrmms.2014.09.024

Pros, A., Diez, P., Molins, C., 2012. Modeling steel fiber reinforced concrete: numerical immersed boundary approach and a phenomenological mesomodel for concrete-fiber interaction. Int. J. Numer. Methods Eng. 90, 65–86. doi:10.1002/nme

Qi, M., Shao, J.F., Giraud, A., Zhu, Q.Z., Colliat, J.B., 2016. Damage and plastic friction in initially anisotropic quasi brittle materials. Int. J. Plast. 82, 260–282. doi:10.1016/j.ijplas.2016.03.008

Radtke, F.K.F., Simone, A., Sluys, L.J., 2011. Apartition of unity finite element method for simulating non-linear debonding and matrix failure in thin fibre composites. Int. J. Numer. Methods Eng. 86, 453–476. doi:10.1002/nme

Radtke, F.K.F., Simone, A., Sluys, L.J., 2010. Apartition of unity finite element method for obtaining elastic properties of continua with embedded thin fibre. Int. J. Numer. Methods Eng. 84, 708–732. doi:10.1002/nme

Rasheed, M.A., Prakash, S.S., 2018. Behavior of hybrid-synthetic fiber reinforced cellular lightweight concrete under uniaxial tension – Experimental and analytical studies. Constr. Build. Mater. 162, 857–870. doi:10.1016/j.conbuildmat.2017.12.095

Reeder, J.R., 2006. 3D Mixed-Mode Delamination Fracture Criteria–An Experimentalist's Perspective James R. Reeder, in: American Society for Composites, 21st Annual Technical Conference. Dearborn, MI, US, pp. 1–19.

Reeder, J.R., 1993. A bilinear failure criterion for mixed-mode delamination. Compos. Mater. Des. 11, 303–322. doi:10.1520/stp12636s

Reeder, J.R., Crews, J.H., 1990. Mixed-mode bending method for delamination testing. AIAA J. 28, 1270–1276. doi:10.2514/3.25204

Reinhardt, H., 1984. Fracture mechanics of fictitious crack propagation in concrete. Heron 29, 3–42.

Reinhardt, H.W., Cornelissen, H. a. W., 1984. Post-peak cyclic behaviour of concrete in uniaxial tensile and alternating tensile and compressive loading. Cem. Concr. Res. 14, 263–270. doi:10.1016/0008-8846(84)90113-3

Reinhardt, H.W., Cornelissen, H.A.W., Hordijk, D.A., 1986. Tensile tests and failure analysis of concrete. J. Struct. Eng. 112, 2462–2477. doi:10.1061/(ASCE)0733-9445(1986)112:11(2462)

Reinhardt, H.W., Xu, S., 2000. A practical testing approach to determine mode II fracture energy GIIF for concrete. Int. J. Fract. 105, 107–125. doi:10.1023/A:1007649004465

Ren, G.M., Wu, H., Fang, Q., Liu, J.Z., Gong, Z.M., 2016. Triaxial compressive behavior of UHPCC and applications in the projectile impact analyses. Constr. Build. Mater. 113, 1–14. doi:10.1016/j.conbuildmat.2016.02.227

Reyes, E., Gálvez, J.C., Casati, M.J., Cendón, D.A., Sancho, J.M., Planas, J., 2009. An embedded cohesive crack model for finite element analysis of brickwork masonry fracture. Eng. Fract. Mech. 76, 1930–1944. doi:10.1016/j.engfracmech.2009.05.002

Rezakhani, R., Cusatis, G., 2014. Asymptotic expansion homogenization of discrete fine-scale models with rotational degrees of freedom for the simulation of quasi-brittle materials. J. Mech. Phys. Solids 88, 320–345. doi:10.1016/j.jmps.2016.01.001

Robert, L., Nazaret, F., Cutard, T., Orteu, J.J., 2007. Use of 3-D digital image correlation to characterize the mechanical behavior of a fiber reinforced refractory castable. Exp. Mech. 47, 761–773. doi:10.1007/s11340-007-9062-8

Robinson, M.J., 1985. The strength of Indiana limestone under multiaxial loading conditions. MS Thesis, University of Colorado, Boulder, Colo (Taken from Shreyer 1989).

Rokugo, K., Uchida, Y., Moriyama, M., Lim, S.C., 2007. Direct tensile behavior and size effect of strain-hardening fiber- reinforced cement-based composites (SHCC), in: 6th International Conference on Fracture Mechanics of Concrete and Concrete Structures.

Rots, J.G., 1991. Smeared and discrete representations of localized fracture. Int. J. Fract. 51, 45–59. doi:10.1007/BF00020852

Rudnicki, J.W., Rice, J.R., 1975. Conditions for the localization of deformation in pressure-sensitive dilatant materials. J. Mech. Phys. Solids 23, 371–394. doi:10.1016/0022-5096(75)90001-0

Russell, A.R., Chapman, M., Teh, S.H., Wiedmann, T., 2017. Cost and embodied carbon reductions in cutter soil mix walls through fibre reinforcement. Geosynth. Int. 24, 280–292. doi:10.1680/jgein.17.00001

Sadrnejad, S.A., Shakeri, S., 2017. Fabric assessment of damaged anisotropic geo-materials using the multi-laminate model. Int. J. Rock Mech. Min. Sci. 91, 90–103. doi:10.1016/j.ijrmms.2016.11.013

Saeb, S., Amadei, B., 1992. Modelling rockjoints under shear and normal loading. Int. J. Rock Mech. Min. Sci. 29, 267–278.

Salari, M.R., Saeb, S., Willam, K.J., Patchet, S.J., Carrasco, R.C., 2004. A coupled elastoplastic damage model for geomaterials. Comput. Methods Appl. Mech. Eng. 193, 2625–2643. doi:10.1016/j.cma.2003.11.013

Samaniego, E., Belytschko, T., 2005. Continuum – discontinuum modelling of shear bands. Int. J. Numer. Methods Eng. 62, 1857–1872. doi:10.1002/nme.1256

Sanborn, S.E., Prevost, J.H., 2011. Frictional slip plane growth by localization detection and the extended finite element method (XFEM). Int. J. Numer. Anal. Methods Geomech. 35, 1278–1298. doi:10.1002/nag

Sancho, J.M., Planas, J., Cendón, D.A., Reyes, E., Gálvez, J.C., 2007. An embedded crack model for finite element analysis of concrete fracture. Eng. Fract. Mech. 74, 75–86. doi:10.1016/j.engfracmech.2006.01.015

Savage, H.M., Brodsky, E.E., 2011. Collateral damage: Evolution with displacement of fracture distribution and secondary fault strands in fault damage zones. J. Geophys. Res. Solid Earth 116. doi:10.1029/2010JB007665

Sayer, M., Bektaş, N.B., Sayman, O., 2010. An experimental investigation on the impact behavior of hybrid composite plates. Compos. Struct. 92, 1256–1262. doi:10.1016/j.compstruct.2009.10.036

Schädlich, B., Schweiger, H.F., 2013. A multilaminate constitutive model accounting for anisotropic small strain stiffness. Int. J. Numer. Anal. methods Geomech. 37, 1337–1362. doi:10.1002/nag

Schauffert, E., Cusatis, G., 2011. Lattice discrete particle model for Fibre-Reinforced Concrete. I: Theory. J. Eng. Mech. 137, 826–833. doi:10.1061/(ASCE)EM

Schauffert, E.A., Cusatis, G., Pelessone, D., O'Daniel, J.L., Baylot, J.T., 2012. Lattice discrete particle model for Fiber-Reinforced Concrete. II: Tensile fracture and multiaxial loading behavior. J. Eng. Mech. 138, 834–841. doi:10.1061/(ASCE)EM.1943-7889.0000392

Scheider, I., Brocks, W., 2003. Simulation of cup - cone fracture using the cohesive model. Eng. Fract. Mech. 70, 1943–1961. doi:10.1016/S0013-7944(03)00133-4

Scholtès, L., Donzé, F.V., Khanal, M., 2011. Scale effects on strength of geomaterials, case study: Coal. J. Mech. Phys. Solids 59, 1131–1146. doi:10.1016/j.jmps.2011.01.009

Schreyer, H.L., Sulsky, D.L., Munday, L.B., Coon, M.D., Kwok, R., 2006. Elastic-decohesive constitutive model for sea ice. J. Geophys. Res. Ocean. 111, 1–21. doi:10.1029/2005JC003334

Schultz, R.A., Siddharthan, R., 2005. A general framework for the occurrence and faulting of deformation bands in porous granular rocks. Tectonophysics 411, 1–18. doi:10.1016/j.tecto.2005.07.008

Schweiger, H.F., Wiltafsky, C., Scharinger, F., Galavi, V., 2009. A multilaminate framework for modelling induced and inherent anisotropy of soils. Géotechnique 59, 87–101. doi:10.1680/geot.2008.3770

Seo, Y.S., Jeong, G.C., Kim, J.S., Ichikawa, Y., 2002. Microscopic observation and contact stress analysis of granite under compression. Eng. Geol. 63, 259–275.

Sfer, D., Carol, I., Gettu, R., Etse, G., 2002. Study of the behavior of concrete under triaxial compression. J. Eng. Mech. 128, 156–163. doi:10.1061/(ASCE)0733-9399(2002)128:2(156)

Shao, J.F., Chau, K.T., Feng, X.T., 2006a. Modeling of anisotropic damage and creep deformation in brittle rocks. Int. J. Rock Mech. Min. Sci. 43, 582–592. doi:10.1016/j.ijrmms.2005.10.004

Shao, J.F., Jia, Y., Kondo, D., Chiarelli, A.S., 2006b. A coupled elastoplastic damage model for semi-brittle materials and extension to unsaturated conditions. Mech. Mater. 38, 218–232. doi:10.1016/j.mechmat.2005.07.002

Shao, J.F., Rudnicki, J.W., 2000. Microcrack-based continuous damage model for brittle geomaterials. Mech. Mater. 32, 607–619. doi:10.1016/S0167-6636(00)00024-7

Sheldon, H.A., Barnicoat, A.C., Ord, A., 2006. Numerical modelling of faulting and fluid flow in porous rocks: An approach based on critical state soil mechanics. J. Struct. Geol. 28, 1468–1482. doi:10.1016/j.jsg.2006.03.039

Shen, W.Q., Shao, J.F., 2016a. An elastic-plastic model for porous rocks with two populations of voids. Comput. Geotech. 76, 194–200. doi:10.1016/j.compgeo.2016.03.011

Shen, W.Q., Shao, J.F., 2016b. An incremental micro-macro model for porous geomaterials with double porosity and inclusion. Int. J. Plast. 83, 37–54. doi:10.1016/j.ijplas.2016.04.002

Shi, C., Dam, A.G. Van, Mier, J.G.M. Van, Sluys, B., 2000. Crack interaction in concrete, in: Wittmann, F.H. (Ed.), Proceedings of the Material for Building and Structures. Wiley-VCH, Winheim, German, pp. 125–31.

Simo, J.C., Ju, J.W., 1987. Strain- and stress-based continuum damage models-I. formulation. Int. J. Solids Struct. 23, 821–840. doi:10.1016/0020-7683(87)90083-7

Simon, J.W., Höwer, D., Stier, B., Reese, S., Fish, J., 2017. A regularized orthotropic continuum damage model for layered composites: intralaminar damage progression and delamination. Comput. Mech. 60, 445–463. doi:10.1007/s00466-017-1416-1

Sirijaroonchai, K., El-Tawil, S., Parra-Montesinos, G., 2010. Behavior of high performance fiber reinforced cement composites under multi-axial compressive loading. Cem. Concr. Compos. 32, 62–72. doi:10.1016/j.cemconcomp.2009.09.003

Skarzyński, Tejchman, J., 2016. Experimental investigations of fracture process in concrete by means of X-ray micro-computed tomography. An Int. J. Exp. Mech. 52, 26–45. doi:10.1111/str.12168

Sloan, I.H., Womersley, R.S., 2004. Extremal Systems of Points and Numerical Integration on the Sphere. Adv. Comput. Math. 21, 107–125. doi:10.1023/B:ACOM.0000016428.25905.da

Slowik, V., Villmann, B., Bretschneider, N., Villmann, T., 2006. Computational aspects of inverse analyses for determining softening curves of concrete. Comput. Methods Appl. Mech. Eng. 195, 7223–7236. doi:10.1016/j.cma.2005.04.021

Soriano, I., Ibraim, E., Andò, E., Diambra, A., Laurencin, T., Moro, P., Viggiani, G., 2017. 3D fibre architecture of fibre-reinforced sand. Granul. Matter 19, 75. doi:10.1007/s10035-017-0760-3

Souley, M., Lopez, P., Boulon, M., Thoraval, A., 2015. Experimental Hydromechanical Characterization and Numerical Modelling of a Fractured and Porous Sandstone. Rock Mech. Rock Eng. 48, 1143–1161. doi:10.1007/s00603-014-0626-5

Soulioti, D. V, Barkoula, N.M., Paipetis, A., Matikas, T.E., 2011. Effects of fibre geometry and volume fraction on the flexural behaviour of steel-fibre reinforced concrete. Strain 47, 535–541. doi:10.1111/j.1475-1305.2009.00652.x

Spada, A., Giambanco, G., Rizzo, P., 2009. Damage and plasticity at the interfaces in composite materials and structures. Comput. Methods Appl. Mech. Eng. 198, 3884–3901. doi:10.1016/j.cma.2009.08.024

Spiezia, N., Salomoni, V.A., Majorana, C.E., 2016. Plasticity and strain localization around a horizontal wellbore drilled through a porous rock formation. Int. J. Plast. 78, 114–144. doi:10.1016/j.ijplas.2015.10.013

Srikar, G., Anand, G., Suriya Prakash, S., 2016. A Study on residual compression behavior of structural Fiber Reinforced Concrete exposed to moderate temperature using Digital Image Correlation. Int. J. Concr. Struct. Mater. 10, 75–85. doi:10.1007/s40069-016-0127-x

Stang, H., Shah, S.P., 1986. Failure of fibre-reinforced composites by pull-out fracture. J. Mater. Sci. 21, 953–957. doi:10.1007/BF01117378

Suárez, F., Gálvez, J., Cendón, D., 2018. A material model to reproduce mixed-mode fracture in concrete. Fatigue Fract. Eng. Mater. Struct. 223–238. doi:10.1111/ffe.12898

Swoboda, G., Yang, Q., 1999a. An energy-based damage model of geomaterials - I. Formulation and numerical results. Int. J. Solids Struct. 36, 1719–1734. doi:10.1016/S0020-7683(98)00036-5

Swoboda, G., Yang, Q., 1999b. An energy-based damage model of geomaterials - II. Deduction of damage evolution laws. Int. J. Solids Struct. 36, 1735–1755. doi:10.1016/S0020-7683(98)00164-4

Syroka-Korol, E., Tejchman, J., Mróz, Z., 2013. FE calculations of a deterministic and statistical size effect in concrete under bending within stochastic elasto-plasticity and non-local softening. Eng. Struct. 48, 205–219. doi:10.1016/j.engstruct.2012.09.013

Tang, C.-S., Wang, D.-Y., Cui, Y.-J., Shi, B., Li, J., 2016. Tensile Strength of Fiber-Reinforced Soil. J. Mater. Civ. Eng. 28, 04016031. doi:10.1061/(asce)mt.1943-5533.0001546

Tang, T., Shah, S.P., Ouyang, C., 1992. Fracture Mechanics and Size Effect of concrete in tension. J. Struct. Eng. 118, 3169–3185.

Tejchman, J., Gorski, J., 2008. Deterministic and statistical size effect during shearing of granular layerwithin amicro-polar hypoplasticity. Int. J. Numer. Anal. Methods Geomech. 32, 189–213. doi:10.1002/nag

Teng, J.G., Yu, T., Wong, Y.L., Dong, S.L., 2007. Hybrid FRP-concrete-steel tubular columns: Concept and behavior. Constr. Build. Mater. 21, 846–854. doi:10.1016/j.conbuildmat.2006.06.017

Tengattini, A., Das, A., Nguyen, G.D., Viggiani, G., Hall, S.A., Einav, I., 2014. A thermomechanical constitutive model for cemented granular materials with quantifiable internal variables. Part I - Theory. J. Mech. Phys. Solids 70, 382–405. doi:10.1016/j.jmps.2014.05.022

Thomas, J., Ramaswamy, A., 2007. Mechanical Properties of Steel Fiber-Reinforced Concrete. J. Mater. Civ. Eng. 19, 385–392. doi:10.1061/(ASCE)0899-1561(2007)19:5(385)

Tordesillas, A., Shi, J., Tshaikiwsky, T., 2011. Stress–dilatancy and force chain evolution. Int. J. Numer. Anal. Methods Geomech. 35, 264–292. doi:10.1002/nag

Tran, H.D., Sulsky, D.L., Schereyer, H.L., 2015. An anisotropic elastic-decohesive constitutive relation for sea ice. Int. J. Numer. Anal. Methods Geomech. 32, 988–1013. doi:10.1002/nag

Tvergaard, V., Hutchinson, J.W., 1993. The influence of plasticity on mixed mode interface toughness. J. Mech. Phys. Solids 41, 1119–1135. doi:10.1016/0022-5096(93)90057-M

Unger, J.F., Eckardt, S., Könke, C., 2011. A mesoscale model for concrete to simulate mechanical failure. Comput. Concr. 8. doi:10.12989/cac.2011.8.4.401

Unteregger, D., Fuchs, B., Hofstetter, G., 2015. A damage plasticity model for different types of intact rock. Int. J. Rock Mech. Min. Sci. 80, 402–411. doi:10.1016/j.ijrmms.2015.09.012

Vachaparampil, A., Ghassemi, A., 2017. Failure characteristics of three shales under true-triaxial compression. Int. J. Rock Mech. Min. Sci. 100, 151–159. doi:10.1016/j.ijrmms.2017.10.018

van den Bosch, M.J., Schreurs, P.J.G., Geers, M.G.D., 2008. Identification and characterization of delamination in polymer coated metal sheet. J. Mech. Phys. Solids 56, 3259–3276. doi:10.1016/j.jmps.2008.07.006

van Mier, J.G.M., 1986. Fracture of Concrete Under Complex Stress. Heron 31, 1–90.

van Mier, J.G.M., Schlangen, E., 1993. An experimental and numerical study of mode I (tensile) and mode II (shear) fracture in concrete. J. Mech. Behav. Mater. 4, 179–190.

van Vliet, M.R.A., van Mier, J.G.M., 2000. Experimental investigation of size effect in concrete and sandstone under uniaxial tension. Eng. Fract. Mech. 65, 165–188. doi:10.1016/s0013-7944(99)00114-9

Veiskarami, M., Tamizdoust, M.M., 2017. Bifurcation Analysis in Sands under True Triaxial Conditions with Coaxial and Noncoaxial Plastic Flow Rules. J. Eng. Mech. 143, 1–12. doi:10.1061/(ASCE)EM.1943-7889.0001344.

Voyiadjis, G.Z., Taqieddin, Z.N., Kattan, P.I., 2008. Anisotropic damage-plasticity model for concrete. Int. J. Plast. 24, 1946–1965. doi:10.1016/j.ijplas.2008.04.002

Voyiadjis, G.Z., Woody Ju, J.W., Chaboche, J.L., 1998. Damage mechanics in engineering materials. Elsevier Science Ltd.

Vu, V.D., Mir, A., Nguyen, G.D., Sheikh, A.H., 2017. A thermodynamics-based formulation for constitutive modelling using damage mechanics and plasticity theory. Eng. Struct. 143, 22–39. doi:10.1016/j.engstruct.2017.04.018

Wang, J.G., Ichikawa, Y., Leung, C.F., 2003. A constitutive model for rock interfaces and joints. Int. J. Rock Mech. Min. Sci. 40, 41–53. doi:10.1016/S1365-1609(02)00113-2

Wells, G.N., Sluys, L.J., 2000. Application of embedded discontinuities for softening solids. Eng. Fract. Mech. 65, 263–281. doi:10.3390/molecules14125281

Wiebicke, M., Andò, E., Herle, I., Viggiani, G., 2017. On the metrology of interparticle contacts in sand from x-ray tomography images. Meas. Sci. Technol. 28, 124007. doi:10.1088/1361-6501/aa8dbf

Wille, K., El-Tawil, S., Naaman, A.E., 2014. Properties of strain hardening ultra high performance fiber reinforced concrete (UHP-FRC) under direct tensile loading. Cem. Concr. Compos. 48, 53–66. doi:10.1016/j.cemconcomp.2013.12.015

Wille, K., Kim, D.J., Naaman, A.E., 2011. Strain-hardening UHP-FRC with low fiber contents. Mater. Struct. Constr. 44, 583–598. doi:10.1617/s11527-010-9650-4

Winkler, B., Hofstetter, G., Niederwanger, G., 2001. Experimental verification of a constitutive model for concrete cracking. Proc. Inst. Mech. Eng. Part L J. Mater. Des. Appl. 215, 75–86. doi:10.1177/146442070121500202

Wong, T., Baud, P., Klein, E., 2001. Localized failure modes in a compactant porous rock. Geophys. Res. Lett. 28, 2521–2524.

Wong, T.F., Baud, P., 2012. The brittle-ductile transition in porous rock: A review. J. Struct. Geol. 44, 25–53. doi:10.1016/j.jsg.2012.07.010

Wong, T.-F., David, C., Zhu, W., 1997. The transition from brittle faulting to cataclasic flow in porous sandstones:Mechanical deformation. J. Geophys. Res. 102, 3009–3025. doi:10.1029/96JB03282

Wu, Z., Yin, J., 2003. Fracturing behaviors of FRP-strengthened concrete structures. Eng. Fract. Mech. 70, 1339–1355. doi:10.1016/S0013-7944(02)00100-5

Xenos, D., Grégoire, D., Morel, S., Grassl, P., 2015. Calibration of nonlocal models for tensile fracture in quasi-brittle heterogeneous materials. J. Mech. Phys. Solids 82, 48–60. doi:10.1016/j.jmps.2015.05.019

Xie, J., Elwi, A.E., Macgregor, J.G., 1995. Mechanical properties of three high-Strength concretes containing silica fume. ACI Mater. J. 2, 135–143.

Xie, N., Zhu, Q.Z., Shao, J.F., Xu, L.H., 2012. Micromechanical analysis of damage in saturated quasi brittle materials. Int. J. Solids Struct. 49, 919–928. doi:10.1016/j.ijsolstr.2011.12.006

Xie, N., Zhu, Q.Z., Xu, L.H., Shao, J.F., 2011. A micromechanics-based elastoplastic damage model for quasi-brittle rocks. Comput. Geotech. 38, 970–977. doi:10.1016/j.compgeo.2011.07.014

Yaghoobi, A., Chorzepa, M.G., 2015. Meshless modeling framework for fiber reinforced concrete structures. Comput. Struct. 161, 43–54. doi:10.1016/j.compstruc.2015.08.015

Yan, X., Du, S., Wang, D., 1991. An engineering method of determining the delamination fracture toughness of composite laminates. Eng. Fract. Mech. 39, 623–627.

Yan, Z.G., Zhang, Y., Woody Ju, J., Chen, Q., Zhu, H.H., 2019. An equivalent elastoplastic damage model based on micromechanics for hybrid fiber-reinforced composites under uniaxial tension. Int. J. Damage Mech. 28, 79–117. doi:10.1177/1056789517744425

Yazdani, N., Beneberu, E., Riad, M., 2019. Nondestructive evaluation of FRP-concrete interface bond due to surface defects. Adv. Civ. Eng. 2019, 1–10. doi:10.1155/2019/2563079

Yeo, I.W., de Freitas, M.H., Zimmerman, R.W., 1998. Effect of shear displacement on the aperture and permeability of a rock fracture. Int. J. Rock Mech. Min. Sci. doi:10.1016/S0148-9062(98)00165-X

Yetimoglu, T., Salbas, O., 2003. A study on shear strength of sands reinforced with randomly distributed discrete fibers. Geotext. Geomembranes 21, 103–110. doi:10.1016/S0266-1144(03)00003-7

Yin, Z.Y., Chang, C.S., 2013. Stress–dilatancy behavior for sand under loading and unloading conditions. 2International J. Numer. Anal. Methods Geomech. 37, 855–870. doi:10.1002/nag

Yin, Z.Y., Zhao, J., Hicher, P.Y., 2014. A micromechanics-based model for sand-silt mixtures. Int. J. Solids Struct. 51, 1350–1363. doi:10.1016/j.ijsolstr.2013.12.027

Yoo, D.Y., Kim, S.W., Park, J.J., 2017. Comparative flexural behavior of ultra-high-performance concrete reinforced with hybrid straight steel fibers. Constr. Build. Mater. 132, 219–229. doi:10.1016/j.conbuildmat.2016.11.104

Yoshinaka, R., Yoshida, J., Shimizu, T., Arai, H., Arisaka, S., 1993. Scale effect in shear strength and deformability of rock joints, in: In: Pinto Da Chunha A (ed) Proc Symp Scale Effects in Rock Masses 93. Libson, Portugal. Balkema, Rotterdam, pp. 143–149.

Yu, M.H., Zan, Y.W., Zhao, J., Yoshimine, M., 2002. A Unified Strength criterion for rock material. Int. J. Rock Mech. Min. Sci. 39, 975–989. doi:10.1016/S1365-1609(02)00097-7

Yuan, Z., Fish, J., 2016. Are the cohesive zone models necessary for delamination analysis? Comput. Methods Appl. Mech. Eng. 310, 567–604. doi:10.1016/j.cma.2016.06.023

Zeng, T., Shao, J.F., Xu, W.Y., 2015. A micromechanical model for the elastic-plastic behavior of porous rocks. Comput. Geotech. 70, 130–137. doi:10.1016/j.compgeo.2015.08.001

Zhang, H., Huang, Y.J., Yang, Z.J., Xu, S.L., Chen, X.W., 2018. A discrete-continuum coupled finite element modelling approach for fibre reinforced concrete. Cem. Concr. Res. 106, 130–143. doi:10.1016/j.cemconres.2018.01.010

Zhang, J., Ju, X., 2011. Investigation on stress-crack opening relationship of engineered cementitious composites using inverse approach. Cem. Concr. Res. 41, 903–912. doi:10.1016/j.cemconres.2011.04.010

Zhang, Y., Lackner, R., Zeiml, M., Mang, H.A., 2015. Strong discontinuity embedded approach with standard SOS formulation: Element formulation, energy-based crack-tracking strategy, and validations. Comput. Methods Appl. Mech. Eng. 287, 335–366. doi:10.1016/j.cma.2015.02.001

Zhao, L.-Y., Zhu, Q.-Z., Shao, J.-F., 2018. A micro-mechanics based plastic damage model for quasi-brittle materials under a large range of compressive stress. Int. J. Plast. 100, 156–176. doi:10.1016/j.ijplas.2017.10.004

Zhou, A., Büyüköztürk, O., Lau, D., 2017. Debonding of concrete-epoxy interface under the coupled effect of moisture and sustained load. Cem. Concr. Compos. 80, 287–297. doi:10.1016/j.cemconcomp.2017.03.019

Zhu, Q.Z., Shao, J.F., 2015. A refined micromechanical damage-friction model with strength prediction for rock-like materials under compression. Int. J. Solids Struct. 60, 75–83. doi:10.1016/j.ijsolstr.2015.02.005

Zhu, Q.Z., Zhao, L.Y., Shao, J.F., 2016. Analytical and numerical analysis of frictional damage in quasi brittle materials. J. Mech. Phys. Solids 92, 137–163. doi:10.1016/j.jmps.2016.04.002

Zhu, Y., 2017. A micromechanics-based damage constitutive model of porous rocks. Int. J. Rock Mech. Min. Sci. 91, 1–6. doi:10.1016/j.ijrmms.2016.11.005

Ziegler, H., 1983. An introduction to Thermomechanics, 1st ed. North Holland, Amsterdam.

Zreid, I., Kaliske, M., 2016. An implicit gradient formulation for microplane Drucker-Prager plasticity. Int. J. Plast. 83, 252–272. doi:10.1016/j.ijplas.2016.04.013

Appendix A

Modelling jointed rock mass as a continuum with an embedded cohesive-frictional model

Le, L.A., Nguyen, G.D., Bui, H.H., Sheikh, A.H., Kotousov, A., Khanna, A., 2017. Modelling jointed rock mass as a continuum with an embedded cohesive-frictional model. *Engineering Geology* 228, 107–120. doi:10.1016/j.enggeo.2017.07.011

Statement of Authorship

Title of Paper	Modelling jointed rock mass as a continuum with an embedded cohesive-frictional model
Publication Status	☑ Published ☐ Accepted for Publication ☐ Submitted for Publication ☐ Unpublished and Unsubmitted w ork w ritten in manuscript style
Publication Details	Le, L.A., Nguyen, G.D., Bui, H.H., Sheikh, A.H., Kotousov, A., Khanna, A., 2017. Modelling jointed rock mass as a continuum with an embedded cohesive-frictional model. Eng. Geol. 228, 107–120. doi:10.1016/j.enggeo.2017.07.011

Principal Author

Name of Principal Author (Candidate)	Linh A. Le		
Contribution to the Paper	Developed the cohesive-frictional model including technical details, implementation and verification. Performed numerical analysis and model validation. Wrote and revised the manuscript.		
Overall percentage (%)	70		
Certification:	This paper reports on original research I conducted during the period of my Higher Degree by Research candidature and is not subject to any obligations or contractual agreements with a third party that would constrain its inclusion in this thesis. I am the primary author of this paper.		
Signature		Date	26/03/2019

Co-Author Contributions

By signing the Statement of Authorship, each author certifies that:

i. the candidate's stated contribution to the publication is accurate (as detailed above);

ii. permission is granted for the candidate in include the publication in the thesis; and

iii. the sum of all co-author contributions is equal to 100% less the candidate's stated contribution.

Name of Co-Author	Giang D. Nguyen		
Contribution to the Paper	Developed the general framework for the double-scale approach and generic form of the cohesive-frictional model. Supervised the technical developments. Evaluated & revised the manuscript.		
Signature		Date	27 / 03 / 2019

Name of Co-Author	Ha H. Bui		
Contribution to the Paper	Developed the generic form of the cohesive-frictional model & contributed to the development of the double-scale approach in generic form. Supervised the technical developments. Evaluated & revised the manuscript.		
Signature		Date	27 / 03 / 2019

Name of Co-Author	Abdul Hamid Sheikh		
Contribution to the Paper	Supervised the technical developments. Evaluated & revised the manuscript.		
Signature		Date	28/03/2019

Name of Co-Author	Andrei Kotousov		
Contribution to the Paper	Supervised the technical developments. Evaluated & revised the manuscript.		
Signature		Date	27/03/2019

Name of Co-Author	Aditya Khanna		
Contribution to the Paper	Evaluated & revised the manuscript.		
Signature		Date	27/03/2019

Engineering Geology 228 (2017) 107–120

Contents lists available at ScienceDirect

Engineering Geology

journal homepage: www.elsevier.com/locate/enggeo

Modelling jointed rock mass as a continuum with an embedded cohesive-frictional model

Linh A. Le[a], Giang D. Nguyen[a,*], Ha H. Bui[b], Abdul H. Sheikh[a], Andrei Kotousov[c], Aditya Khanna[c]

[a] School of Civil, Environmental and Mining Engineering, The University of Adelaide, Adelaide, SA 5005, Australia
[b] Department of Civil Engineering, Monash University, Clayton, VIC 3800, Australia
[c] School of Mechanical Engineering, The University of Adelaide, Adelaide, SA 5005, Australia

ARTICLE INFO

Keywords:
Jointed rock mass
Constitutive modelling
Double scale
Coupled damage-plasticity
Cohesive model

ABSTRACT

The mechanical and hydraulic properties of a jointed rock mass are strongly affected by the characteristics of joints within the intact rock mass. In this study, a constitutive model for jointed rock masses is developed by incorporating the contributions of both the joint and its surrounding rock mass. The behaviour of the joint is represented by a new coupled damage-plasticity cohesive-frictional model taking into account its dilation evolution and the reduction of both strength and stiffness, while the surrounding rock behaviour is assumed to behave elastically. The interactions between the joint and the surrounding rock are described by a set of kinematic enhancements and internal equilibrium equations across the interface of the joint. The formulation of the proposed model is presented along with its implementation algorithms and validation with experimental data. The enhanced kinematics facilitates the incorporation of both behaviour and orientation of the joint, together with the size and behaviour of the surrounding rock, allowing capturing key characteristics of jointed rock mass responses under mixed-mode loading conditions at different spatial scales.

1. Introduction

The mechanical and hydraulic properties of a rock mass are strongly affected by the presence of discontinuities such as joints, fractures or faults. The effects of these features, generally referred to as joints, can be very significant in many problems in geology or geophysics, mining or petroleum engineering, hydrogeology and waste management, therefore, it is important to be able to locate and characterise them remotely within a rock mass using geophysical methods (Cook, 1992). In general, the behaviour of a rock mass is discontinuous, anisotropic, inhomogeneous and inelastic (Harrison and Hudson, 2000). There are two approaches which are normally used to model these features. The first approach describes joints or system of joints as aggregate effects within a representative volume element to come up with a practicable continuum model. Some studies following this approach can be listed as Cai and Horii (1992), Lee (1998), Chalhoub and Pouya (2008), Martinez et al. (2012). The other approach treats joints as discrete entities. Studies which incorporated this approach include Plesha (1987), Haberfield and Johnston (1994), Huang et al. (2002), Grasselli and Egger (2003), Mihai and Jefferson (2013), Schreyer and Sulsky (2016). One of the advantages of treating joints as discrete entities is that the mechanical responses of components (i.e. intact rock, joints) and the interactions between them are taken into account in details within a constitutive model. This would be very useful for further developing those constitutive models to continuum models. The current work utilises the second approach as it allows more realistic description of various deformation effects and mechanisms.

It is well recognised that understanding the mechanical behaviour of rock joints plays a very important role in designing rock structures such as underground excavations, rock slopes (Singh and Rao, 2005). As reported in many studies (Bandis et al., 1983; Desai and Fishman, 1991; Jing, 1990), the deformation behaviour of rock joints is complicated. Under shear displacements, rock joints would exhibit dilatant behaviour which is strongly associated with the development of shear and normal stresses across the joints plane. Several models were proposed to simulate the shear stress–displacement relationships of rock joints with combinations of empirically based relations and mechanical formulations. For example, Patton (1966) and Ladanyi and Archambault (1969) were among the first to develop empirical shear strength formulations for rock joints accounting for the effect of its roughness nature. These roughness factors were then generalised as joint roughness coefficient (JRC) in the commonly used empirical shear strength model by Barton and Choubey (1977). This empirical model is capable of predicting the shear strength under the normal compression

* Corresponding author.
E-mail address: g.nguyen@adelaide.edu.au (G.D. Nguyen).

http://dx.doi.org/10.1016/j.enggeo.2017.07.011
Received 14 February 2017; Received in revised form 19 July 2017; Accepted 28 July 2017
Available online 02 August 2017

but the progressive development of stresses during shearing is missing. To address this shortcoming, Li et al. (1989) proposed an elasto-plastic model to link the normal stress and the shear stress of a contact unit in the rough crack surface. Igcacio et al. (1997) presented a normal/shear cracking model for quasi-brittle materials. Su et al. (2004) developed a continuum-level phenomenological interface constitutive model which accounts for both reversible elastic behaviour, as well as irreversible inelastic separation-sliding deformations prior to failure for rock joints. Although the joint behaviour can be mimicked in these models, the interactions between the joint and the bulk material are totally neglected. This would hinder the model's extension for modelling the rock mass where joints are distributed within and interact with the surrounding rock. Wang et al. (2003) proposed a constitutive model with an ellipse yield function and associated flow rules for the rock joint. In this model, a shape function is used along with the yield function to incorporate the shear anisotropy of the joints. However, this might not be applicable for modelling in situ joints where anisotropy usually is not of interest and hard to characterise. Recently, in 2016, Schreyer and Sulsky (2016) proposed a nonlinear elasticity model where the joint widths are taken into account to enable the modelling of either pre-existing gaps or the formation of new joints. Nonetheless, in this research, three separate yield surfaces and separate softening/hardening rules were used to capture key characteristics of the joints. The discontinuity at apexes where these three yield surfaces intersect might bring difficulties and require treatments in the implementation. In addition, only joints that are parallel to the sides of square finite elements can be taken into account in this approach (Schreyer and Sulsky, 2016).

Glossary

$\boldsymbol{\sigma}$	Average stress vector
$\boldsymbol{\sigma}_o$	Stress vector of the material outside the joint
$\boldsymbol{\sigma}_i$	Stress vector of the material inside the joint
σ_n	Constant normal stress in shear test
σ_c	Compression strength of the material
$\boldsymbol{\varepsilon}$	Average strain vector
$\boldsymbol{\varepsilon}_o$	Strain vector of the material outside the joint
$\boldsymbol{\varepsilon}_i$	Strain vector of the material inside the joint
ε	Tolerance of the traction continuity condition
$\mathbf{a}_o$	Elastic stiffness matrix of the bulk material
$[\![\mathbf{u}]\!]$	Displacement jump vector of the joint in global coordinate system
$[\![\dot{u}_c]\!]$	Displacement jump vector of the joint in local coordinate system
u_n	Total normal displacement jump of the joint in local coordinate system
u_n^p	Plastic normal displacement jump of the joint in local coordinate system
u_s	Total shear displacement jump of the joint in local coordinate system
u_s^p	Plastic shear displacement jump of the joint in local coordinate system
u_p	Effective plastic factor
h	Width of the joint
H	Characterised length of the joint
Ω_o	Volume of the bulk material outside the joint
Ω_i	Volume of the joint
η	Volume fracture of the joint
Γ_i	Area of the joint
$\mathbf{t}_i$	Traction vector of the joint in global coordinate system
$\mathbf{t}_c$	Traction vector of the joint in local coordinate system
$\mathbf{t}_c^{trial}$	Trial traction vector of the joint in local coordinate system
t_n	Normal traction of the joint in local coordinate system
t_s	Shear traction of the joint in local coordinate system
τ_y	Shear strength in shear test
$\mathbf{K}^t$	Inelastic tangent stiffness matrix of the joint in global coordinate system
$\mathbf{K}_c^E$	Elastic tangent stiffness matrix of the joint in local coordinate system
$\mathbf{K}_c^t$	Inelastic tangent stiffness matrix of the joint in local coordinate system
K_n	Elastic normal stiffness of the joint in local coordinate system
K_s	Elastic shear stiffness of the joint in local coordinate system
D	Damage variable of the joint
f_n	Tension strength of the material
m	Parameter controlling the curvature of the initial yield surface
μ_0	Parameter controlling the inclination of the initial yield surface
μ	Parameter controlling the inclination of the failure yield surface
ϕ	Internal friction angle
λ	Factor of proportionality in flow rule
y	The yield surface of the cohesive model
g	The potential function of cohesive model's non-associated flow rule
δ_0	Displacement corresponding to shear strength
α	Parameter controlling energy dissipation
γ	Parameter controlling the dilation during the shear
E	Young's modulus of the bulk material
G_{comp}	Fracture energy computed from the model
G_f	Fracture energy measured from the experiment
r	Residual stress of the traction continuity
n	Normal vector of the joint face in Voight notation
ν	Poisson's ratio of the bulk material
R	Transformation matrix from global to local coordinate system

One of the difficulties in analysing jointed rock masses is its diversity in natural characteristics. Because rock mass is a natural material, rock joints are formed under different stress states and continuous loadings from dynamic movements of the upper crust of the Earth such as tectonic movements, earthquakes, glaciation cycles. This complex and long history of formation makes the in situ characteristics of rock joints hard to be determined. Experiments on rock joints are mostly based on small specimens corresponding to a certain location within the rock mass. The geometry and roughness of the joints are usually presented by the joint roughness coefficient (JRC) which is often estimated by visibly comparing to standard profiles (Barton and Choubey, 1977; Li and Zhang, 2015). However, it is widely recognised that the mechanical behaviour of rock joints can vary as a function of scale, although the extent is arguable (Tatone and Grasselli, 2013, 2009).

In the past decades, many studies have been carried out to characterise the effects of the scale on the mechanical behaviour of jointed rock masses. A relatively comprehensive review of statistical scale effects on jointed rock behaviour from previous studies is presented in the work done by Bahaaddini et al. (2014). Bahaaddini et al. (2014, 2013) also used the discrete element method (DEM) to investigate the shear behaviour and statistical scale effects of the rock joints. Although such explicit simulations are good for understanding the mechanical mechanisms of the joints, they might need several millions of particles for modelling a rock mass and its joints, and hence are too expensive for practical purposes. Phenomenological approaches could be a good choice to deal with this difficulty by using curve fitting-based techniques to yield similar results by experiments or to obtain empirical equations for a certain experimental data. However, focusing on one particular path with a precise matching to experimental data cannot always warrant a success in light of the uncertainty associated with both the properties of in situ joints and the variety of stress paths

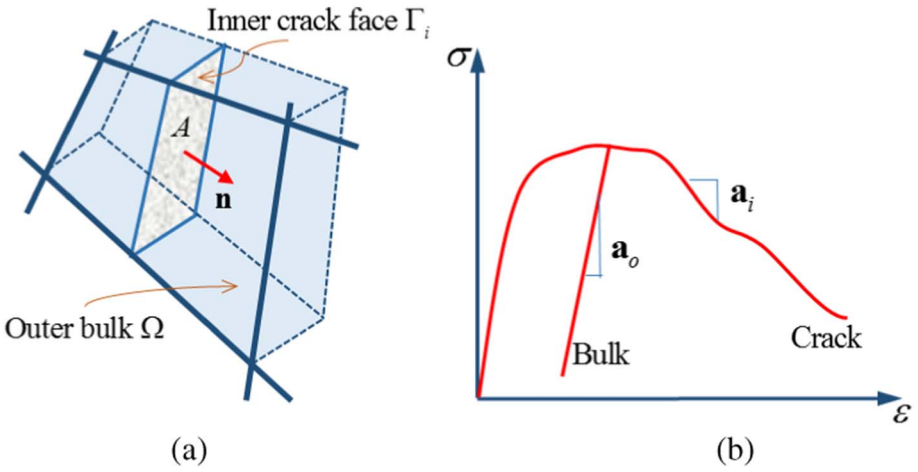

Fig. 1. (a) Illustration of a volume element Ω containing a discontinuity representing the joint, and (b) corresponding material responses inside and outside the localisation zone (after Nguyen et al., 2012).

inherent in most problems (Schreyer and Sulsky, 2016). On the other hand, most (if not all) of research works on jointed rock masses focuses on statistical size effects of the joints due to randomness of strength, while the deterministic size effects due to localised failure (Bazant, 2000; Bažant and Yu, 2009) of the joint in a rock mass is usually missing or not addressed at length. Hence, in this research, to deal with the uncertainty of in situ joints, and deterministic size effects due to localised failure of a jointed rock mass an approach that includes essential characteristics of both the joints and the surrounding intact rock is developed. These include frictional effects, degradation of both strength and stiffness, and joint dilation evolution under asperity damage, together with the size of the rock mass containing the joint. These characteristics can provide a model with sufficient flexibility to cover possible responses of joints in a variety of geological settings.

The review presented above shows the importance of both mechanical behaviour and geometrical details of joints as well as surrounding intact rocks in governing the responses of a jointed rock mass, together with the challenges in incorporating them in a computationally efficient approach for practical purposes. In this study, we adopt a balanced approach in which only essential details, including mechanical and geometrical features of both the joint and the surrounding intact rock, are included in a kinematically enriched constitutive model. The enhanced kinematics provides more flexibility to the constitutive model for accommodating both the mechanical behaviour and geometrical details at two scales: the scale of the joint, and the scale of the rock mass containing the joint. The terminology “double-scale” is hence adopted as it reflects the key characteristics of the proposed approach in bridging the two spatial scales, and facilitating the analysis of a jointed rock mass at the constitutive (material) level. While it is reasonable to assume elastic behaviour for the surrounding intact rock, the joint responses are represented by a new damage-plasticity cohesive-frictional model. The proposed cohesive model uses only a single combined yield-failure surface, which gradually transforms from initial yield to ultimate failure with residual frictional strength, under the evolution of asperity damage. This enables the modelling of a joint at different stages of deformation under mixed-mode loading conditions. In particular, key inelastic responses including residual deformations, strength and stiffness reduction, evolution of dilation due to asperity damage, and unilateral behaviour upon unloading-reloading are accounted for.

The paper is organised as follows. Section 2 presents the double-scale framework with keys features in both formulation and implementation. Section 3 introduces the proposed cohesive model for mixed-mode loading of rock joints. Section 4 presents the implementation of the cohesive model into the overall double-scale framework to obtain a constitutive relation for a jointed rock mass. Numerical examples to validate the model are provided in Section 5 followed by conclusions in Section 6.

2. A double-scale approach

In a rock mass, the size of the rock mass is in the order of meters while the size of a joint width usually is in the order of millimetres, therefore the joints can be treated as a weak plane of rubble between two beds of rock (Schreyer and Sulsky, 2016). Thus, from the modelling point of view, the joint can be considered as a very thin band surrounded by a bulk material of intact rock. Although the mechanical behaviour of the joint is nonlinear and different from the responses of the bulk material, all these features contribute to the overall stress-strain relation of the jointed rock mass. Hence, it is necessary for a reliable constitutive model to have a coupling between responses of the joint and the bulk, so that the behaviour of jointed rock mass can be represented appropriately. To achieve this, the double-scale modelling framework developed by Nguyen et al. (2012, 2014a, 2016) is employed. The key idea of this framework is to enhance the constitutive behaviour with an additional kinematics mode and a corresponding length scale related to the width of the localisation zone to correctly describe localised failure of materials (Nguyen et al., 2014a). The interaction between the joint and the surrounding rock is described by the internal equilibrium conditions across the interface of the joint. By doing so, the two scales including the behaviour of the joint and the overall stress-strain relation of the jointed rock mass are incorporated into a single constitutive model. In other words, the framework connects these two scales to obtain a constitutive relationship at the macro level in which inelastic behaviour is governed by the mechanisms of joint damage at a lower scale. This explains why the terminology “double-scale” is used for this model, as stated in the earlier works by Nguyen et al. (2012, 2014a, 2016). This section briefly presents the double-scale constitutive framework specifically tailored for accommodating the cohesive model; more details are available in Nguyen et al. (2012, 2014a). It should be noted that because the behaviour of the material is assumed to be rate-independent, the time derivative can be used as increments in the computational procedure.

Without losing generality, the constitutive model is developed for a material volume Ω comprising of an inner joint Ω_i and an outer bulk material Ω_o as shown in Fig. 1. The joint may be expressed in terms of its area Γ_i and thickness h (i.e. $\Omega_i = h\Gamma_i$) where the joint thickness is usually very small ($h \to 0$) compared to the rock mass as mentioned earlier. The area of the joint in the form of a damage localisation band and the normal vector of this area are denoted as A ($=\Gamma_i$) and n. The stress and strain vectors of the joint are denoted as $\sigma_i$and ε_i, respectively. The stress and strain vectors of the outer bulk material are denoted as $\sigma_o$and ε_o, while the volume-averaged overall stress and strain vectors of this volume element are σ and ε, respectively. Following the Voight notations, these above quantities are expressed in the global coordinate system as:

$$\boldsymbol{\sigma} = [\sigma_{11}\ \sigma_{22}\ \sigma_{33}\ \sigma_{12}\ \sigma_{23}\ \sigma_{31}]^{\mathrm{T}} \quad ; \quad \boldsymbol{\varepsilon} = [\varepsilon_{11}\ \varepsilon_{22}\ \varepsilon_{33}\ \varepsilon_{12}\ \varepsilon_{23}\ \varepsilon_{31}]^{\mathrm{T}}$$
$$\mathbf{n} = \begin{bmatrix} n_1 & 0 & 0 & n_2 & 0 & n_3 \\ 0 & n_2 & 0 & n_1 & n_3 & 0 \\ 0 & 0 & n_3 & 0 & n_2 & n_1 \end{bmatrix}^{\mathrm{T}} \tag{1}$$

Fig. 1 also illustrates the stress-strain response of the inner rock joint and the outer bulk material. From the figure, it can be seen that the joint is considered to be inelastic while the outer bulk is considered to undergo elastic unloading. This is the typical behaviour observed in brittle/quasi-brittle materials when a crack appears within the material. Since the displacements at the two sides of a joint will be different during loading of the rock mass, there will be relative displacements between these two sides. It was these relative displacements that have a significant impact on the behaviour of the joint, leading to an influence on the overall responses of the considered volume element. Thus, in order to link the behaviour of the joint to the overall stress-strain relation of the jointed rock mass, the strain rate of the joint having a infinitesimally small thickness ($h \to 0$) can be expressed in terms of the strain rate of the bulk material and a kinematically enhanced strain rate component which can further be approximated as (Kolymbas, 1981, 2009 and Vardoulakis et al., 1978):

$$\dot{\boldsymbol{\varepsilon}}_{\mathrm{i}} = \dot{\boldsymbol{\varepsilon}}_{\mathrm{o}} + \frac{1}{h}\mathbf{n}[\![\dot{\mathbf{u}}]\!] \approx \frac{1}{h}\mathbf{n}[\![\dot{\mathbf{u}}]\!] \tag{2}$$

where $[\![\dot{\mathbf{u}}]\!] = [\dot{u}_1\ \ \dot{u}_2\ \ \dot{u}_3]^T$ is the rate of relative displacements between two sides of the joint in the global coordinate system. It should be noted that the rate of the relative displacement is denoted as $[\![\dot{\mathbf{u}}]\!]$ to differentiate itself from absolute displacement rates of two joint sides which are used for normal strain computation. In the above equation, the first term $\dot{\boldsymbol{\varepsilon}}_o$ can be ignored as it is very small compared to the second term since $h \to 0$. The contribution of the joint and the bulk material to the overall strain of the jointed rock mass is formulated based on their volume fractions by using the rule of mixtures. Following this rule, the overall strain rate of the jointed rock mass can be expressed in terms of the inner and outer strain rates:

$$\dot{\boldsymbol{\varepsilon}} = \eta\dot{\boldsymbol{\varepsilon}}_{\mathrm{i}} + (1-\eta)\dot{\boldsymbol{\varepsilon}}_{\mathrm{o}} \tag{3}$$

where $\eta = h/H$ is the volume fraction of the joint and $\eta \to 0$ when h is very small. The length H characterises the relative size of the volume element Ω which can be defined as $H = \Omega/A$. Substituting Eq. (2) into Eq. (3) and using the above relationship ($\eta = h/H$), Eq. (3) can be expressed as:

$$\dot{\boldsymbol{\varepsilon}} = \eta\frac{1}{h}\mathbf{n}[\![\dot{\mathbf{u}}]\!] + (1-\eta)\dot{\boldsymbol{\varepsilon}}_{\mathrm{o}} = \frac{1}{H}\mathbf{n}[\![\dot{\mathbf{u}}]\!] + \dot{\boldsymbol{\varepsilon}}_{\mathrm{o}} \tag{4}$$

On the other hand, the behaviour of the joint and the bulk material are connected to the overall response of the volume element Ω through their contributions to the overall virtual work done in this volume. This can be achieved using the Hill-Mandel condition (Hill, 1963) as follows:

$$\boldsymbol{\sigma}^T\dot{\boldsymbol{\varepsilon}} = \eta\boldsymbol{\sigma}_{\mathrm{i}}^T\dot{\boldsymbol{\varepsilon}}_{\mathrm{i}} + (1-\eta)\boldsymbol{\sigma}_{\mathrm{o}}^T\dot{\boldsymbol{\varepsilon}}_{\mathrm{o}} \tag{5}$$

Using Eqs. (2)–(4) and the condition $\eta \to 0$, Eq. (5) can be rewritten as:

$$(\boldsymbol{\sigma}^{\mathrm{T}} - \boldsymbol{\sigma}_{\mathrm{o}}^{\mathrm{T}})\dot{\boldsymbol{\varepsilon}}_{\mathrm{o}} + \frac{1}{H}(\boldsymbol{\sigma}^{\mathrm{T}}\mathbf{n} - \boldsymbol{\sigma}_{\mathrm{i}}^{\mathrm{T}}\mathbf{n})[\![\dot{\mathbf{u}}]\!] = (\boldsymbol{\sigma}^{\mathrm{T}} - \boldsymbol{\sigma}_{\mathrm{o}}^{\mathrm{T}})\dot{\boldsymbol{\varepsilon}}_{\mathrm{o}} + \frac{1}{H}(\boldsymbol{\sigma}^{\mathrm{T}}\mathbf{n} - \mathbf{t}_{\mathrm{i}}^{\mathrm{T}})[\![\dot{\mathbf{u}}]\!] = 0 \tag{6}$$

where the contribution of the inner stress for the joint is expressed in terms its traction vector $\boldsymbol{\sigma}_{\mathrm{i}}^{\mathrm{T}}\mathbf{n} = \mathbf{t}_{\mathrm{i}}^{\mathrm{T}} = [t_1\ \ t_2\ \ t_3]$. In order to satisfy Eq. (6) for any arbitrary values of $\dot{\boldsymbol{\varepsilon}}_{\mathrm{o}}$ and $[\![\dot{\mathbf{u}}]\!]$, followings conditions need to be satisfied: (i) the overall stress of the volume element Ω coincides with the stress of the bulk material $\boldsymbol{\sigma} = \boldsymbol{\sigma}_{\mathrm{o}}$, and (ii) the continuity of traction across the boundary of the joint is satisfied, i.e. $\mathbf{n}^T\boldsymbol{\sigma} = \mathbf{t}_{\mathrm{i}}$. This traction continuity plays a very important role as it helps to link the behaviour of the joint to the response of the surrounding bulk material.

A generic relationship between the rate of traction and the rate of displacement jump can be written as:

$$\dot{\mathbf{t}}_{\mathrm{i}} = \mathbf{K}^{\mathrm{t}}[\![\dot{\mathbf{u}}]\!] \tag{7}$$

in which $\mathbf{K}^{\mathrm{t}}$ is the tangent stiffness matrix of the joint in the global coordinate system, Now the condition of traction continuity in its rate form $\mathbf{n}^{\mathrm{T}}\dot{\boldsymbol{\sigma}}_{\mathrm{o}} = \dot{\mathbf{t}}_{\mathrm{i}}$ can be rewritten using Eq. (7) and the constitutive relation of the outer bulk material ($\dot{\boldsymbol{\sigma}}_{\mathrm{o}}=\mathbf{a}_{\mathrm{o}}\dot{\boldsymbol{\varepsilon}}_{\mathrm{o}}$) along with Eq. (4) as:

$$\mathbf{n}^{\mathrm{T}}\mathbf{a}_{\mathrm{o}}\left(\dot{\boldsymbol{\varepsilon}} - \frac{1}{H}\mathbf{n}[\![\dot{\mathbf{u}}]\!]\right) = \mathbf{K}^{\mathrm{t}}[\![\dot{\mathbf{u}}]\!] \tag{8}$$

After some arrangements of the above equation, the rate of displacement jump can be derived as:

$$[\![\dot{\mathbf{u}}]\!] = \left[\frac{1}{H}\mathbf{n}^{\mathrm{T}}\mathbf{a}_{\mathrm{o}}\mathbf{n} + \mathbf{K}^{\mathrm{t}}\right]^{-1}\mathbf{n}^{\mathrm{T}}\mathbf{a}_{\mathrm{o}}\dot{\boldsymbol{\varepsilon}} = \mathbf{C}^{-1}\,\mathbf{n}^{\mathrm{T}}\mathbf{a}_{\mathrm{o}}\dot{\boldsymbol{\varepsilon}} \tag{9}$$

Using the above-mentioned conditions ($\boldsymbol{\sigma} = \boldsymbol{\sigma}_{\mathrm{o}}$), the constitutive relation of the bulk material along with Eqs. (4) and (9), the constitutive relationship of the jointed rock material can be derived as:

$$\dot{\boldsymbol{\sigma}} = \mathbf{a}_{\mathrm{o}}\left[\dot{\boldsymbol{\varepsilon}} - \frac{1}{H}\mathbf{n}[\![\dot{\mathbf{u}}]\!]\right] = \left[\mathbf{a}_{\mathbf{o}} - \frac{1}{H}\mathbf{a}_{\mathrm{o}}\mathbf{n}\mathbf{C}^{-1}\mathbf{n}^{\mathrm{T}}\mathbf{a}_{\mathrm{o}}\right]\dot{\boldsymbol{\varepsilon}} \tag{10}$$

As seen in the above formulation, both of the joint and the surrounding rock responses contribute to the constitutive model through a set of kinematic parameter and internal equilibrium conditions across the boundary of the joint. This helps to incorporate the elastic response of the bulk material and the inelastic loading of the joint in the overall response of the volume element. The stress-strain relationship Eq. (10) could be readily implemented within an existing numerical method such as finite element method for a structural analysis simulation without any modifications. Moreover, as the constitutive model incorporates the mechanical behaviour and orientation of the joint along with the size and behaviour of the surrounding rock, the deterministic size effect can be handled naturally at the constitutive level. The inclusion of the normal vector of the joint would also help the model to handle joints with any orientations.

3. A cohesive model for rock joint

To model the behaviour of the joint, a new cohesive model based on a coupled damage-plasticity framework is proposed. The model focuses on reproducing important features of the post-peak deformation and damage development of cohesive fracture under mixed mode loading conditions in both tensile and compressive regimes. These include strength and stiffness reductions, irreversible displacements, residual frictional strength at the failure state and the evolution of dilation under the effects of asperity degradation. All these features were either missing or not addressed at length in Nguyen et al. (2012, 2014a, 2016). The formulation allows the modelling of rock joints at different stages of the calculation with or without cohesion. In general, the proposed cohesive model can be used not only for rock joints, but also for material where cohesive cracks exist including brittle/quasi-brittle material like concrete or granular material like soil and sand. This section describes the formulation of the proposed cohesive model for rock joint.

3.1. Model formulation

The typical responses of a rock joint in the case of shear under constant normal stress and the case of compression were summarised by Barton (1976) and Saeb and Amadei (1992) and are illustrated in Fig. 2. It can be seen from this figure that for the case of shearing, the shear stiffness degrades after reaching the stress peak. The shear stress then gradually reduces and reaches the plateau. On the other hand, there is no degradation of stiffness in the case of normal compression. Instead, the inelasticity seems to occur right after the loading in this case. Based on these considerations, the tractions-displacement jumps relations at a joint should be formulated in a way that only shear stiffness is degraded

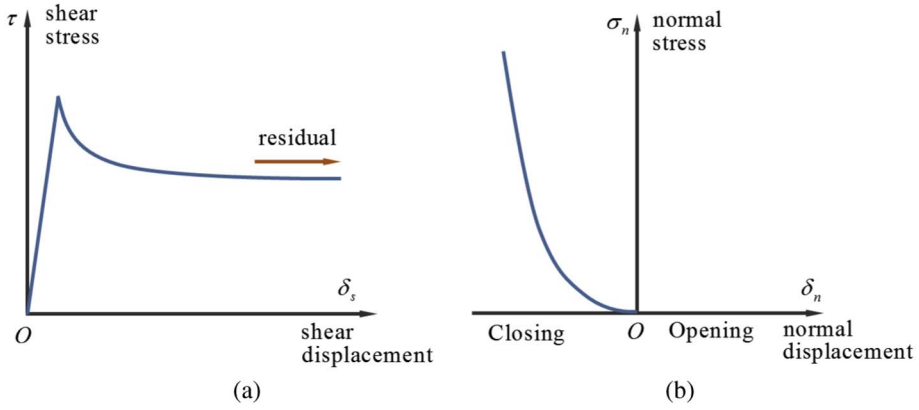

Fig. 2. Typical behaviour of rock joint (a) shear under constant normal stress (after Barton, 1976) and (b) under increasing normal compression (after Saeb and Amadei, 1992).

during the loading. Thus, in the proposed cohesive model, the tractions-relative displacement relationship at a joint is described in the form:

$$t_n = K_n(u_n - u_n^P)$$
$$t_s = (1 - D)K_s(u_s - u_s^P) \quad (11)$$

where t_n, t_s are respectively the normal and shear tractions of the joint. K_n and K_s are the cohesive elastic stiffness for normal and shear cases; u_n, u_s are the normal and shear relative displacement (displacement jump) while u_n^P, u_s^P are inelastic (frictional) displacement jumps between 2 sides of the joint surface. It should be noted that the shear traction is comprised of two other shear tractions in the local s1-axis and s2-axis $t_s = \sqrt{t_{s1}^2 + t_{s2}^2}$ as illustrated in Fig. 3. This means that the relative shear displacement u_s is also comprised of two members of the s1-axis and s2-axis in the local coordinate system as presented for traction t_s. In this paper, the normal traction is defined to be positive in case of tension and negative in compression. In Eq. (11), D is the damage state of the material ranging within 0 and 1 (i.e. $0 \le D \le 1$). As discussed earlier, the damage variable does not appear in the normal traction equation as seen in Eq. (11). Thus, different from conventional damage formulations where damage variable D represents the isotropic stiffness degradation in all directions, the damage variable in this model represents the degradation of shear stiffness only. $D = 0$ represents the state where all asperities of the joint are intact and the joint behaviour is in elastic range with fully shear stiffness K_s. On the other hand, $D = 1$ represents fully damaged material state where asperities are worn off and shear stiffness are fully degraded. In the paper, the nonlinear behaviour of the joint in normal direction due to the breaking of asperities leading to compaction (Schreyer and Sulsky, 2016) is not accounted for. Although for all validation examples in this study this is not an issue, we acknowledge this shortcoming and will address it in future work.

It can be seen from the formulation of tractions that the responses of the rock joint before yielding is linearly elastic, governed by elastic stiffness K_n and K_s. This implication agrees with the experimental observations (Asadollahi et al., 2010; Barton, 2013; Gentier et al., 2000; Grasselli and Egger, 2003; Li et al., 2016; Saeb and Amadei, 1992; Sun et al., 1985). As suggested by other researchers (Bandis et al., 1983; Goodman, 1976; Jing, 1990; Wang et al., 2003), the shear stiffness

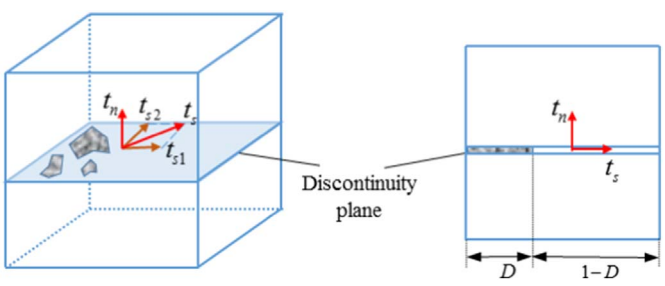

Fig. 3. Tractions and damage illustration in a cohesive zone.

should be a linear function of applied normal stress. However, because the research focuses on post-peak behaviour, these two stiffnesses are kept constants. It can be seen later that this choice does not significantly affect the results. Moreover, other empirical equations or more complicated calculation for these normal and shear stiffness can be used in the model if required.

Along with the tractions-displacement jumps relation, a loading function for the damage development and plasticity is needed in order to determine whether the behaviour of the joint is in elastic or inelastic (plastic-damage) regime. A loading function is also necessary for computing the elastic/plastic displacement parts, as well as the evolution of tractions during loading/unloading. The proposed loading function is written in the following form:

$$y(t_n, t_s, D) = t_s^2 - [(1 - D)\mu_0^2 + D\mu^2][t_n - (1 - D)f_n]^2 - m\sigma_c(1 - D)[t_n - (1 - D)f_n] \quad (12)$$

where f_n is the tension strength of the cohesive zone. For rock joint case, because two sides of the jointed rock were pre-separated, the tensile strength is negligible compared to shear strength. Thus, in this paper, the tension strength f_n is assumed to be zero. But it is worthy to note that for other cases of materials such as concrete or soil, there exists a tensile cohesive and thus this parameter would be nonzero. In the above equation, σ_c is the compression strength of the rock; m and μ_0 are the parameters controlling the shape of the initial yield surface; μ is the parameters controlling the shape of failure surface. It should be noted that by changing values of these parameters, the shape of the yield surface could be adapted to different rock joint responses corresponding to different geological settings, as illustrated in Fig. 4a. This feature gives the model a certain level of flexibility while dealing with different cases of material and loading paths.

The shape of the loading function and its evolution following the development of the damage variable is illustrated in Fig. 4b. The initial yield surface corresponding to the case of $D = 0$ (the blue curve in Fig. 4b) gradually evolves as the damage variable D increases and reaches the failure surface corresponding to $D = 1$ (red line). Substituting $D = 1$ into Eq. (12) yields a linear relationship between the normal and shear tractions, i.e. $t_s = \pm \mu t_n$. This relationship corresponds to the well-known Mohr Coulomb criterion, where μ plays the role of internal frictional coefficient, e.g. $\mu = \tan\phi$ in Mohr-Coulomb model with ϕ being the friction angle of the joint as described in many studies (Gentier et al., 2000; Grasselli and Egger, 2003; Li et al., 2016; Singh and Singh, 2012). From Eq. (11), it can be seen that when damage variable D reaches 1, the shear traction would theoretically be zero. However, as presented in Fig. 4, the values of the joint tractions lie on the failure surface where shear traction could have a non-zero value. Thus, in the practical calculation, damage variable asymptotically approaches 1 but never reaches this value. It can be seen from the formulation of the model that both damage and plasticity and their coupling are taken into account in a unified form of loading function. This

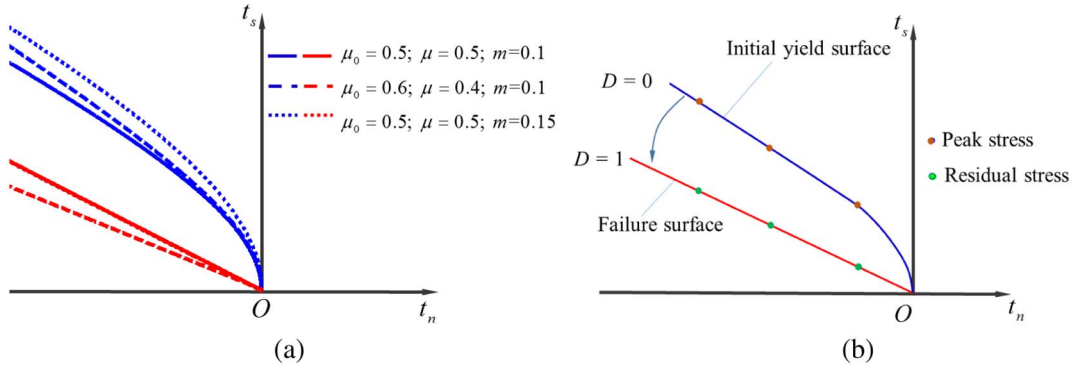

Fig. 4. Illustration of the proposed cohesive model (a) effects of parameters on initial yield ($D = 0$, blue) and failure surface ($D = 1$; red); (b) shape and evolution of loading function from initial yield to final failure surface. (For interpretation of the references to colour in this figure legend, the reader is referred to the web version of this article.)

helps the model evolve from initial yield to failure smoothly without any additional separate criteria for damage and plasticity.

As non-associated flow rule is needed for a constitutive model of rock joint to better describe the dilation and plastic deformation of the interface (Wang et al., 2003), the following plastic potential is used:

$$g(t_n, t_s, D) = \gamma t_s^2 - [(1-D)\mu_0^2 + D\mu^2][t_n - (1-D)f_n]^2 - m\sigma_c(1-D)[t_n - (1-D)f_n] \quad (13)$$

where γ is a parameter controlling the dilation of the material under shearing. The relative normal and shear plastic displacements following non-associated flow rule become:

$$\dot{u}_n^p = \dot{\lambda}\frac{\partial g}{\partial t_n} \quad \text{and} \quad \dot{u}_s^p = \dot{\lambda}\frac{\partial g}{\partial t_s} \quad (14)$$

where $\dot{\lambda}$ is a positive scalar factor of proportionality which is nonzero only when plastic deformations occurs. As seen from this equation, the partial derivatives of potential function govern the ratio or the relative magnitudes of the plastic displacement components $\dot{u}_s^p$ and $\dot{u}_n^p$, and parameter γ helps control the dilation rate effectively.

To complete the cohesive model, an evolution of damage variable D is provided to capture the damage propagation. Because the damage here represents the degradation of shear stiffness which is a non-decreasing process, in general, the evolution of damage could be in any form as long as it produces a non-decreasing value of damage from 0 to 1 when plastic displacement increases. For the case of rock joint, from experimental results (Barton, 2013; Gentier et al., 2000; Grasselli and Egger, 2003; Li et al., 2016), it is seen that right after the peak, the shear stress at first reduces rapidly. However, with further shearing, this rate of reduction slows down. This could be explained that after reaching the shear strength, the asperities in the joint begin to be worn off rapidly and later slide on each other with less wearing off. Therefore, in this research, the evolution of damage variable is chosen to be an exponential function of the so-called effective plastic factor, u_p, so that the damage variable increases rapidly at first and then gradually slows down. The form of the damage variable in the research is taken as:

$$D = 1 - e^{-u_p};\quad \dot{u}_p = \alpha\sqrt{\left(\frac{\dot{u}_n^p}{\delta_0}\right)^2 + \left(\frac{\dot{u}_s^p}{\delta_0}\right)^2} \quad (15)$$

where α is the parameter controlling the contribution of normal and shear plastic displacement to the damage of the material; δ_0 is the displacement corresponding to shear strength (i.e. stress peak). The only purpose of putting δ_0 into damage formulation is to represent the damage variable D in dimensionless form.

As presented, a tractions-displacement jumps relationship, a non-associated flow rule together with the evolutions of internal variables (i.e. damage D, plastic displacement jump u_n^p, u_s^p and effective plastic factor u_p) complete the cohesive model. In the proposed cohesive model, only one loading surface is employed from the initial yielding to the final failure surface. This allows a natural description of softening with the transition to frictional behaviour under mixed-mode loading. Because the damage evolution is in association with the plastic strain, the effects of coalescence and frictional sliding are taken into account together during the material failure. These features give the model a good prediction capability under different loading cases.

3.2. Model parameters

The first step before using the proposed model for any simulation is to calibrate parameters used in the model. In other words, the model needs to be adjusted to fit with a specific type of the material as well as the length-scale of the interested problem before being used for simulation. This section presents the calibration of the model's parameters against experimental data of shearing under Constant Normal Load (CNL) owing to its wide availability in the literature.

In terms of physical meaning, the shear elastic stiffness K_s is the slope of the stress-displacement curve in from experimental data and normal elastic stiffness K_n is the elastic stiffness of the rock joint in compression. Thus, given a data set of shear experiment, K_s can be calculated by $K_s = \tau_y/\delta_0$ where τ_y is the shear stress peak and δ_0 is the corresponding displacement as illustrated in Fig. 5a. Because K_n is the elastic stiffness of the rock joint, it can be calculated from elastic Young's Modulus E divided by the thickness of the joint $K_n = E/h$. Since rock joint is considered to have zero thickness, i.e. $h \to 0$, normal elastic stiffness theoretically equals to infinity i.e. $K_n \to +\infty$. Thus, for numerical simulation, K_n is chosen to be large enough compared to other stiffness (K_s, E) to be considered as infinity without affecting the outcome of the model.

Based on the residual shear stress, the internal friction coefficient μ can be calculated as $\mu = \tan(\phi)$, as illustrated in Fig. 5. Therefore, the remaining parameters in the model that need to be calibrated include loading surface parameters m, μ_0, damage parameter α and dilation parameter γ. The loading shape parameters m and μ_0 can be calibrated via the shape of initial loading surface using the peak shear stress. As illustrated in Fig. 5b, if the shear is superposed with compression ($t_n < 0$), the peak of the shear stress would correspond to the point on initial yield surface where damage initiates ($D = 0$). Thus, by adjusting m and μ_0 to make the loading surface fit with the experimental data, these parameters then can be used for modelling the joint in other loading cases.

The next calibration is the dilation parameter γ. The explicit form of Eq. (14) shows that γ controls the ratio between the shear and the normal components of the incremental plastic displacement vector. Hence, it is this parameter that has a significant influence on the magnitude of the dilation during the shearing. As a result, the calibration of γ can be performed using "trial and error" method for a single data set of dilation which is usually available for brittle material. In this

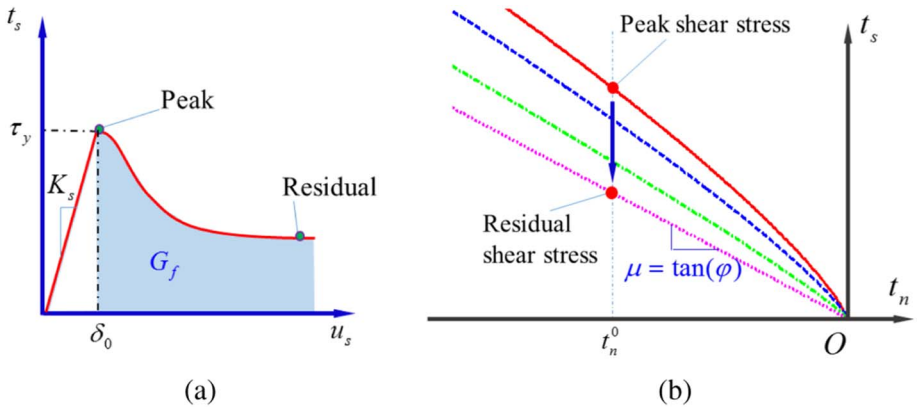

Fig. 5. Illustration of parameters calibration (a) experimental data set of CNL shear for calibration and (b) calibration of loading shape parameters.

process, γ will be adjusted until the dilation brought from the model fit well with that from experimental results. Once the parameter is calibrated by a single set of experiment data corresponding to a given normal pressure, it can be used to predict the behaviour for other loading paths.

Finally, the value of parameter α controlling the damage evolution is needed to make the model ready for calculation. Owing to the fact that α controls the way in which damage evolves during loading process as seen in Eq. (15), this parameter has a strong relation with the area under the shear stress-displacement curve in inelastic range illustrated in Fig. 5a. Therefore, the parameter α could be calibrated so that the resultant quantity from computation $G_{comp} = \Sigma t_s \Delta u_s$ is equal to that calculated from the experimental curve.

3.3. Tangent stiffness of the cohesive model for a rock joint

From Eq. (7) of the framework, it can be seen that in order to implement the proposed cohesive model to above-mentioned double-scale approach, the tangent stiffness matrix $\mathbf{K}^t$ has to be formulated. This matrix is calculated from the stiffness in the local coordinate system $\mathbf{K}_c^t$ as:

$$\mathbf{K}^t = \mathbf{R}^T \mathbf{K}_c^t \mathbf{R} \tag{16}$$

where $\mathbf{R}$ is the transformation matrix from the global coordinate system to the local coordinate system; $\mathbf{K}_c^t$ is the tangent stiffness matrix of the joint representing the rate of traction vector $\dot{\mathbf{t}}_c = [\dot{t}_n \;\; \dot{t}_{s1} \;\; \dot{t}_{s2}]^T$ to the rate of relative displacement vector $[\![\dot{\mathbf{u}}_c]\!] = [\dot{u}_n \;\; \dot{u}_{s1} \;\; \dot{u}_{s2}]^T$ in the local coordinate system $\dot{\mathbf{t}}_c = \mathbf{K}_c^t [\![\dot{\mathbf{u}}_c]\!]$. Similar to the conventional plasticity theory, K_c^t in inelastic range is a function of all internal variables including the damage variable D, relative plastic displacements u_n^p, u_{s1}^p, u_{s2}^p and the effective plastic factor u_p, which has to be calculated in each iteration of the numerical simulation. Therefore, for loading case, in addition to the tractions, all internal variables, as well as displacement jumps, have to be updated iteratively throughout the calculation.

Firstly, the governing Eq. (11) is rewritten in the compact form as

$$\mathbf{t}_c = f(D, \mathbf{u}_c, \mathbf{u}_c^p) \tag{17}$$

By taking derivative of this equation, the incremental form of this relation is then obtained as

$$\dot{\mathbf{t}}_c = \frac{\partial \mathbf{t}_c}{\partial \mathbf{u}_c} [\![\dot{\mathbf{u}}_c]\!] + \frac{\partial \mathbf{t}_c}{\partial \mathbf{u}_c^p} [\![\dot{\mathbf{u}}_c^p]\!] + \frac{\partial \mathbf{t}_c}{\partial D} \dot{D} \tag{18}$$

From Eq. (15), the damage increment is presented by:

$$\dot{D} = e^{-u_p} \dot{u}_p = \frac{\alpha e^{-u_p}}{\delta_o} \sqrt{\left(\frac{\partial g}{\partial t_n}\right)^2 + \left(\frac{\partial g}{\partial t_s}\right)^2}\, \dot{\lambda} = P\dot{\lambda} \tag{19}$$

The consistency condition requires that the obtained tractions for the next iteration $i+1$ still satisfy the yielding condition of the cohesive model $y(\mathbf{t}_c^i, D^i) = y(\mathbf{t}_c^{i+1}, D^{i+1}) = 0$. This results in

$$\dot{y} = \frac{\partial y}{\partial \mathbf{t}_c} \dot{\mathbf{t}}_c + \frac{\partial y}{\partial D} \dot{D} = 0 \tag{20}$$

By substituting Eqs. (14), (18) and (19) into consistency condition in Eq. (20) and solving for $\dot{\lambda}$, one obtains:

$$\dot{\lambda} = \frac{-\frac{\partial y}{\partial \mathbf{t}_c} \frac{\partial \mathbf{t}_c}{\partial \mathbf{u}_c} [\![\dot{\mathbf{u}}_c]\!]}{\frac{\partial y}{\partial \mathbf{t}_c} \frac{\partial \mathbf{t}_c}{\partial \mathbf{u}_c^p} \frac{\partial g}{\partial \mathbf{t}_c} + \frac{\partial y}{\partial \mathbf{t}_c} \frac{\partial \mathbf{t}_c}{\partial D} P + \frac{\partial y}{\partial D} P} = \mathbf{N} [\![\dot{\mathbf{u}}_c]\!] \tag{21}$$

From $\dot{\lambda}$, other internal variables increments (i.e. $\dot{D}$, $\dot{u}_p$, $[\![\dot{\mathbf{u}}_c^p]\!]$) are computed easily following Eqs. (14)–(15). The tangent stiffness in the loading case for the traction-displacement jump relationship is then withdrawn as:

$$\dot{\mathbf{t}}_c = \left[\frac{\partial \mathbf{t}_c}{\partial \mathbf{u}_c} + \frac{\partial \mathbf{t}_c}{\partial \mathbf{u}_c^p} \frac{\partial g}{\partial \mathbf{t}_c} \mathbf{N} + P \frac{\partial \mathbf{t}_c}{\partial D} \mathbf{N} \right] [\![\dot{\mathbf{u}}_c]\!] = \mathbf{K}_c^{\text{tangent}} [\![\dot{\mathbf{u}}_c]\!] \tag{22}$$

3.4. Stress return algorithm for the cohesive model

As seen from Section 3.3, the rate of the traction could be calculated from incremental displacement jump using the tangent stiffness. However, because this tangent stiffness is explicitly calculated from the current state (state A as illustrated in Fig. 6) which does not lie on the yield surface, it only provides good results when the incremental step is sufficiently small. Thus, an implicit calculation is preferred as it could produce relatively good results with larger steps. In addition, similar to the plasticity formulation where a stress return is needed for the implicit calculation, a stress return procedure is also required for the proposed cohesive model to work well with the overall stress-strain implicit calculation. The proposed stress return is based on a special form of the backward-Euler scheme presented by Crisfield (2000). The idea of this method is illustrated in Fig. 6 where the yield surface is approximated by First Taylor expansion at trial point B and the yield criteria (i.e. $y(\mathbf{t}_c, D) = 0$) is applied to obtain the rate of the scalar factor

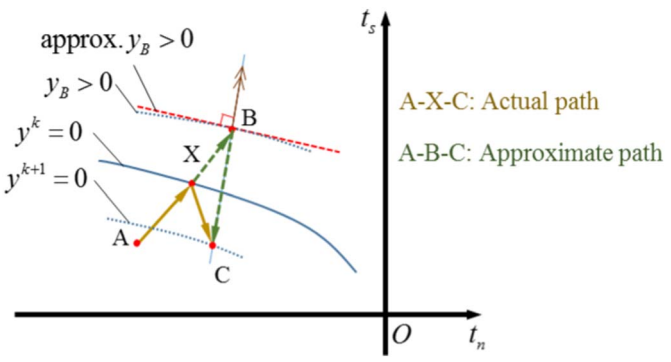

Fig. 6. Illustration of stress return for the proposed cohesive model: A is current state, X is yielding state, B is a trial state, C is a new state.

$\dot{\lambda}$ for the yield evolution. By doing so, the procedure does not have to calculate the exact yielding point X and the yielding criteria is still satisfied.

The increment of the traction from the current point A to trial point B is elastic $\dot{\mathbf{t}}_c^{\text{trial}} = \mathbf{H}\mathbf{K}_c^{\text{E}}[\![\dot{\mathbf{u}}_c]\!]$ where matrices $\mathbf{H}$ and $\mathbf{K}_c{}^E$ is obtained from Eq. (11) as $\mathbf{H} = \text{diag}(1, 1-D, 1-D)$ and $\mathbf{K}_c{}^E = \text{diag}(K_n, K_s, K_s)$. The yield surface at point B is approximated at trial point B by first-order Taylor expansion and then in association with Eq. (18), the stress state is moved from trial point B to new yielding point C on the new yielding surface. The new yielding surface is then enforced to be zero as:

$$y^{k+1} = y_B + \frac{\partial y}{\partial \mathbf{t}_c}\bigg|_B (\mathbf{t}_c^C - \mathbf{t}_c^B) + \frac{\partial y}{\partial D}\bigg|_B \dot{D} = y_B + \frac{\partial y}{\partial t}\bigg|_B \left[\frac{\partial \mathbf{t}_c}{\partial \mathbf{u}_c^p}\dot{\mathbf{u}}_c^p + \frac{\partial \mathbf{t}_c}{\partial D}\dot{D}\right] + \frac{\partial y}{\partial D}\bigg|_B P\dot{\lambda} = 0 \tag{23}$$

Noted that in the above equation, the elastic part when moving from B to C is equal to zero due to the fact that it was already used to move from A to trial point B as presented. By substituting Eqs. (14) and (19) into Eq. (23) and solving for scalar $\dot{\lambda}$, one obtains:

$$\dot{\lambda} = \frac{-y_B}{\frac{\partial y}{\partial \mathbf{t_c}}\Big|_B \frac{\partial \mathbf{t}_c}{\partial \mathbf{u}_c^p}\frac{\partial \mathbf{g}}{\partial \mathbf{t}_c} + \frac{\partial y}{\partial \mathbf{t}_c}\Big|_B \frac{\partial \mathbf{t}_c}{\partial D}P + \frac{\partial y}{\partial D}\Big|_B P} \tag{24}$$

From this scalar factor, increments for other internal variables can be calculated following Eqs. (14), (15) and (19) easily. The traction rate is then computed by:

$$\dot{\mathbf{t}}_c = \dot{\mathbf{t}}_c^{\text{trial}} + \frac{\partial \mathbf{t}_c}{\partial \mathbf{u}_c^p}\dot{\mathbf{u}}_c^p + \frac{\partial \mathbf{t}_c}{\partial D}P\dot{\lambda} \tag{25}$$

4. Stress return algorithm for double-scale approach

Once the relation between the tractions and the relative displacements at the joints is established, it can be implemented into the double-scale model described in Section 2 to obtain a constitutive relation for modelling rock joints. As presented earlier, the responses of the joints and the surrounding materials are included in a single constitutive model and interact with each other via traction continuity condition as shown in Eq. (8). Thus, it is necessary to have an appropriate numerical algorithm to describe this coupling so that both the overall stress-strain of the rock mass and the traction-relative displacement of the joints are updated and compatible with each other iteratively. This section hence presents the numerical algorithm for stress update based on a given total strain increment and previous state of the material point. The paper uses the implicit algorithm as it could give a relatively good result with a larger increment as compared to the explicit algorithm.

In the implicit algorithm, the stress and joint tractions are firstly computed with the assumption of elastic joint behaviour. An iterative procedure is then applied to correct the current stress and tractions to ensure that the traction continuity is obtained with a certain pre-defined tolerance. This enables the algorithm to yield relatively accurate results with larger steps compared to the explicit algorithm. To serve this purpose, a vector of residual traction is defined in the global coordinate system as

$$\mathbf{r} = \mathbf{n}^{\text{T}}\boldsymbol{\sigma} - \mathbf{t} \tag{26}$$

By using the first order Taylor expansion of the residual vector at a state of the last iteration $k-1$, the residual of the current iteration k is given by:

$$\mathbf{r}^k = \mathbf{r}^{k-1} + \mathbf{n}^{\text{T}}\delta\boldsymbol{\sigma} - \delta\mathbf{t} = \mathbf{r}^{k-1} - \frac{1}{H}\mathbf{n}^{\text{T}}\mathbf{a}_o\mathbf{n}\delta[\![\mathbf{u}]\!]_k - \mathbf{K}^t\delta[\![\mathbf{u}]\!]_k \tag{27}$$

where $\delta\boldsymbol{\sigma}$ and $\delta\mathbf{t}$ are respectively the corrective stress and traction vectors at step k. It should be noted that for the above equation, the strain increment $\Delta\boldsymbol{\varepsilon}$ is omitted because it had already been used in explicit step. By zeroing the residual for the current iteration $\mathbf{r}^k = 0$, the corrective displacement for the current step is calculated by:

$$\delta[\![\mathbf{u}]\!]_k = \left[\frac{1}{H}\mathbf{n}^{\text{T}}\mathbf{a}_o\mathbf{n} + \mathbf{K}^{\text{t}}\right]^{-1}\mathbf{r}^{k-1} \tag{28}$$

This corrective displacement is then used to calculate corrective traction $\delta\mathbf{t}_c$ and to update internal variables in the cohesive model as presented in Section 3.4. The corrective stress is now computed as

$$\delta\boldsymbol{\sigma}_k = -\frac{1}{H}\mathbf{a}_o\mathbf{n}\delta[\![\mathbf{u}]\!]_k \tag{29}$$

The process of correcting the stress and tractions is performed until convergence is obtained. The traction continuity is thus satisfied at that point. The pseudo implicit algorithm for stress update is presented in Algorithm 1.

Algorithm 1. Implicit stress update input: $\Delta\boldsymbol{\varepsilon}$, output: $\Delta\boldsymbol{\sigma}$.

1. Compute $\mathbf{C} = \left[\frac{1}{H}\mathbf{n}^{\text{T}}\mathbf{a}_o\mathbf{n} + \mathbf{R}^{\text{T}}\mathbf{K}_c^{\text{E}}\mathbf{R}\right]$ (assume elastic loading/unloading)
2. Compute trial displacement $\Delta[\![\mathbf{u}]\!]^{trial} = \mathbf{C}^{-1}\mathbf{n}^T\mathbf{a}_o\Delta\boldsymbol{\varepsilon}$ then $\Delta[\![\mathbf{u}_c]\!]^{trial} = \mathbf{R}\Delta[\![\mathbf{u}]\!]^{trial}$
3. Compute trial stress $\boldsymbol{\sigma}^{\text{trial}} = \boldsymbol{\sigma} + \Delta\boldsymbol{\sigma}^{\text{trial}} = \boldsymbol{\sigma} + \mathbf{a}_o\left[\Delta\boldsymbol{\varepsilon} - \frac{1}{H}\mathbf{n}\Delta[\![\mathbf{u}]\!]^{\text{trial}}\right]$
4. Compute local trial traction $\mathbf{t}_c^{trial} = \mathbf{t}_c + \mathbf{R}\mathbf{n}^T\Delta\boldsymbol{\sigma}^{trial}$
5. **If**$y(\mathbf{t}^{trial}) < 0$: elastic loading/unloading **then**
6. Compute stress increment $\Delta\boldsymbol{\sigma} = \Delta\boldsymbol{\sigma}^{trial}$
7. Update local traction $\mathbf{t}_c = \mathbf{t}_c^{trial}$
8. Update local displacement $[\![\mathbf{u}_c]\!] = [\![\mathbf{u}_c]\!] + \Delta[\![\mathbf{u}_c]\!]^{trial}$
9. **Else if**$y(\mathbf{t}^{trial}) \geq 0$: plasticity loading
10. Compute $\Delta\mathbf{t}_c$ from $\Delta[\![\mathbf{u}_c]\!]^{trial}$ following Section 3.4
11. Update traction $\mathbf{t}_c = \mathbf{t}_c + \Delta\mathbf{t}_c$ and calculate residual $\mathbf{r}\mathbf{r} = \mathbf{n}^T\boldsymbol{\sigma}^{trial} - \mathbf{R}^T\mathbf{t}_c$
12. **While**$\|\mathbf{r}\| \geq \varepsilon$**do**
13. Calculate $\mathbf{K}_c{}^t$ with new updated internal variable
14. Calculate $\delta[\![\mathbf{u}]\!] = \left[\frac{1}{H}\mathbf{n}^{\text{T}}\mathbf{a}_o\mathbf{n} + \mathbf{R}^{\text{T}}\mathbf{K}_c^{\text{t}}\mathbf{R}\right]^{-1}\mathbf{r}$ then $\delta[\![\mathbf{u}_c]\!] = \mathbf{R}\delta[\![\mathbf{u}]\!]$
15. Compute $\delta\mathbf{t}_c$ from $\delta[\![\mathbf{u}_c]\!]$ following Section 3.4
16. Compute $\delta\boldsymbol{\sigma} = -\frac{1}{H}\mathbf{a}_o\mathbf{n}\delta[\![\mathbf{u}]\!]$
17. Update $\boldsymbol{\sigma}$, $\mathbf{t}_c$ and $\mathbf{r}$
18. **End while**
19. **End if**

5. Model validation

A number of examples are presented in this section to illustrate the performance of the proposed model for analysing jointed rock behaviour. The main focus of the current paper is the rock joint shear under constant normal load (CNL). The material properties from published data and the model's parameters obtained from the calibration are summarised in Table 1 for all examples considered in this paper.

The current double scale model is based on the stress-strain relation of a volume element Ω containing a crack, and the responses of this crack are also taken into the constitutive relation. Therefore, the model is capable of simulating the shear test at material point level as long as the characterised length H is adopted into the model. As described in Section 2, the characterised length H is calculated from the area of the joint and the volume of the considered material body $H = \Omega/A$. Therefore, the values of H for all examples are calculated from the given geometry of the specimens and are presented in Table 1.

It is noted that in all examples, besides the peak and residual strengths used to calibrate the yield and failure surfaces, a single data set including shear stress-shear strain response and dilation behaviour at a given normal pressure was used for the calibration of other model parameters. The calibrated parameters are then utilised to predict the mechanical response of the joint under other normal pressures. The

Table 1
Rock material/joint properties and model parameters for numerical simulation.

Parameter	Material/joint properties from experimental data						δ_0 mm	H mm	Model's parameters			
	E GPa	ν	σ_c MPa	K_n MPa/mm	K_s MPa/mm	μ			m	μ_0	α	γ
Example 1	30.8	0.2	75	10^3	34.73	0.8	0.55	90	0.2	0.7	1.2	1.9
Example 2	14.9	0.2	46	10^3	3.07	1.1	2.1	100	0.15	0.7	1.8	1.6
Example 3	48.4	0.2	173	10^3	7.07	0.8	0.65	140	0.015	0.5	0.7	1.8

behaviour predicted by the model is compared with those obtained from experimental studies as well as previous models by other authors.

5.1. Example 1: data from Gentier et al.

The first example is a simulation of the direct shear test of granite mortar replicas, carried under various constant compressive normal stress $\sigma_n = 7, 14$ and 21 MPa. The samples of these replicas were cored across a natural joint of Guéret granite from France (Gentier et al., 2000). This experiment was conducted by Gentier et al. (2000) and was also recently investigated numerically by Mihai and Jefferson (2013). The geometry and arrangement of this test are shown in Fig. 7. The shear plane of the specimen is circular with a diameter of 90 mm as shown in this figure. In this example, the first data test ($\sigma_n = 7$ MPa) was used to calibrate the model. The calibrated parameters and other model parameters are presented in the first row of Table 1. The results for other normal stress level tests were generated using these calibrated parameters.

The shear stress - shear displacement responses predicted by the proposed model are plotted in Figs. 8–10 along with the experimental data by Gentier et al. (2000) as well as results of the model simulation by Mihai and Jefferson (2013). Because, in the experiment scheme adopted by Gentier et al., four separate tests were conducted for each normal stress level, there are four experimental results for each normal stress level. It is seen from the figures that the results from the proposed model agree well with the experimental data and also those by Mihai and Jefferson (2013) in terms of both shear responses and dilation behaviour. It also can be seen that in all three cases, the peak stresses predicted by the proposed model agree well with those from experiments. This indicates that the initial yield surface governing the peak shear strengths follows well the observed behaviour at different normal stresses. It should also be noted that the proposed model does not require geometrical characteristics of the joints roughness. Instead, this information is lumped in the evolution of the yield surface from initial yield to final failure. This feature would be useful for modelling the jointed rock in reality where the information about the joints geometry is usually limited. In addition, even though the initiation of dilation is slightly different, the magnitude predicted by the model is in good agreement with experimental results. This implies that the proposed evolution from initial yield to final failure and non-associated flow rule can capture key features of the jointed rock behaviour.

It is noted that the patterns of the stress and the dilation evolution from the model are relatively similar to those from experiments. In specific, the shear stress-displacement curve brought by the model includes 4 phases. Firstly, it begins with a linear elastic part where contact area between two sides of the joint increases. In this stage, the specimen also experiences contraction owing to the misfit of the two crack sides. This contraction mostly depends on the nature of the joint surfaces and their contact with each other. The value of the contraction is usually small compared to the dilation (Barton, 1976) and thus is not the main focus of the paper. This phase keeps going until the shear stress reaches its peak. At this point, the traction state (i.e. t_n, t_s) lies on the initial yield surface. The second phase is the peak shear stress phase where asperities of the joint begin to be worn off and slide on each other. In this phase, the dilation initiates with the maximum rate as most of the asperities have not been worn off yet and these asperities slide on each other, resulting in more dilation. Thus the joint roughness is at its highest value in this stage. The damage, as well as plastic displacements, also starts increasing from zero with the highest rate in this phase. This pattern of damage evolution agrees well with the experimental observation made by Gentier et al. (2000). The shear stiffness hence begins to degrade with the highest rate in this phase. The third phase is the post-peak phase, where softening takes place. In this phase, the failure of asperities progressively increases along with the increase of the contact area between two sides of the joint. As a result, the damage increases together with the contraction of yield surface during this phase. The dilation still increases in this phase but with a lower rate compared to the previous one. Finally, the residual strength is reached. Since there is only friction caused by the remaining roughness of the joint, the shear stress is relatively constant with further shearing in this phase. The dilation might be unchanged or continue increasing at a lower rate compared to previous phases. From the above analysis, it can be seen that the progress of shearing obtained by the model is totally similar to that observed from experiment except for the first phase where a short pre-peak inelastic part presents. This leads to five phases of shearing instead of four as obtained from the proposed model. However, the general pattern and the magnitude of the results brought by the model agree well with the experimental results.

5.2. Example 2: data from Li et al.

The second example to be considered is a shear test of precast rock joints from replicas, which was recently conducted by Li et al. (2016). The geometry and roughness of the jointed rock sample are shown in Fig. 11. The sample was fabricated with an estimated joint roughness coefficient (JRC) profile 14–16 representing undulating rock joint

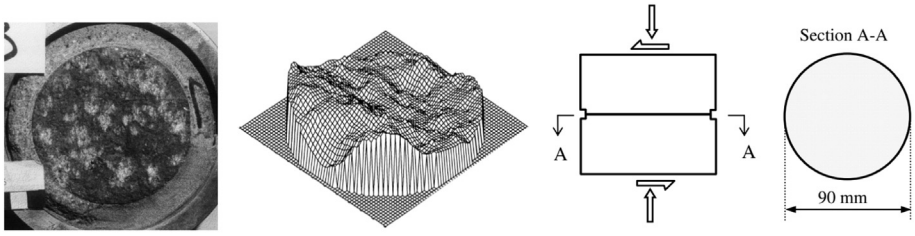

Fig. 7. The Gentier's experiment set up (a) real upper surface of the specimen, (b) 3D representation of the specimen upper surface and (c) test arrangement (after Gentier et al., 2000 & Mihai and Jefferson, 2013).

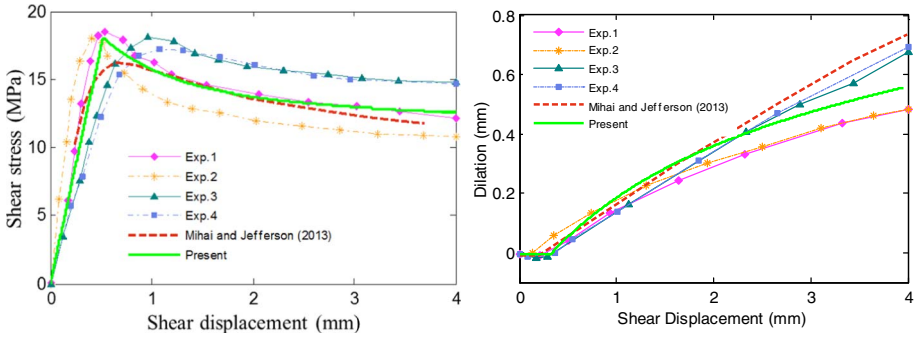

Fig. 8. Shear behaviour and dilation response under normal compression $\sigma_n = 7$ MPa.

(Barton and Choubey, 1977). The length of the specimen is 100 mm. The test was conducted under constant normal load (CNL) σ_n = 2; 3.5; 5 MPa. The material properties and model parameters for this example are presented in Table 1. The experimental data set in the case σ_n = 2 MPa was used for the calibration of model parameters.

The shear stress against shear displacement and dilation behaviour predicted by the model are plotted in Fig. 12 in comparison with their experimental counterparts for different levels of normal stress. The results from the model proposed by Li et al. (2016) are also presented in the figure for comparison purpose. It can be seen from the figure that the results from the current model are generally in good agreement with the experimental data. Although there are still discrepancies between these two sets of results, it can be said that the performance of the model is satisfactory. In spite of the difference of the dilation initiation, the magnitude of the dilation predicted by the model agrees well with those from the experiment, especially for $\sigma_n = 5$ MPa. It is also seen that the dilation decreases when the normal stress increases. This is understandable because for shearing, under higher normal stresses, the contact tractions between two sides of the joint increases correspondingly. As a result, the asperities tend to be damaged more at higher normal stresses. The dilation under shearing hence becomes smaller as expected. Another point is that the proposed model uses limited information from the experiments for the calibration. This would be useful in the simulation of rock joint in the practical context where details on the joint geometries are difficult to obtain. Along with its simplicity and easiness for implementation in conventional Finite Element Method, the proposed model could also be a good choice for modelling brittle/quasi-brittle material or further developing for rock mass in practice.

From the results plotted in Fig. 12, it can be seen that the behaviour of the jointed rock before the peak is linear and it exhibits a nonlinear softening response immediately after the peak. This is due to the assumption that the degradation of asperities takes place only after the peak, resulting damage being activated only after that point. This may not be always the case for all rock joints as damage of the asperities may start before the peak due to the mismatch of the joint's two surfaces (Gentier et al., 2000). However, this pre-peak degradation does not significantly affect the post-peak behaviour, which is the focus of the paper, as can be seen in the model predictions. Nonetheless, we acknowledge this short coming and would address it in our future study.

5.3. Example 3: data from Grasselli and Egger

Next, the model is validated with data set from an experiment conducted by Grasselli and Egger (2003). The experimental test as shown in Fig. 13 was used as replicas to examine the behaviour of granite rock joints. The joint roughness coefficient (JRC) profile of the joints was estimated as 18 (Grasselli and Egger, 2003). The replicas were sheared under different values of constant normal stress levels σ_n = 1.275; 2.55; 5.1; 6.1 MPa. The model's parameters for this test were presented in Table 1. For this example, the experimental data for the case normal stress $\sigma_n = 6.1$ MPa was used for calibration.

The numerical shear stress-shear displacement results of the test are plotted in Fig. 14 in comparison with those from experiments. In addition, the results from numerical simulation by Mihai and Jefferson (2013) are also plotted in the figure. Because there are no experimental data regarding dilation provided, the dilation of this test is not included in the paper. It is seen from the figure that the results from the proposed model are in good agreement with those by experiment and numerical simulation by Mihai and Jefferson (2013), confirming the suitability of the proposed approach. It should also be noted that after the first yielding, the shear stress goes slightly higher than the initial yielding stress, especially for the cases of $\sigma_n = 5.1$ and 6.1 MPa. However, as presented by Barton (1976) and confirmed by many experimental results (Asadollahi et al., 2010; Bahaaddini et al., 2013, 2014; Barton, 2013; Fardin et al., 2001; Li et al., 2016; Saeb and Amadei, 1992), the slight hardening after peak is not the typical behaviour of jointed rock in shear under constant normal stress. And because the main focus of the proposed model is to reflect the typical responses of the rock joint, the model fails to accurately capture this untypical response of this experiment. Nonetheless, the overall responses are adequately described by the proposed model.

5.4. Size effects at the constitutive level

The possession of a length scale in the constitutive structure, as can

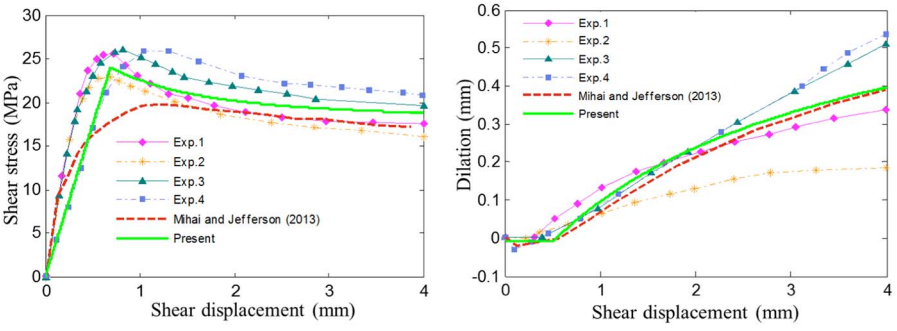

Fig. 9. Shear behaviour and dilation response under normal compression $\sigma_n = 14$ MPa.

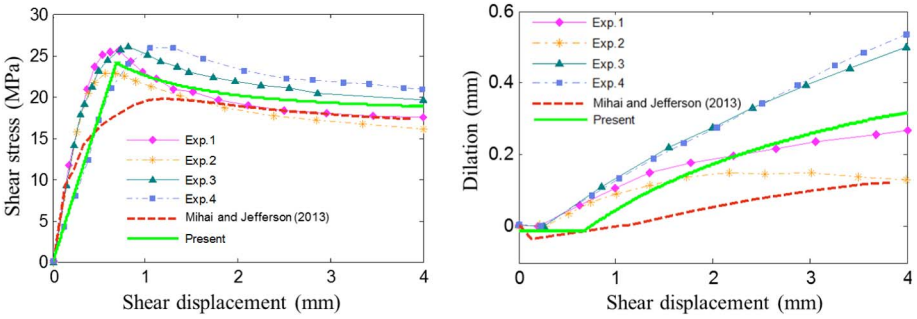

Fig. 10. Shear behaviour and dilation response under normal compression $\sigma_n = 21$ MPa.

be seen in the model description in Section 2, allows capturing the spatial scaling of the constitutive behaviour due to the localisation of deformation. In the context of jointed rock mass behaviour, localised inelastic deformation mostly at the joint, while the surrounding rock mass can be reasonably assumed to be under elastic deformation. A parametric study is used in this section to demonstrate the capability of the proposed model in capturing the deterministic size effects in modelling a rock mass containing a joint. We note that this deterministic size effect due to localised failure is different from the statistical ones due to randomness of strength (Bažant and Yu, 2009; Bazant, 2000), which has been both experimentally (Yoshinaka et al., 1993) and numerically (Bahaaddini et al., 2014) investigated in rock joints.

The deterministic size effect of a jointed rock mass behaviour is due to relative size of the rock joint and its surrounding intact rock. The thickness and behaviour of the joint contained within a rock mass are invariant and irrespective of the size of the rock mass, leading to the scaling of the behaviour of the jointed rock mass with its size. In the proposed model, apart from the inclusion of the characterised length H to represent the relative size of the joint and the surrounding rock, the total deformation is also decomposed into displacement jump at the joint and strain in the intact rock. This helps the model obtain the deterministic scale effect naturally. The model is thus capable of simulating a jointed rock mass at constitutive level (or one element based simulation) and hence can help save computational costs in modelling jointed rock masses.

To illustrate the scale effect in the model, the jointed rock mass in the first experiment (carried by Gentier et al., 2000) with normal stress $\sigma_n = 7$ MPa is chosen for the parametric study. By changing the rock mass size, the relative size of the rock joint and the surrounding bulk body would be changed and the resultant responses of the material will be obtained. The experiment will be simulated with four different scales as shown in Fig. 15 in which the specimen 1 is the original sample with the length of $h = 0.09$ m and the lengths of other specimens (2 3 4) are respectively $0.18, 0.36, 0.72$ m.

In addition to the simulation at constitutive level (one element based simulation) as described in the previous sections, numerical simulations using finite element method (FEM) consisting of several elements are also carried out to verify the performance of the proposed size-dependent constitutive model. For the FE (finite element) simulations, the proposed constitutive model is implemented into the commercial software ABAQUS in the form of a user-defined material model (UMAT). In this simulation, a layer of elements (the red layer shown in Fig. 15b) is used to represent the rock joint with the proposed double-scale constitutive model while the remaining elements represent the surrounding intact rock with elastic behaviour. The thickness of this layer is taken as constant $h = 0.5$ cm for simulations of all rock mass specimens having different sizes to reflect the fact that the joint thickness is the same for different rock mass specimens. Each specimen simulation is discretised with approximately 1200 elements, which means element sizes are different for simulations of different specimens. In these simulations, the elastic parameters of the FE model are obtained by matching its elastic responses with that of the proposed double-scale constitutive model, while all other parameters governing inelastic behaviour are the same in both models (as taken from example 1).

The corresponding stress - displacement responses under shear predicted by the proposed constitutive model and the FE analysis are plotted in Fig. 16. It can be seen that the increase of sample size results in a reduction of elastic shear stiffness of the rock mass and an increase of peak displacement δ_0. This shows that by taking both the joint and the surrounding rock behaviour into the developing the constitutive model, the deterministic size effect can be captured at the constitutive level. However, the values of the shear strengths by the model are unchanged with different scales. This is because of the missing statistical size effects in the current model. The present constitutive approach does not possess such a capability as it represents the constitutive relation with a few variables to save computational costs. It is, of course, natural for a much richer micromechanical approach (e.g. Bahaaddini et al., 2014, 2013) to have such statistical details for better predictions, at a price of much higher computational costs.

It can also be seen in Fig. 16 that the results obtained from the FE analysis and constitutive model are almost the same. This highlights the capability of the proposed model in capturing the behaviour of a jointed rock mass at different spatial scales. This advantage of the model will help save the computational cost while at the same time being able to capture essential features of a jointed rock mass.

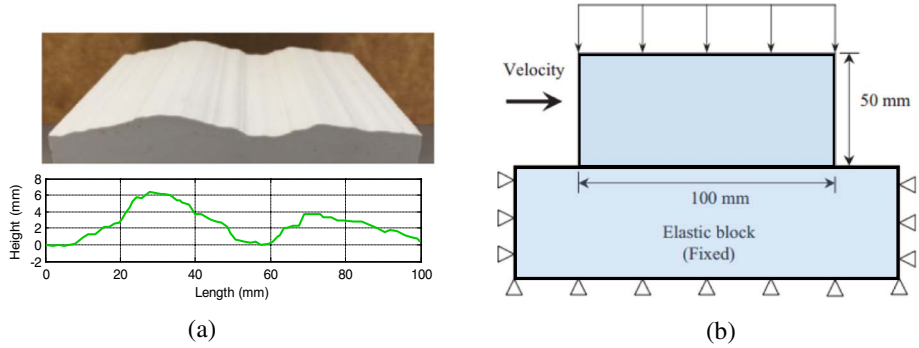

Fig. 11. The experiment set up for the second example (a) the geometry of the sample and (b) test arrangement (after Li et al., 2016).

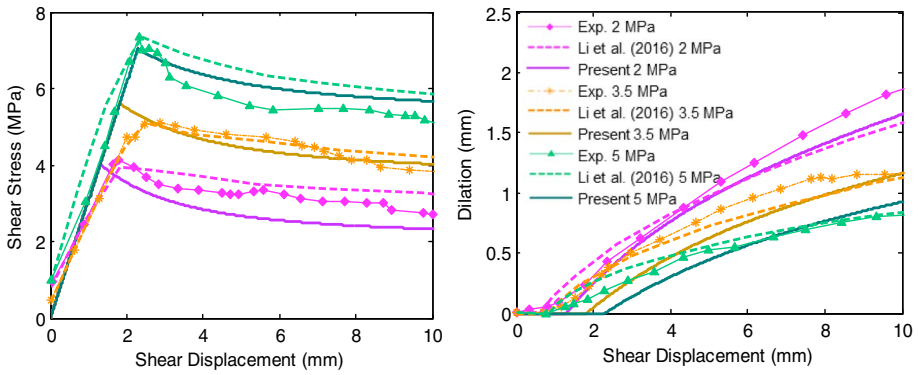

Fig. 12. Shear stress-displacement relation and dilation under different normal stress.

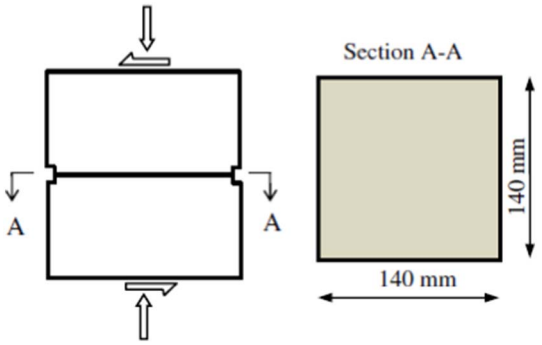

Fig. 13. Geometry and test arrangement of rock joint (after Grasselli and Egger, 2003).

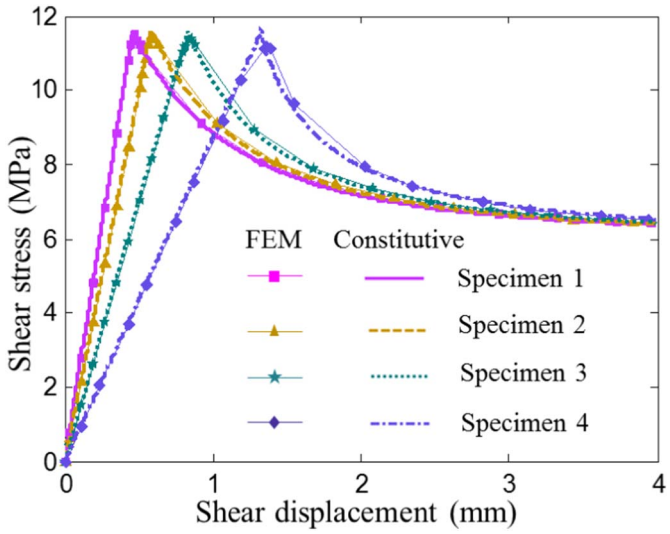

Fig. 15. Geometries of specimens used for scale effect investigation: (a) four specimen sizes in constitutive simulation and (b) four corresponding discretisations in FEM simulation. (For interpretation of the references to colour in this figure, the reader is referred to the web version of this article.)

6. Conclusions

The paper presents a double-scale approach for modelling the shear behaviour of jointed rock mass under constant normal load (CNL) condition. In the model, the mechanical behaviour of the joints and the surrounding rock are incorporated into a constitutive model where their interactions are controlled by a set of kinematic parameters and static conditions across the joint interface. By doing so, the contributions of these two components are naturally taken into the constitutive model along with their interactions. This helps give the model a better description of the jointed rock mass in different loading cases. Another advantage obtained by incorporating the joint in the rock mass is that the joint orientation and the scale effect could be taken into calculation in a continuum constitutive model. A coupled damage-plasticity cohesive model is proposed to describe this inelasticity of the joint in mixed-mode loading condition. By using a single unified loading function, the newly proposed cohesive model can naturally capture the behaviour of the joint from initial yielding to final failure. The proposed model is then validated against experimental results of jointed rock. The numerical results show a good agreement between the proposed model and experimental data, as well as numerical results in previous studies. In addition, the coupling between surrounding rock and joint together with their relative size and orientation of the joint enable the double-scale approach to naturally capture the scale effects of jointed rock mass behaviour. This shows the potential of the proposed approach in modelling rock mass at larger scales.

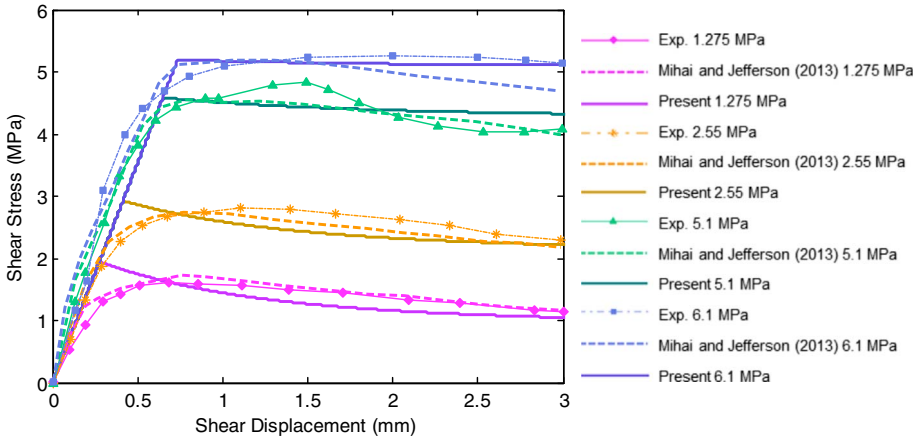

Fig. 14. Stress-displacement relation and dilation of example 3.

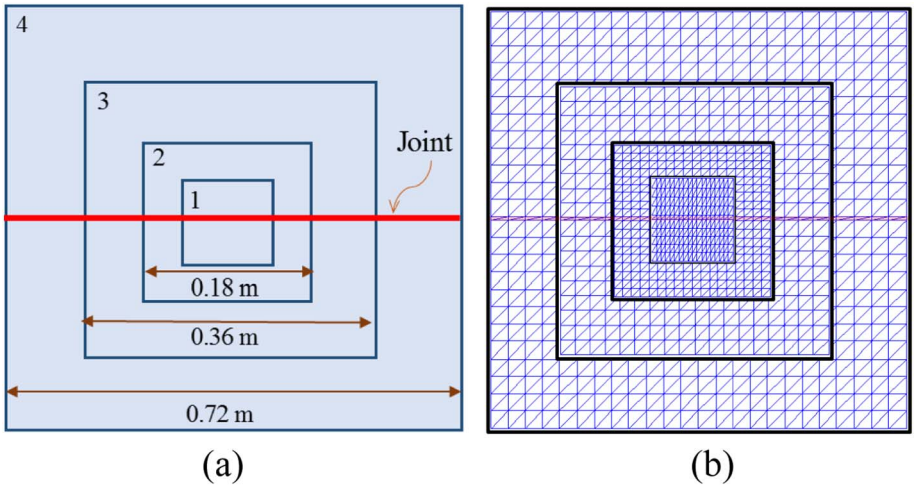

Fig. 16. Shear stress displacement from the FEM and constitutive simulation.

The promising features of the proposed approach and the cohesive model show that they have potentials for modelling the hydro-mechanical coupling in hydraulic fracturing (Alm, 1999; Cammarata et al., 2007; Fidelibus, 2007; Petrovitch et al., 2013, 2014; Souley et al., 2015; Yeo et al., 1998). The most straightforward way, in our opinion, is to modify the hydraulic conductivity of the material taking into account the fracture opening obtained from the embedded cohesive model, in addition to the hydraulic conductivity of the host rock mass. It should be noted that the proposed approach allows the hydro-mechanical coupling to be carried out at the material (constitutive level), as has been discussed as a conceptual approach in Nguyen et al. (2014b), making it very attractive for our new approach (Bui and Nguyen, 2017) for fluid-solid interaction within the framework of the Smoothed Particle Hydrodynamics for geomaterials (Bui et al., 2008).

Acknowledgements

Giang D. Nguyen and Ha H. Bui gratefully acknowledge support from the Australian Research Council via Discovery Projects FT140100408 (Nguyen), DP160100775 (Bui), and DP170103793 (Nguyen & Bui).

References

Alm, P., 1999. Hydro-mechanical Behavior of a Pressurized Single Fracture: An In Situ Experiment. Chalmers University, Sweden.
Asadollahi, P., Invernizzi, M.C.A., Addotto, S., Tonon, F., 2010. Experimental validation of modified Barton's model for rock fractures. Rock Mech. Rock. Eng. 43, 597–613. http://dx.doi.org/10.1007/s00603-010-0085-6.
Bahaaddini, M., Sharrock, G., Hebblewhite, B.K., 2013. Numerical direct shear tests to model the shear behaviour of rock joints. Comput. Geotech. 51, 101–115. http://dx.doi.org/10.1016/j.compgeo.2013.02.003.
Bahaaddini, M., Hagan, P.C., Mitra, R., Hebblewhite, B.K., 2014. Scale effect on the shear behaviour of rock joints based on a numerical study. Eng. Geol. 181, 212–223. http://dx.doi.org/10.1016/j.enggeo.2014.07.018.
Bandis, S.C., Lumsden, A.C., Barton, N.R., 1983. Fundamentals of rock joint deformation. Int. J. Rock Mech. Min. Sci. 20, 249–268. http://dx.doi.org/10.1016/0148-9062(83)90595-8.
Barton, N., 1976. Rock mechanics review: the shear strength of rock and rock joints. Int. J. Rock Mech. Min. Sci. 13, 255–279. http://dx.doi.org/10.1016/0148-9062(76)90003-6.
Barton, N., 2013. Shear strength criteria for rock, rock joints, rockfill and rock masses: problems and some solutions. J. Rock Mech. Geotech. Eng. 5, 249–261. http://dx.doi.org/10.1016/j.jrmge.2013.05.008.
Barton, N., Choubey, V., 1977. The shear strength of rock joints in theory and practice. Rock Mech. 10, 1–54. http://dx.doi.org/10.1007/BF01261801.
Bazant, Z.P., 2000. Size effect. Int. J. Solids Struct. http://dx.doi.org/10.1016/S0020-7683(99)00077-3.
Bažant, Z.P., Yu, Q., 2009. Universal size effect law and effect of crack depth on quasi-brittle structure strength. J. Eng. Mech. 135, 78–84. http://dx.doi.org/10.1061/(ASCE)0733-9399(2009)135:2(78).
Bui, H.H., Nguyen, G.D., 2017. A coupled fluid-solid SPH approach to modelling flow through deformable porous media. Int. J. Solids Struct. 0, 1–21. http://dx.doi.org/10.1016/j.ijsolstr.2017.06.022.
Bui, H.H., Fukagawa, R., Sako, K., Ohno, S., 2008. Lagrangian meshfree particles method (SPH) for large deformation and failure flows of geomaterial using elastic–plastic soil constitutive model. Int. J. Numer. Anal. Methods Geomech. 32, 1537–1570.
Cai, M., Horii, H., 1992. A constitutive model of highly jointed rock masses. Mech. Mater. 13, 217–246. http://dx.doi.org/10.1016/0167-6636(92)90004-W.
Cammarata, G., Fidelibus, C., Cravero, M., Barla, G., 2007. The hydro-mechanically coupled response of rock fractures. Rock Mech. Rock. Eng. 40, 41–61. http://dx.doi.org/10.1007/s00603-006-0081-z.
Chalhoub, M., Pouya, A., 2008. Numerical homogenization of a fractured rock mass: a geometrical approach to determine the mechanical representative elementary volume. Electron. J. Geotech. Eng. 13, 1–12.
Cook, N.G.W., 1992. Natural joints in rock: mechanical, hydraulic and seismic behaviour and properties under normal stress. Int. J. Rock Mech. Min. Sci. 29, 198–223. http://dx.doi.org/10.1016/0148-9062(92)93656-5.
Crisfield, M.A., 2000. Non-linear Finite Element Analysis of Solids and Structures. John Wiley and Sons Ltd., New York. http://dx.doi.org/10.1017/CBO9781107415324.004.
Desai, C.S., Fishman, K.L., 1991. Plasticity-based constitutive model with associated testing for joints. Int. J. Rock Mech. Min. Sci. 28, 15–26. http://dx.doi.org/10.1016/0148-9062(91)93229-Y.
Fardin, N., Stephansson, O., Jing, L., 2001. The scale dependence of rock joint surface roughness. Int. J. Rock Mech. Min. Sci. 38, 659–669. http://dx.doi.org/10.1016/S1365-1609(01)00028-4.
Fidelibus, C., 2007. The 2D hydro-mechanically coupled response of a rock mass with fractures via a mixed BEM–FEM technique. Int. J. Numer. Anal. Methods Geomech. 31, 1329–1348. http://dx.doi.org/10.1002/nag.
Gentier, S., Riss, J., Archambault, G., Flamand, R., Hopkins, D., 2000. Influence of fracture geometry on shear behavior. Int. J. Rock Mech. Min. Sci. 37, 161–174. http://dx.doi.org/10.1016/S1365-1609(99)00096-9.
Goodman, R., 1976. Methods of Geological Engineering in Discontinuous Rocks. West Publishing Company, San Francisco.
Grasselli, G., Egger, P., 2003. Constitutive law for the shear strength of rock joints based on three-dimensional surface parameters. Int. J. Rock Mech. Min. Sci. 40, 25–40.
Haberfield, C.M., Johnston, I.W., 1994. A mechanistically-based model for rough rock joints. Int. J. Rock Mech. Min. Sci. 31, 279–292. http://dx.doi.org/10.1016/0148-9062(94)90898-2.
Harrison, J.P., Hudson, J.A., 2000. Engineering Rock Mechanics. Part 2: Illustrative Workable Examples. Pergamon, Elsevier, Oxford.
Hill, R., 1963. Elastic properties of reinforced solids: some theoretical principles. J. Mech. Phys. Solids 11, 357–372. http://dx.doi.org/10.1016/0022-5096(63)90036-X.
Huang, T.H., Chang, C.S., Chao, C.Y., 2002. Experimental and mathematical modeling for fracture of rock joint with regular asperities. Eng. Fract. Mech. 69, 1977–1996. http://dx.doi.org/10.1016/S0013-7944(02)00072-3.
Igcacio, C., Pere, C.P., Lopez, C.M., 1997. Normal/shear cracking model: application to discrete crack analysis. J. Eng. Mech. 123, 765–773.
Jing, L., 1990. Numerical Modelling of Jointed Rock Masses by Distinct Element Method for Two, and Three-dimensional Problems. Lulea University of Technology (PhD Theis).
Kolymbas, D., 1981. Bifurcation analysis for sand samples with a non-linear constitutive equation. Ingenieur-Archiv 50, 131–140. http://dx.doi.org/10.1007/BF00539697.
Kolymbas, D., 2009. Kinematics of shear bands. Acta Geotech. 4, 315–318. http://dx.doi.org/10.1007/s11440-009-0092-5.
Ladanyi, B., Archambault, G., 1969. Simulation of shear behavior of a jointed rock mass. In: The 11th US Rock Mechanics Symposium (USRMS), Berkeley, CA, pp. 105–125.
Lee, U., 1998. A theory of smeared continuum damage mechanics. J. Mech. Sci. Technol. 12, 233–243. http://dx.doi.org/10.1007/BF02947168.
Li, Y., Zhang, Y., 2015. Quantitative estimation of joint roughness coefficient using statistical parameters. Int. J. Rock Mech. Min. Sci. 77, 27–35. http://dx.doi.org/10.1016/j.ijrmms.2015.03.016.
Li, B., Maekawa, K., Okamura, H., 1989. Contact density model for stress transfer across

cracks in concrete. J. Fac. Eng. 40, 9–52 The University of Tokyo.
Li, Y., Oh, J., Mitra, R., Hebblewhite, B., 2016. A constitutive model for a laboratory rock joint with multi-scale asperity degradation. Comput. Geotech. 72, 143–151. http://dx.doi.org/10.1016/j.compgeo.2015.10.008.
Martinez, M.J., Newell, P., Bishop, J.E., 2012. Coupled multiphase flow and geomechanics for analysis of caprock damage during CO2 sequestration operations. In: XIX International Conference on Water Resources CMWR 2012. University of Illinois at Urbana-Champaign, USA.
Mihai, I., Jefferson, A., 2013. A multi-asperity plastic-contact crack plane model for geomaterials. Int. J. Numer. Anal. Methods Geomech. 37, 1492–1509. http://dx.doi.org/10.1002/nag.
Nguyen, G.D., Elzein, A., Bennett, T., 2014b. A conceptual approach to two-scale constitutive modelling for hydro-mechanical coupling. In: 7th International Congress on Environmental Geotechnics ICEG2014. Engineers Australia (EA), Melbourne, Australia.
Nguyen, G.D., Einav, I., Korsunsky, A.M., 2012. How to connect two scales of behaviour in constitutive modelling of geomaterials. Géotech. Lett. 2, 129–134. http://dx.doi.org/10.1680/geolett.12.00030.
Nguyen, G.D., Korsunsky, A.M., Einav, I., 2014a. A constitutive modelling framework featuring two scales of behaviour: fundamentals and applications to quasi-brittle failure. Eng. Fract. Mech. 115, 221–240. http://dx.doi.org/10.1016/j.engfracmech.2013.11.006.
Nguyen, G.D., Nguyen, C.T., Nguyen, V.P., Bui, H.H., Shen, L., 2016. A size-dependent constitutive modelling framework for localised failure analysis. Comput. Mech. 1–24. http://dx.doi.org/10.1007/s00466-016-1293-z.
Patton, F., 1966. Multiple modes of shear failure in rock. In: 1st International Society for Rock Mechanics. International Society for Rock Mechanics, Lisbon, Portugal, pp. 509–515 (October).
Petrovitch, C.L., Nolte, D.D., Pyrak-Nolte, L.J., 2013. Scaling of fluid flow versus fracture stiffness. Geophys. Res. Lett. http://dx.doi.org/10.1002/grl.50479.
Petrovitch, C.L., Pyrak-Nolte, L.J., Nolte, D.D., 2014. Combined scaling of fluid flow and seismic stiffness in single fractures. Rock Mech. Rock. Eng. 47, 1613–1623. http://dx.doi.org/10.1007/s00603-014-0591-z.
Plesha, M., 1987. Constitutive models for rock discontinuities with dilatancy and surface degradation. Int. J. Numer. Anal. Methods Geomech. 11, 345–362. http://dx.doi.org/10.1002/nag.1610110404.
Saeb, S., Amadei, B., 1992. Modelling rock joints under shear and normal loading. Int. J. Rock Mech. Min. Sci. 29, 267–278.
Schreyer, H., Sulsky, D., 2016. Constitutive and numerical framework for modeling joints and faults in rock. Int. J. Numer. Anal. Methods Geomech. 40, 1253–1283. http://dx.doi.org/10.1002/nag.
Singh, M., Rao, K.S., 2005. Empirical methods to estimate the strength of jointed rock masses. Eng. Geol. 77, 127–137. http://dx.doi.org/10.1016/j.enggeo.2004.09.001.
Singh, M., Singh, B., 2012. Modified Mohr-Coulomb criterion for non-linear triaxial and polyaxial strength of jointed rocks. Int. J. Rock Mech. Min. Sci. 51, 43–52. http://dx.doi.org/10.1016/j.ijrmms.2011.12.007.
Souley, M., Lopez, P., Boulon, M., Thoraval, A., 2015. Experimental hydromechanical characterization and numerical modelling of a fractured and porous sandstone. Rock Mech. Rock. Eng. 48, 1143–1161. http://dx.doi.org/10.1007/s00603-014-0626-5.
Su, C., Wei, Y.J., Anand, L., 2004. An elastic-plastic interface constitutive model: application to adhesive joints. Int. J. Plast. 20, 2063–2081. http://dx.doi.org/10.1016/j.ijplas.2003.12.008.
Sun, Z., Gerrard, C., Stephansson, O., 1985. Rock joint compliance tests for compression and shear loads. Int. J. Rock Mech. Min. Sci. 22, 197–213. http://dx.doi.org/10.1016/0148-9062(85)92948-1.
Tatone, B.S.A., Grasselli, G., 2009. A method to evaluate the three-dimensional roughness of fracture surfaces in brittle geomaterials. Rev. Sci. Instrum. 80. http://dx.doi.org/10.1063/1.3266964.
Tatone, B.S.A., Grasselli, G., 2013. An investigation of discontinuity roughness scale dependency using high-resolution surface measurements. Rock Mech. Rock. Eng. 46, 657–681. http://dx.doi.org/10.1007/s00603-012-0294-2.
Vardoulakis, I., Goldscheider, M., Gudehus, G., 1978. Formation of shear bands in sand bodies as a bifurcation problem. Int. J. Numer. Anal. Methods Geomech. 2, 99–128. http://dx.doi.org/10.1002/nag.1610020203.
Wang, J.G., Ichikawa, Y., Leung, C.F., 2003. A constitutive model for rock interfaces and joints. Int. J. Rock Mech. Min. Sci. 40, 41–53. http://dx.doi.org/10.1016/S1365-1609(02)00113-2.
Yeo, I.W., de Freitas, M.H., Zimmerman, R.W., 1998. Effect of shear displacement on the aperture and permeability of a rock fracture. Int. J. Rock Mech. Min. Sci. http://dx.doi.org/10.1016/S0148-9062(98)00165-X.
Yoshinaka, R., Yoshida, J., Shimizu, T., Arai, H., Arisaka, S., 1993. Scale effect in shear strength and deformability of rock joints. In: Pinto Da Chunha, A. (Ed.), Proc Symp Scale Effects in Rock Masses 93. Balkema, International Society for Rock Mechanics, Rotterdam, Libson, Portugal, pp. 143–149.

Appendix B

Localised failure mechanism as the basis for constitutive modelling of geomaterials

Le, L.A., Nguyen, G.D., Bui, H.H., Sheikh, A.H., Kotousove, A., 2018. Localised failure mechanism as the basis for constitutive modelling of geomaterials. *International Journal of Engineering Science* 133, 284–310.

Statement of Authorship

Title of Paper	Localised failure mechanism as the basis for constitutive modelling of geomaterials
Publication Status	☑ Published ☐ Accepted for Publication ☐ Submitted for Publication ☐ Unpublished and Unsubmitted w ork w ritten in manuscript style
Publication Details	Le, L.A., Nguyen, G.D., Bui, H.H., Sheikh, A.H., Kotousove, A., 2018. Localised failure mechanism as the basis for constitutive modelling of geomaterials. Internaltional J. Eng. Sci. 133, 284–310.

Principal Author

Name of Principal Author (Candidate)	Linh A. Le	
Contribution to the Paper	Developed the double-scale modelling featuring two localisation bands including technical details, implementation and verification. Performed numerical analysis and model validation. Wrote and revised the manuscript.	
Overall percentage (%)	70	
Certification:	This paper reports on original research I conducted during the period of my Higher Degree by Research candidature and is not subject to any obligations or contractual agreements with a third party that would constrain its inclusion in this thesis. I am the primary author of this paper.	
Signature		Date 26/03/2019

Co-Author Contributions

By signing the Statement of Authorship, each author certifies that:

i. the candidate's stated contribution to the publication is accurate (as detailed above);

ii. permission is granted for the candidate in include the publication in the thesis; and

iii. the sum of all co-author contributions is equal to 100% less the candidate's stated contribution.

Name of Co-Author	Giang D. Nguyen		
Contribution to the Paper	Developed the generic thermodynamic framework for the double-scale approach and generic Fortran code for triaxial compression test. Supervised the technical developments. Evaluated & revised the manuscript.		
Signature		Date	27 / 03 / 2019

Name of Co-Author	Ha H. Bui		
Contribution to the Paper	Developed generic Fortran code for triaxial compression test & contributed to the development of the thermodynamic based double-scale approach in generic form. Supervised the technical developments. Evaluated & revised the manuscript.		
Signature		Date	27 / 03 / 2019

Name of Co-Author	Abdul Hamid Sheikh		
Contribution to the Paper	Supervised the technical developments. Evaluated & revised the manuscript.		
Signature		Date	03/04/2019

Name of Co-Author	Andrei Kotousov		
Contribution to the Paper	Supervised the technical developments. Evaluated & revised the manuscript.		
Signature		Date	27/03/2019

International Journal of Engineering Science 133 (2018) 284–310

Contents lists available at ScienceDirect

International Journal of Engineering Science

journal homepage: www.elsevier.com/locate/ijengsci

Localised failure mechanism as the basis for constitutive modelling of geomaterials

Linh A. Le[a], Giang D Nguyen[a,*], Ha H. Bui[b], Abdul Hamid Sheikh[a], Andrei Kotousov[c]

[a] School of Civil, Environmental and Mining Engineering, The University of Adelaide, Adelaide, SA 5005, Australia
[b] Department of Civil Engineering, Monash University, Clayton, VIC 3800, Australia
[c] School of Mechanical Engineering, The University of Adelaide, Australia

ARTICLE INFO

Article history:
Received 20 August 2018
Revised 14 September 2018
Accepted 15 September 2018

Keywords:
Constitutive modelling
Geomaterials
Localised failure
Lode angle
Size effect
Localisation band
Cohesive-frictional

ABSTRACT

Localised failure of geomaterials in the form of cracks or shear bands always requires special attention in constitutive modelling of solids and structures. This is because the validity of classical constitutive models based on continuum mechanics is questionable once localised inelastic deformation has occurred. In such cases, due to the fact that the macro inelastic responses are mainly governed by the deformation and microstructural changes inside the localisation zone, internal variables, representing these microstructural changes, should be defined inside this zone. In this paper, the localised failure mechanism is identified and employed as an intrinsic characteristic upon which a constitutive model is based on at the first place, instead of being dealt with after developing the model using various regularisation techniques. As a result, inelastic responses of the model are correctly associated with the localisation bands, and not smeared out over the whole volume element as in classical continuum constitutive models. It is shown that this inbuilt localisation mechanism in a constitutive model can naturally capture important features of the material and possess intrinsic regularisation effects while minimising the use of additional phenomenological treatments, and also possessing intrinsic regularisation effects. The development of the proposed model is based on an additional kinematic enhancement to account for high gradient of deformation across the localisation band. This enrichment allows the introduction of an additional constitutive relationship for the localisation band, which is represented in the form of a cohesive-frictional model describing traction-displacement jump relationship across two sides of the localisation band. The model, formulated within a thermodynamically consistent approach, possesses constitutive responses of the bulk material and two localisation bands connected through internal equilibrium conditions. Its key characteristics are demonstrated and validated against experimental data from different types of geomaterials under different loading conditions at both material and structural levels.

* Corresponding author.
E-mail addresses: giang.nguyen@trinity.oxon.org, g.nguyen@adelaide.edu.au (G.D. Nguyen).

https://doi.org/10.1016/j.ijengsci.2018.09.004
0020-7225/

Glossary

$\mathbf{a}_o$	Elastic stiffness of material
$\mathbf{C}$	Kinematic constraint
D_k	Damage of crack k
E	Young's modulus
f_t	Tensile strength
f_c	Compressive strength
g	Potential function of cohesive-frictional crack
G_I	Mode I fracture energy
G_{II}	Mode II fracture energy
h_k	Thickness of crack k
H_k	Characteristic length of crack k
I_1	First invariant of stress tensor
J_2,J_3	Second and Third invariants of deviatoric stress tensor
K_n, K_s	Elastic normal and shear stiffness of crack
$\mathbf{K}_c^{sec}$	Secant stiffness of crack in local coordinate system
$\mathbf{K}_{ck}^{sec}$	Secant stiffness of crack k in local coordinate system
$\mathbf{K}_k^{sec}$	Secant stiffness of crack k in global coordinate system
$\mathbf{K}_k^{tan}$	Tangent stiffness of crack k in global coordinate system
m	Model parameters controlling shape of yield surface
n_i	Normal vectors of crack in index notation
$\mathbf{n}_k$	Normal vector of crack k in matrix form
p	Hydrostatic pressure
q	Deviatoric stress component
$\mathbf{r}_k$	Residual vector of crack k
$\mathbf{R}_k$	Transformation matrix from global to local coordinate system of crack k
$\mathbf{t}_k$	Traction of crack k in global coordinate system
$\mathbf{t}_k^{tr}$	Trial traction of crack k in global coordinate system
$\mathbf{t}_k^{cor}$	Corrective traction of crack k in global coordinate system
$\mathbf{t}_c = [\ t_n \quad t_{s1} \quad t_{s2}\ ]^T$	Traction of crack in local coordinate system
$\mathbf{t}_{ck} = [\ t_{k,n} \quad t_{k,s1} \quad t_{k,s2}\ ]^T$	Traction of crack k in local coordinate system
u_p	Accumulated displacement parameter
$\mathbf{u}_k$	Total displacement jump of crack k in global coordinate system
$\mathbf{u}_c = [\ u_n \quad u_{s1} \quad u_{s2}\ ]^T$	Total displacement jump of crack in local coordinate system
$\mathbf{u}_{ck} = [\ u_{k,n} \quad u_{k,s1} \quad u_{k,s2}\ ]^T$	Total displacement jump of crack k in local coordinate system
$\mathbf{u}_c^e$	Elastic displacement jump of crack in local coordinate system
$\mathbf{u}_c^p = [\ u_n^p \quad u_{s1}^p \quad u_{s2}^p\ ]^T$	Plastic displacement jump of crack in local coordinate system
$\mathbf{u}_k^{tr}$	Trial displacement jump of crack k in global coordinate system
$\mathbf{u}_k^p$	Plastic displacement jump of crack k in global coordinate system
y	Yield-failure function crack
α_0, β	Parameters controlling damage evolution
γ	Parameter controlling the non-associativity
Γ_k	Area of crack k
δ_0	Displacement corresponding to peak stress in pure tension
$\boldsymbol{\varepsilon} = [\varepsilon_{11}\ \varepsilon_{22}\ \varepsilon_{33}\ \gamma_{12}\ \gamma_{23}\ \gamma_{31}]^T$	Overall strain of RVE
$\boldsymbol{\varepsilon}_o = [\varepsilon_{o,11}\ \varepsilon_{o,22}\ \varepsilon_{o,33}\ \gamma_{o,12}\ \gamma_{o,23}\ \gamma_{o,31}]^T$	Strain of outer bulk material
η_k	Volume fraction of crack k
θ	Lode angle
$\dot{\lambda}$	Plastic multiplier
$\boldsymbol{\Lambda}$	Lagrangian multipliers
μ_0, μ	Model parameters controlling shape of yield surface
ν	Poisson's ratio
$\boldsymbol{\xi}_k$	Strain of crack k
$\boldsymbol{\sigma}_{ij}$	Stress of RVE in index notation form
$\sigma_i;\ i = 1,\ 2,\ 3$	Principal stress 1, 2 and 3
$\boldsymbol{\sigma}^{tr}$	Trial stress of RVE
$\boldsymbol{\sigma}_o$	Stress of outer bulk material
$\boldsymbol{\sigma} = [\sigma_{11}\ \sigma_{22}\ \sigma_{33}\ \sigma_{12}\ \sigma_{23}\ \sigma_{31}]^T$	Stress of RVE in matrix form
φ, κ	Failure plane orientation of crack
Φ	Dissipation potential of RVE

Φ_{Γ_k}	Dissipation potential of crack face k
ϕ	Material frictional angle
$\overline{\boldsymbol{\chi}}_{\mathrm{o}}$	True generalised stress of outer bulk material
$\overline{\boldsymbol{\chi}}_{\Gamma_k}$	True generalised stress of crack face k
$\boldsymbol{\chi}_{\mathrm{o}}$	Dissipative generalised stress of outer bulk material
$\boldsymbol{\chi}_{\Gamma_k}$	Dissipative generalised stress of crack face k
Ψ	Helmholtz free energy potential of RVE
Ψ_o	Helmholtz free energy potential of outer bulk material
Ψ_{Γ_k}	Helmholtz free energy potential of crack face k
Ω	Representative volume element (RVE)
Ω_{o}	Outer bulk material
Ω_k	Crack band k

1. Introduction

Geomaterials usually experience a wide range of loading conditions. For concrete and its structural applications, the applied loads usually result in the material being under tension and/or shearing under low confining pressures. Rocks, on the other hand, often experience shearing under a wide range of confining pressures. Nevertheless, both concrete and rocks usually show brittle responses at low confining pressures (Ingraham, Issen, & Holcomb, 2013; Klein & Reuschlé, 2003; Yang, Jiang, Xu, & Chen, 2008) and ductile behaviour under high confining pressures (Ingraham et al., 2013; Wong & Baud, 2012).

Despite the fact that geomaterials display a wide range of responses, it is well-known that localised failure, in the form of localisation bands, is commonly observed in most loading conditions. To the best of our knowledge, this localised failure is the key mechanism underlying the responses and several characteristics of the geomaterials. In tension, the localisation band is usually perpendicular to the applied tensile load (Jensen, 2016) and under mode I fracture. The corresponding material behaviour, in this case, is usually quasi-brittle, mainly governed by the tensile strength f_t and mode I fracture energy G_I. In triaxial compression (Ingraham et al., 2013; Ma & Haimson, 2016), geomaterials show a wide range of responses at different levels of confinement associated with different modes of localised failure. In particular, when confining pressure increases, the localisation band orientation changes from highly inclined to less inclined and/or even perpendicular to the axial principal stress (Klein & Reuschlé, 2003; Ma & Haimson, 2016). The macro responses experience a transition from brittle to ductile behaviour associated with two mechanisms: shear localisation at low confining pressures with dilatant behaviour and compaction failure at high confining pressures with grain crushing and porosity reduction (Wong & Baud, 2012).

One of the effects of localised failure mechanism on geomaterial behaviour is the deterministic size effect, which has been extensively observed in experiments on concrete and rock (Bažant, 1999; Karihaloo, Abdalla, & Xiao, 2003; van Mier, 1986) and also investigated numerically (Rezakhani & Cusatis, 2014; Syroka-Korol, Tejchman, & Mróz, 2013; Tejchman & Gorski, 2008). Different from statistical size effect, caused by the randomness of material strength, deterministic size effect, in this case, is a result of stress redistribution caused by the stable propagation of fracture and dissipation released from inelastic responses inside the localisation band. In addition, the dependence of yield locus and material responses on the Lode angle, observed in true triaxial tests (Haimson & Rudnicki, 2010; Ingraham et al., 2013; Vachaparampil & Ghassemi, 2017), can also be linked with the localised failure. In particular, at sufficiently low confining pressures, shear banding is the mechanism that triggers material failure (Eichhubl, Hooker, & Laubach, 2010; Ma & Haimson, 2016; Wong & Baud, 2012). The behaviour of shear band is, in fact, closely linked with the true triaxial stress condition, which can be represented by three stress invariants, I_1, J_2, and J_3 (or alternatively the Lode angle θ, with $\cos 3\theta = \frac{3\sqrt{3}}{2} J_3/J_2^{3/2}$), in which I_1 is the first invariant of the stress tensor; J_2 and J_3 are the second and the third invariants of the deviatoric stress tensor. As can be seen in several experiments (Lee & Haimson, 2011; Ma & Haimson, 2016; Vachaparampil & Ghassemi, 2017), a change of true triaxial condition leads to a corresponding variation of the failure plane orientation. As a consequence, the dependence of material yield/failure on the Lode angle comes naturally as a result of localised shear failure. With the increase of confining pressure, the failure mechanism gradually transitions from shear to compaction localisation and finally diffuse compaction, in conjunction with the brittle-ductile transition (Ma & Haimson, 2016; Wong & Baud, 2012). During this transition, the influence of shear on material behaviour reduces and thus the yield locus gradually becomes less dependent on the Lode angle as experimentally observed in Ingraham et al. (2013). Therefore, the Lode angle dependence, along with size effect, localisation band orientation and other features (i.e., hydrostatic pressure dependence, tension-compression difference) can and should be considered as consequences of the localised failure mechanism.

Given the localised failure as the key mechanism governing the responses of geomaterials, this mechanism should be considered as the basis and intrinsic feature in the development of constitutive models before any other features such as Lode angle dependence, hydrostatic pressure dependence or size effect. However, to the best of our knowledge, this key mechanism is usually separated from the development of constitutive models and incorporated afterwards in the form of regularisation techniques to deal with softening related issues in the analysis of Boundary Value Problems (BVPs). This separation is, in fact, useful as it simplifies the development of a model, as seen in several examples in the literature. These include elasto-plastic models (Chemenda & Mas, 2016; Lu, Du, Wang, Zhou, & Li, 2016; Navarro, Alonso, Calvo, & Sánchez, 2010; Shen & Shao, 2016; Spiezia, Salomoni, & Majorana, 2016), elastic/plastic-damage models (Brünig & Michalski, 2017; Grassl, Xenos, Nyström, Rempling, & Gylltoft, 2013; Karrech, Regenauer-Lieb, & Poulet, 2011; Mir, Nguyen, & Sheikh,

2018; Paliwal, Hammi, Moser, & Horstemeyer, 2017; Zhu, Zhao, & Shao, 2016) and even some micromechanics based models (Cheng, Qian, & Zhao, 2016; Das et al., 2014; Qi, Shao, Giraud, Zhu, & Colliat, 2016; Tengattini et al., 2014; Zhao, Zhu, & Shao, 2018). The merits along with success of the above models in capturing stress-strain responses are unquestionable, especially for diffuse failure where the implicit assumption of homogeneous deformation used in these models is appropriate. However, these classical constitutive models for geomaterials are not physically meaningful beyond the onset of localisation, and hence do not possess behaviour intrinsically linked with localised failure mechanism that is experimentally observed under a wide range of conditions. As a consequence, additional phenomenological relationships are usually needed for these models in the analysis of BVPs, as remedies for the lack of intrinsic localised failure mechanism to deal with softening and localisation. For instance, regularisations based on the smeared crack approach (Cervera & Chiumenti, 2006; Grassl et al., 2013), viscous enhancements (Das et al., 2014; Tengattini et al., 2014; Zhao et al., 2018) or nonlocal enrichment (Nguyen & Korsunsky, 2008; Xenos, Grégoire, Morel, & Grassl, 2015), are usually required to avoid the mesh-dependent issues in the analysis of BVPs involving localisation and/or softening.

In addition, as initial yield states in classical continuum models are governed by the yield criterion solely, phenomenological expression of the yield functions containing the third stress invariant J_3 (or alternatively Lode angle parameter θ) is also required in some models to capture the dependence of initial yield and mechanical responses on the Lode angle (Chemenda & Mas, 2016; Grassl et al., 2013; Paliwal et al., 2017; Veiskarami & Tamizdoust, 2017). Although providing good improvements to the constitutive behaviour, these treatments are usually of phenomenological nature as a consequence of missing the underlying intrinsic mechanism of the material failure. In this respect, we acknowledge micro-/meso-mechanical approaches (i.e., Nguyen, Bui, Nguyen, & Kodikara, 2017; Xenos et al., 2015) as powerful ones that can naturally resolve several issues of continuum modelling listed above. They are however much more computationally expensive and thus are not covered within the scope of this paper.

The essentials of the localised failure mechanism in constitutive modelling have been addressed partly in some studies through the incorporation of cracks where inelastic behaviour takes place (Caner & Bažant, 2013; Misra & Yang, 2010; Schreyer, 2007). However, the work by Schreyer and co-authors (Sanchez, Schreyer, Sulsky, & Wallstedt, 2015; Schreyer, 2007; Tran, Sulsky, & Schereyer, 2015) only focuses on crack orientation and still rely on the smeared crack regularisation to deal with softening related issues in the analysis of BVPs. The microplane models (Bažant & Caner, 2014; Caner & Bažant, 2013; Etse, Nieto, & Steinmann, 2003; Li, Caner, Chau, & Bažant, 2017) and other similar micromechanics-based models (Misra & Poorsolhjouy, 2016; Misra & Yang, 2010) include the effects of different failure plane orientations on the mechanical responses and hence can handle complex loading conditions with multiple localisation bands/cracks. However, these models still do not account for the mechanism of localised failure when mapping all these effects to a single macro stress–strain relationship. In other words, the assumption of homogeneous deformation was implicitly employed in these models and as a consequence, they still rely on regularisations for analysing BVPs (e.g., Daneshyar & Ghaemian, 2017). In another kind of approach, Pietruszczak and co-authors (Haghighat & Pietruszczak, 2015; Pietruszczak & Haghighat, 2015) provided comprehensive treatments for the inclusion of a single localisation band and its size in a constitutive structure. However, a strong basis for the development of constitutive models that can capture a wide range of behaviour under different loading conditions was not addressed and investigated. In addition, although the regularisation effects and crack propagations were satisfactory for benchmark problems in Haghighat and Pietruszczak (2015), the use of a single localisation band required an extra treatment (i.e., level-set method) in the determination of the crack orientation to better control the crack propagation and avoid stress-locking issue.

From the microscopic point of view, the localisation band is, in fact, a system of macro-, meso- and/or micro-cracks which are formed during the loading, as addressed by Hillerborg, Modéer, and Petersson (1976), later confirmed by experimental observations at micro/meso-scale (Brooks, 2013; Skarzyński & Tejchman, 2016) and field scales (Savage & Brodsky, 2011). As analysed in these studies, a fracture process zone (FPZ) usually consists of both primary and secondary cracks with different orientations. The formation and evolution of this zone significantly affect the toughness and ductility of the material (Hu & Duan, 2008). This finite-width FPZ is usually and practically idealised as a single zero-thickness crack, lumping the contributions of several cracks at lower (micro/meso) scales into a cohesive-frictional model. Despite the practical usefulness, this simplification contains potential issues in the calculation of fracture energy from standard experiments, and also in the numerical simulation of structural failure/fracture. The former is the boundary effect on the produced fracture energy and is not the focus of this work, given the use of averaged fracture energy from standard tests. The latter is related to the evolution of the FPZ during failure. It has been well-known that unphysical stress-locking issue in numerical simulations of concrete fracture, even under proportional loading conditions, is due to taking and fixing the orientation of a single crack at the onset of cracking. Special attentions and numerical treatments are thus needed at the level of the discretisation scheme to obtain a proper crack propagation. These include crack tracking/tracing (Dias-da-Costa, Alfaiate, Sluys, & Júlio, 2009; Haghighat & Pietruszczak, 2015; Lloberas-Valls, Huespe, Oliver, & Dias, 2016; Parvaneh & Foster, 2016; Zhang, Lackner, Zeiml, & Mang, 2015) and rotating crack approach (He, Wu, Liew, & Wu, 2006; Jirásek, 2000; Sancho, Planas, Cendón, Reyes, & Gálvez, 2007). However, due to the use of a single localisation band/crack, such models are inadequate under non-proportional loading conditions with changes of loading paths and hence stress locking still occurs if a new (secondary) crack/band is not allowed in the models. We will show later that allowing secondary cracking at the constitutive level is a natural way to remove stress locking issues and correctly capture the propagation of the macro-crack. Since this enhancement is at the constitutive level, the implementation of the proposed approach in any mesh-based or mesh-free methods is

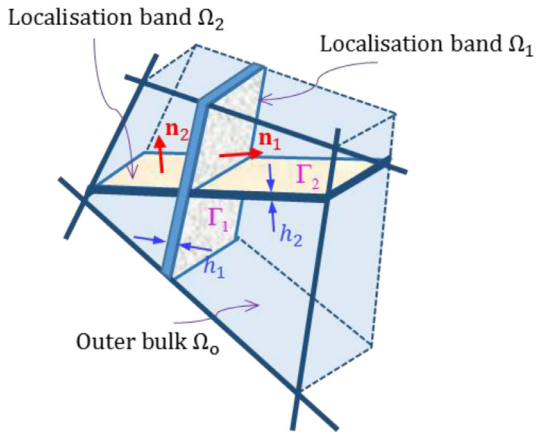

Fig. 1. Illustration of a representative volume element (RVE) with two cracks.

essentially the same, as it requires only a length scale related to the size of the volume element to bridge the constitutive and structural responses.

In this research, we incorporate the intrinsic mechanisms of localised failure explicitly and systematically to obtain a constitutive model with essential features of the material while minimising the involvement of phenomenological relationships. A new thermodynamics-based formulation is developed to accommodate the kinematic enrichment due to the presence of more than one cracks crossing a volume element. This is totally different from earlier work (Nguyen, Einav, & Korsunsky, 2012; Nguyen, Korsunsky, & Einav, 2014; Nguyen, Nguyen, Nguyen, Bui, & Shen, 2016b), the enhanced assumed strain or strong discontinuity approach (i.e., Borja, 2000), and that by Pietruszczak and co-authors (Haghighat & Pietruszczak, 2015; Pietruszczak & Haghighat, 2015), where a single localisation band and its corresponding kinematic enrichments were used. The thermodynamic formulation in this paper will provide a better way to connect the bulk behaviour with those of two cohesive-frictional cracks embedded in it, to naturally obtain both macro stress and internal equilibrium without requiring additional or arbitrary assumptions. The cohesive-frictional crack is further developed from a new cohesive model (Le et al., 2017), which is based on damage-plasticity formulation with a unified yield-failure surface for mixed-mode loading cases. This cohesive model naturally provides both onset and orientation of the localisation band, through the activation of its inelastic behaviour with respect to an orientation depending on the stress state. No further treatment or enforcement of the band orientation is needed as essentially required in several previous studies. Therefore, in the simulations of localised failure at structural scale, the proposed approach can naturally remove stress locking and correctly capture the propagation of a macro-crack, consisting of several meso-cracks due to secondary cracking. Size effects and the dependence of yield locus on all three stress invariants I_1, J_2 and J_3 are also automatically captured without requiring any further treatments.

2. A mechanism-based constitutive model

A new thermodynamic formulation is presented in this section to connect all components of the proposed kinematically enriched constitutive model. This has not been achieved in earlier work (Nguyen et al., 2014) where ad hoc relationships outside the thermodynamic formulation were needed. The proposed approach is developed in a generic form and hence can be used with any constitutive models to describe the nonlinear responses inside the localisation zone.

2.1. Thermodynamic formulation of the kinematically enriched approach

The constitutive model is developed for a Representative Volume Element (RVE) Ω comprising an outer bulk material Ω_o and two localisation bands $\Omega_k = \Gamma_k h_k$ $(k = 1,\ 2)$, represented by its area Γ_k and thickness h_k as shown in Fig. 1. The localisation bands are also characterised by their orientations, which are represented by normal vectors $\mathbf{n}_k$. Assuming homogeneous behaviour, the tractions at the boundaries between the localisation bands and the bulk material in the global coordinate system and strain vectors of the bands are denoted as $\mathbf{t}_k$ and $\dot{\boldsymbol{\xi}}_k$ respectively. The stress and strain vectors of the outer bulk material are $\boldsymbol{\sigma}_o$ and $\boldsymbol{\varepsilon}_o$, while the volume-averaged stress and strain vectors of the RVE are denoted as $\boldsymbol{\sigma}$ and $\boldsymbol{\varepsilon}$. It should be noted that the notation k represents localisation band number and has nothing to do with index notation (i.e. $\dot{\boldsymbol{\xi}}_1$ denotes the strain vector of the localisation band #1).

To link the behaviour of the localisation bands to the overall stress-strain relationship of the RVE, the strain rates $\dot{\boldsymbol{\xi}}_k$ inside the localisation bands can be expressed in terms of the homogeneous strain rate of the bulk material $\dot{\boldsymbol{\varepsilon}}_o$ and an enhancing strain rate (Neilsen & Schreyer, 1993):

$$\dot{\boldsymbol{\xi}}_1 = \dot{\boldsymbol{\varepsilon}}_o + \frac{1}{h_1}\mathbf{n}_1\dot{\mathbf{u}}_1 \ \text{and}\ \dot{\boldsymbol{\xi}}_2 = \dot{\boldsymbol{\varepsilon}}_o + \frac{1}{h_2}\mathbf{n}_2\dot{\mathbf{u}}_2 \tag{1}$$

where $\dot{\mathbf{u}}_1$ and $\dot{\mathbf{u}}_2$ are the velocity jumps between two sides of the bands in the global coordinate system. The inclusion of the bulk behaviour in this approach allows the use of only a few localisation bands to capture behaviour with and without localised failure. This is different from some existing micromechanics-based approaches (Caner & Bažant, 2013; Kedar & Bažant, 2015; Misra & Poorsolhjouy, 2016) that ignore the difference between the strain inside the localisation band and the macro strain (or the strain in the bulk) and hence require contributions from as many orientations as possible to form the macro strain. Having more bands would improve the flexibility of the model but, at the same time, complicates the implementation and computation (for the stress update at both macro and localisation band level). Therefore, we only use a maximum of two localisation bands at a material point, which is sufficient to capture the behaviour of geomaterials in many cases as will be shown later in the numerical examples. The macro strain rate is obtained using Eq. (1) and a simple volume averaging homogenisation, assuming the strain in each region is uniform:

$$\dot{\boldsymbol{\varepsilon}} = (1-\eta_1-\eta_2)\dot{\boldsymbol{\varepsilon}}_{\mathrm{o}} + \eta_1\dot{\boldsymbol{\xi}}_1 + \eta_2\dot{\boldsymbol{\xi}}_2 = \dot{\boldsymbol{\varepsilon}}_{\mathrm{o}} + \frac{1}{H_1}\mathbf{n}_1\dot{\mathbf{u}}_1 + \frac{1}{H_2}\mathbf{n}_2\dot{\mathbf{u}}_2 \tag{2}$$

where $\eta_k = \frac{\Omega_k}{\Omega} = \frac{\Gamma_k h_k}{\Omega}$ $(k = 1,\ 2)$ is the volume fraction of localisation band k in the RVE. For $H_k = \frac{\Omega}{\Gamma_k}$, defined as the characteristic length of the RVE in relation to the localisation band k, we have $\eta_k = \frac{h_k}{H_k}$.

The above kinematic enrichment is then employed in the framework of generalised thermodynamics proposed by Houlsby and Puzrin (2000) for the model formulation. Following this framework, the constitutive relation of the material, its internal variables and their evolutions will be derived from two explicitly defined energy potentials: free energy potential, and dissipation potential. The enhanced kinematic condition in Eq. (2) will be treated as a kinematic constraint. The procedures established beforehand by Houlsby and Puzrin (2000) will directly result in a kinematically enriched model involving the combined responses of two localisation bands idealised as two cohesive-frictional cracks and the bulk material. No further assumptions, as used previously by Nguyen et al. (2012, 2014), will be required. For isothermal processes, the Helmholtz free energy potential Ψ takes the following form, with contributions from both the bulk (Ψ_{o}) and crack faces (Ψ_{Γ_1} and Ψ_{Γ_2}):

$$\Psi = \Psi_{\mathrm{o}} + \frac{1}{\Omega}\left(\Psi_{\Gamma_1}\Gamma_1 + \Psi_{\Gamma_2}\Gamma_2\right) + \mathbf{C}^{\mathrm{T}}\boldsymbol{\Lambda} = \frac{1}{2}\boldsymbol{\varepsilon}_{\mathrm{o}}{}^{\mathrm{T}}\mathbf{a}_{\mathrm{o}}\boldsymbol{\varepsilon}_{\mathrm{o}} + \frac{1}{H_1}\Psi_{\Gamma_1} + \frac{1}{H_2}\Psi_{\Gamma_2} + \mathbf{C}^{\mathrm{T}}\boldsymbol{\Lambda} \tag{3}$$

where $\boldsymbol{\Lambda}$ is the vector of Lagrangian multipliers; $\mathbf{a}_{\mathrm{o}}$ is the stiffness matrix of the material in elastic range; $\mathbf{C}$ is the kinematic constraint based on Eq. (2):

$$\mathbf{C} = \boldsymbol{\varepsilon} - \left(\boldsymbol{\varepsilon}_{\mathrm{o}} + \frac{1}{H_1}\mathbf{n}_1^{\mathrm{T}}\mathbf{u}_1 + \frac{1}{H_2}\mathbf{n}_2^{\mathrm{T}}\mathbf{u}_2\right) = \mathbf{0} \tag{4}$$

The dissipation potential, in this case, consists of two components corresponding to two cracks, assuming the bulk is always elastic:

$$\Phi = \frac{1}{\Omega}\left(\Phi_{\Gamma_1}\Gamma_1 + \Phi_{\Gamma_2}\Gamma_2\right) = \frac{1}{H_1}\Phi_{\Gamma_1}\left(\mathbf{u}_1^{\mathrm{p}}, D_1\right) + \frac{1}{H_2}\Phi_{\Gamma_2}\left(\mathbf{u}_2^{\mathrm{p}}, D_2\right) \tag{5}$$

We note that Ψ_{Γ_1}, Ψ_{Γ_2}, Φ_{Γ_1} and Φ_{Γ_2} are surface-based quantities, corresponding to the dissipation per unit surface of area. This naturally leads to the involvement of the length scale $H_k = \Omega/\Gamma_k$ when writing the energy potential and dissipation potential for a unit volume. The assumption of elastic bulk is generally not correct for the case of shearing under very high confining pressure but provides reasonable responses for a wide enough range of responses under both tension and compression. We acknowledge this shortcoming and will address it in future studies. The behaviour across crack surfaces Γ_1 and Γ_2 can be reasonably assumed to be cohesive-frictional, represented by a damage-plasticity cohesive model, in which $\mathbf{u}_k^{\mathrm{p}}$ and D_k are respectively the plastic displacement jump and damage variable. Details on this model will be presented in Section 2.3.

Following the procedures established in Houlsby and Puzrin (2000) for the derivation of constitutive models, the true and generalised stresses are:

$$\boldsymbol{\sigma} = \frac{\partial\Psi}{\partial\boldsymbol{\varepsilon}} = \boldsymbol{\Lambda} \tag{6}$$

$$\overline{\boldsymbol{\chi}}_{\mathrm{o}} = -\frac{\partial\Psi}{\partial\boldsymbol{\varepsilon}_{\mathrm{o}}} = -(\mathbf{a}_{\mathrm{o}}\boldsymbol{\varepsilon}_{\mathrm{o}} - \boldsymbol{\Lambda}) \tag{7}$$

$$\overline{\boldsymbol{\chi}}_{\Gamma_1} = -\frac{\partial\Psi}{\partial\mathbf{u}_1} = -\frac{1}{H_1}\left(\frac{\partial\Psi_{\Gamma_1}}{\partial\mathbf{u}_1} - \mathbf{n}_1^{\mathrm{T}}\boldsymbol{\Lambda}\right) \tag{8}$$

$$\overline{\boldsymbol{\chi}}_{\Gamma_2} = -\frac{\partial\Psi}{\partial\mathbf{u}_2} = -\frac{1}{H_2}\left(\frac{\partial\Psi_{\Gamma_2}}{\partial\mathbf{u}_2} - \mathbf{n}_2^{\mathrm{T}}\boldsymbol{\Lambda}\right) \tag{9}$$

The corresponding dissipative generalised stresses are obtained from the dissipation potential as follows:

$$\boldsymbol{\chi}_{\mathrm{o}} = \frac{\partial \Phi}{\partial \dot{\boldsymbol{\varepsilon}}_{\mathrm{o}}} = \mathbf{0} \tag{10}$$

$$\boldsymbol{\chi}_{\Gamma_1} = \frac{\partial \Phi}{\partial \dot{\mathbf{u}}_1} = \mathbf{0} \tag{11}$$

$$\boldsymbol{\chi}_{\Gamma_2} = \frac{\partial \Phi}{\partial \dot{\mathbf{u}}_2} = \mathbf{0} \tag{12}$$

The orthogonality conditions (Houlsby & Puzrin, 2000; Ziegler, 1983), $\overline{\boldsymbol{\chi}}_{\mathrm{o}} = \boldsymbol{\chi}_{\mathrm{o}}$, $\overline{\boldsymbol{\chi}}_{\Gamma_1} = \boldsymbol{\chi}_{\Gamma_1}$, and $\overline{\boldsymbol{\chi}}_{\Gamma_2} = \boldsymbol{\chi}_{\Gamma_2}$ lead to the following relationships:

$$\boldsymbol{\sigma} = \boldsymbol{\Lambda} = \mathbf{a}_{\mathrm{o}} \boldsymbol{\varepsilon}_{\mathrm{o}} \tag{13}$$

$$\mathbf{t}_1 = \frac{\partial \Psi_{\Gamma_1}}{\partial \mathbf{u}_1} = \mathbf{n}_1^{\mathrm{T}} \boldsymbol{\Lambda} = \mathbf{n}_1^{\mathrm{T}} \boldsymbol{\sigma} \tag{14}$$

$$\mathbf{t}_2 = \frac{\partial \Psi_{\Gamma_2}}{\partial \mathbf{u}_2} = \mathbf{n}_2^{\mathrm{T}} \boldsymbol{\Lambda} = \mathbf{n}_2^{\mathrm{T}} \boldsymbol{\sigma} \tag{15}$$

in which $\mathbf{t}_1$ and $\mathbf{t}_2$ are the tractions acting on crack surfaces Γ_1 and Γ_2, respectively. It can be seen that, in addition to the kinematic condition in Eq. (2), the bulk material and the cracks are linked through the internal equilibrium conditions (14) and (15). As the terms in the energy and dissipation potentials are separated into three parts, corresponding to the bulk material and two cracks as seen in Eqs. (3) and (5), the constitutive descriptions of these two cracks can be decoupled and dealt with separately. For example, the elastic bulk in this case does not produce dissipation and its behaviour can be directly obtained from the Helmholtz free energy Ψ_o, while the free energy potential Ψ_{Γ_k} and dissipation potential Φ_{Γ_k} written for a unit surface area can be used to obtain the constitutive behaviour of cohesive-frictional crack k, following procedures in Houlsby and Puzrin (2000). This separation of models facilitates the formulation of the cohesive-frictional model, which will be described in Section 2.3.

2.2. Structure of the proposed constitutive model

For now, the generic form $\dot{\mathbf{t}}_k = \mathbf{K}_k^{\tan} \dot{\mathbf{u}}_k, \ (k = 1, \ 2)$ of the cohesive crack in the global coordinate system is used for the construction of the constitutive model, with $\mathbf{K}_k^{\tan}$ being the tangent stiffness of the cohesive crack k. The proposed model consists of two constitutive relationships, $\dot{\mathbf{t}}_k = \mathbf{K}_k^{\tan} \dot{\mathbf{u}}_k$, and $\boldsymbol{\sigma} = \mathbf{a}_{\mathrm{o}} \boldsymbol{\varepsilon}_{\mathrm{o}}$ (13), connected through the internal equilibrium conditions (14) and (15). The derivation of the macro response connecting macro stress rate $\dot{\boldsymbol{\sigma}}$ with macro strain rate $\dot{\boldsymbol{\varepsilon}}$ will give us a better idea about the links between several components in the structure of the proposed constitutive model.

By substituting $\dot{\mathbf{t}}_k = \mathbf{K}_k^{\tan} \dot{\mathbf{u}}_k$ into the rate forms of traction continuity conditions in Eqs. (14) and (15), we have

$$\begin{cases} \mathbf{n}_1^{\mathrm{T}} \dot{\boldsymbol{\sigma}} = \mathbf{n}_1^{\mathrm{T}} \mathbf{a}_{\mathrm{o}} \dot{\boldsymbol{\varepsilon}}_{\mathrm{o}} = \mathbf{K}_1^{\tan} \dot{\mathbf{u}}_1 \\ \mathbf{n}_2^{\mathrm{T}} \dot{\boldsymbol{\sigma}} = \mathbf{n}_2^{\mathrm{T}} \mathbf{a}_{\mathrm{o}} \dot{\boldsymbol{\varepsilon}}_{\mathrm{o}} = \mathbf{K}_2^{\tan} \dot{\mathbf{u}}_2 \end{cases} \tag{16}$$

From Eq. (2), the bulk strain rate $\dot{\boldsymbol{\varepsilon}}_{\mathrm{o}}$ can be expressed in terms of macro strain rate $\dot{\boldsymbol{\varepsilon}}$ and velocity jump $\dot{\mathbf{u}}_k$. Substitution of $\dot{\boldsymbol{\varepsilon}}_{\mathrm{o}}$ into Eq. (16), followed by some transformations and arrangements, results in:

$$\begin{cases} \left(\dfrac{1}{H_1} \mathbf{n}_1^{\mathrm{T}} \mathbf{a}_{\mathrm{o}} \mathbf{n}_1 + \mathbf{K}_1^{\tan} \right) \dot{\mathbf{u}}_1 + \dfrac{1}{H_2} \mathbf{n}_1^{\mathrm{T}} \mathbf{a}_{\mathrm{o}} \mathbf{n}_2 \dot{\mathbf{u}}_2 = \mathbf{n}_1^{\mathrm{T}} \mathbf{a}_{\mathrm{o}} \dot{\boldsymbol{\varepsilon}} \\ \dfrac{1}{H_1} \mathbf{n}_2^{\mathrm{T}} \mathbf{a}_{\mathrm{o}} \mathbf{n}_1 \dot{\mathbf{u}}_1 + \left(\dfrac{1}{H_2} \mathbf{n}_2^{\mathrm{T}} \mathbf{a}_{\mathrm{o}} \mathbf{n}_2 + \mathbf{K}_2^{\tan} \right) \dot{\mathbf{u}}_2 = \mathbf{n}_2^{\mathrm{T}} \mathbf{a}_{\mathrm{o}} \dot{\boldsymbol{\varepsilon}} \end{cases} \tag{17}$$

This equation can be re-arranged in matrix form as:

$$\begin{bmatrix} \dfrac{1}{H_1} \mathbf{n}_1^{\mathrm{T}} \mathbf{a}_{\mathrm{o}} \mathbf{n}_1 + \mathbf{K}_1^{\tan} & \dfrac{1}{H_2} \mathbf{n}_1^{\mathrm{T}} \mathbf{a}_{\mathrm{o}} \mathbf{n}_2 \\ \dfrac{1}{H_1} \mathbf{n}_2^{\mathrm{T}} \mathbf{a}_{\mathrm{o}} \mathbf{n}_1 & \dfrac{1}{H_2} \mathbf{n}_2^{\mathrm{T}} \mathbf{a}_{\mathrm{o}} \mathbf{n}_2 + \mathbf{K}_2^{\tan} \end{bmatrix} \begin{bmatrix} \dot{\mathbf{u}}_1 \\ \dot{\mathbf{u}}_2 \end{bmatrix} = \begin{bmatrix} \mathbf{n}_1^{\mathrm{T}} \mathbf{a}_{\mathrm{o}} \\ \mathbf{n}_2^{\mathrm{T}} \mathbf{a}_{\mathrm{o}} \end{bmatrix} \dot{\boldsymbol{\varepsilon}} \tag{18}$$

The velocity jumps of the two cracks can be then calculated from a given macro strain rate as:

$$\begin{bmatrix} \dot{\mathbf{u}}_1 \\ \dot{\mathbf{u}}_2 \end{bmatrix} = \begin{bmatrix} \dfrac{1}{H_1} \mathbf{n}_1^{\mathrm{T}} \mathbf{a}_{\mathrm{o}} \mathbf{n}_1 + \mathbf{K}_1^{\tan} & \dfrac{1}{H_2} \mathbf{n}_1^{\mathrm{T}} \mathbf{a}_{\mathrm{o}} \mathbf{n}_2 \\ \dfrac{1}{H_1} \mathbf{n}_2^{\mathrm{T}} \mathbf{a}_{\mathrm{o}} \mathbf{n}_1 & \dfrac{1}{H_2} \mathbf{n}_2^{\mathrm{T}} \mathbf{a}_{\mathrm{o}} \mathbf{n}_2 + \mathbf{K}_2^{\tan} \end{bmatrix}^{-1} \begin{bmatrix} \mathbf{n}_1^{\mathrm{T}} \mathbf{a}_{\mathrm{o}} \\ \mathbf{n}_2^{\mathrm{T}} \mathbf{a}_{\mathrm{o}} \end{bmatrix} \dot{\boldsymbol{\varepsilon}} = \begin{bmatrix} \mathbf{M}_1 \\ \mathbf{M}_2 \end{bmatrix} \dot{\boldsymbol{\varepsilon}} \tag{19}$$

where $\mathbf{M}_1$ and $\mathbf{M}_2$ are 3-by-6 matrices for 3D cases. The constitutive relation of the RVE crossed by two cracks can then be written as

$$\dot{\boldsymbol{\sigma}} = \mathbf{a}_{\mathrm{o}} \left[\dot{\boldsymbol{\varepsilon}} - \frac{1}{H_1} \mathbf{n}_1 \dot{\mathbf{u}}_1 - \frac{1}{H_2} \mathbf{n}_2 \dot{\mathbf{u}}_2 \right] = \mathbf{a}_{\mathrm{o}} \left[\mathbf{1} - \frac{1}{H_1} \mathbf{n}_1 \mathbf{M}_1 - \frac{1}{H_2} \mathbf{n}_2 \mathbf{M}_2 \right] \dot{\boldsymbol{\varepsilon}} \tag{20}$$

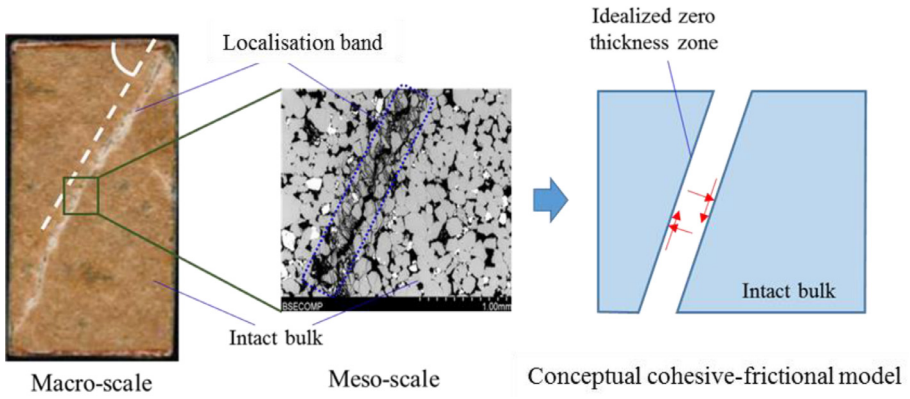

Fig. 2. Experimental observation of localised zone at Coconino sandstone (after Ma & Haimson, 2016) and the proposed conceptual model.

As shown in the above formulation, both responses of the cracks and their surrounding bulk are included in the constitutive model through the application of a set of kinematic enrichments and internal equilibrium conditions across the boundaries of the cracks. Because the constitutive model is constructed within the thermodynamic framework, the model automatically complies with the First and Second Laws of thermodynamics. It can also be seen that the orientations, relative sizes and mechanical responses of the cracks, along with the behaviour of the surrounding bulk material, are incorporated in the macro behaviour. Size effect can thus be captured naturally at the constitutive level, and the generic model also possesses in-built regularisation effects thanks to the natural appearance of the sizes H_k in the constitutive structure (20). We will show later that this will naturally lead to convergence of numerical results with respect to the discretisation in the analysis of BVPs and no other regularisations are needed. In addition, it can also be seen in the constitutive structure (20) that the macro behaviour is governed by the responses of two embedded localisation bands that can be activated or deactivated depending on the stress conditions. This generic structure requires appropriate models at the scale of the localisation band, where inelastic behaviour actually takes place. Therefore, incorrect smearing of inelastic behaviour over the whole volume element is totally removed. In other words, phenomenology in this case has been transferred to the lower scale of the localisation band and this requires the development of a cohesive-frictional model, which will be described in the next sub-section.

2.3. Cohesive-frictional model for localisation band

A generic cohesive-frictional crack model (Le et al., 2017) is further tailored in this study to capture the behaviour of the localisation band under both tensile and compressive conditions. Different from models that simply use empirical relationships between stress and crack opening with linear, exponential or bilinear laws, this model focuses on reproducing significant aspects of the post-peak deformation as a result of asperities degradation (i.e., damage) and irreversible displacements (i.e., plasticity). This helps describe crack behaviour in different scenarios, such as pure tension, pure shear or mixed-mode loading conditions. The model was validated against data on jointed rock masses and was proven to be effective for modelling cracks under mixed-mode loading conditions. However, as the previous work (Le et al., 2017) deals with rock joint, it only covers the compression and frictional behaviour of the material. Therefore this cohesive-frictional model should be enhanced to cover a wider range of behaviour, and this section describes both the generic formulation for the sake of completeness and the specifications for cohesive-frictional behaviour in tension/compression, shear and mixed mode conditions. It is worth noting that the cohesive-frictional model and its variables, described in this section, are defined in the local coordinate system of the localisation band. They are hence transformed to the global coordinate system, where needed, using the transformation matrix $\mathbf{R}_k$ during the calculation.

2.3.1. Cohesive-frictional model summary

Experimental observations (illustrated in Fig. 2) show that the interlocking and cohesion of aggregates in a localisation band of finite thickness govern the behaviour of the material at macro-scale. From the modelling point of view, it is reasonable and practical to idealise the localisation band as a zero thickness zone and describe its responses using a cohesive-frictional model. The description of the localisation band in this form naturally facilitates its integration into the constitutive model presented in the previous section without any adjustment. The proposed cohesive-frictional model was constructed based on a damage-plasticity framework to reflect the close link of the localised damage and irreversible deformations addressed in several studies (Antoni, 2017; Lu, Hsu, & Asce, 2007; Scerrato, Giorgio, Madeo, Limam, & Darve, 2014).

For the coupling between damage and plasticity, the cohesive-frictional zone is assumed to comprise of two parts: the damaged part represented by damage variable D (i.e., $0 \le D \le 1$), and the undamaged part represented by $(1 - D)$. The traction acting on two faces of the crack is denoted as $\mathbf{t}_c = [\ t_n \quad t_{s1} \quad t_{s2}\ ]^{\mathrm{T}}$, representing the normal and two shear tractions, respectively. The displacement jump between the two crack faces, $\mathbf{u}_c$, is decomposed into an elastic part $\mathbf{u}_c^e$ and an irreversible (plastic) part $\mathbf{u}_c^p$ as $\mathbf{u}_c = \mathbf{u}_c^e + \mathbf{u}_c^p$.

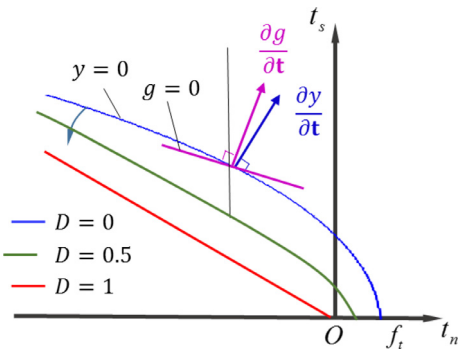

Fig. 3. Illustration of yield surface evolution and non-associated flow rule.

The traction-displacement relationship is described as:

$$\mathbf{t}_c = \begin{bmatrix} t_n \\ t_{s1} \\ t_{s2} \end{bmatrix} = \begin{bmatrix} 1 - DH(t_n) & 0 & 0 \\ 0 & 1-D & 0 \\ 0 & 0 & 1-D \end{bmatrix} \begin{bmatrix} K_n & 0 & 0 \\ 0 & K_s & 0 \\ 0 & 0 & K_s \end{bmatrix} \begin{bmatrix} u_n - u_n^p \\ u_{s1} - u_{s1}^p \\ u_{s2} - u_{s2}^p \end{bmatrix} = \mathbf{HK}\left(\mathbf{u}_c - \mathbf{u}_c^p\right) \tag{21}$$

where $\mathbf{K}_c^{\text{sec}} = \mathbf{HK}$ is the secant stiffness of the cohesive zone in the local coordinate system; K_n, K_s represent the normal and shear elastic stiffness of the cohesive crack; $u_n, u_{s1,\,2}$ are the normal and shear displacement jumps, and u_n^p, $u_{s1,\,2}^p$ represent the plastic displacement jumps. The normal traction is defined as positive in tension, and the sign of the displacement jump follows its corresponding traction. The inclusion of the Heaviside function $H(t_n)$ here means that the damaged part only affects the normal traction in the case where tension exists. This is a difference of this model compared to the one in Le et al. (2017) where the damage effect in tension does not appear in the constitutive relationship. The presence of damage and irreversible displacements in the traction-displacement relationship also allows the model to naturally capture the strength/stiffness reduction due to micro-cracking.

As observed in experiments, the development of microcracks is always accompanied by irreversible deformations (Lu et al., 2007). Therefore, a combined yield-failure function including damage as a function of accumulated plastic displacement is used to capture this interaction. This function needs to be smooth to ensure a continuous transition from pure normal/compression or shear to mixed mode conditions. In addition, experimental observations of shearing tests (Liao, Lee, Wu, & Lai, 2011) show a residual shear strength at the end of cracking due to friction caused by the waviness and roughness of asperities. Based on the foregoing considerations, the proposed damage-plastic yield model takes the form:

$$y = \left(t_{s1}^2 + t_{s2}^2\right) - \left[(1-D)\mu_0^2 + D\mu^2\right]\left[t_n - (1-D)f_t\right]^2 + mf_c(1-D)\left[t_n - (1-D)f_t\right] \tag{22}$$

in which f_t is the tensile strength; f_c is the compressive strength of the material; and m, μ_0 are the parameters controlling the shape of the initial yield surface. Different from the previous model (Le et al., 2017) where rock joint have no tensile strength, $f_t = 0$, the current model is tailored for a cohesive-frictional crack with tensile strength $f_t \neq 0$. As a result, apart from compression-shear mixed mode conditions as in the original model, the current model can also be used for tension-shear loading cases. For the case of final failure, $D = 1$, the yield surface becomes $t_s = \sqrt{t_{s1}^2 + t_{s2}^2} = \pm\mu t_n$, which is the classical frictional Mohr–Coulomb criterion, where μ plays the role of internal frictional coefficient of the material (i.e., $\mu = \tan\phi$ where ϕ is the friction angle). As a result, the residual shear strength can be described by the current yield surface. Thanks to the inclusion of damage in the yield criterion, illustrated in Fig. 3, the initial yield surface (blue curve corresponding to the case of $D = 0$) gradually evolves as the damage variable D increases and reaches the final failure surface (red line corresponding to $D = 1$). This unified form of loading function helps the model evolve from initial yield to final failure smoothly, without requiring any additional criterion for damage and plasticity. The corresponding plastic potential for non-associated flow rules is defined by:

$$g = \gamma\left(t_{s1}^2 + t_{s2}^2\right) - \left[(1-D)\mu_0^2 + D\mu^2\right]\left[t_n - (1-D)f_t\right]^2 + mf_c(1-D)\left[t_n - (1-D)f_t\right] \tag{23}$$

where γ is the parameter controlling the non-associativity. With $\dot{\lambda}$ being the plastic multiplier, the flow rules are:

$$\dot{u}_n^p = \dot{\lambda}\frac{\partial g}{\partial t_n};\quad \dot{u}_{s1}^p = \dot{\lambda}\frac{\partial g}{\partial t_{s1}};\quad \dot{u}_{s2}^p = \dot{\lambda}\frac{\partial g}{\partial t_{s2}} \tag{24}$$

To complete the cohesive model, an evolution law of damage variable D is provided to capture the damage propagation caused by the plastic displacement jumps. The experimental data for different loading cases on concrete and sandstone (Ingraham et al., 2013; Liao et al., 2011; Shi, Dam, Mier, & Sluys, 2000) shows that the material responses change rapidly just after reaching its yielding point, and then the rate of variation slows down with further loading. This indicates that a reasonable damage evolution should increase quickly at first, and then more slowly. Hence, in the paper, an exponential

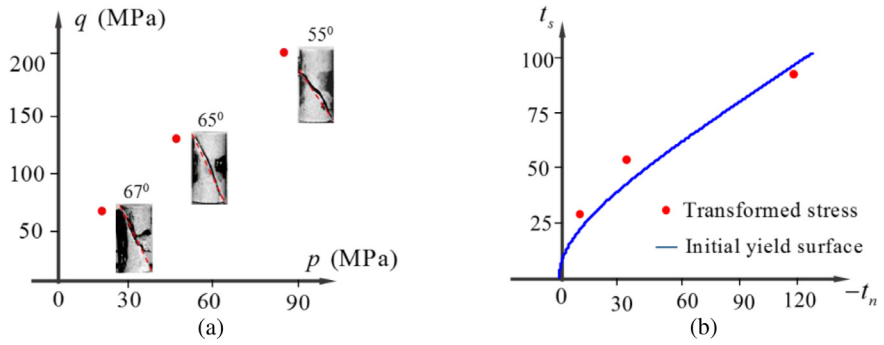

Fig. 4. Illustration of yield surface calibration: (a) experimental data (Klein et al., 2001) and (b) converted traction and calibrated yield surface by the model.

function is used for damage evolution:

$$D = 1 - e^{-u_p}, \text{ with } \Delta u_p = \sqrt{\left(\frac{\alpha \Delta u_n^p}{\delta_0}\right)^2 + \left(\frac{\beta \Delta u_{s1}^p}{\delta_0}\right)^2 + \left(\frac{\beta \Delta u_{s2}^p}{\delta_0}\right)^2} \tag{25}$$

where u_p is the accumulated plastic displacement parameter in non-dimensional form; α and β are non-dimensional parameters controlling the contributions of normal and shear plastic displacements to the damage evolution; δ_0 is defined as the displacement corresponding to peak stress in pure tension, and is used just to make u_p non-dimensional. In the case of shearing under compression, the normal plastic displacement is a result of the dilation behaviour due to sliding of asperities against each other. Therefore, its contribution to the damage development should be smaller than that in pure tension where normal displacement is the direct cause of the damage development. This effect is taken into account in the model using the following function:

$$\alpha = \alpha_0 e^{\frac{-\langle -t_n \rangle}{f_t}} \tag{26}$$

where $\langle . \rangle$ are the Macaulay brackets; α_0 is calculated from mode I fracture energy G_I as shown in the next sub-section. The appearance of tensile strength f_t in the formulation is just to make α non-dimensional as it should be. The use of Eq. (26) in this case is satisfactory as demonstrated later in all numerical examples, and we acknowledge that this should be backed up with further investigations based on micromechanics in future work.

2.3.2. Parameter identification of the proposed cohesive-frictional model

Apart from material properties (i.e., tensile strength f_t, compressive strength f_c, friction angle ϕ), parameters that need to be calibrated include $\mu_0, m, \alpha_0, \beta$ and γ. As discussed earlier, the parameters μ_0 and m control the shape of the initial yield surface, which defines the crack initiation. Therefore, in order to calibrate these parameters, an experimental dataset of localisation onset (i.e., yielding points) should be used. As the majority of the yield surface is in compression, the ideal dataset can be obtained from triaxial compression tests in which the stress states at yielding are recorded along with the crack patterns. To illustrate the calibration of these parameters, the triaxial test results of Bentheim sandstone conducted by Klein, Baud, Reuschlé, and Wong (2001) are used. The experimental results of the differential stress $q = |\sigma_1 - \sigma_3| = \sqrt{3J_2}$ and the hydrostatic stress $p = \frac{\sigma_1 + 2\sigma_3}{3} = -I_1/3$, where localisation initiates, are plotted in Fig. 4(a) along with their failure plane orientation extracted from the experiments. In association with these orientation of failure, stress states are converted to stresses (tractions) in the local coordinate system of the localisation band (as illustrated in Fig. 2). The two parameters μ_0 and m are then calibrated to fit the experimental data in the local coordinate system. The calibrated initial yield surface is illustrated in Fig. 4(b) using two parameters: $\mu_0 = 0.55$ and $m = 1.1$.

The relationship between the parameter α_0 and mode I fracture energy G_I is found from the analytical derivation of pure tension case where shear traction is considered to be zero, $t_s = 0$. The plastic shear displacement rate is thus written as:

$$\dot{u}_s^p = \dot{\lambda} \frac{\partial g}{\partial t_s} = 2\dot{\lambda} t_s \gamma = 0 \tag{27}$$

As a result, the normal plastic displacement jump solely drives the damage evolution. The rate of accumulated displacement parameter then becomes:

$$\dot{u}_p = \alpha_0 \frac{\dot{u}_n^p}{\delta_0} = \frac{1}{1-D}\dot{D} \quad \text{and thus} \quad \dot{u}_n^p = \frac{\delta_0}{\alpha_0}\frac{1}{1-D}\dot{D} \tag{28}$$

From the yielding condition $y = 0$, in association with the condition $t_s = 0$, the normal traction is calculated by:

$$t_n = (1-D) f_t = (1-D) K_n \left(u_n - u_n^p\right) \tag{29}$$

This equation results in:

$$\left(u_n - u_n^p\right) = \frac{f_t}{k_n} \quad \text{thus} \quad \dot{u}_n = \dot{u}_n^p = \frac{\delta_0}{\alpha_0}\frac{1}{1-D}\dot{D} \tag{30}$$

By using Eqs. (28)–(30), the mode I fracture energy can be analytically calculated by:

$$G_I = \int_0^{+\infty} t_n \mathrm{d}u_n = \int_0^1 (1-D) f_t \frac{\delta_0}{\alpha_0}\frac{1}{1-D}\mathrm{d}D = f_t\frac{\delta_0}{\alpha_0} \;\rightarrow \alpha_0 = \frac{f_t\delta_0}{G_I} \tag{31}$$

From this equation, it can be seen that the parameter α_0 in the proposed cohesive model is directly linked with and can be calculated from the mode I fracture energy G_I.

Similarly, the parameter β has a strong link with mode II fracture energy G_{II} in pure shear tests. Unfortunately, this relationship cannot be explicitly established by analytical derivation. The parameter β is hence determined using a numerical procedure given α_0 is known. Lastly, the parameter γ controlling the ratio between plastic normal and shear displacement jumps (i.e., $\dot{u}_n^p$ and $\dot{u}_s^p$) can be calibrated based on dilation responses. An example of such calibration using experimental data on rock joints can be found in Le et al. (2017).

3. Model implementation

3.1. Crack initiation and its orientation

For crack initiation, studies such as Červenka and Papanikolaou (2008), Dong, Wu, Xu, Zhang, and Fang (2010) and Unger, Eckardt, and Könke, (2011) used the Rankine criterion, where crack initiates when the maximum principal stress exceeds the material tensile strength. In this case, the crack orientation is always perpendicular to the maximum principal direction. Although this criterion is useful in tension, it is not applicable to cases where tension is not the failure mechanism (i.e., compression, shear loadings). Originated from the pioneering work by Rudnicki and Rice (1975), acoustic tensor has been used for the onset of localisation and given reasonable results in several studies (Chemenda, 2009; Das et al., 2011, 2013, 2014; Nguyen, Nguyen, Bui, & Nguyen, 2016a; Nguyen et al., 2016b; Tengattini et al., 2014). Following this approach, the orientation associated with the minimum determinant of the acoustic tensor is selected as localisation band orientation. Given the lack of localisation mechanisms and associated models, the use of the acoustic tensor for the determination of localisation band orientation is reasonable in classical continuum models.

However, in this study, the cohesive-frictional model used to describe the behaviour of the localisation band gives us a more natural way to not only detect the onset and orientation of the band but also to track its evolution. In particular, for a given stress state, all possible crack orientations are scanned and checked for crack initiation. For each potential orientation, the normal traction t_n and shear traction t_s acting on that plane are calculated using continuum mechanics equations:

$$t_n = n_i\sigma_{ij}n_j \text{ and } t_s = \sqrt{\| \sigma_{ij}n_j \|^2 - t_n^2} \tag{32}$$

where n_i is the normal vector of the plane, and σ_{ij} is stress state of the material in index notation form. A crack will appear if there exists a traction vector (t_n^*, t_s^*) that maximises the initial yield function: $y(t_n^*, t_s^*) = \max_{\forall \mathbf{n}}\{y(t_n, t_s, D=0)\} \geq 0$. The orientation corresponding to this traction vector is the crack orientation at that material point, and it is used for the rest of the calculation. The determination of the characteristic length as the ratio between the RVE volume and the surface area of the localisation band (Eq. 2 and Fig. 1) can then be performed automatically. In the research, this procedure will be used as the crack initiation criterion for both first and second cracks: if the material is intact, the criterion is used to check if the first crack is formed; and if a crack already exists, it will check for the activation of the second crack.

3.2. Stress return algorithm

In order to update the stress state given a strain increment, an implicit algorithm is employed because it can give relatively good results for larger increments compared to the explicit algorithm. Given that the algorithm for the model featuring one crack was clearly described previously in Le et al. (2017), only the case where two cracks with two orientations $\mathbf{n}_1$ and $\mathbf{n}_2$ have been triggered, is presented here.

For a given strain increment, if a crack is under loading (i.e., opening, shearing), its behaviour is inelastic and if it is under unloading (i.e., closing), the behaviour is elastic and hence secant stiffness is used. Therefore, both cracks are first assumed to be elastic to calculate the trial displacement increment in global coordinate system $\Delta\mathbf{u}_k^{\mathrm{tr}}$ $(k = 1,\ 2)$ following Eq. (19), with $\mathbf{K}_k^{\tan}$ replaced by $\mathbf{K}_k^{\sec}$. The secant stiffness of crack k in the global coordinate system is $\mathbf{K}_k^{\sec} = \mathbf{R}_k^T\mathbf{K}_{ck}^{\sec}\mathbf{R}_k$, where $\mathbf{K}_{ck}^{\sec}$ is secant stiffness, presented in Eq. (21), in the local coordinate system and $\mathbf{R}_k$ is the transformation matrix of crack k. The trial stress increment $\Delta\boldsymbol{\sigma}^{\mathrm{tr}}$ is calculated by using Eq. (20) and the trial traction in the global coordinate system is then computed by:

$$\Delta\mathbf{t}_k^{\mathrm{tr}} = \mathbf{n}_k^T\Delta\boldsymbol{\sigma}^{\mathrm{tr}} \text{ and } \mathbf{t}_k^{\mathrm{tr}} = \mathbf{t}_k + \Delta\mathbf{t}_k^{\mathrm{tr}},\ k = 1,\ 2 \tag{33}$$

The trial traction of each crack is transformed to the local coordinate system and then substituted back into the yield function in Eq. (22) to test the assumptions of elasticity made previously. If the yield function value of a crack is negative,

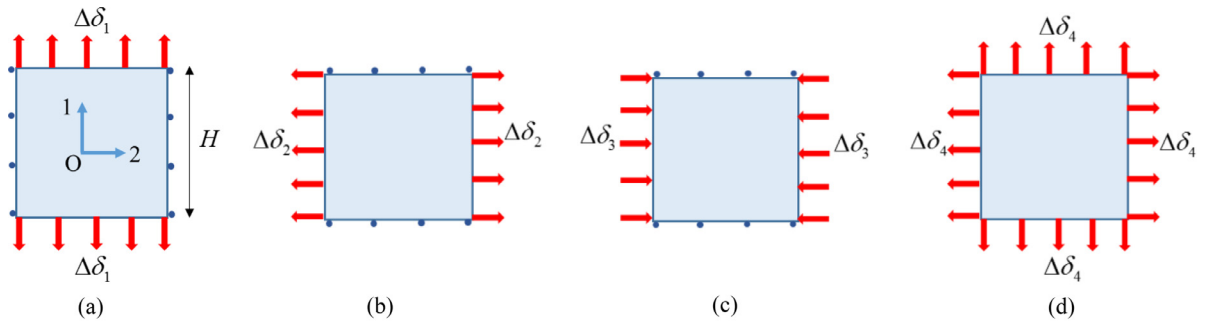

Fig. 5. Different loading phases (i.e. phase 1 to phase 4) to examine the model behaviour.

the assumption of elasticity is correct. Otherwise, the assumption is not correct and the crack is in inelastic state. As there are two cracks in the model, one of the following four possible scenarios will happen: (i) both cracks are closing; (ii) crack 1 is closing, crack 2 is opening; (iii) crack 1 is opening, crack 2 is closing; and (iv) both cracks are activated. For each scenario, the tractions are updated by corrective traction $\Delta\mathbf{t}_k^{\text{cor}}$ in the global coordinate system corresponding to each crack state ($\Delta\mathbf{t}_k^{\text{cor}} = \mathbf{0}$ if the crack is closing). The algorithm for calculating the corrective traction in inelastic case follows procedures described by Section 3.4 in Le et al. (2017) with appropriate transformation. The traction in the global coordinate system is then updated by:

$$\mathbf{t}_k = \mathbf{t}_k^{\text{tr}} + \Delta\mathbf{t}_k^{\text{cor}};\ k = 1, 2 \tag{34}$$

Up to this point, the traction in each crack is returned to its proper value with respect to the crack state, but the overall stress is still at the trial state $\boldsymbol{\sigma}^{\text{tr}} = \boldsymbol{\sigma} + \Delta\boldsymbol{\sigma}^{\text{tr}}$. Therefore, the internal equilibrium conditions in Eqs. (14) and (15), $\mathbf{n}_k^{\text{T}}\boldsymbol{\sigma}^{\text{tr}} - \mathbf{t}_k = 0$, are not met. An iterative procedure is thus used to correct the stress with the aim of meeting internal equilibrium conditions. To do this, two residual traction vectors corresponding to two cracks are defined as

$$\mathbf{r}_1 = \mathbf{n}_1^{\text{T}}\boldsymbol{\sigma} - \mathbf{t}_1 \ \text{and} \mathbf{r}_2 = \mathbf{n}_2^{\text{T}}\boldsymbol{\sigma} - \mathbf{t}_2 \tag{35}$$

By using the first order Taylor expansion for the residual at the current iteration n, the traction residual of the next iteration $n+1$ is given by:

$$\mathbf{r}_1^{n+1} = \mathbf{r}_1^n + \mathbf{n}_1^T\delta\boldsymbol{\sigma} - \delta\mathbf{t}_1 \ \text{and}\ \mathbf{r}_2^{n+1} = \mathbf{r}_2^n + \mathbf{n}_2^T\delta\boldsymbol{\sigma} - \delta\mathbf{t}_2 \tag{36}$$

where $\delta\boldsymbol{\sigma}$, $\delta\mathbf{t}_1$ and $\delta\mathbf{t}_2$ are the iterative stress and tractions from iteration n to $n+1$. Then, the stress increment in Eq. (20) is substituted into Eq. (36) with suitable tangent stiffness $\mathbf{K}_k^{\tan}$ to solve for the iterative displacement increment $\delta\mathbf{u}_1$ and $\delta\mathbf{u}_2$. With some arrangements, one obtains:

$$\begin{cases} \mathbf{r}_1^{n+1} = \mathbf{0} \\ \mathbf{r}_2^{n+1} = \mathbf{0} \end{cases} \rightarrow \begin{bmatrix} \delta\mathbf{u}_1 \\ \delta\mathbf{u}_2 \end{bmatrix} = \begin{bmatrix} \frac{1}{H_1}\mathbf{n}_1^T\mathbf{a}_0\mathbf{n}_1 + \mathbf{K}_1^{\tan} & \frac{1}{H_2}\mathbf{n}_1^T\mathbf{a}_0\mathbf{n}_2 \\ \frac{1}{H_1}\mathbf{n}_2^T\mathbf{a}_0\mathbf{n}_1 & \frac{1}{H_2}\mathbf{n}_2^T\mathbf{a}_0\mathbf{n}_2 + \mathbf{K}_2^{\tan} \end{bmatrix}^{-1} \begin{bmatrix} \mathbf{r}_1^n \\ \mathbf{r}_2^n \end{bmatrix} \tag{37}$$

It is worth noting that in the calculation of $\delta\mathbf{u}_1$ and $\delta\mathbf{u}_2$, the strain increment is neglected because it is already used in the trial step. The obtained displacement increments are then transformed back to the local coordinate system and used to update tractions following standard procedures described in Section 3.4 in Le et al. (2017). The iterative stress is then calculated as

$$\delta\boldsymbol{\sigma} = -\frac{1}{H_1}\mathbf{a}_0\mathbf{n}_1\delta\mathbf{u}_1 - \frac{1}{H_2}\mathbf{a}_0\mathbf{n}_2\delta\mathbf{u}_2 \tag{38}$$

This process is repeated until a convergence criterion is satisfied: $\|\mathbf{r}_k\| < \text{tolerance}$.

4. Model behaviour and validation at constitutive level

4.1. Illustration of model behaviour under different loading paths

In this section, a series of loading conditions, as shown in Fig. 5, is applied to a square representative volume element (RVE) to illustrate the performance of the proposed model. The material properties for concrete are taken as follows: tensile strength f_t =2.86 MPa; compressive strength f_c=38.4 MPa; mode I fracture energy $G_I = 0.063$ KN/m. The model parameters are $\mu_0 = 0.1$; $m = 4.5$; $\alpha_0 = 0.63$, $\beta = 0.0017$; $\gamma = 1.9$; $K_n = K_s = 10^{10}$ KPa/m and the RVE size $H = 0.1$ m. The RVE experiences four different displacement-controlled loading phases as follows. Phase 1 is tensile loading in the vertical direction up to $\Delta\delta_1 = 0.3$ mm. Phase 2 is tensile loading in the horizontal direction up to $\Delta\delta_2 = 0.5$ mm. Phase 3 is unloading in the horizontal direction up to $\Delta\delta_3 = 0.2$ mm. Phase 4 is reloading in both directions up to $\Delta\delta_4 = 0.9$ mm. It should be noted that during the loading/unloading in one direction, displacement in the other direction is kept constant.

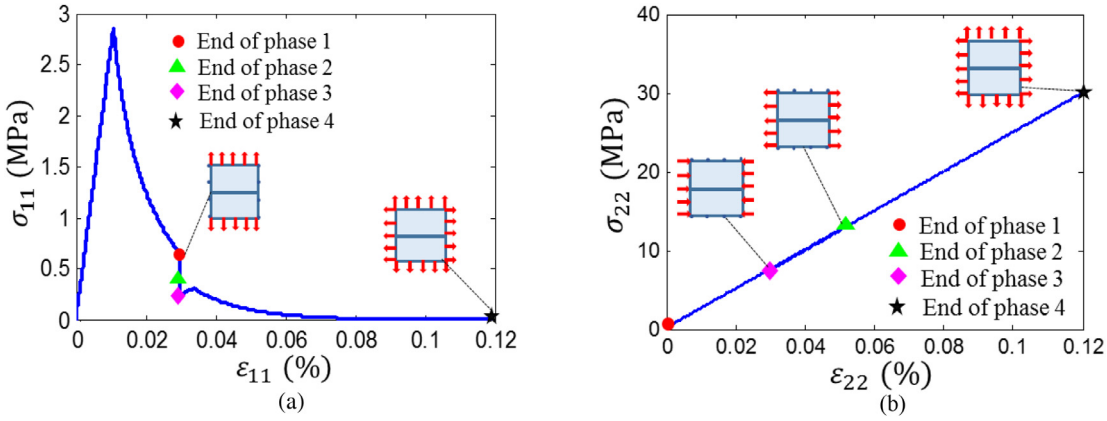

Fig. 6. Behaviour of the original model during loading phases: (a) $\sigma_{11} - \varepsilon_{11}$ and (b) $\sigma_{22} - \varepsilon_{22}$.

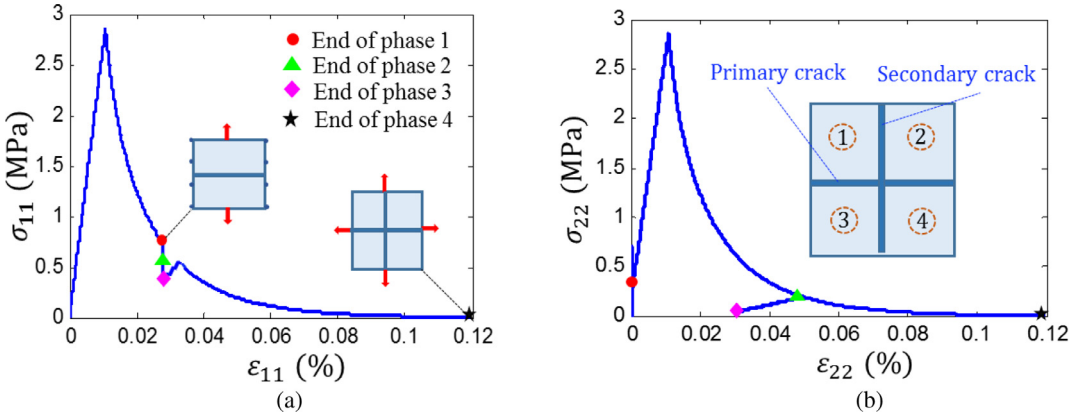

Fig. 7. Behaviour of the proposed model during loading phases: (a) $\sigma_{11} - \varepsilon_{11}$ and (b) $\sigma_{22} - \varepsilon_{22}$.

To illustrate why the model should feature two cracks, the original double-scale model featuring one crack (Le et al., 2017; Nguyen et al., 2012, 2014) is used to show its weakness in solving the above problem. The stress-strain responses produced by this one-crack model, plotted in Fig. 6, show that in phase 1, the vertical stress σ_{11} increases linearly up to the tensile strength, where a crack appears, and then comes to softening as expected. The stress σ_{22}, however, keeps increasing during phase 2, passing tensile strength, and reaches 12 MPa at the end of phase 2 as seen in Fig. 6(b). It then reduces to 8 MPa in phase 3, owing to the unloading, before increasing up to 30 MPa at the end of phase 4. Because only one crack is allowed in this one-crack model, it cannot cope with the change in loading path and the stress unphysically goes far beyond the tensile strength. As discussed previously in the introduction, this is a serious issue with existing models in the literature that allow only a single localisation band or crack.

The problem is now solved by the proposed two-crack model to show that incorporating two cracks in the constitutive model naturally helps overcome the stress-locking encountered in the above analysis. The stress-strain responses, plotted in Fig. 7, show that during phase 1, σ_{11} quickly reaches tensile strength and then experiences softening after the appearance of a horizontal crack (the primary crack) as seen in Fig. 7(a). In this phase, owing to displacement restraint in the horizontal direction and the Poisson effect, σ_{22} increases up to 0.7 MPa while σ_{11} increases, and then decreases to 0.3 MPa when σ_{11} decreases. In phase 2, with the applied displacement along the horizontal direction, σ_{22} linearly increases up to the tensile strength, and decreases after the formation of a vertical crack (a secondary crack). These two cracks divide the RVE into 4 blocks as illustrated in Fig. 7(b). At the beginning of phase 2, owing to the increase of σ_{22} and the displacement restraint along the vertical direction, the intact blocks shrink vertically and force the primary crack to continue opening. However, after σ_{22} reaches tensile strength, and experiences softening, all four blocks expand vertically leading to closure of the primary crack. In phase 3, because the unloading is applied in the horizontal direction, the secondary crack closes and thus σ_{22} decreases. This phase shows that the secant stiffness of the cracks is degraded because of the damage development during previous phases (shown in Fig. 7(b)). Similar to phase 2, the primary crack keeps closing in phase 3, resulting in a vertical drop of σ_{11} (Fig. 7(a)). During phase 4, because displacements are applied to both directions, it is clear that both cracks should further open. Therefore, stresses σ_{11} and σ_{22} both increase elastically at first (as they are both in the elastic state) and then experience inelastic softening once they reach their yield points again. This analysis shows that a

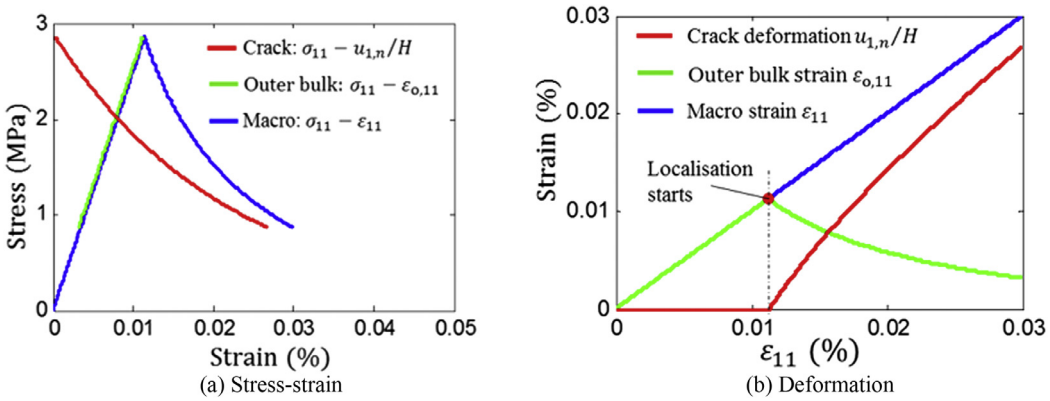

Fig. 8. Detailed stress-strain responses and deformation during phase 1.

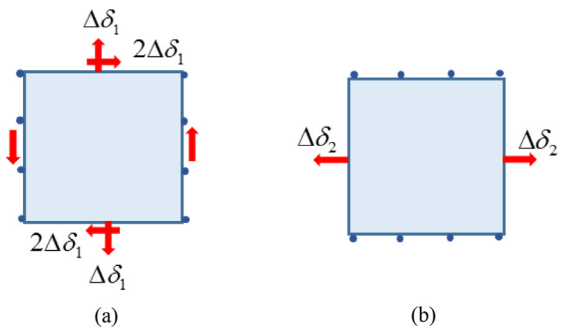

Fig. 9. Different loading phases: (a) phase 1 and (b) phase 2.

secondary crack is a must to better describe the behaviour of geomaterials in general loading cases where loading/unloading or change of loading paths occur. It should be noted that by using the same argument, a third crack might be necessary for 3D formulations to stop stress σ_{33} from increasing. However, this is beyond the scope of this paper and will be addressed in future studies.

In addition, Fig. 8 shows details of the localisation band, the outer bulk material and the overall (macro) responses during phase 1 to further illustrate the capability of the proposed model in capturing the localised deformation observed in geomaterials. It is seen that the outer bulk strain in 1-axis direction, $\varepsilon_{o,11}$, is equal to the macro (overall) strain ε_{11} before localisation takes place. Once localisation of deformation initiates, the outer bulk material is under unloading, with both strain and stress decreasing (see Fig. 8). The localisation band, on the other hand, is under inelastic loading (i.e., opening) with a decrease in stress and an increase in $u_{1,n}$ which is the normal displacement jump of the first crack in its local coordinate system. The macro behaviour of the material, presented by the blue curve in Fig. 8(a) and (b), is a combination of these two responses with respect to their contributions as described in the constitutive Eq. (20). This change of loading paths in both intact bulk material and the localisation band within a continuum model is a key feature that distinguishes the proposed model from other continuum-based model (Brünig & Michalski, 2017; Grassl et al., 2013; Karrech et al., 2011; Mir et al., 2018; Paliwal et al., 2017; Zhu et al., 2016) and micromechanics based models (i.e., Das et al., 2014, Das, Nguyen, & Einav, 2011, Tengattini et al., 2014) where such responses cannot be captured.

A different loading path, shown in Fig. 9, is used to further illustrate a more general case with two cracks not perpendicular to each other. In this loading path, the RVE experiences two displacement-controlled loading phases. Phase 1 is a mixed-mode loading with normal displacement in the vertical direction up to $\Delta\delta_1 = 0.1$ mm, shear displacement $\Delta\delta_{12} = 2\Delta\delta_1$ and $\Delta\delta_2 = 0$. Phase 2 is tensile loading in the horizontal direction up to $\Delta\delta_2 = 0.5$ mm while $\Delta\delta_1 = \Delta\delta_{12} = 0$.

The stresses in two directions with respect to calculation step (6000 steps in total) are plotted in Fig. 10 for both one-crack and two-crack models. It is seen that for the one-crack model, a crack with an inclination angle of 30^0 is formed at the end of phase 1. In phase 2, even though this crack opens under the given horizontal displacement, stress can still be transferred through it, leading to an unphysical increase of σ_{22} up to 10 MPa as shown in Fig. 10(a). This is the well-known stress locking issues, described in previous studies (Jirásek, 2000; Rots, 1991; Sancho et al., 2007). When secondary cracking is introduced, it helps avoid this unphysical locking as shown in Fig. 10(b). As shown in this figure, the first and second cracks are not necessarily perpendicular with each other which gives the proposed constitutive model flexibilities in capturing the formation and evolution of FPZ that consists of several smaller cracks in different orientations during FEA simulations.

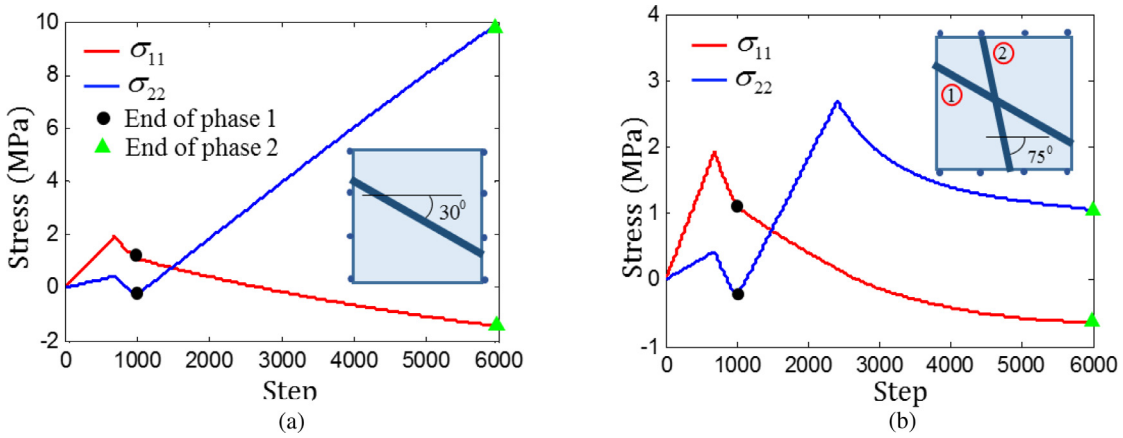

Fig. 10. Model behaviour: (a) one-crack model and (b) two-crack model.

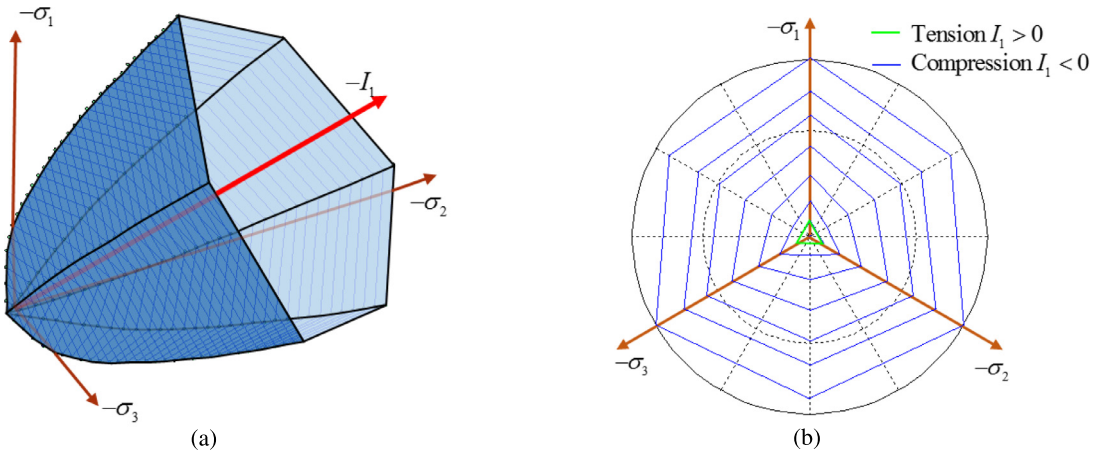

Fig. 11. A typical yield locus produced by the proposed model: (a) yield locus in principal stress space and (b) yield locus in the octahedral plane at different hydrostatic pressure levels.

4.2. General features of the yield locus produced by the proposed model

A typical yield locus produced by the proposed model, plotted in Fig. 11, clearly shows its dependence on the hydrostatic pressure and the Lode angle. As can be seen, this is a characteristic of macro behaviour generated by the embedded mechanism of localisation in the proposed constitutive structure while the third stress invariant is not present in the proposed model. In tension range, the resulting yield locus has a triangular shape in octahedral plane (Fig. 11(b)). With an increase of compressive pressure, the triangular yield locus gradually becomes more radically symmetrical. This feature by the model distinguishes itself from the Mohr–Coulomb yield model which has the same shape in different octahedral planes given the same set of parameters. Although the yield locus has non-smooth corners, the proposed model will not encounter singularity problems when taking derivatives of the yield function, as in the Rankine, Tresca and Mohr–Coulomb models. This is because the material yielding in the model is produced from the embedded localised failure mechanism, controlled by the cohesive-frictional model whose yield surface is continuous and defined on the failure plane. Therefore, there is no explicit macro yield function as in classical continuum models and thus the singularity issues experienced in such models do not present here.

However, it can be seen that the yield locus is not a closed surface in the compressive direction, which indicates that if a material point is loaded along the compressive hydrostatic path ($\sigma_1 = \sigma_2 = \sigma_3 < 0$), it never yields. This is a direct consequence of the open-shaped cohesive model defined on the failure plane meaning that failure will not appear in pure compression and the bulk behaviour is elastic. This problem can be overcome by introducing a close-shaped cohesive model and/or inelastic bulk behaviour to mimic failure due to material crushing under high confining pressures. This issue will be resolved in future work.

Another important feature of the proposed model is that every yielding point on the yield locus is associated with a corresponding failure plane as illustrated in Figs. 12 and 13 for typical loading paths, including tension, triaxial compression

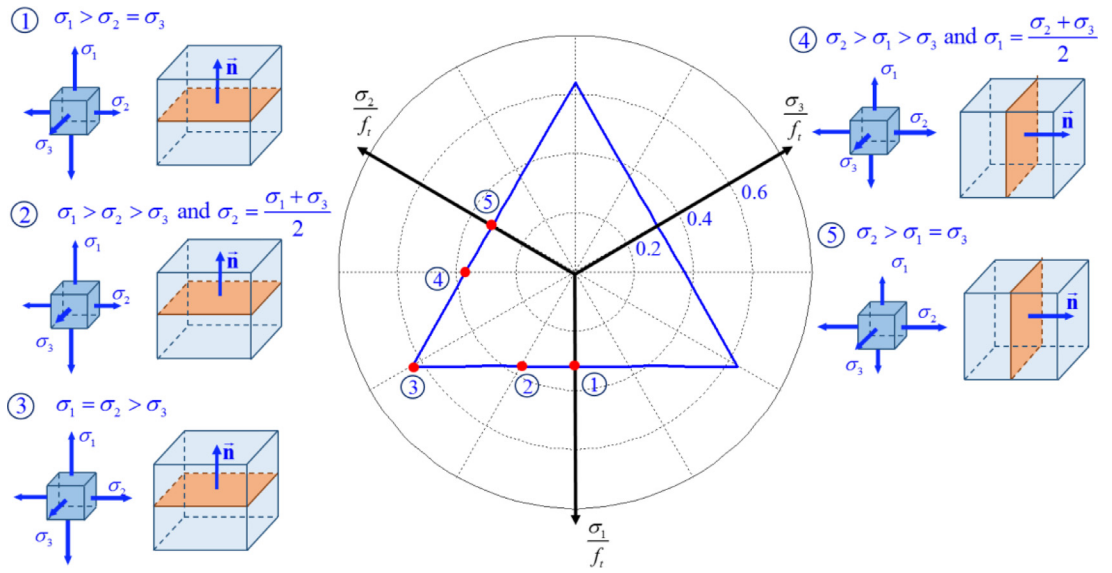

Fig. 12. Example of dimensionless failure locus in octahedral plane for tension.

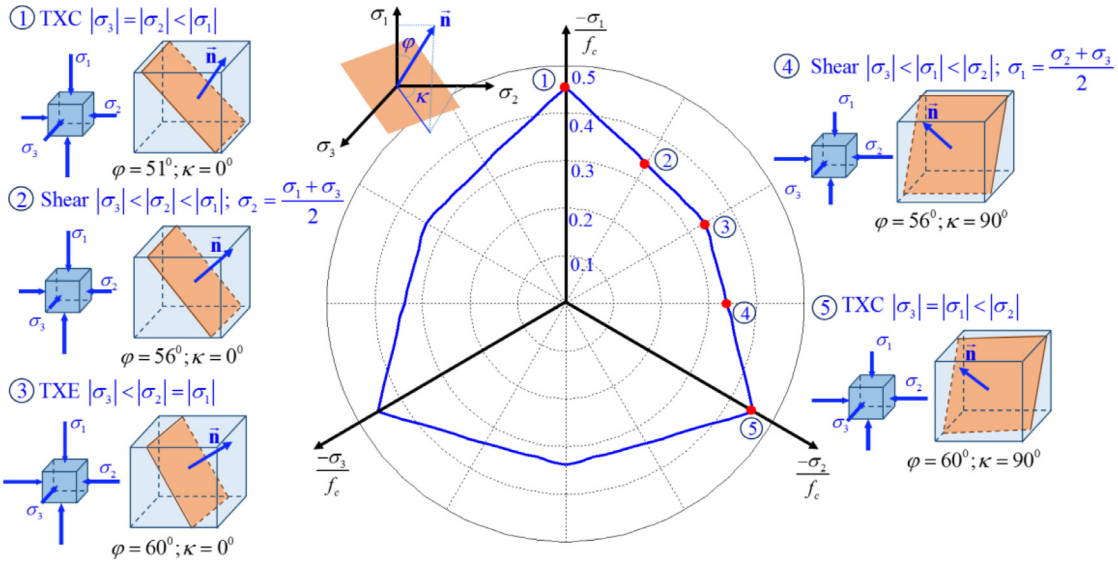

Fig. 13. Example of dimensionless failure locus in octahedral plane for compression.

(TXC), shear and triaxial extension (TXE). In the tension case, the crack orientation only changes when the direction of the maximum principal stress changes. This is reasonable because, in this case, the crack orientation only depends on the maximum principal stress direction, which coincides with the Rankine criterion. For compression, the failure plane orientation by the model evolves with changes in the loading path as also observed in experiments (Ingraham et al., 2013; Klein & Reuschlé, 2003; Ma & Haimson, 2016; Vachaparampil & Ghassemi, 2017). All of these results are naturally produced by the model without requiring adding the third stress invariant (or Lode angle parameter) in the yield function.

The experimental data from true triaxial tests conducted on Laxiwa granite by Li, Xu, and Liu (1994) and later interpreted by Yu, Zan, Zhao, and Yoshimine (2002) is used to validate the yield loci produced by the model. The tests were performed at different hydrostatic pressure levels $p = 75,\ 100,\ 130,\ 160$ MPa and for each test, the stresses at yielding states are recorded to calculate the deviatoric stress component $q = \sqrt{3J_2}$. The rock properties are taken as: uniaxial compressive strength $f_c = 157$ MPa and tensile strength $f_t = 9.3$ MPa. The model parameters, $m = 0.6$ and $\mu_0 = 0.54$, are calibrated from the case of $p = 75$ MPa and then used for other cases.

The results of yield loci, predicted by the model in Fig. 14, show good agreements with experimental observations. Thanks to the inclusion of the localised failure in the constitutive relationship, the model can naturally capture the Lode-angle dependence of the yield loci without needing the third stress invariant (or Lode angle parameter) in the expression of the macro yield function. In addition, each yielding state predicted by the proposed model is also accompanied by an orientation

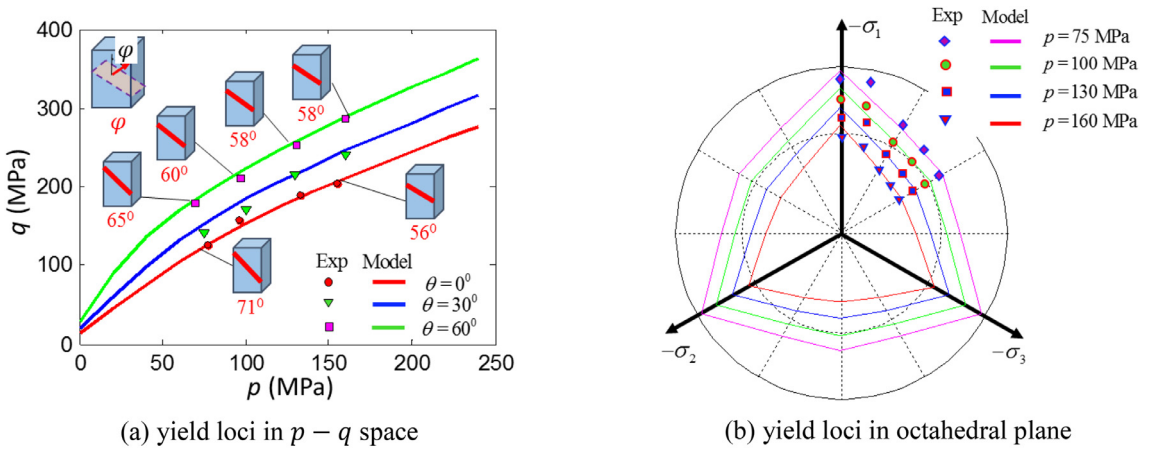

Fig. 14. Failure locus produced by the model against experimental results for Laxiwa granite.

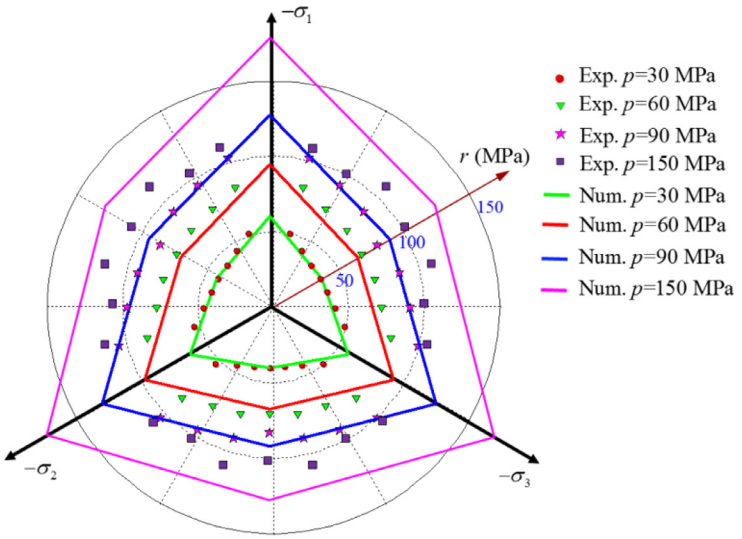

Fig. 15. Failure loci in octahedral plane against experimental results for Castlegate sandstone.

of the localisation failure plane. It can be seen that with an increase of hydrostatic stress, the failure plane orientation decrease as also observed in experiments (Ingraham et al., 2013; Ma & Haimson, 2016; Vachaparampil & Ghassemi, 2017). Moreover, at the same level of mean stress, the failure plane orientation of the axisymmetric compression (i.e., $|\sigma_1| > |\sigma_2| = |\sigma_3|$) is smaller than that in axisymmetric extension (i.e. $|\sigma_1| = |\sigma_2| > |\sigma_3|$) as experimentally observed (Ingraham et al., 2013; Ma & Haimson, 2016). This feature highlights the importance and benefits of embedding the mechanisms of localised failure in the proposed model, and also its advantage in removing the phenomenological use of third stress invariant over other continuum models in the literature.

The capability of the model in predicting yield loci are also validated against experimental data for Castlegate sandstone whose properties are taken as $f_t = 1$ MPa and $f_c = 16$ MPa. Model parameters including $m = 1.7$ and $\mu_0 = 0.5$ are calibrated from the case of $p = 30$ MPa.

Results of yield loci predicted by the model in Fig. 15 agree well with their experimental counterparts (Ingraham et al., 2013) at low confining stress levels. However, for the case of higher confining stress (i.e., $p = 30$ MPa), the model is not successful in capturing the shape of the yield locus. This is because at high confining stresses the failure mechanism gradually changes from localisation to diffusion associated with grain crushing, a mechanism that the proposed model does not possess yet. This is why the experimental data shows a circular-shaped yield locus at high confining stress levels, while the model prediction is still a hexagon. As explained earlier, work is underway to take into account this transition of failure mechanism governing the observed behaviour.

4.3. Model validation against triaxial test results for Bentheim sandstone

In this section, the performance of proposed model is assessed against triaxial tests conducted by Klein et al. (2001) on cylindrical Bentheim sandstone samples having a diameter of 20 mm and height of 40 mm. For convenience, the pressure

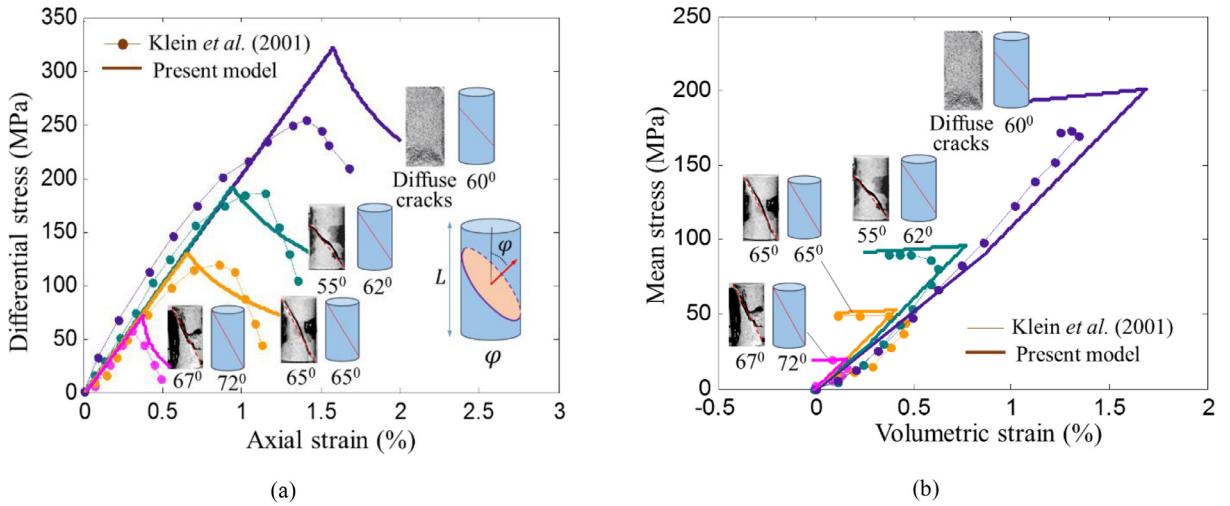

Fig. 16. Triaxial test results for Bentheim sandstone: (a) differential stress – axial strain and (b) mean stress – volumetric strain.

in this example follows geomechanics conventions, where compressive stress is considered to be positive. The tests were carried out at different confining pressure levels (0, 10, 30 and 90 MPa) where the axial and lateral strains were recorded to calculate the volumetric strain throughout the experiment. The differential stress q and mean stress p were then calculated, along with the axial/volumetric strain for each stage of the test.

As illustrated in Section 4.2, because the proposed model includes the behaviour of the localisation band, it is capable of capturing size effect responses at the constitutive level. The material properties are taken as follows: Young's modulus $E = 21$ GPa; Poisson's ratio $\nu = 0.24$; compressive strength $f_c = 60$ MPa; tensile strength $f_t = 1$ MPa; mode I fracture energy $G_f = 0.146$ kNm/m^2. For modelling the triaxial test, the parameters of the model were calibrated using the experimental data at confining stress $\sigma_3 = 10$ MPa, resulting in the following model parameters: $\alpha_0 = \frac{f_t \delta_0}{G_f} = 0.34$; $\beta = 0.046$; $m = 1.1$; $\mu_0 = 0.55$; $\mu = 0.32$; $\gamma = 0.8$. The elastic stiffness of the cohesive-frictional model in this case can take a large value, $K_n = K_s = 10^{10}$ KPa/m. Once the localisation band appears, the characteristic length H is calculated as $H = \Omega/\Gamma = L\cos\varphi$, where L is the specimen height and φ is the localisation band orientation as illustrated in Fig. 16(a).

Fig. 16 shows that both experimental stress-strain results and failure patterns (Klein et al., 2001) are fairly captured by the model. In particular, the orientations of the localisation bands under different confining pressures are predicted following the procedures described in Section 3.1 and compared well with their experimental counterparts. For each confining pressure, the material behaviour is accompanied by a failure plane as experimentally observed in the tests. This is one of the key features produced by the model that cannot be found in classical continuum models. It is seen that an increase in the confining pressure results in a decrease in the angle between the failure plane and the horizontal axis, reflecting the experimental observations. The dilation behaviour associated with this change of failure plane orientation can also be captured well, as shown in Fig. 16(b). However at high confining pressure (90 MPa), because the model fails to capture the compaction failure mechanism associated with grain crushing, the predicted results are much higher than their experimental counterparts.

A parametric study is performed on the same sandstone using confining pressure $\sigma_3 = 30$ MPa to illustrate the size-dependent behaviour of the material at constitutive level. Fig. 17(a) shows the stress-strain results of the triaxial test for different specimen lengths $L = 40$, 60 and 80 mm, respectively, while keeping the radius unchanged. It is seen that the longer the specimen is, the more brittle the behaviour becomes. This prediction by the model agrees well with experimental observations on size effects (van Mier, 1986). Fig. 17(b) shows the invariance of traction–displacement responses in the local coordinate system of the failure plane, which indicates the invariance of dissipation rate regardless of specimen sizes. These features are direct outcomes of incorporating the localised failure mechanism in the proposed constitutive model and also show the in-built regularisation effects of the proposed model.

4.4. Model validation against triaxial test results for concrete

The proposed model is also validated against triaxial tests conducted by Imran and Pantazopoulou (1997) on cylindrical concrete specimens with the length of 115 mm and diameter of 54 mm. The material properties are: Young's modulus $E = 21.25$ GPa; Poisson's ratio $\nu = 0.21$; compressive strength $f_c = 21.2$ MPa; tensile strength $f_t = 2.86$ MPa and mode I fracture energy $G_f = 0.063$ kN.m/m^2. Other model parameters are: $\alpha_0 = 0.63$; $m = 0.48$; $\mu_0 = 0.1$; $\mu = 1.05$; $\gamma = 1.5$; $\beta = 0.006$; $K_n = K_s = 10^{10}$ KPa/m. The characteristic length H is calculated once the localisation band appears using the same formulation described in the preceding example on sandstone.

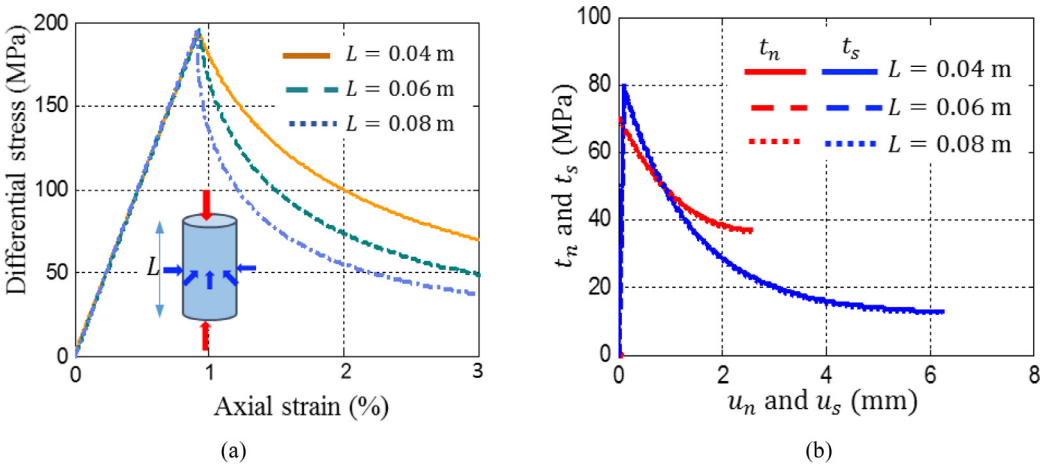

Fig. 17. Parametric study on size effect: (a) stress-strain curves for different specimen lengths and (b) traction – displacement in local failure plane up to the same damage level ($D = 0.9$).

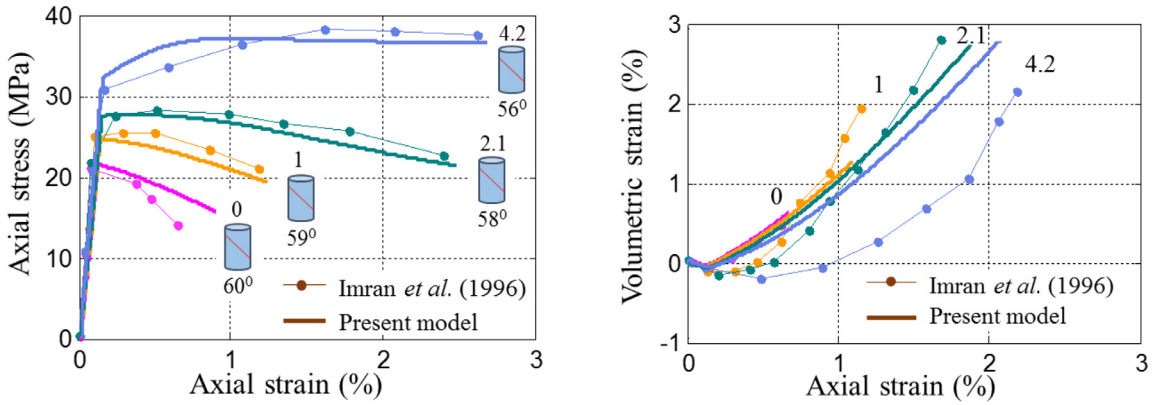

Fig. 18. Triaxial test results for concrete at different confinement (0, 1, 2.1 and 4.2 MPa): axial stress–axial strain and volumetric strain–axial strain.

The predictions, plotted in Fig. 18, show that the transition from softening (at zero or low confining pressure) to hardening behaviour (at higher confining pressure) exhibited by the specimen is well-captured by the model. The model prediction of failure patterns, characterised by the failure plane angle φ in Fig. 18, also reflects the general trend of localised failure in triaxial compression tests, where an increase of confining pressure leads to a decrease in the failure plane angle. While the stress-strain results show a good agreement, there are discrepancies between volumetric strain measured in the experiments and that predicted by the model for high confining pressure cases, despite the agreement in the trend. This could be due to the measuring method used in the experiment where only one strain gauge with a limited length was attached to the specimen at mid-height to measure the lateral strain (Imran & Pantazopoulou, 1997). The volumetric strain calculated from this lateral strain, therefore, might not be a good representative for the volumetric response of the specimen.

The size-dependent behaviour is also illustrated in Fig. 19 for the case of confining pressure $\sigma_3 = 2.1$ MPa using three different lengths $L_1 = 115$ mm, $2L_1$ and $4L_1$. The traction – displacement responses in the local coordinate system are the same, regardless of the length scale as illustrated in Fig. 19(b). This again highlights the importance and benefits of including localised failure mechanism in the development of constitutive models.

5. Model validation at the structural level

In this section, the proposed model is implemented into the commercial package ABAQUS as a user-defined material model (UMAT) for the analysis of BVPs including tension tests of double-edge notch specimens, mixed-mode tests of a double-edge notch specimen and L-shaped structure. Because the responses of the materials in those experiments are mostly softening, displacement-controlled loading is used for the simulations. The mechanical properties of the materials are summarised in Table 1. The friction angle of concrete is taken as 37°, based on a generally-accepted value in Fujita, Ishimaru, Hanai, and Suenga (1998) for all examples. The elastic normal and shear stiffness of the cohesive-frictional model are taken

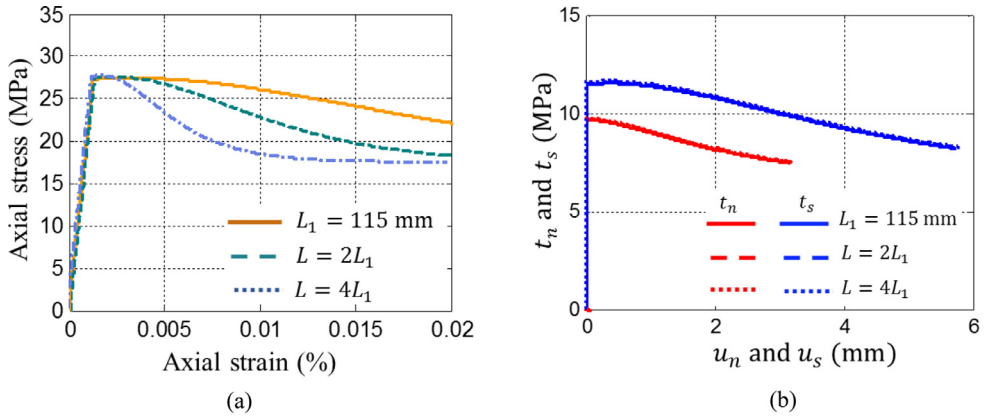

Fig. 19. Parametric study on size effect: (a) stress-strain curves for different specimen lengths and (b) traction – displacement in local failure plane up to the same damage level ($D = 0.9$).

Table 1
Mechanical properties of the material used in experiments.

Properties	Example 1	Example 2	Example 3
Young's Modulus E (GPa)	24	32	25.8
Poisson's ratio ν	0.2	0.2	0.18
Compressive strength f_c(MPa)	38.4	38.4	31
Tensile strength f_t(MPa)	2.86	3	2.7
Fracture energy G_I (N/mm)	0.063	0.11	0.065
Specimen thickness (mm)	10	50	100
Friction angle ϕ (^{0})	37	37	37

Table 2
Other model parameters.

Parameters	Example 1	Example 2	Example 3
α_0	0.63	0.38	0.58
β	0.002	0.002	0.001
m	0.4	0.43	0.4
μ_0	0.4	0.35	0.5

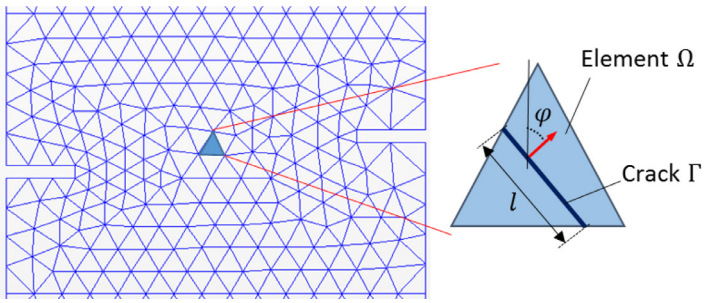

Fig. 20. Illustration for the characteristic length calculation in FEAs.

as $K_n = K_s = 10^{10}$ and dilation parameter $\gamma = 1.1$ is used. Other model parameters needed for the cohesive-frictional model are presented in Table 2.

In the paper, all simulations are performed in 2D using 3-node triangular elements. Strictly, the characteristic length of each element should be calculated by definition as $H = \frac{\Omega}{\Gamma} = \frac{A}{l}$ where A is the area of the element and l is the length of the localisation band crossing the element as illustrated in Fig. 20. Theoretically, H can be calculated during the simulation using the predicted localisation orientation φ, nodal coordinates of the element and geometric manipulations. However, to avoid this dependence on element geometry and also reduce the computational time, a simple and more practical way, with $H = \sqrt{A}$, is employed in this study. This simple approximation also helps facilitate the discretisation independence of the implementation for both mesh-free and mesh-based methods. The convergence of numerical solutions upon mesh refinement in this Section demonstrates that this simplification works well and hence can be adopted.

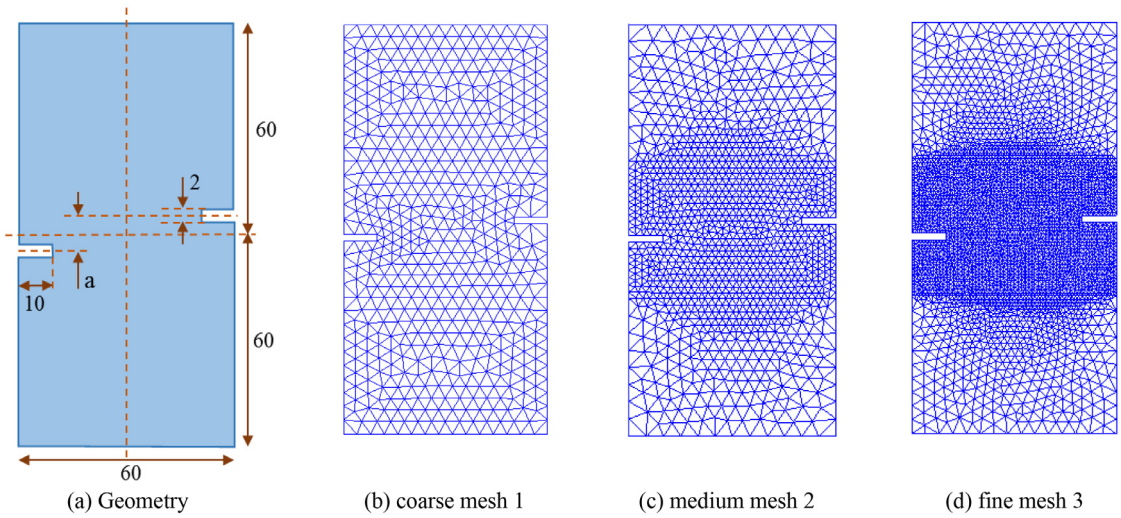

Fig. 21. Specimen geometry and mesh sizes for the tension test.

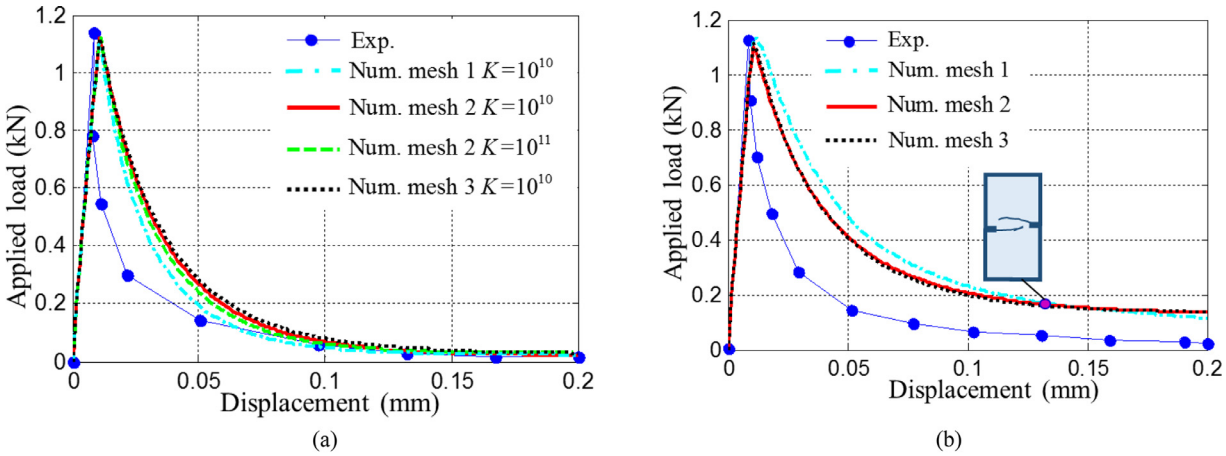

Fig. 22. Load-displacement responses for tension test: (a) $a = 0$ and (b) $a = 5$.

5.1. Tension test of the double-edge-notched specimen

Tension tests of two double-edge-notched concrete specimens, shown in Fig. 21 (in cm), are simulated to illustrate the model capability. Based on the experimental setup (Shi et al., 2000), the top edge is pulled upwards and the bottom edge is fixed in the simulation. The tests were conducted with two different values of the vertical distance a between two notches (i.e., symmetrical, $a = 0$, and asymmetric, $a = 5$ cm).

The predicted force-displacement responses are presented in Fig. 22, for three different meshes, mesh 1 (635 elements), mesh 2 (1242 elements) and mesh 3 (2598 elements). It can be seen that the model prediction fairly agrees with the experimentally measured response which shows sharp softening after the peak due to the brittle attribute of concrete behaviour. During this process, a large amount of energy is quickly dissipated via the crack development, and the load-displacement curve hence drops down rapidly. It can also be observed from this figure that the numerical results converge upon mesh refinement, thanks to the characteristic length H included in the model. The results corresponding to two values of cohesive stiffness K(K=10^{10} and K=10^{11}), presented in Fig. 22 for the case of $a = 0$, are almost unchanged. This shows that as long as these stiffness values are high enough, the choice of the actual values does not significantly affect the simulation results. Fig. 23 and Fig. 24 show a good agreement between simulated crack patterns (using mesh 2) and those from experiments.

5.2. Mixed-mode loading test of the double-edge-notched specimen

The capability of the model in capturing mixed-mode responses is demonstrated via the simulation of a double-edge-notched concrete specimen under combined shear and tension, shown in Fig. 25. The loading path 2a (Nooru, Schlangen,

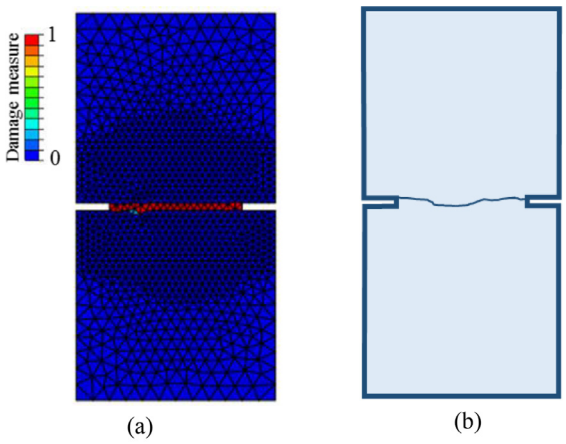

Fig. 23. Crack patterns for symmetrical notch a = 0: (a) macro crack by the model and (b) from experiment (redrawn from Shi et al., 2000).

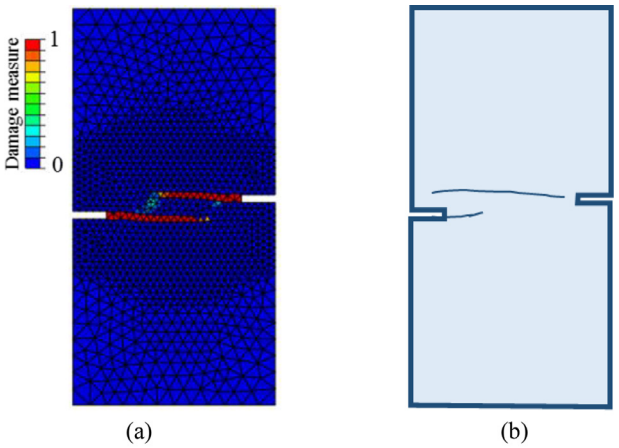

Fig. 24. Crack patterns for unsymmetrical notch a = 5: (a) macro crack by the model and (b) from experiment (redrawn from Shi et al., 2000).

& Van Mier, 1993), where a normal (horizontal) and shear (vertical) displacements are applied equally ($\delta_n = \delta_s$) on the specimen, is considered here. In the experiment, displacements were measured at points M, M', N, N', P and P' and then used to calculate the average displacement as $\delta_n = (\delta_n^M - \delta_n^{M'} + \delta_n^N - \delta_n^{N'})/2$ and $\delta_s = (\delta_s^P - \delta_s^{P'})/2$. However, because incorporating such conditions in numerical simulation is difficult, an alternative boundary condition, proposed by Jefferson (2003), is used in this study. Following this alternative, the movements of two rigid plates were applied to the upper-left and top edges of the specimens while the lower-right and bottom edges were fixed in both directions.

The results in Fig. 26 show reasonable agreements in trends between the numerical results and their corresponding experimental counterparts. As the results produced by two meshes (mesh 1, 1821 elements and mesh 2, 3984 elements shown in Fig. 25) are almost the same, they again demonstrate the convergence of the numerical results upon mesh refinement. Fig. 27 highlights the agreement between the predicted and experimentally observed crack patterns. The damage variable values at the final state of the simulation in Fig. 27(a) demonstrates that two parallel macro cracks formed and propagated during the simulation, as also experimentally observed (Nooru et al., 1993).

5.3. Mixed-mode test of the L-shaped structure

The final example to illustrate the model capability is a mixed-mode test of an L-shaped structure carried out by Winkler, Hofstetter, and Niederwanger (2001) with structural geometry and boundary condition shown in Fig. 28. A vertical displacement was applied through a loading plate near the right edge while the bottom of the specimen was fixed in both directions. This figure also shows the two meshes used in the numerical simulation: mesh 1 (1432 elements) and mesh 2 (2563 elements).

The load versus vertical displacement presented in Fig. 29(a) shows a relatively good agreement between responses predicted by the model and the experimentally observed ones. Although there is a slight difference in residual force values in the final stage of failure, the softening branch of the results is captured by the proposed two-crack model (model 2).

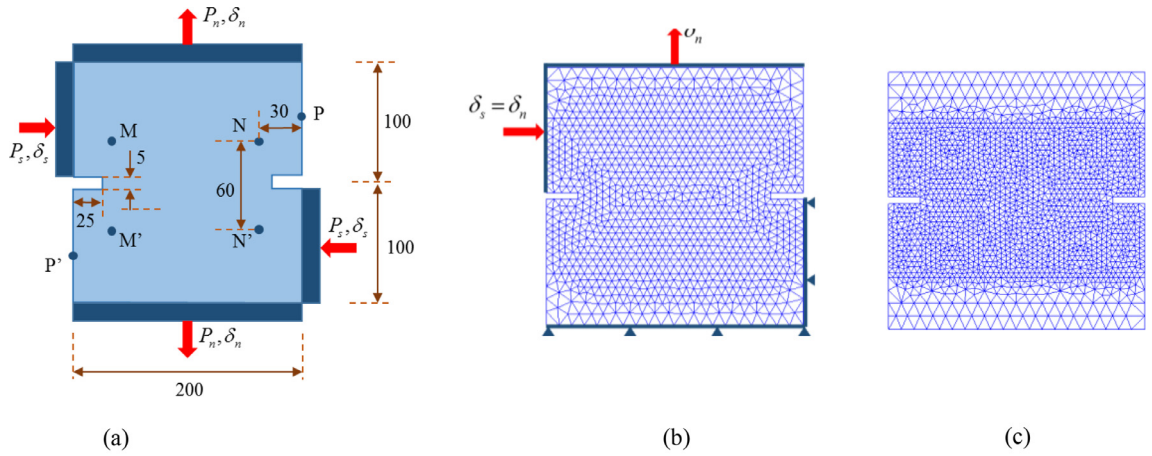

Fig. 25. Mixed mode test: (a) experiment set-ups; (b) mesh 1 and (c) mesh 2.

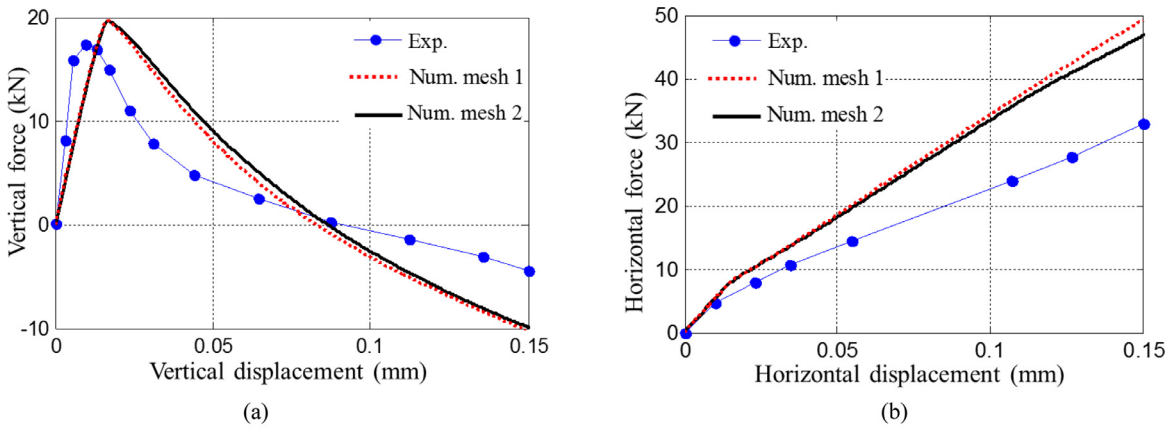

Fig. 26. Load-displacement responses for the mixed-mode test: (a) in vertical and (b) in the horizontal direction.

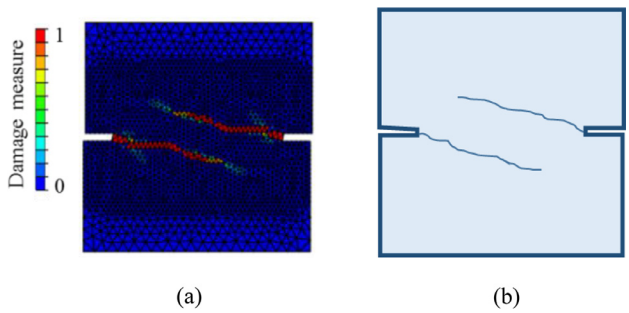

Fig. 27. Crack pattern of the mixed-mode test: (a) macro crack from simulation; and (b) from experiments (redrawn from Nooru et al., 1993).

The figure also shows the result obtained using a model that allows the activation of a single crack only (model 1) with the same set of parameters. It can be seen that the result obtained by this single crack model is much stiffer showing a remarkable hardening response before the softening. This discrepancy can be explained in Fig. 29(b), where the crack development at the early stage of cracking (point A in Fig. 29(a)) is plotted. As can be seen, the primary cracks, denoted by green lines, in shaded elements are not well aligned with the overall macroscopic crack direction, which is almost horizontal as shown in Fig. 30. For the one-crack model (Nguyen et al., 2012, 2014, Le et al., 2017), a significant amount of stress is still transferred through these shaded elements as illustrated previously in Section 4.1, leading to over-stiff responses. In the two-crack model is used, secondary cracks, denoted by red lines in Fig. 29(c), are activated and help release this spurious stress transfer. This allows the macroscopic crack to develop in an appropriate direction and yield more reasonable results. This again illustrates that the proposed model with more than one cracks can capture well the development of the FPZ

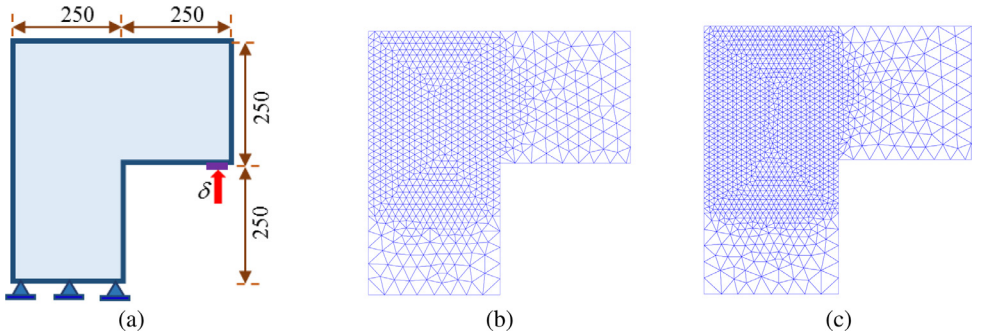

Fig. 28. The L-shaped test: (a) experiment set-ups (b) mesh 1 and (c) mesh 2.

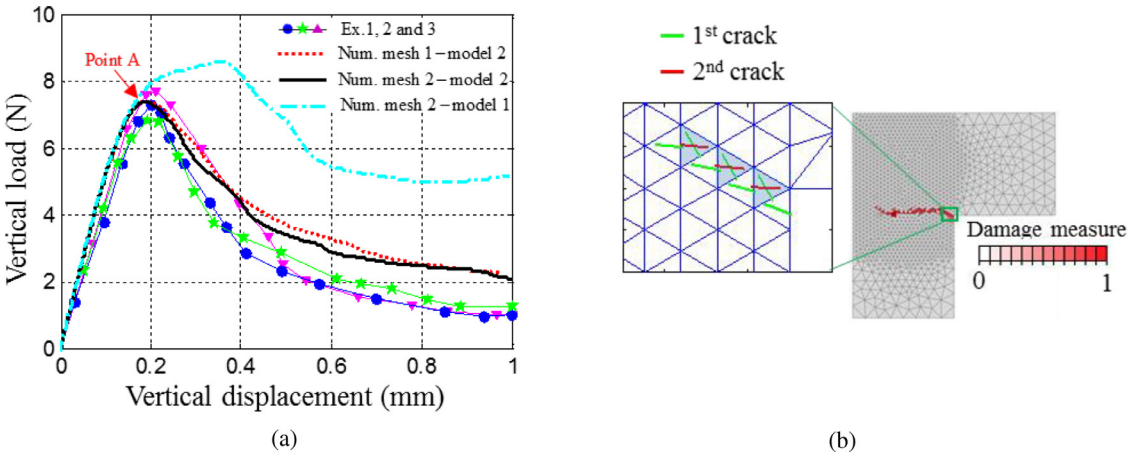

Fig. 29. Results of L-shaped structure test: (a) Load-displacement responses, (b) embedded crack development at point A.

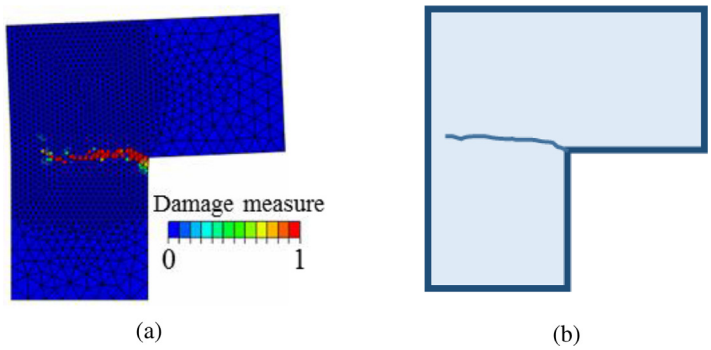

Fig. 30. Crack pattern of the mixed-mode test: (a) macro crack from simulation (magnification factor of 50) and (b) from experiments (redrawn from Winkler et al., 2001).

without requiring any additional treatment for crack orientation. As shown in Fig. 30, the crack pattern obtained from the model agrees well with its experimental counterpart with a major crack initiating from the corner and then propagating to the left side of the specimen.

6. Conclusions

This work addresses the importance of failure mechanisms in governing the mechanical responses of geomaterials and describes an approach to integrate them in constitutive modelling to naturally capture intrinsic features of geomaterials failure. The analysis of experimental data on both macro stress-strain responses and the underlying failure mechanisms show the correlation between localised failure observed in experiments and several important behavioural characteristics such as Lode angle dependence and size effects. This correlation leads to essential requirements in enriching the structure of

constitutive models to accommodate this localised failure mechanism as a basis for the development of a model for geomaterials. The proposed approach is developed within the framework of thermodynamics, with new forms of energy potentials proposed to encapsulate localised failure mechanisms. The thermodynamics-based formulation naturally leads to a new constitutive structure containing the responses of both the bulk and localisation bands idealised as two cohesive-frictional cracks, the orientations of which depend on both stress state and material properties. The interactions of these phases (bulk and localisation bands) are obtained as part of the standard procedures in the thermodynamic formulation and help connect them to drive the macro response of the volume element. The obtained constitutive model possesses key features of geomaterial, all of which are the results of the underlying localised failure mechanism embedded in the proposed constitutive structure. No phenomenological treatments for the Lode angle dependence of the mechanical behaviour and for the regularisation in the analysis of Boundary Value Problems are required, as usually the case in classical continuum models. In addition, the introduction of secondary cracking help naturally removes stress locking issues in the analysis of localised failure at structural scale. Good agreements with experimental results at both constitutive and structural levels illustrate the capabilities of the proposed model in analysing the materials responses and their failure patterns in a wide range of loading cases, from tension to triaxial compression, under different confining pressure levels. The proposed approach thus shows promising features in constitutive modelling geomaterials based on their underlying mechanisms of localised failure. The capabilities of the approach can be further extended in the near future to capture compaction failure mechanism by introducing compaction modes with grain crushing to the currently elastic bulk and/or to the cohesive-frictional model at the scale of the compaction band.

Acknowledgements

Giang D. Nguyen and Ha H. Bui gratefully acknowledge support from the Australian Research Council via Discovery Projects FT140100408 (Nguyen), DP160100775 (Bui), and DP170103793 (Nguyen and Bui). Professional editor, Leticia Mooney, is acknowledged for proof-reading the first draft of the manuscript.

Supplementary materials

Supplementary material associated with this article can be found, in the online version, at doi:10.1016/j.ijengsci.2018.09.004.

References

Antoni, N. (2017). A further analysis on the analogy between friction and plasticity in Solid Mechanics. *International Journal of Engineering Science, 121*, 34–51. http://doi.org/10.1016/j.ijengsci.2017.08.012.

Bažant, Z. P. (1999). Size effect on structural strength: A review. *Archive of Applied Mechanics, 69*(9-10), 703–725. http://doi.org/10.1007/s004190050252.

Bažant, Z. P., & Caner, F. C. (2014). Impact comminution of solids due to local kinetic energy of high shear strain rate: I. Continuum theory and turbulence analogy. *Journal of the Mechanics and Physics of Solids, 64*(1), 223–235. http://doi.org/10.1016/j.jmps.2013.11.008.

Borja, R. I. (2000). A finite element model for strain localization analysis of strongly discontinuous fields based on standard Galerkin approximation. *Computer Methods in Applied Mechanics and Engineering, 190*, 1529–1549.

Brooks, Z. (2013). *(PhD thesis)*. Fracture process zone: microstructure and nanomechanics in quasi-brittle materials. Massachusetts Institute of Technology.

Brünig, M., & Michalski, A. (2017). A stress-state-dependent continuum damage model for concrete based on irreversible thermodynamics. *International Journal of Plasticity, 90*, 31–43. http://doi.org/10.1016/j.ijplas.2016.12.002.

Caner, F. C., & Bažant, Z. P. (2013). Microplane model M7 for plain concrete. I: Formulation. *Journal of Engineering Mechanics, 139*(12), 1724–1735. http://doi.org/10.1061/(ASCE)EM.1943-7889.0000571.

Červenka, J., & Papanikolaou, V. K. (2008). Three dimensional combined fracture-plastic material model for concrete. *International Journal of Plasticity, 24*(12), 2192–2220. http://doi.org/10.1016/j.ijplas.2008.01.004.

Cervera, M., & Chiumenti, M. (2006). Smeared crack approach: Back to the original track. *International Journal for Numerical and Analytical Methods in Geomechanics, 30*(12), 1173–1199. http://doi.org/10.1002/nag.518.

Chemenda, A. I. (2009). The formation of tabular compaction-band arrays: Theoretical and numerical analysis. *Journal of the Mechanics and Physics of Solids, 57*(5), 851–868. http://doi.org/10.1016/j.jmps.2009.01.007.

Chemenda, A. I., & Mas, D. (2016). Dependence of rock properties on the Lode angle: Experimental data, constitutive model, and bifurcation analysis. *Journal of the Mechanics and Physics of Solids, 96*, 477–496. http://doi.org/10.1016/j.jmps.2016.08.004.

Cheng, J., Qian, X., & Zhao, T. (2016). Rheological viscoplastic models of asphalt concrete and rate-dependent numerical implement. *International Journal of Plasticity, 81*, 209–230. http://doi.org/10.1016/j.ijplas.2016.01.004.

Daneshyar, A., & Ghaemian, M. (2017). Coupling microplane-based damage and continuum plasticity models for analysis of damage-induced anisotropy in plain concrete. *International Journal of Plasticity, 95*, 216–250. http://doi.org/10.1016/j.ijplas.2017.04.011.

Das, A., Nguyen, G. D., & Einav, I. (2011). Compaction bands due to grain crushing in porous rocks: A theoretical approach based on breakage mechanics. *Journal of Geophysical Research, 116*(8), 1–14. http://doi.org/10.1029/2011JB008265.

Das, A., Nguyen, G. D., & Einav, I. (2013). The propagation of compaction bands in porous rocks based on breakage mechanics. *Journal of Geophysical Research: Solid Earth, 118*(5), 2049–2066. http://doi.org/10.1002/jgrb.50193.

Das, A., Tengattini, A., Nguyen, G. D., Viggiani, G., Hall, S. A., & Einav, I. (2014). A thermomechanical constitutive model for cemented granular materials with quantifiable internal variables. Part II – Validation and localization analysis. *Journal of the Mechanics and Physics of Solids, 70*(1), 382–405. http://doi.org/10.1016/j.jmps.2014.05.022.

Dias-da-Costa, D., Alfaiate, J., Sluys, L. J., & Júlio, E. (2009). A discrete strong discontinuity approach. *Engineering Fracture Mechanics, 76*(9), 1176–1201. http://doi.org/10.1016/j.engfracmech.2009.01.011.

Dong, Y., Wu, S., Xu, S. S., Zhang, Y., & Fang, S. (2010). Analysis of concrete fracture using a novel cohesive crack method. *Applied Mathematical Modelling, 34*(12), 4219–4231. http://doi.org/10.1016/j.apm.2010.04.019.

Eichhubl, P., Hooker, J. N., & Laubach, S. E. (2010). Pure and shear-enhanced compaction bands in Aztec Sandstone. *Journal of Structural Geology, 32*(12), 1873–1886. http://doi.org/10.1016/j.jsg.2010.02.004.

Etse, G., Nieto, M., & Steinmann, P. (2003). A micropolar microplane theory. *International Journal of Engineering Science, 41*(13-14), 1631–1648. http://doi.org/10.1016/S0020-7225(03)00031-4.

Fujita, Y., Ishimaru, R., Hanai, S., & Suenga, Y. (1998). Study on internal friction angle and tensile strength. In *Proceedings of FRAMCOS-3* (pp. 325–334). 1994.
Grassl, P., Xenos, D., Nyström, U., Rempling, R., & Gylltoft, K. (2013). CDPM2: A damage-plasticity approach to modelling the failure of concrete. *International Journal of Solids and Structures, 50*(24), 3805–3816. http://doi.org/10.1016/j.ijsolstr.2013.07.008.
Haghighat, E., & Pietruszczak, S. (2015). On modeling of discrete propagation of localised damage in cohesive-frictional material. *International Journal for Numerical and Analytical Methods in Geomechanics, 39*, 1774–1790.
Haimson, B., & Rudnicki, J. W. (2010). The effect of the intermediate principal stress on fault formation and fault angle in siltstone. *Journal of Structural Geology, 32*(11), 1701–1711. http://doi.org/10.1016/j.jsg.2009.08.017.
He, W., Wu, Y. F., Liew, K. M., & Wu, Z. (2006). A 2D total strain based constitutive model for predicting the behaviors of concrete structures. *International Journal of Engineering Science, 44*(18-19), 1280–1303. http://doi.org/10.1016/j.ijengsci.2006.07.007.
Hillerborg, A., Modéer, M., & Petersson, P. E. (1976). Analysis of crack formation and crack growth in concrete by means of fracture mechanics and finite elements. *Cement and Concrete Research, 6*(6), 773–781. http://doi.org/10.1016/0008-8846(76)90007-7.
Houlsby, G. T., & Puzrin, A. M. (2000). Thermomechanical framework for constitutive models for rate-independent dissipative materials. *International Journal of Plasticity, 16*(9), 1017–1047. http://doi.org/10.1016/S0749-6419(99)00073-X.
Hu, X., & Duan, K. (2008). Size effect and quasi-brittle fracture: The role of FPZ. *International Journal of Fracture, 154*(1-2), 3–14. http://doi.org/10.1007/s10704-008-9290-7.
Imran, I., & Pantazopoulou, S. J. (1997). Experimental study of plain concrete under triaxial stress. *ACI Material Journal, 93*(93), 589–601.
Ingraham, M. D., Issen, K. A., & Holcomb, D. J. (2013). Response of Castlegate sandstone to true triaxial states of stress. *Journal of Geophysical Research: Solid Earth, 118*(2), 536–552. http://doi.org/10.1002/jgrb.50084.
Jefferson, A. D. (2003). Craft – A plastic-damage-contact model for concrete. II. Model implementation with implicit return-mapping algorithm and consistent tangent matrix. *International Journal of Solids and Structures, 40*, 6001–6022.
Jensen, S. S. (2016). Experimental study of direct tensile strength in sedimentary rocks. *(PhD thesis).*
Jirásek, M. (2000). Comparative study on finite elements with embedded discontinuities. *Computer Methods in Applied Mechanics and Engineering, 188*(1-3), 307–330. http://doi.org/10.1016/s0045-7825(99)00154-1.
Karihaloo, B. L., Abdalla, H. M., & Xiao, Q. Z. (2003). Size effect in concrete beams. *Engineering Fracture Mechanics, 70*(7-8), 979–993. http://doi.org/10.1016/S0013-7944(02)00161-3.
Karrech, A., Regenauer-Lieb, K., & Poulet, T. (2011). A damaged visco-plasticity model for pressure and temperature sensitive geomaterials. *International Journal of Engineering Science, 49*(10), 1141–1150. http://doi.org/10.1016/j.ijengsci.2011.05.005.
Kedar, K., & Bažant, Z. P. (2015). Microplane damage model for fatigue of quasibrittle materials : Sub-critical crack growth, lifetime and residual strength. *International Journal of Fatigue, 70*, 93–105. http://doi.org/10.1016/j.ijfatigue.2014.08.012.
Klein, E., Baud, P., Reuschlé, T., & Wong, T. F. (2001). Mechanical behaviour and failure mode of Bentheim sandstone under triaxial compression. *Physics and Chemistry of the Earth, Part A: Solid Earth and Geodesy, 26*(1-2), 21–25. http://doi.org/10.1016/S1464-1895(01)00017-5.
Klein, E., & Reuschlé, T. (2003). A model for the mechanical behaviour of bentheim sandstone in the brittle regime. *Pure and Applied Geophysics, 160*(5), 833–849. http://doi.org/10.1007/PL00012568.
Le, L. A., Nguyen, G. D., Bui, H. H., Sheikh, A. H., Kotousove, A., & Khanna, A. (2017). Modelling jointed rock mass as a continuum with an embedded cohesive-frictional model. *Engineering Geology, 228*, 107–120.
Lee, H., & Haimson, B. C. (2011). True triaxial strength, deformability, and brittle failure of granodiorite from the San Andreas Fault Observatory at Depth. *International Journal of Rock Mechanics and Mining Sciences, 48*(7), 1199–1207. http://doi.org/10.1016/j.ijrmms.2011.08.003.
Li, C., Caner, F. C., Chau, V. T., & Bažant, Z. P. (2017). Spherocylindrical microplane constitutive model for shale and other anisotropic rocks. *Journal of the Mechanics and Physics of Solids, 103*, 155–178. http://doi.org/10.1016/j.jmps.2017.03.006.
Li, X. C., Xu, D. J., & Liu, S. H. (1994). The experimental research of the strength, deformation and failure properties of Laxiwa granite under the status of true triaxial stresses. In *Proceedings of the third conference of chinese society of rock mechanics and engineering* (pp. 153–159). Beijing China: China Science and Technology Press.
Liao, C. J., Lee, D. H., Wu, J. H., & Lai, C. Z. (2011). A new ring-shear device for testing rocks under high normal stress and dynamic conditions. *Engineering Geology, 122*(1-2), 93–105. http://doi.org/10.1016/j.enggeo.2011.03.018.
Lloberas-Valls, O., Huespe, A. E., Oliver, J., & Dias, I. F. (2016). Strain injection techniques in dynamic fracture modeling. *Computer Methods in Applied Mechanics and Engineering, 308*, 499–534. http://doi.org/10.1016/j.cma.2016.05.023.
Lu, D., Du, X., Wang, G., Zhou, A., & Li, A. (2016). A three-dimensional elastoplastic constitutive model for concrete. *Computers and Structures, 163*, 41–55. http://doi.org/10.1016/j.compstruc.2015.10.003.
Lu, X., Hsu, C. T., & Asce, F. (2007). Stress-strain relations of high-strength concrete under triaxial compression. *Journal of Materials in Civil Engineering, 19*(3), 261–268. http://doi.org/10.1061/(ASCE)0899-1561(2007)19:3(261).
Ma, X., & Haimson, B. C. (2016). Failure characteristics of two porous sandstones subjected to true triaxial testing. *Journal of Geophysical Research: Solid Earth, 121*(9), 6477–6498. http://doi.org/10.1002/2016JB012979.
Mir, A., Nguyen, G. D., & Sheikh, A. H. (2018). A thermodynamics-based model for brittle to ductile behaviour and localised failure of porous rocks. *International Journal of Solids and Structures* (In press). https://www.sciencedirect.com/science/article/pii/S0020768318302579.
Misra, A., & Poorsolhjouy, P. (2016). Granular micromechanics model of anisotropic elasticity derived from Gibbs potential. *Acta Mechanica, 227*(5), 1393–1413. http://doi.org/10.1007/s00707-016-1560-2.
Misra, A., & Yang, Y. (2010). Micromechanical model for cohesive materials based upon pseudo-granular structure. *International Journal of Solids and Structures, 47*(21), 2970–2981. http://doi.org/10.1016/j.ijsolstr.2010.07.002.
Navarro, V., Alonso, J., Calvo, B., & Sánchez, J. (2010). A constitutive model for porous rock including effects of bond strength degradation and partial saturation. *International Journal of Rock Mechanics and Mining Sciences, 47*(8), 1330–1338. http://doi.org/10.1016/j.ijrmms.2010.08.003.
Neilsen, M. K., & Schreyer, H. L. (1993). Bifurcations in elastic-plastic materials. *International Journal of Solids and Structures, 30*(4), 521–544. http://doi.org/https://doi.org/10.1016/0020-7683(93)90185-A.
Nguyen, G. D., Einav, I., & Korsunsky, A. M. (2012). How to connect two scales of behaviour in constitutive modelling of geomaterials. *Géotechnique Letters, 2*, 129–134. http://doi.org/10.1680/geolett.12.00030.
Nguyen, G. D., & Korsunsky, A. M. (2008). Development of an approach to constitutive modelling of concrete: Isotropic damage coupled with plasticity. *International Journal of Solids and Structures, 45*(20), 5483–5501. http://doi.org/10.1016/j.ijsolstr.2008.05.029.
Nguyen, G. D., Korsunsky, A. M., & Einav, I. (2014). A constitutive modelling framework featuring two scales of behaviour : Fundamentals and applications to quasi-brittle failure. *Engineering Fracture Mechanics, 115*, 221–240. http://doi.org/10.1016/j.engfracmech.2013.11.006.
Nguyen, G. D., Nguyen, C. T., Bui, H. H., & Nguyen, V. P. (2016a). Constitutive modelling of compaction localisation in porous sandstones. *International Journal of Rock Mechanics and Mining Sciences, 83*, 57–72. http://doi.org/10.1016/j.ijrmms.2015.12.018.
Nguyen, G. D., Nguyen, C. T., Nguyen, V. P., Bui, H. H., & Shen, L. (2016b). A size-dependent constitutive modelling framework for localised failure analysis. *Computational Mechanics, 58*(2), 257–280. http://doi.org/10.1007/s00466-016-1293-z.
Nguyen, N. T. H., Bui, H. H., Nguyen, G. D., & Kodikara, J. (2017). A cohesive damage-plasticity model for DEM and its application for numerical investigation of soft rock fracture properties. *International Journal of Plasticity, 98*, 175–196. http://doi.org/10.1016/j.ijplas.2017.07.008.
Nooru-Mohamed, M. B., Schlangen, E., & Van Mier, J. G. (1993). Experimental and numerical study on the behavior of concrete subjected to biaxial tension. *Advanced Cement Based Materials, 1*, 22–37.
Paliwal, B., Hammi, Y., Moser, R. D., & Horstemeyer, M. F. (2017). A three-invariant cap-plasticity damage model for cementitious materials. *International Journal of Solids and Structures, 108*, 186–202. http://doi.org/10.1016/j.ijsolstr.2016.12.015.

Parvaneh, S. M., & Foster, C. D. (2016). On numerical aspects of different updating schedules for tracking fracture path in strain localization modeling. *Engineering Fracture Mechanics, 152*, 26–57. http://doi.org/10.1016/j.engfracmech.2015.11.011.

Pietruszczak, S., & Haghighat, E. (2015). Modeling of deformation and localized failure in anisotropic rocks. *International Journal of Solids and Structures, 67-68*, 93–101. http://doi.org/10.1016/j.ijsolstr.2015.04.004.

Qi, M., Shao, J. F., Giraud, A., Zhu, Q. Z., & Colliat, J. B. (2016). Damage and plastic friction in initially anisotropic quasi brittle materials. *International Journal of Plasticity, 82*, 260–282. http://doi.org/10.1016/j.ijplas.2016.03.008.

Rezakhani, R., & Cusatis, G. (2014). Asymptotic expansion homogenization of discrete fine-scale models with rotational degrees of freedom for the simulation of quasi-brittle materials. *Journal of the Mechanics and Physics of Solids, 88*, 320–345. http://doi.org/10.1016/j.jmps.2016.01.001.

Rots, J. G. (1991). Smeared and discrete representations of localized fracture. *International Journal of Fracture, 51*(1), 45–59. http://doi.org/10.1007/BF00020852.

Rudnicki, J. W., & Rice, J. R. (1975). Conditions for the localization of deformation in pressure-sensitive dilatant materials. *Journal of the Mechanics and Physics of Solids, 23*(6), 371–394. http://doi.org/10.1016/0022-5096(75)90001-0.

Sanchez, J., Schreyer, H., Sulsky, D., & Wallstedt, P. (2015). Solving quasi-static equations with the material-point method. *International Journal for Numerical Method in Engineering, 103*, 60–78. http://doi.org/10.1002/nme.

Sancho, J. M., Planas, J., Cendón, D. A., Reyes, E., & Gálvez, J. C. (2007). An embedded crack model for finite element analysis of concrete fracture. *Engineering Fracture Mechanics, 74*, 75–86. http://doi.org/10.1016/j.engfracmech.2006.01.015.

Savage, H. M., & Brodsky, E. E. (2011). Collateral damage: Evolution with displacement of fracture distribution and secondary fault strands in fault damage zones. *Journal of Geophysical Research: Solid Earth, 116*(3), 1–14. http://doi.org/10.1029/2010JB007665.

Scerrato, D., Giorgio, I., Madeo, A., Limam, A., & Darve, F. (2014). A simple non-linear model for internal friction in modified concrete. *International Journal of Engineering Science, 80*, 136–152. http://doi.org/10.1016/j.ijengsci.2014.02.021.

Schreyer, H. L. (2007). Modelling surface orientation and stress at failure of concrete and geological materials. *International Journal For Numerical and Analytical Methods in Geomechanics, 31*, 147–171. http://doi.org/10.1002/nag.

Shen, W. Q., & Shao, J. F. (2016). An elastic-plastic model for porous rocks with two populations of voids. *Computers and Geotechnics, 76*, 194–200. http://doi.org/10.1016/j.compgeo.2016.03.011.

Shi, C., Dam, A. G. Van, Mier, J. G. M. Van, & Sluys, B. (2000). Crack interaction in concrete. In F. H. Wittmann (Ed.), *Proceedings of the material for building and structures* (pp. 125–131). Winheim, German: Wiley-VCH.

Skarzyński, L., & Tejchman, J. (2016). Experimental investigations of fracture process in concrete by means of X-ray micro-computed tomography. *An International Journal for Experimental Mechanics, 52*(1), 26–45. http://doi.org/10.1111/str.12168.

Spiezia, N., Salomoni, V. A., & Majorana, C. E. (2016). Plasticity and strain localization around a horizontal wellbore drilled through a porous rock formation. *International Journal of Plasticity, 78*, 114–144. http://doi.org/10.1016/j.ijplas.2015.10.013.

Syroka-Korol, E., Tejchman, J., & Mróz, Z. (2013). FE calculations of a deterministic and statistical size effect in concrete under bending within stochastic elasto-plasticity and non-local softening. *Engineering Structures, 48*, 205–219. http://doi.org/10.1016/j.engstruct.2012.09.013.

Tejchman, J., & Gorski, J. (2008). Deterministic and statistical size effect during shearing of granular layerwithin amicro-polar hypoplasticity. *International Journal for Numerical and Analytical Methods in Geomechanics, 32*(March 2007), 189–213. http://doi.org/10.1002/nag.

Tengattini, A., Das, A., Nguyen, G. D., Viggiani, G., Hall, S. A., & Einav, I. (2014). A thermomechanical constitutive model for cemented granular materials with quantifiable internal variables. Part I – Theory. *Journal of the Mechanics and Physics of Solids, 70*(1), 382–405. http://doi.org/10.1016/j.jmps.2014.05.022.

Tran, H. D., Sulsky, D. L., & Schereyer, H. L. (2015). An anisotropic elastic-decohesive constitutive relation for sea ice. *International Journal for Numerical and Analytical Methods in Geomechanics, 32*, 988–1013. http://doi.org/10.1002/nag.

Unger, J. F., Eckardt, S., & Könke, C. (2011). A mesoscale model for concrete to simulate mechanical failure. *Computers and Concrete, 8*(4), 401–423. http://doi.org/10.12989/cac.2011.8.4.401.

Vachaparampil, A., & Ghassemi, A. (2017). Failure characteristics of three shales under true-triaxial compression. *International Journal of Rock Mechanics and Mining Sciences, 100*, 151–159. http://doi.org/10.1016/j.ijrmms.2017.10.018.

van Mier, J. G. M. (1986). Fracture of concrete under complex stress. *Heron, 31*(3), 1–90.

Veiskarami, M., & Tamizdoust, M. M. (2017). Bifurcation analysis in sands under true triaxial conditions with coaxial and noncoaxial plastic flow rules. *Journal of Engineering Mechanics, 143*(10), 1–12. http://doi.org/10.1061/(ASCE)EM.1943-7889.0001344.

Winkler, B., Hofstetter, G., & Niederwanger, G. (2001). Experimental verification of a constitutive model for concrete cracking. *Proceedings of the Institution of Mechanical Engineers, Part L: Journal of Materials: Design and Applications, 215*(2), 75–86. http://doi.org/10.1177/146442070121500202.

Wong, T. F., & Baud, P. (2012). The brittle-ductile transition in porous rock: A review. *Journal of Structural Geology, 44*, 25–53. http://doi.org/10.1016/j.jsg.2012.07.010.

Xenos, D., Grégoire, D., Morel, S., & Grassl, P. (2015). Calibration of nonlocal models for tensile fracture in quasi-brittle heterogeneous materials. *Journal of the Mechanics and Physics of Solids, 82*, 48–60. http://doi.org/10.1016/j.jmps.2015.05.019.

Yang, S. Q., Jiang, Y. Z., Xu, W. Y., & Chen, X. Q. (2008). Experimental investigation on strength and failure behavior of pre-cracked marble under conventional triaxial compression. *International Journal of Solids and Structures, 45*(17), 4796–4819. http://doi.org/10.1016/j.ijsolstr.2008.04.023.

Yu, M. H., Zan, Y. W., Zhao, J., & Yoshimine, M. (2002). A unified strength criterion for rock material. *International Journal of Rock Mechanics and Mining Sciences, 39*(8), 975–989. http://doi.org/10.1016/S1365-1609(02)00097-7.

Zhang, Y., Lackner, R., Zeiml, M., & Mang, H. A. (2015). Strong discontinuity embedded approach with standard SOS formulation: Element formulation, energy-based crack-tracking strategy, and validations. *Computer Methods in Applied Mechanics and Engineering, 287*, 335–366. http://doi.org/10.1016/j.cma.2015.02.001.

Zhao, L.-Y., Zhu, Q.-Z., & Shao, J.-F. (2018). A micro-mechanics based plastic damage model for quasi-brittle materials under a large range of compressive stress. *International Journal of Plasticity, 100*(October 2017), 156–176. http://doi.org/10.1016/j.ijplas.2017.10.004.

Zhu, Q. Z., Zhao, L. Y., & Shao, J. F. (2016). Analytical and numerical analysis of frictional damage in quasi brittle materials. *Journal of the Mechanics and Physics of Solids, 92*, 137–163. http://doi.org/10.1016/j.jmps.2016.04.002.

Ziegler, H. (1983). *An introduction to thermomechanics*. Amsterdam: North Holland 1st ed.

Appendix C

Incorporation of micro-cracking and fibre bridging phenomena in constitutive modelling of fibre reinforced concrete

Le, L.A., Nguyen, G.D., Bui, H.H., Sheikh, A.H., Kotousov, A., 2019. Incorporation of micro-cracking and fibre bridging phenomena in constitutive modelling of fibre reinforced concrete. *In preparation*

Statement of Authorship

Title of Paper	Incorporation of micro-cracking and fibre bridging phenomena in constitutive modelling of fibre reinforced concrete
Publication Status	☐ Published ☐ Accepted for Publication ☐ Submitted for Publication ☑ Unpublished and Unsubmitted w ork w ritten in manuscript style
Publication Details	Le, L.A., Nguyen, G.D., Bui, H.H., Sheikh, A.H., Kotousov, A., 2019. Incorporation of micro-cracking and fibre bridging phenomena in constitutive modelling of fibre reinforced concrete. In preparation

Principal Author

Name of Principal Author (Candidate)	Linh A. Le		
Contribution to the Paper	Developed the model for fibre reinforced concrete. Implemented the model & performed numerical analysis and model validation. Wrote and revised the manuscript.		
Overall percentage (%)	70		
Certification:	This paper reports on original research I conducted during the period of my Higher Degree by Research candidature and is not subject to any obligations or contractual agreements with a third party that would constrain its inclusion in this thesis. I am the primary author of this paper.		
Signature		Date	26/03/2019

Co-Author Contributions

By signing the Statement of Authorship, each author certifies that:

i. the candidate's stated contribution to the publication is accurate (as detailed above);

ii. permission is granted for the candidate in include the publication in the thesis; and

iii. the sum of all co-author contributions is equal to 100% less the candidate's stated contribution.

Name of Co-Author	Giang D. Nguyen		
Contribution to the Paper	Developed the general framework for the model. Supervised the technical developments. Evaluated & revised the manuscript.		
Signature		Date	27 / 03 / 2019

Name of Co-Author	Ha H. Bui		
Contribution to the Paper	Supervised the technical developments. Evaluated & revised the manuscript.		
Signature		Date	27 / 03 / 2019

Name of Co-Author	Abdul Hamid Sheikh		
Contribution to the Paper	Supervised the technical developments. Evaluated & revised the manuscript.		
Signature		Date	28/03/2019

Name of Co-Author	Andrei Kotousov		
Contribution to the Paper	Supervised the technical developments. Evaluated & revised the manuscript.		
Signature		Date	27/03/2019

Incorporation of micro-cracking and fibre bridging phenomena in constitutive modelling of fibre reinforced concrete

Linh Anh Le[a], Giang Dinh Nguyen[a*], Ha H. Bui[b], Abdul H. Sheikh[a], Andrei Kotousov[c]

[a]School of Civil, Environmental and Mining Engineering, The University of Adelaide, Adelaide, SA 5005, Australia

[b]Department of Civil Engineering, Monash University, Clayton, VIC 3800, Australia

[c]School of Mechanical Engineering, The University of Adelaide, Adelaide, SA 5005, Australia

Abstract

Experimental studies have shown that the appearance and development of micro/meso cracks followed by fibre bridging effect is the underlying mechanism governing the responses of fibre reinforced concrete (FRC). These two coupled phenomena largely affect the ductility and transition of the failure modes from diffusive to localised fracture. Nevertheless, the appearance of cracks causes the stress and strain defined over the considered volume element no longer homogeneous. Thus, a separate set of constitutive laws should be involved in the constitutive model besides classical continuum formulations to describe the inelasticity taking place within the cracking zone. In this paper, the cracking mechanism is incorporated directly into the structure of constitutive model by a set of kinematic enhancements and internal equilibrium equations across the crack interface. This straightforwardly allows an explicit introduction of both fibre bridging effect caused by randomly oriented short fibres and cohesive resistance from cementitious concrete, into a continuum constitutive model. As a result, the micro/meso-structural changes of both fibres-matrix interactions and degradation of cohesion inside the cracking zone are naturally taken into account together with its relative size. The material responses in both diffuse and localised stages are thus correctly captured, requiring no additional regularisations in the analysis of Boundary Value Problems. The constitutive formulations are presented in the paper together with its validation against experimental data at both material and structural levels.

Keywords: *Constitutive modelling; fibre reinforced concrete (FRC); fibre bridging; cohesive crack*

Nomenclature

$\mathbf{a}_{\mathrm{o}}$	Elastic stiffness of material
D	Damage variable
d_f	Fibre diameter
E_f	Fibre elastic Young's modulus
E_m	Concrete elastic Young's modulus
f	Snub coefficient
f_y	Fibre yield strength
f_c, f_t	Concrete compressive and tensile strength, respectively
g	Plastic potential function
G_I	Mode I specific fracture energy
h	Localisation band thickness
h_{f1}, h_{f2}	Fibre hook length
H	Characteristic length of localisation band
$\mathbf{K}^f$	Stiffness of fibre bridging effect in global coordinate system
$\mathbf{K}^c$	Stiffness of crack cohesion in global coordinate system
K_n, K_s	Elastic normal and shear stiffness of crack cohesion
L	Fibre embedded length
L_f	Fibre total length
P	Single fibre pull-out force
$\mathbf{n}$	Normal vector of localisation band
n_c	Number of crack within specimen
S	Fibre-matrix interfacial slip
$\mathbf{t} = [t_1 \quad t_2 \quad t_3]^T$	Total traction of crack in global coordinate system
$\mathbf{t}^c = [t_1^c \quad t_2^c \quad t_3^c]^T$	Traction of crack cohesion in global coordinate system
$\mathbf{t}_l^c = [t_n^c \quad t_{s1}^c \quad t_{s2}^c]^T$	Traction of crack cohesion in local coordinate system
$\mathbf{t}_l^f = \left[t_n^f \quad t_{s1}^f \quad t_{s2}^f\right]^T$	Traction of fibre bridging in local coordinate system
$\mathbf{t}^f = \left[t_1^f \quad t_2^f \quad t_3^f\right]^T$	Traction of fibre bridging in global coordinate system
t^f	Axial fibre bridging stress local coordinate system
$\mathbf{u} = [u_1 \quad u_2 \quad u_3]^T$	Displacement jump of crack in global coordinate system
$\mathbf{u}_l = [u_n \quad u_{s1} \quad u_{s2}]^T$	Displacement jump of crack in local coordinate system
$\mathbf{u}_l^{\mathrm{p}} = \left[u_n^p \quad u_{s1}^p \quad u_{s2}^p\right]^T$	Plastic displacement jump of crack in local coordinate system
u_p	Accumulated displacement parameter
V_f	Fibre volume fraction
y	Yield-failure function
α, β	Parameters controlling damage evolution
β_f	Frictional sliding parameter
δ	Crack opening
δ_0	Displacement corresponding to peak stress in pure tension

$\boldsymbol{\varepsilon} = [\varepsilon_{11}\ \varepsilon_{22}\ \varepsilon_{33}\ \gamma_{12}\ \gamma_{23}\ \gamma_{31}]^T$	Overall strain of RVE
$\boldsymbol{\varepsilon}_{\mathrm{o}} = \left[\varepsilon_{\mathrm{o},11}\ \varepsilon_{\mathrm{o},22}\ \varepsilon_{\mathrm{o},33}\ \gamma_{\mathrm{o},12}\ \gamma_{\mathrm{o},23}\ \gamma_{\mathrm{o},31}\right]^T$	Strain of outer bulk material
η	Volume fraction of localisation band
θ	Fibre hook angle
$\dot{\lambda}$	Plastic multiplier
μ_0, μ, m	Model parameters controlling shape of yield surface
μ_f	Fibre-matrix frictional coefficient
ν	Material Poisson's ratio
$\boldsymbol{\xi}$	Strain inside localisation band
$\boldsymbol{\varrho}$	Stress inside localisation band
$p(\phi)$	Density function of fibre orientation
$p(z)$	Density function of fibre centroidal distance
$\boldsymbol{\sigma} = [\sigma_{11}\ \sigma_{22}\ \sigma_{33}\ \sigma_{12}\ \sigma_{23}\ \sigma_{31}]^T$	Overall stress of RVE
$\boldsymbol{\sigma}_{\mathrm{o}} = \left[\sigma_{\mathrm{o},11}\ \sigma_{\mathrm{o},22}\ \sigma_{\mathrm{o},33}\ \sigma_{\mathrm{o},12}\ \sigma_{\mathrm{o},23}\ \sigma_{\mathrm{o},31}\right]^T$	Stress of outer bulk material
τ	Shear stress acting on fibre-matrix interface
τ_0	Initial fibre-matrix cohesion
φ	Material friction angle
ϕ	Fibre orientation angle
Γ	Localisation band area
Ω	Representative Volume Element (RVE)
Ω_{i}	Inner localisation band
Ω_{o}	Outer bulk material

1. Introduction

It is well-known that adding short fibres into cementitious concrete can substantially improve the overall ductility, energy absorption and fracture toughness. The improvement of these key mechanical properties of fibre reinforced concrete (FRC) is directly associated with the effect of the added fibres on the formation and development of micro- and macro-cracks under progressive loading [1,2]. When a crack is formed within a material volume, the displacements of crack faces under loading trigger the fibre bridging mechanism. The activated fibres transfer stresses across the crack surface and delay its opening and/or coalescence. This leads to the overall reduction of the crack driving force and promoting the formation of new cracks in adjacent regions, which finally result in the dissipation of the applied load over a larger volume. As a result, the material can absorb more energy and its behaviour becomes more ductile. The fibre bridging continues until all fibres across the crack are completely pulled out of the matrix. The number of cracks formed within the material body and the amount of energy absorbed, as well as the overall material responses, depend on this fibre bridging effect [3–7], which is in

turn governed by the mechanical properties of fibres, matrix and more importantly, their interactions.

Given the fibre bridging effect and cohesion in a crack as intrinsic mechanisms, driving the material behaviour, they should be the foremost basis in developing a constitutive model for FRC. In this sense, constitutive models, drawn from statistical regression of experimental results on specific groups of tests [8–12], or exploiting fracture mechanics formulations of damage variable to account for the presence of fibres [13,14] or merely proposing empirical stress-strain responses [15–17] are of phenomenological nature as they totally left out the underlying mechanism of material failure addressed above. Even though these models are simple and useful for structural modelling, they heavily rely on curve-fitting for the calibration of model parameters since the real mechanical failure mechanism governing the macro observable behaviour is missing. They are thus strongly influenced by experimental data, which needs to be obtained for different loading conditions and for a particular composition and material properties of the FRC. As a consequence, the predictive capabilities of these models are bounded by the types of FRC and testing conditions from which they were built and calibrated.

Alternatively, discrete models such as lattice models [18–21] can successfully capture both complex meso-structural changes and fibre bridging mechanism by explicit modelling of coarse aggregates and individual fibre responses with their embedded lengths and orientations. In a similar way, semi-discrete models account for the contribution of fibres by mapping the individual fibre influence back to the finite mesh by using the partition of unity property of enriched shape functions [22,23], strong discontinuity formulations [24], morphological kinematical descriptor [1,25], fibre-aligned mesh with interface elements [26] or meshless formulations [27]. The displacement field from extended finite element method (X-FEM) [28,29] or from smeared crack approach [30,31] was also used to reflect the discontinuity of the material. Even though these models had demonstrated relatively good results and are very useful for understanding the failure mechanism of FRC, the high computational cost is still the main drawback that impedes them from being applied extensively to analysing large-scale structures having hundreds of thousands of fibres.

Another approach to modelling FRC is the micro-mechanics based continuum modelling which opts for a balance between accuracy and computational cost. By incorporating the failure mechanism into constitutive models, the approach is able to reflect the complex meso-structural changes while, at the same time, maintaining computational efficiency for structural

simulations. In these models, the fibre-matrix interactions and fibre-bridging mechanism are described by only influential variables such as the fibre orientation distribution, volume fraction and fibre shape besides the relevant material properties. The main advantage of this approach is that it could capture the macroscopic behaviour of the material with physical representations at the meso-scale yet still remains simple and computationally efficient. The incorporation of fibre bridging effect into the micro-mechanical constitutive model can be done by introducing damage variables, which represent the stiffness degradation of crack bridged by fibres [32–36], or by superposing the stress borne by fibres and matrix with further homogenisation of the overall mechanical response [37–39]. In this theme, Dutra et al. [40] incorporated the fibre effect on the material strength by using a static approach of the limit analysis together with a homogenisation scheme. Despite a significant improvement in the efficiency of the numerical simulation, these studies largely focused only on the macro strength without full material responses and thus cannot be applied to structural modelling where a constitutive relationship describing the mechanical responses from intact to ultimate failure is needed. Alternatively, the microplane models [41,42], extended from a series of models for plain concrete, included the effect of fibre bridging by using multiple failure plane orientations with the implicit homogeneous deformation assumption. Micromechanical constitutive models proposed by Mihai and Jefferson [43,44] take into account fibre the bridging effect and aggregates interlocking in multiple directions by using Budiansky and O' Connell's solution [45] for an elastic solid containing a penny-shaped crack and a homogenisation scheme based on the Mori-Tanaka method. Similar to the microplane models, the macro-strain in these models by Mihai and Jefferson was obtained by integrating the contributions from several directional micro-cracks. In addition, on each crack plane, two contact surface functions were employed for various crack states (i.e., open, interlocked and close crack state) to describe differences in tension/compression behaviour. Even though abovementioned approaches obtained relatively good results for benchmark problems, they largely rely on regularisations on top of the models for the analysis of Boundary Value Problems (BVPs). Essentially, the constitutive behaviour should scale with the resolution of the discretisation used in the Finite Element Analysis (FEA) so that the requirement of the energy dissipation is met (i.e. cracked elements should reproduce an invariant dissipation with respect to the size of the element). This important length scale is either missing [28–31], or had to be obtained by phenomenological treatments of characteristic length [41,43,44] from crack band theory [46] or by changing model parameters for every analysis [42] to fit the fracture properties produced by the experiments.

This research, thus, proposes a model for fibre reinforced concrete by incorporating the failure mechanism of cracking directly into the constitutive model to encapsulate both the fibre bridging effect and frictional-cohesive resistance across the crack plane. The cracking failure mechanism is considered as the basis for the model development and is incorporated into the constitutive model via a set of kinematic enhancements and internal equilibrium equations across the crack interface. The fibre bridging model is developed based on the concept proposed by Li et al. [47,48] for straight fibre with modifications suggested by Alwan et al. [49], to account for the load-resistance of fibre shape (hooks) and slip-softening law. The cohesive resistance and effects of interlocking from cementitious concrete are described by the newly developed cohesive-frictional model [50], which is based on a damage-plasticity framework with a unified yield-failure surface. Thanks to the incorporation of cracking failure mechanism at constitutive level, the responses of the FRC, from hardening with multiple cracking to softening with a localisation band can be naturally captured. The key features of the proposed model include: i) the contributions of both nonlinear inelasticity inside cracks and linear elasticity of intact bulk material are taken into account directly; ii) fibre bridging effect and cohesive resistance within a crack are independently incorporated within a continuum-based formulations; iii) intrinsic scaling and mesh independence without requiring ad hoc regularisations; iv) diffuse/localisation failure mechanism and their transitions for different fibre contents can be captured at both constitutive and structural levels.

The paper is organised as follows. The experimental results elucidating the governing failure mechanism of FRC together with the proposed conceptual model are presented in Section 2. The theoretical background and formulations of the fibre bridging effect and cohesive-frictional models, incorporated systematically within the double-scale framework, are described in Section 3. Systematic validation of the proposed model against experimental data at constitutive and structural levels are presented in Section 4, followed by conclusions and further prospects in final Section 5.

2. Proposed double-scale modelling for FRC

2.1. Mechanisms of cracking and bridging effect: experimental observation & theoretical idealisation.

The mechanisms governing the behaviour of fibre reinforced concrete (FRC) can be observed and identified using typical experimental results of tension tests, shown in Fig. 1, for both plain and reinforced concrete. As seen in the figure, the response of the plain concrete specimen is

sharp softening after stress reaches material tensile strength with the appearance of a major crack. This is because a localised zone quickly develops and dissipates all of the energy given by the load, resulting in brittle behaviour as also observed in many experiments [4,51–53]. On the other hand, substantial improvements in toughness and fracture resistance can be observed from the stress-strain responses of FRC [3,4,51–56], which can be divided into three phases. In phase I, illustrated by the curve AB in Fig. 1, the response of the FRC is relatively linear elastic, which is similar to the case of plain concrete. This means that the fibres have not been mobilised yet and the FRC behaves just like plain concrete in this phase. However, a significant increase of strength and ductility is observed in phase II from B to C of the curve (see Fig. 1) with numerous cracks distributed throughout the specimen. This is because when the first crack initiates and opens, the fibres across the crack are activated (i.e., resist the crack opening) and begin to debond from the matrix. These bridging fibres help transfer stresses between two sides of the crack and hamper it from opening freely as illustrated at meso-scale in Fig. 2. This forces the material to form new small cracks in surrounding regions to dissipate the energy provided by the applied load. The density of cracks throughout the specimen and the elongation of phase II depend on the fibre bridging forces, governed by the number of fibres across the crack planes, the mechanical properties of fibres, matrix and their interactions. As small cracks are uniformly distributed, the strain is relatively homogenous throughout the specimen length during this phase. In phase III, material behaviour is found to be softening with the formation of a localisation band at the weakest plane, illustrated by a red curve in experimental failure pattern in Fig. 1. In this phase, the fibres across this localisation band are subsequently pulled out of the matrix, making the bridging effect weaker and consequently fostering the localisation band to develop further. The deformation in the localisation band increases quickly while cracks at other locations close owing to the decrease of stress as illustrated in Fig. 1. This process takes place until the specimen fails completely.

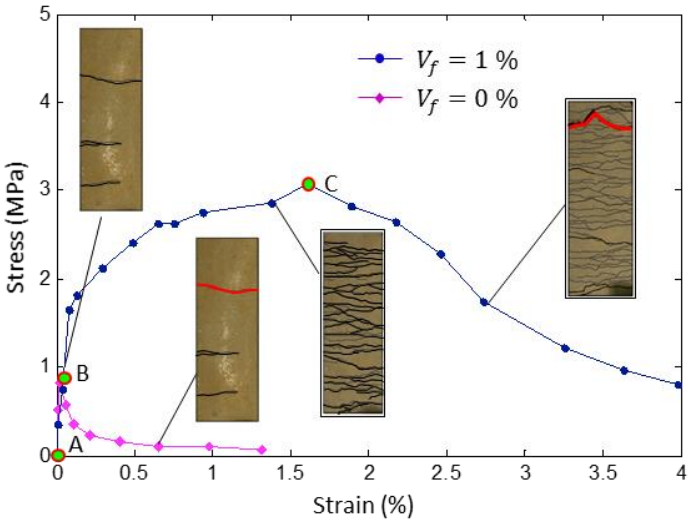

Fig. 1. Uniaxial tensile responses of plain concrete and concrete reinforced by Spectra fibre along with failure pattern as reported by Sirijaroonchai et al. [57]

Therefore, once cracks appear within the material, the inelastic response and energy dissipation take place predominantly within these cracks, where stresses are transferred via: (i) cohesive resistance from crack and (ii) bridging fibres across the crack. This stress transfer process within the cracks is the intrinsic mechanism behind mechanical responses of the material at mesoscale as well as structural scale. The conceptual model, shown in Fig. 2, is hence built to incorporate this stress transfer as the basis for the model development. As the stress and strain over the volume element are no longer uniform due to the presence of crack, the conceptual model comprises a localisation band describing the crack and a bulk material representing the intact surrounding FRC, each of which has its own constitutive behaviour. The explicit presence of the localisation band in the constitutive model allows a straightforward inclusion of both fibre bridging forces, illustrated by red force vectors and the concrete cohesive resistance, denoted by blue force vectors in Fig. 2. The separation of fibre bridging forces and cohesion resistance in the localisation allows these two constitutive relationships to be developed independently. Therefore, the proposed model is generic in the sense that it can incorporate any fibre bridging law of any fibre types with different geometries and mechanical properties. Once the stress transfer in a crack is captured, the diffuse-localised failure, where uniformly distributed cracks develop and form a single localisation band, can be incorporated afterwards. In particular, the fibre volume content governs the density of cracks (presented by the number of cracks in the specimen) during phase II (i.e., diffuse cracking), which in turn governs the macro behaviour and energy absorption capability of the structure. A phenomenological relationship will be used in the model to reflect this intimate link and to facilitate the modelling of diffuse cracking phase. The details of these components and their

incorporations into a continuum-based constitutive model will be addressed in the following section.

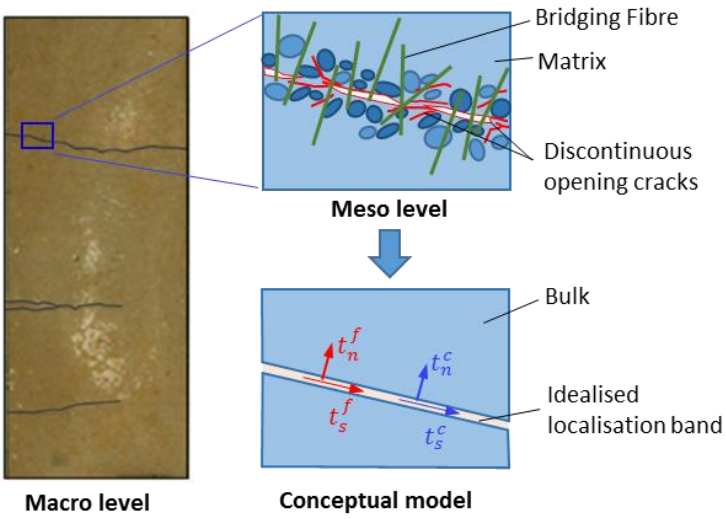

Fig. 2. Illustration of the proposed model concept

2.2. Proposed model for fibre reinforced concrete

2.2.1. Double-scale modelling

Without losing generality, the constitutive model is constructed using a Representative Volume Element (RVE) which features an outer bulk material Ω_o and an inner localisation band $\Omega_i = \Gamma h$, represented by its area Γ and thickness h as shown in Fig. 3. To facilitate the formulations, the stress and strain vectors of the outer bulk material are denoted as $\boldsymbol{\sigma}_o = [\sigma_{o,11}\ \sigma_{o,22}\ \sigma_{o,33}\ \sigma_{o,12}\ \sigma_{o,23}\ \sigma_{o,31}]^T$ and $\boldsymbol{\varepsilon}_o = [\varepsilon_{o,11}\ \varepsilon_{o,22}\ \varepsilon_{o,33}\ \gamma_{o,12}\ \gamma_{o,23}\ \gamma_{o,31}]^T$, while the volume-averaged overall stress and strain vectors of the RVE are $\boldsymbol{\sigma} = [\sigma_{11}\ \sigma_{22}\ \sigma_{33}\ \sigma_{12}\ \sigma_{23}\ \sigma_{31}]^T$ and $\boldsymbol{\varepsilon} = [\varepsilon_{11}\ \varepsilon_{22}\ \varepsilon_{33}\ \gamma_{12}\ \gamma_{23}\ \gamma_{31}]^T$.

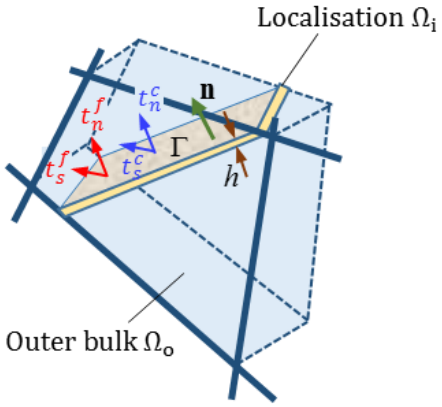

Fig. 3. Illustration of a representative volume element (RVE)

Assuming uniform behaviour throughout the localisation area, its strain rate $\dot{\boldsymbol{\xi}}$ can be expressed in terms of homogeneous strain rate of the bulk material $\dot{\boldsymbol{\varepsilon}}_o$ and an enhancing strain rate as [58]:

$$\dot{\boldsymbol{\xi}} = \dot{\boldsymbol{\varepsilon}}_o + \frac{1}{h}\mathbf{n}\dot{\mathbf{u}} \approx \frac{1}{h}\mathbf{n}\dot{\mathbf{u}} \tag{1}$$

where $\dot{\mathbf{u}} = [\dot{u}_1 \quad \dot{u}_2 \quad \dot{u}_3]^T$ is the velocity jump between two sides and $\mathbf{n}$ is the normal vector in the Voigt notation form of the localisation band in the global coordinate system. In this equation, the first term of Eq. (1) are much smaller than the other component and can be neglected as the localisation band can be reasonably idealised as a zero thickness crack plane; $h \to 0$. The homogenised or macro strain rate of the RVE, $\dot{\boldsymbol{\varepsilon}}$, can be calculated by a simple volume averaging homogenisation of the strain in the localisation band and the bulk material as:

$$\dot{\boldsymbol{\varepsilon}} = (1-\eta)\dot{\boldsymbol{\varepsilon}}_o + \eta\dot{\xi} = \dot{\boldsymbol{\varepsilon}}_o + \frac{1}{H}\mathbf{n}\dot{\mathbf{u}} \tag{2}$$

where $\eta = \frac{\Omega_i}{\Omega} = \frac{\Gamma h}{\Omega}$ is the volume fraction of the localisation band in relation to the RVE and $H = \frac{\Omega}{\Gamma} = \frac{h}{\eta}$ is defined as the characteristic length of the RVE.

Eq. (2) shows that the characteristic length is directly withdrawn from the model formulations and represents the relative size between the localisation band and the RVE. The resulting constitutive behaviour thus automatically scales with the discretisation used in the Finite Element Analysis (FEA) and the energy dissipated by the localisation in the element is properly reflected as addressed at length and illustrated by numerical examples in Le et al. [50]. This feature is one of the main advantages, distinguishing the proposed model from previous studies [41–44], where characteristic lengths have to be used after the model formulations as a parameter to scale the behaviour with respect to the element resolution during the FEA.

The incorporation of the localisation band behaviour into the overall responses of the RVE is also carried out via the principle of virtual work [59] which requires that the summation of virtual work done by the localisation band and its surrounding bulk material is equal to the work done by the RVE:

$$\boldsymbol{\sigma}^T \delta\boldsymbol{\varepsilon} = \eta \boldsymbol{\varrho}^T \delta\xi + (1-\eta)\boldsymbol{\sigma}_{\mathrm{o}}^T \delta\boldsymbol{\varepsilon}_{\mathrm{o}} \tag{3}$$

where $\boldsymbol{\varrho}$ is the stress inside the localisation band; $\delta\boldsymbol{\xi}$, $\delta\boldsymbol{\varepsilon}_{\mathrm{o}}$ and $\delta\boldsymbol{\varepsilon}$ are, respectively, the virtual strain of the localisation band, the outer bulk material and the volume element. By substituting the kinematic enhancement in Eqs. (1) and (2) into the above statement for virtual work in Eq. (3), one obtains:

$$(1-\eta)(\boldsymbol{\sigma}^T - \boldsymbol{\sigma}_{\mathrm{o}}^T)\delta\boldsymbol{\varepsilon}_{\mathbf{o}} + \frac{1}{H}(\boldsymbol{\sigma}^T\mathbf{n} - \boldsymbol{\varrho}^T\mathbf{n})\delta\mathbf{u} = 0 \tag{4}$$

in which $\delta\mathbf{u}$ is the virtual displacement jump across the localisation band. Since the work conservation has to be satisfied for arbitrary values of virtual deformations $\delta\boldsymbol{\varepsilon}_{\mathbf{o}}$ and $\delta\mathbf{u}$, two following equilibriums are obtained: i) the averaged stress of the volume element coincides with the stress of the outer bulk material $\boldsymbol{\sigma} = \boldsymbol{\sigma}_{\mathrm{o}}$ and ii) satisfaction of traction continuity across the crack plane $\boldsymbol{\sigma}^T\mathbf{n} = \boldsymbol{\varrho}^T\mathbf{n} = \mathbf{t}^T$, where $\mathbf{t} = [t_1 \quad t_2 \quad t_3]^T$ is the traction acting on the crack plane in the global coordinate system.

As stated above, when a crack opens, both bridging forces from fibres $\mathbf{t}^f = \begin{bmatrix} t_1^f & t_2^f & t_3^f \end{bmatrix}^T$ and cohesive resistance from plain concrete $\mathbf{t}^c = [t_1^c \quad t_2^c \quad t_3^c]^T$ are activated simultaneously. The traction acting on this crack plane thus comprises these two components as:

$$\dot{\mathbf{t}} = \dot{\mathbf{t}}^f + \dot{\mathbf{t}}^c = \mathbf{K}^f\dot{\mathbf{u}} + \mathbf{K}^c\dot{\mathbf{u}} = (\mathbf{K}^f + \mathbf{K}^c)\dot{\mathbf{u}} \tag{5}$$

where $\mathbf{K}^f$ and $\mathbf{K}^c$ are, respectively, the tangent stiffness of the fibre bridging force and cohesion law expressed in the global coordinate system, which will be addressed in sections 3.2 and 3.3. By substituting Eq. (5) back into the rate form of traction continuity ($\mathbf{n}^T\dot{\boldsymbol{\sigma}} = \dot{\mathbf{t}}$), together with Eq. (2) and some arrangements, the velocity jump from a given strain increment can be written as:

$$\dot{\mathbf{u}} = \left(\frac{1}{H}\mathbf{n}^T\mathbf{a}_{\mathrm{o}}\mathbf{n} + \mathbf{K}^f + \mathbf{K}^c\right)^{-1}\mathbf{n}^T\mathbf{a}_{\mathrm{o}}\dot{\boldsymbol{\varepsilon}} \tag{6}$$

In the above formulation, the intact bulk material is assumed to be elastic with stiffness $\mathbf{a}_{\mathrm{o}}$ and the inelastic response of the material is assumed to happen only in the embedded crack. The constitutive relation of the FRC can be then written as:

$$\dot{\boldsymbol{\sigma}} = \dot{\boldsymbol{\sigma}}_{\mathrm{o}} = \mathbf{a}_{\mathrm{o}}\left[\dot{\boldsymbol{\varepsilon}} - \frac{1}{H}\mathbf{n}\dot{\mathbf{u}}\right] = \left[\mathbf{a}_{\mathrm{o}} - \frac{1}{H}\mathbf{a}_{\mathrm{o}}\mathbf{n}\left(\frac{1}{H}\mathbf{n}^{T}\mathbf{a}_{\mathrm{o}}\mathbf{n} + \mathbf{K}^{f} + \mathbf{K}^{c}\right)^{-1}\mathbf{n}^{T}\mathbf{a}_{\mathrm{o}}\right]\dot{\boldsymbol{\varepsilon}} \tag{7}$$

The obtained constitutive relationship shows that the response of localisation band, driven by both the fibre bridging effect and concrete cohesion, is systematically and directly incorporated into a continuum-based constitutive model. As seen in Eqs. (6) and (7), the constitutive model, in this form, is generic and able to feature any type of fibre bridging and cohesive laws via the tangent stiffness $\mathbf{K}^{f}$ and $\mathbf{K}^{c}$. As a result, it can be used for different types of fibres with different geometries and mechanical specifications while maintaining the cracking mechanism as the central component of modelling.

2.2.2. Cohesive-frictional crack model

In this study, the resistance of a cohesive crack within the cementitious matrix, $\dot{\mathbf{t}}^{c} = \mathbf{K}^{c}\dot{\mathbf{u}}$, is described by the recently proposed cohesive-frictional crack model [50,60], which was proven to be effective for geomaterials (i.e. concrete, rock) in tension, compression, shear and mixed mode loading conditions. The essential feature of this model is to capture the post-peak behaviour of cracks as a result of asperities degradation and irreversible displacements by coupling the damage and plasticity within a unified yield-failure function and traction-displacement relationship. As the model and its associated variables are expressed in the local coordinate system of the crack plane in this section, they would be transformed to the global coordinate system by a transformation matrix $\mathbf{R}$ where needed for modelling.

The cohesive-frictional crack comprises two parts: the damaged part represented by damage variable D (i.e. $0 \leq D \leq 1$), and the undamaged part represented by $(1 - D)$. The traction-displacement relationship takes the form:

$$\begin{aligned}\mathbf{t}_{l}^{c} = \begin{bmatrix} t_{n}^{c} \\ t_{s1}^{c} \\ t_{s2}^{c} \end{bmatrix} &= \begin{bmatrix} 1 - DH(t_{n}) & 0 & 0 \\ 0 & 1 - D & 0 \\ 0 & 0 & 1 - D \end{bmatrix}\begin{bmatrix} K_{n} & 0 & 0 \\ 0 & K_{s} & 0 \\ 0 & 0 & K_{s} \end{bmatrix}\begin{bmatrix} u_{n} - u_{n}^{p} \\ u_{s1} - u_{s1}^{p} \\ u_{s2} - u_{s2}^{p} \end{bmatrix} \\ &= \mathbf{HK}\left(\mathbf{u}_{l} - \mathbf{u}_{l}^{\mathrm{p}}\right)\end{aligned} \tag{8}$$

where $\mathbf{t}_l^c$ is the traction in the local coordinate system of the crack plane, comprising of the normal traction t_n^c and two shear tractions t_{s1}^c and t_{s2}^c; K_n and K_s represent the normal and shear elastic stiffness of the cohesive crack; $u_n, u_{s1,2}$ are the normal and shear displacement jumps, and $u_n^p, u_{s1,2}^p$ represent the plastic displacement jumps; $H(t_n)$ is the Heaviside step function, implying that the damaged part only affects the normal traction in the case where tension exists. Our previous study [50] shows that as long as the values of elastic stiffness, K_n, K_s, are high enough, the choice of actual values does not affect the model results. They are thus taken as $K_n = K_s = 10^{10}$ KPa/m in all examples of this research. The proposed initial-failure function is taken as:

$$\begin{aligned} y = (t_{s1}^2 + t_{s2}^2) - [(1-D)\mu_0^2 + D\mu^2][t_n - (1-D)f_t]^2 \\ + mf_c(1-D)[t_n - (1-D)f_t] \end{aligned} \tag{9}$$

in which f_t, f_c are, respectively, tensile and compressive strengths of plain concrete; m, μ_0 are parameters controlling the shape of initial yield surface while $\mu = \tan\varphi$ plays the role of material frictional coefficient where φ is the friction angle. In this study, the friction angle of concrete is taken as $\varphi = 37^0$ from Fujita et al. [61] for all examples. The non-associated flow rules used in this study are:

$$\dot{u}_n^p = \dot{\lambda}\frac{\partial g}{\partial t_n};\ \ \dot{u}_{s1}^p = \dot{\lambda}\frac{\partial g}{\partial t_{s1}};\ \ \ \dot{u}_{s2}^p = \dot{\lambda}\frac{\partial g}{\partial t_{s2}} \tag{10}$$

where $\dot{\lambda}$ is the plastic multiplier and g is the corresponding plastic potential function, defined as:

$$\begin{aligned} g = \gamma(t_{s1}^2 + t_{s2}^2) - [(1-D)\mu_0^2 + D\mu^2][t_n - (1-D)f_t]^2 \\ + mf_c(1-D)[t_n - (1-D)f_t] \end{aligned} \tag{11}$$

with γ being the parameter controlling the non-associativity. Fig. 4 illustrates the evolution from initial yield surface (blue curve) to the final failure (red line) along with the corresponding plastic potential function (illustrated at point A by a purple line). The coupling between damage and plasticity is also addressed through the damage evolution law as:

$$D = 1 - e^{-u_p}, \text{ with } \Delta u_p = \sqrt{\left(\frac{\alpha\Delta u_n^p}{\delta_0}\right)^2 + \left(\frac{\beta\Delta u_{s1}^p}{\delta_0}\right)^2 + \left(\frac{\beta\Delta u_{s2}^p}{\delta_0}\right)^2} \tag{12}$$

in which u_p is the accumulated plastic displacement parameter in non-dimensional form calculated from plastic normal and shear displacements of the crack; α and β are non-dimensional parameters controlling the contributions of these two plastic displacements to the damage evolution; δ_0 is defined as the displacement corresponding to peak stress in pure tension. As the only purpose of δ_0 is to make u_p a non-dimensional quantity, it is taken as $\delta_0 = 0.015$ mm for all examples in this research.

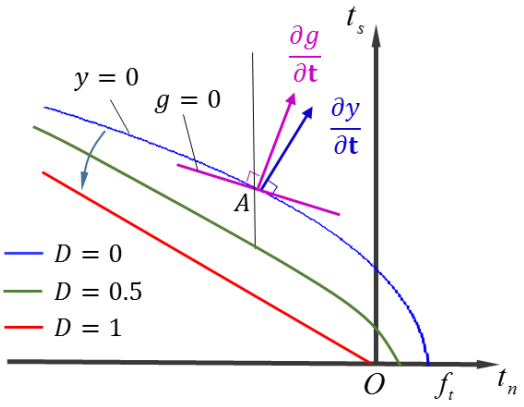

Fig. 4. Illustration of yield surface evolution and non-associated flow rule (after Le et al. [50]).

The coupling of damage and plasticity, as considered in above formulations, is simple yet effective to describe the irreversible deformation and asperities degradation of the plain concrete. A smooth transition from the initial yield surface to final failure corresponding to the damage in the crack allows the modelling of the material response in different loading paths. Details of stress return algorithm, physical descriptions and parameters calibration can be found in Le et al. [50,60].

2.2.3. Crack bridging from fibres

The constitutive equation in Eq. (7) indicates that apart from a cohesive law for the cementitious matrix, the model also requires a fibre bridging law, describing the stress transfer by randomly distributed fibres across the crack. Since the model is formulated in a generic form as mentioned earlier, either phenomenological fibre bridging laws [62–64] or more complicated micromechanics-based models [65–67] can be used within the constitutive model described above. In this study, the pull-out force – displacement relationship (i.e., $P - \delta$) of smooth polymer fibres follows formulations proposed by Lin and Li [48] which is based on micromechanical analysis of single fibre pull-out test. The model is simple with a few parameters and was proven to be effective for modelling the fibre bridging effect of FRC

[43,44]. For hooked end fibre, the pull-out force – displacement relationship is obtained by solving the differential equation in Lin and Li [48] with slip-softening law in association with the pull-out resistance of the fibre hooks proposed by Alwan et al. [49].

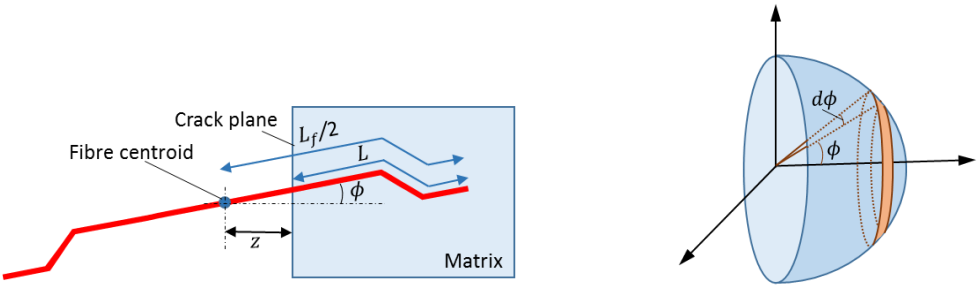

(a) (b)

Fig. 5. Illustration of fibre bridging effect integration: (a) z and ϕ definitions for a hooked fibre and (b) integration scheme

The fibre bridging stress t^f in the local coordinate system of the crack plane is then derived by integrating the individual pull-out contribution of all fibres across the crack plane using probability density functions for the fibre orientation $p(\phi)$ and for fibre centroidal distance from the crack plane $p(z)$ as [48]:

$$t^f(\delta) = \frac{4V_f}{\pi {d_f}^2} \int_{\phi} \int_{z} P(\delta)\, p(\phi) p(z) dz d\phi \tag{13}$$

where d_f is the diameter of the fibre; V_f is the fibre volume fraction within the material; ϕ is the orientation angle of the fibre and z is the distance between the centroid of a fibre and the crack plane as illustrated in Fig. 5; $P(\delta)$ is the pull-out force carried by a single fibre with respect to crack opening, $\delta = \|\mathbf{u}\|$.

Thanks to the integration with corresponding probability density functions, the fibre bridging force can be constructed from the contributions of individual fibres without having to explicitly take into account the influence of every fibre. This allows the calculation of fibre bridging stress from single fibre pull-out where micro-structural changes and failure mechanisms are taken into consideration. The macro responses of the FRC can thus be captured with a proper bridging force from fibres. In addition, the model can be flexibly used for different types of fibre distributions (i.e., unidirectional fibres, random fibres) by changing these density functions appropriately. The formulations of bridging stress t^f for two most

common fibres, including smooth polymer fibres and hook-end steel fibre, are presented in the following.

Fibre bridging effect for smooth polymer fibres

As proposed by Lin and Li [48], the pull-out process of a single polymer fibre comprises two stages: (i) debonding stage where interfacial fibre-matrix cohesion is debonded and (ii) subsequent pull-out stage governed by the frictional slipping of fibres over the matrix. The relationship between the fibre-matrix interfacial shear stress τ and the slip S is assumed to be linear hardening as follows:

$$\tau = \tau_0(1 + \beta_f \frac{S}{d_f}) \tag{14}$$

where d_f is the diameter of the fibre; τ_0 is the initial cohesion between fibre and matrix and $\beta_f > 0$ is the hardening parameter for the frictional sliding. For the case of uniformly random distribution of fibres (i.e., $p(\phi) = \sin\phi$; $p(z) = \frac{2}{L_f}$), together with fibre snubbing effect, the fibre bridging law can be written as [48]:

$$\frac{t^f}{t^*} = \begin{cases} \frac{2}{k}\left\{\left[1 - \frac{1}{k}\cosh^{-1}\left(1 + \zeta\frac{\delta}{\delta^*}\right)\right]\sqrt{\left(1 + \zeta\frac{\delta}{\delta^*}\right)^2 - 1} + \frac{\zeta\delta}{k\delta^*}\right\} & 0 \le \delta \le \delta^* \\ \left(1 + \frac{\beta_f}{d_f}\delta\right)\left(1 - \frac{2\delta}{L_f}\right) & \delta^* \le \delta \le \frac{L_f}{2} \end{cases} \tag{15}$$

with $t^* = 0.5w\tau_0 V_f(1 + \varsigma)\frac{L_f}{d_f}$; $w = \frac{2}{4+f^2}\left(1 + e^{\pi f/2}\right)$; $k = \frac{\omega L_f}{2d_f}$; $\zeta = \cosh(k) - 1$; $\omega = \sqrt{4\tau_0\beta_f(1 + \varsigma)/E_f}$; $\varsigma = \frac{V_f E_f}{(1-V_f)E_m}$; $\delta^* = \frac{2d_f}{\beta_f}[\cosh(k) - 1]$. In the above formulations, L_f is the fibre length; f is snubbing coefficient of the fibre; E_f and E_m are, respectively, Young's modulus of the fibre and the cement matrix.

Fibre bridging effect for hooked-end steel fibres

Experimental results of single fibre pull-out [62,63] show that hooked-end fibres have greater load-bearing capacity compared to straight fibre owing to the extra effort needed to straighten the hooks before pulling it out of the matrix. The present study followed the concepts used in the analytical formulation of Alwan et al. [49] to determine the mechanical contribution from the hooks to the fibre load-resistance by formulating the hook straightening as a pulling process through frictional pulleys where plastic hinges are integrated. This contribution from

hook-straightening is incorporated into the model of straight fibre by Lin and Li [48] to obtain a pull-out model for hooked-end fibre. As a result, in addition to debonding and pull-out phases as for straight fibre, the pull-out process of a hooked-end fibre is considered to experience two extra phases for hook straightening process, as illustrated in Fig. 6. During phase 1, the fibre is debonded from the cementitious matrix by a pull-out force as illustrated by the blue curve in Fig. 6b. In phase 2, both parts of the hook (i.e., h_{f1} and h_{f2}) are straightened at two plastic hinges illustrated by image (2) in Fig. 6a. The additional pull-out force to perform the cold work needed to for this process is $\Delta P_1 = P_2 - P_1$, corresponding to the extra pull-out distance h_{f1}. The force-displacement relationship in this phase is illustrated in Fig. 6b by the red curve. In phase 3, the remaining part of the hook, h_{f2}, is straightened and pulled out by an additional force $\Delta P_2 = P_3 - P_1$, as illustrated by a purple curve in the figure. After being straightened, the fibre is then pulled out of the matrix by the same frictional pulling mechanism as experienced by a normal straight fibre in phase 4. The force-displacement relationship for this phase is illustrated by a green curve in the figure. By using an equivalent frictional pulley model to calculate the cold work needed for straightening the steel hooks at plastic hinges, ΔP_1 and ΔP_2 can be calculated as [49]:

$$\Delta P_1 = \frac{f_y \pi {d_f}^2}{12\cos\theta\left(1-\mu_f \sin\frac{\theta}{2}\right)^2} \quad \text{and} \quad \Delta P_2 = \frac{f_y \pi {d_f}^2}{24\cos\theta\left(1-\mu_f \sin\frac{\theta}{2}\right)} \tag{16}$$

where f_y is the fiber yield strength; θ is the hook angle and μ_f is the frictional coefficient between the fibre surface and the surrounding cementitious matrix.

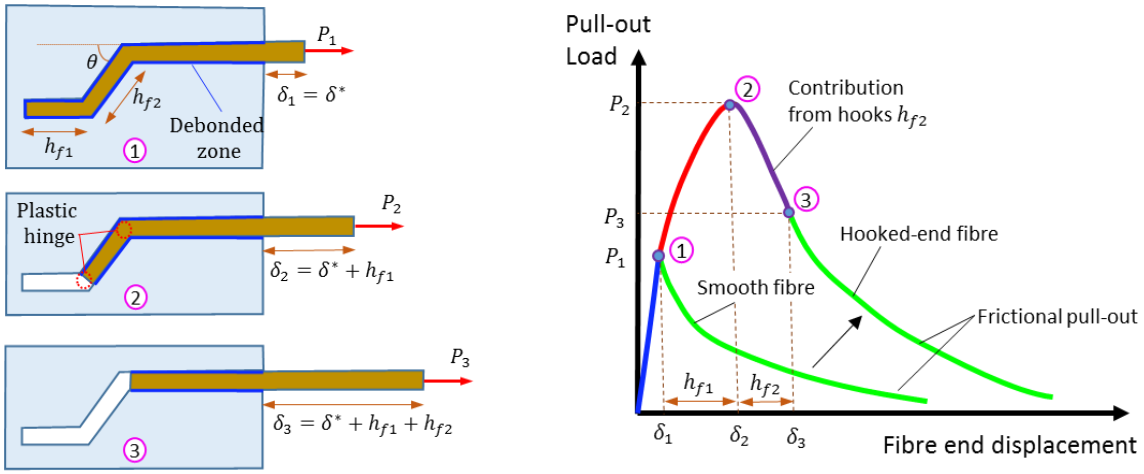

(a) (b)

Fig. 6. Illustration of a hooked-end fibre pull-out: (a) pull-out process and (b) corresponding load-displacement curve

Different from polymer fibres where fibre debris from surface abrasion creates "jamming" effect and results in slip-hardening behaviour, experimental results for steel fibres [49,62,63] show a softening shear-slip relationship, which can be represented as:

$$\tau = \tau_0(1 - \beta_f \frac{S}{d_f}) \tag{17}$$

We thus integrated this relationship into the procedure for polymer fibres described in [48] to obtain single fibre pull-out force for straight steel fibre (see Appendix A). It can be seen that due to the difference in the shear-slip relationship, the solution of the differential equation for the pull-out force, in this case, is totally different from that for polymer fibre. Together with the contributions from the hooks, presented above, the single fibre pull-out force for hooked-end steel fibre is written as (see Appendix A):

$$P = \begin{cases} P_I = \dfrac{\pi {d_f}^2 \tau_0}{\omega}(1+\varsigma)\sqrt{1-\left(1-\dfrac{\beta_f \delta}{2d_f}\right)^2} & 0 \le \delta \le \delta^* \\ P_{II} = P_0 + \dfrac{\Delta P_1}{h_{f1}}(\delta - \delta^*) & \delta^* \le \delta \le \delta^* + h_{f1} \\ P_{III} = P_0 + \Delta P_1 + \dfrac{\Delta P_2 - \Delta P_1}{h_{f2}}\left(\delta - h_{f1} - \delta^*\right) & \delta^* + h_{f1} \le \delta \le \delta^* + h_{f1} + h_{f2} \\ P_{IV} = \dfrac{\pi {d_f}^2 \tau_0{}'}{\omega}\sin\left[\dfrac{\omega}{d_f}(L - \delta + \delta^*)\right] - \pi\beta_f \tau_0'(\delta - \delta^*)(L - \delta + \delta^*) & \delta^* + h_{f1} + h_{f2} \le \delta \le L + \delta^* \end{cases} \tag{18}$$

where $\delta^* = \frac{2d_f}{\beta}\left[1 - \cos(\frac{\omega L}{d_f})\right]$; $\tau_0{}' = \frac{P_0 + \Delta P_2}{\frac{\pi {d_f}^2}{\omega}\sin\left[\frac{\omega}{d_f}(L - h_{f1} - h_{f2})\right] - \pi\beta_f(h_{f1} + h_{f2})(L - h_{f1} - h_{f2})}$;

$P_0 = \frac{\pi {d_f}^2 \tau_0}{\omega}(1+\varsigma)\sqrt{1-(1-\frac{\beta_f \delta^*}{2d_f})^2}$; ω and ς are defined in Eq. (15) and L is the fibre embedded length within the cementitious matrix. The fibre bridging model for hooked-end steel fibres is then obtained by substituting this pull-out law into Eq. (13) (see Appendix B) as:

$$\frac{t^f}{t^*} = \begin{cases} \dfrac{\pi {d_f}^2 \tau_0}{\omega}(1+\varsigma)\sqrt{1-\left(1-\dfrac{\beta_f \delta}{2d_f}\right)^2} & 0 \le \delta \le \delta^* \\ P_0 + \dfrac{\Delta P_1}{h_{f1}}(\delta - \delta^*) & \delta^* \le \delta \le \delta^* + h_{f1} \\ P_0 + \Delta P_1 + \dfrac{\Delta P_2 - \Delta P_1}{h_{f2}}\left(\delta - h_{f1} - \delta^*\right) & \delta^* + h_{f1} \le \delta \le \delta^* + h_{f1} + h_{f2} \\ \dfrac{z_4}{z_2}\left[\dfrac{\pi {d_f}^2 \tau_0{}'}{\omega}\sin\left[\dfrac{\omega}{d_f}\left(\dfrac{L_f}{4} - \delta + \delta^*\right)\right] - \pi\beta_f \tau_0'(\delta - \delta^*)\left(\dfrac{L_f}{4} - \delta + \delta^*\right)\right] & \delta^* + h_{f1} + h_{f2} \le \delta \le \dfrac{L_f}{2} + \delta^* \end{cases} \tag{19}$$

where δ^*, $\tau_0{}'$ are calculated by Eq. (18) with $L = L_f/4$; $z_2 = \frac{L_f}{2} - h_{f1} - h_{f2}$; $z_4 = \frac{L_f}{2} - \delta +$ δ^* and $t^* = \frac{4V_f}{\pi {d_f}^2} \frac{1+e^{\frac{\pi f}{2}}}{4+f^2}$.

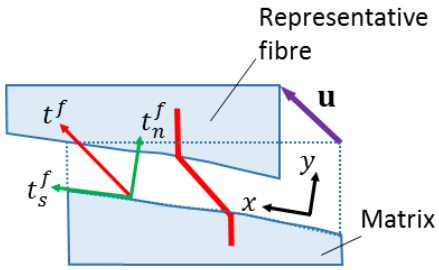

Fig. 7. Deformation and projections of force transferred by a bridging fibre due to crack opening

With the assumption that the bridging fibres deform in accordance with the relative displacement of the crack faces as illustrated in Fig. 7 for 2D case, the rate of fibre bridging stress rate, $\dot{t}^f = K_l^f \dot{\delta}$, along the fibre axis can be projected onto the local coordinate system of the crack plane to get the local bridging law as

$$\dot{\mathbf{t}}_l^f = \begin{bmatrix} \dot{t}_n^f \\ \dot{t}_{s1}^f \\ \dot{t}_{s2}^f \end{bmatrix} = \begin{bmatrix} K_l^f & 0 & 0 \\ 0 & K_l^f & 0 \\ 0 & 0 & K_l^f \end{bmatrix} \begin{bmatrix} \dot{u}_n \\ \dot{u}_{s1} \\ \dot{u}_{s2} \end{bmatrix} = \mathbf{K}_l^f \dot{\mathbf{u}}_l \tag{20}$$

The rate form of fibre bridging law in the global coordinate system, $\dot{\mathbf{t}}^f = \mathbf{K}^f \dot{\mathbf{u}}$, can now be obtained from its local relationship by using coordinate transformations technique and incorporated into the double-scale model presented in section 3.1 for modelling FRC.

2.2.4. Enhancement to account for effects of fibre content on cracking and mechanical response

It is known that the inhomogeneity of material in specimens could not be captured by solely using homogenous models with Finite Element Analysis, especially for FRC where crack development is strongly affected by the randomness of fibre distribution. Moreover, as shown in experimental results [54–56], for a specific set of material mixture (i.e. concrete and fibre), fibre content (i.e. volume fraction) is the decisive factor, controlling the crack density and elongation of phase II where cracks are diffusely distributed among specimens as addressed in Section 2.1. Crack density, in this case, can be considered as a "property" of a material mixture governed by the fibre volume fraction. However, to the best of our knowledge, there is no explicit relationship between fibre content and crack density in failure of FRC that was reported

in the literature. Given limited experimental proofs and theoretical supports on the issue, a phenomenological law is used in the model to reflect this intimate relationship and to alleviate the mismatch of inhomogeneity between the real material and that in the modelling. The relationship of the so-called crack density and fibre volume content V_f is reflected through the number of crack, n_c, initiating throughout the considered RVE, formulated as:

$$n_c = \frac{1}{\varepsilon_0} V_f e^{100V_f - \vartheta - \frac{0.01\varepsilon_m}{\varepsilon_0}} + 1 \tag{21}$$

where $\varepsilon_m = \max(\varepsilon_1,\ \varepsilon_2,\ \varepsilon_3)$ is the largest value of principal strain of the RVE; $\varepsilon_0 = \delta_0/H$ with δ_0 defined as the displacement corresponding to peak stress in pure tension as presented in Eq. (12) and H is the characteristic length of considered RVE (or element during the simulation by FEA); ϑ is a parameter controlling the crack density throughout the considered volume. This law is inspired from experimental observations [3,54,68–71] that the number of crack increases with the increase of volume content. The number of crack, formulated in this form, also approaches 1 with the increase of strain to reflect the transition from diffuse cracking to localisation mode as earlier analysed in Section 2.1.

A parametric study, shown in Fig. 8a, further illustrates this relationship with respect to different values of parameter ϑ by plotting the number of crack, calculated over a length $L = 20\text{cm}$ at a stage $\varepsilon_m = 2\varepsilon_0$ with various volume fraction values (i.e., $V_f = 0 - 4\%$). It can be seen that for the case of plain concrete (i.e., $V_f = 0\%$), the number of crack across the RVE is 1 which agrees with experimental observations [4,51–53] and the analyses made in section 2.1. With the increase of the fibre volume fraction, the number of crack increases at different rates depending on the parameter ϑ. In addition, the crack number is plotted against various deformation values (i.e., ε_m ranges from ε_0 to 3%) in Fig. 8b for volume fraction $V_f = 3\%$. It is seen that with the increase of deformation, the number of crack gradually decreases and approaches 1. The phenomenological law, in this form, would help the model reflect the transition from diffuse cracking phase to localised failure mode smoothly. It also gives the model flexibility to adapt itself to different types of FRC.

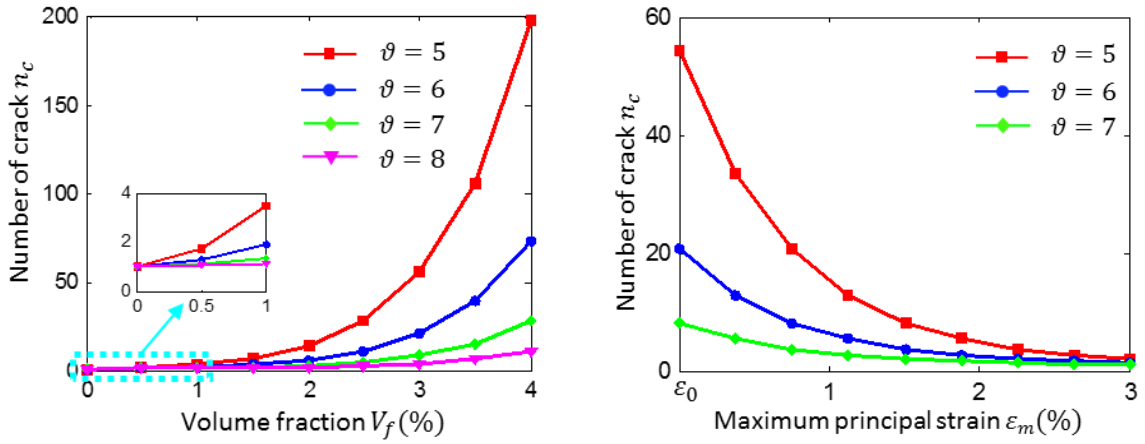

(a) (b)

Fig. 8. Parametric study on parameter ϑ: (a) number of crack with different volume fraction values and (b) with deformation evolution

With the increase in the number of cracks/localisation bands, as illustrated in Fig. 9a, the proportion of localisation band with respect to the RVE in Eq. (2) now becomes $\eta = \frac{n_c \Omega_{\mathrm{i}}}{\Omega} = \frac{n_c h}{H}$. Following the same procedure in section 3.1 (i.e., Eq. (2)-(6)), the constitutive equation, Eq. (7) is rewritten as:

$$\dot{\boldsymbol{\sigma}} = \mathbf{a}_{\mathrm{o}} \left[\dot{\boldsymbol{\varepsilon}} - \frac{n_c}{H} \mathbf{n} \dot{\mathbf{u}} \right] = \mathbf{a}_{\mathrm{o}} \left[\mathbf{1} - \frac{n_c}{H} \mathbf{n} \left(\frac{n_c}{H} \mathbf{n}^T \mathbf{a}_{\mathrm{o}} \mathbf{n} + \mathbf{K}^f + \mathbf{K}^b \right)^{-1} \mathbf{n}^T \mathbf{a}_{\mathrm{o}} \right] \dot{\boldsymbol{\varepsilon}} \tag{22}$$

The reasoning behind this enhancement is illustrated through an example of a RVE of FRC having the length $L = 20$ cm and $V_f = 1$ % as shown in Fig. 9b (the experimental failure pattern is taken from Sirijaroonchai et al. [57]). Under tensile loading, let us assume that there are 20 cracks appearing in the considered RVE, making the averaged crack density $\zeta_{\mathrm{cr}} = 20/0.2 = 100$ cracks/m. In the modelling, if the RVE is meshed with two elements using the proposed model, each element, having characteristic length $H = 10$cm, has to theoretically reflect the interactions of 10 cracks and their surrounding bulk material. The number of crack in each element is calculated as $n_c = 10.4$ by Eq. (21) with $\vartheta = 2.94$ and $\varepsilon_m = 2\varepsilon_0$. On the other hand, when the RVE is simulated using only one element having characteristic length $H = 20$cm, the number of cracks can be recalculated using the same parameter $\vartheta = 2.96$ and the result is $n_c = 19.8$ (cracks). This means that in both cases, the crack density remains constant of approximately $\zeta_{\mathrm{cr}} = 100$ cracks/m as it should be. This simple modification allows the proposed model to properly capture the diffuse cracking phase at different

discretisation resolutions during the modelling with FEA. It should also be noticed that the number of crack used in the model described above is just a value to represent for the level of diffuse cracking in the specimen and thus its value can be a real number. The use of Eq. (21) is satisfactory as demonstrated by numerical examples and we acknowledge that it should be backed up with further investigations based on micromechanics and experiments in future work.

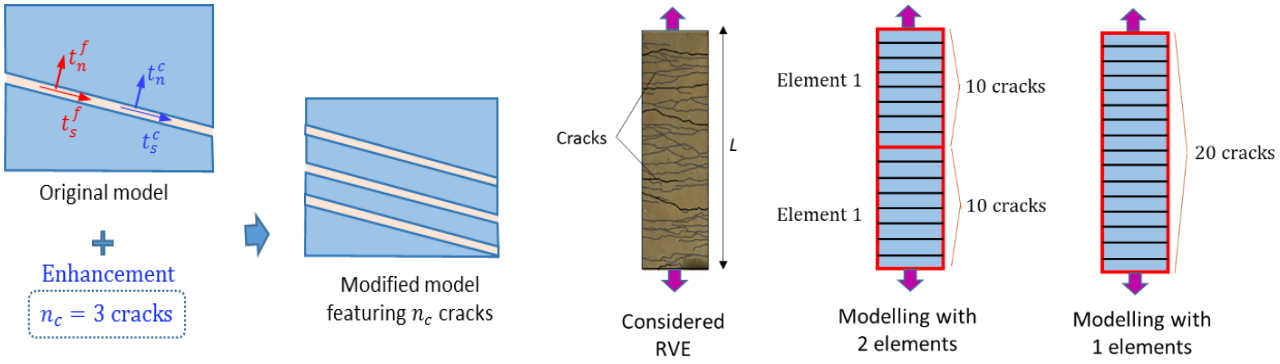

Fig. 9. Illustration of enhancement to capture constant crack density during simulation

3. Numerical examples

3.1. Single fibre pull-out test

The proposed pull-out model for hooked-end fibres is validated via a series of pull-out tests, shown in Fig. 10, where a hooked steel fibre is pulled out of a cementitious matrix. The experiments were performed by Alwan et al. [49] with commercial Dramix fibres having a diameter $d_f = 0.5$ mm and two embedded lengths $L = 12.5$ and 25 mm while the cement Young's modulus is $E_m = 20$ GPa. The fibre properties are: yield strength $f_y = 896$ MPa; Young's modulus $E_f = 210$ GPa; hook geometries $h_{f1} = h_{f2} = 1.5$ mm and hook angle $\theta = 45^0$. The model parameters are taken as $\tau_0 = 1.1$ KPa; $\beta_f = 0.04$; $\mu_f = 0.5$.

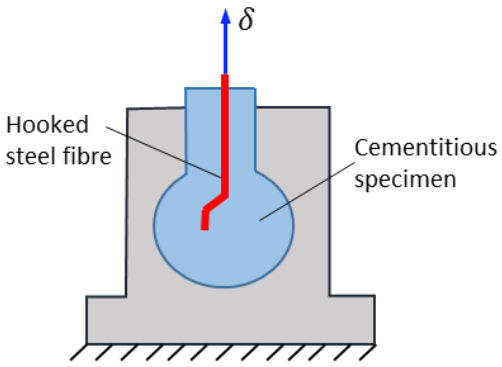

Fig. 10. Pull-out test set-up of a single hooked-end steel fibre

The load-displacement responses, plotted in Fig. 11 for both embedded lengths, show good agreements between the model results and experimental ones. Following the model, under a very small displacement, the fibres are debonded from the matrix and the straightening process starts quickly. The softening behaviour, where all hooks are straightened and the fibre is subsequently pulled out of the matrix, is well-captured by the model. Thanks to the considerations of fibre-matrix slip and hook straightening at microscopic level, the model can predict the overall pull-out force with a few physically meaningful parameters, which can be experimentally determined. The responses, including the contributions from the hooks, are produced from fibre mechanical properties and geometries without the need of information about the force-displacement curve in advance as in previous models [62] or phenomenological models heavily based on curve-fitting [63,64]. Even though the fibre pull-out responses from the model are not smooth, this simple model is capable of capturing the general trend and behaviour of single fibre pull-out thanks to the mechanism of debonding and hook straightening.

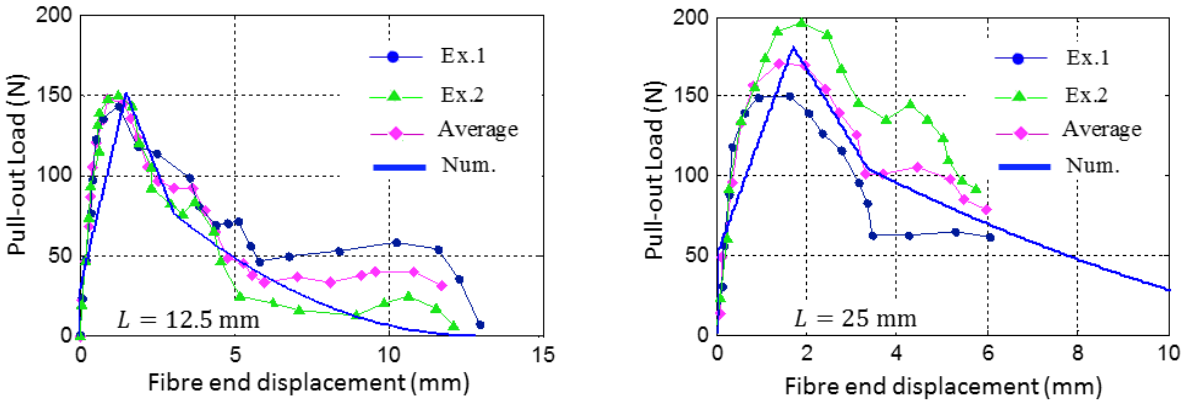

Fig. 11. Pull-out test results for different embedded lengths L

3.2. Single point simulations of uniaxial tension tests

The uniaxial tension tests, with set-up shown in Fig. 12, are used to investigate the capability of the proposed constitutive model for FRC. A series of tests were conducted by Li et al. [4] with commercial Dramix fibres and polymer polyvinyl alcohol (PVA) fibres with different volume fraction $V_f = 0\%, 2\%, 3\%$ and 6%. The properties of the concrete are taken as: Young's modulus $E_m = 50$ GPa; Poisson's ratio $\nu = 0.18$; uniaxial compressive strength $f_c = 46.3$ MPa; tensile strength $f_t = 3.7$ MPa; fracture energy $G_I = 0.27$ N/mm from which the model parameter α can be calculated as $\alpha = 0.2$. As the plain concrete used for all specimens comes from the same batch, model parameters for the matrix are taken as: $m = 0.3$; $\beta = 0.05$; $\mu_0 = 0.6$; $\gamma = 1.2$. The mechanical properties of fibres used in the experiments and related model parameters are listed in Table 1.

Table 1: Mechanical properties and parameters of the fibres used in experiments

	Fibre properties						Model parameters			
	E_f (GPa)	d_f (mm)	L_f (mm)	τ_0 (MPa)	h_{f1} (mm)	h_{f1} (mm)	μ_f	f	β_f	ϑ
Dramix	200	0.5	30	1.2	2	2	0.5	0.8	0.03	7.9
PVA	30	0.66	30	1.1	-	-	-	0.85	1.9	10.6

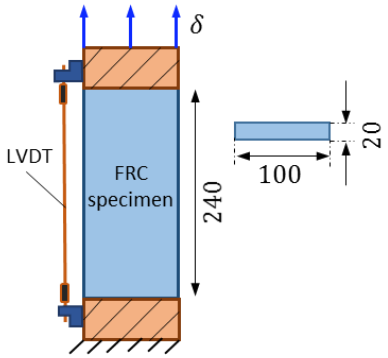

Fig. 12. Schematic set-up of tension tests, measured in mm.

Numerical results of the model for Dramix fibre reinforced concrete, plotted in Fig. 13, show fair agreements with its corresponding experimental counterparts for different values of fibre volume fraction. It is seen that the general trend of the material response from softening to hardening is well-captured by the model. Fig. 15b shows detailed contributions of both concrete cohesion and fibre bridging effect at a crack plane for the case $V_f = 3\%$. It can be seen that after the first crack appears in the specimen (point A in the figure), fibres bridging stress t_1^f, illustrated by a green curve, is activated and starts transferring stress across the crack plane while the matrix cohesion t_1^c begins to gradually lose its strength (illustrated by the blue curve). The overall stress of the specimen, σ_{11}, illustrated by the red curve, is a combination of these two responses as shown in the figure. This verifies that the failure mechanism of FRC where fibres help bear the loading and stop crack from opening, addressed in section 2, is well captured by the proposed model.

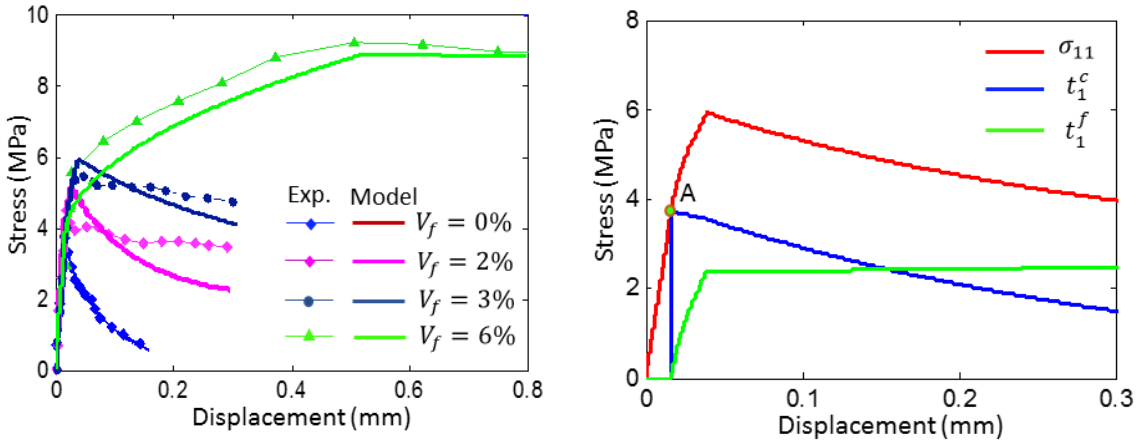

(a) (b)

Fig. 13. Tension test results of concrete reinforced by Dramix fibre: (a) Stress-displacement for different volume fractions and (b) detailed contributions for $V_f = 3\%$.

A parametric study is conducted for the two values of volume fraction $V_f = 3$ and 6% to investigate the influence of parameter ϑ on the overall responses of the specimen. Fig. 14, plotting the stress – displacement with respect to different values of ϑ, shows that with larger values of the parameter, the material behaviour becomes more ductile. This is understandable as when ϑ increases ($\vartheta = 7.3;\ 7.9$ and 8.5), the number of cracks (and hence crack density) also increases (at displacement $\delta = 0.1mm$, $n_c = 2.9;\ 4.8;\ 7.5$ for the case $V_f = 3\%$; and $n_c = 79;\ 144;\ 262$ for the case $V_f = 6\%$). This allows the energy to be dissipated gradually via the formation and development of more cracks, leading to more ductile behaviour. The impact of parameter ϑ (and also the phenomenological law) on the behaviour is also seen to be stronger in the case of higher volume fraction.

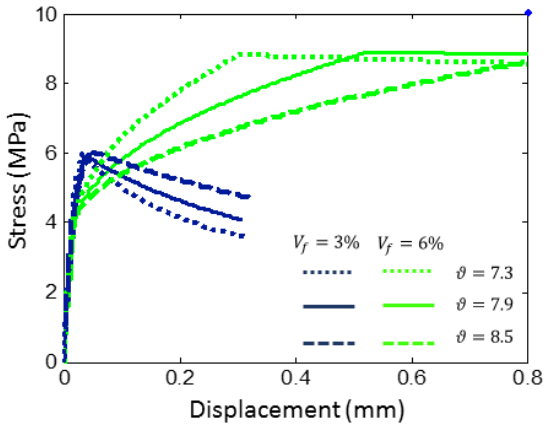

Fig. 14. Stress – displacement responses with different values of parameter ϑ

Fig. 15a shows reasonable agreements between numerical results and its experimental counterparts for concrete reinforced with PVA fibres. As observed in experimental studies, the results for PVA fibres show modest improvements of strength and ductility with low volume fractions (i.e., 2-3%) and they only become significant with very high contents of fibres (i.e., 6%). Similar to the case of Dramix reinforced concrete, the detailed responses, plotted in Fig. 15b, show that the overall specimen response is a combination of the fibre bridging effect and the matrix cohesion. In addition, the figure shows that after a crack initiates (i.e., point A), the stress $\sigma_{o,11}$ and strain $\varepsilon_{o,11}$ of the intact bulk material, illustrated by the cyan curve, continue to increase up to the peak owing to the increase of the overall stress σ_{11}. However, when the overall stress decreases, they both decrease (i.e., the outer bulk shrinks) making stress – train response a straight line on the elastic trajectory, which contrasts with the increase of deformations in the opening crack. This shows that both linear-elastic behaviour of the outer bulk material and inelastic responses of the crack where cohesion and fibre bridging take place, are interconnected within a continuum model and they all contribute to the overall responses of the material following their own constitutive relationships. This is one of the key features that distinguishes the proposed model from other continuum-based model [41–44] where such behaviour cannot be captured.

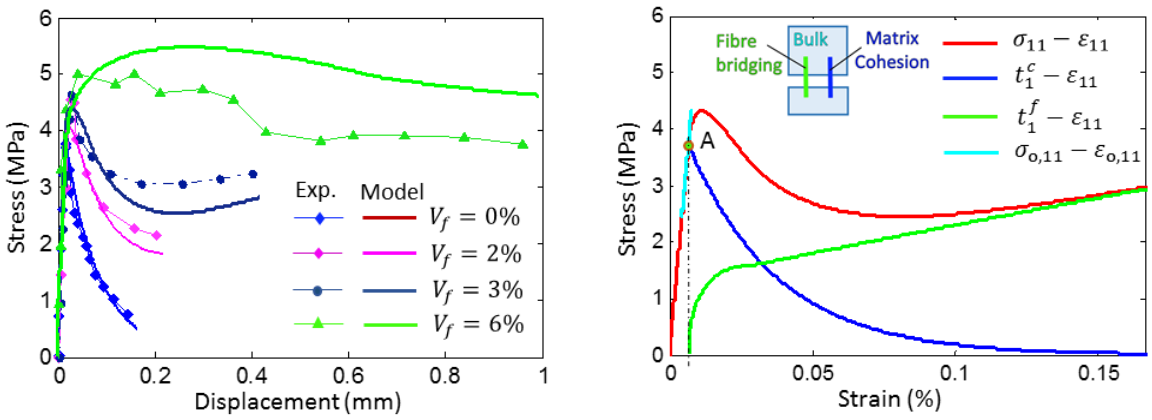

(a) (b)

Fig. 15. Tension test results of concrete reinforced with PVA fibre: (a) Stress-displacement for different volume fractions and (b) detailed contributions for $V_f = 3\%$.

3.3. Finite element analysis (FEA) of dog-bone tension tests

In this section, the proposed model is implemented into the commercial package ABAQUS as a user-defined material model (UMAT) for the FEA of dog-bone tension tests, whose set-up is shown in Fig. 16a. The simulations are performed in 2D plane stress using a mesh comprising

of 1347 three-node triangular elements as shown in Fig. 16b, with displacement-controlled loading condition. The experiments were conducted by Kamal et al. [3] with ultra-high performance concrete (UHPC) reinforced by high strength polyethylene (PE) fibres whose geometries and properties are listed in Table 2 and Table 3.

As addressed in our previous study [50], the characteristic length of each element can be calculated by definition in Eq. (2) once a crack appears by using the predicted crack orientation and nodal coordinates of the element. However, for simplicity purpose, the characteristic length is approximated as the square root of element area $H_i = \sqrt{A_i}, i = 1, 2, \dots N_e$ where N_e is the number of element in the simulation. The previous study [50] shows that this simple approximation is effective in facilitating the implementation during the simulation without losing the effectiveness of the regularisation and hence can be adopted.

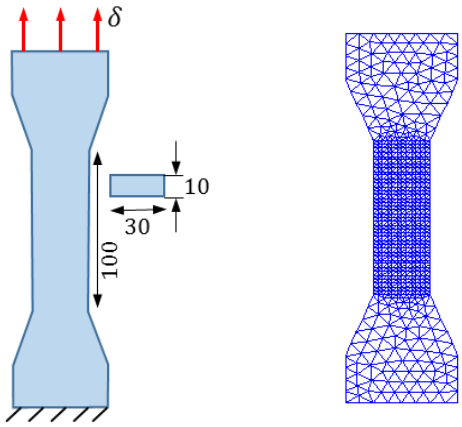

(a) (b)

Fig. 16. Dog-bone tests: (a) Schematic experimental set-up and (b) Finite element mesh

Table 2: Fibres properties and related model parameters

	Fibre properties						Related parameters			
	E_f (GPa)	d_f (mm)	L_f (mm)	τ_0 (MPa)	h_{f1} (mm)	h_{f1} (mm)	μ_f	f	β_f	ϑ
PE	32	0.012	6	1.1	-	-	-	0.92	0.001	4.5
Dramix	210	0.63	50	1.8	2	2	0.6	0.85	0.015	5.2

Table 3: Concrete properties and related model parameters

	Concrete properties					Related parameters			
	E_m (GPa)	ν	f_c (MPa)	f_t (MPa)	G_I (N/mm)	β	m	μ_0	γ

Dog-bone	33	0.2	94	3.7	0.15	0.1	0.9	0.8	1.1
Bending	40	0.2	81	2.5	0.07	0.08	0.8	0.78	2.2

Fig. 17 shows fair agreements between numerical results and those from the experiment for three volume fractions $V_f = 0.5, 1$ and 1.5%. With the increase of fibre content, the fibre bridging force becomes stronger, resulting in more cracks within the specimen and significant improvement in material ductility as also observed in experiments [3,54,68]. The damage profiles, in Fig. 18a, show that for the case of $V_f = 0.5$ %, after the appearance of the first crack, a localisation band forms and develops quickly among the specimen. This is clearly seen in the strain profiles across the specimen length at three instants of the analysis (see Fig. 18b). With high volume content (i.e., for the case $V_f = 1.5$ %), the deformation is more homogenous, thanks to the stronger fibre bridging force shown in Fig. 18c. The homogeneity of strain is maintained in the hardening phase, during which cracks form and develop uniformly throughout the specimen as seen in the damage contours in Fig. 18a. This reflects the analysis made in section 2 that the fibre bridging stress forces the specimen to form a system of uniformly distributed small cracks to dissipate the given energy.

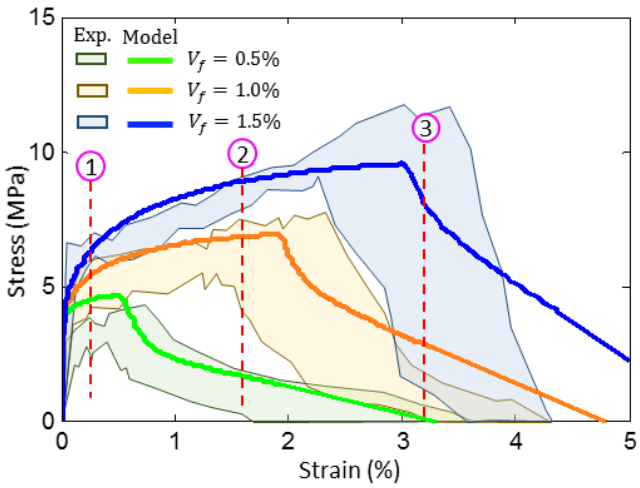

Fig. 17. Stress-strain responses of dog-bone tests

In all cases of fibre content, once a localisation is formed, most of the deformations take place in this region causing bridging fibres to be quickly pulled out of the concrete matrix and the material response becomes softening as observed in experiments. In this sense, the addition of fibres, represented by the fibre bridging effect illustrated in Fig. 18c, prolongs the formation and development of localisation within the specimen and thus enhances its capability of energy absorption. The plot of tractions in the localisation band (i.e., Fig. 18c) with respect to local strain shows that the overall load resistance of the specimen comes from both the matrix cohesion, vanishing quickly and the fibre bridging force, being the main load-bearing

component until failure. The influence of fibre bridging effect is stronger with the increase of fibre content, leading to the change of specimen behaviour, described above. These underlying mechanisms driving the macro responses and failure patterns that match experimental counterparts are naturally captured by the model thanks to the embeded localisation band in the constitutive equations. This highlights the benefits of the in-built intrinsic failure mechanism of the model.

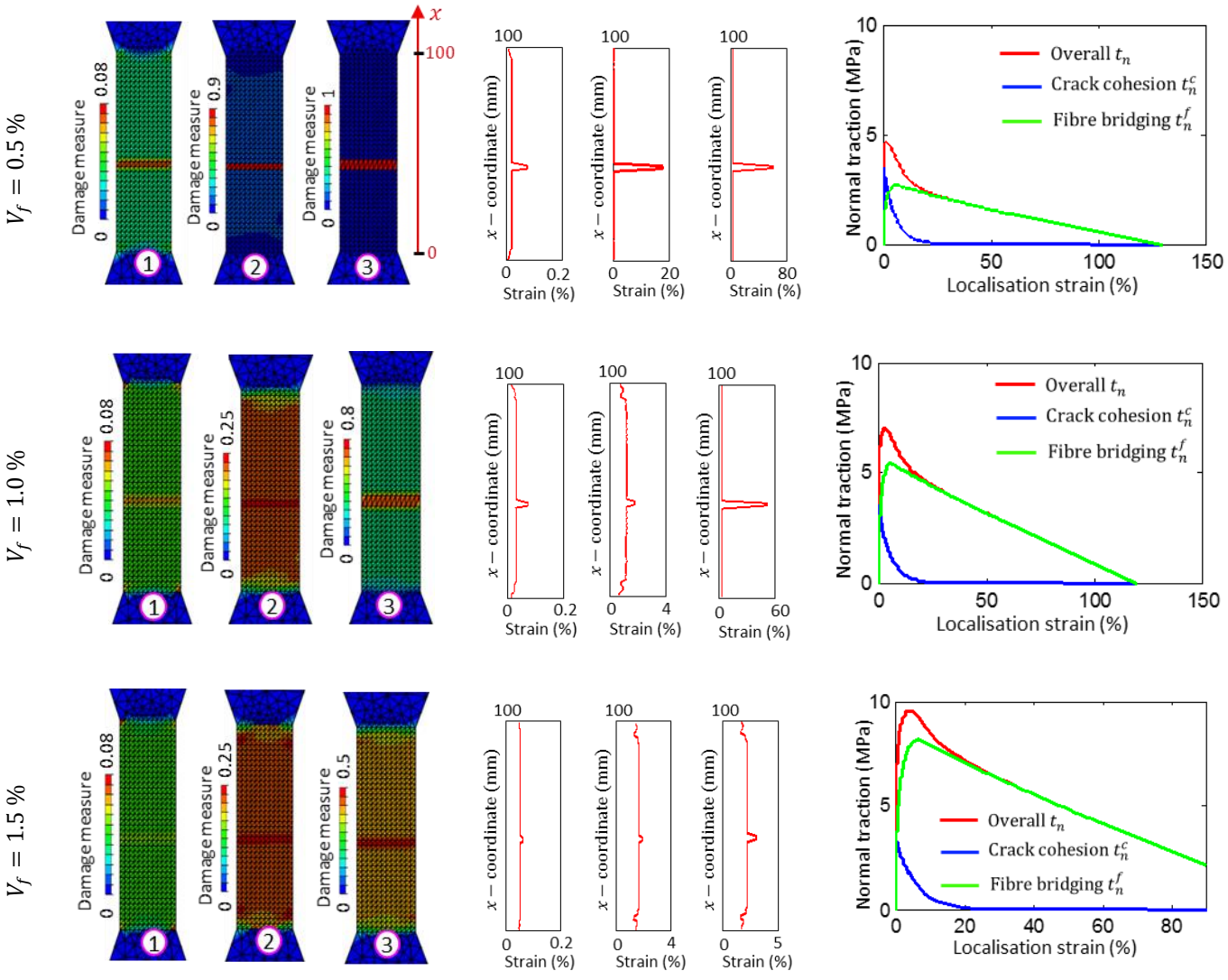

Fig. 18. Dog-bone tests results: (a) Damage contour; (b) Strain profiles and (c) Detailed contribution at the localisation

Further detailed analysis of strains at two sections (i.e., A-A and B-B) in Fig. 19 clearly shows the difference in the deformations inside and outside the localisation band during the loading. At first, strains of the two sections are relatively the same, which verifies the homogeneous deformation profiles shown in Fig. 18a. A sudden increase in strain at section

A-A, compared to section B-B, indicates the formation of a localisation band. After that, the localisation band keeps opening while the strain in other regions, represented by section B-B, decreases as shown by the zoom-in image in Fig. 19. This, together with the examples presented in Section 3.2, shows the robustness of the proposed model capturing the interaction of the localisation and its outer bulk material at both constitutive and structural modelling levels.

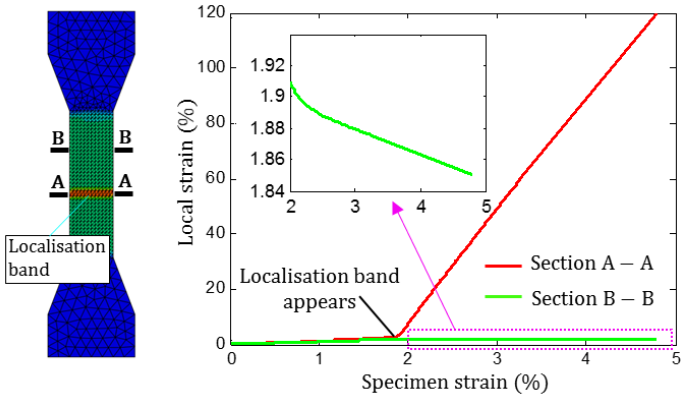

Fig. 19. Detailed analysis of local strains at 2 sections in the case $V_f = 1$ %

3.4. Finite element analysis of 3-point bending tests

In this section, the capability of the proposed model is validated against experimental results of 3-point bending tests, conducted by Bencardino et al. [74] with set-up and boundary condition shown in Fig. 20a. The specimens in these tests were cast with high-performance concrete, whose mechanical properties are listed Table 2 and steel hooked-end Dramix fibres whose geometries and properties are presented in Table 3. The simulations in this example use 3-node triangular elements and displacement-controlled loading in 2D plane stress condition with two meshes, mesh 1 (1107 elements) and mesh 2 (2636 elements), as shown in Fig. 20b.

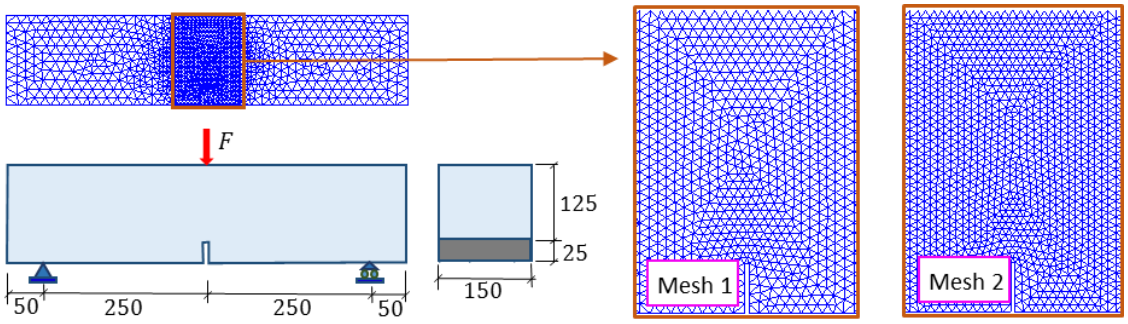

(a) (b)

Fig. 20. Three-point bending tests: (a) Schematic experiment set-up and (b) Meshes used for simulations

The load-displacement responses by the model, presented in Fig. 21, show good agreements with their experimental counterparts. While the plain concrete shows a sharp softening response after reaching its peak, FRC vividly shows significant improvements in ductility and strength with hardening behaviour. These improvements again have an intimate relationship with the failure mechanism of the material. Fracture patterns at different stages, depicted in Fig. 22a, show that for the case of plain concrete, a narrow crack band initiates from the notch and quickly develops toward the top of the specimen. Section cuts across the damaged area in Fig. 22b further show that the horizontal strain of plain concrete beam concentrates on a narrow region (i.e. a localisation) throughout the analysis. In this case, a small amount of energy, represented by the small area under the load-displacement curve in Fig. 21, is dissipated via the formation and rapid development of this major crack. The failure pattern of the FRC beam, on the other hand, shows that a bigger region of damage forms and develops up to the end of the experiments with respect to the increase of fibre content, as also observed in experimental data [69,71,70]. This is further illustrated by section cuts of deformation in Fig. 22b, where strain spreads in a wider area and cracks are more diffused with higher fibre volume fraction.

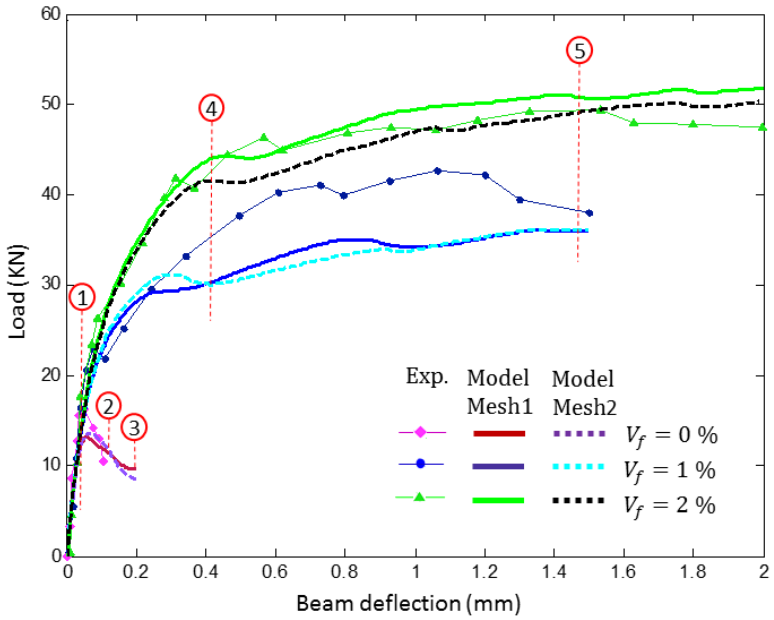

Fig. 21. Load-deflection responses of 3-point bending tests

In addition, Fig. 21 also shows that the numerical results for the two meshes are comparable, demonstrating the convergence of the proposed model with mesh refinement. Even though the structural responses, in this case, are hardening, the material behaviour shown in Fig. 22c is, in fact, softening, followed by a hardening period. Regularisation is thus always

needed when solving BVPs to reflect the proper amount of energy dissipated within a crack for different mesh resolutions. As crack is included in the model with its relative size, represented by the characteristic length H, the constitutive behaviour naturally scales with the resolution of discretisation while the dissipation in crack remains the same. Results from the proposed model are thus independent of the mesh size without employing any external regularisation. This advantage is one of the features distinguishing the proposed model from existing ones [41–44].

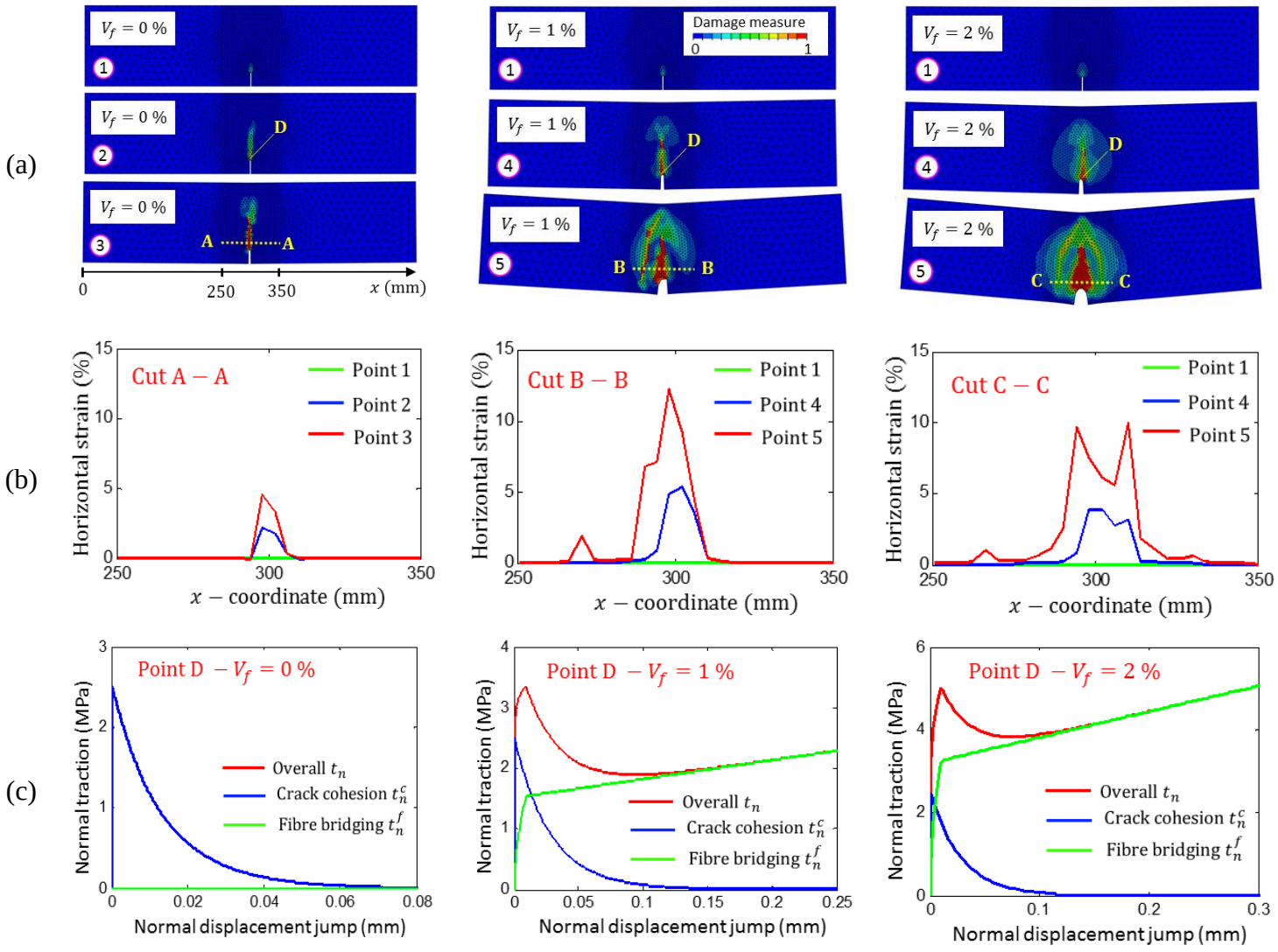

Fig. 22. Detailed analysis of 3-point bending tests: (a) damage contour with magnification factor of 10 (mesh1); (b) corresponding section cut of horizontal strain and (c) local traction-displacement at point D of the beam

All of these structural responses and failure pattern, described above, are actually driven by the constitutive behaviour shown in Fig. 22c at a point just above the beam notch (i.e. point D in Fig. 22a) for all three cases. Under loading, the material quickly loses its cohesive resistance, represented by blue curves and activates the fibre bridging forces, described as green

curves in the figure. The loading resistance of the element is a combination of both cementitious cohesion and the fibre bridging effect as previously addressed in section 2.1. The cohesive resistance from plain material and bridging effect from fibres hinders a crack from opening and force the specimen to initiate more cracks in surrounding areas to dissipate the provided energy. The interaction between these two contributions is further illustrated in Fig. 23, where normal tractions contour at point 4 of the analysis are plotted for the case $V_f = 2\%$. It shows that up to this point, concrete loses the majority of its cohesive resistance in the major crack. This is presented in the figure by a blue thin area where local cohesive traction is approximately zero. However, stresses are still transferred across this crack, thanks to the fibre bridging effect illustrated in the figure. The overall traction, being a sum of both fibre bridging effect and cohesion, still can carry a significant amount and thus the structure can absorb much more energies before failure, shown by a substantially bigger area under the load-displacement curve compared to that of plain concrete (see Fig. 21). This detailed analysis again shows that the structural responses are naturally captured with corresponding failure patterns driven by the underlying mechanism of fibre bridging effect at constitutive level. This proves the robustness and effectiveness of featuring the crack as the failure mechanism in the constitutive modelling.

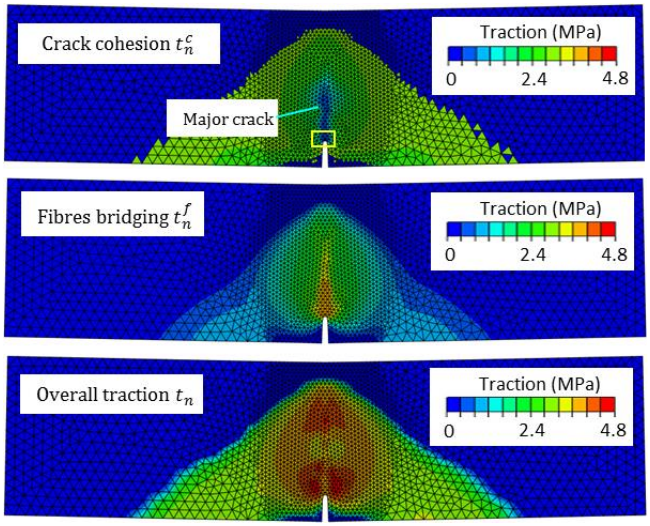

Fig. 23. Normal traction contour at point 4 for $V_f = 2\%$

4. Conclusions

In this research, the fibre bridging effect and cohesive resistance acting on an opening crack are taken as the fundamental mechanism in developing a constitutive model for randomly distributed short fibre reinforced concrete. Both the effect of fibres-matrix bonding and aggregates interlocking/cohesion within a crack are incorporated into a continuum-based constitutive model via kinematic enhancements and traction continuity conditions. The

enrichment adapted in the present form allows the inclusion of a separate fibre bridging law, where micro-mechanical considerations of fibre debonding, hook straightening and fibre pull-out are taken into account. The direct inclusion of the crack with its relative size into the constitutive model also produces an in-built regularisation effect to overcome the mesh-dependency problem during the simulation of Boundary Value Problems. The macro responses and failure patterns of the material, from hardening with multiple-cracking to softening with a localisation band, are naturally captured by the model as demonstrated by numerical examples in both constitutive modelling and Boundary Value Problems simulations. The proposed approach shows good potential to be extended to other materials such as fibre reinforced soil or sand with more complex underlying mechanisms and micro/meso constitutive laws.

5. Acknowledgements

Giang D. Nguyen and Ha H. Bui gratefully acknowledge support from the Australian Research Council via Discovery Projects FT140100408 (Nguyen), DP160100775 (Bui), and DP170103793 (Nguyen and Bui).

Appendix A. Derivation of single fibre pull-out with slip-softening interface

Debonding phase

Following the concept proposed by Lin and Li [48] for pull-out process of a straight fibre depicted in Fig. A.1, interfacial fibre-matrix slip, S in the debonding phase can be calculated from the differential equation:

$$\frac{d^2S}{dx^2} + \frac{\omega^2}{{d_f}^2} S = \frac{\omega^2}{\beta_f d_f} \tag{A.1}$$

where ω and other parameters are defined earlier as in Eq. (15). The boundary conditions of this equation are $S = 0$ and $\frac{dS}{dx} = 0$ at $x = 0$.

The solution for this second order differential equation (A.1) can be found as:

$$S(x) = \frac{d_f}{\beta_f}\left[1 - \cos\left(\frac{\omega x}{d_f}\right)\right] \tag{A.2}$$

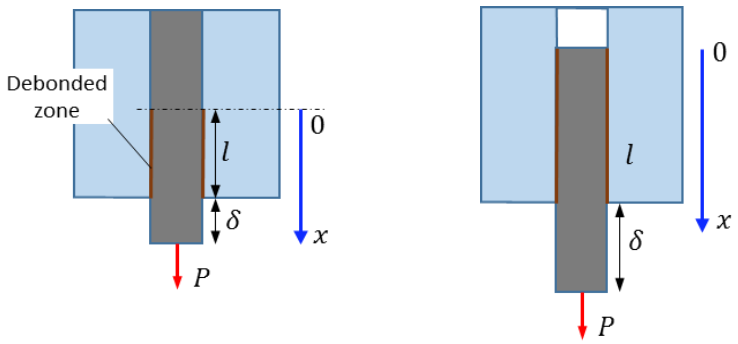

(a) (b)

Fig. A.1. Schematic of straight fibre pull-out: (a) debonding phase and (b) pull-out phase

By substituting Eq. (A.2) into Eq. (17), the shear stress acting along the fibre can be expressed as:

$$\tau(x) = \tau_0 \cos\left(\frac{\omega x}{d_f}\right) \tag{A.3}$$

The averaged interfacial shear stress in the debonded region can thus be obtained as:

$$\bar{\tau} = \frac{1}{l}\int_0^l \tau(x)dx = \frac{d_f}{\omega l}\tau_0 \sin(\frac{\omega l}{d_f}) \tag{A.4}$$

where l is the debonded length of the fibre as shown in Fig. A.1. As a result, the pull-out force in the debonding phase can be written as [48]:

$$P = \pi d_f l \bar{\tau}(1+\varsigma) = \frac{\pi {d_f}^2 \tau_0}{\omega}(1+\varsigma)\sin(\frac{\omega l}{d_f}) \tag{A.5}$$

By eliminating l from Eq. (A.5) and using two-side pull-out distance $\delta = 2S(x = l)$, the pull-out force with respect to pull-out displacement is obtained as:

$$P = \frac{\pi {d_f}^2 \tau_0}{\omega}(1+\varsigma)\sqrt{1-(1-\frac{\beta_f \delta}{2d_f})^2} \tag{A.6}$$

Finally, the force and displacement corresponding to the stage of fully debonded can be expressed as:

$$P_0 = \frac{\pi {d_f}^2 \tau_0}{\omega}(1+\varsigma)\sqrt{1-(1-\frac{\beta_f \delta^*}{2d_f})^2} \text{ and } \delta^* = 2S(x = L) = \frac{2d_f}{\beta}\left[1-\cos(\frac{\omega L}{d_f})\right] \tag{A.7}$$

Pull-out phase

In this phase, the fibre is assumed to be frozen and pulled out of the matrix with frictional sliding as illustrated in Fig. A.1. The slip formulation can now be expressed as:

$$S = \frac{d_f}{\beta_f}\left[1 - \cos(\frac{\omega x}{d_f})\right] + (\delta - \delta^*) \tag{A.8}$$

Consequently, the expression for the pull-out force can be written as:

$$\begin{aligned} P &= \pi d_f \int_0^{L-\delta+\delta^*} \tau(x)dx \\ &= \frac{\pi {d_f}^2 \tau_0}{\omega} \sin\left[\frac{\omega}{d_f}(L - \delta + \delta^*)\right] - \pi\beta_f\tau_0(\delta - \delta^*)(L - \delta + \delta^*) \end{aligned} \tag{A.9}$$

The incorporation of the hook contributions, Eq. (16), into the debonding and pull-out phases in Eqs. (A.6) and (A.9) is illustrated in Fig. 6b, where phase 2 and 3 are simply taken as a linear process. With some algebraic manipulations, the four-phase force-displacement relationship of a single hook-end fibre can be obtained as described in Eq. (18).

Appendix B. Derivation of fibre bridging stress from single fibre pull-out

As described in Eq. (13), the fibre bridging law for hooked-end fibre can be obtained by integrating the pull-out contributions (i.e., Eq.(18)) of fibres across the crack plane. Fig. 5 shows the relative position of a fibre to the matrix, represented by its orientation ϕ and centrodial distance to the crack plane, from which the embedded length can be determined as:

$$L = \frac{L_f}{2} - \frac{z}{\cos\phi} \rightarrow z = \left(\frac{L_f}{2} - L\right)\cos\phi \tag{B.1}$$

Because the proposed pull-out force expression for hooked-end fibre in Eq.(18) is valid only for embedded length $h_{f1} + h_{f2} \le L \le L_f/2$, the integration of bridging law, for simplicity purpose, only counts the contributions from fibres in this range as illustrated in Fig. B.1. As a result, the boundaries for the integration are $0 \le \phi \le \pi/2$ and $0 \le z \le \left(\frac{L_f}{2} - h_{f1} - h_{f2}\right)\cos\phi = z_2\cos\phi$ and the density functions for uniformly random distribution

are taken as $p(\phi) = \sin\phi$ and $p(z) = \frac{1}{z_2}$. In addition, the pull-out force for inclined fibres (i.e., $\phi \neq 0$) can be calculated from perpendicular fibres (i.e., $\phi = 0$) as:

$$P|_{\phi} = e^{f\phi} P|_{\phi=0} \tag{B.2}$$

where f is the snubbing coefficient, proposed by Li et al. [47,75]. The integration for the fibre bridging effect now expressed as:

$$t^f(\delta) = \frac{4V_f}{\pi z_2 {d_f}^2} \int_{\phi=0}^{\frac{\pi}{2}} \int_{z=0}^{z_2\cos\phi} P(\delta) e^{f\phi} \sin\phi dz\, d\phi \tag{B.3}$$

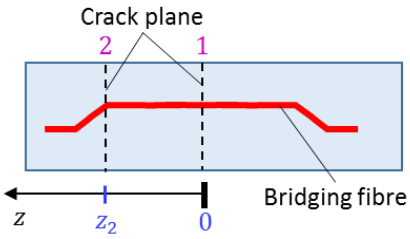

Fig. B.1. Illustration of fibre boundaries for the integration

As the pull-out force P is obtained separately for four different phases (i.e., debonding, straightening hook h_{f1}, straightening hook h_{f2} and frictional pull-out), the integration in Eq. (B.3) can simply be calculated for four phases. To simplify the integration process, the force P of fibres whose embedded lengths range from 0 to $L_f/2$, is approximated by taking an averaged embedded length of $L_f/4$. This approximation helps obtain a simple yet effective model for fibre bridging effect in this study but we acknowledge that a more accurate and complex calculation can be used to acquire better consistencies throughout the model.

In phase I ($0 \leq \delta \leq \delta^*$), the fibre bridging stress can be obtained from the pull-out force as:

$$\begin{aligned} t^f(\delta) &= \frac{4V_f}{\pi z_2 {d_f}^2} \int_{\phi=0}^{\frac{\pi}{2}} \int_{z=0}^{z_2\cos\phi} P_I e^{f\phi} \sin\phi dz\, d\phi \\ &= P_I \frac{4V_f}{\pi z_2 {d_f}^2} \int_{\phi=0}^{\frac{\pi}{2}} \int_{z=0}^{z_2\cos\phi} e^{f\phi} \sin\phi dz d\phi = \frac{4V_f}{\pi {d_f}^2} \frac{1 + e^{\frac{\pi f}{2}}}{4 + f^2} P_I = t^* P_I \end{aligned} \tag{B.4}$$

Similarly, the bridging law for phase II and III can be simply written as $t^* P_{\mathrm{II}}$ and $t^* P_{\mathrm{III}}$. However, since during phase IV, some fibres are completely pulled out of the matrix and have

no more contribution to the bridging effect, the upper limit of the integration changes. As formulated in Eq. (18), a fibre contributes to the bridging as long as its embedded length satisfies $\delta \leq L + \delta^*$. By substituting Eq. (B.1) into this condition, one obtains:

$$\delta \leq \frac{L_f}{2} - \frac{z}{\cos\phi} + \delta^* \rightarrow z \leq \left(\frac{L_f}{2} - \delta + \delta^*\right)\cos\phi = z_4\cos\phi \tag{B.5}$$

This upper integration limit ensures that for a given crack opening, only fibres that are actually bridging the crack, are counted. The bridging stress is then calculated as:

$$\begin{aligned} t^f(\delta) &= \frac{4V_f}{\pi z_2 {d_f}^2}\int_{\phi=0}^{\frac{\pi}{2}}\int_{z=0}^{z_4\cos\phi} P_{IV}(\delta)e^{f\phi}\sin\phi dz\, d\phi = \frac{4V_f}{\pi z_2 {d_f}^2}P_{IV}z_4\,\frac{1+e^{\frac{\pi f}{2}}}{4+f^2} \\ &= \frac{4V_f z_4}{\pi {d_f}^2 z_2}\frac{1+e^{\frac{\pi f}{2}}}{4+f^2}P_{IV} = \sigma^*\frac{z_4}{z_2}P_{IV} \end{aligned} \tag{B.6}$$

References

[1] J. Oliver, D.F. Mora, A.E. Huespe, R. Weyler, A micromorphic model for steel fiber reinforced concrete, Int. J. Solids Struct. 49 (2012) 2990–3007. doi:10.1016/j.ijsolstr.2012.05.032.

[2] P. Guerrero, A.E. Naaman, Effect of mortar fineness and adhesive agents on pullout response of steel fibers, ACI Struct. J. 97 (2000) 12–20. doi:10.14359/800.

[3] A. Kamal, M. Kunieda, N. Ueda, H. Nakamura, Evaluation of crack opening performance of a repair material with strain hardening behavior, Cem. Concr. Compos. 30 (2008) 863–871. doi:10.1016/j.cemconcomp.2008.08.003.

[4] Z. Li, F. Li, T.Y. Chang, Y.-W. Mai, Uniaxial tensile behaviour of concrete reinforced with randomly distributed short fibres, ACI Mater. J. 95 (1998) 564–574.

[5] C. Lu, V.C. Li, C.K.Y. Leung, Flaw characterization and correlation with cracking strength in Engineered Cementitious Composites (ECC), Cem. Concr. Res. 107 (2018) 64–74. doi:10.1016/j.cemconres.2018.02.024.

[6] J. Yu, J. Yao, X. Lin, H. Li, J.Y.K. Lam, C.K.Y. Leung, I.M.L. Sham, K. Shih, Tensile performance of sustainable Strain-Hardening Cementitious Composites with hybrid PVA and recycled PET fiber.pdf, Cem. Concr. Res. 107 (2018) 110–123.

[7] A. Abrishambaf, M. Pimentel, S. Nunes, Influence of fibre orientation on the tensile behaviour of ultra-high performance fibre reinforced cementitious composites, Cem. Concr. Res. 97 (2017).

[8] A.A. Abdul-Razzak, A.A. Mohammed Ali, Modelling and numerical simulation of high strength fibre reinforced concrete corbels, Appl. Math. Model. 35 (2011) 2901–2915. doi:10.1016/j.apm.2010.11.073.

[9] V. Slowik, B. Villmann, N. Bretschneider, T. Villmann, Computational aspects of inverse analyses for determining softening curves of concrete, Comput. Methods Appl. Mech. Eng. 195 (2006) 7223–7236. doi:10.1016/j.cma.2005.04.021.

[10] A.A. Abdul-Razzak, A.A. Mohammed Ali, Influence of cracked concrete models on the nonlinear analysis of High Strength Steel Fibre Reinforced Concrete corbels, Compos. Struct. 93 (2011) 2277–2287. doi:10.1016/j.compstruct.2011.03.016.

[11] A. Blanco, P. Pujadas, S. Cavalaro, A. De La Fuente, A. Aguado, Constitutive model for fibre reinforced concrete based on the Barcelona test, Cem. Concr. Compos. 53 (2014) 327–340. doi:10.1016/j.cemconcomp.2014.07.017.

[12] J.L.A. de O. e Sousa, R. Gettu, Determining the Tensile Stress-Crack Opening Curve of Concrete by Inverse Analisis, J. Eng. Mech. 132 (2006) 141–148. doi:10.1061/_ASCE_0733-9399_2006_132:2_141.

[13] D. Fanella, D. Krajcinovic, Continuum damage mechanics of fibre reinforced concrete, J. Eng. Mech. 111 (1985) 995–1009.

[14] F. Li, Z. Li, Continuum damage mechanics based modeling of fiber reinforced concrete in tension, Int. J. Solids Struct. 38 (2001) 777–793. doi:10.1016/S0020-7683(00)00034-2.

[15] M.C. Nataraja, N. Dhang, A.P. Gupta, Stress–strain curves for steel-fiber reinforced concrete under compression, Cem. Concr. Compos. 21 (1999) 383–390. doi:10.1016/S0958-9465(99)00021-9.

[16] J.A.O. Barros, J.A. Figueiras, Flexural behaviour of SFRC: Testing and modelling, J. Mater. Civ. Eng. 11 (1999) 331–339.

[17] S.A. Ezeldin, P.N. Balaguru, High strength fiber reinforced concrete under compression, J. Mater. Civ. Eng. 4 (1990) 415–429.

[18] C. Jin, N. Buratti, M. Stacchini, M. Savoia, G. Cusatis, Lattice discrete particle modeling of fiber reinforced concrete: Experiments and simulations, Eur. J. Mech. A/Solids. 57 (2016) 85–107. doi:10.1016/j.euromechsol.2015.12.002.

[19] E. Schauffert, G. Cusatis, Lattice dícrete particle model for Fibre-Reinforced Concrete. I: Theory, J. Eng. Mech. 137 (2011) 826–833. doi:10.1061/(ASCE)EM.

[20] E.A. Schauffert, G. Cusatis, D. Pelessone, J.L. O'Daniel, J.T. Baylot, Lattice discrete particle model for Fiber-Reinforced Concrete. II: Tensile fracture and multiaxial loading behavior, J. Eng. Mech. 138 (2012) 834–841. doi:10.1061/(ASCE)EM.1943-7889.0000392.

[21] J. Kang, K. Kim, Y.M. Lim, J.E. Bolander, Modeling of fiber-reinforced cement composites: Discrete representation of fiber pullout, Int. J. Solids Struct. 51 (2014) 1970–1979. doi:10.1016/j.ijsolstr.2014.02.006.

[22] F.K.F. Radtke, A. Simone, L.J. Sluys, Apartition of unity finite element method for simulating non-linear debonding and matrix failure in thin fibre composites, Int. J. Numer. Methods Eng. 86 (2012) 453–476. doi:10.1002/nme.

[23] F.K.F. Radtke, A. Simone, L.J. Sluys, Apartition of unity finite element method for obtaining elastic properties of continua with embedded thin fibre, Int. J. Numer. Methods Eng. 84 (2012) 708–732. doi:10.1002/nme.

[24] C. Octávio, D. Dias-da-Costa, J. Alfaiate, E. Júlio, Modelling the behaviour of steel fibre reinforced concrete using a discrete strong discontinuity approach, Eng. Fract. Mech. 154 (2016) 12–23. doi:10.1016/j.engfracmech.2016.01.006.

[25] A.E. Huespe, J. Oliver, D.F. Mora, Computational modeling of high performance steel fiber reinforced concrete using a micromorphic approach, Comput. Mech. 52 (2013) 1243–1264. doi:10.1007/s00466-013-0873-4.

[26] H. Zhang, Y.J. Huang, Z.J. Yang, S.L. Xu, X.W. Chen, A discrete-continuum coupled finite element modelling approach for fibre reinforced concrete, Cem. Concr. Res. 106 (2018) 130–143. doi:10.1016/j.cemconres.2018.01.010.

[27] A. Yaghoobi, M.G. Chorzepa, Meshless modeling framework for fiber reinforced concrete structures, Comput. Struct. 161 (2015) 43–54. doi:10.1016/j.compstruc.2015.08.015.

[28] Pike, C. Oskay, Three-dimensional modeling of short fiber-reinforced composites with Extended Finite-Element Method, J. Eng. Mech. (2015) 1–12. doi:10.1061/(ASCE)EM.1943-7889.0001149.

[29] Pike, C. Oskay, XFEM modeling of short microfiber reinforced composites with cohesive interfaces, Finite Elem. Anal. Des. 106 (2015) 16–31. doi:10.1016/j.finel.2015.07.007.

[30] V.M.C.F. Cunha, J.A.O. Barros, J.M. Sena-cruz, An integrated approach for modelling the tensile behaviour of steel fibre reinforced self-compacting concrete, Cem. Concr. Res. 41 (2011) 64–76. doi:10.1016/j.cemconres.2010.09.007.

[31] V.M.C.F. Cunha, J.A.O. Barros, J.M. Sena-Cruz, A finite element model with discrete embedded elements for fibre reinforced composites, Comput. Struct. 94-95 (2012) 22–33. doi:10.1016/j.compstruc.2011.12.005.

[32] H.K. Lee, S. Simunovic, A damage constitutive model of progressive debonding in aligned discontinuous fiber composites, Int. J. Solids Struct. 38 (2001) 875–895. doi:10.1016/S0020-7683(00)00060-3.

[33] H.K. Lee, S. Simunović, D.K. Shin, A computational approach for prediction of the damage evolution and crushing behavior of chopped random fiber composites, Comput. Mater. Sci. 29 (2004) 459–474. doi:10.1016/j.commatsci.2003.12.008.

[34] B.N. Nguyen, M.A. Khaleel, A mechanistic approach to damage in short-fiber composites based on micromechanical and continuum damage mechanics descriptions, Compos. Sci. Technol. 64 (2004) 607–617. doi:10.1016/S0266-3538(03)00293-8.

[35] X. Peng, C. Meyer, A continuum damage mechanics model for concrete reinforced with randomly distributed short fibers, Comput. Struct. 78 (2000) 505–515.

[36] R. Hameed, A. Sellier, A. Turatsinze, F. Duprat, Metallic fiber-reinforced concrete behaviour: Experiments and constitutive law for finite element modeling, Eng. Fract. Mech. 103 (2013) 124–131. doi:10.1016/j.engfracmech.2012.11.022.

[37] A. Diambra, E. Ibraim, A. Russell, D. Muir Wood, Modelling the undrained response of fibre reinforced sands, Soils Found. 51 (2011) 625–636. http://cat.inist.fr/?aModele=afficheN&cpsidt=24723480.

[38] A. Diambra, E. Ibraim, A.R. Russell, D. Muir Wood, Fibre reinforced sands: from experiments to modelling and beyond, Int. J. Numer. Anal. Methods Geomech. 37 (2013) 2427–2455. doi:10.1002/nag.

[39] A. Diambra, E. Ibraim, A.R. Russell, D. Muir Wood, Fibre reinforced sands: From experiments to modelling and beyond, Geotext. Geomembranes. 28 (2010) 238–250. doi:10.1002/nag.2142.

[40] V.F. Pasa Dutra, S. Maghous, A. Campos Filho, A homogenization approach to macroscopic strength criterion of steel fiber reinforced concrete, Cem. Concr. Res. 44 (2013) 34–45. doi:10.1016/j.cemconres.2012.10.009.

[41] A. Beghini, Z.P. Bažant, Y. Zhou, O. Gouirand, F.C. Caner, Microplane model M5f for multiaxial behavior and fracture of fiber-reinforced concrete, J. Eng. Mech. 133 (2007) 66–75. doi:10.1061/(asce)0733-9399(2007)133:1(66).

[42] F.C. Caner, Z.P. Bažant, R. Wendner, Microplane model M7f for fiber reinforced concrete, Eng. Fract. Mech. 105 (2013) 41–57. doi:10.1016/j.engfracmech.2013.03.029.

[43] I.C. Mihai, A.D. Jefferson, P. Lyons, A plastic-damage constitutive model for the finite element analysis of fibre reinforced concrete, Eng. Fract. Mech. 159 (2016) 35–62. doi:10.1016/j.engfracmech.2015.12.035.

[44] I.C. Mihai, A.D. Jefferson, A micromechanics based constitutive model for fibre reinforced cementitious composites, Int. J. Solids Struct. 110-111 (2017) 152–169. doi:10.1016/j.ijsolstr.2017.01.032.

[45] B. Budiansky, R.J. O'connell, Elastic moduli of a cracked solid, Int. J. Solids Struct. 12 (1976) 81–97. doi:10.1016/0020-7683(76)90044-5.

[46] Z.P. Bažant, B.H. Oh, Crack band theory of concrete, Mater. Struct. 16 (1983) 155–177. doi:10.1007/BF02486267.

[47] V.C. Li, Y. Wang, S. Backer, A micromechanical model of tension- softening and bridging toughening of short random fiber reinforced brittle, J. Mech. Phys. Solids. 39 (1991) 607–625.

[48] Z. Lin, V.C. Li, Crack bridging in fiber reinforced cementitious composites with slip-hardening interfaces, J. Mech. Phys. Solids. 45 (1997) 763–787.

[49] J.M. Alwan, A.E. Naaman, P. Guerrero, Effect of mechanical clamping on the pull-out response of hooked steel fibers embedded in cementitious matrices, Concr. Sci. Eng. 1 (1999) 15–25. http://rilem.net/gene/main.php?base=600026&id_publication=391&id_papier=7278.

[50] L.A. Le, G.D. Nguyen, H.H. Bui, A.H. Sheikh, A. Kotousove, A thermodynamics-based double-scale approach to modelling localised failure of geomaterials, Internaltional J. Eng. Sci. 133 (2018) 284–310.

[51] V.S. Gopalaratnam, S.P. Shah, Tensile failure of steel fiber-reinforced mortar, J. Eng. Mech. 113 (1987) 635–652. doi:10.1061/(ASCE)0733-9399(1987)113:5(635).

[52] K. Wille, S. El-Tawil, A.E. Naaman, Properties of strain hardening ultra high performance fiber reinforced concrete (UHP-FRC) under direct tensile loading, Cem. Concr. Compos. 48 (2014) 53–66. doi:10.1016/j.cemconcomp.2013.12.015.

[53] V.C. Li, W. Hwai-Chung, M. Mohamed, M. Dhanada, Tensile behaviour of cement-based composite with random discontinuous steel fibers, J. Am. Ceram. Soc. 79 (1996) 74–78.

[54] V.C. Li, S. Wang, C. Wu, Tensile strain-hardening behaviour of Polyvinyl Alcohol Engineered Cementitious Composites (PVA-ECC), ACI Mater. J. (2001) 483–492. doi:10.14359/10851.

[55] S.H. Park, D.J. Kim, G.S. Ryu, K.T. Koh, Tensile behavior of ultra high performance hybrid fiber reinforced concrete, Cem. Concr. Compos. 34 (2012) 172–184. doi:10.1016/j.cemconcomp.2011.09.009.

[56] K. Wille, D.J. Kim, A.E. Naaman, Strain-hardening UHP-FRC with low fiber contents, Mater. Struct. Constr. 44 (2011) 583–598. doi:10.1617/s11527-010-9650-4.

[57] K. Sirijaroonchai, S. El-Tawil, G. Parra-Montesinos, Behavior of high performance fiber reinforced cement composites under multi-axial compressive loading, Cem. Concr. Compos. 32 (2010) 62–72. doi:10.1016/j.cemconcomp.2009.09.003.

[58] M.K. Neilsen, H.L. Schreyer, Bifurcations in elastic-plastic materials, Int. J. Solids Struct. 30 (1993) 521–544. doi:https://doi.org/10.1016/0020-7683(93)90185-A.

[59] R. Hill, Elastic properties of reinforced solids: Some theoretical principles, J. Mech. Phys. Solids. 11 (1963) 357–372. doi:10.1016/0022-5096(63)90036-X.

[60] L.A. Le, G.D. Nguyen, H.H. Bui, A.H. Sheikh, A. Kotousove, A. Khanna, Modelling jointed rock mass as

a continuum with an embedded cohesive- frictional model, Eng. Geol. 228 (2017) 107–120.

[61] Y. Fujita, R. Ishimaru, S. Hanai, Y. Suenga, Study on Internal Friction Angle and Tensile Strength, Proc. Fram. (1998) 325–334.

[62] F. Laranjeira, C. Molins, A. Aguado, Predicting the pullout response of inclined hooked steel fibers, Cem. Concr. Res. 40 (2010) 1471–1487. doi:10.1016/j.cemconres.2010.05.005.

[63] S. Abdallah, M. Fan, D.W.A. Rees, Analysis and modelling of mechanical anchorage of 4D/5D hooked end steel fibres, Mater. Des. 112 (2016) 539–552. doi:10.1016/j.matdes.2016.09.107.

[64] V.M.C.F. Cunha, J.A.O. Barros, J.M. Sena-Cruz, Pullout Behavior of Steel Fibers in Self-Compacting Concrete, J. Mater. Civ. Eng. 22 (2010) 1–9. doi:10.1061/(ASCE)MT.1943-5533.0000001.

[65] H. Stang, S.P. Shah, Failure of fibre-reinforced composites by pull-out fracture, J. Mater. Sci. 21 (1986) 953–957. doi:10.1007/BF01117378.

[66] A.E. Naaman, G.G. Namur, J.M. Alwan, H.S. Najm, Fiber Pullout and Bond Slip. I: Analytical Study, J. Struct. Eng. 117 (1992) 2769–2790. doi:doi:10.1061/(ASCE)0733-9445(1991)117:9(2791).

[67] C. Lu, C.K.Y. Leung, Theoretical evaluation of fiber orientation and its effects on mechanical properties in Engineered Cementitious Composites (ECC) with various thicknesses, Cem. Concr. Res. 95 (2017) 240–246. doi:10.1016/j.cemconres.2017.02.024.

[68] S.H. Park, D.J. Kim, G.S. Ryu, K.T. Koh, Tensile behavior of ultra high performance hybrid fiber reinforced concrete, Cem. Concr. Compos. 34 (2012) 172–184. doi:10.1016/j.cemconcomp.2011.09.009.

[69] I. Paegle, G. Fischer, Phenomenological interpretation of the shear behavior of reinforced Engineered Cementitious Composite beams, Cem. Concr. Compos. 73 (2016) 213–225. doi:10.1016/j.cemconcomp.2016.07.018.

[70] D. V Soulioti, N.M. Barkoula, A. Paipetis, T.E. Matikas, Effects of fibre geometry and volume fraction on the flexural behaviour of steel-fibre reinforced concrete, Strain. 47 (2011) 535–541. doi:10.1111/j.1475-1305.2009.00652.x.

[71] J. Zhang, X. Ju, Investigation on stress-crack opening relationship of engineered cementitious composites using inverse approach, Cem. Concr. Res. 41 (2011) 903–912. doi:10.1016/j.cemconres.2011.04.010.

[72] P. Tjiptobroto, W. Hansen, Tensile strain hardening and multiple cracking in high-performance cement-based composites containing discontinuous fibers, ACI Mater. J. 90 (1993) 16–25. doi:10.1016/j.actbio.2011.11.020.

[73] X. Wu, S.-M. Han, Multiple cracking model of fiber reinforced high performance cementitious composites under uniaxial tension, Int. J. Concr. Struct. Mater. 3 (2009) 71–77. doi:10.4334/IJCSM.2009.3.1.071.

[74] F. Bencardino, L. Rizzuti, G. Spadea, R.N. Swamy, Experimental evaluation of fiber reinforced concrete fracture properties, Compos. Part B Eng. 41 (2010) 17–24. doi:10.1016/j.compositesb.2009.09.002.

[75] V.C. Li, Y. Wang, S. Backer, Effect of inclining angle, bundling and surface treatment on synthetic fibre pull-out from a cement matrix, Composites. 21 (1990) 132–140. doi:10.1016/0010-4361(90)90005-H.

Appendix D

Capturing localised failure of geomaterials at the constitutive level by embedding a cohesive crack in a continuum modelling approach

Le, L.A., Nguyen, G.D., Bui, H.H., Sheikh, A.H., Kotousov, A., 2018. Capturing localised failure of geomaterials at the constitutive level by embedding a cohesive crack in a continuum modelling approach. *The 3rd Australasian Conference on Computational Mechanics, ACCM 2018,* Geelong February 12-14

Statement of Authorship

Title of Paper	Capturing localised failure of geomaterials at the constitutive level by embedding a cohesive crack in a continuum modelling approach
Publication Status	☑ Published ☐ Accepted for Publication ☐ Submitted for Publication ☐ Unpublished and Unsubmitted w ork w ritten in manuscript style
Publication Details	Le, L.A., Nguyen, G.D., Bui, H.H., Sheikh, A.H., Kotousov, A., 2018. Capturing localised failure of geomaterials at the constitutive level by embedding a cohesive crack in a continuum modelling approach. The 3rd Australasian Conference on Computational Mechanics, ACCM 2018, Geelong February 12-14.

Principal Author

Name of Principal Author (Candidate)	Linh A. Le		
Contribution to the Paper	Developed the model. Implemented the model, performed numerical analysis and model validation. Wrote and revised the manuscript.		
Overall percentage (%)	70		
Certification:	This paper reports on original research I conducted during the period of my Higher Degree by Research candidature and is not subject to any obligations or contractual agreements with a third party that would constrain its inclusion in this thesis. I am the primary author of this paper.		
Signature		Date	26/03/2019

Co-Author Contributions

By signing the Statement of Authorship, each author certifies that:

i. the candidate's stated contribution to the publication is accurate (as detailed above);

ii. permission is granted for the candidate in include the publication in the thesis; and

iii. the sum of all co-author contributions is equal to 100% less the candidate's stated contribution.

Name of Co-Author	Giang D. Nguyen		
Contribution to the Paper	Developed the general framework for the double-scale model and generic form of the cohesive-frictional model. Supervised the technical developments. Evaluated & revised the manuscript.		
Signature		Date	27 / 03 / 2019

Name of Co-Author	Ha H. Bui		
Contribution to the Paper	Developed the generic form of the cohesive-frictional model & contributed to the development of the double-scale approach in generic form. Supervised the technical developments. Evaluated & revised the manuscript.		
Signature		Date	27 / 03 / 2019

Name of Co-Author	Abdul Hamid Sheikh		
Contribution to the Paper	Supervised the technical developments. Evaluated & revised the manuscript.		
Signature		Date	28/03/2019

Name of Co-Author	Andrei Kotousov		
Contribution to the Paper	Supervised the technical developments. Evaluated & revised the manuscript.		
Signature		Date	27/03/2019

Capturing localised failure of geomaterials at the constitutive level by embedding a cohesive crack in a continuum modelling approach

Linh Anh Le[1,a], Giang Dinh Nguyen[1,b *], Ha H. Bui[2,c], Abdul H. Sheikh[1,d], Andrei Kotousov[3,e]

[1]School of Civil, Environmental and Mining Engineering, The University of Adelaide, Adelaide, SA 5005, Australia

[2]Department of Civil Engineering, Monash University, Clayton, VIC 3800, Australia

[3]School of Mechanical Engineering, The University of Adelaide, Adelaide, SA 5005, Australia

[a]linh.a.le@adelaide.edu.au, [b]g.nguyen@adelaide.edu.au, [c]ha.bui@monash.edu, [d]abdul.sheikh@adelaide.edu.au, [e]andrei.kotousov@adelaide.edu.au

Keywords: Geomaterials, localised failure, cohesive crack, double-scale approach

Abstract. The accumulation of localised failure in the form of cracks is well-known as the main failure mechanism of geomaterials such as rock and concrete. The mechanical behaviours of the material are hence governed by the mixed-mode behaviour of the crack and its interaction with the surrounding intact bulk material. In this study, a new constitutive model is developed for modelling geomaterials by incorporating a new damage-plasticity cohesive crack model into a continuum-based approach that possesses connections between different spatial scales. The interaction between the inelastic crack and the bulk material is described by a set of kinematic and internal equilibrium conditions across the crack interfaces. As the behaviour of the localised crack, along with its orientation and relative size, is incorporated in the constitutive relation, key features of the material behaviour including softening, yield locus and size effect can be naturally captured without requiring any enhancement or regularisation. The validation of the model against experimental results shows that the proposed constitutive model is capable of capturing key characteristics of localised failure under different loading conditions.

1. Introduction

Geomaterials such as soft rock, sandstone or concrete have been playing a very important role in the construction industry for centuries. Their localised failure mechanisms, however, have not always been thoroughly understood and/or adequately addressed in continuum constitutive modelling. It is well-known that the accumulation of damage/failure in the form of localised cracks is the primary failure mechanism in most loading cases [1,2]. The behaviour of the crack is usually driven by the aggregate interlocking and cohesion of two crack faces while the surrounding intact material usually undergoes elastic deformation. The energy is thus mainly dissipated via irreversible displacements and damage evolution within the cracking zone during the loading process. As a result, the inelastic behaviour of the material is primarily governed by the responses of the crack.

Existing constitutive models are not found to address the abovementioned fundamental localised failure mechanisms satisfactorily. For instance, in classical continuum models such as damage or damage-plasticity models, the stress and strain are considered to be homogenous over the entire representative volume element used for deriving the constitutive model without incorporating any mechanism to reflect the contribution of the localised crack. As a result, the macroscopic anisotropy of the structural behaviour has to be captured by means of the finite element (FE) approximation within the resolution of the adopted mesh [3], which can cause mesh-dependent issues. Although treatments using smeared crack approach [4–6] has some advantages over the classical continuum models as they produce mesh-independent dissipations, this regularisation effect is a result of scaling the fracture properties with the discretisation size to meet the requirement of energy dissipation. This scaling of the fracture energy can cause an inadmissible snap back instability when the discretisation size is not small enough [7,8]. The underlying reason behind this problem is the lack of a correct representation of the localised failure mechanism at the material (constitutive) level.

The paper thus presents a constitutive model that features intrinsic mechanisms of localised failure, so that essential features of the material responses in both pre-peak and post-peak regimes can be automatically captured with a continuum approach without requiring any ad hoc regularisation. In order to do this, the behaviour of the localised crack will be incorporated in the proposed model following the double-scale approach [7,9] to get the overall stress-strain relation. A set of kinematic parameters and internal equilibrium conditions across the crack interface are used to describe the interaction between the localisation zone and the surrounding material. The damage-plasticity responses of the crack is modelled by our newly proposed cohesive crack model [10] while the surrounding material is assumed to be elastic. Because the localisation and its responses are included in the model, the anisotropy, discontinuity and its orientation automatically appear within a continuum modelling approach. Numerical examples are then performed to illustrate the predictive capability and features of the model. Other important aspects and applications of the model are further investigated in our recent work [11].

2. The proposed model for geomaterial

In this work, the double-scale approach [7,9] is employed to feature the behaviour of localised crack in the overall stress-strain response of the material while the localised responses are simulated by our recently developed cohesive model [10]. The general concept and formulations of these two model are thus presented in this section. More details on the model formulation can be found in [10, 11], and some applications in modelling soil cracking and rock fracture with the Smoothed Particle Hydrodynamics in [12–14].

The double-scale approach. The key idea of the double-scale approach is to link the behaviour of the localised crack to the overall continuum relation by using a set of kinematic strain enhancement parameters and work conservation condition. The constitutive model is constructed for a material volume Ω comprising of an inner localised crack Ω_i and an outer bulk material of volume Ω_o as shown in Fig. 1. As shown in the figure, the inner cracking zone $\Omega_i = \Gamma_i h$ is represented by its area Γ_i and thickness h which is very small compared to its areas ($h \to 0$ for the case of geomaterial cracking). The normal vector of the localised surface is denoted as $\mathbf{n}$. The stress and strain vectors of the outer bulk material are denoted in Voigt notations as $\boldsymbol{\sigma}_o$ and $\boldsymbol{\varepsilon}_o$ while the volume-averaged overall stress and strain vectors of this volume element are $\boldsymbol{\sigma}$ and $\boldsymbol{\varepsilon}$, respectively.

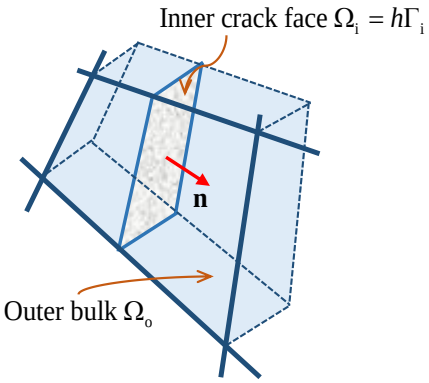

Fig. 1 Illustration of a volume element Ω with a localised crack Ω_i (after [10])

In order to link the behaviour of the localised crack with the overall stress-strain relation, the strain rate of the crack can be expressed in terms of the strain rate of the surrounding bulk and an enhanced strain rate component [15,16] as:

$$\dot{\boldsymbol{\varepsilon}}_i = \dot{\boldsymbol{\varepsilon}}_o + \frac{1}{h}\mathbf{n}\dot{\mathbf{u}} \approx \frac{1}{h}\mathbf{n}\dot{\mathbf{u}} \tag{1}$$

where $\dot{\mathbf{u}}$ is the rate of relative displacements between two sides of the localisation in the global coordinate system. The first term $\boldsymbol{\varepsilon}_o$ in this equation is ignored because it is very small compared to the second term since $h \to 0$. Using Eq. (1) and the rule of mixtures, the relationship between localised crack strain and overall/total strain is obtained as:

$$\dot{\boldsymbol{\varepsilon}} = \eta\dot{\boldsymbol{\varepsilon}}_{\mathrm{i}} + (1-\eta)\dot{\boldsymbol{\varepsilon}}_{\mathrm{o}} = \dot{\boldsymbol{\varepsilon}}_{\mathrm{o}} + \frac{1}{H}\mathbf{n}\dot{\mathbf{u}} \tag{2}$$

where $\eta = {}^{\Omega_{\mathrm{i}}}/_{\Omega} = {}^{h}/_{H}$ is the volume fraction of the localisation zone within the volume element and $H = {}^{\Omega}/_{\Gamma_{\mathrm{i}}}$ is the characteristic length of the localised band, representing the relative size of the band compared to the whole volume element. Thanks to the presence of this characteristic length, the length scale would be naturally captured by the model, as will be shown later. By using the Hill-Mandel condition [17] for the conservation of work, the traction continuity at the localised crack surface can be obtained as $\boldsymbol{\sigma}^T\,\mathbf{n} = \mathbf{t}$, where $\mathbf{t}$ is the traction acting on the localised crack. Given the relationship between the rates of this traction and the relative displacement in the general form $\dot{\mathbf{t}} = \mathbf{K}^t\dot{\mathbf{u}}$, where $\mathbf{K}^t$ is the tangent stiffness of the cohesive model, the constitutive relation can be obtained as [10]:

$$\dot{\boldsymbol{\sigma}} = \mathbf{a}_0\left[\dot{\boldsymbol{\varepsilon}} - \frac{1}{H}\mathbf{n}\dot{\mathbf{u}}\right] \text{ and } \dot{\mathbf{u}} = \left[\frac{1}{H}\mathbf{n}^T\mathbf{a}_0\mathbf{n} + \mathbf{K}^{\mathbf{t}}\right]^{-1}\mathbf{n}^T\mathbf{a}_0\dot{\boldsymbol{\varepsilon}} \tag{3}$$

As seen in the above formulations, both contributions of the localised crack and the surrounding bulk material are included in a continuum model through a set of kinematic parameters and internal equilibrium conditions across the boundaries of the cracks. This helps incorporate the orientations, relative sizes and mechanical responses of the localised band into the overall behaviour of the material naturally without any regularisation. Further details on other aspects such as the stress return algorithm can be found in [10,11].

The cohesive crack model. To capture the behaviour of the crack, our recently developed cohesive crack model [10], is employed. The model is based on the damage-plasticity framework with a unified yield-failure surface which evolves gradually corresponding to the damage accumulation. This framework along with the unified yield-failure surface provides a simple but versatile model with enough generality for applications not only in concrete/rock fracture but also in rock joint failure [10]. This model can be cast in a thermodynamically consistent formulation, but this is not addressed here for the sake of simplicity. The readers can refer to our recent works [18,19] on thermodynamically consistent cohesive models if interested. For the cohesive crack, it is known that the aggregate interlocking and cohesion between of two sides of the localised crack govern the behaviour of the localisation during the loading process. In this sense, the localised crack can be considered as a cohesive zone, albeit partially damaged as illustrated in Fig. 2a, and still maintain its load bearing capability by transferring stresses across the zone.

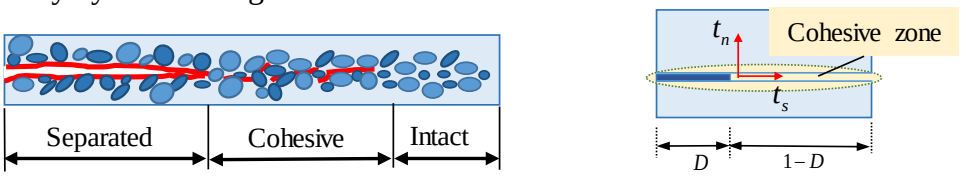

(a) (b)

Fig. 2 Illustration of cohesive zone (a) and its conceptual model (b)

The conceptual model for the cohesive zone, as illustrated in Fig. 2b, is comprised of two parts: damaged part represented by the damage variable D (i.e. $0 \le D \le 1$) and undamaged part represented by $(1-D)$. The traction acting on two faces in the local coordinate system is denoted as $\mathbf{t_c}$. The relative displacement of the two crack faces is denoted as $\mathbf{u}_c$ which is decomposed in the elastic part $\mathbf{u}_c^e$ and irreversible plastic part $\mathbf{u}_c^p$: $\mathbf{u}_c = \mathbf{u}_c^e + \mathbf{u}_c^p$. The traction-separation relation is described as:

$$\mathbf{t}_c = \begin{bmatrix} t_n \\ t_{s1} \\ t_{s2} \end{bmatrix} = \begin{bmatrix} 1-DH(t_n) & 0 & 0 \\ 0 & 1-D & 0 \\ 0 & 0 & 1-D \end{bmatrix} \begin{bmatrix} K_n & 0 & 0 \\ 0 & K_s & 0 \\ 0 & 0 & K_s \end{bmatrix} \begin{bmatrix} u_n - u_n^p \\ u_{s1} - u_{s1}^p \\ u_{s2} - u_{s2}^p \end{bmatrix} = \mathbf{HK}\left(\mathbf{u}_c - \mathbf{u}_c^p\right) \quad (4)$$

where K_n, K_s are cohesive elastic stiffness corresponding to normal and shear cases, respectively; $H(t_n)$ is the Heaviside function with respect to t_n. The inclusion of the Heaviside function indicates that the damaged part is assumed to affect the normal traction in tension case only. The presence of damage and irreversible displacements in this relation allows the model to capture the loading as well as unloading path during the modelling.

A yield surface, used to identify whether the cohesive zone is under elastic or plastic deformation, is defined as [10]:

$$y = (t_{s1}^2 + t_{s2}^2) - [(1-D)\mu_0^2 + D\mu^2][t_n - (1-D)f_t]^2 + mf_c(1-D)[t_n - (1-D)f_t] \quad (5)$$

in which f_t is the tensile strength; f_c is the compressive strength of the material; m, μ and μ_0 are the parameters controlling the shape of the initial and final yield surface. As can be seen from the formulation, the inclusion of damage in the yield criterion helps the yield surface evolve gradually as damage develops during the loading process. This unified form of loading function helps the model translate from the initial yield to the final failure smoothly. The corresponding potential function is defined by modifying the yield function as:

$$g = \tan\gamma(t_{s1}^2 + t_{s2}^2) - [(1-D)\mu_0^2 + D\mu^2][t_n - (1-D)f_t]^2 + mf_c(1-D)[t_n - (1-D)f_t] \quad (6)$$

where γ is the parameter controlling the non-associated flow rules which are stated as:

$$\dot{u}_n^p = \dot{\lambda}\frac{\partial g}{\partial t_n};\ \ \dot{u}_{s1}^p = \dot{\lambda}\frac{\partial g}{\partial t_{s1}};\ \ \dot{u}_{s2}^p = \dot{\lambda}\frac{\partial g}{\partial t_{s2}} \quad (7)$$

The damage evolution is then defined as:

$$D = 1 - e^{-u_p};\ \dot{u}_p = \sqrt{\left(\frac{\alpha\dot{u}_n^p}{\delta_0}\right)^2 + \left(\frac{\beta\dot{u}_{s1}^p}{\delta_0}\right)^2 + \left(\frac{\beta\dot{u}_{s2}^p}{\delta_0}\right)^2} \quad (8)$$

where u_p is the so-called normalised plastic factor; α and β are parameters controlling the contribution of normal and shear plastic displacements during the damage evolution; δ_0 is the critical displacement measured in a tension test at its peak stress. It is noted that the parameters α and β are highly connected with mode I and mode II fracture energy G_I and G_{II} as shown in our work [11].

According to the cohesive model formulation, the tangent stiffness matrix appeared in the traction-separation relationship $\dot{\mathbf{t}} = \mathbf{K}^t\dot{\mathbf{u}}$ can be readily obtained as shown by Le et al. [10]. The cohesive model is then implemented into the double-scale approach via Eq. (3) to obtain a complete continuum constitutive model.

3. Model validation

The capability of the proposed model is illustrated through two examples: biaxial test of rectangular specimens and bending test of a notched beam. The material used in both tests is concrete. The material properties and model parameters used for each example are presented in Table 1. The critical displacement $\delta_0 = 0.014$ mm for both examples is adopted from the tension test by Shi et al. [20].

Table 1 Material properties and model parameters

Parameter	Material properties							Model parameters					
	E GPa	ν	f_c MPa	f_t MPa	K_n	K_s	G_I N/mm	μ	μ_0	m	α	β	γ
Example 1	29.5	0.17	39	3.82	10^8	10^8	7	1.1	0.8	0.35	0.76	0.01	2.7
Example 2	48.4	0.2	80	2.5	10^8	10^8	5.2	0.6	0.7	0.8	0.72	0.005	3.2

Biaxial test on concrete. In this section, the validation of the model is carried out using results obtained from the biaxial test conducted by Sang-Keun et al. [21] on concrete specimens from a standard Korean nuclear containment building. The specimens, with the dimension 200×200×60 mm, were tested under different biaxial loading conditions. For this validation, the characteristic length H used in the model will be calculated during the simulation once the localised crack appears by $H = {\Omega}/{\Gamma_i} = {L}/{\cos\alpha}$, where L is the specimen height and α is the crack orientation as illustrated in Fig.3.

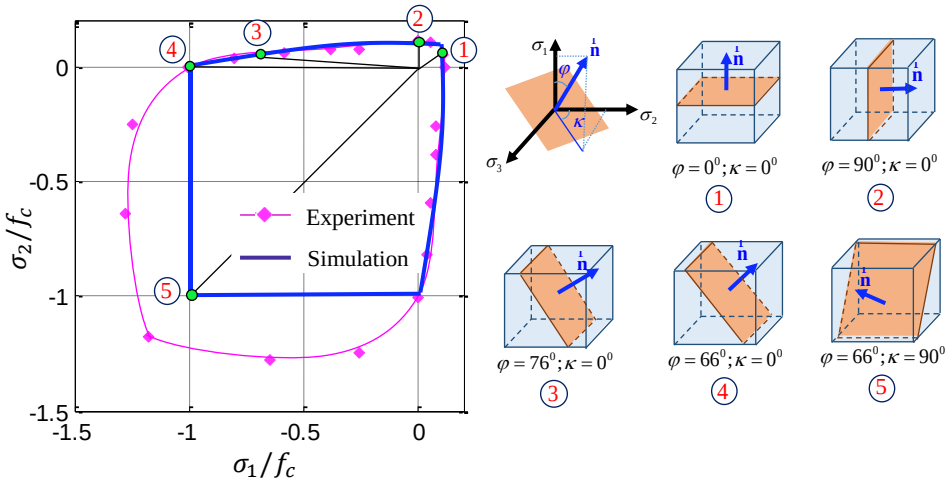

Fig. 3 Yield locus and corresponding localised failure of concrete specimens under biaxial loading

Fig.3 shows the yield locus produced by the model in comparison with that obtained from the experiment. It is seen that the prediction of yielding by the model agrees well with those obtained from the experiment in tension/tension quadrant and tension/compression quadrants. Moreover, each predicted yield state is accompanied by a crack orientation. In tension/tension regime (eg. case 1 and 2 in Fig.3), the mechanism of localised failure is the excess of stress compared to tensile strength. The localisation orientation thus depends on the maximum principal stress direction as illustrated in Fig.3. On the other hand, in the tension/compression regime (eg. case 3 and 4 in Fig.3), the failure mechanism gradually becomes shear under compression along a shear band. Thanks to the inclusion of a crack in the constitutive model, the proposed model could capture such transition naturally along with the intrinsic mechanism. However, in the compression/compression regime, there is a significant difference between results predicted by the model and that by the experiment. Even though the overall shape and failure mechanism could be fairly captured by the model, the yield locus predicted by the model is much smaller than that from the experiment. We believe that the discrepancies are due to the difference between the behaviour at structural scale and "material scale" (or constitutive behaviour). In particular, the prediction of initial yield/failure by the constitutive model is independent of size and based on the assumption of homogeneous stress. On the other hand, the experimental study used a rectangular specimen with one dimension much smaller than the other two. There is inhomogeneous stress distribution prior to yielding/failure that leads to failure patterns different from that predicted using the assumption homogeneous stress. This problem could be overcome by a 3D finite element simulation consisting of multiple elements to model the exact dimensions of the specimen and to some extent material inhomogeneity, instead of using a single element for extracting the results as in the present case. We, however, acknowledge this discrepancy and will address it in future work.

The stress-strain curves for some typical loading paths are plotted in Fig. 4 to illustrate the post-peak behaviour predicted by the model. In these loading cases, the stress component σ_2 is kept as constant while the strain component ε_1 is applied gradually to simulate biaxial compression or tension tests. The third stress/strain component is taken as zero in all cases. It can be seen that the post-peak behaviour of the material is sharply softening in tension case. After reaching the peak stress (tensile strength), the stress quickly drops and become asymptotic to zero as expected. In biaxial compression, the post-peak behaviour is still softening in both tension/compression and compression/compression regime. The same phenomenon can be observed from similar experiments for comparable materials [22–24]. This illustrates the predictive capability of the model when featuring the localised failure mechanism in the constitutive model.

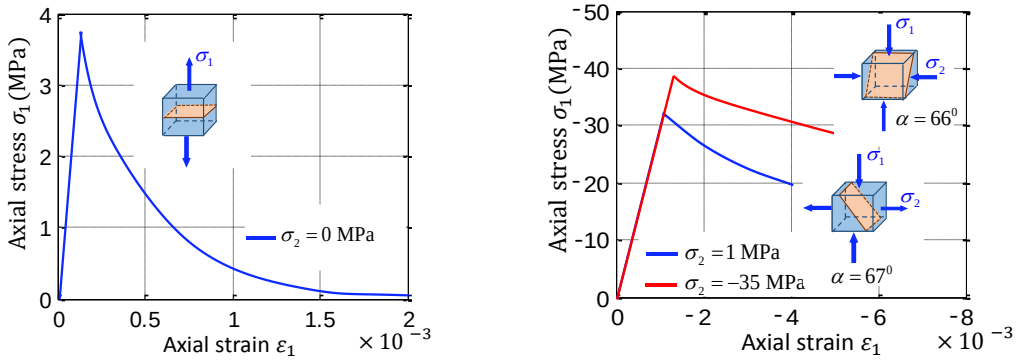

Fig. 4 Numerical results for biaxial test: (a) in tension and (b) in biaxial compression

The scale effect in the model is now investigated by performing unconfined uniaxial compression test ($\sigma_2 = \sigma_3 = 0$ MPa) taking different values of the specimen size L. Fig. 5 shows the variation of the post peak behaviour for different spatial scales. It is seen that the bigger the specimen is, the more brittle the material becomes. This is because when the specimen size increases, followed by an increase of the characteristic length H, the contribution of the localised crack decreases as seen from Eq. (2). As a result, at the same stress state, a smaller specimen would have larger strain values compared to a bigger specimen, meaning that the smaller specimen produces less energy dissipation comparing to that of the larger one. The behaviour thus becomes more brittle with increasing size. Thanks to the inclusion of the localised crack with its relative size in the constitutive model, the length scale is naturally captured without requiring any ad hoc regularisation.

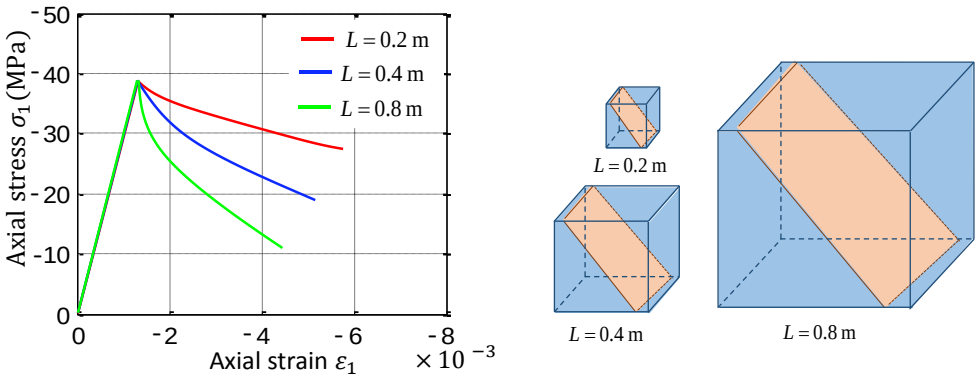

Fig. 5 Illustration of the scale effect produced by the proposed model

Three-point bending test of a notched beam. The proposed model is then implemented into a commercially available FE package (ABAQUS) as a user-defined material model (UMAT) to simulate the three-point bending test which was conducted by Bencardio et al. [25]. The notched beam as shown in Fig. 6a is modelled taking the dimensions L = 500mm, c = 25mm, D = 150mm , b = 150mm , a_0 = 25mm, and the notch width w = 2mm. Two different meshes, a coarse mesh (931 elements) and a fine mesh (3324 elements) as shown in Fig. 6b, are used for the simulation to investigate the convergence of results with respect to mesh size. For the FE simulation, the

characteristic length for each material point (Gauss point) is taken as the square root of area (A) of an element i.e. $H = \sqrt{A}$.

The results obtained from the numerical simulation are presented in the form of load-deflection curves in Fig. 7a along with that obtained from the experiment to illustrate the predictive capability of the model. It is seen that the predicted results agree well with the experiment results. Three distinct stages are recorded during the loading: linear elastic response up to P_1; hardening behaviour until the peak load P_2; and finally, softening until the beam is considered to be failed. It can also be observed that the results from the two meshes are very close to each other, which indicates that the proposed constitutive model with an embedded length scale naturally leads to mesh independent solutions. Thanks to the including the length scale H in the constitutive model, the model could capture the contribution change of the localised failure to the overall stress-strain response when element size changes. This helps the model obtain the scale effect in numerical simulation naturally without having to resort to any additional regularisation. The crack pattern predicted by the model is also shown in Fig. 7b. As observed in the experiment, the numerical results have shown that a major crack is initiated from the notch and propagates toward the top surface of the beam during the loading process. This again illustrates the effectiveness of the model for the analysis of the localised failure in geomaterials.

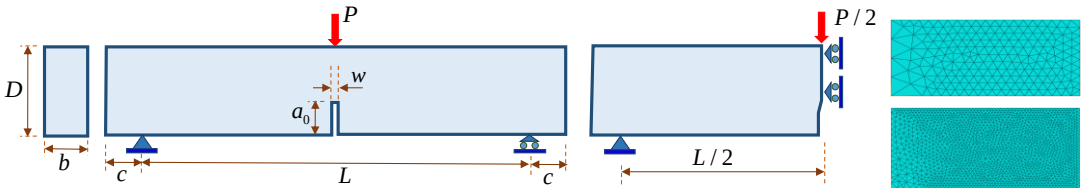

(a) (b)

Fig. 6 (a) Experiment set-ups and half beam model used for simulation; (b) two FE meshes used in numerical simulation

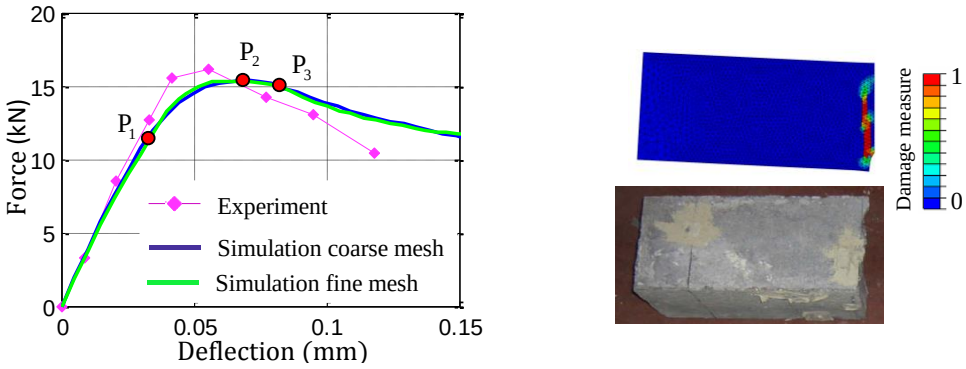

(a) (b)

Fig. 7 Results for three-point bending test: (a) force-displacement curve and (b) failure pattern

4. Conclusion

The paper presents a continuum model to analyse the localised failure of geomaterials by incorporating the contribution of the localised band into the overall constitutive relationship within a double-scale modelling approach. The cohesive crack model with a unified yield surface is used to capture the damage-plasticity behaviour of the localised band. The intrinsic localised failure mechanism is thus incorporated to capture the key features of the material response in its post-peak regime. The numerical results illustrate that the model is able to model the softening responses, scale effect and localised failure surface naturally at both constitutive and structural levels. This highlights the robustness of the proposed approach in modelling failure of geomaterials and also its potentials for predicting cracking in both structural mechanics and geomechanics.

Acknowledgements

Giang D. Nguyen and Ha H. Bui gratefully acknowledge support from the Australian Research Council via Discovery Projects FT140100408 & DP140100945 (Nguyen), DP160100775 (Bui), and DP170103793 (Nguyen & Bui).

References

[1] B. Paliwal, K.T. Ramesh, An interacting micro-crack damage model for failure of brittle materials under compression, Journal of the Mechanics and Physics of Solids. 56 (2008) 896–923. doi:10.1016/j.jmps.2007.06.012.
[2] H.L. Schreyer, Modelling surface orientation and stress at failure of concrete and geological materials, International Journal For Numerical and Analytical Methods in Geomechanics. 31 (2007) 147–171. doi:10.1002/nag.
[3] M. Cervera, M. Chiumenti, Smeared crack approach: Back to the original track, International Journal for Numerical and Analytical Methods in Geomechanics. 30 (2006) 1173–1199. doi:10.1002/nag.518.
[4] Z.P. Bažant, B.H. Oh, Crack band theory of concrete, Materials and Structures. 16 (1983) 155–177. doi:10.1007/BF02486267.
[5] A. Hillerborg, M. Modéer, P.E. Petersson, Analysis of crack formation and crack growth in concrete by means of fracture mechanics and finite elements, Cement and Concrete Research. 6 (1976) 773–781. doi:10.1016/0008-8846(76)90007-7.
[6] Y.R. Rashid, Ultimate strength analysis of prestressed concrete pressure vessels, Nuclear Engineering and Design. 7 (1968) 334–344. doi:10.1016/0029-5493(68)90066-6.
[7] G.D. Nguyen, I. Einav, A.M. Korsunsky, How to connect two scales of behaviour in constitutive modelling of geomaterials, Géotechnique Letters. 2 (2012) 129–134. doi:10.1680/geolett.12.00030.
[8] M. Jirasek, Particale model for quasibrittle fracture and application to sea ice, Journal of Engineering Mechanics. 121 (1995) 1016–1025.
[9] G.D. Nguyen, A.M. Korsunsky, I. Einav, A constitutive modelling framework featuring two scales of behaviour : Fundamentals and applications to quasi-brittle failure, Engineering Fracture Mechanics. 115 (2013). doi:10.1016/j.engfracmech.2013.11.006.
[10] L.A. Le, G.D. Nguyen, H.H. Bui, A.H. Sheikh, A. Kotousove, A. Khanna, Modelling jointed rock mass as a continuum with an embedded cohesive- frictional model, Engineering Geology. 228 (2017) 107–120.
[11] L.A. Le, G.D. Nguyen, H.H. Bui, A.H. Sheikh, A. Kotousove, A thermodynamics-based double-scale approach to modelling localised failure of geomaterials, In Preparation. (n.d.).
[12] H.T. Tran, H.H. Bui, G.D. Nguyen, J. Kodikara, A Continuum Based Approach to Modelling Tensile Cracks in Soils, in: Sixth Biot Conference on Poromechanics, Paris, France, 2017: pp. 337–344.
[13] Y. Wang, H.H. Bui, G.D. Nguyen, P.G. Ranjith, A Mesh-Free Continuum Based Computational Approach to Modelling Rock Fracture, in: Sixth Biot Conference on Poromechanics, Paris, France, 2017: pp. 2041–2048.
[14] Y. Wang, H.H. Bui, G.D. Nguyen, R.P. Gamage, Numerical Simulation of Size Effect on Rock Fracture using SPH and a Size-dependent Constitutive Model, in: 9th Australasian Congress on Applied Mechanics, Sydney, Australia, 2017.
[15] D. Kolymbas, Kinematics of shear bands, Acta Geotechnica. 4 (2009) 315–318. doi:10.1007/s11440-009-0092-5.
[16] I. Vardoulakis, M. Goldscheider, G. Gudehus, Formation of shear bands in sand bodies as a bifurcation problem, International Journal for Numerical and Analytical Methods in Geomechanics. 2 (1978) 99–128. doi:10.1002/nag.1610020203.
[17] R. Hill, Elastic properties of reinforced solids: Some theoretical principles, Journal of the Mechanics and Physics of Solids. 11 (1963) 357–372. doi:10.1016/0022-5096(63)90036-X.
[18] N.H.T. Nguyen, H.H. Bui, G.D. Nguyen, J. Kodikara, S. Arooran, P. Jitsangiam, A thermodynamics-based cohesive model for discrete element modelling of fracture in cemented materials, International Journal of Solids and Structures. 117 (2017) 159–176. doi:10.1016/j.ijsolstr.2017.03.027.
[19] G.D. Nguyen, H.H. Bui, The Roles and Effects of Friction in Cohesive Zone Modelling: A Thermodynamics-Based Formulation, in: 4th Congrès International de Géotechnique - Ouvrages -Structures. CIGOS, Lecture Notes in Civil Engineering, vol 8. Springer, Singapore, 2017: pp. 288–296.
[20] C. Shi, A.G. Van Dam, J.G.M. Van Mier, B. Sluys, Crack interaction in concrete, in: F.H. Wittmann (Ed.), Material for Building and Structures, Wiley-VCH, Winheim, German, 2000: pp. 125–31.
[21] S.K. Lee, Y.C. Song, S.H. Han, Biaxial behavior of plain concrete of nuclear containment building, Nuclear Engineering and Design. 227 (2004) 143–153. doi:10.1016/j.nucengdes.2003.09.001.
[22] H. Kupfer, H.K. Hilsdorf, H. Rusch, Behavior of concrete under biaxial stress, ACI Structural Journal. 66 (1969) 656–666. doi:10.14359/7388.
[23] I. Imran, S.J. Pantazopoulou, Experimental Study of plain concrete under triaxial stress, ACI Material Journal. 93 (1997) 589–601.
[24] E. Klein, T. Reuschlé, A model for the mechanical behaviour of bentheim sandstone in the brittle regime, Pure and Applied Geophysics. 160 (2003) 833–849. doi:10.1007/PL00012568.
[25] F. Bencardino, L. Rizzuti, G. Spadea, R.N. Swamy, Experimental evaluation of fiber reinforced concrete fracture properties, Composites Part B: Engineering. 41 (2010) 17–24.

Appendix E

Localisation and lode-angle dependence of geomaterial behaviour

Le, L.A., Nguyen, G.D., Bui, H.H., Sheikh, A.H., Kotousov, A., 2018. Localisation and lode-angle dependence of geomaterial behaviour. *The 25th Australasian Conference on Mechanics of Structures and Materials, ACMSM25*, Brisbane, Australia, December 4 – 7

Statement of Authorship

Title of Paper	Localisation and lode-angle dependence of geomaterial behaviour
Publication Status	☑ Published ☐ Accepted for Publication ☐ Submitted for Publication ☐ Unpublished and Unsubmitted w ork w ritten in manuscript style
Publication Details	Le, L.A., Nguyen, G.D., Bui, H.H., Sheikh, A.H., Kotousov, A., 2018. Localisation and lode-angle dependence of geomaterial behaviour. 25th Australasian Conference on Mechanics of Structures and Materials, ACMSM25, Brisbane, Australia, December 4 – 7.

Principal Author

Name of Principal Author (Candidate)	Linh A. Le		
Contribution to the Paper	Developed the model. Implemented the mode, performed numerical analysis and model validation. Wrote and revised the manuscript.		
Overall percentage (%)	70		
Certification:	This paper reports on original research I conducted during the period of my Higher Degree by Research candidature and is not subject to any obligations or contractual agreements with a third party that would constrain its inclusion in this thesis. I am the primary author of this paper.		
Signature		Date	26/03/2019

Co-Author Contributions

By signing the Statement of Authorship, each author certifies that:

i. the candidate's stated contribution to the publication is accurate (as detailed above);

ii. permission is granted for the candidate in include the publication in the thesis; and

iii. the sum of all co-author contributions is equal to 100% less the candidate's stated contribution.

Name of Co-Author	Giang D. Nguyen		
Contribution to the Paper	Developed the general framework for the double-scale approach and generic form of the cohesive-frictional model. Supervised the technical developments. Evaluated & revised the manuscript.		
Signature		Date	27 / 03 / 2019

Name of Co-Author	Ha H. Bui		
Contribution to the Paper	Developed the generic form of the cohesive-frictional model & contributed to the development of the double-scale approach in generic form. Supervised the technical developments. Evaluated & revised the manuscript.		
Signature		Date	27 / 03 / 2019

Name of Co-Author	Abdul Hamid Sheikh		
Contribution to the Paper	Supervised the technical developments. Evaluated & revised the manuscript.		
Signature		Date	28/03/2019

Name of Co-Author	Andrei Kotousov		
Contribution to the Paper	Supervised the technical developments. Evaluated & revised the manuscript.		
Signature		Date	27/03/2019

25th Australasian Conference on Mechanics of Structures and Materials (ACMSM25)
Edited by C.M. Wang, J.C.M. Ho and S. Kitipornchai
Brisbane, Australia, December 4 – 7, 2018

LOCALISATION AND LODE-ANGLE DEPENDENCE OF GEOMATERIAL BEHAVIOUR

L.A. LE[1], G.D. NGUYEN[1,*], H.H. BUI[2], A.H. SHEIKH[1], A. KOTOUSOV[3]

[1]School of Civil, Environmental and Mining Engineering, The University of Adelaide, SA 5005, Australia

[2]Department of Civil Engineering, Monash University, Clayton, VIC 3800, Australia

[3]School of Mechanical Engineering, The University of Adelaide, SA 5005, Australia

Emails: linh.a.le@adelaide.edu.au, g.nguyen@adelaide.edu.au, ha.bui@monash.edu, abdul.sheikh@adelaide.edu.au, andrei.kotousov@adelaide.edu.au

*Corresponding author

Abstract. *True triaxial test results of geomaterials have shown a strong dependence of the material responses on the third invariant of the deviatoric stress (or alternatively Lode angle). In constitutive modelling, this dependence is usually captured by incorporating different forms of the Lode angle (i.e. Lode angle parameter, third invariant of deviatoric stress) into the macroscopic yield function phenomenologically. In this paper, the mechanism of localised failure is analysed and identified as the underlying cause of the Lode angle dependence, from which a constitutive model is developed. The model includes an additional kinematic field with its own set of governing relationships to account for the high deformation gradient across the boundary of the localisation band. Since the mechanism of localised failure and its initiation, governed by true triaxial stress states, are included, the Lode-angle dependent behaviour is naturally captured without requiring any phenomenological relationships. In this short correspondence, the key characteristics of the proposed approach are outlined together with its preliminary results validated against experimental data.*

Keywords: Localised failure, Lode-angle dependence, Geomaterial

1. INTRODUCTION

Geomaterials such as soft rock, sandstone or concrete have been serving as basic materials in the construction industry for centuries. The accumulation of damage in the form of localisation bands is well-known as the main failure mechanism of the material in most loading conditions (Paliwal and Ramesh, 2008; Schreyer, 2007). However, its link with Lode-angle dependence of the yield locus, observed in experiments (Ingraham et al., 2013; Ma and Haimson, 2016; Vachaparampil and Ghassemi, 2017), has not been adequately addressed in the literature. Most of the existing models focus on reproducing this dependence by adding a Lode angle parameter, θ, or related parameters (i.e. third invariant of deviatoric stress J_3) into the macroscopic yield function (Chemenda and Mas, 2016; Liolios and Exadaktylos, 2017; Lü et al., 2016; Paliwal et al., 2017). Although giving good predictions, these treatments are of phenomenological nature and do not reflect the links with the failure mechanism.

This paper proposes a new approach to the Lode-angle dependence of the yield surface by considering the localisation failure mechanism as a foundation for the constitutive model. In

particular, the behaviour of the localisation band is incorporated into the model following the double-scale approach (Nguyen et al., 2014, 2012) that employs a set of kinematic enhancements and an internal equilibrium condition across the interfaces of the band. The behaviour of the localisation band, including its yielding, is governed by a cohesive-frictional model (Le et al., 2017, 2018). Because the localisation and its responses are incorporated explicitly in the model, the dependence of the yield locus on the Lode angle is captured naturally. In this paper, key concepts and preliminary results are briefly outlined to demonstrate the potential of the proposed approach. Further details on other important aspects and applications of the model can be found in our recent work (Le et al., 2017, 2018).

2. FAILURE MECHANISM AND LODE-ANGLE DEPENDENT YIELD LOCUS

Some early triaxial compression tests on cylindrical specimens (Ansari and Li, 1998; Ingraham et al., 2013; Lade, 1997; Xu and Geng, 1985) as well as recent true triaxial tests on cubic specimens (Ma and Haimson, 2016; Macari and Hoyos Jr, 2001; Vachaparampil and Ghassemi, 2017) conducted on sandstone, concrete and soil show that the yield surface is highly dependent on the Lode-angle θ, defined by $\cos 3\theta = J_3/2(3/J_2)^{3/2}$. The yield loci and stress-strain responses together with localisation failure patterns from tests conducted on Castlegate sandstone in Figure 1 can be considered as typical behaviour of geomaterials in true triaxial compression. It is seen that for different Lode angle values, the material yields at different deviatoric stress levels: the yielding in axisymmetric extension $\theta = -30^0$ (i.e. $\sigma_1 = \sigma_2 > \sigma_3$) falls below that in pure shear $\theta = 0^0$ and axisymmetric compression $\theta = 30^0$ (i.e. $\sigma_1 > \sigma_2 = \sigma_3$). This phenomenon is clearly observed at low confining stress where yield loci have triangle-like shapes. At such stress levels, the material responses are usually brittle and the failure plane appear to have a high inclination (see Figure 1b). With the increase of confining stress, the dependence of the yield surface on the Lode angle becomes less dominant. This can be seen in the yield locus, becoming more rotationally symmetrical and almost circular at high confining stress (see Figure 1a). During this transition, the material responses change from brittle to more ductile, while the angle of inclination of the failure plane reduces gradually, and disappears at relatively high stress levels (see Figure 1b, where NA indicates no clear band observed).

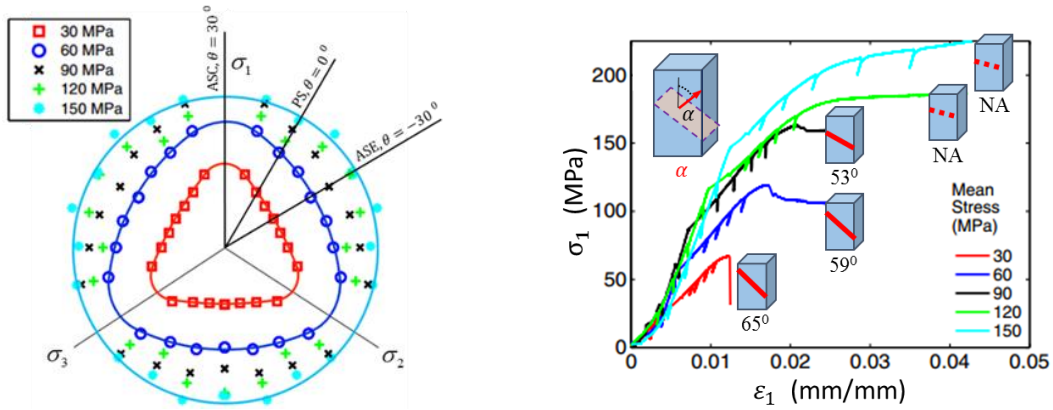

Figure 1. Experimental observations of Castlegate sandstone (after Ingraham et al., 2013): (a) Yield loci at different confining stress levels and (b) Stress-strain & failure pattern for $\theta = 0^0$

From the above test results, it is seen that the Lode-angle dependence of the yield surface is closely related to the failure mechanism of the material. This dependence should be interpreted as one of the consequences of the failure mechanism. In particular, at low confining stress, along with highly inclined failure planes, shear band is the mechanism responsible for the

material failure (Ma and Haimson, 2016; Wong and Baud, 2012). The stress acting on this shear band is closely linked with the true triaxial stress conditions, represented by the stress invariants I_1, J_2 and J_3. Because the shear stress component is dominant in controlling the behaviour of the shear band, for different values of the invariants J_2, J_3 and consequently the Lode angle θ, the material responses would change significantly. The change of the yield surface with respect to different Lode angle values thus comes naturally as a result of shear band failure mechanism. As the confining stress increases, the failure plane becomes less inclined and the failure mechanism changes from localised shear band to diffuse compaction (with no clear localisation bands), in conjunction with the brittle – ductile transition (Ma and Haimson, 2016; Wong and Baud, 2012). As a result, the influence of shear stress on the material yielding/failure decreases. This explains why the yield locus gradually becomes less dependent on the Lode angle during this transition as shown in Figure 1a. Based on this analysis, the dependence of the yield surface on the Lode angle can be considered as an indirect consequence of the failure mechanism and closely links with the localised failure band orientation.

In order to capture the Lode-angle dependence during the modelling, the localisation and its underlying mechanisms should be considered and adequately included in the model. This inclusion not only helps capture the Lode-angle dependence naturally but also serves as a basis to obtain other intrinsic features of geomaterial failure.

3. EMBEDDING FAILURE MECHANISM IN A MODEL

3.1. Incorporating localisation band in continuum models

In order to include the localised failure into the model, the constitutive relation is derived using a material representative volume element (RVE) Ω having an inner localisation band Ω_i and an outer elastic bulk material Ω_o as shown in Figure 2a. The inner localisation zone Ω_i is represented by its area Γ_i and thickness h as $\Omega_i = \Gamma_i h$. The normal vector of the localisation band is denoted as $\mathbf{n}$. The stress and strain vectors of the outer bulk material are denoted as $\boldsymbol{\sigma}_o$ and $\boldsymbol{\varepsilon}_o$ while $\boldsymbol{\sigma}_i$ and $\boldsymbol{\varepsilon}_i$ stand for the stress and strain vectors of the inner localisation zone. The volume-averaged overall stress and strain vectors of the element are expressed by $\boldsymbol{\sigma}$ and $\boldsymbol{\varepsilon}$. The key idea of the double-scale approach is to link the size and responses of the localisation band to the overall continuum behaviour by using a set of kinematic strain enhancements and the balance of virtual work.

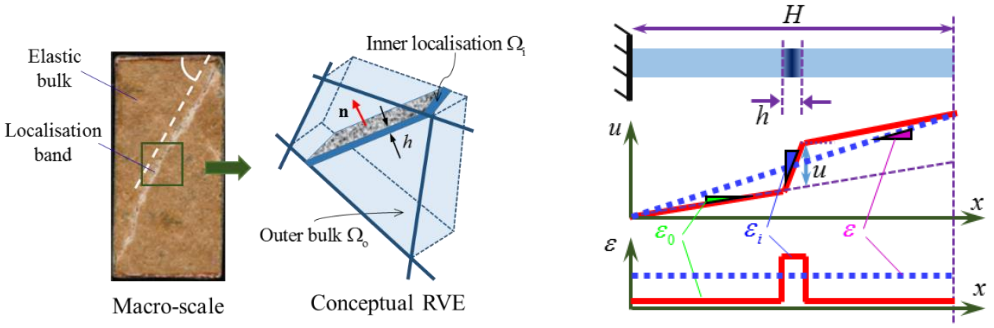

(a) (b)

Figure 2. The conceptual model based on failure mechanism at mesoscale (a) and 1D illustration of kinematic enhancement across the localisation band (b)

Following earlier work (Kolymbas, 2009; Neilsen and Schreyer, 1993), the strain rate of the localisation band can be expressed by:

$$\dot{\boldsymbol{\varepsilon}}_{\mathrm{i}} = \dot{\boldsymbol{\varepsilon}}_{\mathrm{o}} + \frac{1}{h}\mathbf{n}\dot{\mathbf{u}} \tag{1}$$

where $\dot{\mathbf{u}}$ is the rate of relative displacements between two sides of the localisation band in the global coordinate system. It can be seen from the above equation that the high strain rate in the localisation band consists of a homogeneous term representing the strain rate of the outer bulk material, and an enhancement term involving the relative displacement rate across two sides of the band. Assuming homogeneous behaviour inside and outside the band, the overall strain rate of the RVE can be approximated using the rule of mixtures in association with Eq. (1) as:

$$\dot{\boldsymbol{\varepsilon}} = \eta\dot{\boldsymbol{\varepsilon}}_{\mathrm{i}} + (1-\eta)\dot{\boldsymbol{\varepsilon}}_{\mathrm{o}} = \dot{\boldsymbol{\varepsilon}}_{\mathrm{o}} + \frac{1}{H}\mathbf{n}\dot{\mathbf{u}} \tag{2}$$

where $\eta = \Omega_{\mathrm{i}}/\Omega = h/H$ is the volume fraction of the localisation band with respect to the volume element and $H = \Omega/\Gamma_{\mathrm{i}}$ represents the relative size of the band compared to the volume element. This kinematic enhancement is illustrated in Figure 2b for 1D case where the inhomogeneous deformation over the element is illustrated by the red solid line and the averaged macro strain is presented by the dotted blue line. It can be seen that even though the overall strain appears to be constant over the region, it actually comprises of deformations from both the localisation band and the outer bulk material. This helps take the contribution of the localisation band into account naturally. In addition, the summation of virtual work done by the localisation band and its surrounding bulk material should be equal to the work done by the macro stress and virtual strain rate:

$$\boldsymbol{\sigma}^T\delta\boldsymbol{\varepsilon} = \eta\boldsymbol{\sigma}_{\mathrm{i}}^T\delta\boldsymbol{\varepsilon}_{\mathbf{i}} + (1-\eta)\boldsymbol{\sigma}_{\mathrm{o}}^T\delta\boldsymbol{\varepsilon}_{\mathbf{o}} \tag{3}$$

where $\delta\boldsymbol{\varepsilon}$, $\delta\boldsymbol{\varepsilon}_{\mathbf{i}}$ and $\delta\boldsymbol{\varepsilon}_{\mathbf{o}}$ are, respectively, the virtual strain increment of the RVE, inner localisation band and outer bulk material, respectively. By substituting Eq. (1)-(2) into (3), one obtains:

$$(\boldsymbol{\sigma}^T - \boldsymbol{\sigma}_{\mathrm{o}}^T)\delta\boldsymbol{\varepsilon}_{\mathbf{o}} + \frac{1}{H}(\boldsymbol{\sigma}^T\mathbf{n} - \boldsymbol{\sigma}_{\mathrm{i}}^T\mathbf{n})\delta\mathbf{u} + \eta\boldsymbol{\sigma}_{\mathrm{o}}^T\delta\boldsymbol{\varepsilon}_{\mathbf{o}} - \eta\boldsymbol{\sigma}_{\mathrm{i}}^T\delta\boldsymbol{\varepsilon}_{\mathbf{o}} = 0 \tag{4}$$

where $\delta\mathbf{u}$ is the virtual displacement increment across the localisation. In the paper, because the localisation band is idealised as a zero thickness region, e.g. $h \to 0$ (and consequently $\eta \to 0$), the last two terms in Eq. (4) can be neglected as they are much smaller than the other components. In order to satisfy Eq. (4) for arbitrary values of virtual strain rate $\delta\boldsymbol{\varepsilon}_{\mathbf{o}}$ and virtual velocity jump $\delta\mathbf{u}$, the following conditions have to be satisfied: i) the overall stress of the volume element coincides with the stress of the outer bulk material $\boldsymbol{\sigma} = \boldsymbol{\sigma}_o$ and ii) the traction continuity condition at the localisation surface is written as $\boldsymbol{\sigma}^T\mathbf{n} = \boldsymbol{\sigma}_{\mathrm{i}}^T\mathbf{n} = \mathbf{t}$, where $\mathbf{t}$ is the traction acting on the localisation band.

The relationship between the traction $\mathbf{t}$ and the relative displacement (separation) $\mathbf{u}$ in the localisation band can be written in a generalised rate form as $\dot{\mathbf{t}} = \mathbf{K}^t\dot{\mathbf{u}}$ where $\mathbf{K}^t$ is the tangent stiffness of the band. In the paper, this relationship is governed by our newly developed cohesive-frictional model (Le et al., 2017, 2018) based on a damage-plasticity framework. The unified yield-failure surface of this model is written as:

$$y = t_s^2 - [(1-D)\mu_0^2 + D\mu^2][t_n - (1-D)f_t]^2 + mf_c(1-D)[t_n - (1-D)f_t] \tag{5}$$

where $t_s = \sqrt{t_{s1}^2 + t_{s2}^2}$ and t_n are shear and normal tractions acting on the localisation plane in the local coordinate system; t_{s1} and t_{s2} are two components of the shear traction along the two perpendicular axes; f_t is the tensile strength of the material; f_c is its compressive strength; D is damage variable ($0 \le D \le 1$); m, μ and μ_0 are the parameters controlling the shape of the initial yield and final failure surfaces. As can be seen from the above formulation, the inclusion

of damage parameter in the yield-failure surface helps it evolve from initial yield to final failure smoothly when the damage in the localisation band develops (see Le et al., 2017). As the focus of this study is the material yielding associated with the onset of localisation, only the initial yield surface is needed:

$$y^{\text{ini}} = y(D=0) = t_s^2 - \mu_0^2(t_n - f_t)^2 + mf_c(t_n - f_t) \tag{6}$$

Once the tangent stiffness is established from the cohesive-frictional model, with some mathematic manipulations, the constitutive relationship of the RVE can be derived as (Le et al, 2017 & 2018):

$$\dot{\boldsymbol{\sigma}} = \mathbf{a}_0\left[\dot{\boldsymbol{\varepsilon}} - \frac{1}{H}\mathbf{n}\dot{\mathbf{u}}\right] \text{ and } \dot{\mathbf{u}} = \left[\frac{1}{H}\mathbf{n}^T\mathbf{a}_0\mathbf{n} + \mathbf{K}^{\mathbf{t}}\right]^{-1}\mathbf{n}^T\mathbf{a}_0\dot{\boldsymbol{\varepsilon}} \tag{7}$$

This equation clearly shows that contributions from both the localisation band and the surrounding bulk material are included in the continuum constitutive model. This helps incorporate the localised failure, including its orientation, relative sizes and mechanical responses, into the model. As a result, the dependence of material responses on the localisation band and consequently the Lode angle is captured naturally in the model without adding J_3 or Lode angle parameter in the yield function.

3.2. Localisation band initiation

Because the yielding of the material is controlled by a criterion at the localisation band level, a scheme is needed to determine the onset and orientation of the localisation. In the study, a simple procedure, exploiting the proposed yield surface, is used for this purpose. At a given stress state, all possible orientations are scanned to detect the onset of localisation. The normal traction t_n and shear traction t_s acting on each potential plane are calculated by:

$$t_n = n_i\sigma_{ij}n_j \text{ and } t_s = \sqrt{\left\|\sigma_{ij}n_j\right\| - {t_n}^2} \tag{8}$$

where n_i is the normal vector of the potential plane, and σ_{ij} is the stress state of the material in index notation form. The material yielding is triggered if there exists a traction set (t_n^*, t_s^*) that violates the yield condition in Eq. (6), as:

$$y^{\text{ini}}({t_n}^*, {t_s}^*) = \max_{\forall \boldsymbol{n}}\{y^{\text{ini}}(t_n, t_s)\} \geq 0 \tag{9}$$

The orientation corresponding to this set would be used as the localisation band orientation for the rest of the calculation.

4. MODEL CAPABILITY TO CAPTURE THE LODE-ANGLE DEPENDENCE

4.1. Typical yield surface produced by the proposed approach

In this paper, macroscopic yield surface is produced by applying different loading conditions (i.e. axisymmetric extension, pure shear, axisymmetric compression) to a cubic element (constitutive modelling). For each step of a loading condition, the scheme described in section 3.2 is used to check and record the stress state if the yielding happens. All of these stress states are then plotted in principal stress space to obtain a macroscopic yield surface. A typical yield surface in principal stress space and yield loci in octahedral planes produced by the proposed approach are shown in Figure 3. It shows that the shape of the yield surface (Figure 3a) is similar to that of the Mohr-Coulomb model. However, it can be seen in Figure 3b, when the confining pressure increases from low to high, the yield loci show a transition from highly dependent to less dependent on the Lode-angle. This feature cannot be obtained by the Mohr-

Coulomb model where yield loci have the same shape regardless of confining pressure level for a given set of parameters. In addition, while conventional models such as Mohr-Coulomb or Tresca control the material yielding by macro loading functions, the proposed model uses a smooth yield function based on the traction acting on the localisation plane. As a result, even though the macro yield locus produced by the proposed model is non-smooth, it would not encounter singularity problem during the calculation as experienced in these conventional models. This again highlights the benefit of incorporating localised failure mechanism explicitly in the constitutive model.

Figure 3 shows that the yield surface is open in the compression direction, meaning that the material would never yield if it is loaded along the hydrostatic axis (e.g. $\sigma_1 = \sigma_2 = \sigma_3$). This is due to the open shape of the yield criterion at the localisation band level which indicates that the band would not yield under pure compression. This implies that the model is unable to capture the diffuse compaction failure caused by grain crushing under very high confining pressure as observed in experiments (Ma and Haimson, 2016; Vachaparampil and Ghassemi, 2017; Wong and Baud, 2012). This drawback can be overcome by replacing the yield surface in Eq. (5) by a close-shaped yield function or using inelastic behaviour for the bulk material. This issue will be addressed in our future work.

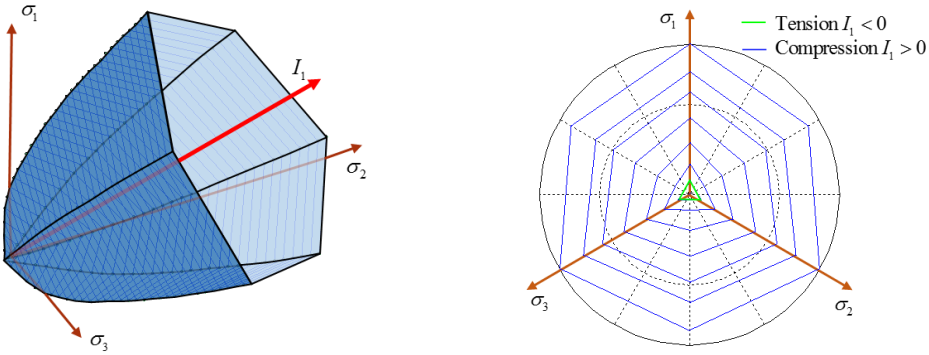

(a) (b)

Figure 3. A typical yield surface produced by the proposed model: (a) yield surface in stress space and (b) yield loci in the octahedral plane at different confining pressure levels.

4.2. Experimental validation

In this section, the yield loci produced by the proposed model is validated against experimental data conducted by Robinson (1985) for Indiana limestone and later interpreted by Aubertin et al. (1999). The material properties are: compression strength $f_c = 28$ MPa and tensile strength $f_t = 4$ MPa and model parameters are taken as $\mu_0 = 0.7$ and $m = 0.28$. The yield surface in the hydrostatic – deviatoric stress space and the octahedral plane, predicted by the model, are presented in Figure 4 along with the experimental data. It can be seen that the yielding predicted by the model agrees well with its experimental counterpart. The Lode-angle dependence of the yield surface is seen clearly in the hydrostatic – deviatoric stress space where yield locus of axisymmetric extension $\theta = -30^0$ falls below that of axisymmetric compression $\theta = 30^0$.

Figure 4 also shows the orientation of the localised failure predicted by the model for $I_1 = 30, 60$ and 90 MPa. The figure shows that when the confining stress increases, the failure plane orientation decreases, which coincides with experimental observations (Ingraham et al., 2013; Klein and Reuschlé, 2003; Ma and Haimson, 2016; Vachaparampil and Ghassemi, 2017). In addition, at the same mean stress level, the orientation of failure plane in axisymmetric

compression is smaller than that in axisymmetric extension, which agrees with experimental observations (Ingraham et al., 2013; Ma and Haimson, 2016). All of these results are naturally produced by the proposed model without adding the third stress invariant (or Lode angle) to the expression of the yield surface. This highlights the benefits of considering the intrinsic failure mechanism at the very beginning step of the model construction.

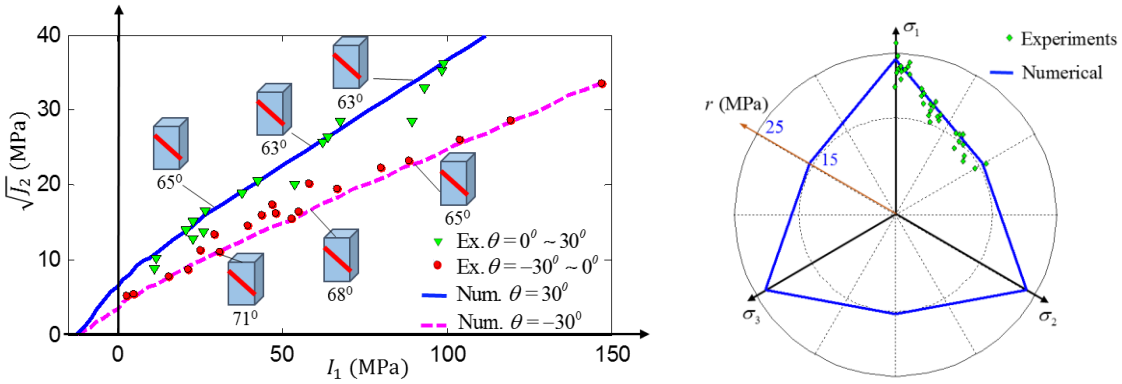

Figure 4. Failure locus in hydrostatic – deviatoric stress space and octahedral plane ($I_1 = 50\ MPa$) against experimental results of Limestone

5. CONCLUSION

The localised failure mechanism is identified as the cause of the Lode-angle dependence and hence used as the basis to develop a constitutive model for geomaterials. In this model, the yielding is activated using a criterion based on stress state of a plane which provides both onset and orientation of the localisation. The results show that macroscopic yield surface constructed by this way naturally features the Lode-angle dependence without requiring the addition of the third stress invariant or Lode angle parameter. Further work is in progress to capture the full mechanical responses with the influence of Lode angle.

Acknowledgements

Giang D. Nguyen and Ha H. Bui gratefully acknowledge support from the Australian Research Council via Discovery Projects FT140100408 & DP140100945 (Nguyen), DP160100775 (Bui), and DP170103793 (Nguyen & Bui).

REFERENCES

Ansari, F., Li, Q., (1998). High-Strength Concrete Subjected to Triaxial Compression. Journal of American Concrete Institute 95, 747–755.

Aubertin, M., Li, L., Simon, R., Khalfi, S., (1999). Formulation and application of a short-term strength criterion for isotropic rocks. Canadian Geotechnical Journal 36, 947–960.

Chemenda, A.I., Mas, D., (2016). Dependence of rock properties on the Lode angle: Experimental data, constitutive model, and bifurcation analysis. Journal of the Mechanics and Physics of Solids 96, 477–496. doi:10.1016/j.jmps.2016.08.004

Ingraham, M.D., Issen, K.A., Holcomb, D.J., (2013). Response of Castlegate sandstone to true triaxial states of stress. Journal of Geophysical Research: Solid Earth 118, 536–552. doi:10.1002/jgrb.50084

Klein, E., Reuschlé, T., (2003). A model for the mechanical behaviour of bentheim sandstone in the brittle regime. Pure and Applied Geophysics 160, 833–849.

doi:10.1007/PL00012568

Kolymbas, D., (2009). Kinematics of shear bands. Acta Geotechnica 4, 315–318. doi:10.1007/s11440-009-0092-5

Lade, P. V, (1997). Modelling the strength of engineering materials in three dimensions. Mechanics of Cohesive-Frictional Materials 2, 339–356.

Le, L.A., Nguyen, G.D., Bui, H.H., Sheikh, A.H., Kotousov, A., Khanna, A., (2017). Modelling jointed rock mass as a continuum with an embedded cohesive-frictional model. Engineering Geology 228, 107–120. doi:10.1016/j.enggeo.2017.07.011

Le, L.A., Nguyen, G.D., Bui, H.H., Sheikh, A.H., Kotousove, A., (2018). A thermodynamics-based double-scale approach to modelling localised failure of geomaterials. In preparation.

Liolios, P., Exadaktylos, G., (2017). Hyperbolic hardening model for quasibrittle materials. International Journal of Solids and Structures 120, 1339–1351. doi:10.1016/j.ijsolstr.2017.05.011

Lü, X., Huang, M., Andrade, J.E., (2016). Strength criterion for cross-anisotropic sand under general stress conditions. Acta Geotechnica 11, 1339–1350. doi:10.1007/s11440-016-0479-z

Ma, X., Haimson, B.C., (2016). Failure characteristics of two porous sandstones subjected to true triaxial testing. Journal of Geophysical Research: Solid Earth 121, 6477–6498. doi:10.1002/2016JB012979

Macari, M., Hoyos Jr, L., (2001). Mechanical Behavior of an Unsaturated Soil Under Multi-Axial Stress States. American Society for Testing and Materials 24, 14–22. doi:10.1520/GTJ11278J

Neilsen, M.K., Schreyer, H.L., (1993). Bifurcations in elastic-plastic materials. International Journal of Solids and Structures 30, 521–544. doi:https://doi.org/10.1016/0020-7683(93)90185-A

Nguyen, G.D., Einav, I., Korsunsky, A.M., (2012). How to connect two scales of behaviour in constitutive modelling of geomaterials. Géotechnique Letters 2, 129–134. doi:10.1680/geolett.12.00030

Nguyen, G.D., Korsunsky, A.M., Einav, I., (2014). A constitutive modelling framework featuring two scales of behaviour : Fundamentals and applications to quasi-brittle failure. Engineering Fracture Mechanics 115, 221–240. doi:10.1016/j.engfracmech.2013.11.006

Paliwal, B., Hammi, Y., Moser, R.D., Horstemeyer, M.F., (2017). A three-invariant cap-plasticity damage model for cementitious materials. International Journal of Solids and Structures 108, 186–202. doi:10.1016/j.ijsolstr.2016.12.015

Paliwal, B., Ramesh, K.T., (2008). An interacting micro-crack damage model for failure of brittle materials under compression. Journal of the Mechanics and Physics of Solids 56, 896–923. doi:10.1016/j.jmps.2007.06.012

Robinson, M.J., (1985). The strength of Indiana limestone under multiaxial loading conditions. MS Thesis, University of Colorado, Boulder, Colo (Taken from Shreyer 1989).

Schreyer, H.L., (2007). Modelling surface orientation and stress at failure of concrete and geological materials. International Journal For Numerical and Analytical Methods in Geomechanics 31, 147–171. doi:10.1002/nag

Vachaparampil, A., Ghassemi, A., (2017). Failure characteristics of three shales under true-triaxial compression. International Journal of Rock Mechanics and Mining Sciences 100, 151–159. doi:10.1016/j.ijrmms.2017.10.018

Wong, T.F., Baud, P., (2012). The brittle-ductile transition in porous rock: A review. Journal of Structural Geology 44, 25–53. doi:10.1016/j.jsg.2012.07.010

Xu, D., Geng, N., (1985). The variation law of rock strength with increase of intermediate principal stress. Acta Mechanica Solida Sinica 7, 72–80.